Green Materials for Electronics

Green Materials for Electronics

Edited by Mihai Irimia-Vladu, Eric D. Glowacki,
Niyazi S. Sariciftci, and Siegfried Bauer

WILEY-VCH

Editors

Dr. Mihai Irimia-Vladu
Joanneum Res. Forschungsgesellschaft mbH
Department of Materials
Franz-Pichler Str. 30
8160 Weiz
Austria

Dr. Eric D. Glowacki
Linköping University
Norrköping campus
Department of Science and Technology
Laboratory of Organic Electronics
Bredgatan 33
Norrköping 60221
Sweden

Prof. Niyazi S. Sariciftci
Johannes Kepler University Linz
Department of Physical Chemistry
Linz Institute for Organic Solar Cells
Altenberger Str. Nr. 69
4040 Linz
Austria

Prof. Siegfried Bauer
Johannes Kepler University Linz
Department of Soft Matter Physics
Altenberger Str. 69
4040 Linz
Austria

Cover
Small image: Reprinted by permission from Macmillan Publishers Ltd: Nature, Heung Cho Ko *et al*. Vol 454 Number 7205, 2008.
Background image: fotolia_134593869.jpg

Library of Congress Card No.: applied for

British Library Cataloguing-in-Publication Data
A catalogue record for this book is available from the British Library.

Bibliographic information published by the Deutsche Nationalbibliothek
The Deutsche Nationalbibliothek lists this publication in the Deutsche Nationalbibliografie; detailed bibliographic data are available on the Internet at <http://dnb.d-nb.de>.

Print ISBN: 978-3-527-33865-8
ePDF ISBN: 978-3-527-69293-4
ePub ISBN: 978-3-527-69296-5
Mobi ISBN: 978-3-527-69294-1
oBook ISBN: 978-3-527-69295-8

Cover Design Adam Design, Weinheim, Germany
Typesetting SPi Global Private Limited, Chennai, India
Printing and Binding

Printed on acid-free paper

10 9 8 7 6 5 4 3 2 1

Contents

List of Contributors

Maria R. Antognazza
Center for Nano Science and Technology
Istituto Italiano di Tecnologia
20133 Milano
Italy

Siegfried Bauer
Johannes Kepler University Linz
Department of Soft Matter Physics
4040 Linz
Austria

Melanie Baumgartner
Johannes Kepler University Linz
Department of Soft Matter Physics
4040 Linz
Austria

and

Johannes Kepler University Linz
Institute of Polymer Science
4040 Linz
Austria

Fabio Benfenati
Center for Synaptic Neuroscience and Technology
Istituto Italiano di Tecnologia
16132 Genoa
Italy

and

University of Genova
Department of Experimental Medicine
16132 Genova
Italy

Magnus Berggren
Linköping University
Department of Science and Technology
Laboratory of Organic Electronics
60174 Norrköping
Sweden

Eloïse Bihar
Ecole Nationale Supérieure des Mines
CMP-EMSE, MOC
Department of Bioelectronics
Gardanne 13541
France

and

MicroVitae Technologies
Hôtel Technologique Europarc Sainte Victoire
Europarc Sainte Victoire
Meyreuil 13590
France

and

Ecole Nationale Supérieure des Mines
CMP-EMSE, MOC
Department of Flexible Electronics
Gardanne 13541
France

Stefania R. Cicco
CNR-ICCOM Bari
Dipartimento di Chimica
4-70126 BARI
Italy

Maria E. Coppola
Joanneum Research
Forschungsgesellschaft mbH
Department of Materials
Weiz 8160
Austria

and

Politecnico di Milano
Department of Chemistry, Materials
and Chemical Engineering
"Giulio Natta"
Piazza Leonardo da Vinci 32
Milano 20133
Italy

Andrea Desii
Center for Nano Science and
Technology
Istituto Italiano di Tecnologia
20133 Milano
Italy

Jessamyn A. Fairfield
National University of Ireland Galway
School of Physics
University Road
Galway
H91 CF50
Ireland

Gianluca M. Farinola
Università degli Studi di Bari
"Aldo Moro"
Dipartimento di Chimica
70126 Bari
Italy

Erik O. Gabrielsson
Linköping University
Department of Science and
Technology
Laboratory of Organic Electronics
60174 Norrköping
Sweden

Eric D. Glowacki
Linköping University
Norrköping campus
Department of Science and
Technology
Laboratory of Organic Electronics
60174 Norrköping
Sweden

Eliot F. Gomez
University of Cincinnati
Department of Electrical Engineering
and Computer Science
Nanoelectronics Laboratory
Cincinnati OH 45221-0030
USA

Suk-Won Hwang
Korea University
KU-KIST Graduate School of
Converging Science and Technology
Seoul 02841
Republic of Korea

Mihai Irimia-Vladu
Joanneum Research
Forschungsgesellschaft mbH
Department of Materials
Weiz 8160
Austria

Dimitrios A. Koutsouras
Ecole Nationale Supérieure des Mines
CMP-EMSE, MOC
Department of Bioelectronics
Gardanne 13541
France

Guglielmo Lanzani
Center for Nano Science and Technology
Istituto Italiano di Tecnologia
20133 Milano
Italy

and

Politecnico di Milano
Dip.to di Fisica
Piazza Leonardo Da Vinci 32
20133 Milano
Italy

Maria Magliulo
Università degli Studi di Bari
"Aldo Moro"
Dipartimento di Chimica
70126 Bari
Italy

George G. Malliaras
Ecole Nationale Supérieure des Mines
CMP-EMSE, MOC
Department of Bioelectronics
Gardanne 13541
France

Kyriaki Manoli
Università degli Studi di Bari
"Aldo Moro"
Dipartimento di Chimica
70126 Bari
Italy

Takeo Miyake
Waseda University
Graduate School of Information Production and System
Kitakyushu
Fukuoka, 808-0135
Japan

Mohammad Yusuf Mulla
Università degli Studi di Bari
"Aldo Moro"
Dipartimento di Chimica
70126 Bari
Italy

Ronald Österbacka
Åbo Akademi University
Center for Functional Materials and Faculty of Science and Engineering
Laboratory of Physics
Turku
Finland

Gerardo Palazzo
Università degli Studi di Bari
"Aldo Moro"
Dipartimento di Chimica
70126 Bari
Italy

Jouko Peltonen
Åbo Akademi University
Center for Functional Materials and Faculty of Science and Engineering
Laboratory of Physical Chemistry
Turku
Finland

Roberta Ragni
Università degli Studi di Bari
"Aldo Moro"
Dipartimento di Chimica
70126 Bari
Italy

John A. Rogers
University of Illinois at Urbana-Champaign
Department of Materials Science and Engineering
Frederick Seitz Materials Research Laboratory
Urbana, IL 61801
USA

Marco Rolandi
University of California
Santa Cruz Department of Electrical Engineering
Santa Cruz
CA 95064
USA

Mohamed Saadaoui
Ecole Nationale Supérieure des Mines
CMP-EMSE, MOC
Department of Flexible Electronics
Gardanne 13541
France

Niyazi S. Sariciftci
Johannes Kepler University Linz
Department of Physical Chemistry
Linz Institute for Organic Solar Cells
4040 Linz
Austria

Preethi Seshadri
Università degli Studi di Bari
"Aldo Moro"
Dipartimento di Chimica
70126 Bari
Italy

Daniel T. Simon
Linköping University
Department of Science and Technology
Laboratory of Organic Electronics
60174 Norrköping
Sweden

Mandeep Singh
Università degli Studi di Bari
"Aldo Moro"
Dipartimento di Chimica
70126 Bari
Italy

Eva-Kathrin Sinner
University of Natural Resources and Life Sciences, BOKU
Department of Nanobiotechnology
Institute of Synthetic Bioarchitectures
1190 Vienna
Austria

Andrew J. Steckl
University of Cincinnati
Department of Electrical Engineering and Computer Science
Nanoelectronics Laboratory
Cincinnati, OH 45221-0030
USA

Cherng-Wen Darren Tan
University of Natural Resources and Life Sciences, BOKU
Department of Nanobiotechnology
Institute of Synthetic Bioarchitectures
1190 Vienna
Austria

Amber Tiwari
Università degli Studi di Bari
"Aldo Moro"
Dipartimento di Chimica
70126 Bari
Italy

Martti Toivakka
Åbo Akademi University
Center for Functional Materials and Faculty of Science and Engineering
Laboratory of Paper Coating and Converting
Turku
Finland

Luisa Torsi
Università degli Studi di Bari
"Aldo Moro"
Dipartimento di Chimica
70126 Bari
Italy

Danilo Vona
Università degli Studi di Bari
"Aldo Moro"
Dipartimento di Chimica
70126 Bari
Italy

Preface

Bioorganic electronics is rapidly growing, motivating the writing of this book as a commentary on the state of the art of the field. We are indebted to all contributors for their excellent chapters, which we hope the reader will find illuminating and informative as this exciting new field develops.

Bioelectronics has been a dream of cybernetics for quite some time. The pioneering work of Peter Fromherz (Max Planck Institute for Biochemistry, Germany) interfacing neurons with silicon circuits dates back several decades. Bioelectronics has been limited to silicon circuits for quite some time. Recently, the expansion of organic electronic devices has opened up a new avenue to realize this dream of interfacing biological systems with electronic circuits.

Organic conducting materials can speak the language of biological systems with their unique properties of hybrid ionic/electronic conduction, combined with electrochemical activity. Organic semiconductors, especially biocompatible semiconductors, display a list of properties important for the interfacing of biological systems with the electronic world. Their biocompatibility, nontoxicity, processability, and increasingly operational stability in aqueous media offer unique benefits inaccessible to their inorganic counterparts.

To make an interface with biosystems, electrical information must be transformed into ionic and protonic signals. Biosystems are often based on ionic charge transport and on signal transduction based on electrochemical systems, as opposed to the electronic world relying on electronic conduction of solid-state materials. In transforming signals from the electronic world to the bioworld, we need materials and systems such as transducers, which sustain electronic as well as ionic conduction. Organic electronic materials offer this possibility also because of their chemical tenability. As several chapters in this book will show, the derivatization of organic semiconductors enables unique electronic device functions. Therefore, we envision that the future of cybernetics might be using more and more organic/bio-organic semiconductors (Figure 1).

On the other hand, we believe it is highly useful to stress the concept of *green* electronics to sustain a sound and healthy environment. We already have today a severe problem with electronic waste in our world. Humanity is currently not able to create a sustainable cycle for the production, use, and end-of-life of electronic gadgets and instruments. Often such products are disposed in ordinary garbage dumps, polluting our environment and wasting highly valuable materials as well (Figure 2).

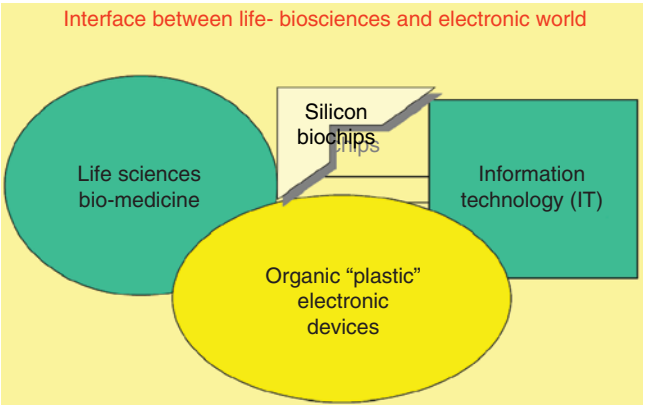

Figure 1 Future cybernetics as an important mission of organic electronics.

Figure 2 A child at an electronic dumping ground in China sits among a pile of wires and e-waste. The e-waste is exported from all over the world to less developed countries, mostly in Asia and Africa, where children often handle e-waste containing many hazardous chemicals. (Image reproduced with permission from Greenpeace International.)

Akio Morita, the founding chairman of SONY once stated:

"We are moving from consumer electronics to consumable electronics."

Upon this premise we clearly see that electronic waste is and will be an increasing problem. By using plastic materials for organic solar cells, organic light-emitting diodes, and so on, we will face a mounting problem of plastic waste, already polluting our oceans. Polyolefins and commodity plastics are often not biodegradable and impose a problem when they end up in the biosphere.

These problems may be mitigated with the use of biodegradable and nontoxic materials. Several chapters in this book cover a creative repurposing of mass-produced materials for *green* electronics, such as paper, DNA, diatomous silica, and various bioresorbable materials. These materials can be tailored to be biodegradable by the end of their life cycle, or to degrade transiently *in vivo* for medical applications.

Such ideas and many more propositions are found in the chapters of this book. Of course the editors do not claim completeness of coverage of this topic with this book; the field is vast and fortunately growing rapidly. We do believe that several core concepts are introduced and these concepts will retain their relevance in future bioelectronic technologies. We sincerely hope that in some years many such books will be available, carrying the flag further in different territories of science. We wish all colleagues embarking on new science in this field the best of luck.

Siegfried Bauer
Eric Daniel Glowacki
Mihai Irimia-Vladu
Niyazi Serdar Sariciftci

1

Emerging "Green" Materials and Technologies for Electronics

Melanie Baumgartner[1,2], Maria E. Coppola[3,4], Niyazi S. Sariciftci[5], Eric D. Glowacki[6], Siegfried Bauer[1], and Mihai Irimia-Vladu[3]

[1] *Johannes Kepler University Linz, Department of Soft Matter Physics, Altenberger Str. Nr. 69, 4040, Linz, Austria*
[2] *Johannes Kepler University Linz, Institute of Polymer Science, Altenberger Str. Nr. 69, 4040, Linz, Austria*
[3] *Joanneum Research Forschungsgesellschaft mbH, Department of Materials, Franz-Pichler Str. Nr. 30, 8160, Weiz, Austria*
[4] *Politecnico di Milano, Department of Chemistry, Materials and Chemical Engineering "Giulio Natta", Piazza Leonardo da Vinci 32, 20133, Milano, Italy*
[5] *Johannes Kepler University Linz, Department of Physical Chemistry, Linz Institute for Organic Solar Cells, Altenberger Str. Nr. 69, 4040 Linz, Austria*
[6] *Linköping University, Norrköping campus, Laboratory of Organic Electronics, Department of Science and Technology, Bredgatan 33, Norrköping 60174, Sweden*

1.1 Introduction to "Green" Materials for Electronics

We are currently witnessing an evolution of technologies blurring the lines between the physical, digital, and biological spheres. Electronics become highly flexible and even mechanically stretchable, with applications ranging from wearable consumer electronics to mobile health, sports, and well-being. The materials aspects of flexible and stretchable electronics is covered in depth by many pioneers in the field, summarizing also the latest developments spanning from stretchable interconnects to the level of highly sophisticated electronic skin [1–5]. A wide class of materials is available in thin film forms, ranging from dielectrics and semiconductors to metals, as well as a cornucopia of industrially relevant processing methods. Initial attempts toward biocompatible electronics paved the way toward epidermal [6] and implantable electronics [7–9]. Sustainable use of material resources is a major concern of our society, challenging research with the ever-growing amount of electronic waste, estimated to be 41.8 million metric tons (Mt) at the end of 2014 and forecasted to reach 50 million Mt by 2018 [10].

Inspiration from nature led to the first approaches to biodegradable forms of electronics, finally culminating in the development of transient electronics that simply degrades after service life [11]. The state of the art in "green" electronics has been summarized in a recent review, covering degradable substrates and materials for encapsulation, as well as dielectrics, semiconductors, and metals for basic electronic circuit elements [12]. In this chapter we will provide a brief overview on "green" materials for degradable circuit boards and organic electronics, including the latest developments in the field. We first summarize

Green Materials for Electronics, First Edition.
Edited by Mihai Irimia-Vladu, Eric D. Glowacki, Niyazi S. Sariciftci, and Siegfried Bauer.

the use of paper, followed by a discussion of natural and nature inspired materials, including DNA and nucleobases; silk; saccharides; Aloe Vera, natural waxes, and gums; cellulose and its derivatives; resins; proteins, peptides, and amino acids; and finally natural and nature-inspired semiconductors for biodegradable and biocompatible electronics. We expect that in the future we will be as comfortable with highly flexible and degradable forms of electronics, embedded everywhere, in textiles, on skin, and even within our body as we are now familiar with smartphones and tablet computers.

1.2 Paper

More than 2000 years ago the Chinese inventive genius brought to light what is to date of incommensurable importance for humanity: paper, a natural-origin and sustainable (renewable and degradable) material. Good tunable physical properties, such as transparency or roughness, make paper desirable for large-area products. Paper wins over other flexible substrate materials owing to its low cost (below 0.1 USD m^{-2}), high flexibility, and the possibility for large-scale roll-to-roll manufacturing with speeds of processing exceeding 25 m s^{-1} [13]. When the cultivation of wood, the basic material for paper, is executed environmentally sustainably and when recycled paper is used in the fabrication process, paper outrivals most candidates for substrates in biodegradable devices. Apart from its classic usages for packaging, information storage, and as support for displays, paper recently developed into a substrate for a wide variety of unconventional electronics. Paper electronics is continuously drawing attention in the scientific community and is highlighted in this book extensively in Chapter 6 by Martti Toivakka *et al.* for a plethora of applications. In the following, we will only briefly present the usage of paper as substrate and dielectric for basic electronic circuits. Martins *et al.* have utilized, for example, both the above-mentioned assets of paper in a low power electronic Complementary Metal-Oxide-Semiconductor (CMOS) inverter circuit layered on a flexible and recyclable fiber-based paper substrate. The paper gate dielectric offers a large capacitance per area at low frequencies because of its fiber-based foam-like structure. Figure 1.1a displays an image of a CMOS inverter on paper, tested under different supply voltages. Figure 1.1b shows the voltage transfer characteristics (*VTC*s) of the inverters, which are used to extract the high and low states, associated with the input and output voltages. Gain and leakage current are extracted from Figure 1.1c [14]. Although the reported results are not impressive in terms of CMOS performance, the use of paper for a dual function of substrate and dielectric is highly promising since it enables layering of various semiconductor structures (dielectrics and semiconductors). The demonstration opens the door for implementing paper for a plethora of applications that can be broadly grouped under the umbrella of "green" electronics (memory elements and integrated systems, smart labels, tags, sensors, and electrochromic paper displays, to name a few).

The rough surface of paper, combined with its high absorbance tendency for various liquids, makes very challenging the processing of solution-based active layers on top of it. Pettersson *et al.* eliminated the problem of semiconductor absorption into the paper substrate by using a mixture containing a semiconductor

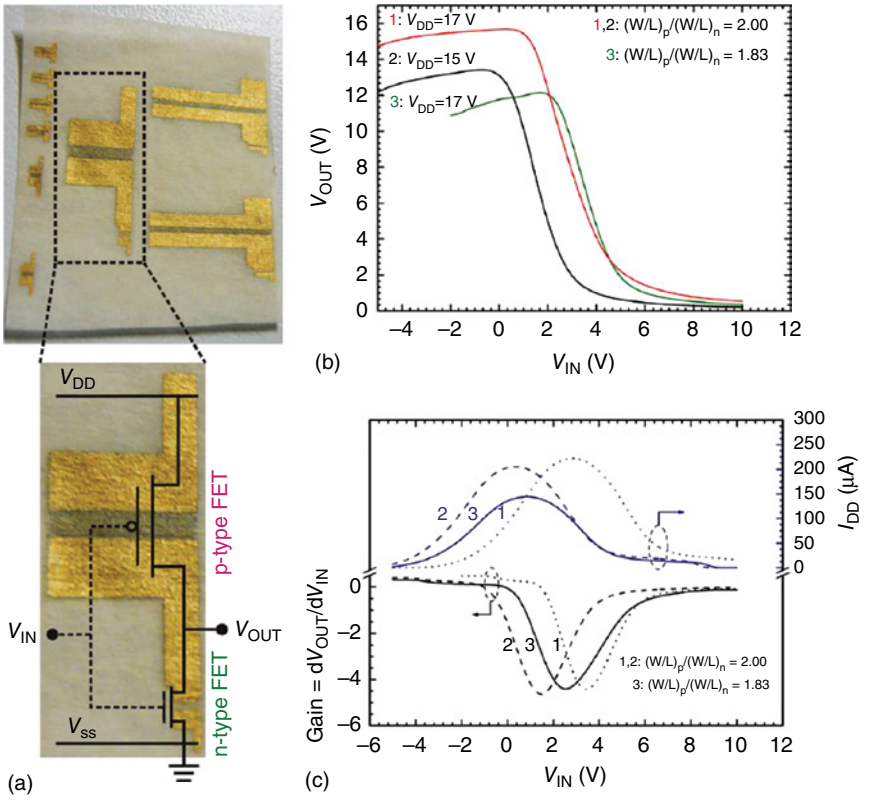

Figure 1.1 The potential of paper for the fabrication of future CMOS architectures: (a) photograph of a low-power electronic CMOS inverter circuit on paper; (b) the voltage transfer characteristics of the CMOS inverters; and (c) the gain, dV_{out}/dV_{in}, and the leakage current, I_{DD}. (Martins *et al*. 2011 [14]. Reproduced with permission of John Wiley and Sons.)

and a biodegradable polymer insulator [15]. In this compound, spontaneous phase separation occurs, and a thin semiconducting layer is formed on top (Figure 1.2Aa). Owing to this preparation step, the sensitive semiconductor was separated from the paper substrate. Importantly, the rough surface of paper does not play an important role anymore, in that it does not transpose its unevenness through the dielectric and to the dielectric–semiconductor interface where the charge transport occurs. Another aspect of utmost importance is the stability of devices fabricated on paper. Pettersson *et al*. examined the bias–stress stability and the shelf life of transistors on paper [16]. These transistors were connected in advanced circuits, including NOR gates and D-latches. Stabilities of up to 3 weeks were observed, currently limiting the usage of such paper electronic devices to short-term applications only. To prove the operation principle, a logic NOR-gate was fabricated with two transistors and one 5.6 MΩ resistor. For NOR gates, a high output (i.e., value of 1) results if both the inputs to the gate are low (i.e., both display a value of 0). Figure 1.2B shows the output of such logic circuit device with a low operating voltage and fast switching of the states, from one state to the other [16].

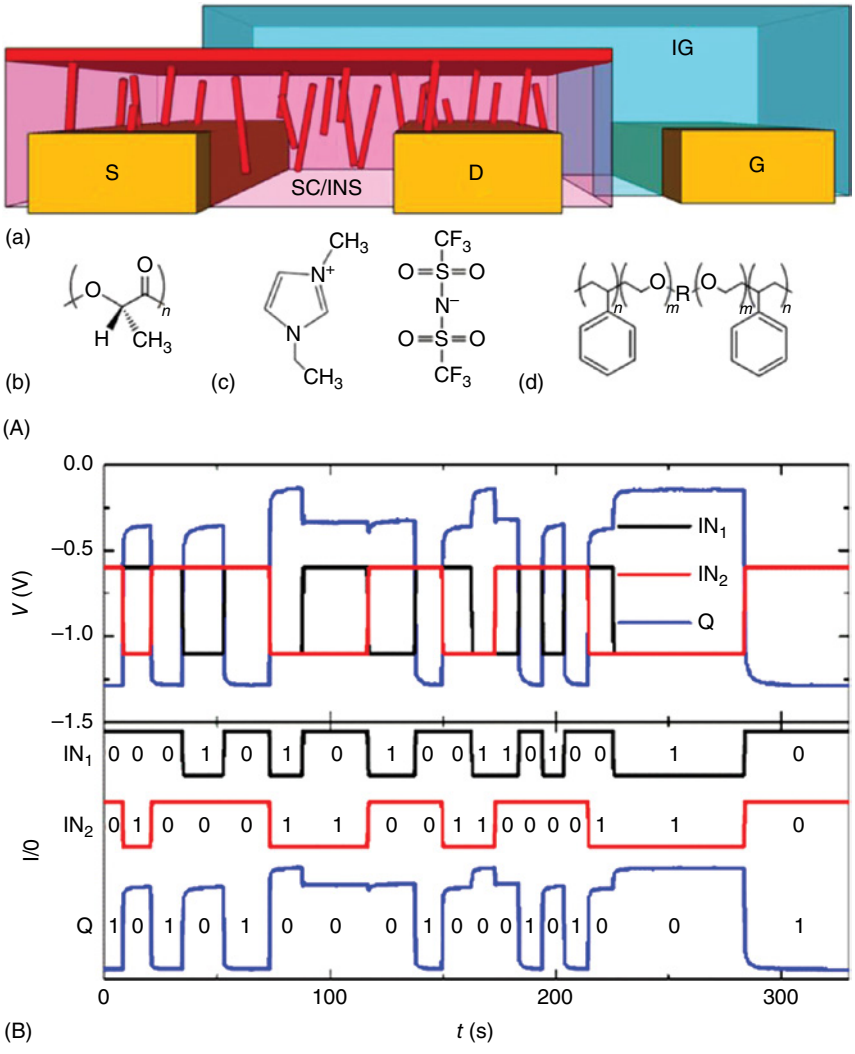

Figure 1.2 (A) (a) Schematic of the OFET structure containing the gate (G), source (S), and drain (D) electrodes, the ion gel (*IG*,) and the self-separating semiconductor insulator blend (SC/INS); (b) the chemical structure of the poly(L-lactic acid) (*PLLA*); (c) the chemical structure of the ion gel used, 1-ethyl-3-methylimidazolium bis(trifluoromethylsulfonyl)imide (EMIM:TFSI); and (d) the chemical structure of the triblock copolymer, PS:PEO:PS (7 wt%), used as a gelling agent for the ion gel. (Pettersson *et al*. 2014 [15]. Reproduced with permission of Cambridge University Press.). (B) Output data of the NOR-gate with a supply voltage, V_{DD}, of −1.3 V. The raw signals are superimposed in the top graph and presented deconvoluted in the bottom graph. (Pettersson *et al*. 2015 [16]. Reproduced with permission of John Wiley and Sons.)

Paper, although a challenging material for device preparation, opens the door to low-cost disposable electronics. Electronic devices fabricated on paper will need also a power supply, and for such purpose paper-based photovoltaics could be a perfect complement. Paper appears to be an ideal support material for photovoltaic cells,

being ~1000 times less expensive than glass and ~100 times less expensive than common plastics. Barr *et al.* demonstrated the potential of unmodified paper for photovoltaics fabrication [17]. The paper photovoltaic arrays reported by the group generated impressive performance: an open circuit voltage approaching 50 V and a current of ~10 μA capable of powering electronic displays under ambient indoor lighting for at least 6000 h of uninterrupted power supply. Moreover, the photovoltaic arrays could be tortuously flexed and folded without loss of function. In 2014 Leonat *et al.* showed that nearly doubling the Power Conversion Efficiency (PCE) (i.e., reaching efficiencies of 4%) compared to the one reported in reference [17] for an individual polymer-based photovoltaic cell on paper is possible [18]. Figure 1.3a displays the component materials used in the fabrication process of the organic solar cell on a double-side coated image printer paper that is displayed in Figure 1.3b.

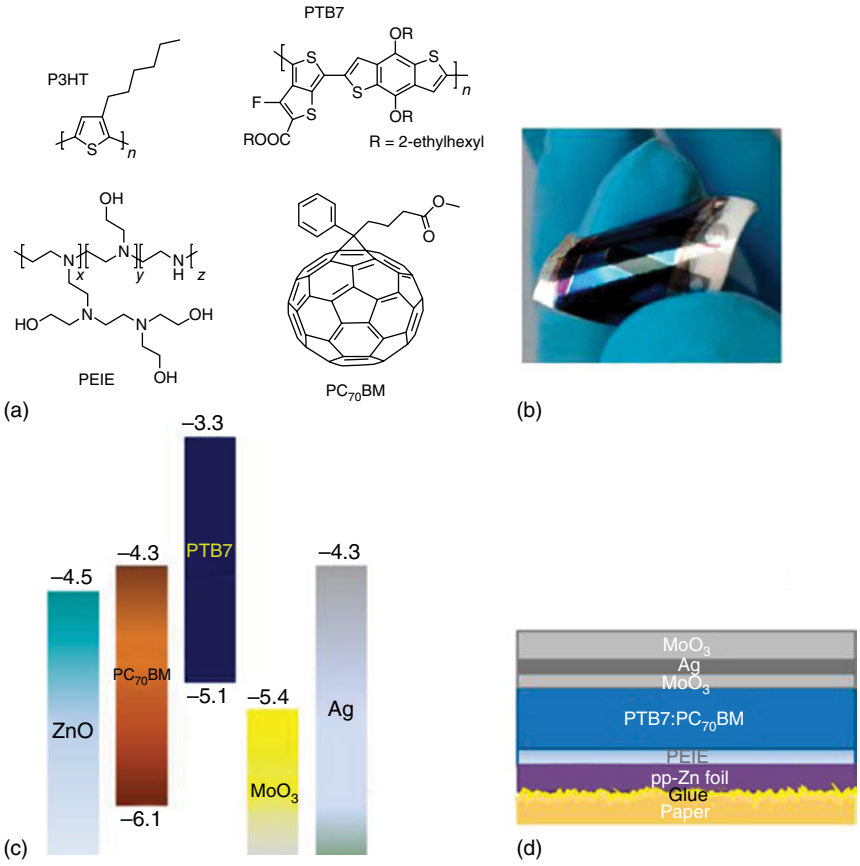

Figure 1.3 (a) Chemicals employed in bulk fabrication of heterojunction solar cell devices: standard P3HT and novel PTB7 polymers as electron donors; $PC_{70}BM$ as electron acceptor; polyethylenimine (*PEIE*) deposited in a thin layer (10 nm) coating to improve the work function and injection of ZnO back electrode; (b) photograph of a 4% efficient organic solar cell on a flexible paper support; (c) energetic levels of the photovoltaic layers; (d) schematic of the fabricated device showing the sequence of the layers. (Leonat *et al.* 2014 [18]. Reproduced with permission of American Chemical Society.)

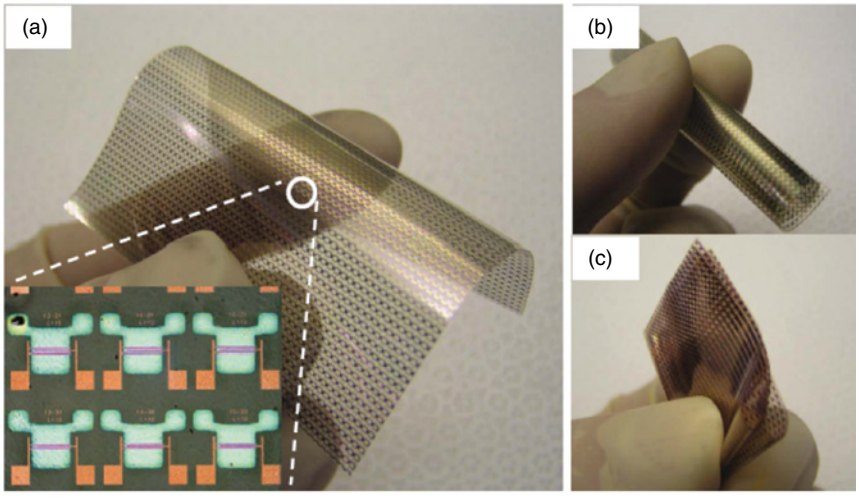

(A)

	1	2	3	4	5	6	7	8	9	10
A	0.24	0.19	0.30	0.25	0.21	0.26	0.22	0.24	0.04	0.13
B	0.23	0.00	0.29	0.21	0.28	0.35	0.40	0.14	0.19	0.20
C	0.34	0.36	0.26	0.24	0.36	0.48	0.26	0.44	0.21	0.26
D	0.16	0.29	0.22	0.16	0.01	0.00	0.40	0.35	0.06	0.39
E	0.14	0.35	0.45	0.43	0.43	0.28	0.02	0.34	0.19	0.23
F	0.16	0.20	0.22	0.38	0.36	0.30	0.02	0.34	0.05	0.19
G	0.16	0.36	0.11	0.27	0.40	0.33	0.57	0.23	0.13	0.38
H	0.16	0.47	0.12	0.24	0.18	0.24	0.38	0.04	0.29	0.23
I	0.27	0.34	0.24	0.06	0.14	0.27	0.17	0.05	0.56	0.17
J	0.34	0.33	0.26	0.44	0.23	0.32	0.37	0.07	0.28	0.25

Mobility	No. of TFTs
0.00 – 0.04	7
0.05 – 0.09	5
0.10 – 0.14	7
0.15 – 0.19	12
0.20 – 0.24	19
0.25 – 0.29	16
0.30 – 0.34	10
0.35 – 0.39	12
0.40 – 0.44	7
0.45 – 0.49	3
0.50 – 0.54	0
0.55 – 0.59	2
	Σ 100

(B)

Figure 1.4 (A) (a) Photograph and a magnified image by optical microscopy of transparent, nanopaper-based OTFT array. Photographs revealing the (b) bending and (c) folding deformation modes endured by the substrate. (Fujisaki *et al*. 2014 [19]. Reproduced with permission of John Wiley and Sons.) (B) Field-effect mobility map of the transistor array on 5€ paper banknote with an area of $10 \times 8\,mm^2$ showing the distribution of the field-effect mobility. (Zschieschang *et al*. 2011 [20]. Reproduced with permission of John Wiley and Sons.)

The coating is based on a zinc metalized polypropylene thin film, where propylene serves as smoothener of the rough paper surface and prevents capillary penetration of the solution-processed active layers into the paper substrate, while zinc is employed as the metallic electrode of the device. Energy band diagrams of the components and the layered sketch of the device are presented in Figure 1.3c,d respectively [18].

A next step will be the realization of truly 3D-shaped paper electronics; in this respect Kirigami techniques seem promising to make paper not only flexible but even stretchable. Highly flexible, sustainable optoelectronics may soon become a reality with the aid of highly transparent paper. Cellulose nanopaper (made from nano-sized cellulose fibers) was selected as substrate for flexible electronics, as reported by Fujisaki *et al.* [19] Initial work employed a 20 µm thin transparent paper, made from native wood cellulose nanofibers only, as substrate for fabrication of high-mobility organic thin film transistor (TFT) arrays. Figure 1.4Aa depicts a photograph and an optical microscopic image of a 20 µm thin transparent nanopaper-based OTFT array. Figure 1.4Ab,c demonstrate the amenability of the substrate material to withstand torturous deformation, in a similar way to conventional paper.

OTFT arrays might also be a good option for anti-counterfeiting and tracking feature applications, especially when printed directly on banknotes. Zschieschang *et al.* demonstrated the fabrication of complex circuits with high yield and reproducibility directly on the rough surface of paper bills [20]. Such circuits could form advanced electronic safety features for counterfeit protection (Figure 1.4B). In a recent report Kim and coworkers demonstrated for the first time one-dimensional photonic nanocavities on paper after their transfer printing with the aid of a micro-sized stamp [21].The nanocavity exhibits lasing (Figure 1.5) and displays a wavelength shift dependent on the amount of hydration of the paper substrate, proving also its amenability to function as a sensor. Although the *Q*-factor is

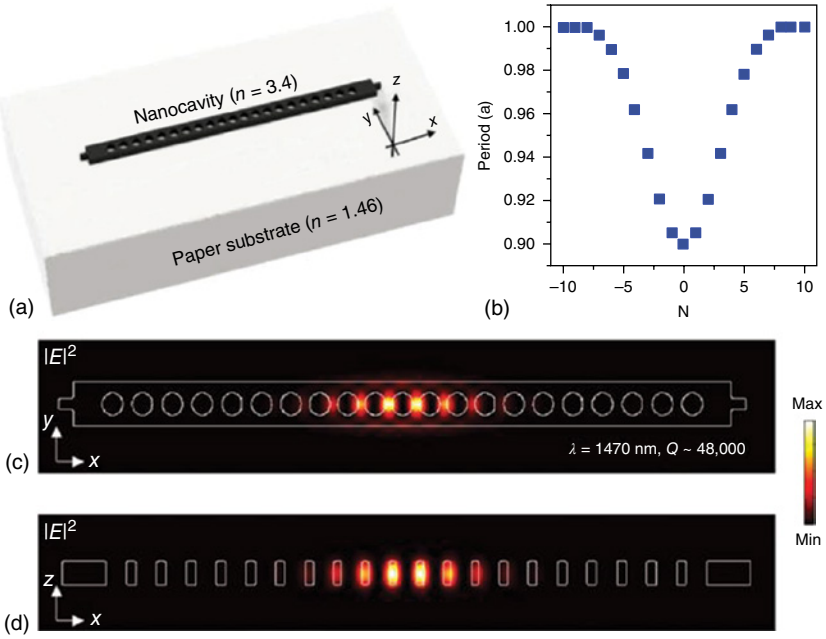

Figure 1.5 (a) Schematic of a semiconductor photonic nanocavity laser deposited via transfer printing on a paper substrate; (b) the Gaussian-modulated period of hole-to-hole distances along the *x*-axis from 0.9a to 1.0a. (c) The electric field intensity of the photonic crystal on the *x*–*y* plane and (d) the electric field intensity of the photonic crystal on the *x*–*z* plane. (Kim *et al.* 2016 [21]. Reproduced with permission of John Wiley and Sons.)

reduced by a factor of 10 when the paper substrate is introduced as support for the free-standing nanocavity crystal, the lasing threshold remains low, at ~0.2 mW. When employing the communication wavelength of 1.55 μm, the paper substrate provides a sufficiently high *Q*-factor for lasing, potentially paving a way for telecommunication applications. The selected research examples discussed here serve to illustrate the huge potential of paper for future development of sustainable electronics and photonic devices.

1.3 DNA and Nucleobases

In 1953, Watson and Crick published the helical structure of deoxyribonucleic acid, better known as *DNA* [22]. This investigation led to a better understanding of the main building block of every living organism on Earth and its genetic code transmittance responsible for growth, development, functioning, and reproduction. The long fibrous DNA molecule consists of a very long backbone chain formed by repeated units of a sugar group (deoxyribose) and a phosphate group alternately bonded to nucleobase molecules (the purines adenine and guanine, and the pyrimidines cytosine and thymine). Although the DNA-based research represented from its inception the bread and butter of genomics [23], the molecule stirred increasing interest over the past decade as a material for organic electronics, in the intention to bridge functional electronics with living organisms. Yumusak *et al.* demonstrated a bio-organic field-effect transistor (*BioOFET*) based on a cross-linked DNA gate dielectric, purified from salmon waste [24]. DNA is soluble only in aqueous solutions, which makes implementation of standard processing techniques from organic solvents difficult. The authors engineered a DNA–lipid complex that became water insoluble and processible in high quality films from organic solvents using standard device fabrication techniques such as spin coating. Steckl *et al.* paved the way for using DNA in organic light-emitting diodes (*OLED*s) and emphasized the potential of DNA as an inexpensive and biodegradable source material for the development of optical waveguides and laser structures [25, 26]. Thin films of DNA incorporated into the fluorescent emitting materials for OLEDs can increase the brightness of the respective devices by one order of magnitude compared to OLEDs produced from standard materials. The authors found that the DNA layer behaves as a highly efficient electron-blocking layer (*EBL*) while not hampering hole transport. Therefore, the thin DNA layer enhances the probability of exciton formation and eventually of photon emission in fluorescent OLEDs decorated with specific fluorophores (i.e., standard AlQ3 for green and NPB for blue emission respectively) as visualized in Figure 1.6a [27]. When DNA-surfactant thin films are incorporated in phosphorescent OLEDs, the brightness and efficiency of the DNA-based devices outperforms their phosphorescent counterparts, as revealed in Figure 1.6b.

DNA capping layers also enhance charge injection in OFETs, as demonstrated by Zhang *et al.* [28]. In their work, DNA works as an interlayer for n-type and ambipolar semiconductor OFETs fabrication with gold as top source and drain electrodes. The DNA layer in the device, schematically shown in Figure 1.7Aa, allows for the injection of both charge carriers. The OFET was prepared either

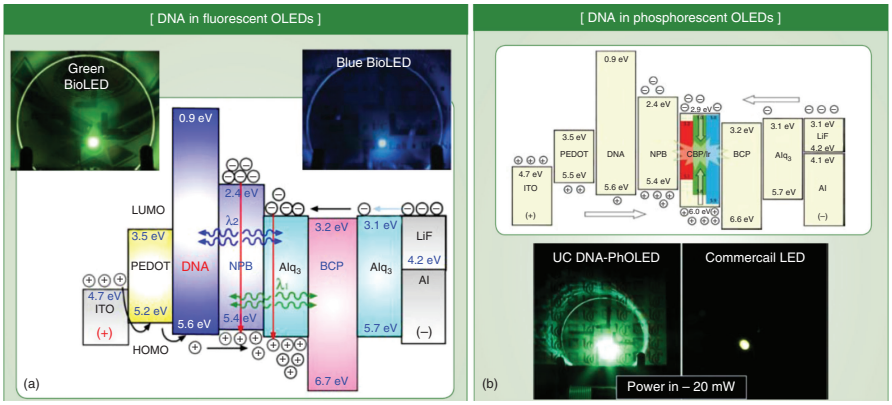

Figure 1.6 (a) Fluorescent OLEDs with DNA surfactant as electron-blocking layer employing AlQ3 fluorophore for green emission and NPB for blue emission. The bottom schematic displays the energy diagram of the layered structure; (b) DNA surfactant employed in the fabrication of phosphorescent OLEDs: the energy diagrams (top) of the layered structure, and the comparison of DNA-based OLED with a commercially available phosphorescent LED, with both devices biased at 20 mW (bottom). (Steckl *et al*. 2011 [27]. Reproduced with permission of Optics & Photonics News.)

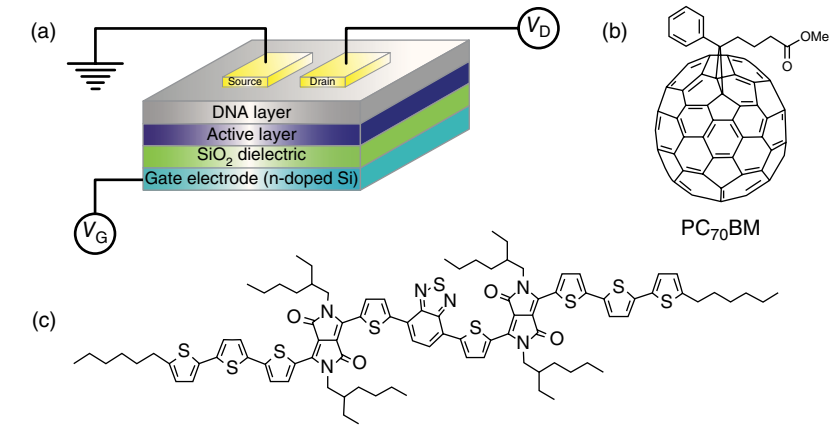

(A)

	μ_{lin} (*e*) ($cm^2\ V^{-1}\ s^{-1}$)	μ_{sat} (*e*) ($cm^2\ V^{-1}\ s^{-1}$)	μ_{sat} (*h*) ($cm^2\ V^{-1}\ s^{-1}$)	V_{th} (V)[a]
$PC_{70}BM$	7.5×10^{-3}	9×10^{-3}	N/A	16
$PC_{70}BM$/DNA	1.7×10^{-2}	1.6×10^{-2}	N/A	10
BTDPP2	4.8×10^{-4}	4.4×10^{-3}	6×10^{-3}	12
BTDPP2/DNA	2.3×10^{-3}	1.1×10^{-2}	2.1×10^{-2}	6.5

(B) [a] V_{th} is determined from the linear regime under electron accumulation mode.

Figure 1.7 (A) (a) Schematic of the device structure with DNA used a charge injection layer and (b–c) chemical structure of the semiconductors employed. (Zhang *et al*. 2012 [28]. Reproduced with permission of John Wiley and Sons.) (B) Device parameters of OFETs fabricated using $PC_{70}BM$, $PC_{70}BM$/DNA, BTDPP2, and BTDPP2/DNA.

with an n-type semiconductor material, [6,6]-phenyl-C_{71}-butyric acid methyl ester($PC_{70}BM$) (with the structure depicted in Figure 1.7Ab) and 4,7-bis{2-[2,5-bis(2-ethylhexyl)-3-(5-hexyl-2,2′:5′,2″-terthiophene-5″-yl)-pyrrolo[3,4-*c*]pyrrolo-1,4-dione-6-yl]-thiophene-5-yl}-2,1,3-benzothiadiazole (BTDPP2) (shown in Figure 1.7Ac) or with an ambipolar semiconductor, diketopyrrolopyrrole (*DPP*). The fabricated OFETs having DNA as injection layer showed an increase in field-effect mobility of up to one order of magnitude as compared to the samples that have no such interlayer (see Figure 1.7B).

Far easier to process than DNA are its constituent nucleobases that are widely available in crystalline powder form; they can be used without purification, or alternatively can be scrupulously purified to a desired extent via the train sublimation method. AFM surface investigations of vacuum-sublimed thin films deposited on glass substrates demonstrated a root mean square (*rms*) roughness of ~3 nm for guanine, ~14.5 nm for adenine, ~24 nm for cytosine, and ~65 nm for thymine [29]. The authors showed that ultrathin layers of natural adenine, guanine, thymine, and cytosine can be used as stand-alone dielectric or in combination with one another in alternating layers.

Irimia-Vladu *et al.* widely investigated the use of various such permutations that were reported in several publications [29–31]. For example, four alternating layers of adenine and guanine as dielectric in a fully biodegradable and biocompatible OFET were implemented, resulting in a specific capacitance of 5.1 nF cm^{-2}, stemming from a calculated dielectric constant of ~3.85 for adenine and ~4.35 for guanine measured at 1 kHz. The authors showed that in spite of the final roughness of the combined layer, the alternating adenine and guanine films produce an insulator that is sufficiently dense to work as dielectric layer in OFETs fabricated on a variety of biodegradable substrate materials: hard gelatine, caramelized sugar, or even on ecological nursery foils [30]. Because nucleobases are amenable for thin-film processing by vacuum deposition, they are ideally suited as thin capping layers for dipole-rich metal oxide dielectric interfaces. Figure 1.8

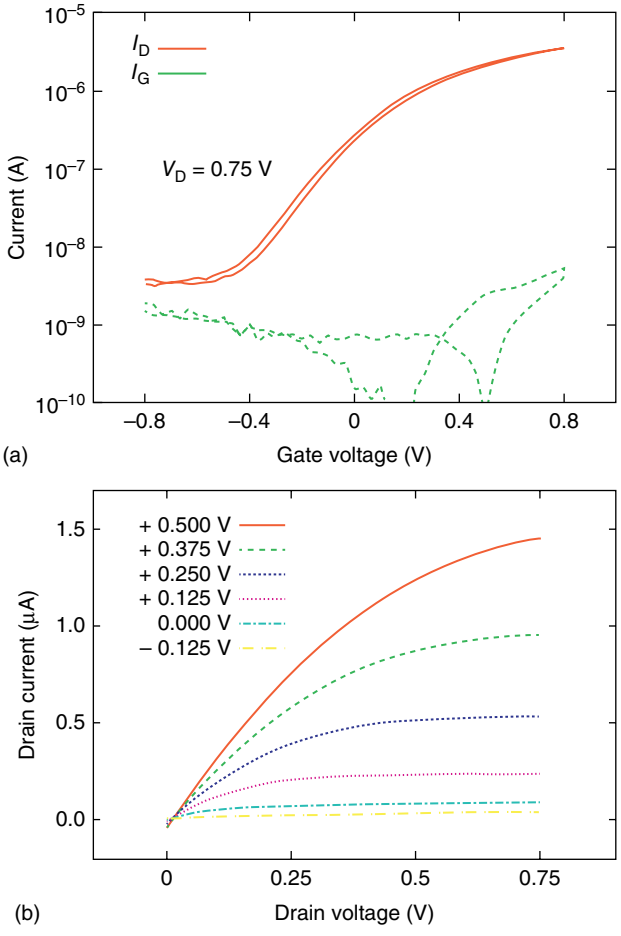

Figure 1.8 (a) Transfer and (b) output characteristics of a low-operating voltage OFET with adenine employed as capping layer on electrochemically grown aluminum oxide layer. Hot wall epitaxial-deposited C_{60} acts as organic semiconductor and aluminum as contact electrodes. (Schwabegger *et al.* 2011 [32]. Reproduced with permission of Elsevier.)

shows such an example through the transfer and output characteristics of an AlO_x–adenine gate dielectric. A thin film of vacuum processed adenine was used by the authors as a capping layer for the electrochemically grown aluminum oxide layer, resulting in a combined organic–inorganic dielectric having a high specific capacitance of ~0.1 μF cm^{-2} and consequently contributing to a remarkable field-effect mobility of the hot-wall epitaxially deposited fullerene C_{60} organic semiconductor of ~3.4 cm^2 V^{-1} s^{-1} [32].

Nucleobases showed promising applications not only in OFETs but also in organic light-emitting diodes, OLEDs. Gomez *et al.* investigated the nucleobases thymine (T) and adenine (A) as EBLs that lead to a high photoemission efficiency in OLEDs [33]. In their following work they also included guanine (G), cytosine (C), and uracil (U) into the investigation as EBL as also as hole-blocking layer (*HBL*) in the OLED structure along with a thorough study of their thin-film and electronic properties [34]. Nucleobases have similar Highest Occupied Molecular Orbital (HOMO)–Lowest Unoccupied Molecular Orbital (LUMO) energy gaps as DNA (i.e., ranging from 3.6 to 4.1 eV), but differently, they have a fairly large range of electron affinity values (1.8–3.0 eV) that allow for an additional degree of freedom in device design. Table 1.1 summarizes the peak performance of different nucleobases tested as EBL and HBL.

Table 1.1 Performance summary of the investigated nucleobases as electron-blocking layers (EBL) and hole-blocking layers (HBL) in organic light-emitting diodes.

	Turn-on (V)	Maximum luminance (cd m^{-2})	Maximum current efficacy (cd A^{-1})	Maximum luminous efficacy (lum W^{-1})	Quantum efficiency (%)	
					Ext	Int
(a) EBL type II						
Baseline	3.25	95.179	38.5	22.3	10.7	59.4
G	4.75	17.191	44.3	21.9	12.3	68.3
A	5.0	82.289	51.8	21.2	14.3	79.4
C	5.0	5.646	36.1	14.5	10.0	55.6
T	7.75	3.844	22.6	6.9	6.3	35.0
U	7.0	21	3.3	1.2	0.9	5.0
DNA–CTMA	3.75	60.061	43.3	25.6	12.0	66.7
(b) HBL type III						
G	6.0	16	1.3	0.6	0.4	2.2
A	5.5	215	1.0	0.4	0.3	1.6
C	5.5	217	5.2	2.1	1.5	8.3
T	5.5	362	15.1	5.0	4.2	23.3
U	4.25	4 045	16.3	7.4	4.6	25.6

Source: Gomez *et al.* 2015 [34]. Reproduced with permission of John Wiley and Sons.

For the devices tested as HBL/ETL, uracil performed the best of all nucleobases as HBL, having the largest current, the best efficiency, and the highest luminance. C-based OLEDs display both EBL and HBL tendencies. For the devices tested as HBL/EBL, uracil performed the best of all nucleobases as HBL, having the largest current, the best efficiency, and the highest luminance.

With the above exemplified reports, the door now stands widely open for the employment of DNA and its constituent nucleobases in the field of electronics. Low cost and easy process routines make DNA and its nucleobases interesting and appealing for interfacing electronics with living matter. Particularly its use in sensing and optoelectronics is very promising, and perhaps soon DNA will add one more word to its denomination of "molecule of life"; it could become "the molecule of light" [27].

1.4 Silk

When the production of silk in woven fibers was implemented in China more than 3500 years BC, the shiny precious material was reserved only for local aristocracy. Later on it found its way through the silk road to Europe's royalty and wealthy class. Silk is naturally produced from hundreds of different silkworm species, with the mulberry silkworm as its most famous representative [35]. Today silk is not only desired for fashion purpose, rather more as an interesting part of research, especially in the fields of tissue engineering and regenerative medicine because of its biocompatibility stemming mainly from its protein constituency [36]. Owing to its biodegradability and biocompatibility, silk has also come into the focus of organic electronics in recent years for a wide range of applications. Hota *et al.* used natural silk fibroin protein to fabricate a transparent biomemristor and investigated the endurance and retention characteristics of the device [37]. As proved in Figure 1.9a, metal–insulator–metal (*MIM*) capacitors with silk fibroin protein showed memory resistor and rectifying characteristics at the same time, and were therefore memristive in nature. The schematic design of the device is shown in the insets of the figure. In Figure 1.9b the retention characteristics of the memristor device is shown, with attainable switching ratios of approximately 10–11 times.

The dynamic mechanical and dielectric properties of amorphous regenerated films of silk fibroin were studied by Magoshi and Magoshi in 1975 [38]. In 2011 Wang *et al.* fabricated a flexible organic thin-film transistor with a silk fibroin gate dielectric by coating a thin layer of silk fibroin film onto a Polyethylene terephthalate (PET) substrate patterned with a gold gate electrode [39]. The silk dielectric had to be dip-cast to achieve a continuous layer. Pentacene was thermally evaporated onto the dry silk film for the organic semiconductor layer and the device was finalized with gold as source and drain contacts. Figure 1.10a shows a photograph of the rollable pentacene OTFT and in Figure 1.10b the transfer characteristics of the device are presented, displaying a very small hysteresis, indicative of a very low level of charge trap density at or near the pentacene–silk fibroin interface [39]. Another example for silk as dielectric in organic electronics was offered by the work of Capelli *et al.* who integrated silk protein in OFETs and organic light-emitting transistors (*OLET*s) respectively, with the latter devices yielding a light

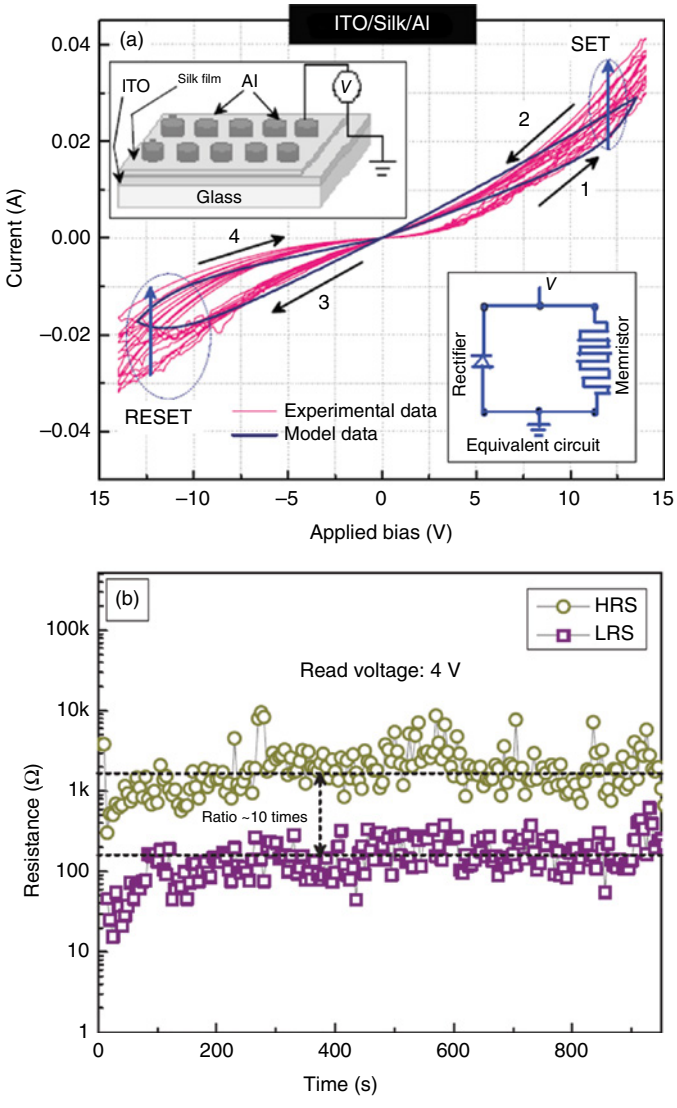

Figure 1.9 (a) Reversible and nonvolatile switching characteristics of memristor devices with silk fibroin protein showing good match between the experimental and the model data and (b) retention test of the high resistance states (*HRS*) and low resistance states (*LRS*) of the ITO/silk/Al capacitor structures under a positive bias operation, with resistances read at 4 V. (Hota *et al*. 2012 [37]. Reproduced with permission of John Wiley and Sons.)

emission of 100 nW [40]. In a more recent publication, Chang *et al*. employed major ampulate spider silk as polyelectrolyte gate dielectric for OFETs with pentacene semiconductor and analyzed the important role of hydration of the silk dielectric for obtaining reproducible results at different levels of relative humidity [41]. Various other research groups harvested the excellent properties of silk, such as flexibility, good mechanical properties, and the ability to stand alone as a film, and employed it in the development of organic electronic devices. One such

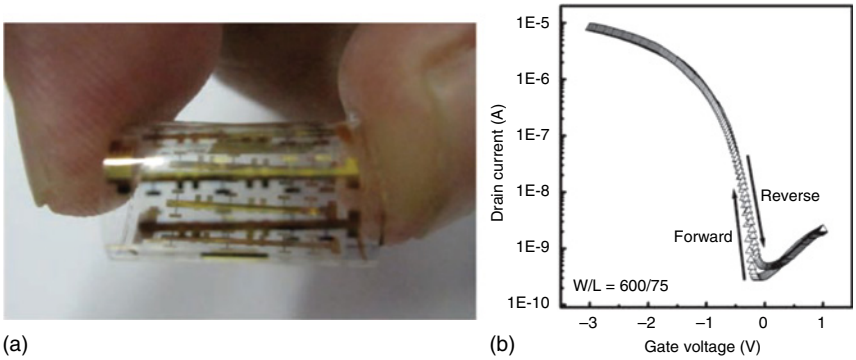

Figure 1.10 (a) Photograph of the rollable OTFT with pentacene semiconductor and silk fibroin gate dielectric and (b) transfer characteristics of the transistor. (Wang *et al*. 2011 [39]. Reproduced with permission of John Wiley and Sons.)

example was offered by Kim *et al*. who presented in their work an interesting way to transfer metal electrodes to a thin, freestanding silk film [42].

Figure 1.11 shows the process routine of the transfer printing with a schematic diagram on the left and a corresponding high-resolution image on the right and optical microscopy images of the circuits in the insets. In the fabrication sequence described in Figure 1.11, metal oxide field-effect transistors were first placed on a Poly(methyl methacrylate (PMMA) carrier wafer. Afterwards the devices where lifted on a poly(dimethylsiloxane) *PDMS* stamp, displayed in Figure 1.11b. With this setup the electrodes could be transferred to a silk film on a silicon wafer (Figure 1.11c) or even to a freestanding silk film (Figure 1.11d), thereby contributing to the development of bioresorbable electronics. In a follow-up report of the same group, Hwang *et al*. designed devices capable of interfacing electronics with living tissue for biomedical applications [43]. In their work, silk with various degrees of crystallinity was used as a programmable dissolving substrate and encapsulation for a wide series of devices. The group demonstrated transistors, diodes, inductors, capacitors, and resistors, all made out of thin active layers of magnesium and magnesium oxides, silicon nanomembranes and silicon dioxides, with controllable transient times dictated by the controlled dissolution of silk encapsulate and substrates. In several follow-up contributions, the group of John Rogers cemented the indispensability of silk in the development of transient electronics. The respective field is covered extensively by Huang and Rogers in Chapter 5 of this book.

Another interesting approach was to employ silk fibers and dye them with a conducting conjugated polyelectrolyte, as shown by Müller *et al*. [44]. The group fabricated an electrochemical transistors (*ECT*s) by arranging the coated fibers in a simple cross-junction configuration. Conducting fibers could be woven into pristine fiber segments. Intelligent clothing with silk fibers will surely be an exciting option for the future. The good insulating properties and its simple processibility from aqueous solutions make silk a good alternative as dielectric for electronic devices. The highest potential of silk lies in its good programmability of its dissolution in liquids, notably in bodily fluids, and these amazing characteristics have secured the use of silk in the fabrication recipes of future transient electronic devices.

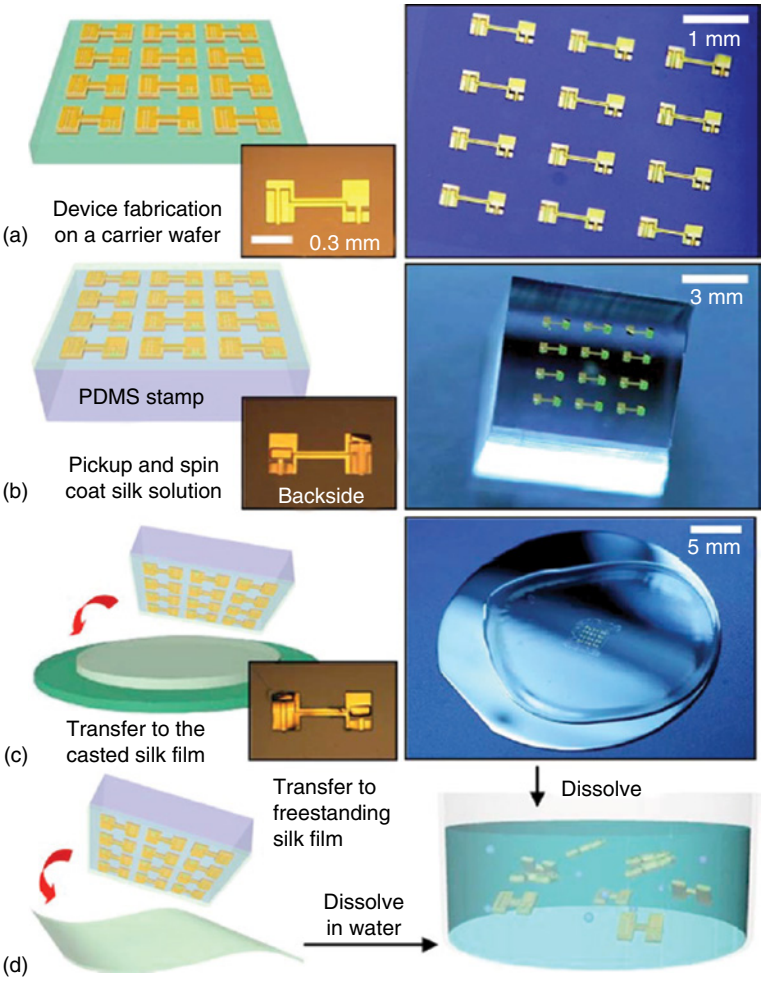

Figure 1.11 (a) (left) Schematic diagram and the microscope image as inset of devices fabricated on carrier wafer; (right) high-resolution image of the ultrathin devices on a carrier wafer; (b) devices lifted onto the surface of a PDMS stamp; (c) spin coating of thin silk film on silicon wafer onto which the devices are transferred; and (d) (left) transfer printing onto a freestanding silk film and (right) dissolution of the devices. (Kim *et al*. 2009 [42]. Reproduced with permission of AIP Publishing.)

1.5 Saccharides

Sweet things come to our mind, when we hear the word sugar. Sugar molecules have a long history in chemistry and biochemistry and were first reported more than 250 years ago [45]. This substance of plant origin can be grouped into three categories: monosaccharides, such as fructose, glucose, and galactose; disaccharides, such as lactose, maltose, and sucrose; and finally oligosaccharides. When targeting the fabrication of biodegradable and biocompatible electronics, the simplest small molecules of the sugar family are highly eligible, owing to their nontoxicity, good

acceptance in society, and simple processing routes from aqueous solvents. Irimia-Vladu *et al.* investigated the dielectric properties of spin-coated glucose and lactose films and their applicability in OFETs. Solution-processed sugars have excellent film-forming properties. Such spin cast films show an rms roughness in the range of 0.5–1 nm, which helps in the subsequent deposition of high-quality layers of semiconductors and contact electrodes [29, 30]. The measured specific capacitance of a 2.6 μm thick film cast from a glucose solution in deionized water was 2.15 nF cm^{-2}. The film of glucose was employed as dielectric layer in the fabrication of OFETs; Figure 1.12 shows transfer and output characteristics of such an OFET with fullerene C_{60} acting as the semiconducting layer [29]. In another

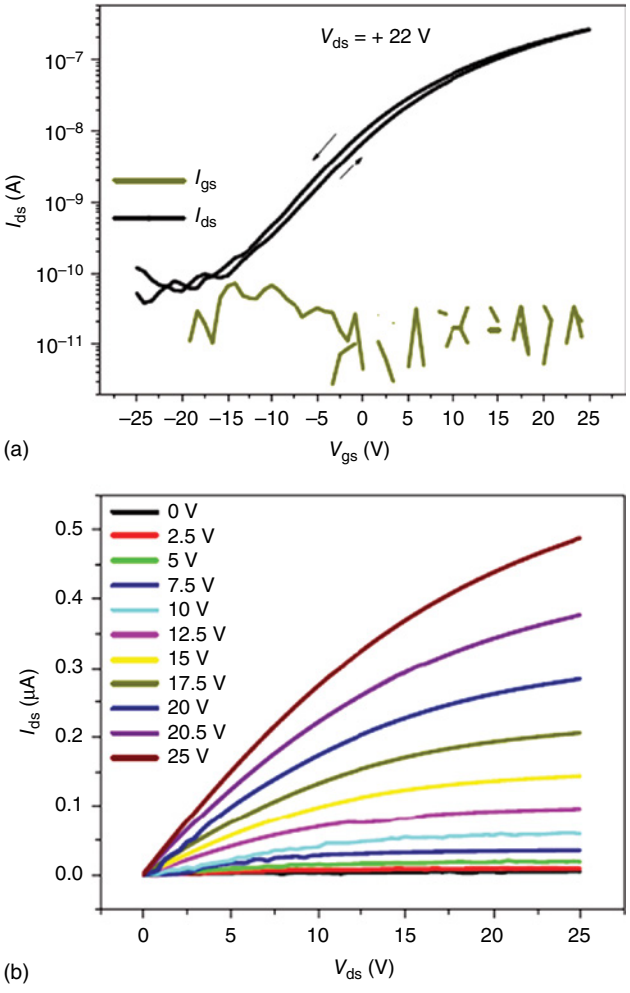

Figure 1.12 Transfer (a) and output (b) characteristics of an OFET with solution-processed glucose gate dielectric and C_{60} semiconductor channel showing minimal hysteresis and excellent insulating characteristics (very low leakage currents) of glucose dielectric. (Irimia-Vladu *et al.* 2010 [29]. Reproduced with permission of Elsevier.)

Table 1.2 Mechanical properties of the investigated polymer composite samples of gelatine (G) and sucrose (S) in Poly(vinyl alcohol) (PVA) matrix.

Sample	Ultimate Stress (MPa)	Tensile Strain at Break (%)	Young's Modulus (MPa)
PVA	40.5 ± 2.9	76 ± 9.2	1304.8 ± 218.5
0.1 G	115.6 ± 17.1	2.6 ± 0.6	3022.7 ± 378.7
0.5 G	42.4 ± 2.7	4.3 ± 0.7	1699.9 ± 167.9
1 G	41.2 ± 5.3	1.9 ± 0.2	1384.5 ± 107.8
2 G	50.7 ± 12.1	3.7 ± 0.9	1182.7 ± 64.7
0.1 S	40.6 ± 3.6	184.4 ± 19.6	513.9 ± 40.8
0.5 S	22.1 ± 1.1	313.7 ± 8.3	45.7 ± 2.3
1 S	21.7 ± 1.9	419.1 ± 22.1	28.7 ± 4.2
2 S	7.1 ± 1.4	333.1 ± 34.5	8.7 ± 0.8

Source: Acar *et al*. 2014 [46]. Reproduced with permission of John Wiley and Sons.

contribution, the same group showed that caramelized glucose is also an appropriate substrate for organic electronic devices [30].

Other research groups have tried to take advantage of the plasticizing effect of sugars in combination with polymers. Acar *et al*. integrated sucrose in a polymer matrix to fabricate a tunable material for transient electronics [46]. The addition of sucrose shifted the glass transition temperature (T_g) to lower temperatures, which resulted in more elastic composites at temperatures above T_g. Table 1.2 lists the Young's modulus, tensile strength, and tensile strain at break measured from the stress–strain curves. Increasing the concentration of sucrose in the Poly(vinyl alcohol) (PVA)/sucrose composite also increases the solubility of the resulting compound, which recommends the blend as an ideal candidate for the development of programmable transient materials for biomedical applications.

Sugar can play a major role in organic electronics, especially in transient electronics, because of its nontoxicity, good water solubility, low cost, and easy processibility. The sugar family has many members, besides the already mentioned ones, that still wait for close investigation and implementation in organic electronics, such as ribose, the inner constituent of DNA molecules.

1.6 Aloe Vera, Natural Waxes, and Gums

Aloe barbadensis miller, better known as *Aloe Vera*, is a succulent plant growing in the dry regions of Africa, Asia, and Americas. A variety of ancient cultures used the plant for medical treatment and as a skin care product. In traditional medicine, Aloe Vera gel is widely used as anti-inflammatory drug for the relief of sunburns or insect bites. The fleshy Aloe Vera leaves contain an inner clear gel that consists up to 99% of water. The remaining 1% includes glucomannans,

amino acids, lipids, sterols, and vitamins [47]. Aloe Vera as an active layer in electronic devices is cost efficient, easy to process, and suitable for biodegradable and biocompatible devices. Aloe Vera found its way into electronics development through the work of Khor and Cheong who investigated the dielectric properties of commercially purchased Aloe Vera gel. The group found a dielectric constant of ~3.4 for a screen-printed Aloe Vera layer [48]. Based on this knowledge they built an n-type OFET. In Figure 1.13a, the schematic design of the OFET is presented, including the dielectric layer consisting of a mixture of extracted natural Aloe Vera paste from fresh leaves with added 1.5 wt% of SiO_2 nanoparticles. The SiO_2 nanoparticles were introduced in order to enhance the compatibility of the semiconductor, C_{60} with the Aloe Vera gel. Figure 1.13b shows the output characteristic of the device with the first measurement taken immediately after its fabrication and the second one after 14 days. Stored under ambient condition, the OFET showed diminished device performance explained by the authors as a change in hydration of the dielectric layer; but it could be also largely credited to the oxidation of the semiconductor layer and of the contact electrodes [49].

Other materials of plant origin that found applicability in organic electronics development are natural gums and waxes. Gum Arabic, also known as *acacia gum*, segregates from various species of acacia trees. Ancient Egyptians already knew of the good adhesive properties of gum Arabic and used it in combination with mineral pigments for paintings [50, 51]. Nowadays, gum Arabic is widely employed in food industry as an ingredient of chewing gum. Gum mastic, another natural gum used for more than 2500 years in traditional Greek medicine, is obtained from the mastic tree, *Pistacia lentiscus* [52]. Nowadays, this brittle and translucent resin is still used in folk medicine and food industry. Another plant-derived exudate is carnauba wax, mostly harvested in Brazil from the palm tree *Copernicia cerifera*. It is the hardest natural wax that melts at ~80–87 °C and is usually added to other waxes to increase their melting point. It is also used for encapsulation in pharmacy and food industry owing to its excellent water repellent properties [53]. In the field of organic electronics these materials are very suitable as dielectrics when either hydrophilic (gums) or hydrophobic (waxes) layers are sought for device development. Stadlober *et al.* studied a variety of natural-origin materials for bioelectronics, such as gum Arabic, gum mastic, paraffin, beewax, and carnauba wax [54]. The dielectric constant measured at 1 kHz is 2.9 for carnauba wax and higher for the materials processed from aqueous solutions, that is, 4.1 for gum Arabic and 3.9 for gum mastic. In combination with a hybrid gate dielectric, such as electrochemically grown aluminum oxide (Al_2O_3), the gums and the waxes form a sufficiently dense and highly insulating gate dielectric. They also show excellent surface characteristics to assist the growth of the subsequently deposited organic semiconductor layer of OFETs. Figure 1.14Aa shows the output and transfer characteristics of a pentacene OFET with a hybrid bilayer dielectric of gum Arabic on Al_2O_3, assisting in obtaining a high mobility of 0.56 $cm^2 V^{-1} s^{-1}$ for the pentacene semiconductor [54]. In another report, Glowacki *et al.* combined the naturally occurring oligo ethylene, tetratetracontane (*TTC*), with aluminum oxide for obtaining a hybrid organic–inorganic dielectric layer and

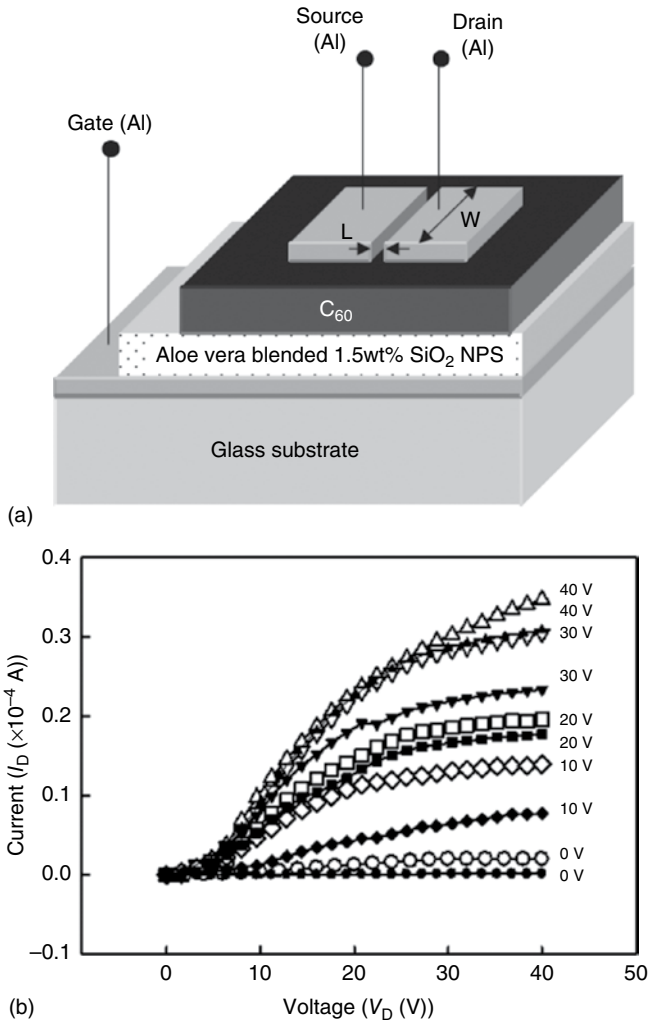

Figure 1.13 (a) Schematic of the employed architecture for the fabrication of OFETs with Aloe Vera gate dielectric including 1.5 wt% SiO_2 filler and (b) output characteristics of one representative device showing the initial measurement (open symbols) and the one recorded after 14 days (filled symbols). The significant drop in output current is presumably due to changes in the hydration level of the dielectric layer, with oxidation of the semiconductor and contact electrodes that could have also played a role. (Qian Khor and Cheong 2013 [49]. Reproduced with permission of The Electrochemical Society.)

the hydrogen-bonded semiconducting pigment quinacridone in OFET devices [55]. This air-stable semiconductor pigment quinacridone shows a very high T_{80} value of its mobility retention (time elapsed so that the mobility decreases to 80% of its initial value), as shown in Figure 1.14B, and can be operated in air without significant degradation for at least 140 days [55].

The main advantage of all these above exemplified materials, as well as of many other waxes and gums that wait to be reported for the organic electronics

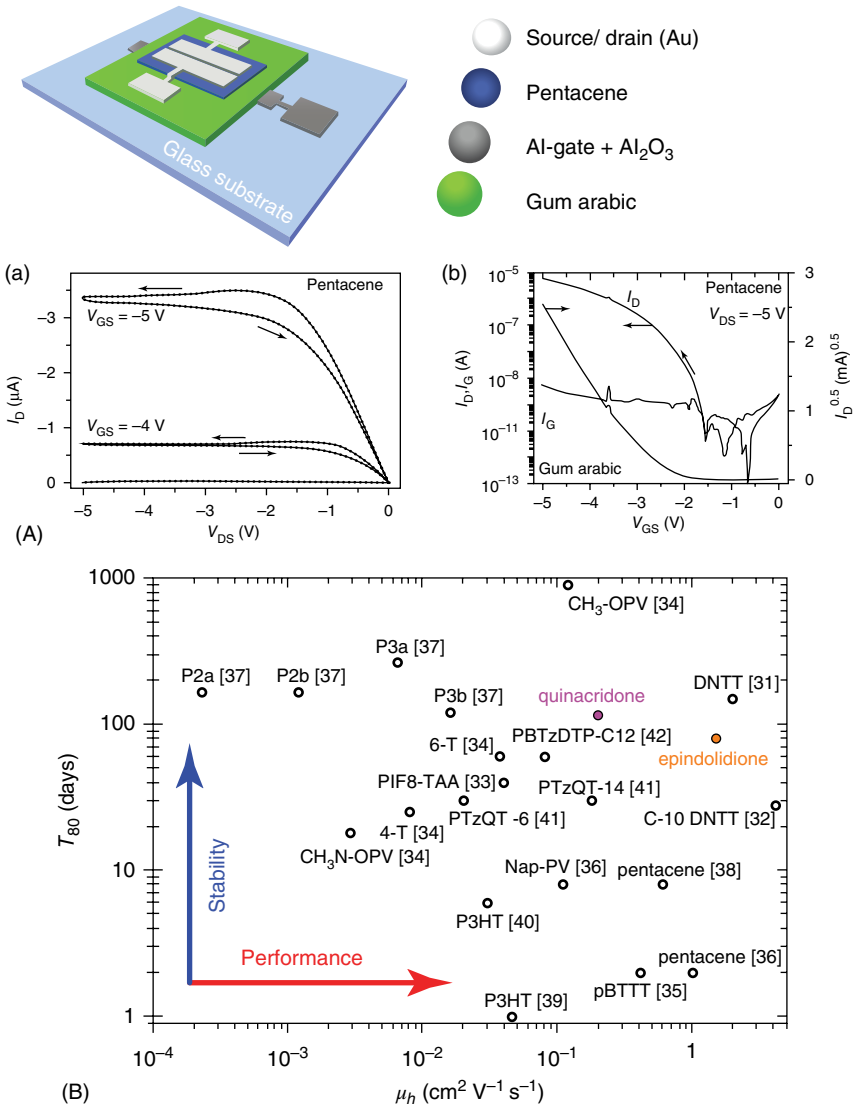

Figure 1.14 (A, top) Schematic of the fabricated OFET with gum Arabic capping layer on Al_2O_3 dielectric and pentacene semiconductor; (A, a,b) transfer and output characteristics of the device, which shows minimal hysteresis and high mobility of the organic semiconductor. Stadlober *et al*. 2015 [54]. Reproduced with permission of IEEE.; (B) degradation time T_{80}, expressed in days required for the mobility of the organic semiconductor to drop to 80% of its initial value. Devices with polyethylene oligomer, tetratetracontane (i.e., $C_{44}H_{90}$) dielectric showed impressive performance with epindolidione and quinacridone semiconductors. (Glowacki *et al*. 2013 [55]. Reproduced with permission of John Wiley and Sons.)

development, is their low cost and easy processibility. All gums are processible from aqueous solvents, whereas waxes are amenable for doctor blading or screen-printed deposition technique in their melted form.

1.7 Cellulose and Cellulose Derivatives

Cellulose as a carbohydrate surpasses the non-carbohydrate lignin for the position of the most prominent biopolymer on Earth, and is one of the most substantial biomass materials. Cellulose-first an integral part of papyrus and later of paper-was indirectly employed by the humanity to document events and spread its knowledge; cellulose became part of ascending research interest over the past 150 years. Some highlights regarding the implementation of cellulose in electronics will be offered below. Good dielectric properties make cellulose ideal as dielectric in complex circuit designs and also as substrate for circuits in general [56]. In fact, one of the most noticeable properties of cellulose to be harvested in bioelectronics is its high dielectric constant for an organic material [57]. Unfortunately, its high molecular weight and complexity make cellulose difficult to process in significant amounts in virtually any type of solvent. Attaching functional groups to impart solubility to cellulose was demonstrated by Petritz *et al.* who investigated the solution processible cellulose derivative tri-methyl silyl cellulose *TMSC* as an ultrathin dielectric film for complementary inverter fabrication [58]. The group employed a hybrid organic–inorganic dielectric containing electrochemically grown aluminum oxide, Al_2O_3, and TMSC as capping layer for the inverter fabrication, and showed that TMSC alone can function with good performance too. Figure 1.15a shows the performance of such a complementary inverter circuit as VTCs and gain curves for an operation window between 0 and 7 V. Figure 1.15b displays the noise margin (*NM*) and mismatch ΔV_M of the threshold voltage V_M as a function of the supply voltage, whereas Figure 1.15c exemplifies the "maximum equal criterion" method to extract the noise margin by displaying the maximum size of a square that fits between the inverter curve and the mirrored inverter curve [58]. Owing to its excellent smoothness and low trap density characteristics, the TMSC dielectric contributed to recording of impressive gains in excess of 1000 and noise margins over 90% for a low operating voltage of the complementary inverter circuit. The significant degree of hydrophobicity of cellulose derivative TMSC was harvested by the same group in a follow-up publication demonstrating the functionality of a complementary-like inverter based on a single type of ambipolar semiconductor (6,6′-Cl-Indigo) [59]. Another approach is the utilization of cellulose in cellulose-based ionogels as high capacitance gate dielectric for the fabrication of electrolyte-gated field-effect transistors on paper, as shown in the report of Thiemann *et al.* [60]. In this case, the gate dielectric of the TFT is a thin flexible electrolyte film that is ionically conducting but highly electronically insulating, rendering its superior dielectric properties to cellulose ionogel that has a high specific capacitance varying from 4.6 to 15.6 μF cm^{-2}. Figure 1.16a shows a schematic illustration of electrolyte-gated TFT with ZnO nanorods semiconductor and a lateral gate on multilayer-coated paper with laminated cellulose ionogel as dielectric; Figure 1.16b displays the optical image of a ZnO nanorod TFT on multilayer-coated paper. The fabricated TFTs turn on at 0.8 V and have on/off ratios of about 100, as presented in Figure 1.16c. Owing to the flexibility of the paper, the TFT samples could also be measured during inward bending as shown in Figure 1.16d, with a slight degradation recorded during a compressive strain test.

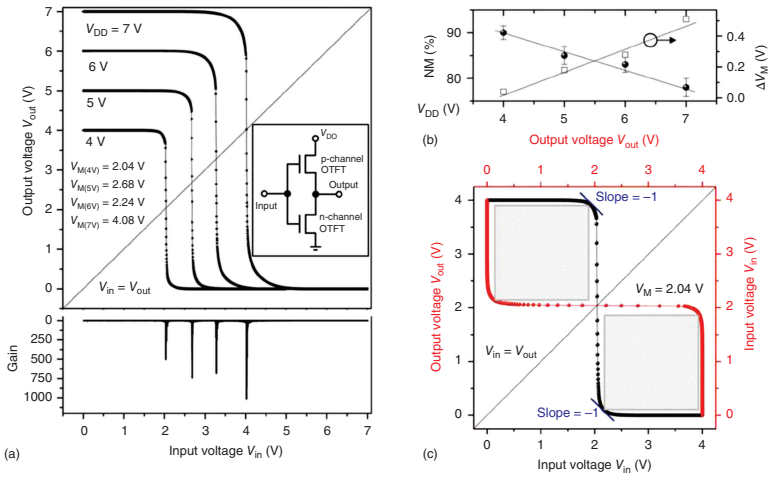

Figure 1.15 (a) Inverter performance expressed as voltage transfer curves (*VTCs*) for a complementary inverter with fullerene, C_{60}, and pentacene as organic semiconductors and TMSC-Al_2O_3 dielectric. The bottom graph displays the measured gain that reached 1600 for a champion device; (b) the noise margin (NM) and the mismatch ΔV_M of the threshold voltage as a function of the supply voltage; and (c) "maximum equal criterion," the method employed for noise margin estimation by calculating the maximum size of a square that fits between the inverter curve and the mirrored inverter curve, at a supply voltage V_{DD} of only 4 V [58]. (Petritz *et al.* 2015, http://onlinelibrary.wiley.com/doi/10.1002/adma.201404627/full. Used under CC-BY-4.0 http://creativecommons.org/licenses/by/4.0/.)

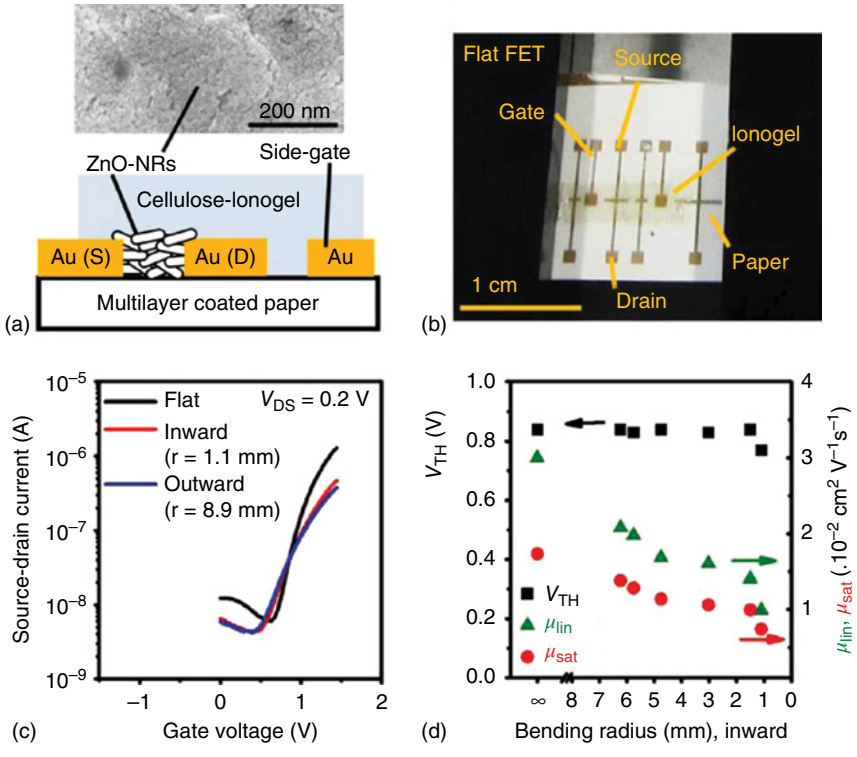

Figure 1.16 (a) Schematic of electrolyte-gated TFT structure with ZnO nanorods and side gate fabricated on multilayer-coated paper with laminated cellulose ionogel; the inset displays a scanning electron microscopy image of the short ZnO nanorods (typical length ~14 nm) on paper; (b) image of the tested device taken before the bending test; (c) transfer characteristics of the TFT recorded before and during inward and outward bending tests (radius 1.1 and 8.9 mm respectively) at a drain–source voltage V_{ds} = 0.2 V; and (d) threshold voltages (V_{th}) and field-effect mobilities (calculated in the linear and the saturated regimes) versus the inward bending radius. (Thiemann *et al.* 2013 [60]. Reproduced with permission of John Wiley and Sons.)

Beside its good dielectric properties, cellulose is highly suitable as substrate for organic electronics. Transparency, lightweight, and flexibility are the key properties of cellulose that Gomez and Steckl harvested for the fabrication of OLEDs [61]. The goal of that research was to pave the way for the fabrication of OLEDs based on fully natural materials. Figure 1.17 shows the schematic device that has adenine as the hole injection layer on a cellulose/epoxy substrate.

With respect to the substrates, especially nanocellulose-based paper sheets show very good transparency and smoother surfaces than regular paper. This material is highly biocompatible and therefore suitable for medical applications, which in combination with electronics could lead to improved diagnostic monitoring for patients [62]. The combination of the technical use of nanocellulose and electronics is considerable. Cellulose nanopapers are well suited as ultrafiltration membranes [63]. Evaporated electronics could, for example, monitor the durability of the filter and give notice when the filter has to be changed.

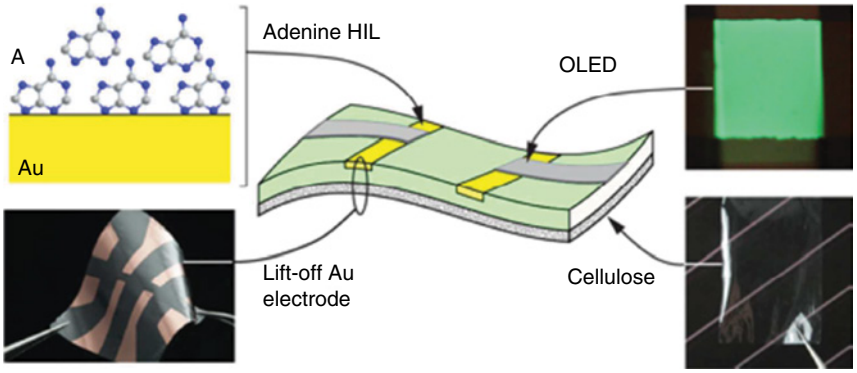

Figure 1.17 Device structure of an OLED with cellulose substrate, gold electrode, and adenine as hole injection layer. (Gomez and Steckl 2015 [61]. Reproduced with permission of American Chemical Society.)

One interesting avenue to follow will be the investigation of bacterial cellulose, which is different than plant cellulose in that it is more chemically pure, has ultrafine network architecture, contains no hemicellulose or lignin, and has a higher hydrophilicity and better tensile strength. Bacterial grown cellulose can be molded in any form and shape owing to the degrees of freedom offered by the polymerization reaction [64]. The dawn of implementation of cellulose in organic electronics has arrived and it will be interesting to see how this "green" and abundant material will find applications targeting sustainable developments for electronics.

1.8 Resins

A resin is a natural material either of plant or animal origin. Plant resins are generally referred to as *sap* or *sticky exudates* and are lipid-soluble mixtures of volatile and nonvolatile terpenoid and/or phenolic secondary compounds that are usually secreted in specialized structures located either internally or on the surface of the plant and have potential significance in ecological interactions. Irrespective of their origin (plant or animal), natural resins are traditionally classified into three main classes: hard resins (as copal, shellac or mastic), soft resins (as frankincense and myrrh), and oleoresins (mainly from Pinaceae genus), including turpentines, balsams, and elemis. Most of the resins belonging to these three classes have attracted deep interest for their medicinal properties and/or have been exploited in the industrial production of varnishes and lacquers and in the preparation of incenses and perfumes. Often mistaken with other plant exudates, that is, gums, the resins are fundamentally different. While gums are complex polysaccharides mixtures that decompose completely upon heating without melting, resins melt and progressively release volatile oils when the temperature is increased over their melting point [65]. As a rule of thumb, resins are processible in alcoholic solutions but insoluble in water, whereas gums are exactly the opposite; another class of exudates is formed by gum resins, which are to some extent a mixture of the two

and are soluble to some degree in both types of solvents exemplified above [66]. Typical building blocks of most of the resins produced by plants are terpenes and terpenoids, organic compounds widespread in nature as constituents of essential oils as well as major components of turpentine, the fluid obtained by the distillation of resins mainly from trees belonging to the pine family. Most prominent examples of plant resins are amber and copal, which are listed in most of the physics textbooks as examples of highly insulating materials. Although natural resins secreted by plants are overwhelming in their numbers, animal origin resins also exist. An example of animal origin resin with industrial significance is shellac, which is secreted by one tiny insect, *Tachardia Lacca* (with its subspecies *Kerria Lacca* and *Kerria Chinensis*) and deposited on the branches of insect colonies supporting trees in India, Thailand, and China. This red insect produces an excretion that acts as protective coating for its larvae against UV radiation. The amber-colored substance known as *lac* is the raw material of shellac manufacture that sums up to 20 000 tons per year worldwide [67, 68]. Most popular for its use as binder for phonograph records of the 78 rpm era, it is nowadays employed mostly as barrier coating to prevent moisture loss in citric fruits (its major worldwide application) as well as enteric coating for medical capsules intended to pass unaffected the upper part of the gastrointestinal tract and probe the colon [69]. In 1979 Goswami investigated the dielectric behavior of the constituents of the natural resin shellac [70] and in the year 2013, Irimia-Vladu *et al*. employed shellac as dielectric in OFETs [71]. Fresh shellac flakes readily dissolve in alcoholic solvents, preferably ethanol, and can be processed into films of different thickness via either drop casting or spin coating. Those drop cast or spin-coated layers can be cross-linked by heating the samples, not exceeding a temperature of 100 °C, with a resulting film displaying remarkable surface smoothness [71, 72]. In one such investigation, Irimia-Vladu *et al*. prepared a 30 nm shellac dielectric layer in an OFET device and also a 500 μm thick shellac substrate. Impressive smoothness of the film with rms roughness of ~1 nm revealed by AFM investigations, coupled with the absence of dipolar or ionic relaxation mechanisms in the frequency range of 10^{-3}–10^{4} Hz demonstrated by means of dielectric spectroscopy, make shellac ideal for utilization in organic electronics [71]. Figure 1.18a,b shows the transfer characteristics of (a) a C_{60} OFET and (b) a pentacene OFET fabricated on a 500 μm thick drop cast shellac substrate, with 250 nm thin shellac as gate dielectric layer. In both cases, the devices showed no hysteresis, indicating that the trap density for electrons or holes at the semiconductor interface is negligibly small. Shellac is versatile and easily modifiable chemically, so future applications in organic electronics are likely to come. In addition, a wide range of resins of plant origin still await investigation and implementation in electronic devices. In a pioneering work, Coppola *et al*. investigated a large number of plant-origin resins as dielectrics for OFET fabrication: amber, copal, frankincense, mhyrr, damar, sandarac, guggul, spruce, cedar, rosin, mastic, and elemi (Coppola *et al*., manuscript in preparation). Two examples of such investigation are presented in Figure 1.18c,d for spruce and myrrh dielectrics in OFETs with pentacene semiconductor. An interesting feature of all the resins investigated is the absence or occurrence of very minimal hysteresis in OFETs, an astonishing feat that happens in spite of their chemical complexity and composition diversity.

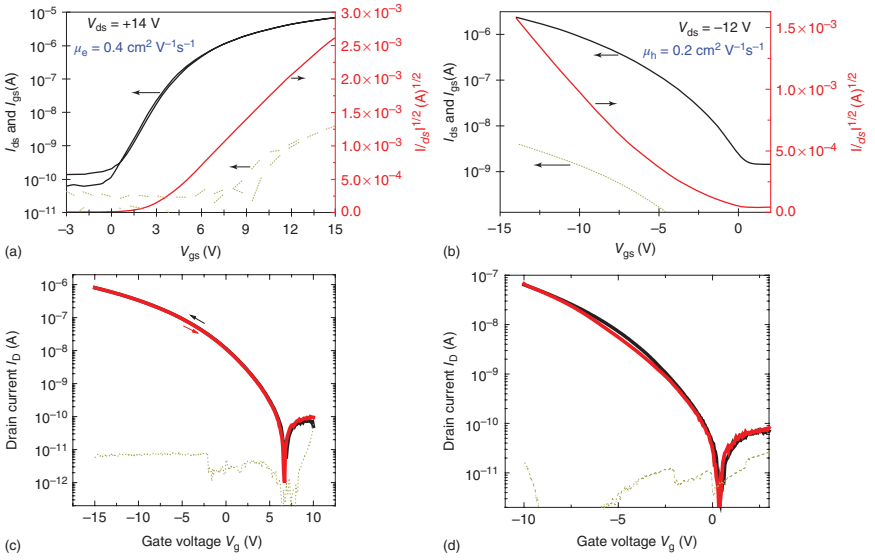

Figure 1.18 Hysteresis-free OFETs with natural resins processed from ethanol (~200–250 nm thick films) and used as capping layer of 32 nm thick aluminum oxide dielectric. (a) OFET with Shellac as capping layer on aluminum oxide dielectric and fullerene semiconductor; (b) OFET with Shellac as capping layer on aluminum oxide dielectric and pentacene semiconductor (Irimia-Vladu *et al.* 2013 [71]. Reproduced with permission of The Royal Society of Chemistry.); (c) spruce resin, and (d) myrrh resin as dielectrics processed from ethanol with vacuum-deposited pentacene as organic semiconductor in both cases.

1.9 Gelatine

Gelatine is a widely used common commodity material with a very long history. Studies show that ancient Egyptians already boiled bone and animal leather, which contained natural collagen as glue. Scientists assume however that the knowledge of the adhesive strength of collagen goes far back in time. Gelatine became popular as a food product because of its stabilizing effect, odorless taste, and gelling properties. Furthermore, gelatine has been used in photography, medicine, and pharmacy [73]. As multifunctional and multifarious material, gelatine has found its way into modern science, mostly employed as culture media for microbiological purposes. In 2010, gelatine entered the field of electronics through the demonstration of the first fully biodegradable and biocompatible OFET with hard gelatine as substrate [30]. Hard gelatine has a rather smooth surface with an rms roughness of 30 nm. For electronics fabrication it is important that the roughness of the substrate be minimized because that roughness will be transferred during the fabrication process to all layers above and will ultimately impair the functionality of interfaces between the dielectric and semiconductor and semiconductor and electrode layers.

As shown in Figure 1.19, the additional deposition of a smoothening layer, such as rosolic acid spin coated from ethanol solution, reduced the rms roughness of the hard gelatin down to ~9 nm, which was more amenable for device fabrication and led to improved transistor characteristics exemplified in very low leakage currents not exceeding 1 nA, five orders of magnitude on–off current, and low operating voltage. Besides the use of hard gelatine as substrate, the application of solution-based gelatine as dielectric was investigated by Mao *et al.* [74]. In a follow-up contribution, the group enhanced the dielectric properties of the solution-based gelatine with an additional TTC layer to form a TTC–gelatine bilayer [75]. Figure 1.20 shows the schematic of the corresponding device. The thermally evaporated TTC layer on the spin-coated gelatine film acts as a passivation layer and reduces the hysteresis loop and leakage currents of the p-channel pentacene OFET and the n-channel PTCDI-C_8 OFET compared to OFETs having only a

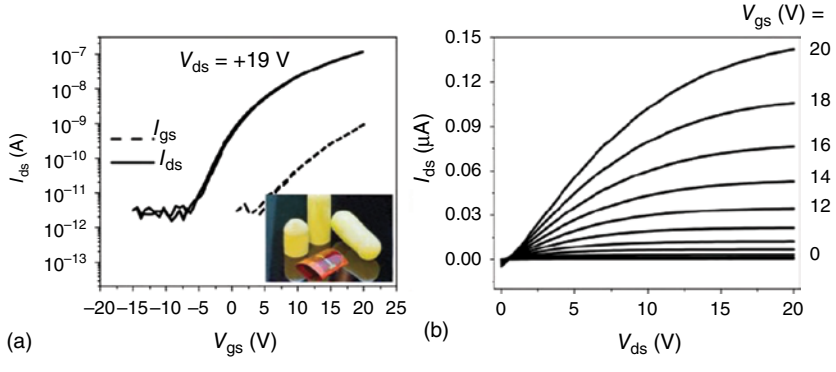

Figure 1.19 (a) Transfer and (b) output characteristics of OFETs fabricated on hard gelatine capsule. (Irimia-Vladu *et al.* 2010 [30]. Reproduced with permission of John Wiley and Sons.)

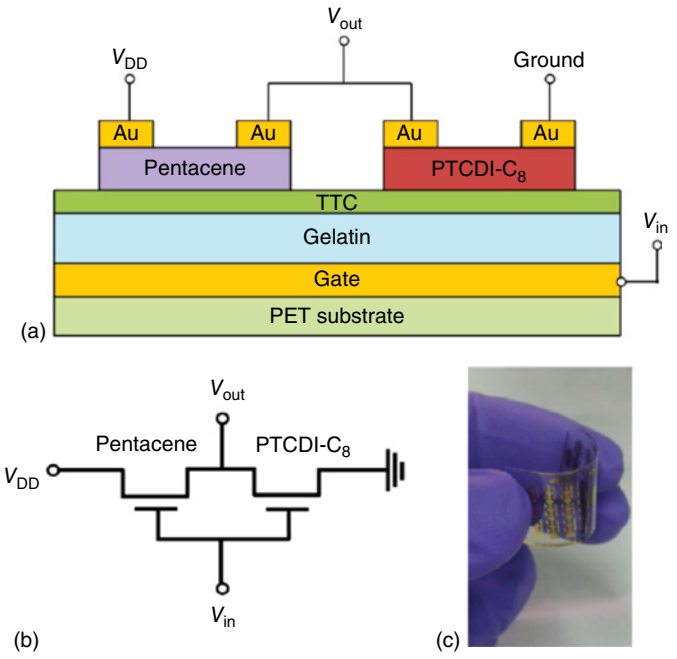

Figure 1.20 (a) Schematic of the inverter device fabricated on plastic substrate with gelatin as gate dielectric; (b) diagram of the circuit; and (c) photograph of the flexible CMOS inverter. (Mao *et al*. 2015 [75]. Reproduced with permission of Elsevier.)

solution-based gelatine dielectric and no TTC. Another interesting application of gelatine is in the field of polymer composites. The emerging field of degradable bioelectronics and biomedical devices requires materials that have tunable properties such as solubility and degradation over a well-defined period of time. The work of Acar *et al*. [46] demonstrated that gelatine filler, when added to PVA as polymer matrix, can significantly influence the material performance. The biodegradability and nontoxicity of both materials is very well known, which make them ideal candidates for transient electronics [76]. In this respect, the work of Acar *et al*. showed that an increasing amount of gelatine in the PVA–gelatine composite leads to a decreasing solubility of the polymer film and therefore to a controlled dissolution of the layer when employed in electronics fabrication.

Another very interesting approach was the fabrication of an edible supercapacitor made out of food-based components by Wang *et al*. who used gelatine as a packaging material [77]. A schematic structure of the "green" supercapacitor is presented in Figure 1.21.

By employing all edible materials (activated charcoal for the electrodes, Gatorade fluid for the electrolyte, seaweed for the separator membrane, cheese as the segregation layer, gold leaf for collector electrodes, and gelatine as encapsulate), the authors demonstrated the amenability of the design to successfully act as electric source. The edible supercapacitor design was able to support the functionality of a USB camera when connecting in series 5 such fully charged 4 cm × 4 cm square (electrode area) supercapacitors. The series of supercapacitors was able to supply

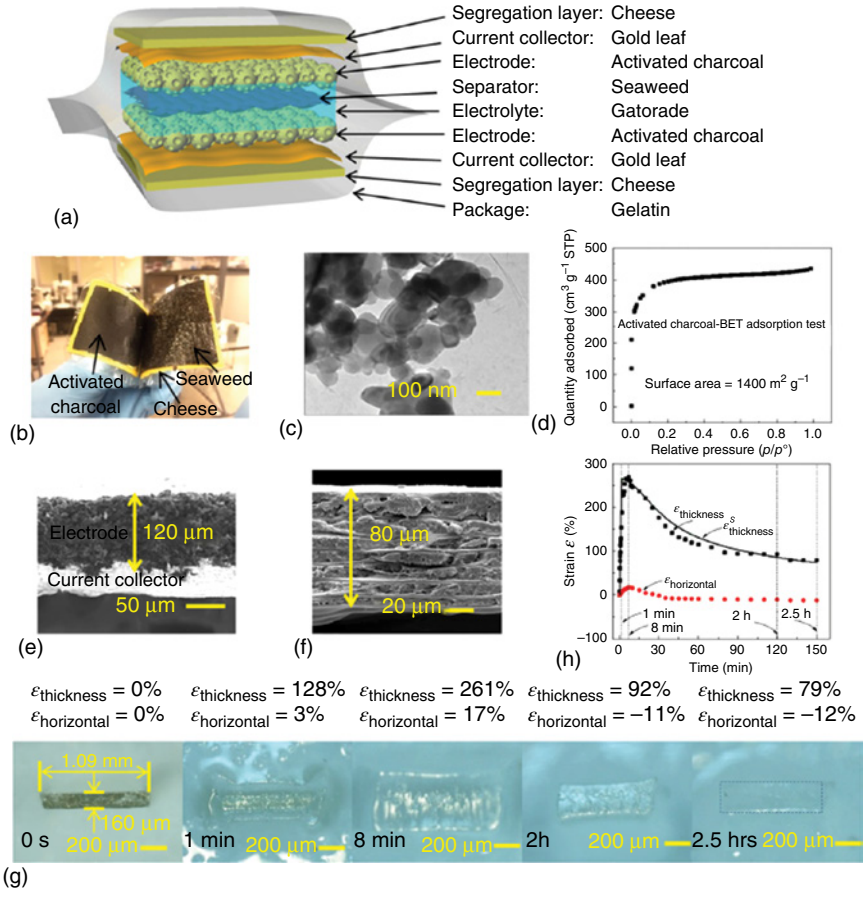

Figure 1.21 (a) Schematic of the materials employed for the fabrication of edible supercapacitors; (b) photograph of the device; (c) transmission electron microscopy image of the activated charcoal; (d) the employed test, Brunauer–Emmett–Teller, to calculate the surface area of the activated charcoal; (e) scanning electron microscopy image of the cross section of the activated charcoal electrode; (f) cross-section SEM image of the seaweed separator; (g) dissolution test of the gelatine encapsulate; and (h) the time evolutions of the strains showing both experiments and simulations. (Wang *et al*. 2016 [77]. Reproduced with permission of John Wiley and Sons.)

the required 3.3 V necessary to power the camera, which recommends the design for further development of implantable biomedical devices.

From an ecological point of view, gelatine is a non-problematic material. Gelatine is produced from leftovers in meat processing plants that would otherwise be discarded, and therefore it is sustainable. Its composition is a mixture of peptides and proteins produced by partial hydrolysis of collagen extracted from the bones, skin, and connective tissues of animals. It seems reasonable to believe that future electronics development will harvest the high versatility of gelatine imparted by many possibilities of its chemical modification for the achievement of biocompatible stretchable and conformable electronic devices.

1.10 Proteins, Peptides, Aminoacids

New developments in science and technology demand sophisticated materials of very high quality. An unusual source of inspiration for electronic materials comes from things we see or touch on a daily routine. One very good example is the work of Chang *et al.* [78] who used albumen, nothing else but the chicken egg white, as gate dielectric in pentacene- and C_{60}-based OFETs. The albumen film showed impressive dielectric behavior and surface smoothness, with a measured rms roughness of ~1.5 nm, which made it suitable for OFET device fabrication. Figure 1.22A left frame shows the schematic of the device. The specific capacitance of albumen is 12 nF cm^{-2} with a dielectric constant of 5.3–6.1. Figure 1.22Ba,b shows output and transfer characteristics of a pentacene-based OFET with albumen as gate dielectric. Samples prepared with a C_{60} semiconducting layer show similarly remarkable characteristics. Noticeably, both the n- and the

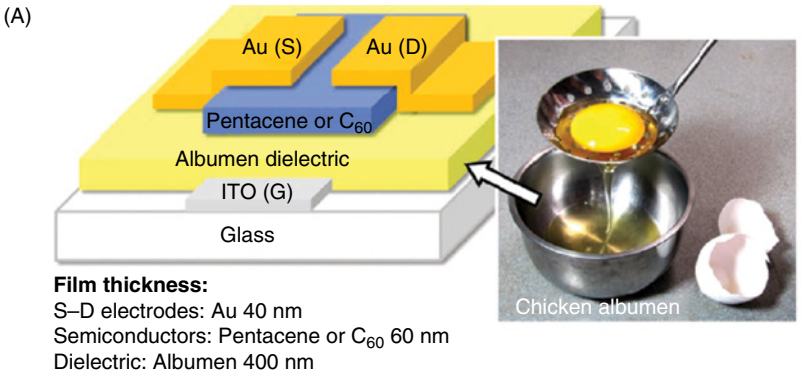

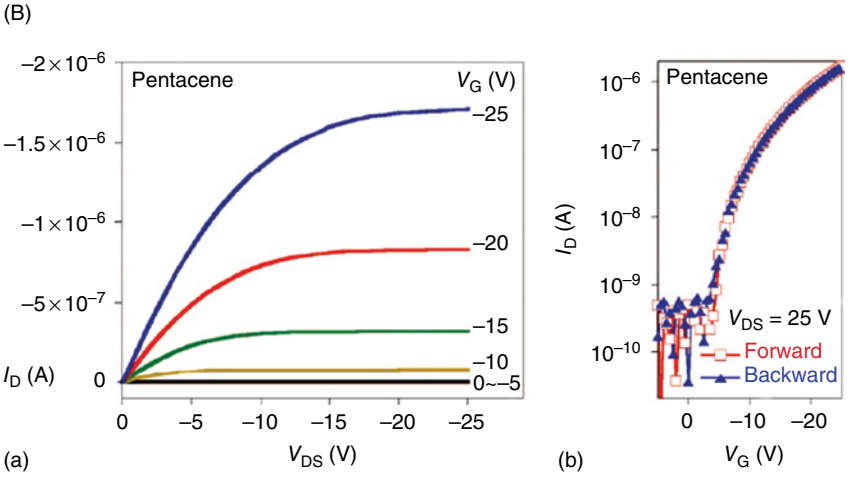

Figure 1.22 (A) OFET schematic employing cross-linked egg white and pentacene for the organic dielectric semiconductor respectively and (B) transfer and output characteristics for the fabricated devices. (Chang *et al.* 2011 [78]. Reproduced with permission of John Wiley and Sons.)

p-type devices display no obvious hysteresis, credited to the low trap density and smoothness of the dielectric layer.

In a very interesting publication, Wu *et al.* showed that by carefully controlling the level of hydration in egg white layer dielectric, and therefore the proton migration in polypeptide chains under electric field, one can mimic the synaptic activity in brain by using multiple in-plane gates in an indium tin oxide, ITO floating gate with indium zinc oxide, IZO semiconductor field-effect transistor (Figure 1.23Aa) [79]. Figure 1.23Ab shows the transfer curves of the TFT, where the nonvolatile memory effect is shown for various scan rates and ranges of the gate voltage with a maximal hysteresis window of 4 V obtained at 8 V applied V_{gs} voltage. The interesting characteristic of this configuration is that the synaptic device can form a

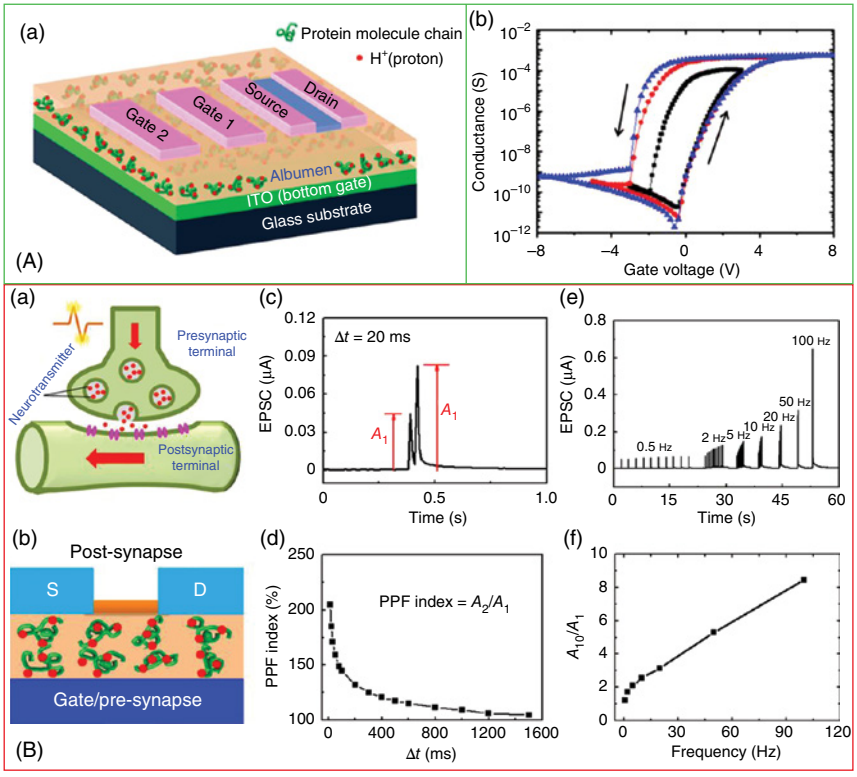

Figure 1.23 (A) (a) Schematic of the albumen-gated IZO-based synaptic transistor with two in-plane gates used to trigger the current spike formation; (b) recorded nonvolatile memory measurements at various scan rates and voltage ranges; (B) (a,b) schematic of the neuronal synapse and the fabricated TFT device that mimics the biological function; (c–f) various figures of merit of spikes modulation and their recording: (c) a pair of applied presynaptic spikes called paired pulse facilitation (*PPF*) triggering the EPSC under an interspike interval of 20 ms; (d) the PPF index plotted versus interspike interval Δt; (e) the dynamic filter behavior of the albumen-gated synaptic transistors a function of the stimulus train for various applied frequencies; (f) the EPSC amplitude gain as a function of pulse frequency [79]. (Wu *et al.* 2016, http://www.nature.com/srep/2016/160324/srep23578/full/srep23578.html. Used under CC-BY-4.0 http://creativecommons.org/licenses/by/4.0/.)

connected network with the in-plane gates through strongly lateral electric-double-layer (EDL) coupling, and thus mimic the spike-modulated movement of the neurotransmitters in biological synapses such as in the human brain. In our brain, the most important functions, including learning, signal processing, and memory, are controlled by precise modulation of ion fluxes through neurons and synapses. Neurotransmitters are transported through ion fluxes and can modulate the synapse efficiency by establishing a connection between the presynaptic and postsynaptic neurons (Figure 1.23Ba). The figure of merit of the synaptic strength is the ionic excitatory postsynaptic potential (*EPSP*), which is nothing else but a momentary current caused by the movement of ions into the postsynaptic neuron as a consequence of the presynaptic neuron spike. In this ingenuous representation of

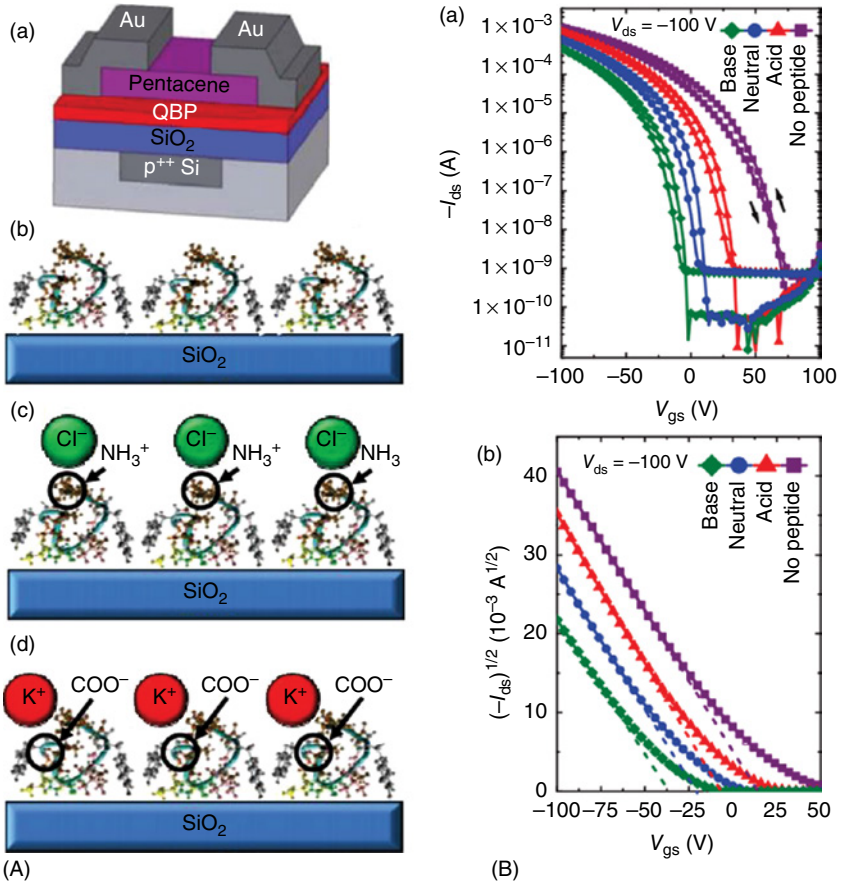

Figure 1.24 (A) (a) Schematic of a peptide-modified thin-film transistor; studied cases of peptide assembly in: water (b) where no ions are present to pair with peptide termini; in acidic solution (c) where, the N-termini of the peptide pair with chloride ions to produce a dipole pointing away from the substrate surface; and in basic solution (d) where the C-termini pair with potassium ions to produce a dipole pointing toward the substrate surface. (B) Transfer characteristics of the device showing the controllable shift of the threshold voltage. (Dezieck *et al*. 2010 [80]. Reproduced with permission of AIP Publishing.)

an electronic circuit that mimics biological actions, the ITO bottom-gate electrode and IZO source/drain electrodes containing channel layer are nothing but the presynaptic and postsynaptic terminals, respectively; the albumen film and its constituent ions (protons) are regarded as the synaptic fork and neurotransmitters respectively; the channel current (I_{ds}) is regarded as the excitatory postsynaptic current (*EPSC*), which is considered here instead of the potential (EPSP) to demonstrate the existence of the presynaptic spike (Figure 1.23Bb). It is in fact this presynaptic spike supplied by the gate electrodes G1 and/or G2 that triggers the proton transport within the albumen and consequently the modulation of the channel current.

An OFET has parameters that can be tuned in order to improve device performance. One such important factor is the threshold voltage (V_T). Dezieck *et al.* found a way to control V_T in organic thin-film transistors with a dielectric layer modified by a genetically engineered polypeptide [80]. Controlling V_T can yield higher circuit performance and lower power consumption in electronics. In their work they used a genetically engineered peptide for inorganics (*GEPI*s), basically a quartz binding polypeptide (*QBP*) of a specific amino acid sequence, which preferentially and strongly binds to silicon dioxide (SiO_2). The authors prepared different solutions of aqueous QBP with varying pHs to modify the organic semiconductor–SiO_2 interface in an OTFT and tune the threshold voltage through the control of the peptide assembling conditions as shown in Figure 1.24. OTFTs modified with QBP were assembled on SiO_2 under basic, neutral, and acidic conditions with and without peptide. A positive shift in V_T was observed when QBP was assembled in acidic conditions, whereas a negative shift in V_T was observed when QBP was assembled in basic solutions.

1.11 Natural and Nature-Inspired Semiconductors

There are a number of molecular materials of natural origin that are intrinsically semiconducting and can be used as active components in (opto) electronic devices. Some of the compounds responsible for photosynthesis, for example, are chromophores with extensive conjugation, such as porphyrins and polyenes. Their chemical structures closely resemble the ones of many of the synthetic, conjugated semiconductors. Tang and Albrecht processed thin films of chlorophyll *a* to produce sandwich-type photovoltaic diodes in 1975, representing a seminal example of harnessing a naturally available semiconductor in a solid-state device [81]. Since then, chlorophyll was used in solid-state photovoltaic diodes; however, low power conversion efficiency and poor charge transport, and in particular operational stability were major problems of those pioneering devices. In the early 1990s, Moses *et al.* explored the consequences of the similarity of beta-carotene with the well-known conducting polymer polyacetylene [82]. Like polyacetylene, carotene was found by the authors to have spinless solitons upon doping, which indicated its suitability for applications in organic electronics. Beta-carotene semiconductor was solution processed from chloroform solution to make films suitable for thin-film transistors, with hole mobility of $1 \times 10^{-4}\,cm^2\,V^{-1}\,s^{-1}$ and also explored in bulk heterojunction organic photovoltaic

devices, nevertheless with modest performance [83, 84]. As in the case of chlorophyll *a*, operational stability was a major problem, as beta-carotene rapidly oxidized when exposed to ambient oxygen. Evolution has not endowed these natural conjugated chromophores with long-term stability. Indeed, the metabolism of living systems continuously regenerates these molecules.

Over the course of human history, people were surrounded by natural colors, but found that very few of them could be used to make stable pigments or dyes. Through a long selection process, a few natural-origin chromophores emerged as suitable colorants for artistic purposes [85, 86]. Nearly all of the organic materials utilized as dyes and pigments prominently feature both intra- and intermolecular hydrogen bonding, which leads to the desired coloristic properties and most importantly promotes stability. These molecules are relatively small one or two condensed ring structures with carbonyl and often amine functional groups, which are sometimes colorless when dissolved in true solutions [87–89]. Hydrogen bonding mediates aggregation and crystallization and leads to marked bathochromic shifts in absorption upon aggregation. In this way, small molecules that are intrinsically stable assemble into crystals with a strong UV–vis absorption and additional stability afforded by high crystal lattice energy. It is this family of so-called hydrogen-bonded pigments that holds promise as a natural source of stable semiconductors. Indigo is one of the most well-known natural-origin dyes used throughout history, with different derivatives obtainable from plant and animal sources (Figure 1.25a,b) [91, 92]. Owing to its high crystal lattice energy, indigo is not soluble in its neutral form; therefore, fabric dyeing technique relies first on a chemical reduction step to obtain a water-soluble leucoindigo (Figure 1.25c).

After allowing leucoindigo to penetrate into the fibers, the textile is withdrawn into air where oxygen oxidizes the leucoindigo back into the insoluble neutral blue-colored form, giving a permanent coloration to the fabric. This process of so-called vat dyeing highlights also the versatile and reversible redox states of these types of molecules. Besides being known to be nontoxic (i.e., indigo carmine, the sodium sulfate salt of indigo is an approved food colorant), indigo is the single most widely produced industrial dyestuff, with 20 000 tons per year used only for the dyeing of blue denim fabric [93]. Reproducing the vat dyeing technique of indigo processibility for organic electronics fabrication is not desirable because of the inherent ionic content of the deposited film. Interestingly though, indigo sublimes and can be scrupulously cleaned through train sublimation technique; thin films of pure indigo can be therefore deposited via vacuum sublimation at temperatures below 300 °C in high vacuum chambers. Mainly due to its stability (indigo has reasonably good fading resistance against UV radiation) and easy processibility, indigo was identified as a promising semiconducting material for organic electronics. Irimia-Vladu *et al.* reported in 2012 that indigo was an ambipolar semiconductor with balanced electron and hole mobilities of $1 \times 10^{-2}\,cm^2\,V^{-1}\,s^{-1}$ and good stability against degradation. In their seminal work, the authors vacuum-processed an indigo semiconductor using TTC as a gate dielectric material (discussed in Section 1.6) and shellac resin as a substrate (Section 1.8) [72]. Their effort represented the first thin-film transistor fabricated exclusively from natural-origin materials (Figure 1.26).

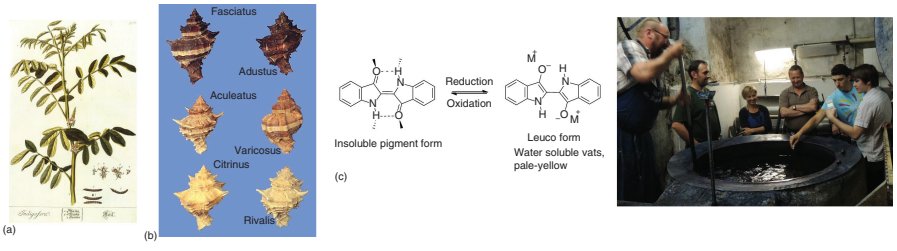

Figure 1.25 (a) Image of *Indigofera tinctoria*, the tropical source of indigo; (b) various snails from the Muricidae and Thaisidae families represented the natural source of Tyrian purple dyes; (c) the chemistry of vat dyeing involving the reduction of indigos to produce an aqueous solution of $Indigo^{-1}$ (indigo radical), and $indigo^{-2}$ (fully reduced, known as leuco or "white" indigo) with various metal counterions, most typically K^+ and Na^+. The photo shows two of the authors visiting a traditional indigo vat dyeing facility in Bad Leonfelden, Austria (EDG-right, white shirt, and MIV-left, green shirt). (Głowacki *et al*. 2013 [90]. Reproduced with permission of John Wiley and Sons.)

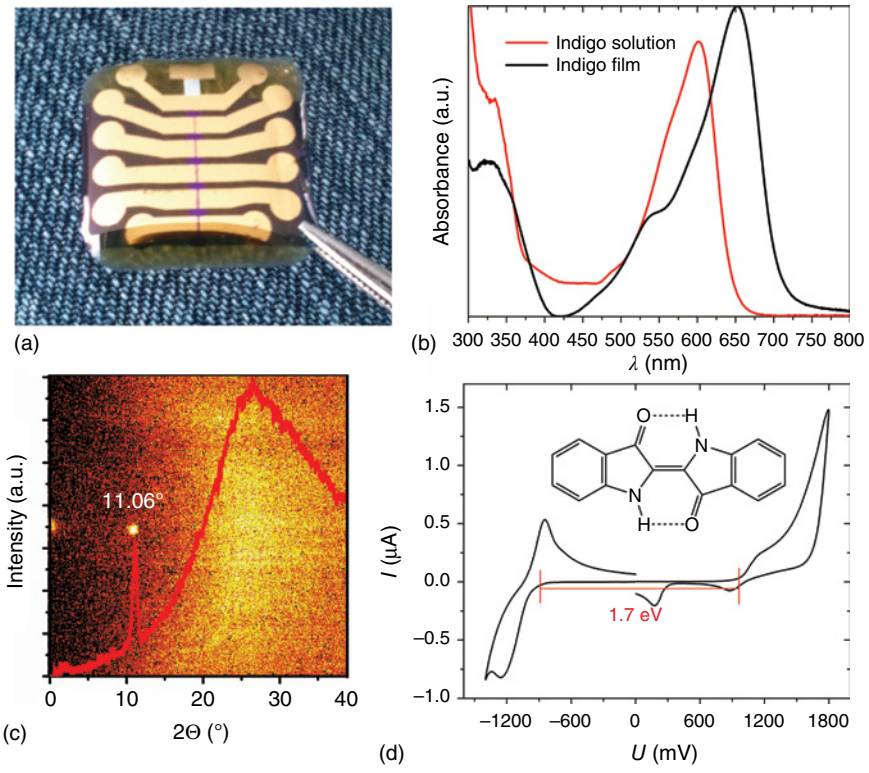

Figure 1.26 Indigo field-effect transistors: (a) Photograph of ambipolar indigo transistors fabricated on shellac with aluminum oxide-tetratetracontane dielectric and gold source and drain electrodes; (b) optical absorption spectra of an indigo solution in chloroform (red) and of a thin evaporated indigo film (black), showing a bathochromic shift of absorbance onset of ~100 nm in the indigo film in comparison to the solution; (c) XRD of an indigo thin film grown by thermal evaporation on tetratetracontane; and (d) cyclic voltammetry scans of indigo films using ITO|indigo as the working electrode. The quasireversible two electron exchange electrochemistry correctly predicts the possibility of ambipolar transport in indigo molecule. (Irimia-Vladu *et al.* 2012 [72]. Reproduced with permission of John Wiley and Sons.)

Tyrian purple, 6,6′-dibromoindigo, a natural pigment extracted historically from Mediterranean Sea snails (Figure 1.25b) was also found to be an ambipolar semiconductor in transistors and was used to fabricate near-infrared-absorbing heterojunction diodes with silicon [94–96]. van der Waals interactions between bromine atoms promote enhanced π–π stacking in Tyrian purple, leading to balanced electron and hole mobilities in the range of $0.4\,cm^2\,V^{-1}\,s^{-1}$ [95]. The crystal structures of both molecules helps explaining the observed charge transport behavior (Figure 1.27). While intermolecular hydrogen bonds cause the indigo molecules to arrange into hydrogen-bonded chains, these chains π–π stack along the axis perpendicular to the hydrogen-bonding axis. It was found in various studies that the orientation of the growing crystals with respect to the substrate has a profound effect on the occurrence of charge transport [97, 98]. The π–π stacking axis, for instance, must be parallel to the gate dielectric in order to

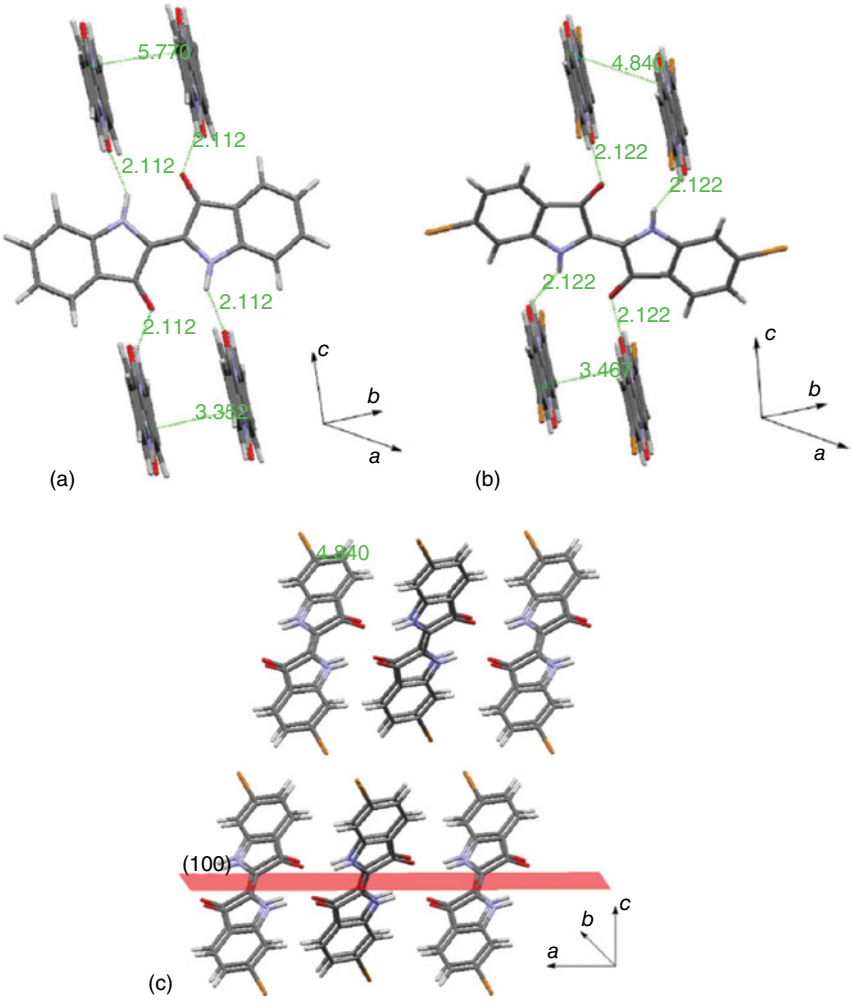

Figure 1.27 (a) Indigo crystal structure showing the interplanar spacing along the b-axis between two stacked indigo molecules (3.352 Å) and the interatomic distances between two equivalent positions (5.77 Å); (b) Tyrian purple (6,6′-dibromoindigo) crystal structure, having an interplanar spacing of 3.46 Å, and an interatomic distance between two equivalent positions of 4.84 Å; and (c) Tyrian purple view along the b-axis (stacking direction). The only visible peaks of Tyrian purple when grown on hydrophobic (low surface energy) gate dielectrics are [100] and other [*h*00]. This kind of stacking parallel to the substrate is ideal for obtaining charge transport between source and drain electrodes in OFET design. (Głowacki *et al*. 2013 [90]. Reproduced with permission of John Wiley and Sons.)

obtain good charge mobility in thin-film transistor geometry [72, 90, 99]. Several successful examples of chemically modified indigos, some with extended π-conjugation, have been shown in organic transistor applications [100, 101]. The substitution of indigo can alter packing and crystallization and lead to large changes in mobility. Moreover, the anisotropic nature of transport, wherein one crystallographic axis dominates in contributing to charge transport, leads to vast

differences in observed charge transport behavior, depending on substrate properties and deposition conditions.

The term hydrogen-bonded pigments, although accurate in describing the naturally derived materials discussed above, historically originated with respect to organic-molecular solid-state colorants of synthetic origin [102]. This term entered the field of industrial organic pigments since the introduction of hydrogen-bonded groups was recognized for promoting stability and allowing control on aggregation behavior (i.e., polymorphism and crystallochromy), which ultimately led to obtaining the desired colors [103]. Industrial pigment chemists and technologists, however, normally categorize colorants by their chemical "family" – for example, azo compounds, phthalocyanines, and quinacridones. Many compounds from these families can be considered as belonging to the hydrogen-bonded pigment class [104]. Most of these materials are generally considered nontoxic; due to their intense lack of solubility they are simply not bioavailable, but only synthetically produced. Only a few of these materials have been studied in detail with results published in scientific literature with respect to their electro-optical properties or even biodegradation amenabilities. A much larger body of knowledge exists, however, in the realm of patents and technological and engineering bulletins, but the reported properties of those dyes and pigments are restricted to their practical colorant properties. Some pigments have been studied for their toxicological and environmental impact, in the context of their deployment on a large scale in consumer products such as outdoor paint formulations, printing inks, various cosmetic formulations as well as tattoos [105].

One of the most prominent synthetic hydrogen-bonded pigments, produced on an industrial scale, is quinacridone [106]. Quinacridone is best known as the magenta pigment for printing inks, but is also found in paints and cosmetic products [104]. Quinacridone was explored as an active material for solar cells [107] and thin-film transistors, achieving hole mobilities of $0.1\,cm^2\,V^{-1}\,s^{-1}$, with about one order of magnitude lower electron mobility [55]. Quinacridone, however, is characterized by excellent operation stability in devices operated in ambient air without encapsulation [55]. Another interesting hydrogen-bonded molecule with an outstanding stability is epindolidione, which is nothing else but a structural isomer of indigo. Different than quinacridone, epindolidione does not have a straight forward synthetic route, but alternatively can be synthesized by a high-temperature solid-state thermal rearrangement of indigo in high vacuum [55, 108]. Epindolidione also shows ambipolar charge transport as its isomer indigo, but outplays indigo in performance, affording hole mobilities greater than $1\,cm^2\,V^{-1}\,s^{-1}$ [109]. Quinacridone and epindolidione are luminescent both in dilute solution and in solid state, whereas indigo is not, because of the ultrafast photoinduced proton transfer that leads to very efficient nonradiative deactivation of its excited state (Figure 1.28). Epindolidione and quinacridone demonstrate various excimeric and defect-luminescence behavior in solid state, apparently due to the intermolecular hydrogen-bonding interaction, which contributes to efficient delocalization of excited states between neighboring molecules [109, 110]. For bioelectronics applications, epindolidione and quinacridone have promising properties mainly because of their stability and amenability for further functionalization. Glowacki *et al.* showed that thin-film transistors with

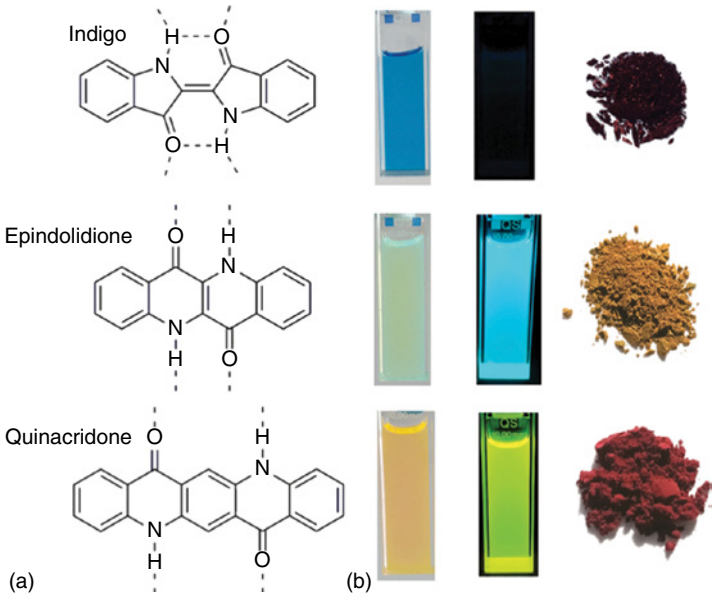

Figure 1.28 (a) Molecular structures of indigo, its isomer epindolidione, and quinacridone, with dashed lines indicating hydrogen bonding; (b) solutions of 0.1 mM of each material in dimethyl sulfoxide (*DMSO*), with photoluminescence excitation at 365 nm. Epindolidione and quinacridone are highly emissive, while indigo shows very low luminescence quantum yield. On the right, the powders of the three pigments are shown, where the bathochromically shifted absorption and tinctorial strength are visible compared to their respective solution. (Głowacki *et al*. 2015 [109]. Reproduced with permission of John Wiley and Sons.)

epindolidione semiconductor could be fabricated to operate in a low-voltage window by using ultrathin alumina dielectric layers (Figure 1.29) [109]. Such devices operated stably in a pH range from 3 to 10 over hundreds of cycles in direct contact with electrolytic solutions, without the need of passivation. Both epindolidione and quinacridone can be bioconjugated easily via nucleophilic attack of the amine functional groups on *N*-succinimidyl esters, which can in turn be used as linkers to covalently attach biomolecules of interest to the surface of the hydrogen-bonded semiconductor (Figure 1.30) [111]. The authors demonstrated successful linking of a photosynthetic reaction center protein to the semiconductor epindolidione and quinacridone molecules, with confirmed preservation of both protein and semiconductor functions after bridging. The outstanding stability of epindolidione and quinacridone in aqueous solutions is further underscored in their photoelectrocatalytic performance in reducing oxygen selectively to hydrogen peroxide, which represents a valuable molecule for a plethora of biological contexts. Jakešová *et al*. showed that these photocathodic reactions can proceed in a pH range from 1 to 12 over at least 4 days of continuous operation, with some experiments recording more than 2 weeks of stable operation at pH 1 (Figure 1.31) [112]. The unique photocatalytic ability of these two pigments is enabled by the combination of a high-lying (and thus highly-reductive) LUMO level with their inherent stability – normally organic

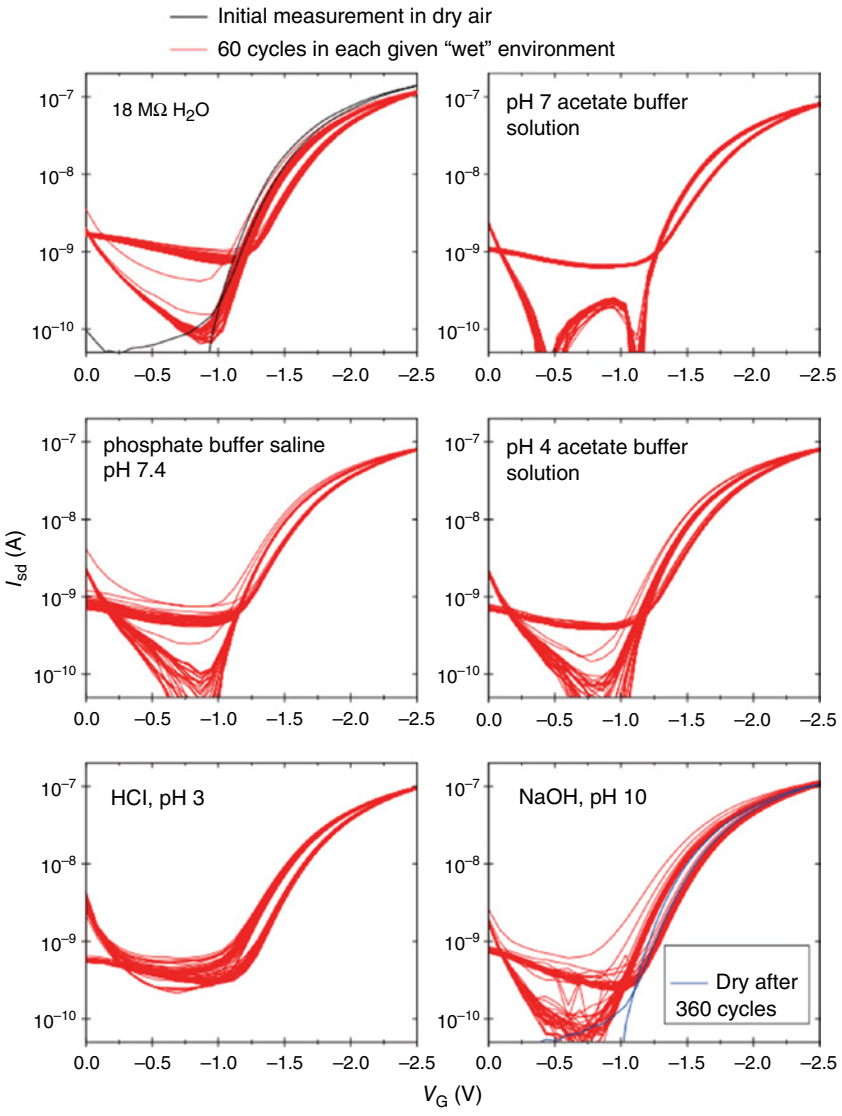

Figure 1.29 Low-voltage operating OFETs with epindolidione semiconductor fabricated on thin aluminum oxide dielectric. The devices were measured with an applied source–drain voltage, $V_{ds} = -0.5$ V in air (black curve) followed by 360 cycles in six different aqueous environments, with 60 cycles carried out in each medium (red curves). Samples were rinsed with deionized water when moving from one electrolyte to another. (Głowacki *et al*. 2015 [109]. Reproduced with permission of John Wiley and Sons.)

semiconductors with such high-lying states are unstable in oxygenated or water-containing environments. The stability of these pigments, enabling catalysis, represents a new direction for organic semiconductors research, and the recent progress of the use of quinacridone in organic semiconducting devices has been recently reviewed [113].

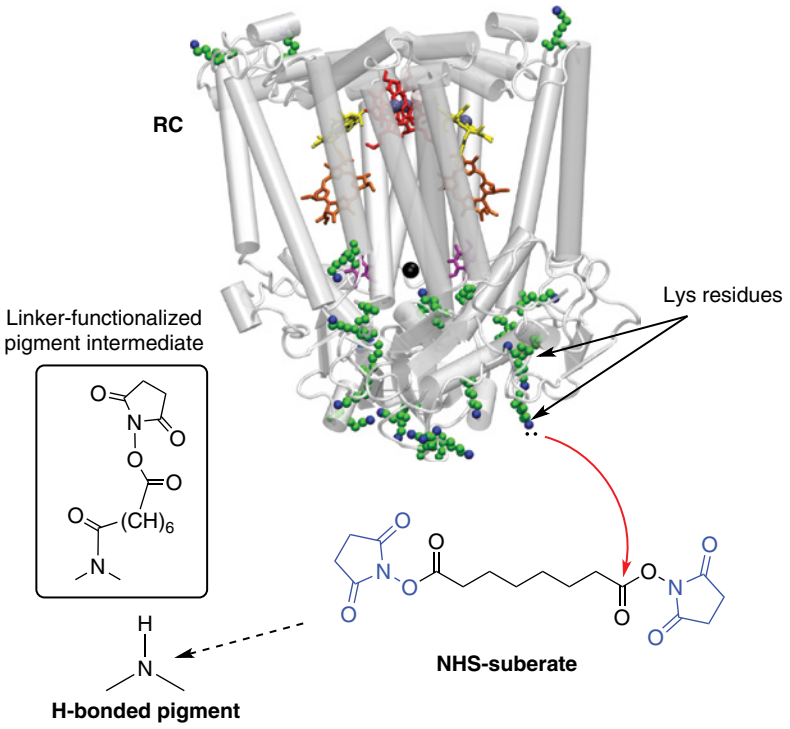

Figure 1.30 The proposed bioconjugation procedure of the *Rhodobacter sphaeroides* photosynthetic reaction center (*RC*) to hydrogen-bonded pigments (quinacridone and epindolidione) using the disuccinimidyl suberate linker. The *N*-succinimidyl ester (NHS) function on the linker is introduced in order to selectively address the amine nucleophiles on the pigments. The NHS groups that are cleaved during the bioconjugation process are shown in blue. The crystal structure of the RC with its 22 lysine residues available for conjugation is shown at the top of the figure [111]. (Glowacki *et al*. 2015, http://pubs.rsc.org/en/Content/ArticleLanding/2015/TC/c5tc00556f#!divAbstract. Used under CC-BY-3.0 http://creativecommons.org/licenses/by/3.0/.)

Apart from indigos and quinacridones, flavanthrone and indanthrone pigments (synthetic derivatives of anthraquinones) are also produced in large scale and widely employed as dyestuffs and cosmetic colorants. They have also shown promising performance in organic transistor devices and light-emitting diodes, as demonstrated through several publications [83, 114, 115].

Many of the above-mentioned compounds and classes of compounds (either hydrogen bonded or not) have as a common feature the high crystal lattice energy that makes their processibility difficult via solution and sometimes even via vacuum sublimation routes. Indeed, some dyes and pigment molecules cannot be processed in their purest form (e.g., vat blue 20, vat green 8 and its isomers, and many others anthraquinones), and can be used only as dispersions afforded by the presence of a specific surfactant. All hydrogen-bonded pigments are characterized in fact by very low solubility in organic or aqueous solvents. Typically, stable solutions can only be obtained in relatively low concentrations on the order of 0.1–0.2 mM in highly polar hydrogen-bond-forming solvents such as dimethyl sulfoxide or

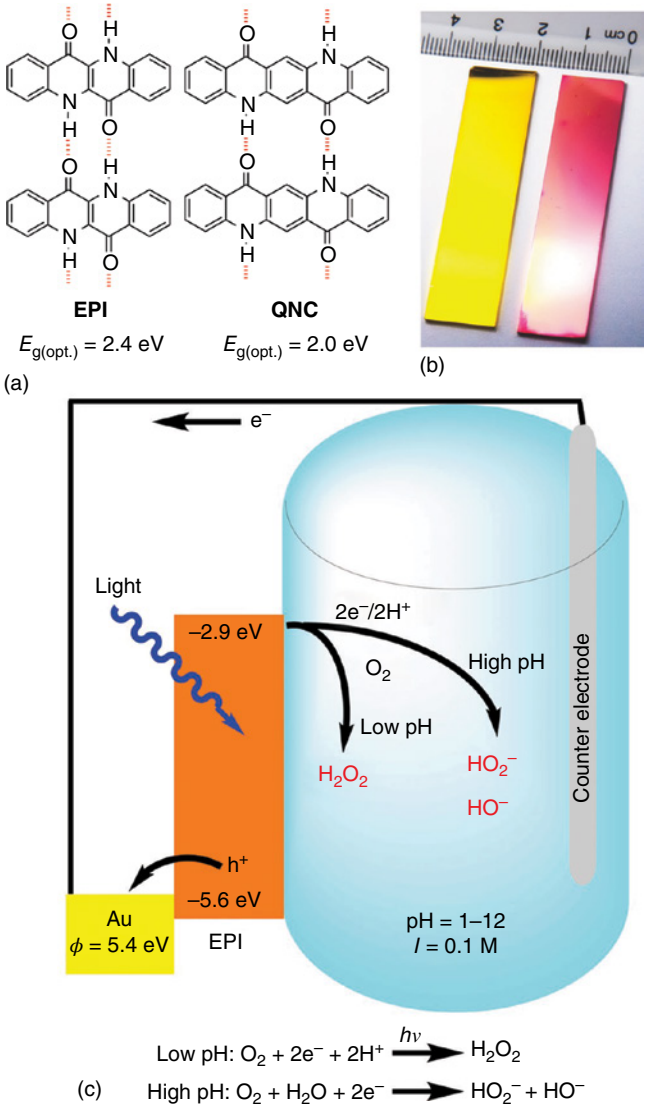

Figure 1.31 (a) Molecular structure of hydrogen-bonded pigment semiconductors epindolidione (*EPI*) and quinacridone (*QNC*) with the measured optical band gap at the bottom; (b) EPI (left) and QNC (right) photoelectrodes, consisting of thin polycrystalline films vacuum deposited on gold coated glass slides; and (c) schematic of the photoelectrochemical measurement setup with EPI semiconductor electrode. The measurement involved aqueous electrolytes in the pH range 1–12. Oxygen reduction reactions at low and high pH levels occur via the equations shown. (Jakešová *et al*. 2016 [112]. Reproduced with permission of John Wiley and Sons.)

dimethylformamide. This property impedes any reliable solution processibility of devices and also limits the range of chemical reactions that can be used to modify the fundamental pigment chromophores. Substituting the pigment-forming molecules with large alkyl chains can impart some solubility in organic solvents, yet

hydrogen bonding leads to rapid aggregation. An alternative strategy is transient substitution of the hydrogen-bonding functional groups with a protecting group that can be cleaved in a controlled way. Zambounis *et al.* reported the so-called latent pigment approach by attaching a *tert*butoxy carbonyl functional group (*tBOC*) to the amine function of the pigments using the highly reactive dianhydride of *t*BOC [116]. This design effectively blocks any hydrogen-bond formation and leads to dyes with very high solubilities in typical organic solvents. The *t*BOC group can be irreversibly degraded by heat treatment or acid vapor exposure, leading to gaseous byproducts. Zambounis *et al.* used this technique for technical coloristic purposes, whereby a latent pigment could be processed and then deprotected at a specific processing step. This procedure can be used to disperse pigment particles uniformly in host polymer films, for example [117]. This method can be used for the solution processing of indigos and quinacridones, and can yield derivatives that are soluble and therefore amenable to multistep synthetic modification [118, 119]. It can also be used to produce blends of indigos with semiconducting polymers such as polythiophenes or to synthesize controlled colloids of nano- and microcrystals. When the *t*BOC protected form of a pigment is dissolved and then chemically or thermally deprotected in the presence of various ligands, colloidal crystals can be grown with tunable size and shape (Figure 1.32). This procedure

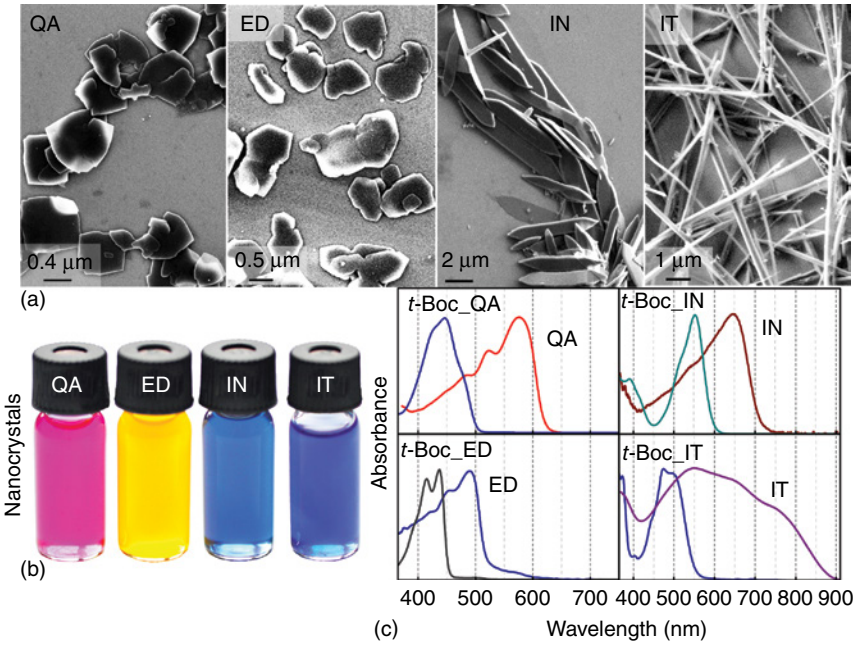

Figure 1.32 (a) Electron micrographs of the colloidal micro-nanocrystals of organic pigments on a Si substrate (*QA*, quinacridone; *ED*, epindolidione; *IN*, indigo; *IT*, indanthrene). The pigments were synthesized by cleavage of the thermolabile *t*BOC protection groups from the latent pigment precursors; (b) image of the vials containing the colloidal dispersions; and (c) absorbance spectra of the latent pigment precursors and the synthesized organic pigment micronanostructures [120]. (Sytnyk *et al.* 2014, https://www.ncbi.nlm.nih.gov/pmc/articles/PMC4277760/. Used under CC-BY-4.0 http://creativecommons.org/licenses/by/4.0/.)

yields semiconducting crystals that can be solution processed and used directly in field-effect transistors or photodiodes [120].

The hydrogen-bonded pigment class of materials holds promise for sustainable electronics since the materials are robust and multifunctional and many are well-developed industrially, providing low cost with proven stability. Application of these materials in organic optoelectronics offers motivation for synthetic chemists to again focus their attention on this "old" materials class, and it is likely that research in functional materials based on hydrogen-bonded pigments will expand in the future.

1.12 Perspectives

A decade ago, the vision of green and sustainable electronics was not more than pie in the sky, with hesitant approaches toward biodegradable and even edible electronics. Initially seen as an exotic category of cross-disciplinary materials science, "green" electronics became a distinct and booming research area. A wealth of nature-inspired and natural substrates, dielectrics, and semiconductors is now available, useful in support structures and thin-film forms for electronic and optoelectronic devices. Nevertheless, there is still a long way to go until we can dream of a technological era with responsible handling of materials and resources. There are ample opportunities for research, ranging from the identification of sufficiently stable natural materials employable for device design, development, and optimization to the fabrication of prototypes close to commercialization. In the end, we may have a pluripotent platform of lasting technologies for electronics and photonics, changing the way we perceive electronic and photonic systems, with applications spanning smart appliances, sports, healthcare, and well-being.

References

1 Rogers, J.A., Someya, T., and Huang, Y. (2010) Materials and mechanics for stretchable electronics. *Science*, **327** (5973), 1603–1607.

2 Wagner, S. and Bauer, S. (2012) Materials for stretchable electronics. *MRS Bull.*, **37** (03), 207–213.

3 Bauer, S., Bauer-Gogonea, S., Graz, I., Kaltenbrunner, M., Keplinger, C., and Schwödiauer, R. (2014) 25th Anniversary article: a soft future: from robots and sensor skin to energy harvesters. *Adv. Mater.*, **26** (1), 149–162.

4 Chortos, A., Liu, J., and Bao, Z. (2016) Pursuing prosthetic electronic skin. *Nat. Mater.*, **15**, 937–950.

5 Rogers, J. and Balooch, G. (2016) A restorative synthetic skin. *Nat. Mater.*, **15**, 828–829.

6 Kim, D.-H., Lu, N., Ma, R., Kim, Y.-S., Kim, R.-H., Wang, S., Wu, J., Won, S.M., Tao, H., Islam, A., Yu, K.J., Kim, T., Chowdhury, R., Ying, M., Xu, L., Li, M., Chung, H.-J., Keum, H., McCormick, M., Liu, P., Zhang, Y.-W., Omenetto, F.G., Huang, Y., Coleman, T., and Rogers, J.A. (2011) Epidermal electronics. *Science*, **333**, 838–843.

7 Kim, Y.J., Chun, S.E., Whitacre, J., and Bettinger, C.J. (2013) Self-deployable current sources fabricated from edible materials. *J. Mater. Chem. B*, **1** (31), 3781–3788.

8 Norton, J.S., Leeb, D.S., Lee, J.W., Lee, W., Kwon, O., Won, P., Jung, S.-Y., Cheng, H., Jeong, J.-W., Akce, A., Umunna, S., Nad, I., Kwon, Y.H., Wang, X.-Q., Liu, Z.J., Paik, U., Huang, Y., Bretl, T., Yeo, W.-H., and Rogers, J.A. (2015) Soft, curved electrode systems capable of integration on the auricle as a persistent brain-computer interface. *Proc. Natl. Acad. Sci. U.S.A.*, **112** (13), 3920–3925.

9 Tao, H., Hwang, S.-W., Marelli, B., An, B., Moreau, J.E., Yang, M., Brenckle, M.A., Kim, S., Kaplan, D.L., Rogers, J.A., and Omenetto, F.G. (2014) Silk-based resorbable electronic devices for remotely controlled therapy and in vivo infection abatement. *Proc. Natl. Acad. Sci. U.S.A.*, **111** (49), 17385–17389.

10 2014) *The Global e-waste Monitor 2014: Quantities, Flows and Resources*, United Nations University, Institute for Advanced Study on Sustainability, pp. 1–80.

11 Kang, S.-K., Murphy, R.K.J., Hwang, S.-W., Lee, S.M., Harburg, D.V., Krueger, N.A., Shin, J., Gamble, P., Cheng, H., Yu, S., Liu, Z., McCall, J.G., Stephen, M., Ying, H., Kim, J., Park, G., Webb, R.C., Lee, C.H., Chung, S., Wie, D.S., Gujar, A.D., Vemulapalli, B., Kim, A.H., Lee, K.-M., Cheng, J., Huang, Y., Lee, S.H., Braun, P.V., Ray, W.Z., and Rogers, J.A. (2016) Bioresorbable silicon electronic sensors for the brain. *Nature*, **530**, 71–76.

12 Irimia-Vladu, M. (2014) Green electronics: biocompatible and biodegradable materials and devices for sustainable future. *Chem. Soc. Rev.*, **43**, 588–610.

13 Tobjörk, D. and Österbacka, R. (2011) Paper electronics. *Adv. Mater.*, **23**, 1935–1961.

14 Martins, R., Nathan, A., Barros, R., Pereira, L., Barquinha, P., Correia, N., Costa, R., Ahnood, A., Ferreira, I., and Fortunato, E. (2011) Complementary metal oxide semiconductor technology with and on paper. *Adv. Mater.*, **23**, 4491–4496.

15 Pettersson, F., Österbacka, R., Koskela, J., Kilpelä, A., Remonen, T., Zhang, Y., Inkinen, S., Wilén, C.-E., Bollström, R., Toivakka, M., Määttänen, A., Ihalainen, P., and Peltonen, J. (2014) Ion-modulated transistors on paper using phase-separated semiconductor/insulator blends. *MRS Commun.*, **4**, 51–55.

16 Pettersson, F., Adekanye, D., and Österbacka, R. (2015) Stability of environmentally friendly paper electronic devices. *Phys. Status Solidi A*, **212**, 2696–2701.

17 Barr, M.C., Rowehl, J.A., Lunt, R.R., Xu, J., Wang, A., Boyce, C.M., Im, S.G., Bulovic´, V., and Gleason, K.K. (2011) Direct monolithic integration of organic photovoltaic circuits on unmodified paper. *Adv. Mater.*, **23**, 3500–3505.

18 Leonat, L., White, M., Glowacki, E., Scharber, M., Zillger, T., Rühling, J., Hübler, A., and Sariciftci, S.N. (2014) 4% efficient polymer solar cells on paper substrates. *J. Phys. Chem. C*, **118**, 16813–16817.

19 Fujisaki, Y., Koga, H., Nakajima, Y., Nakata, M., Tsuji, H., Yamamoto, T., Kurita, T., Nogi, M., and Shimidzu, N. (2014) Transparent nanopaper-based flexible organic thin-film transistor array. *Adv. Funct. Mater.*, **24**, 1657–1663.

20 Zschieschang, U., Yamamoto, T., Takimiya, K., Kuwabara, H., Ikeda, M., Sekitani, T., Someya, T., and Klauk, H. (2011) Organic Electronics on Banknotes. *Adv. Mater.*, **23**, 654–658.

21 Kim, S., Ko, H., Lee, C., Kim, M.K., Kim, K.S., Lee, Y.-H., Shin, K., and Cho, Y.-H. (2016) Semiconductor photonic nanocavity on a paper substrate. *Adv. Mater.*, **28**, 9765–9769, doi: 10.1002/adma.201603368

22 Watson, J.D. and Crick, F.H.C. (1953) A structure for deoxyribose nucleic acid. *Nature*, **171**, 737–738.

23 Paleček, E. and Bartošík, M. (2012) Electrochemistry of nucleic acids. *Chem. Rev.*, **112**, 3427–3481.

24 Yumusak, C., Singh, T.B., Sariciftci, N.S., and Grote, J.C. (2009) Bio-organic field effect transistors based on crosslinked deoxyribonucleic acid (DNA) gate dielectric. *Appl. Phys. Lett.*, **95**, 263304.

25 Steckl, A.J. (2007) DNA – a new material for photonics? *Nat. Photonics*, **1**, 3–5.

26 Hagen, J.A., Li, W., Steckl, A.J., and Grote, J.G. (2006) Enhanced emission efficiency in organic light-emitting diodes using deoxyribonucleic acid complex as an electron blocking layer. *Appl. Phys. Lett.*, **88** (17), 10–13.

27 Steckl, A.J., Spaeth, H., You, H., Gomez, E., and Grote, G. (2011) DNA as an optical material. *Opt. Photonics News*, **22**, 34.

28 Zhang, Y., Zalar, P., Kim, C., Collins, S., Bazan, G.C., and Nguyen, T.-Q. (2012) DNA interlayers enhance charge injection in organic field-effect transistors. *Adv. Mater.*, **24**, 4255–4260.

29 Irimia-Vladu, M., Troshin, P.A., Reisinger, M., Schwabegger, G., Ullah, M., Schwoediauer, R., Mumyatov, A., Bodea, M., Fergus, J.W., Razumov, V., Sitter, H., Bauer, S., and Sariciftci, N.S. (2010) Environmentally sustainable organic field effect transistors. *Org. Electron.*, **11**, 1974–1990.

30 Irimia-Vladu, M., Troshin, P.A., Reisinger, M., Shmygleva, L., Kanbur, Y., Schwabegger, G., Bodea, M., Schwoediauer, R., Mumyatov, A., Fergus, J.W., Razumov, V., Sitter, H., Sariciftci, N.S., and Bauer, S. (2010) Biocompatible and biodegradable materials for organic field effect transistors. *Adv. Funct. Mat.*, **20** (23), 4069–4076.

31 Irimia-Vladu, M., Sariciftci, N.S., and Bauer, S. (2011) Exotic materials for bio-organic electronics. *J. Mater. Chem.*, **21** (5), 1350–1361.

32 Schwabegger, G., Ullah, M., Irimia-Vladu, M., Baumgartner, M., Kanbur, Y., Ahmed, R., Stadler, P., Bauer, S., Sariciftci, N.S., and Sitter, H. (2011) High mobility, low voltage operating C_{60} based n-type organic field effect transistors. *Synth. Met.*, **161**, 2058–2062.

33 Gomez, E.F., Venkatraman, V., Grote, J.G., and Steckl, A.J. (2014) DNA bases thymine and adenine in bio-organic light emitting diodes. *Sci. Rep.*, **4**, 7105.

34 Gomez, E.F., Venkatraman, V., Grote, J.G., and Steckl, A.J. (2015) Exploring the potential of nucleic acid bases in organic light emitting diodes. *Adv. Mater.*, **27**, 7552–7562.

35 Basu, A. (2015) *Advances in Silk Science and Technology*, Elsevier Science & Technology.

36 Kundu, S. (2014) *Silk Biomaterials for Tissue Engineering and Regenerative Medicine*, Woodhead Publishing Ltd.

37 Hota, M.K., Bera, M.K., Kundu, B., Kundu, S.C., and Maiti, C.K. (2012) A natural silk fibroin protein-based transparent bio-memristor. *Adv. Funct. Mater.*, **22**, 4493–4499.

38 Magoshi, J. and Magoshi, Y. (1975) Physical properties and structure of silk. II. Dynamic mechanical and dielectric properties of silk fibroin. *J. Polym. Sci., Part B: Polym. Phys.*, **13**, 1347–1351.

39 Wang, C.-H., Hsieh, C.-Y., and Hwang, J.-C. (2011) Flexible organic thin-film transistors with silk fibroin as the gate dielectric. *Adv. Mater.*, **23**, 1630–1634.

40 Capelli, R., Amsden, J.J., Generali, G., Toffanin, S., Benfenati, V., Muccini, M., Kaplan, D.L., Omenetto, F.G., and Zamboni, R. (2011) Integration of silk protein in organic and light-emitting transistors. *Org. Electron.*, **12**, 1146–1151.

41 Chang, T.-H., Liao, C.-P., Tsai, J.-C., Lee, C.-Y., Hwang, J.-C., Tso, I.M., Chueh, Y.-L., Lyu, P.-C., and Gan, J.-Y. (2014) Natural polyelectrolyte: major ampullate spider silk for electrolyte organic field-effect transistors. *Org. Electron.*, **15**, 954–960.

42 Kim, D.-H., Kim, Y.-S., Amsden, J., Panilaitis, B., Kaplan, D.L., Omenetto, F.G., Zakin, M.R., and Rogers, J.A. (2009) Silicon electronics on silk as a path to bioresorbable, implantable devices. *Appl. Phys. Lett.*, **95**, 133701.1–133701.3.

43 Hwang, S.-W., Tao, H., Kim, D.-H., Cheng, H., Song, J.-K., Rill, E., Brenckle, M.A., Panilaitis, B., Won, S.M., Kim, Y.-S., Song, Y.M., Yu, K.J., Ameen, A., Li, R., Su, Y., Yang, M., Kaplan, D.L., Zakin, M.R., Slepian, M.J., Huang, Y., Omenetto, F.G., and Rogers, J.A. (2012) A physically transient form of silicon electronics. *Science*, **337**, 1640–1644.

44 Müller, C., Hamedi, M., Karlsson, R., Jansson, R., Marcilla, R., Hedhammar, M., and Inganäs, O. (2011) Woven electrochemical transistors on silk fibers. *Adv. Mater.*, **23**, 898–901.

45 Marggraf, A.S. (1747) *Experiences Chimiques Faites Dans le Dessein de Tirer un Veritable Sucre de Diverses Plantes, qui Croissent Dans nos Contrées*, vol. **2**, Histoire de l'académie Royale des Sciences et Belles-lettres de Berlin, pp. 79–90; Chymische Schriften 1767.

46 Acar, H., Çınar, S., Thunga, M., Kessler, M.R., Hashemi, N., and Montazami, R. (2014) Study of physically transient insulating materials as a potential platform for transient electronics and bioelectronics. *Adv. Funct. Mater.*, **24**, 4135–4143.

47 Surjushe, A. and Vasani, R. (2008) Aloe Vera: a short review. *Indian J. Dermatol.*, **53** (4), 163–166.

48 Khor, L.Q. and Cheong, K.Y. (2013) Aloe Vera gel as natural organic dielectric in electronic application. *J. Mater. Sci. – Mater. Electron.*, **24** (7), 2646–2652.

49 Qian Khor, L. and Yew Cheong, K. (2013) N-type organic field-effect transistor based on fullerene with natural aloe vera/SiO2 nanoparticles as gate dielectric. *ECS J. Solid State Sci. Technol.*, **2** (11), P440–P444.

50 Kennedy, J.F., Phillips, G.O., and Williams, P.A. (2015) *Gum Arabic: RSC (Special Publication)*, vol. **1**, Royal Society of Chemistry.

51 Montenegro, M.A., Boiero, M.L., Valle, L., and Borsarelli, C.D. (2012) Gum arabic : more than an edible emulsifier. *Prod. Appl. Biopolym.*, **17** (3), 220.

52 Paraschos, S., Mitakou, S., and Skaltsounis, A.L. (2012) Chios gum mastic: a review of its biological activities. *Curr. Med. Chem.*, **19**, 2292–2302.

53 Lakkis, J.M. (2016) *Encapsulation and Controlled Release Technologies in Food Systems*, John Wiley & Sons, Inc., pp. 289–308.

54 Stadlober, B., Karner, E., Petritz, A., Fian, A., and Irimia-Vladu, M. (2015) Nature as microelectronic fab: bioelectronics: materials, transistors and circuits. *IEEE European Solid-State Device Research Conference 2015*, pp. 10–17

55 Glowacki, E.D., Irimia-Vladu, M., Kaltenbrunner, M., Gsiorowski, J., White, M.S., Monkowius, U., Romanazzi, G., Suranna, G.P., Mastrorilli, P., Sekitani, T., Bauer, S., Someya, T., Torsi, L., and Sariciftci, N.S. (2013) Hydrogen-bonded semiconducting pigments for air-stable field-effect transistors. *Adv. Mater.*, **25** (11), 1563–1569.

56 Steckl, A.J. (2013) Circuits on cellulose. *IEEE Spectr.*, **50** (2), 48–61.

57 Petritz, A., Wolfberger, A., Fian, A., Irimia-Vladu, M., Haase, A., Gold, H., Rothländer, T., Griesser, T., and Stadlober, B. (2013) Cellulose as biodegradable high-k dielectric layer in organic complementary inverters. *Appl. Phys. Lett.*, **103**, 153303.

58 Petritz, A., Wolfberger, A., Fian, A., Griesser, T., Irimia-Vladu, M., and Stadlober, B. (2015) Cellulose-derivative-based gate dielectric for high-performance organic complementary inverters. *Adv. Mater.*, **27**, 7645–7656.

59 Petritz, A., Fian, A., Głowacki, E.D., Sariciftci, N.S., Stadlober, B., and Irimia-Vladu, M. (2015) Ambipolar inverters with natural origin organic materials as gate dielectric and semiconducting layer. *Phys. Status Solidi RRL*, **9**, 358–361.

60 Thiemann, S., Sachnov, S.J., Pettersson, F., Bollström, R., Österbacka, R., Wasserscheid, P., and Zaumseil, J. (2013) Cellulose-based ionogels for paper electronics. *Adv. Funct. Mater.*, **24** (5), 625–634.

61 Gomez, E.F. and Steckl, A.J. (2015) Improved performance of OLEDs on cellulose/epoxy substrate using adenine as a hole injection layer. *ACS Photonics*, **2** (3), 439–445.

62 Klemm, D., Kramer, F., Moritz, S., Lindström, T., Ankerfors, M., Gray, D., and Dorris, A. (2011) Nanocelluloses: a new family of nature-based materials. *Angew. Chem. Int. Ed.*, **50** (24), 5438–5466.

63 Mautner, A., Lee, K.Y., Tammelin, T., Mathew, A.P., Nedoma, A.J., Li, K., and Bismarck, A. (2015) Cellulose nanopapers as tight aqueous ultra-filtration membranes. *React. Funct. Polym.*, **86**, 209–214.

64 Lee, K.Y., Buldum, G., Mantalaris, A., and Bismarck, A. (2014) More than meets the eye in bacterial cellulose: biosynthesis, bioprocessing, and applications in advanced fiber composites. *Macromol. Biosci.*, **14** (1), 10–32.

65 Mantell, C.L. (1950) The natural hard resins—their botany, sources and utilization. *Econ. Bot.*, **4**, 203–242.

66 Langenheim, J.H. (2003) *Plant Resins: Chemistry, Evolution, Ecology and Ethnobotany*, Timber Press Inc..

67 Hicks, E. (1962) *Shellac: its origin and applications*, MacDonald & Co.

68 Bose, P.K., Sankaranarayanan, Y., and Sen Gupta, S.C. (1963) *Chemistry of Lac*, Indian Research Institute.

69 Hagenmaier, R.D. and Shaw, P.E. (1991) Permeability of shellac coatings to gases and water vapor. *J. Agric. Food. Chem.*, **39**, 825–829.

70 Goswami, D.N. (1979) Dielectric behavior of the constituents of the natural resin shellac. *J. Appl. Polym. Sci.*, **24**, 1977–1984.

71 Irimia-Vladu, M., Głowacki, E.D., Schwabegger, G., Leonat, L., Akpinar, H.Z., Sitter, H., Bauer, S., and Sariciftci, N.S. (2013) Natural resin shellac as a substrate and a dielectric layer for organic field-effect transistors. *Green Chem.*, **15**, 1473–1476.

72 Irimia-Vladu, M., Głowacki, E.D., Troshin, P.A., Schwabegger, G., Leonat, L., Susarova, D.K., Krystal, O., Ullah, M., Kanbur, Y., Bodea, M.A., Razumov, V.F.,

Sitter, H., Bauer, S., and Sariciftci, N.S. (2012) Indigo-a natural pigment for high performance ambipolar organic field effect transistors and circuits. *Adv. Mater.*, **24**, 375–380.

73 Schrieber, R. and Gareis, H. (2007) *Gelatine Handbook: Theory and Industrial Practice*, Wiley-VCH Verlag GmbH.

74 Mao, L.K., Hwang, J.C., Chang, T.H., Hsieh, C.Y., Tsai, L.S., Chueh, Y.L., Hsu, S.S.H., Lyu, P.C., and Liu, T.J. (2013) Pentacene organic thin-film transistors with solution-based gelatin dielectric. *Org. Electron. Appl.*, **14** (4), 1170–1176.

75 Mao, L.K., Hwang, J.C., and Tsai, J.C. (2015) Operation voltage reduction and gain enhancement in organic cmos inverters with the ttc/gelatin bilayer dielectric. *Org. Electron.*, **16**, 221–226.

76 Paradossi, G., Cavalieri, F., Chiessi, E., Spagnoli, C., and Cowman, M.Y. (2003) Poly(vinyl alcohol) as versatile biomaterial for potential biomedical applications. *J. Mater. Sci. – Mater. Med.*, **14**, 687–691.

77 Wang, X., Xu, W., Chatterjee, P., Lv, C., Popovich, J., Song, Z., Dai, L., Kalani, M.Y.S., Haydel, S.E., and Jiang, H. (2016) Food-materials-based edible supercapacitors. *Adv. Mater. Technol.*, **1**, 1–7.

78 Chang, J.W., Wang, C.G., Huang, C.Y., Da Tsai, T., Guo, T.F., and Wen, T.C. (2011) Chicken albumen dielectrics in organic field-effect transistors. *Adv. Mater.*, **23** (35), 4077–4081.

79 Wu, G., Feng, P., Wan, X., Zhu, L., Shi, Y., and Wan, Q. (2016) Artificial synaptic devices based on natural chicken albumen coupled electric-double-layer transistors. *Sci. Rep.*, **6**, 23578.

80 Dezieck, A., Acton, O., Leong, K., Oren, E.E., Ma, H., Tamerler, C., Sarikaya, M., and Jen, A.K.Y. (2010) Threshold voltage control in organic thin film transistors with dielectric layer modified by a genetically engineered polypeptide. *Appl. Phys. Lett.*, **97** (1), 1–4.

81 Tang, C.W. and Albrecht, A.C. (1975) Photovoltaic effects of metal–chlorophyll-a–metal sandwich cells. *J. Chem. Phys.*, **62** (6), 2139–2149.

82 Moses, D., Heeger, A.J., Cornil, J., and Brddas, J.L. (1992) Doped beta-carotene films: spinless charge storage stabilized by structural relaxation. *Chem. Phys. Lett.*, **196** (1), 84–90.

83 Głowacki, E.D., Leonat, L., Voss, G., Bodea, M., Bozkurt, Z., Irimia-Vladu, M., Bauer, S., and Sariciftci, N.S. (2011) Natural and nature-inspired semiconductors for organic electronics. *Proceedings of SPIE 2011, vol. 8118, 81180M–81180M–10*.

84 Wang, X., Wang, L., Wang, Z., Wang, Y., Tamai, N., Hong, Z., and Kido, J. (2013) Natural photosynthetic carotenoids for solution-processed organic bulk-heterojunction solar cells. *J. Phys. Chem. C*, **117**, 804–811.

85 Bechtold, T. and Mussak, R. (2009) *Handbook of Natural Colorants*, John Wiley & Sons, Ltd., Chichester.

86 Ferreira, E.S.B., Hulme, A.N., McNab, H., and Quye, A. (2004) The natural constituents of historical textile dyes. *Chem. Soc. Rev.*, **33** (6), 329–336.

87 Głowacki, E.D., Irimia-Vladu, M., Bauer, S., and Sariciftci, N.S. (2013) Hydrogen-bonds in molecular solids – from biological systems to organic electronics. *J. Mater. Chem. B*, **1** (31), 3742–3753.

88 Aakeroy, C.B. and Seddon, K.R. (1993) The hydrogen bond and crystal engineering. *Chem. Soc. Rev.*, **22**, 397–407.

89 Desiraju, G.R. (2011) Reflections on the hydrogen bond in crystal engineering. *Cryst. Growth Des.*, **11** (4), 896–898.

90 Głowacki, E.D., Voss, G., and Sariciftci, N.S. (2013) 25th anniversary article: progress in chemistry and applications of functional indigos for organic electronics. *Adv. Mater.*, **25** (47), 6783–6800.

91 Seefelder, M. (1994) *Indigo in Culture, Science, and Technology*, Ecomed, Landsberg.

92 Zollinger, H. (2003) *Color Chemistry. Syntheses, Properties and Applications of Organic Dyes and Pigments*, Wiley-VCH Verlag GmbH, Weinheim.

93 Steingruber, E.Indigo Indigo Color. (2007) *Ullmann's Encyclopedia of Industrial Chemistry*, Wiley-VCH Verlag GmbH, Weinheim, pp. 1–9.

94 Glowacki, E.D., Leonat, L.N., Voss, G., Badea, M., Bozkurt, Z., Irimia-Vladu, M., Bauer, S., and Sariciftci, N.S. (2011) Ambipolar organic field effect transistors and inverters with the natural material tyrian purple. *AIP Adv.*, **1**, 042132–042137.

95 Kanbur, Y., Irimia-Vladu, M., Glowacki, E.D., Baumgartner, M., Schwabegger, G., Leonat, L.N., Ullah, M., Sitter, H., Schwödiauer, R., Kücükyavuz, Z., Bauer, S., and Sariciftci, N.S. (2012) Vacuum processed polyethylene as a dielectric for low voltage operating organic field effect transistors. *Org. Electron.*, **13**, 919–924.

96 Đerek, V., Głowacki, E.D., Sytnyk, M., Heiss, W., Marciuš, M., Ristić, M., Ivanda, M., and Sariciftci, N.S. (2015) Enhanced near-infrared response of nano- and microstructured silicon/organic hybrid photodetectors. *Appl. Phys. Lett.*, **107**, 83302.

97 Scherwitzl, B., Resel, R., and Winkler, A. (2014) Film growth, adsorption and desorption kinetics of indigo on SiO_2. *J. Chem. Phys.*, **140** (18), 184705.

98 Truger, M., Roscioni, O.M., Röthel, C., Kriegner, D., Simbrunner, C., Ahmed, R., Głowacki, E.D., Simbrunner, J., Salzmann, I., Coclite, A.M., Jones, A.O.F., and Resel, R. (2016) Surface-induced phase of tyrian purple (6,6′-Dibromoindigo): thin film formation and stability. *Cryst. Growth Des.*, **16**, 3647–3655.

99 Anokhin, D.V., Leshanskaya, L.I., Piryazev, A., Susarova, D.K., Dremova, N.N., Shcheglov, E.V., Ivanov, D.A., Razumov, V.F., and Troshin, P.A. (2014) Towards understanding the behavior of indigo thin films in organic field-effect transistors: a template effect of the aliphatic hydrocarbon dielectric on the crystal structure and electrical performance of the semiconductor. *Chem. Commun.*, **50** (57), 7639–7641.

100 Klimovich, I.V., Leshanskaya, L.I., Troyanov, S.I., Anokhin, D.V., Novikov, D.V., Piryazev, A.A., Ivanov, D.A., Dremova, N.N., and Troshin, P.A. (2014) Design of indigo derivatives as environment-friendly organic semiconductors for sustainable organic electronics. *J. Mater. Chem. C*, **2** (36), 7621–7631.

101 Pitayatanakul, O., Higashino, T., Kadoya, T., Tanaka, M., Kojima, H., Ashizawa, M., Kawamoto, T., Matsumoto, H., Ishikawa, K., and Mori, T. (2014) High performance ambipolar organic field-effect transistors based on indigo derivatives. *J. Mater. Chem. C*, **2** (43), 9311–9317.

102 Herbst, W. and Hunger, K. (2004) *Industrial Organic Pigments*, Wiley-VCH Verlag GmbH, Weinheim.

103 Klebe, G., Graser, F., Hädicke, E., and Berndt, J. (1989) Crystallochromy as a solid-state effect: correlation of molecular conformation, crystal packing and colour in perylene-3,4:9,10-bis(dicarboximide) pigments. *Acta Crystallogr., Sect. B: Struct. Sci*, **45** (1), 69–77.

104 Faulkner, E.B. and Schwartz, R.J. (eds) (2009) *High Performance Pigments*, Wiley-VCH Verlag GmbH, Weinheim.

105 Hunger, K. (2005) Toxicology and toxicological testing of colorants. *Rev. Prog. Color. Relat. Top.*, **35**, 76–89.

106 Labana, S.S. and Labana, L.L. (1967) Quinacridones. *Chem. Rev.*, **67** (1), 1–18.

107 Glowacki, E.D., Leonat, L., Irimia-Vladu, M., Schwödiauer, R., Ullah, M., Sitter, H., Bauer, S., and Sariciftci, N.S. (2012) Intermolecular hydrogen-bonded organic semiconductors—quinacridone versus pentacene. *Appl. Phys. Lett.*, **101** (2), 23305.

108 Haucke, G. and Graness, G. (1995) Thermal isomerization of indigo. *Angew. Chem.*, **34** (1), 67–68.

109 Głowacki, E.D., Romanazzi, G., Yumusak, C., Coskun, H., Monkowius, U., Voss, G., Burian, M., Lechner, R.T., Demitri, N., Redhammer, G.J., Sünger, N., Suranna, G.P., and Sariciftci, N.S. (2015) Epindolidiones-versantile and stable hydrogen-bonded pigments for organic field-effect transistors and light-emitting diodes. *Adv. Funct. Mater.*, **25**, 776–787.

110 Rossi, L., Bongiovanni, G., Kalinowski, J., Lanzani, G., Mura, A., Nisoli, M., and Tubino, R. (1996) Ultrafast optical probes of electronic excited states in linear trans-quinacridone. *Chem. Phys. Lett.*, **257**, 545–551.

111 Głowacki, E.D., Tangorra, R.R., Coskun, H., Farka, D., Operamolla, A., Kanbur, Y., Milano, F., Giotta, L., Farinola, G.M., and Sariciftci, N.S. (2015) Bioconjugation of hydrogen-bonded organic semiconductors with functional proteins. *J. Mater. Chem. C*, **3**, 6554–6564.

112 Jakešová, M., Apaydin, D.H., Sytnyk, M., Oppelt, K., Heiss, W., Sariciftci, N.S., and Glowacki, E.D. (2016) Hydrogen-bonded organic semiconductors as stable photoelectrocatalysts for efficient hydrogen peroxide photosynthesis. *Adv. Funct. Mater.*, **26**, 5248–5254.

113 Wang, C., Zhang, Z., and Wang, Y. (2016) Quinacridone-based π-conjugated electronic materials. *J. Mater. Chem. C*, **4**, 9918–9936.

114 Kotwica, K., Bujak, P., Wamil, D., Materna, M., Skorka, L., Gunka, P.A., Nowakowski, R., Golec, B., Luszczynska, B., Zagorska, M., and Pron, A. (2014) Indanthrone dye revisited after sixty years. *Chem. Commun.*, **50** (78), 11543–11546.

115 Kotwica, K., Bujak, P., Data, P., Krzywiec, W., Wamil, D., Gunka, P.A., Skorka, L., Jaroch, T., Nowakowski, R., Pron, A., and Monkman, A. (2016) Soluble flavanthrone derivatives: synthesis, characterization, and application to organic light-emitting diodes. *Chem. A Eur. J.*, **22**, 7978–7986.

116 Zambounis, J.S., Hao, Z., and Iqbal, A. (1997) Latent pigments activated by heat. *Nature*, **388**, 131–132.

117 Hao, Z. and Iqbal, A. (1997) Some aspects of organic pigments. *Chem. Soc. Rev.*, **26** (3), 203.

118 Głowacki, E.D., Voss, G., Demirak, K., Havlicek, M., Sünger, N., Okur, A.C., Monkowius, U., Gąsiorowski, J., Leonat, L., and Sariciftci, N.S. (2013) A facile protection–deprotection route for obtaining indigo pigments as thin films and their applications in organic bulk heterojunctions. *Chem. Commun.*, **49**, 6063–6065.

119 Głowacki, E.D., Apaydin, D.H., Bozkurt, Z., Monkowius, U., Demirak, K., Tordin, E., Himmelsbach, M., Schwarzinger, C., Burian, M., Lechner, R.T., Demitri, N., Voss, G., and Sariciftci, N.S. (2014) Air-stable organic semiconductors based on 6,6′-dithienylindigo and polymers thereof. *J. Mater. Chem. C*, **2** (38), 8089–8097.

120 Sytnyk, M., Daniel, E., Yakunin, S., Voss, G., Schöfberger, W., Kriegner, D., Stangl, J., Trotta, R., Gollner, C., Tollabimazraehno, S., Romanazzi, G., Bozkurt, Z., Havlicek, M., Sariciftci, N.S., and Heiss, W. (2014) Hydrogen-bonded organic semiconductor micro- and nanocrystals: from colloidal syntheses to (opto-)electronic devices. *J. Am. Chem. Soc.*, **136**, 16522–16532.

2

Fabrication Approaches for Conducting Polymer Devices

Dimitrios A. Koutsouras[1], Eloïse Bihar[1,2,3], Jessamyn A. Fairfield[4], Mohamed Saadaoui[3], and George G. Malliaras[1]

[1] *Ecole Nationale Supérieure des Mines, CMP-EMSE, MOC, Department of Bioelectronics, 880, route de Mimet - F-13541 Gardanne, France*
[2] *Microvitae Technologies, Hôtel Technologique, Europarc Sainte Victoire, Route de Valbrillant, Meyreuil, 13590, France*
[3] *Ecole Nationale Supérieure des Mines, CMP-EMSE, MOC, Department of Flexible Electronics, 880, route de Mimet – F-13541 Gardanne, France*
[4] *National University of Ireland Galway, School of Physics, University Road, Galway, H91 CF50, Ireland*

2.1 Introduction

During the past decades the field of organic electronics has attracted increasing attention of the scientific community in an attempt to complement traditional silicon electronics and to broaden their horizons [1]. There are a number of good reasons justifying this trend as organic materials present a unique set of properties. In particular, they allow fabrication of thin, flexible, lightweight, environmentally friendly, and low-cost devices [2]. Moreover, they offer ease of processibility, low-temperature solution-based deposition, and the degree of freedom that comes with their chemically tunable properties [3].

Nevertheless, before this new emerging technology becomes mature enough to influence the electronic industry, the major issue of organic film patterning must be addressed. There is an *inextricable* link between electronic device performance and electronic material patterning and that is the reason why many different methods have been developed through the past years to optimize the fabrication process. Especially when it comes to organic materials, patterning is a challenging task as the technique of choice should be compatible with their special nature.

Unfortunately, despite its comparative advantages, conventional photolithography lacks compatibility with the vast majority of organic electronic materials. This is due to the fact that solvents used during deposition, development, and removal of photoresists have, in most cases, adverse effect on organic films. As a result, the already existing and well-developed industry of conventional silicon-based electronics can only provide limited tools for organic electronics [4]. Thus, the goal of overcoming those incompatibilities is of great importance as it will allow the use of the accumulated knowledge of an already well-established and commercially successful fabrication approach.

Green Materials for Electronics, First Edition.
Edited by Mihai Irimia-Vladu, Eric D. Glowacki, Niyazi S. Sariciftci, and Siegfried Bauer.

Printing techniques have emerged over the last decades as attractive alternatives to photolithography for the manufacturing of electronic devices. These techniques are compatible with roll-to-roll processes and can operate at high speed. Moreover, they only require a limited number of manufacturing steps. They can produce high volume runs, thereby lowering the costs of fabrication. In the second part of this chapter, we will focus on these technologies. A distinction has been made between contact printing technologies (gravure, flexography, screen printing) and noncontact printing technologies (aerosol jet and inkjet). Printed technologies allow the manufacture of a complete device by printing a wide range of inks from conducting to dielectric inks. These new functional inks have been developed to match the electronic requirements and the constraints of industrial processes. Research is ongoing to achieve high resolution down to the micron scale.

In contrast, other nondestructive patterning techniques employed throughout the past years did not manage to live up to their potential. Vapor deposition through shadow masks, soft and hard imprint lithography, thermal transfer process, and laser-assisted printing were originally introduced as alternative approaches promising a convenient and easy way of device fabrication. Nevertheless, all these techniques suffer from numerous drawbacks. In particular, shadow mask deposition is the technique of choice for small-molecule patterning but lacks high-resolution fabrication. Imprint technology, on the other hand, can offer resolution down to 10 nm but it can be used only with a limited number of materials and device architectures [5]. In addition, all of the above techniques have issues with low resolution, poor scalability to larger areas, lack of registration, and the fact that they tend to require complex and costly processing protocols [6]. These disadvantages render them unable to compete with today's state-of-the-art fabrication processes.

In this chapter, we introduce novel approaches for conducting polymer device fabrication, with a particular emphasis on high-throughput, cost-effective, and simple fabrication techniques, applicable to polymers and able to reproducibly create organic devices with high yield and efficiency. We focus on polymer-friendly photolithography and a printing patterning technique.

2.2 Photolithography

2.2.1 History

The term *photolithography* is a compound word made up from the Greek words photo (Φως = light), litho (λίθος = stone), and graphy (γραφή = writing). As implied by its name, photolithography is the process of transferring (writing) a pattern onto a substrate with the help of light.

There are two main historical landmarks in the development of photolithography. The first is the experiments of the Swiss pastor Jean Senebier (1742–1808) of Geneva with resins, in 1782. Senebier noticed that certain resins become insoluble in a solvent (turpentine) after sunlight exposure. The second pivotal moment comes with the work of Nicéphore Niépce on photography in 1826. Niépce,

inspired by Senebier, was the first one to produce an image using the properties of light in Chalon (France). He used bitumen of Judea (a form of asphalt) dissolved in lavender oil, to coat a pewter plate and then he covered it with an etched print on oiled paper. The latter would serve as a mask for the 3 h exposure to sunlight that was to follow. During this time, the exposed parts of the resist became insoluble while the protected ones could easily be removed by a mixture of turpentine and lavender oil corresponding to a photoresist behavior classified later as negative. Nevertheless, the first photolithography pattern transfer took place 5 years later, in 1827, by the Parisian engraver Augustin Francois Lemaître. Lemaître used a strong acid to etch a Niépce plate and to create a copy of a gravure of Cardinal d'Amboise, employing for the first time both photolithography and the chemical etching technique in pattern transfer [7, 8].

Photolithography gradually became popular among the members of the scientific community as many of them started to realize the potential of the new technique. A little more than 100 years later, William Shockley and his coworkers at Bell Laboratories wanted to use photolithography for the fabrication of the first integrated circuit. However, the need for a photoresist that could withstand the hydrofluoric etching of silicon dioxide (an important feature for their microfabrication process) made them turn to Kenneth Mees, Director of the Eastman Kodak Laboratories at Rochester New York. Mees contacted Louis Minsk, who in 1935 developed the first synthetic photopolymer known as *poly(vinyl cinnamate)*, the basis of the first negative photoresist. His idea relied on the photoresist becoming less soluble upon exposure to light. Minsk used that feature in order to define which part of the photoresist would dissolve and which would remain on the substrate. In his approach the dissolved parts would be the ones to create the desired pattern. Five years later, in 1940, Oskar Süß developed a positive photoresist (diazonapthoquinone-DNQ) [8], which worked in the opposite way with the pattern formed by the part of the photoresist that remains after exposure to light.

Today, many more chemical substances have been synthesized, characterized, and used in photolithography both as negative and positive photoresists. At the same time, optimization and variation of radiation sources in lithography (X-ray lithography, charged particles lithography, etc.) allow the patterning with nanometric resolution. The comparison with the 0.5–1 mm accuracy achieved by Lemaître during the first photolithographic attempt shows the extent of progress [7].

2.2.2 Basic Principles

The basic principle behind photolithography is the use of light in order to alter the solubility of a thin film that is exposed to it. A mask is a stencil, usually made out of chromium, which protects selected parts of the photosensitive material while the uncovered ones undergo changes in their properties (solubility) during the exposure. After immersion into a chemical developer, the parts that became more soluble are dissolved leaving the desired pattern on the film behind. It is obvious that the photosensitive material plays a key role in the success of the process. This material is typically an organic polymer, called *photoresist*, which can go through a series of photochemical reactions when exposed to light.

It should also be noted that the term *photolithography* usually refers to the use of ultraviolet light (UV – wavelengths 436 and 365 nm) during patterning. Nevertheless, deep ultraviolet (DUV –wavelengths 248 and 193 nm) and extreme ultraviolet (EUV – wavelengths 5–100 nm) photolithography techniques are both feasible and appealing, as in theory when the wavelength of the light source diminishes the feature resolution increases. Nevertheless, it is difficult to find light sources with enough output power, the proper photoresists, and the optical elements [9] for those short wavelengths. Moving a step further, X-ray lithography, charged particle lithography, or atomic force microscopy (AFM) lithography promise even better resolution, posing at the same time extra technological challenges. In this chapter every time we use the term *photolithography* it will be implied that we refer to UV photolithography.

Returning to photoresists, they can roughly be divided into two categories: positive photoresists (positive tone) and negative ones (negative tone). A positive photoresist is a photoresist, which, when exposed to light, changes chemically and/or structurally becoming more soluble to an organic developer while, ideally, it was insoluble before. The mechanism behind this transformation can be either a polymer chain scission (e.g., poly(methylmethacrylate) (PMMA) photoresist) or a photo-induced change in the polarity of the molecule (e.g., two component DNQ-phenolic novolac resin) [7, 10]. A negative photoresist works in exactly the opposite way. The photoresist is soluble to the developer and exposure to UV light either promotes polymeric cross-linking or starts the polymerization of the monomers. That renders the exposed photoresist insoluble to the developer, and hence unexposed parts of the film are removed during the development step that follows. Common negative tone photoresists are the bis(aryl) azide rubber resists and the Kodak Thin Film Resist (KTFR) (an azide-sensitized poly(isoprene) rubber) [7, 10].

For both these types of photoresists the exposure, the development, and the final pattern formation on the substrate are depicted in Figure 2.1.

In general, positive photoresists are more expensive than negative ones but can offer higher resolution. This feature, along with the fact that positive photoresists can be developed in less toxic water-based developers, made them more popular than their negative counterparts in industry. Nevertheless, many steps forward have been made lately in the synthesis and development of negative resists. As a result, the newer negative tone resists are water developable and can also offer high resolution [7]. In addition, negative photoresists traditionally adhere better to substrates and they are more resistant to wet or dry etching than positive ones [7]. In conclusion, the choice of a proper photoresist depends on many different parameters (cost, resolution, pattern geometry, etc.), all of which need to be taken into account before a decision is made.

Currently, photolithography is the most popular technique of patterning in the integrated circuits industry. It offers a reliable and reproducible way of building electronic devices with great accuracy and high resolution. Its main disadvantage is the limitations in the topography, as it can only be implemented on planar substrates. The process performance can be evaluated through three figures of merit:

- *Resolution*: A measure of the minimum size of a feature that can be patterned. It needs to be as high as possible in order for the feature size to be small.

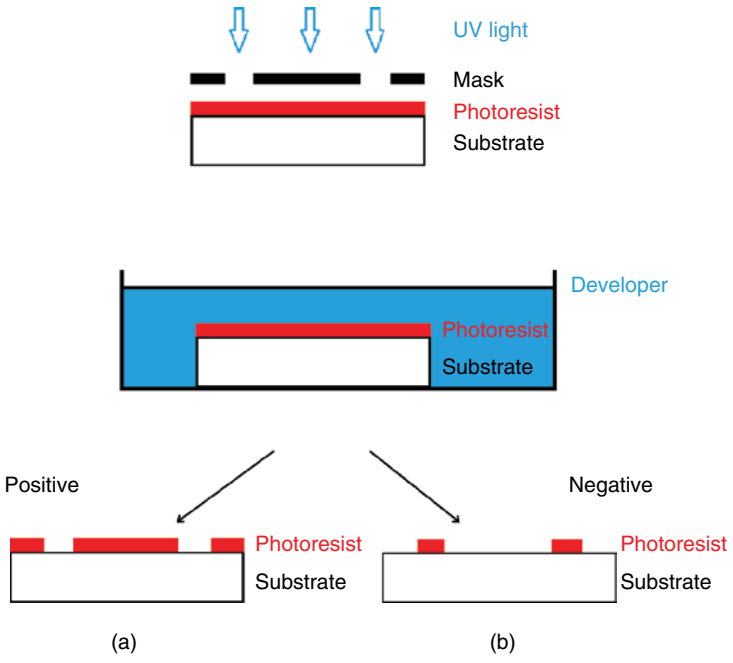

Figure 2.1 Pattern transfer for a positive (a) and a negative (b) photoresist.

- *Registration*: A measure of how accurately patterns on different layers can be aligned with respect to each other.
- *Throughput*: The number of substrates that can be exposed per hour. The higher the throughput the more efficient the process.

2.2.3 Fabrication Steps

The typical fabrication steps that take place during microfabrication are briefly reviewed below.

2.2.3.1 Substrate Cleaning

The first and definitely one of the most important steps in device fabrication is substrate cleaning. Several different types of substrates can be used for electronic circuit development. Silicon wafers are very common, especially in silicon-based semiconductor industry, but other kinds of substrates may also be employed. Glass slides, conformable substrates (like Parylene-C), or even less conventional substrates such as textiles and silk are among them. Despite the fact that some of those substrates may have special requirements or even incompatibilities with the standard cleaning protocols, the cleaning step cannot be easily omitted. Keeping the substrate free of contaminants is a matter of great importance as the degree of its cleanness affects the quality of the deposited film. Moreover, particles on the substrate could potentially lead to damage of the photomask during contact photolithography exposure or even cause, in some cases, undesirable masking effects

due to light diffraction. Among the contaminants that should be removed before coating the substrate with photoresist are atmospheric dust from operators and equipment, organic particles, moisture, H_2O residue films, solvent stains, smoke particles, residual resist, particulates, and chunks of granular matter [7, 11].

The cleanliness of the fabrication environment is of critical importance; hence, all fabrication steps take place in a clean room environment (typically class 100) that allows the presence of up to 100 particles (sized 0.5 μm or larger) per cubic foot of atmosphere. An environment such as this minimizes the amount of unwanted particles in the milieu and as a result it minimizes the number of unwanted contaminants on the device as well. Taking this environment as granted, typical cleaning procedures may include both wet and dry methods. Sonication in water soap baths or solvent baths is normally employed for the removal of particles (both inorganic and organic). In some cases piranha solution (a 3:1 mixture of sulfuric acid and hydrogen peroxide) can also be used to detach organic particles from the substrate. Additional approaches include thermal treatment at high temperature (dehydration bake), plasma cleaning, vapor cleaning, and supercritical cleaning with CO_2 during which supercritical fluid of carbon dioxide is used for removal of inorganic and organic contaminants from cracks and clefts owing to its ability to penetrate into crevices [7, 11].

2.2.3.2 Deposition of the Photoresist

Once substrate cleanness is ensured, deposition of the photoresist on the substrate follows. Among the ways of depositing polymers on a substrate spin-coating is the one that can guarantee uniformity, reproducibility, and precision during deposition. It is a well-known, traditional technique that is easy to use and offers control of the film thickness. The main drawback is the fact that the majority of the processed material is wasted.

Consequently, spin-coating deposition has been the method of choice for photoresist thin-film formation during fabrication for several decades now. During this approach, a small droplet of the photoresist is placed in the middle of the substrate, which is secured on a chuck via vacuum. Centripetal acceleration spreads the photoresist on the substrate. Although almost 98% of the initial material is spun off, eventually a thin film of photoresist is deposited on the substrate, as shown in Figure 2.2.

Thickness h of the photoresist is controlled through specific parameters of the process. The angular spinning speed ω and time t as well as the liquid density ρ, material viscosity η, and evaporation rate e_e are the most important factors affecting the film's formation. During this process, complex nonequilibrium phenomena take place, and it is believed that two parts contribute to the rate by which the thickness of the film changes over time: a part that refers to the effect of the angular spinning speed and a part connected to the evaporation rate of the photoresist e_e. Generally, the spinning cycle can be separated into two stages: a very fast coating stage (when the photoresist is spread on the substrate) and a longer drying stage (during which the solvent evaporates). In any case, the rheology behind the film formation is complex, especially if the evaporation of the photoresist is taken into account. Therefore, the film thickness is usually given by the empirical expression (2.1) [7, 11, 12]

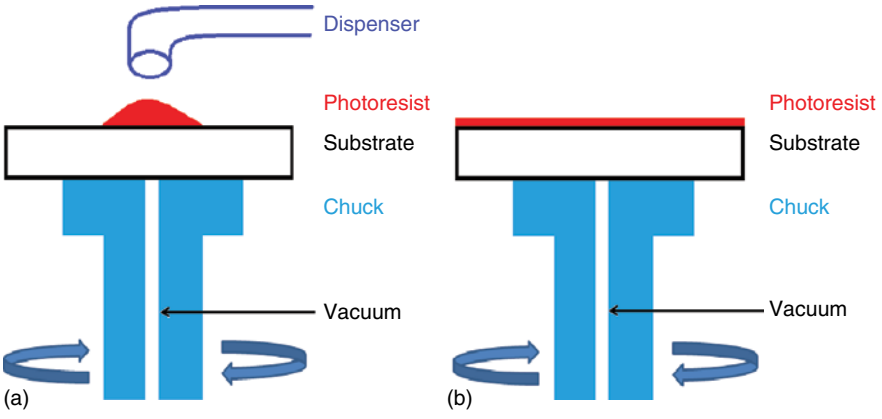

Figure 2.2 (a) Photoresist is placed on the substrate. (b) Film formation due to centripetal acceleration.

$$h = \frac{K\, C^{\beta} \eta^{\gamma}}{\omega^{\alpha}} \tag{2.1}$$

where K is an overall calibration constant, C is the polymer concentration in g/100 ml, and η is the solution's viscosity. The exponential parameters α, β, and γ are determined experimentally. Once these parameters are set, a calibration curve is obtained that can provide the film thickness for a given polymer and solvent. Usually, film thickness is inversely proportional to the square root of the angular spinning speed ω and proportional to the solutions viscosity η to the 0.4–0.6 power [12].

$$h \propto \frac{\eta^{0.4-0.6}}{\sqrt{\omega}} \tag{2.2}$$

There are two common ways to realize the photoresist's dispersion on the substrate: the static dispense and the dynamic dispense. During static dispense a drop of photoresist is deposited on the substrate near its center while it is stationary. The amount of material deposited is in direct correlation with the viscosity of the photoresist (more viscous photoresists require more material to be placed) and the size of the substrate (bigger substrates require more material to ensure the total coverage of the substrate). On the other hand, dynamic dispersion dictates an initial step of spinning at a low speed (typically 500 rpm) while the dispensing takes place. After that, the substrate is accelerated to its final speed. Theoretically, this approach facilitates the wetting of the substrate and consequently the spreading of the material, leading to less waste.

For both approaches, the angular spinning speed and the time of the spinning are the two parameters that affect the final thickness of the film. In general, high speed and longer spinning times lead to thinner film formation.

2.2.3.3 Post-apply Bake

What follows is a thermal treatment step called post-apply bake (PAB) (or soft bake). It usually lasts for a minute or two on a hot plate at 110 °C. The purpose of

this step is to evaporate the remaining solvent from the photoresist and to densify it just before exposure. This renders the coated film more stable and reduces the probability of the covered substrate to stick to the mask during exposure.

2.2.3.4 Use of the Mask/Alignment/Exposure

Exposure stands at the very heart of the fabrication process. The basic principle behind photolithography, after all, is altering a photoresist's solubility by delivering energy to it via radiation. The stencil that is used to transfer the desired pattern on the photosensitive film is called the *mask*. Generally, a mask is made of glass (transparent to UV radiation) with a metal pattern on it (usually a 800 Å chromium film is used). The glass windows allow the radiation to pass through it with very little absorption while the metal pattern protects the underlying photoresist from any interaction with light. Masks are constructed with electron beam lithography, which can result in higher resolution than photolithography [7]. Special care is also taken in the proper alignment of different device layers to each other during the exposure. As previously stated this is one of photolithography's figures of merit (Registration) and is handled with the use of special marks (alignment marks) strategically placed on the different layers [9]. After all, registration is one of the main advantages of photolithography compared to the rest of the techniques, along with high throughput due to its parallel nature.

There are three different ways to perform the exposure: contact, proximity, and projection mode, as shown in Figure 2.3.

2.2.3.4.1 Contact Mode

Contact mode lithography was the first mode to be used in the early 1960s. In this approach the substrate is in physical contact with the mask during the exposure. The alignment of the substrate is performed with the creation of a temporary spatial gap between the two. The resolution of contact printing is rather high as it can go down to the wavelength of the radiation used. Nevertheless, the high risk of mask damage due to the contact with the substrate motivated a search for alternative modes of photolithography.

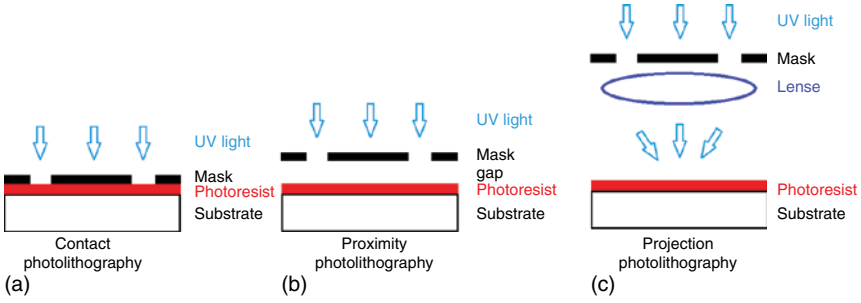

Figure 2.3 Schematic representation of the three exposing modes. (a) Contact photolithography, (b) proximity photolithography, and (c) projection mode.

2.2.3.4.2 Proximity Mode

Here, the mask and the substrate are not in contact as there is a small gap (10–50 μm) maintained between the two. That protects the mask from damage but at the same time lowers resolution due to diffraction effects.

Contact and proximity mode printing are known together as shadow printing. The resolution r for them is given by the formula [9, 11, 12]

$$r = \frac{3}{2}\sqrt{\lambda\left(s + \frac{d}{2}\right)} \tag{2.3}$$

where λ is the radiation wavelength, s is the distance between the mask and the substrate, and d is the photoresist thickness.

2.2.3.4.3 Projection Mode

This is the mode of choice used in semiconductor industry from the mid-1970s to date. In projection printing, there is no direct contact between the mask and the substrate as the mask is projected onto the substrate through a lens system. This approach protects the mask from damage since there is no physical contact involved, as shown in Figure 2.3. In addition, the demagnification of the mask pattern achieved with the optics results in high resolution and makes the mask fabrication a little easier [7].

The resolution r for projection printing is given by [9, 11, 12]

$$r = k\frac{\lambda}{\mathrm{NA}} \tag{2.4}$$

where k is a coefficient that depends on process-related factors and NA is the numerical aperture.

2.2.3.5 Development

After exposure, a development step will allow the latent resist pattern formed to be revealed. Selective dissolution of the resist creates a relief that will serve as a mold for the next fabrication steps. Development is of extreme importance as it controls the quality of the transferred motif.

There are two main approaches to performing this step: wet development and dry development.

2.2.3.5.1 Wet Development

In wet development, aqueous and organic solvents are used to selectively dissolve the exposed photoresist. Positive photoresists are developed in aqueous alkaline solutions while negative photoresists are developed in organic solutions. Aqueous development is preferable for environmental reasons and that is why newer negative resists may also be developed in aqueous solutions [7]. The aqueous solutions are usually tetramethyl ammonium hydroxide (TMAH) based. The solvent is applied either by immersion or by spraying (with or without substrate spinning) [7, 12].

2.2.3.5.2 Dry Development

Dry development is an alternative approach dictated mostly by the need for developing cleaner fabrication techniques. It is based on oxygen-reactive etching for the appearance of the desired pattern. Exposure alters the photoresist's etching resistance rather than its solubility [7, 12]. After development, the substrate is rinsed and dried with dry air or nitrogen. Visual inspection guarantees the quality of the pattern and the lack of defects.

2.2.3.6 Descumming and Post-baking

Descumming is a mild oxygen plasma treatment to remove any residual resist after development. It removes tiny amounts of unwanted material without harming the desired features. Patterned resist is also affected, but as long as only a few hundred angstroms are removed this does not cause any fabrication concerns.

Just before the pattern printed in the photoresist is transferred onto the substrate, a post-baking step (also known as *hard baking*) takes place. Hard baking promotes interfacial adhesion of the film and removes the residual solvent. It usually occurs at the temperature of 120 °C (slightly higher than the temperature used for soft baking), which additionally cross-links the photoresist, making it harder and more resistant to the etching steps that follow. Special care should be taken in order for the temperature not to cause flow or melting of the photoresist as this will degrade the profile of the resist.

2.2.3.7 Pattern Transfer

The previous steps create the desired pattern on the photoresist. The next goal is to transfer this pattern (or its negative) from the photoresist onto the substrate. There are two different methods to achieve this goal: a subtractive process and an additive one [4, 12].

In the subtractive method, first a material film is deposited on the substrate. Photolithography creates a positive image of the pattern and then etching removes the excess material, leaving behind the desired structure. The additive method, on the other hand, uses photolithography to create first a negative image of the pattern and then to realize its positive version via selective deposition of material. Both these methods will be further developed with case studies later in this chapter.

Etching is one of the most crucial parts in fabrication. Selective etching creates the required polymer microstructure during the subtractive approach, while it controls the material deposition in the additive one. In general, etching is a method of removing material that is not protected under the photoresist. It can be done chemically, mechanically, or with a combination of the two mechanisms.

Wet etching was initially the method of choice in the microelectronic industry. An acidic solution was used to erode the thin film not covered by the photoresist, creating a selective 3D structure. However, the method's isotropic nature usually resulted in an undercut profile damaging the overall resolution. Consequently, new dry etching approaches quickly became popular as they could provide etching in an anisotropic way. Plasma etching, in particular, uses plasma (an ionized gas) to anisotropically and selectively etch only the patterned material and not the photoresist above it, allowing fabrication with sub-micrometer resolution.

As dry techniques are easily automated and remove the need for toxic developers, it is not a surprise they quickly rose to dominance [11].

Many different dry etching techniques have been developed, but among them reactive ion etching (RIE) offers the benefits of both the chemical and the physical etching worlds. RIE uses plasma to create ionized atoms that can be accelerated by an electrical field and cause a directional sputtering of the substrate. This is extremely important in giving anisotropy to the technique. The charged molecules gain kinetic energy, which they transfer to the film in the collision, etching it vertically. At the same time they provide the energy for an etching reaction to take place, which is selective due to its chemical nature.

The deposition of the material of interest mentioned above is done with a number of different techniques. Chemical vapor deposition (CVD), physical vapor deposition (PVD), sputtering, and electroplating are among them. Here, we will focus on thermal evaporation as it is widely used for metal film deposition and it will prove to be extremely useful for the fabrication of organic devices that follows.

2.2.3.8 Stripping

The last step of the fabrication process is the removal of the remaining photoresist. That will create patterns by selectively discarding the evaporated material that was deposited on the photoresist while leaving the rest intact. The photoresist acts now as a sacrificial layer and is removed along with the metal layer on top of it, creating the desired metal profile. Photoresist stripping is usually performed with the help of organic solvents. Acetone is very commonly used for this task, along with other phenol-based commercial strippers. Nevertheless, environmental issues favor the use of dry stripping methods such as oxygen plasma. In any case, the ultimate criterion in the stripping approach is not to destroy the target material film. Especially for organic materials, this criterion poses a number of extra difficulties due to incompatibilities with the majority of solvents.

2.2.4 Photolithography in Polymer Device Fabrication

The previously presented steps of conventional photolithography could have theoretically been implemented in polymer device fabrication as well. The main challenge of organics, though, is the incompatibility issues between organic films and the solvents used during optical lithography. Unfortunately, the solvents employed for depositing, developing, and removing photoresists usually have a destructive effect on organic materials (including dissolution, cracking, swelling, and delamination of the polymer film [4]). Two different but representative strategies have been developed during recent years to overcome these limitations, and are presented here.

2.2.4.1 Sacrificial Layer Method

An alternative way of patterning organic materials, developed by DeFranco and coworkers, is based on the use of a poly(monochloro-*p*-xylylane (Parylene-C) sacrificial buffering layer [4]. Parylene-C (a polymer widely used as a barrier layer) is employed to protect the organic film during each step of the photolithography fab-

rication (deposition, development, and strip of the photoresist). After Parylene-C deposition, the formed film is inert and resistant enough to withstand a photolithography step on it.

From this point, two different fabrication methods (an additive and a subtractive one) lead, eventually, to the organic material patterning [4, 13, 14]. For the subtractive method the developed photoresist serves as a mask to selectively etch and remove both the Parylene-C layer and the organic film under it. In the additive method, on the other hand, the photoresist acts as contact mask and an etching step leaves behind voids in the Parylene-C to be filled with the polymer. Both these approaches can give high-quality patterned polymer films, and are shown schematically in Figure 2.4.

The next two case studies are paradigms of the aforesaid additive and subtractive methods implemented in organic device fabrication. The active area of those

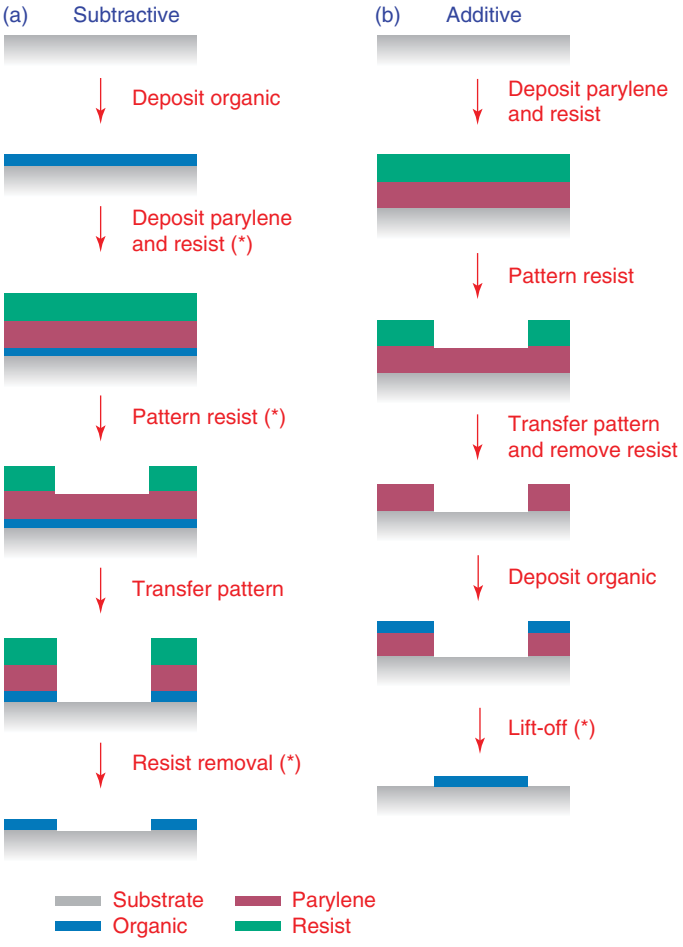

Figure 2.4 (a) Subtractive and (b) additive fabrication approaches. The asterisks indicate the steps where the organics would be damaged during conventional photolithography. (DeFranco *et al*. 2006 [4], Reproduced with permission of Elsevier.)

devices is covered with a thin poly(3,4-ethylenedioxythiophene) doped with poly(styrene sulfonate) (PEDOT:PSS) polymer film while the electrodes and their wiring are gold patterned with the use of conventional photolithography techniques. Both methods are versatile, generic, and can be used for direct patterning of polymer films in a variety of organic devices (polymer-covered electrodes, organic transistors, etc.).

2.2.4.1.1 Subtractive Patterning

A subtractive method that can result in high performing devices was presented in 2011 by Khodagholy and coworkers [15]. In this approach, PEDOT:PSS-covered gold electrodes were fabricated on a 2 μm Parylene-C film that served as a flexible substrate. Initially, gold electrodes, interconnections, and pads were patterned on a Parylene-C film via standard photolithography. A second 2 μm thick film of Parylene-C was used to insulate the device while a second photolithography step followed by oxygen etching (RIE) opened windows over the recording sites and pads. The polymer (PEDOT:PSS) was deposited through spin casting and the devices were coated with a third (sacrificial) layer of Parylene-C. The final photolithography and etching step defined the PEDOT:PSS-coated electrodes. Immersion of the device in deionized water promoted the removal of the Parylene-C sacrificial layer exposing the electrodes (Figure 2.5).

The success of the process relies on the fact that the polymer film adheres better to gold than to the Parylene-C film above it. In addition, due to its hydrophobic character, deionized water facilitates the sacrificial layer's peeling off without affecting the quality and conductivity of the organic film. The conducting film's

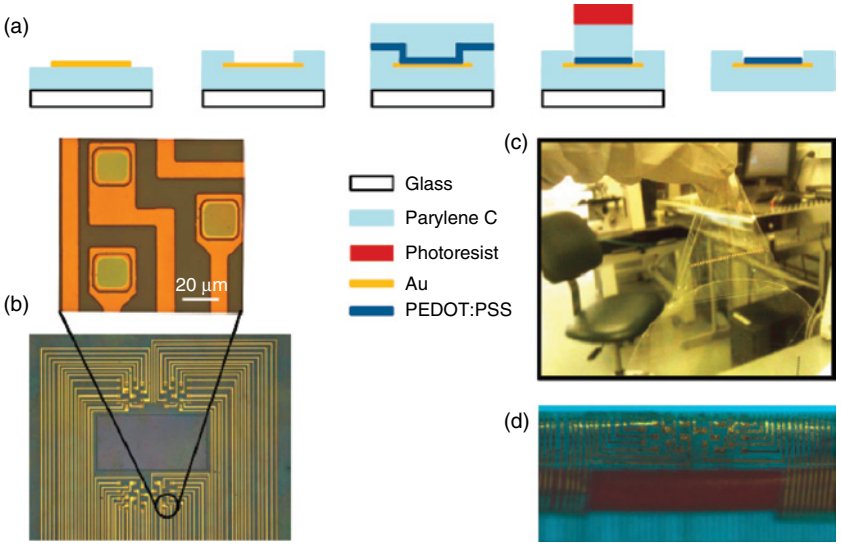

Figure 2.5 (a) The main steps of the fabrication process. The final array of electrodes is mounted on a Parylene-C substrate. (b) Optical image of the electrode array with a close-up on three electrodes. (c) The electrode array can support the weight of a quartz wafer. (d) The array can conform to a cylinder of 2.2 mm radius. (Chang *et al*. 2007 [16]. Reproduced with permission of American Chemical Society.)

integrity is also maintained during the Parylene-C deposition process. The above points render the method generic, versatile, and usable for different types of conducting polymers as they also become hydrophilic when doped.

Parylene-C plays a key role in the fabrication approach studied. It not only protects the organic film, which is sensitive to solvents, but also offers electrical insulation for the device, which is imperative for its functionality. Parylene-C is a member of the greater poly *p*-xylylene family and is produced with the substitution of Cl on the aromatic ring (Figure 2.6).

It has been extensively used in the past for coating purposes. It is a green chemistry polymer as it is chemically inert [16] and needs no initiator for solvent-free deposition as a coating film [17]. Hence it can be easily deposited on and removed from the polymer films without causing their chemical deterioration [15].

The material is deposited from its vapor phase via a CVD method proposed by Gorham. Its dimer is heated at 150 °C ($P = 1$ Torr) creating the vapor phase of the material. A pyrolysis stage follows at 680 °C ($P = 0.5$ Torr) that cracks the dimers to give birth to monomer units. The final polymerization step takes place on the device substrate at 25 °C ($P = 0.5$ Torr) resulting in the formation of a thin polymer film [17]. Most importantly, coating thickness can be controlled accurately and reproducibly through the amount of dimer used.

2.2.4.1.2 Additive Patterning

An additive method of polymer patterning was presented by Sessolo and coworkers in 2013 [3]. Once more, gold electrodes, contact pads, and their interconnections were patterned lithographically on a glass substrate. The device was coated with a 2 μm Parylene-C film that adhered on the substrate with the use of 3-(trimethoxysilyl)propyl methacrylate (–174 Silane). A soap solution was spin cast on Parylene-C to act as an antiadhesive layer between the first and a second 2 μm Parylene-C (sacrificial) film. Photolithography and an etching step were then used to open windows above the electrodes and the pads. After that, the polymer (PEDOT:PSS) was deposit by spin coating on the device, and a final peel-off step defined the final polymer device structure, shown in Figure 2.7.

Once again, the method is generic and versatile, and it can be adapted according to the desired device geometry. Moreover, different conducting polymers can be used as active layers as long as they can be deposited from solution.

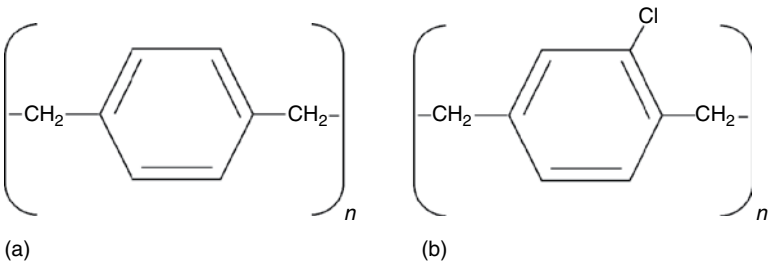

(a) (b)

Figure 2.6 Chemical structure of (a) poly(*p*-xylylene) and (b) (chloro-*p*-xylylene).

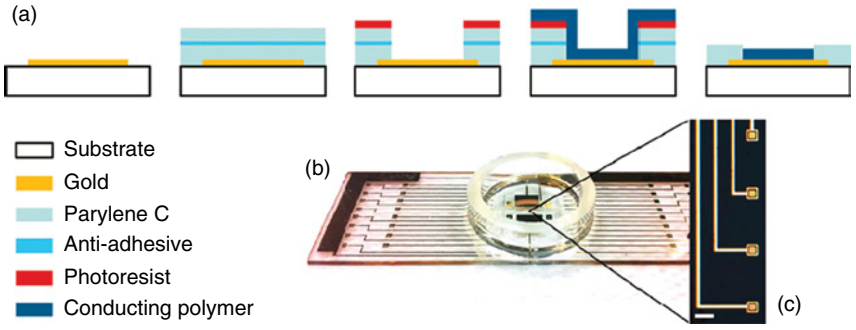

Figure 2.7 (a) The main steps of the fabrication process. The gold electrodes were first patterned lithographically and then Parylene-C was used for the device insulation. A second photolithography step followed by an etching step defines the well for the PEDOT:PSS deposition that follows. A mechanical peel off concludes the fabrication. (b) A microelectrode array device fabricated on a glass slide; (c) a close-up of the PEDOT:PSS covered electrodes (scale bar 50 μm). (Sessolo *et al*. 2013 [3]. Reproduced with permission of John Wiley and Sons.)

2.2.4.2 Orthogonal Photoresist Method

A different way of dealing with the polymer patterning challenge comes with the utilization of orthogonal solvents. The term *orthogonal* refers to solvents in which the organic compounds are insoluble, a feature that allows not only the patterning of organic electronic materials but also their multilayer deposition.

Hydrofluoroethers (HFEs) in particular belong to a class of solvents, which, besides being nontoxic and environment friendly, are also orthogonal to many organic materials [18]. Consequently, they are ideal candidates for polymer patterning as long as a photoresist compatible with them is synthesized.

A photoresist such as this was presented in 2009 by Taylor *et al*. [5]. The HFE compatible material is a copolymer composed of a highly fluorinated monomer **1** (3.3.4.4.5.5.6.6.7.7.8.8.9.9.10.10.10-hepta-decafluorodecyl methacrylate) and a photosensitive monomer **2** (2-nitro-benzyl methacrylate) (Figure 2.8). Its solubility in HFE solvents can be modified after UV exposure due to structural changes to the photosensitive **2** part of the molecule, resulting in a negative tone photoresist. In addition, it is acid stable, a feature extremely useful when it is used to pattern acidic polymers.

As a proof of concept, a bottom-contact organic thin-field transistor was fabricated with a pentacene channel and PEDOT:PSS drain and source electrode by the same group. On a Si wafer, a 360 nm oxide was grown thermally just before PEDOT:PSS was spin cast and baked at 180 °C for 10 min. Photoresist **3** was then spun on the PEDOT:PSS layer and patterned lithographically with HFE-7200 (an isomeric mixture of methyl nonafluorobutyl ether and methyl nonafluoroisobutyl ether) acting as its developer. The image was transferred on the PEDOT:PSS with oxygen etching and the remaining photoresist was lifted off in a propan-2-ol (10% by volume)/HFE-7100 mixture. Photoresist **3** was spun again on the patterned PEDOT:PSS film, this time followed by UV light exposure and a development step. Pentacene was thermally evaporated, and removal of the photoresist by the previously used solvent mixture defined a pentacene channel connecting the PEDOT:PSS source and drain electrodes (Figure 2.9).

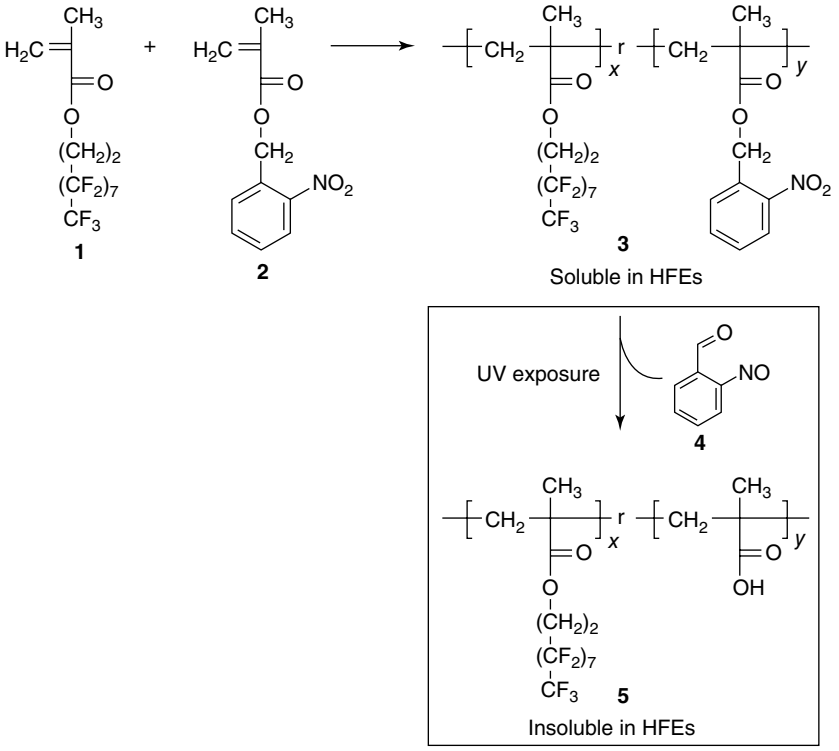

Figure 2.8 Synthesis of the HFE-soluble photosensitive copolymer **3**. Exposure to UV light renders the polymer insoluble in HFEs. (Taylor *et al*. 2009 [5]. Reproduced with permission of John Wiley and Sons.)

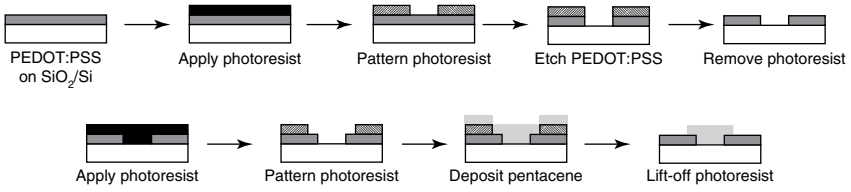

Figure 2.9 Main fabrication steps of the PEDOT:PSS/pentacene bottom-contact organic thin-film transistor. PEDOT:PSS was first spin cast on the substrate and patterned photolithographically with the use of the photoresist 3 as a developer and a following oxygen etching step. The process was repeated for the deposition of the pentacene film giving birth to the organic thin-film transistor. (Taylor *et al*. 2009 [5]. Reproduced with permission of John Wiley and Sons.)

In a similar approach, Hwang and coworkers were able to pattern polymer materials using supercritical carbon dioxide (scCO2) as the solvent [19] to fabricate an organic light-emitting diode (OLED). $ScCO_2$ is an environment-friendly fluid used in the dry photolithography process (DPP) for resist stripping owing to its physical and chemical advantages. Most importantly, it is a poor solvent for most ionic, high molecular weight, and low pressure organic materials.

In their work, a light-emitting polymer (LEP) was patterned on top of a PEDOT:PSS active layer. PEDOT:PSS was first spin cast on glass coated with indium tin oxide (ITO). A negative tone copolymer was synthesized from 1*H*,1*H*,2*H*,2*H*-perfluorodecyl methacrylate (FDMA) and *tert*-butyl methacrylate (TBMA) and deposited on the PEDOT:PSS layer. After UV exposure, $scCO_2$ was used for the development followed by oxygen plasma cleaning treatment and an LEP spin-casting step. A thermally deposited CsF(1 nm)/Al(40 nm) film completed the ITO/PEDOT:PSS/LEP/CsF/Al structure (Figure 2.10).

2.3 Printing

The term *printed electronics* comes from bridging the fields of both printing and electronics; this union of two fields allows for simpler methodology to fabricate inexpensive electronic components. The market for printed electronics has been estimated around 57 billion dollars (US) in 2019 by IDTechEx [20], and there are significant opportunities for companies to enter this market. The advantages of printing techniques include direct ink transfer to substrates and a reduction in the number of manufacturing steps. Furthermore, motivations for the continued use of printing arise from its flexibility, high processing speeds, ease of customization, reduction in manufacturing costs, the possibility of printing on inexpensive flexible plastic or paper substrates, and the ability to print with different types of materials.

Recently, there has been a growing interest to adapt classical printing techniques to be able to print new functional materials, especially with electronic inks for device fabrication. This idea has the potential to open up new markets and opportunities for both industry and academia. By exchanging traditional graphic inks for electrically functional inks, one can directly print or fabricate

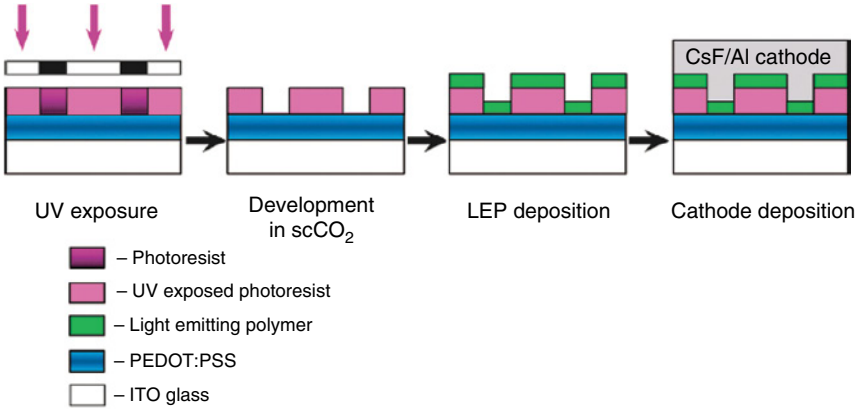

Figure 2.10 The main steps of the OLED fabrication process. PEDOT:PSS was spun on the substrate and a negative tone photoresist was used to pattern the LEP on top of PEDOT:PSS. The developer used was $scCO_2$, which is not harmful to the active material. A CsF(1 nm)/Al(40 nm) film completes the device fabrication [20]. (Glowacki 2015, http://pubs.rsc.org/en/Content/ArticleLanding/2015/TC/c5tc00556f#!divAbstract. Used under CC-BY-3.0 http://creativecommons.org/licenses/by/3.0/.)

interconnections, antennas, sensors, and so on. By using printing techniques, one can avoid the large number of processing steps (lithography, etching, etc.) used in conventional electronic fabrication techniques.

Technologies such as screen printing or inkjet are promising technologies, and have been extensively studied over the last few decades. They are envisaged to replace traditional manufacturing technologies, such as lithography, to fabricate new electronic components. In this part, we will describe the different printing techniques with an emphasis on conducting materials. We will separate the topic into two categories: contact and noncontact printing.

2.3.1 Contact Printing Technologies

2.3.1.1 Gravure

Gravure printing is a process coming from intaglio developed in the nineteenth century. It uses a rotary printing press and operates at high speed processing (up to 100 m min^{-1}). It is adapted for large volume runs such as books or magazines. Gravure is based on the direct transfer of the ink to the substrate from an engraved cylinder to the substrate (Figure 2.11). This cylinder is electroplated, for instance, with copper, and engraved electromechanically or by laser to create microcells. A chromium zinc layer is generally added to protect the cylinder. The volume of the ink that is deposited is determined by the geometry of the microcells. Then, the ink is transferred by capillary force from the microcells to the substrate when pressure is applied between the gravure cylinder and the substrate. Moreover, a doctor blade station is used in order to remove any excess ink and to ensure good film uniformity. Gravure allows designs with high resolution up to 20 μm and presents good printing quality and process reproducibility. It is compatible with a wide range of solvents or water-based inks. The required viscosity of the inks is comprised between 10 and 500 cP. Nevertheless, this process exhibits some limitations in terms of maintenance and cost of manufacturing mainly because of the price and the weight of cylinders.

This technique has been studied for electronic applications such as for the realization of field-effect transistors (FETs) or photovoltaic cells [21]. A few groups tested

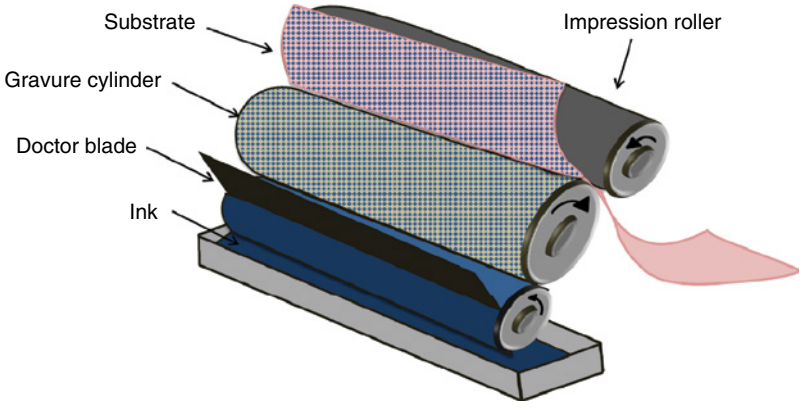

Figure 2.11 Gravure process.

the printability of conducting polymers to print functional multilayers to fabricate FETs [22] or to realize solar cells with laboratory gravure modules [23–25]. Gravure-printed PEDOT:PSS electrodes demonstrated high mechanical flexibility and stretchability in comparison with conventional indium tin oxide (ITO) on flexible substrates. For instance, Hübler *et al.* fabricated photovoltaic cells by printing PEDOT:PSS as the anode and a poly(3-hexylthiophene-2,5-diyl):[6,6]-phenyl-C 61 butyric acid methyl ester blend (P3HT:PCBM) as the photoactive and hole transport layers on paper [24]. Yang *et al.* used an industrial gravure printing proofer to process the photovoltaic module, where they print conducting polymers on flexible substrates already coated with ITO [26]. Recently, gravure has been investigated to realize impedance-based electrochemical biosensors [27], which paves the way to fabricate the new generation of flexible devices for biological applications.

2.3.1.2 Flexography

Conventionally, flexography is used for printing food packages and magazines. Flexography is compatible with flexible substrates such as plastics or cardboards. It is a process combining a system of cylinders and a flexible relief plate (Figure 2.12). An engraved anilox roll is used to transfer the ink from the pan. The amount of the ink is fixed by the volume of the microcells' cylinder. A doctor blade ensures that the thickness of the ink is uniform. Then, the printing of the ink is assured by the contact between the substrate and the plate cylinder. These plates are usually made from rubber or photopolymer materials and produced by photolithography.

This technology is compatible with a wide variety of inks: UV-cured inks and solvent- or water-based inks with a viscosity ranging from 10 to 100 cP. Resolution up to 50 µm can be reached. The use of the plates lowers the cost of fabrication and allows the printing of large volume runs with high processing speed (up to 180 m min^{-1}). The costs are reduced in comparison with gravure but plates can be degraded with the use of solvents. One of the major undesirable effects of this process is the halo that appears on the edge of the printed pattern. The default comes from the deformation of the plate when the pressure is applied between the plate and the substrate squeezing the ink.

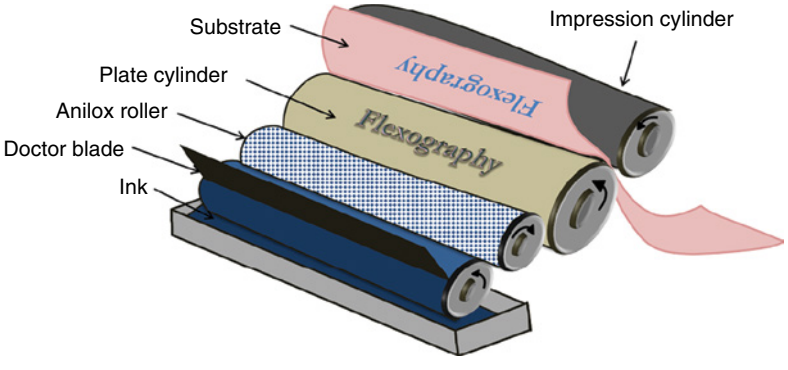

Figure 2.12 Flexography process.

Only few studies chose this approach for printed electronic applications [28, 29]. Hübler *et al.* [30] use a laboratory flexographic test printing device to print the gate and contact electrodes using conducting polymers to fabricate transistors. Krebs *et al.* [31] reported using this process to improve the wettability of surface to slot die conducting polymer while Yu *et al.* [32] printed the silver layer to realize grids to replace ITO in polymer cells.

2.3.1.3 Screen Printing

Screen printing is a simple and versatile technique used in many applications such as textiles or advertisements. It has been originally invented in China, and imported into Europe in the eighteenth century and developed in the second half of the twentieth century. The first patent was published in 1907 by Samuel Simon, and the technique became more popular in the 1960s with artists such as Andy Warhol [33].

Screen printing is a stencil method that uses a mesh stretched over a frame to transfer the ink to the substrate. The ink is pushed into the opening of the mesh through a squeegee (Figure 2.13). The mesh is usually made from nylon, polyester, or a stainless steel. Two different categories of screen printing have been

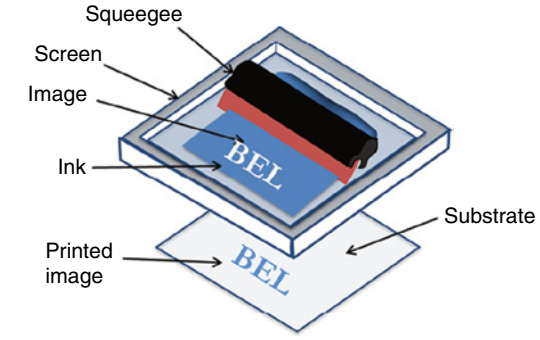

(a)

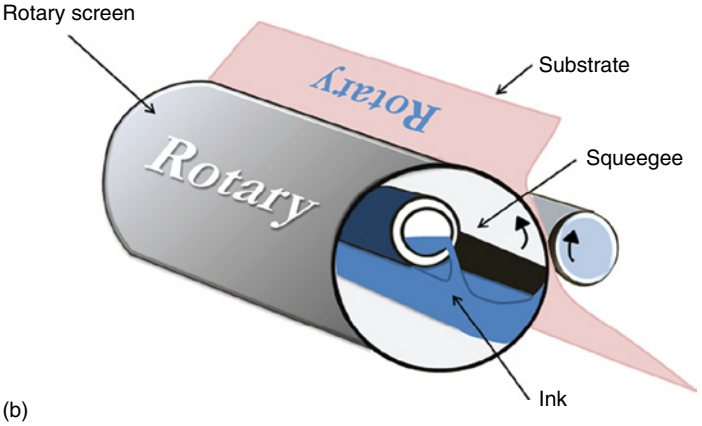

(b)

Figure 2.13 (a) Flatbed screen printing. (b) Rotary screen printing.

developed and can be integrated for roll-to-roll manufacturing: the flatbed screen or the rotary screen. The flatbed screen (Figure 2.13a) is used in laboratories or in production and the rotary is adapted for large-scale process with a production speed up to 100 m min^{-1}. In this case, the squeegee and the ink are placed in the rotary screen (Figure 2.13b), making the maintenance procedure difficult. The printing resolution can be up to 100 µm and depends on parameters such as the surface energy of the substrate, the ink viscosity, the mesh size, and counts.

Screen printing is one of the most robust technologies that have been developed in the last few years as it is compatible with a wide range of substrates such as textiles, clothes, papers, and glass. This process requires high-viscosity inks (up to 10 000 cP) and the deposited thickness can go up to few hundreds of microns. Screen printing is already used to print interconnections for printed circuit boards and antennas for RFIDs (Radio Frequency IDentifications), active layers [34] and electrodes [35, 36] for solar cells or organic thin-film transistors [37], and emitting layers in OLEDS [38–40] (Figure 2.14). Many studies [41–43] and patents [44–46] have reported the use of screen printing for biosensing applications. They demonstrated the feasibility of such devices to detect bioelements or to fabricate amperometric biosensors.

2.3.2 Noncontact Printing Technologies

Noncontact printing technologies are digital writing approaches and present many advantages because they do not require masks and the geometry can be customized and changed on demand. Also, the ink is digitally delivered to the substrate, thus limiting the wastage of materials and allowing processing of designs at low cost.

2.3.2.1 Aerosol Jet

Aerosol jet printing has been developed since the 2000s and shows a promising future for industrial applications. This technology allows printing a large range of ink viscosities (from 1 to 2500 cP). The principle is based on the ejection of fluids even with nanoparticles from a chamber to the substrate (Figure 2.15), a new technology that uses the atomization of suspension by an ultrasonic or a pneumatic system. The formed droplets are guided by a jet stream up to the printing nozzles. The aerosol printing can produce conformal coating and resolution down to 10 µm with processing speed up to 1.2 m min^{-1}.

Few studies mention aerosol printing in literature [47, 48]. Recently, it has been evaluated for diverse applications such as solar cells and thin-film transistors.

Figure 2.14 Screen printer using Clevios™ ink. (Reproduced with permission from Heraeus.)

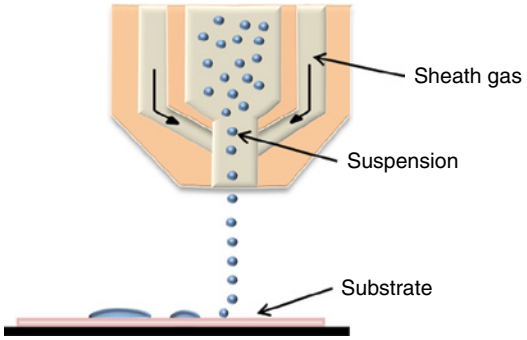

Figure 2.15 Aerosol process.

For instance, aerosol jet has been used to print the conducting polymer as an active layer in solar cells [49] and to fabricate electrodes for TFTs [50]. Aerosol has been also studied for the deposition of DNA or enzymatic layers and for the functionalization of electrodes in biological sensors [51].

2.3.2.2 Inkjet

Inkjet is a noncontact technology commonly used for daily use printing applications (home or office). This process can be integrated in industry in roll-to-roll processes in the production line. Advances in these technologies have been seen recently, for instance, the standardization and commercialization of 3D printing and the creation of new functional inks for electronics.

2.3.2.2.1 History

The physics behind inkjet was first described in 1878 by Lord Rayleigh [52], the pioneer in studying the mechanism of the liquid jets' instability. The first patent was deposited by Elmqvist [53] in 1951 at Siemens-Elema Company.

In the early 1960s, Sweet developed a model [54] in Stanford University, in which he assumed that the trajectory of ejected droplets can be controlled electrostatically through an externally applied electric field. This process has been called continuous inkjet (CIJ) and it is still used for some applications. Later, a drop-on-demand (DOD) technology was proposed in 1972 by Zoltan [55] and Kyser and Sears [56] as an alternative to CIJ. A single droplet is formed and detached by each of the printhead's nozzles.

In the late 1970s, John Vaught [57] from Hewlett Packard and Ichiro Endo [58] from Canon developed a DOD system based on the formation and the ejection of ink using a heating element known as *thermal inkjet*. In the 1990s, and with the standardization of personal computers, inkjet became a technology used daily with the commercialization of inexpensive printers.

2.3.2.2.2 Basic Principles

The inkjet mechanism is based on the formation and the ejection of fluid droplets, released from a chamber under the variation of internal pressure in the printhead cavity and through nozzles. This fluid ejection depends on rheological

parameters such as the ink's properties (surface tension, viscosity, density) and the chamber's pressure. The resolution can reach 20 µm depending on the nozzle diameter, drop volume, surface energy of the substrate, and drop-to-drop spacing. Originally, two technologies have been developed for inkjet: CIJ and DOD technology (Figure 2.16).

CIJ (Continuous Inkjet) Printing

The CIJ technology consists of the generation and the ejection of continuous drops. Those droplets pass through an electrostatic charging electrode and then a high-voltage deflector plate leads trajectory deviation toward a recycling recipient. Two different categories of CIJ have been developed: the binary and the multiple deflections. In a binary deflection system (Figure 2.17) there are two states regulated by the electrostatic deflector. The drops that are charged during the printing step are going directly to the substrate and the non-charged ones are deviated and collected in a gutter and then recycled. In a multiple deflection system, the non-charged drops go to the gutter to be reprocessed while the charged drops are deviated to be deposited onto the substrate.

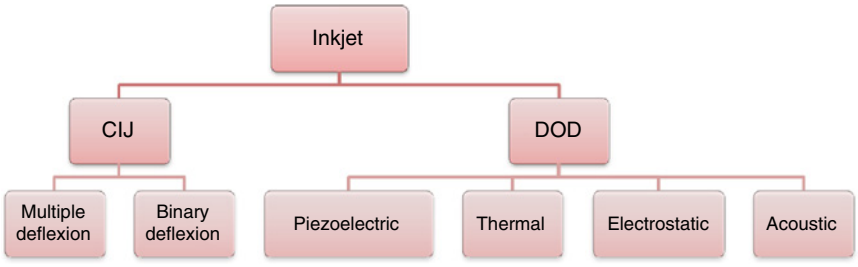

Figure 2.16 Inkjet technology.

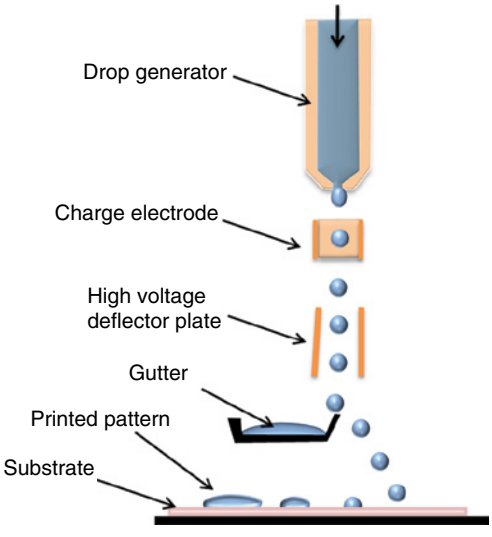

Figure 2.17 Binary continuous inkjet system.

CIJ technology is used in industry for marking and encoding the products before commercialization. It presents advantages such as good printing resolution down to 50 µm, high ejection frequencies of droplets up to 60 kHz at high printing speed, and good process stability without nozzles clogging. However, this technique shows limitations regarding the type of inks to be printed, which have to match the requirements of the system especially for the electrostatic charging step. The ink recycling step can induce materials contamination. Finally, printing of complex designs and customization is not easy because of the continuous ejection of the drops. This is why this technology has never been adopted for printed electronics.

(DOD) Drop-On-Demand Inkjet Printing

The drop-on-demand technique can be divided into four categories: piezoelectric, thermal, electrostatic, and acoustic inkjet. Thermal and piezoelectric inkjets are the most successful technologies adopted in industry and laboratories.

In thermal inkjet, the heating element is integrated within the printhead chamber. A local increase in the temperature of the ink, generally up to 300 °C, creates an air bubble within the ink inside the ejection chamber. This change in local pressure provokes the formation and the ejection of individual droplets (Figure 2.18a). Today, thermal inkjet is widely used for graphic printing and especially for home printers. However, requirements for heating before ejection make this technology very limited in terms of inks. A few studies mentioned the possibility of fabricating biosensors [59, 60]. For instance, Setti *et al.* [61] reported fabricating an amperometric sensor for the detection of glucose.

The piezoelectric inkjet technology is based on the use of a piezo membrane (Figure 2.18b). This membrane is mechanically deformed when an external voltage is applied thus causing a change in the pressure inside the printhead chamber. This causes the formation of the droplet in the aperture in the printhead. The jetting of the ink is given by the pressure release and a large type of inks can be used. Here, the nozzle generates a droplet with a volume of a few picoliters. The ink viscosity ranges from 5 to 20 cP and the resolution down to 20 µm.

With the rise in printed electronics, several companies such as FujiFilm, Ceradrop, and Meyer Burger developed new inkjet machines that can print different functional materials using piezo-DOD technology (Figure 2.19). The printing parameters such as the voltage applied to the piezo element, the drop spacing, the waveform, and the temperature of the ink can be tuned. Some printers offer the possibility to realize the alignment to print complete devices with

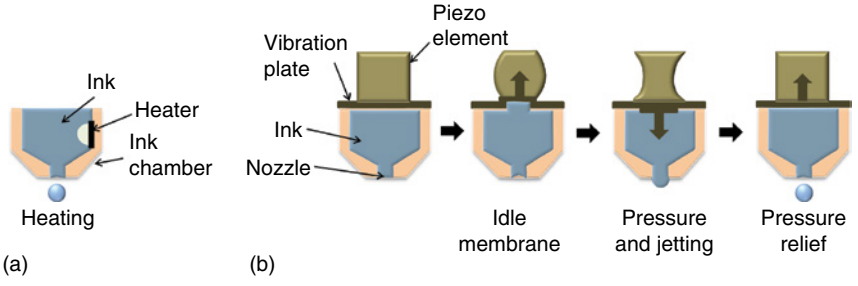

Figure 2.18 (a) Thermal inkjet and (b) drop-on-demand inkjet process.

Figure 2.19 Inkjet printer using Clevios™ ink. (Reproduced with permission from Heraeus.)

several layers and different inks. The machines show flexibility and are easy to use, making the process adaptable to different materials.

Inkjet offers many possibilities for new developments. In the literature, inkjet is widely studied for electronic applications such as for organic thin-film transistors (OTFTs) [62, 63], OLEDs and solar cells or organic photovoltaics (OPVs) [64–68], and sensors [69]. Studies demonstrated the feasibility of using commercial PEDOT:PSS ink to print OTFTs with dimensions in the range of micrometer [70, 71] and sub-micrometer [72] scales by controlling the hydrophobicity of the substrate. Bharathan *et al.* [73] combined inkjet with spin-coating to pattern electroluminescent devices. Inkjet has also been used to print active layers of solar cells [74, 75] with device efficiency above 3%. Printed conducting polymers have also been studied for chemical sensing such as ammonia detection [76, 77].

2.3.2.2.3 Printability Requirements

In the DOD technology, the formation and ejection of the droplet depend on different rheological parameters of the ink such as viscosity, density, and surface tension (Figure 2.20).

Printability of the ink depends on these rheological parameters combined with the characteristics of the printhead (nozzle diameter, frequency of the drops' ejection, applied voltage, channel length, and internal pressure). The rheological behavior of the ink can be described with dimensionless parameters such as the Reynolds number and the Weber number or the Ohnesorge number, defined as

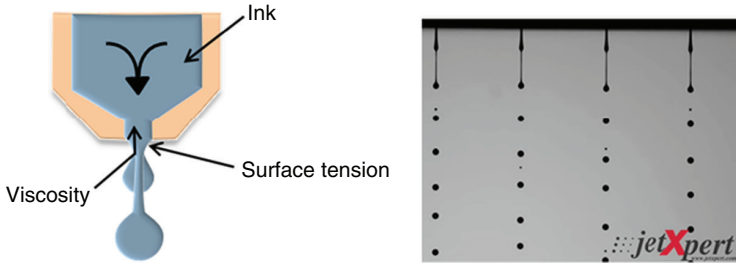

Figure 2.20 (a) Drop formation in the nozzle and (b) ejection of the drop. (JetXpert drop watcher. Reproduced with permission.)

$$Re = \frac{\nu \rho R}{\mu}; \quad We = \frac{\nu^2 \rho R}{\sigma}; \quad Oh = \frac{\sqrt{We}}{Re} = \frac{\mu}{\sqrt{\rho R \sigma}} \tag{2.5}$$

where μ is the viscosity of the ink, ρ is the density, σ is the surface tension, R is the radius of the nozzle, and ν is the velocity.

These numbers are directly dependent on the fluid's rheological properties and they are used to predict the ejection of the ink from the nozzle. In the 1980s, Fromm [78] defined the criteria for ink printability such as $Z = \frac{1}{Oh} > 2$. Later, Reis and Derby [79, 80] discussed Fromm's assumption and propose their own rheological requirements for ink jetting. Using a numerical simulation of drop formation, Reis suggested that the condition $1 < Z < 10$ is more adapted in order to match the ink with the printing requirements. They propose a chart [80] where one can define which area is the most adequate combing the above-mentioned dimensionless number with DOD printing. The lower limit corresponds to a high viscosity domain that prevents the jetting while the upper limit causes the formation of unwanted satellite drops. This theory is often used in the literature [81–83] for the formulation of new functional inks dedicated to inkjet printing technology.

2.3.3 Inks

Graphic inks are widely present on the market and used in daily life. Over the last few years, with concern over environmental issues and to reduce the fabrication costs of electronic components, a new trend has emerged in formulating new functional inks that exhibit different electrical properties. Manufacturers are developing new inks with specific functions that can fit specific requirements for diverse applications such as photovoltaics or thin film transistors (TFTs). In this section, we describe the different categories of inks.

2.3.3.1 Metallic Inks

The inks are usually composed of metallic nanoparticles, for instance, gold, silver, or copper in suspension in solvents. Surfactants can be added to the formulation for the tuning of surface tension to fit the requirements of the printing process. Many manufacturers offer a large choice of metallic inks for printing processes and the market is in expansion. Different methods exist to produce nanoparticles, such as chemical reactions or mechanical attrition. The first method is based on the use of precursors [84] where an organic complex containing metal salt is dissolved in a solvent. For the mechanical attrition, ball milling [85] is usually used to downscale materials to nanoscale. The size of nanoparticles can vary from a few to hundreds of nanometers and they can be produced in different shapes such as nanoplates or nanospheres depending on the preparation conditions. These nanoparticles are subsequently embedded in organic shell polymers for protection against the oxidation and for solubility in water or in vehicle solvents. Poly(vinyl pyrrolidone) (PVP), for example, is one of the most commonly used polymers for the encapsulation of nanoparticles.

Thermal curing is a key step in the fabrication of metal structures. After printing, an annealing step allows the evaporation of organic compounds and the coalescence of nanoparticles. New types of selective curing techniques such as microwave curing [86], laser sintering [87], or photonic sintering [88] permit the coalescence of nanoparticles without thermomechanical degradation or damage to underlying materials such as plastic substrates. Electrical conductivity of between 10% and 30% of that of bulk metal is generally obtained, depending on the thermal cycle and the size and the shape of the nanoparticles [89].

2.3.3.2 Dielectric Inks

Dielectric inks are usually used in printed electronics to fabricate dielectric isolation layers in circuits. They can be UV-based inks also composed of nanoparticles (TiO_2, $BaTiO_3$). UV-curable inks comprise monomers, oligomers, photoinitiators, and additives [90]. Photoinitiators absorb energy from UV leading to the polymerization of the monomers, for instance, acrylic monomers after exposure to UV light (Figure 2.21).

These UV inks offer advantages such as facile processing without clogging the nozzle. They avoid the evaporation of volatile organic compounds from the ink since polymerization occurs without the need for a drying step. The polymerization step takes a few seconds and can be easily integrated in a roll-to-roll process.

2.3.3.3 Conducting Polymer Inks

Since their discovery in the 1970s by Shirakawa *et al.* [91], conducting polymers have been broadly studied because of their electrical conductivity, high mechanical flexibility, and long-term stability. With the emergence of printed electronics, conducting polymers are formulated in new conducting inks. Polyaniline, polypyrroles, polythiophenes, and PEDOT:PSS are especially considered for electronic applications. They are dispersed in organic solvents, and secondary dopant solvents such as ethylene glycol or dimethyl sulfoxide (DMSO) are added to the formulation to boost the conductivity and to fix the viscosity while surfactants such as Triton X-100 adapt the surface tension to match the substrate surface energy.

Polypyrrole is a dielectric polymer that can be doped by oxidation process to reach conductivity up to $100\,S\,cm^{-1}$ [92]. This polymer is usually electrochemically deposited [93] for applications such as capacitors [94] or chemical sensors [95]. Only few studies mention polypyrrole as an ink [96, 97] for printed electronics applications.

Polyaniline is a conducting polymer that combines electronic and optical properties. Polyaniline exists in three stable oxidation states that exhibit different conductivities and colors. Among them, the emeraldine state presents the highest

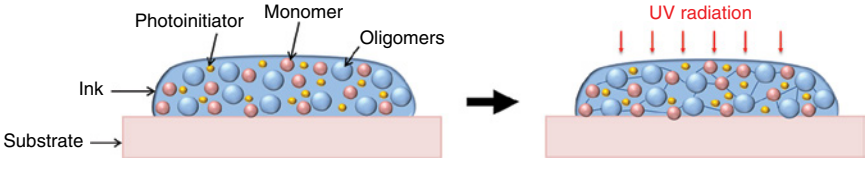

Figure 2.21 UV polymerization.

conductivity in its doped state. Polyaniline has advantages such as stability at room temperature, ease of synthesis, and transparency. Companies such as Panipol are developing polyaniline inks compatible with inkjet and others process. This polymer has been studied for applications such as gas sensing [98], especially ammonia [77, 99], combined with graphene for capacitor electrodes [100] and recently for biomedical applications such as biosensors [101, 102]. However, this polymer is not compatible [103] for implantable biodevices.

PEDOT in its neutral state is a conducting polymer but remains difficult to process mostly because it is insoluble and rapidly oxidizes in air. In combination with PSS, a water-soluble polymer that serves as a charge-balancing counter ion [104], the complex is stable in solution. In its oxidized state, PEDOT:PSS is a stable polymer and it is one of the most studied polymers currently used for printing transparent electrodes [105] or hole transport layers [35] in applications such as solar cells and OLEDs. PEDOT:PSS inks are available commercially in water-based formulations from a few suppliers such as Heraeus and Agfa (Orgacon) that are compatible with printing technologies such as inkjet or screen printing. PEDOT:PSS thin films present high transparency, good thermal stability, and high conductivity, which can be even tuned by doping the polymer with solvents [106]. Recent research [107, 108] highlights PEDOT:PSS as a good candidate for biomedical applications owing to its higher electronic and ionic properties combined with its biocompatibility[109].

2.3.4 Comparison of Printing Techniques

In this section, we focus on specific characteristics of printing technologies (Table 2.1). Screen printing is one of the most advanced techniques in terms of research and development for printed electronics. It allows depositing highly viscous inks resulting in thicker layers than other printing techniques and can fit many electronic applications. It is a mature technology that is already used in industry today. This prerequisite could be achieved by other techniques such as gravure printing by optimizing the size of the engraved cells to reach the micron scale. Both flexography and gravure show promising future in electronics but limits still exist such as the manufacturing costs for gravure or the presence of the halo for the flexography. A compromise must be found between thickness and resolution.

Inkjet is a promising technique especially at the laboratory scale as it allows the digital fabrication of complete devices with low manufacturing costs. Additionally,

Table 2.1 Comparison of printing techniques.

	Gravure	Flexography	Screen printing	Aerosol jet	Inkjet
Printing form	Cylinder engraved	Printing plate	Mesh screen	Digital	Digital
Speed ($m\,min^{-1}$)	8–100	5–180	30–100	1.2	0.02–0.5
Resolution (μm)	20	50	<100	10	20
Viscosity (cP)	10–500	10–100	500–10 000	1–2500	5–20
Thickness (μm)	1–8	1	>10	>0.1	0.1–15

the geometry can be customized on demand. This technique is easy to use to evaluate new designs and inks. Today, inkjet printing is still difficult to use in roll-to-roll processes because of maintenance issues related to nozzle clogging and ink stability. The printing resolution is limited by the rheology of the ink, the characteristics of the printhead, and the physicochemical properties of the substrate. On the other hand, Aerosol jet printing is a recent technique that is versatile and customizable, and could offer an alternative to other processes as it shows flexibility in terms of compatibility with inks (viscosity). The resolution is higher than inkjet but it requires further developments to compete with actual fabrication processes.

2.4 Conclusions

Photolithography has been the technique of choice for device fabrication in the semiconductor industry for many years now. It is a relatively simple, reliable, and reproducible way of fabricating electronic devices in a cost-effective and controllable manner. It can offer high-resolution patterning and the degree of freedom coming from its potential of scalability to large-area substrates. The aforementioned, together with the high throughput that comes hand in hand with its parallel nature, are the technique's comparative advantages over other proposed approaches. Shadow mask evaporation and soft or hard imprint, which were recruited to replace photolithography, do not seem able to compete with it on one or more of its previously mentioned strong points. In addition, one of the drawbacks that these processes share is the issue of registration, a figure of merit that photolithography can easily offer. Above all, photolithography is an appealing organic material patterning technique as it promises to use the knowhow and the added knowledge of the already well-established and mature semiconductor industry.

Photolithography's main challenge, though, remains its implementation in the organic world. Incompatibility issues between the organic materials and the chemicals used during the process have been widely discussed in this chapter along with possible ways to circumvent this problem. Moreover, lithographic patterning requires a controlled environment and consequently clean room facilities. This fact may render the fabrication process a rather complicated one, an issue that can be addressed, nevertheless, by the use of the already existing semiconductor production line. Provided that the proposed organic patterning approaches will be optimized to become generic, versatile, and applicable to any organic material, photolithography has the potential to be the technique of choice in polymer device fabrication for the years to come.

On the other hand, printed technologies also present many advantages such as versatility, flexibility, and low cost. They are compatible with a wide range of materials to formulate inks such as conducting polymers, for instance. They can be sheet-based or roll-to-roll techniques and can use flexible plastics as substrates. They can operate at high speed. They offer new perspectives for electronic applications (OFETS, OLEDs, bioelectronics, etc.) but require further development to reach high resolution.

References

1 Malliaras, G. and Friend, R. (2005) An organic electronics primer. *Phys. Today*, **58** (5), 53–58.
2 Forrest, S.R. (2004) The path to ubiquitous and low-cost organic electronic appliances on plastic. *Nature*, **428** (6986), 911–918.
3 Sessolo, M. *et al.* (2013) Easy-to-fabricate conducting polymer microelectrode arrays. *Adv. Mater.*, **25** (15), 2135–2139.
4 DeFranco, J.A. *et al.* (2006) Photolithographic patterning of organic electronic materials. *Org. Electron.*, **7** (1), 22–28.
5 Taylor, P.G. *et al.* (2009) Orthogonal patterning of PEDOT:PSS for organic electronics using hydrofluoroether solvents. *Adv. Mater.*, **21** (22), 2314–2317.
6 Huang, J. *et al.* (2007) Patterning of organic devices by interlayer lithography. *J. Mater. Chem.*, **17** (11), 1043–1049.
7 Madou, M.J. (2011) *Manufacturing Techniques for Microfabrication and Nanotechnology*, Taylor & Francis.
8 Wilson, C.G., Dammel, R.R., and Reiser, A. (1997) Photoresist Materials: A Historical Perspective, *Proc. SPIE*, (3049), 28–41.
9 Bahreyni, B. (2009) in *Fabrication and Design of Resonant Microdevices* (ed. B. Bahreyni), William Andrew Publishing, Norwich, NY, pp. 9–46.
10 Levinson, H.J. (2005) *Principles of Lithography*, Society of Photo Optical.
11 Thompson, L.F., Willson, C.G., and Bowden, M.J. (1983) *Introduction to Microlithography*, American Chemical Society, Washington, DC.
12 Mack, C. (2008) *Fundamental Principles of Optical Lithography: the Science of Microfabrication*, John Wiley & Sons, Ltd.
13 Ilic, B. and Craighead, H.G. (2000) Topographical patterning of chemically sensitive biological materials using a polymer-based dry lift off. *Biomed. Microdevices*, **2** (4), 317–322.
14 Kymissis, I., Dimitrakopoulos, C.D., and Purushothaman, S. (2002) Patterning pentacene organic thin film transistors. *J. Vac. Sci. Technol., B*, **20** (3), 956.
15 Khodagholy, D. *et al.* (2011) Highly conformable conducting polymer electrodes for In vivo recordings. *Adv. Mater.*, **23** (36), H268–H272.
16 Chang, T.Y. *et al.* (2007) Cell and protein compatibility of parylene-C surfaces. *Langmuir*, **23** (23), 11718–11725.
17 Fortin, J.B. and Lu, T.-M. (2000) Mass spectrometry study during the vapor deposition of poly-para-xylylene thin films. *J. Vac. Sci. Technol., A*, **18** (5), 2459–2465.
18 Zakhidov, A.A. *et al.* (2008) Hydrofluoroethers as orthogonal solvents for the chemical processing of organic electronic materials. *Adv. Mater.*, **20** (18), 3481–3484.
19 Hwang, H.S. *et al.* (2008) Dry photolithographic patterning process for organic electronic devices using supercritical carbon dioxide as a solvent. *J. Mater. Chem.*, **18** (26), 3087–3090.
20 Das, R. and Harrop, P. (2013) *Printed, Organic & Flexible Electronics: Forecasts, Players & Opportunities 2009–2029*, IDTechEx, Cambridge.
21 Pudas, M., Hagberg, J., and Leppävuori, S. (2004) Gravure offset printing of polymer inks for conductors. *Prog. Org. Coat.*, **49** (4), 324–335.

22 Voigt, M.M. *et al.* (2010) Polymer field-effect transistors fabricatfed by the sequential gravure printing of polythiophene, two insulator layers, and a metal Ink gate. *Adv. Funct. Mater.*, **20** (2), 239–246.

23 Kopola, P. *et al.* (2011) Gravure printed flexible organic photovoltaic modules. *Sol. Energy Mater. Sol. Cells*, **95** (5), 1344–1347.

24 Hübler, A. *et al.* (2011) Printed paper photovoltaic cells. *Adv. Energy Mater.*, **1** (6), 1018–1022.

25 Ding, J.M. *et al.* (2009) Patternable polymer bulk heterojunction photovoltaic cells on plastic by rotogravure printing. *Sol. Energy Mater. Sol. Cells*, **93** (4), 459–464.

26 Yang, J. *et al.* (2013) Organic photovoltaic modules fabricated by an industrial gravure printing proofer. *Sol. Energy Mater. Sol. Cells*, **109**, 47–55.

27 Reddy, A.S.G. *et al.* (2011) Gravure printed electrochemical biosensor. *Procedia Eng.*, **25**, 956–959.

28 Mäkelä, T. *et al.* (2007) Continuous roll to roll nanoimprinting of inherently conducting polyaniline. *Microelectron. Eng.*, **84** (5–8), 877–879.

29 Søndergaard, R.R., Hösel, M., and Krebs, F.C. (2013) Roll-to-Roll fabrication of large area functional organic materials. *J. Polym. Sci., Part B: Polym. Phys.*, **51** (1), 16–34.

30 Hübler, A.C. *et al.* (2011) Three-dimensional integrated circuit using printed electronics. *Org. Electron.*, **12** (3), 419–423.

31 Krebs, F.C., Fyenbo, J., and Jørgensen, M. (2010) Product integration of compact roll-to-roll processed polymer solar cell modules: methods and manufacture using flexographic printing, slot-die coating and rotary screen printing. *J. Mater. Chem.*, **20** (41), 8994–9001.

32 Yu, J.-S. *et al.* (2012) Silver front electrode grids for ITO-free all printed polymer solar cells with embedded and raised topographies, prepared by thermal imprint, flexographic and inkjet roll-to-roll processes. *Nanoscale*, **4** (19), 6032–6040.

33 Kamholz, R. (2013) *Andy Warhol and His Process*, http://www.sothebys.com/en/news-video/blogs/all-blogs/21-days-of-andy-warhol/2013/11/andy-warhol-and-his-process.html (accessed 29 March 2017).

34 Shaheen, S.E. *et al.* (2001) Fabrication of bulk heterojunction plastic solar cells by screen printing. *Appl. Phys. Lett.*, **79** (18), 2996–2998.

35 Krebs, F.C. *et al.* (2009) A complete process for production of flexible large area polymer solar cells entirely using screen printing—first public demonstration. *Sol. Energy Mater. Sol. Cells*, **93** (4), 422–441.

36 Krebs, F.C. (2009) All solution roll-to-roll processed polymer solar cells free from indium-tin-oxide and vacuum coating steps. *Org. Electron.*, **10** (5), 761–768.

37 Gray, C. *et al.* (2001) *Screen Printed Organic Thin Film Transistors (OTFTs) on a Flexible Substrate,* In International Symposium on Optical Science and Technology (pp. 89–94). International Society for Optics and Photonics.

38 Pardo, D.A., Jabbour, G.E., and Peyghambarian, N. (2000) Application of screen printing in the fabrication of organic light-emitting devices. *Adv. Mater.*, **12** (17), 1249–1252.

39 Jabbour, G.E., Radspinner, R., and Peyghambarian, N. (2001) Screen printing for the fabrication of organic light-emitting devices. *IEEE J. Sel. Top. Quantum Electron.*, **7** (5), 769–773.

40 Lee, D.-H. *et al.* (2008) Single-layer organic-light-emitting devices fabricated by screen printing method. *Korean J. Chem. Eng.*, **25** (1), 176–180.

41 Tudorache, M. and Bala, C. (2007) Biosensors based on screen-printing technology, and their applications in environmental and food analysis. *Anal. Bioanal.Chem.*, **388** (3), 565–578.

42 O'Halloran, M.P., Pravda, M., and Guilbault, G.G. (2001) Prussian Blue bulk modified screen-printed electrodes for H 2 O 2 detection and for biosensors. *Talanta*, **55** (3), 605–611.

43 Albareda-Sirvent, M., Merkoçi, A., and Alegret, S. (2000) Configurations used in the design of screen-printed enzymatic biosensors. A review. *Sens. Actuators, B*, **69** (1–2), 153–163.

44 Hill, H.A.O. *et al.* (1998) Strip electrode with screen printing. Google Patents, U.S. Patent No 5,820,551.

45 Hill, H.A.O. *et al.* (1996) Strip electrode including screen printing of a single layer. Google Patents, U.S. Patent No 5,509,410.

46 Su, C.S. *et al.* (2006) Electrochemical biosensor by screen printing and method of fabricating same. Google Patents, U.S. Patent No 7,138,041.

47 Krebs, F.C. (2009) Fabrication and processing of polymer solar cells: a review of printing and coating techniques. *Sol. Energy Mater. Sol. Cells*, **93** (4), 394–412.

48 Kopola, P. *et al.* (2012) Aerosol jet printed grid for ITO-free inverted organic solar cells. *Sol. Energy Mater. Sol. Cells*, **107**, 252–258.

49 Girotto, C. *et al.* (2009) Exploring spray coating as a deposition technique for the fabrication of solution-processed solar cells. *Sol. Energy Mater. Sol. Cells*, **93** (4), 454–458.

50 Cho, J.H. *et al.* (2008) Printable ion-gel gate dielectrics for low-voltage polymer thin-film transistors on plastic. *Nat. Mater.*, **7** (11), 900–906.

51 Ingo, G. *et al.* (2010) Surface biofunctionalization and production of miniaturized sensor structures using aerosol printing technologies. *Biofabrication*, **2** (1), 014106.

52 Strutt, J.W. and Rayleigh, L. (1878) On the instability of jets. *Proc. London Math. Soc*, **10**, 4–13.

53 Rune, E. (1951) Measuring instrument of the recording type. Google Patents, U.S. Patent No 2,566,443.

54 Sweet, R.G. (1965) High frequency recording with electrostatically deflected ink jets. *Rev. Sci. Instrum.*, **36** (2), 131–136.

55 Zoltan, S.I. (1972) Pulsed droplet ejecting system. Google Patents, U.S. Patent No 3,683,212.

56 Kyser, E.L. and Sears, S.B. (1976) Method and apparatus for recording with writing fluids and drop projection means therefore. Google Patents, U.S. Patent No. 3,946,398.

57 Donald, D.K., Lee, M.J., and Vaught, J.L. (1982) Method and apparatus for drop-on-demand ink jet printing. Google Patents, U.S. Patent No 4,336,544.

58 Endo, I. *et al.* (1988) Bubble jet recording method and apparatus in which a heating element generates bubbles in a liquid flow path to project droplets. Google Patents, U.S. Patent No 4,723,129.

59 Setti, L. *et al.* (2004) Thermal inkjet technology for the microdeposition of biological molecules as a viable route for the realization of biosensors. *Anal. Lett.*, **37** (8), 1559–1570.

60 Setti, L. *et al.* (2007) An HRP-based amperometric biosensor fabricated by thermal inkjet printing. *Sens. Actuators, B*, **126** (1), 252–257.
61 Setti, L. *et al.* (2005) An amperometric glucose biosensor prototype fabricated by thermal inkjet printing. *Biosens. Bioelectron.*, **20** (10), 2019–2026.
62 Arias, A. *et al.* (2004) All jet-printed polymer thin-film transistor active-matrix backplanes. *Appl. Phys. Lett.*, **85** (15), 3304–3306.
63 Sirringhaus, H., Kawase, T., and Friend, R.H. (2001) High-resolution ink-Jet printing of all-polymer transistor circuits. *MRS Bull.*, **26** (07), 539–543.
64 Hebner, T.R. *et al.* (1998) Ink-jet printing of doped polymers for organic light emitting devices. *Appl. Phys. Lett.*, **72** (5), 519–521.
65 Shimoda, T. *et al.* (2003) Inkjet printing of light-emitting polymer displays. *MRS Bull.*, **28** (11), 821–827.
66 Aernouts, T. *et al.* (2008) Polymer based organic solar cells using ink-jet printed active layers. *Appl. Phys. Lett.*, **92** (3), 033306.
67 Eom, S.H. *et al.* (2009) Polymer solar cells based on inkjet-printed PEDOT:PSS layer. *Org. Electron.*, **10** (3), 536–542.
68 Hoth, C.N. *et al.* (2007) High photovoltaic performance of inkjet Printed polymer:fullerene blends. *Adv. Mater.*, **19** (22), 3973–3978.
69 Abe, K., Suzuki, K., and Citterio, D. (2008) Inkjet-printed microfluidic multianalyte chemical sensing paper. *Anal. Chem.*, **80** (18), 6928–6934.
70 Sirringhaus, H. *et al.* (2000) High-resolution inkjet printing of all-polymer transistor circuits. *Science*, **290** (5499), 2123–2126.
71 Kawase, T. *et al.* (2003) Inkjet printing of polymer thin film transistors. *Thin Solid Films*, **438–439**, 279–287.
72 Wang, J.Z. *et al.* (2004) Dewetting of conducting polymer inkjet droplets on patterned surfaces. *Nat. Mater.*, **3** (3), 171–176.
73 Bharathan, J. and Yang, Y. (1998) Polymer electroluminescent devices processed by inkjet printing: I. Polymer light-emitting logo. *Appl. Phys. Lett.*, **72** (21), 2660–2662.
74 Steirer, K.X. *et al.* (2009) Ultrasonically sprayed and inkjet printed thin film electrodes for organic solar cells. *Thin Solid Films*, **517** (8), 2781–2786.
75 Hoth, C.N. *et al.* (2008) Printing highly efficient organic solar cells. *Nano Lett.*, **8** (9), 2806–2813.
76 Jang, J., Ha, J., and Cho, J. (2007) Fabrication of water-dispersible polyaniline-poly(4-styrenesulfonate) nanoparticles for inkjet-printed chemical-sensor applications. *Adv. Mater.*, **19** (13), 1772–1775.
77 Crowley, K. *et al.* (2008) Fabrication of an ammonia gas sensor using inkjet-printed polyaniline nanoparticles. *Talanta*, **77** (2), 710–717.
78 Fromm, J.E. (1984) Numerical calculation of the fluid dynamics of drop-on-demand jets. *IBM J. Res. Dev.*, **28** (3), 322–333.
79 Reis, N. and Derby, B. (2000) Ink Jet deposition of ceramic suspensions: modeling and experiments of droplet formation. *MRS Proceedings. Cambridge University Press*, **625**, 117–122.
80 Derby, B. (2010) Inkjet printing of functional and structural materials: fluid property requirements, feature stability, and resolution. *Annu. Rev. Mater. Res.*, **40**, 395–414.
81 Denneulin, A. *et al.* (2011) Impact of ink formulation on carbon nanotube network organization within inkjet printed conductive films. *Carbon*, **49** (8), 2603–2614.

82 Angelo, P.D. and Farnood, R.R. (2010) Poly (3, 4-ethylenedioxythiophene): poly (styrene sulfonate) inkjet inks doped with carbon nanotubes and a polar solvent: the effect of formulation and adhesion on conductivity. *J. Adhes. Sci. Technol.*, **24** (3), 643–659.

83 Aleeva, Y. and Pignataro, B. (2014) Recent advances in upscalable wet methods and ink formulations for printed electronics. *J. Mater. Chem. C*, **2** (32), 6436–6453.

84 Grouchko, M. and Magdassi, S. (2013) Inks containing metal precursors nanoparticles. Google Patents U.S. Patent Application No. 14/382,110.

85 Park, B.K. *et al.* (2007) Direct writing of copper conductive patterns by ink-jet printing. *Thin Solid Films*, **515** (19), 7706–7711.

86 Perelaer, J., de Gans, B.-J., and Schubert, U.S. (2006) Ink-jet printing and microwave sintering of conductive silver tracks. *Adv. Mater.* Deerfield Beach Then Weinheim-, **18** (16), 2101.

87 Seung, H.K. *et al.* (2007) All-inkjet-printed flexible electronics fabrication on a polymer substrate by low-temperature high-resolution selective laser sintering of metal nanoparticles. *Nanotechnology*, **18** (34), 345202.

88 Kim, H.-S. *et al.* (2009) Intense pulsed light sintering of copper nanoink for printed electronics. *Appl. Phys. A*, **97** (4), 791–798.

89 Dick, K. *et al.* (2002) Size-dependent melting of silica-encapsulated gold nanoparticles. *J. Am. Chem. Soc.*, **124** (10), 2312–2317.

90 Go, E.C. (2009) *Effects of Oligomer-to-Monomer Ratio on Ink Film Properties of White UV-Curable Gravure Ink for Printing on Biaxially Oriented Polypropylene (BOPP)*, Rochester Institute of Technology.

91 Shirakawa, H. *et al.* (1977) Synthesis of electrically conducting organic polymers: halogen derivatives of polyacetylene,(CH) x. *J. Chem. Soc., Chem. Commun.*, (16), 578–580.

92 Beck, F. and Oberst, M. (1992) Electrocatalytic deposition of polypyrrole in the presence of bromide. *J. Appl. Electrochem.*, **22** (4), 332–340.

93 Li, C. *et al.* (2005) Electrochemical thin film deposition of polypyrrole on different substrates. *Surf. Coat. Technol.*, **198** (1), 474–477.

94 Muthulakshmi, B. *et al.* (2006) Electrochemical deposition of polypyrrole for symmetric supercapacitors. *J. Power Sources*, **158** (2), 1533–1537.

95 Ramanavičius, A., Ramanavičienė, A., and Malinauskas, A. (2006) Electrochemical sensors based on conducting polymer—polypyrrole. *Electrochim. Acta*, **51** (27), 6025–6037.

96 Mabrook, M.F., Pearson, C., and Petty, M.C. (2006) Inkjet-printed polypyrrole thin films for vapour sensing. *Sens. Actuators, B*, **115** (1), 547–551.

97 Gangopadhyay, R. and Molla, M.R. (2011) Polypyrrole–polyvinyl alcohol stable nanodispersion: a prospective conducting black ink. *J. Polym. Sci., Part B: Polym. Phys.*, **49** (11), 792–800.

98 Loffredo, F. *et al.* (2007) Gas sensor devices obtained by ink-jet printing of polyaniline suspensions, in *Macromolecular Symposia*, Wiley Online Library.

99 Hibbard, T., Crowley, K., and Killard, A.J. (2013) Direct measurement of ammonia in simulated human breath using an inkjet-printed polyaniline nanoparticle sensor. *Anal. Chim. Acta*, **779**, 56–63.

100 Xu, Y. *et al.* (2013) Screen-printable thin film supercapacitor device utilizing graphene/polyaniline inks. *Adv. Energy Mater.*, **3** (8), 1035–1040.

101 Morrin, A. *et al.* (2005) Novel biosensor fabrication methodology based on processable conducting polyaniline nanoparticles. *Electrochem. Commun.*, **7** (3), 317–322.

102 Dionisi, A. *et al.* (2014) Biocompatible inkjet resistive sensors for biomedical applications. *2014 IEEE International Instrumentation and Measurement Technology Conference (I2MTC) Proceedings, IEEE*.

103 Huang, L. *et al.* (2008) Synthesis of biodegradable and electroactive multiblock polylactide and aniline pentamer copolymer for tissue engineering applications. *Biomacromolecules*, **9** (3), 850–858.

104 Skotheim, T.A. and Reynolds, J. (2006) *Conjugated Polymers: Theory, Synthesis, Properties, and Characterization*, Taylor & Francis.

105 Cho, C.-K. *et al.* (2011) Mechanical flexibility of transparent PEDOT:PSS electrodes prepared by gravure printing for flexible organic solar cells. *Sol. Energy Mater. Sol. Cells*, **95** (12), 3269–3275.

106 Kim, J.Y. *et al.* (2002) Enhancement of electrical conductivity of poly(3,4-ethylenedioxythiophene)/poly(4-styrenesulfonate) by a change of solvents. *Synth. Met.*, **126** (2–3), 311–316.

107 Leleux, P. *et al.* (2014) Conducting polymer electrodes for electroencephalography. *Adv. Healthc. Mater.*, **3** (4), 490–493.

108 Khodagholy, D. *et al.* (2013) In vivo recordings of brain activity using organic transistors. *Nat. Commun.*, **4**, 1575.

109 Berggren, M. and Richter-Dahlfors, A. (2007) Organic bioelectronics. *Adv. Mater.*, **19** (20), 3201–3213.

3

Biocompatible Circuits for Human–Machine Interfacing

Erik O. Gabrielsson, Daniel T. Simon, and Magnus Berggren

Linköping University, Department of Science and Technology, Laboratory of Organic Electronics, Bredgatan 33, 60174 Norrköping, Sweden

3.1 Introduction

Luigi Galvani is considered to be the pioneer with respect to the study of and early experiments in bioelectricity. In the 1780s, he discovered that detached leg muscles from dead frogs could be stimulated to twitch by electric potentials generated from metal electrodes. Since then, the constant advancement of technology and our understanding of human physiology and neuroscience have spurred the development of devices, implants, and techniques, such as pacemakers and deep-brain stimulation electrodes, that can be used to treat or suppress the effects of diseases and disorders as well as to help us map various biological and chemical processes of importance to the biological and medical sciences.

The physical interface between electronic devices and biological tissues is of particular interest, as this interface bridges the gap between artificial, human-made technologies and biological "circuits." Therefore, this interface illustrates many of the challenges faced by devices intended for human–machine communication. First, the device needs a signal translation function that enables interfacing with the body in a biologically meaningful way, that is, conversion between electronic and biological signals. Some biological processes, for example, contraction of the heart and propagation of action potentials in neurons, are mediated by changes in cell membrane potential, and can thus be sensed or stimulated through purely electrical signals. The majority of biological signals are however mediated biochemically, for example, neurotransmitters released at synapses, long-range-acting hormones, and activation of immune responses through cytokines. Through the specific chemical structure of a given biomolecule, such biosignals can selectively target a single process or pathway. Biomolecule signaling can therefore be more diverse and more specific than signaling mediated by changes in electric potential.

Another important and crucial feature for devices intended for implantation in the human body is biocompatibility, especially for implants intended for long-term therapy [1]. The immune system is programmed to protect us from foreign organ-

Green Materials for Electronics, First Edition.
Edited by Mihai Irimia-Vladu, Eric D. Glowacki, Niyazi S. Sariciftci, and Siegfried Bauer.

isms and substances, and an immune response to an implant can cause drastic local biological changes as well as interference with the function of the implant [2]. Various coatings can be used to render the implant less prone to provoking an immune response [3, 4]. Additionally, tissues are typically soft, and this plasticity is needed to enable a constant change of physical state (movement, growth). Therefore, devices targeted for implantation in such tissues should preferably also be soft and flexible – matching the tissue as well as possible – in order to adapt to, and not damage, the target host environment and target organs *in vivo*.

Well-known examples of devices for human–machine interfacing include the use of single metal electrodes [5], silicon transistors [6], and 3D electrode arrays [7] to measure and induce neuronal activity. The use of metals or typical semiconductors such as silicon is however not always ideal. First, metals and silicon are hard materials, often causing mechanical incompatibility when the bioelectronic device is implanted, resulting in inflammation and additional scar formation [1]. Second, these materials interact with the biological system through electronic charge, and are thus not effective for biochemically mediated signaling pathways, for example, the signal transduction between neurons in a neuromuscular junction governed by the release, diffusion, and recognition of acetylcholine [8].

π-Conjugated polymers, also known as *(semi)conducting polymers* or more generally *organic electronics*, are a class of materials that have emerged as an alternative to metals and silicon in bioelectronic devices [9]. These semiconducting conjugated polymers have found success in a wide range of technical applications, such as the active material in light-emitting diodes [10], transistors [11], and solar cells [12]. For bioelectronics applications, the carbon-based polymer chains offer a wide range of crucial properties and features, such as softness and flexibility [13], are often suited for operation in aqueous media [14], and can be biocompatible [15]. Further, as ions are often present in these materials for charge compensation or doping, conjugated polymers offer a unique interplay between ionic and electronic charge [16]. Early examples on the coupling between conjugated polymers and biology include controlled release of drug molecules, incorporated within the conjugated polymer as dopant ions, through reduction of the polymer [17], and controlling the morphology and growth of cells cultured on a conjugated polymer electrode by the applied potential [18]. Conjugated polymer electrodes have also been shown to outperform the hard silicon or metal electrodes for recording of neuronal activity *in vivo* [14, 19, 20] and enabling detection of neurotransmitters at single-cell resolution [21].

As many biomolecules can be ionized through protonation/deprotonation of acidic or alkali groups (such as amines and carboxyl acids), technology that can manipulate ion flows thus defines an interesting signal translation concept for human–machine interfacing. Organic electronics' coupling of electronic and ionic (and thus biochemical) signals can be enhanced by the use of materials chosen specifically for ionic conduction. For example, ion fluxes can be directed through micrometer-scaled ion-conducting membranes to give spatial control of substance delivery, enabling release of biomolecules in close proximity to a target tissue. Ion-conducting diodes and transistors can be used to build circuits for modulation of ion flow, with the possibility of mimicking the dynamic and nonlinear processes occurring in the body.

This chapter reviews such iontronic devices for signal translation and their application in bioelectronics. We begin with a brief description of the ion transport mechanisms that lay the conceptual groundwork for this type of iontronic devices. Various iontronic devices aimed at bioelectronic applications are then presented. As a conclusion, future possible developments of iontronics for human–machine interfacing are outlined.

3.2 Ion Transport Mechanisms

3.2.1 Ions and Types of Electrolytes

Ions are formed when neutral atoms or molecules gain or lose electric charge so that the number of electrons does not equal the number of protons within the structure. Positively charged ions are called *cations* and negatively charged ones are called *anions*. Examples of ions are simple metal ions (e.g., Na^+), charged biomolecules (e.g., acetylcholine), and polymer chains with multiple charges (e.g., a polyelectrolyte). An electrolyte is a solution with dissolved ions, for example, NaCl dissolved in water, giving Na^+ (aq) and Cl^- (aq). Electroneutrality dictates that the total charge should sum to zero, and electrolytes therefore contain equal amount of charge from both cations and anions.

3.2.2 Ion Transport

Dissolved and dissociated ions in an electrolyte are free to move via migration, diffusion, and/or convection [22]. Electric fields in the electrolyte act on the charged ions to provide migration and concentration gradients drive diffusion, while fluid movement is responsible for convection (Figure 3.1).

3.2.2.1 Migration and Diffusion

A difference in ion concentration Δc between two points in an electrolyte results in ion transport through diffusion. Here, the random movement of molecules strives to level out the concentration difference, giving a net movement of ions from high to low concentration. The diffusion rate is dependent on the diffusion coefficient (D) for the molecule, expressed in square meter per second, and the concentration difference Δc. The flux J (mol $m^{-2} s^{-1}$) due to diffusion is governed by Flick's first law:

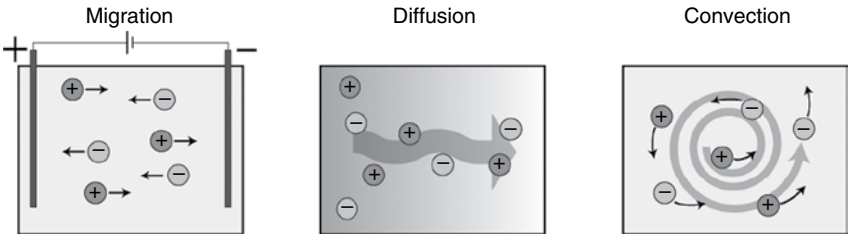

Figure 3.1 Ion transport mechanisms in electrolytes.

$$J = -D\Delta c$$

A potential difference $\Delta\varphi$ between two points in an electrolyte, generated, for example, between two electrodes immersed in the solution, creates an electric field in the electrolyte. The field exerts a force on the ions in the electrolyte, and the resulting transport is termed *migration*. The direction of migration is dependent on the charge of the ion; cations move in the direction of the field while anions migrate in the opposite direction.

Owing to the charge carried by ions, transport through migration and diffusion is linked. A flux of ions due to migration perturbs the ion concentration, resulting in a concentration gradient and thus an opposing diffusion flux. Conversely, two oppositely charged ions with different diffusion coefficients diffusing in a concentration gradient induce an electric field in the electrolyte. This electric field opposes the diffusion movement of the faster diffusing species in order to maintain electroneutrality, and adds a migration component to the flux. The total flux, both accounting for migration and diffusion for an ion with charge z and concentration, c is described by the Nernst–Planck equation:

$$J = -D\Delta c + \left(zF / RT\right) \cdot Dc\Delta\varphi$$

where F is Faraday's constant, R is the gas constant, and T is the temperature. The first part in the Nernst–Planck equation accounts for flux due to diffusion, while the second accounts for migration.

3.2.2.2 Transport Number

As electrolytes contain more than one mobile species, the total flux of ions due to migration or diffusion is the sum of the fluxes for each species. The magnitude of the individual fluxes, and thus their proportion of the total flux, can vary, for example, due to differences in diffusion coefficient or concentration. The transport number describes the fraction of the flux from one specific ion species to the total flux, defined as unity, in the electrolyte. In electrolytes where the ions have similar diffusion coefficients and are at equal concentration, for example, KCl ($D_{K^+} \approx D_{Cl^-} = 2.0 \times 10^{-5}\,\mathrm{cm^2\,s^{-1}}$ [23]), the cation and anion have roughly the same transport number of 0.5 (Figure 3.2). If, on the other hand, the diffusion

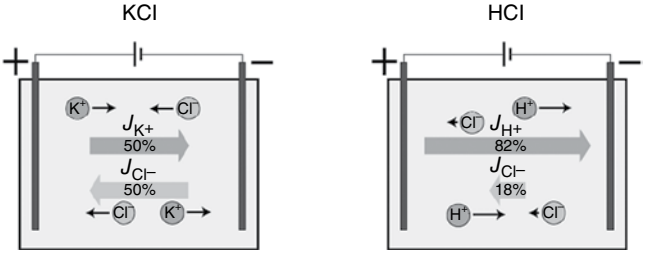

Figure 3.2 Transport numbers. The ionic current in an electrolyte is composed of the total flux for all species present. The transport number describes the contribution from each species, and is higher for ions with higher diffusion coefficient ($D_{H^+} > D_{K^+}$).

coefficients differ, such as for HCl ($D_{H^+} = 9.3 \times 10^{-5}\,cm^2\,s^{-1} > D_{Cl^-}$ [23]), the transport number will be higher for the ion with higher diffusion coefficient ($t_{H^+} = 0.821$ vs $t_{Cl^-} = 0.179$) [24]. Similarly, a relative increase in concentration (compared to other mobile ions in the system) will also increase the transport number.

3.2.3 Ion-Exchange Membranes

Membranes can be used to separate two electrolytes while still allowing transport processes to occur between them, for example, ion transport across an ion-conducing membrane. Ion transport across membranes can also be selective, for example, toward either cations or anions, as in the case of ion-exchange membranes. Such a membrane typically contains fixed ionic charges, either cations or anions, often covalently hosted within a cross-linked polyelectrolyte matrix (Figure 3.3). Additionally, the membrane will contain mobile ions from the surrounding electrolytes. Through electrostatic interaction the fixed charges repel ions of the same charge (coions), while, to maintain electroneutrality, oppositely charged counterions are attracted. Thus, the counterion concentration is higher than the coion concentration inside the membrane. The fraction of counterion concentration c_{cou} in relation to the total number of mobile ions (including

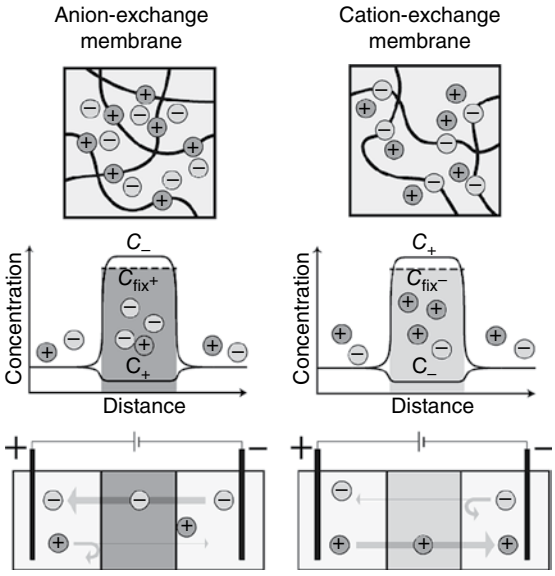

Figure 3.3 Ion-exchange membranes. Anion- and cation-exchange membranes are typically cross-linked polyelectrolytes, where cationic or anionic groups are covalently bound to a polymer chain. These fixed charges are compensated by mobile counterions, carrying opposite charge, while coions, ions with same charge, are repelled. Inside the membrane, the concentration of counterions is relatively higher than that of coions. Migration across ion-exchange membrane is therefore selective toward the counterion, that is, either anions for an anion-exchange membrane or cations for a cation-exchange membrane.

coions c_{co}) depends on the fixed charge concentration X of the membrane and the surrounding electrolyte concentration c_s according to

$$\frac{c_{cou}}{c_{cou}+c_{co}} = \frac{1}{2} + \frac{1}{\sqrt[4]{\left(\frac{1}{4}+\left(\frac{c_S}{4}\right)^2\right)}}$$

Thus, for a highly charged membrane with $X = 1$ M and external electrolyte concentration c_s of 0.1 M, approximately 99% of the mobile ions in the membrane are counterions [25]. This enhances the transport number for the counterion (and reduces the transport number for the coion), giving ion-exchange membranes selective transport for counterions. A cation-exchange membrane contains fixed anions and primarily mobile cations, and vice versa for an anion-exchange membrane; ion-exchange membranes can therefore be regarded as the ionic equivalent to p- and n-type (semi-)conductors. Typical selective ion-exchange membranes have fixed charge concentration of 1–3 M and a counterion transport number of >0.95 [26]. The counterion transport number is, however, reduced when the membrane is in contact with high-concentration electrolytes, as this increases the concentration of coions [27].

3.2.4 Bipolar Membranes

A bipolar membrane is a two-layered membrane with one side having cation-exchange properties and the other anion-exchange properties (Figure 3.4) [28]. The two sides, with either fixed anions or cations, will then contain either cations or anions as counterions, respectively, while the coions are repelled. Thus, the concentration profile for mobile cations and anions varies along the bipolar membrane. This structure is interesting, as it mimics the classical semiconductor pn-junction, and, as expected, bipolar membranes show nonlinear current versus voltage characteristics [29]. The mechanism for ion transport across a bipolar membrane is primarily divided into two regimes, the forward and the reverse bias regimes, depending on the voltage polarity applied to the membrane.

3.2.4.1 Forward Bias Regime

A bipolar membrane is in forward bias when a positive voltage is applied at the cation-exchange side of the membrane. The electric field across the membrane is then directed so that the counterions of both sides of the membrane migrate toward the junction. The ions however cannot pass readily, as they are repelled by the fixed charges of the membrane on the other side of the junction. In contrast to holes and electrons, ions of different polarity do not recombine (except for acid/base with OH^-/H^+). Instead, ions initially accumulate at the junction. However, as the selectivity of an ion-exchange membrane is reduced with increased electrolyte concentration, the accumulation of ions leads to an increased coion transport across the junction. The mobile ions can therefore eventually pass the junction as compensated coions. In forward bias, the ion concentration along the bipolar membrane is high, resulting in high conductivity.

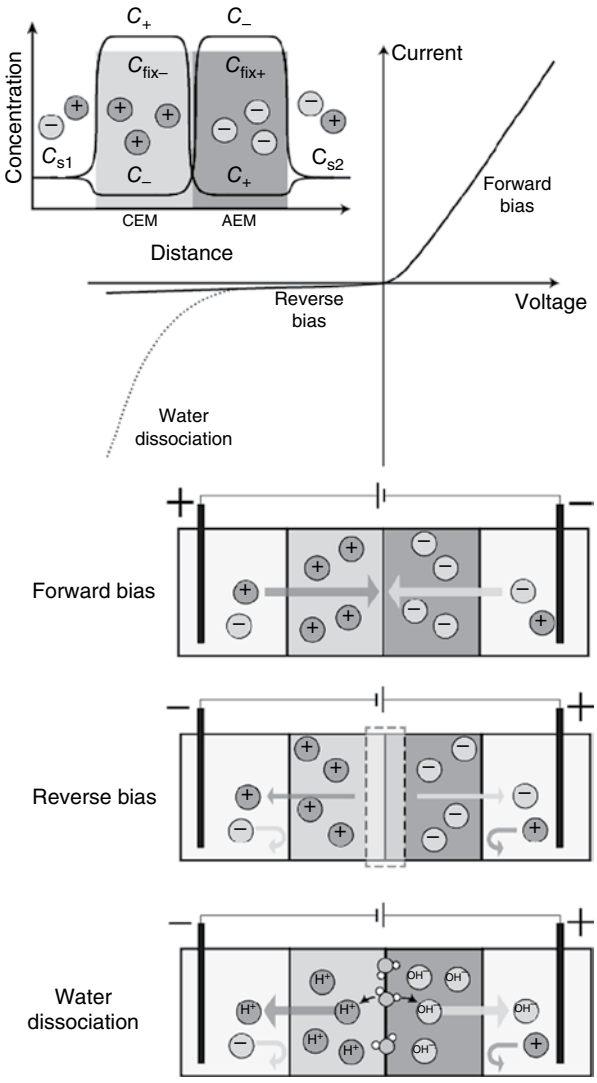

Figure 3.4 Bipolar membrane. The combination of a cation-exchange membrane and an anion-exchange membrane gives a changing ion concentration profile along the membrane, where one side is rich in mobile cations and the other in mobile anions. The current–voltage characteristics for bipolar membranes is nonlinear, showing two regimes: forward and reverse bias. Additionally, some bipolar membranes show accelerated water dissociation in the reverse bias regime.

3.2.4.2 Reverse Bias Regime

Reversing the applied voltage, that is, applying a negative voltage at the cation-exchange side, brings the bipolar membrane into the reverse bias regime. Now, the direction of the electric field forces the counterions to migrate away from the junction. Additionally, only a small amount of coions can migrate toward the junction, as these are mostly repelled at the interfaces toward the electrolytes.

Thus, the flow of counterions out of the junction is higher than the replenishing flow of coions, and the net result is a reduction in ion concentration inside the junction. The low ion concentration in the junction renders the reverse bias less conductive.

The low ion concentration at the interface in a reverse biased bipolar membrane implies a local high electric field across the interface. Together with catalytic groups, such as amines typically present in anion-exchange membranes, the electric field can increase the dissociation rate of water into ions (H^+ and OH^-) [30]. This effect is known as *electric field-enhanced water dissociation*, and is industrially important for separating salts into the corresponding acid and base components [31].

3.2.5 Electrodes

Pairs of electrodes are commonly used to generate ionic currents inside electrolytes.

If the electrodes are polarizable, the surface of the electrode will become electronically charged (negatively or positively) upon electrical biasing. This charge is compensated by a redistribution of ions in the electrolyte in proximity to the electrode, forming an electric double layer (EDL). Closest to the electrode surface, ions with opposite charge, with respect to the electrode, approach the electrode surface to form a so-called Helmholtz layer. Further away from the electrode the diffuse layer is formed, where there is a decaying abundance of oppositely charged ions. The spatial separation of positive and negative charges at the electrode/electrolyte interface resembles a capacitor. The polarizable electrodes can be charged or discharged similarly to an ordinary capacitance depending on the bias applied to the electrode, that is, the (capacitive) current between two polarizable electrodes for a given applied bias decays with time.

In addition, electrochemical reactions can occur at the electrode surface, giving rise to a faradic (charge-transfer) current. Electrolysis of water, where water molecules are split into H_2 and O_2 at the cathode and anode respectively and H^+ and/or OH^- migrate between the electrodes, is an example of such a reaction. For reduction and oxidation to occur at the electrodes, the applied bias must be above the decomposition potential of the electrochemical species, for example, 1.23 V for water. The faradic current can be maintained as long as electrochemically active species are present at the electrode, and the current is thus limited by diffusion of the active species from the bulk of the electrolyte.

Compared to solid metal electrodes, conjugated polymers can be charged not only along the surface but also throughout the bulk of the electrode. They thus offer a large effective electrode area and an increased electrode capacitance [32]. When such an electrode is electrically biased, electrons are inserted into or removed from the polymer backbone, that is, the entire polymer bulk, increasing or decreasing the charge, or doping level, of the conjugated polymer. The change in doping level is compensated by oppositely charged ions migrating in or out from the polymer matrix. In this way, conjugated polymer electrodes can be used as high-capacity electron-to-ion converters, without production of soluble redox products, pH changes, or gases [33].

3.3 Organic Electronic Ion Pump

Devices for *in vivo* drug delivery are commonly based on either diffusion (controlled by a valve-mechanism) or microfluidic flow. Diffusion-based devices typically suffer from a lack of control, for example, as the rate of delivery decays with time and swift on/off responses are typically hard to realize. Microfluidic flow can offer precise control of the delivery, but at the expense of complicated "plumbing" and potential disturbance of the biological processes due to the physical liquid flow. An alternative approach, at least for molecules that are charged or can become charged (through protonation/deprotonation), is electrophoresis. In this technique, the rate of delivery can be tightly controlled electronically, and liquid flow is extensively minimized. The organic electronic ion pump (OEIP) is a microfabricated drug delivery device based on electrophoresis, and has been specifically designed for biomolecule interfacing with cells and tissues *in vivo* and *in vitro*.

The OEIP is designed according to the following principles (Figure 3.5):

- Faradic currents between the two included electrodes immersed in their electrolytes give rise to an electric field. Ions in the electrolytes will migrate in the direction of the field, cations toward the cathode and anions toward the anode.
- The electrolytes are separated by an ion-conductive membrane. If the membrane is cation or anion selective, the transport of ions across it, for a given bias, will primarily be unidirectional and only composed of cations or anions.
- The rate of ion transport (mol s^{-1}) across the membrane is in direct correlation to the faradic current provided through the electrodes, giving temporal control of the ion delivery ($J = i \times F$).
- The membrane can have arbitrary shape, and, for example, have a very thin end on one side. This gives spatial resolution to the delivery.

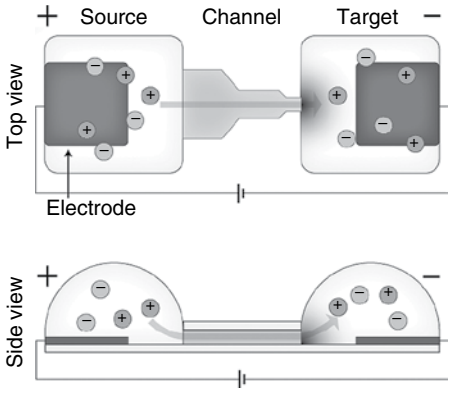

Figure 3.5 The organic electronic ion pump, with two electrodes immersed in electrolytes (designated as source and target), separated by an ion-exchange membrane (here a cation-exchange membrane). A voltage applied between the electrodes drives a selective transport of cations from the source to the target side through the channel.

The very first version of the OEIP was produced on flat plastic sheets coated with poly(3,4-ethylenedioxythiophene):polystyrene sulfonate (PEDOT:PSS). The electrodes and the cation-selective channel were formed through photolithography and dry-etching of the PEDOT:PSS layer. A tapering channel, with the narrower end pointing toward the outlet, gives high spatial resolution without an undesired high resistance. Through chemical overoxidation, the PEDOT:PSS in the channel is rendered electronically isolating while retaining the ionic (cation) conductivity, thus preventing electric short-circuit or electrochemical oxidation fronts in the channel. Lately, the overoxidized PEDOT:PSS material has been replaced by a purer poly(styrenesulfonate) copolymer [34]. An encapsulation layer, using the epoxy-based hydrophobic photoresist SU8, is used to define the inlet and outlet of the channel as well as the storage regions for the electrolytes.

Any type of electrodes can be used, but it is advantageous to have electrodes that can provide large amounts of charge, at low potential loss, without formation of gas, toxic species, or pH changes. Electrodes made of conjugated polymer materials, such as PEDOT:PSS, are therefore attractive, as they have been shown to provide stable faradic currents without significant side reactions [33].

Before using an OEIP, the channel material needs to be hydrated in order to become sufficiently ion conductive. This is typically done by incubation in de-ionized water over extended periods (several hours). Electrolytes are then applied to the source and target reservoir regions. The source electrolyte should contain the ion to be transported, carrying the correct charge (positive or negative depending on channel selectivity). Additionally, it is preferred if the ion to be transported is in higher concentration than any other similarly charged ions in the electrolyte, as this reduces the transport of unintended ions. Extreme pH is therefore undesirable, as this can lead to high transport of H^+ or OH^-. The target electrolyte can be comprised, depending on the application of a simple salt electrolyte, more complex buffers, a cell culture hosted in a medium, or even a tissue or an organ.

Electronically, an OEIP can be regarded as a resistor. The low (ionic) conductivity inside the channel combined with the preferred long and narrow channel geometry leads to a high resistance and typically limits the current through the device. The off-current, when no voltage is applied, is primarily due to diffusion of molecules between the source and target. The on–off ratio for metal ion and biomolecule delivery is typically above 100 [35, 36].

3.3.1 Applications

OEIPs have been used in a number of studies as a drug delivery platform for stimulation of neuronal cells both *in vitro* and *in vivo*. In the first report [35], human cortical neurons (HCN-2) loaded with a Ca^{2+}-sensitive fluorescent probe were cultured at the outlet of the OEIP and were then stimulated by a constant flux of K^+ from a source electrolyte. The increase in K^+ concentration caused opening of cellular Ca^{2+} channels, and cells close to the OEIP outlet showed subsequent increase in the intercellular Ca^{2+}.

A refined design of the OEIP was later presented [36], enabling faster delivery response due to the inclusion of a preload configuration, as well as an increased spatial resolution of the delivery thanks to reduction of the outlet width down to

10 μm. The improvements allowed for triggering of Ca^{2+} responses in cultured SH-SY5Y cells close to the outlet through stimulation with the neurotransmitter acetylcholine, with a response time below 200 ms. Owing to the rapid diffusion of the delivered species away from the outlet, pulsing of the delivery and also varying the pulse length and amplitude allowed for selective stimulation of only the cells located closest to the outlet.

Further, the OEIP has been used for *in vitro* modulation of neuronal activity in mouse brain slices [34]. By delivery of K^+ to neurons in the hippocampus, hyperexcitability, an abnormal electrophysiological neuronal activity associated with epilepsy, could be induced (Figure 3.6a). Conversely, by delivering the inhibitory neurotransmitter γ-aminobutyric acid (GABA), epileptiform activity could be suppressed in the hippocampus after hyperexcitability had been induced by regular electrophysiological methods. Even more recently, the device was further augmented to incorporate a PEDOT:PSS-based electrophysiological sensing electrode at the OEIP outlet [38]. In this way, a 20 μm × 20 μm "bioelectronic pixel" was demonstrated that could both deliver GABA (as the outlet of the OEIP) and sense the local electrophysiological state (as a PEDOT:PSS electrode). Experiments showed that the bioelectronic pixel could perform just as well as the earlier system, which relied on "standard" macroscopic recording electrodes. Thus, the OEIP is an effective tool in regulating neuronal signaling activity in the complex biological settings of real tissues, and is furthermore able to be integrated directly with electrophysiological sensing for feedback-enabled interventions.

It is also possible to couple the chemical delivery from an OEIP together with chemical sensing, for example, of a neurotransmitter. Such systems have been demonstrated for cultured neuroblastoma SH-SY5Y cells, using electrochemical sensors for glutamate or acetylcholine and the OEIP for delivery of acetylcholine [39]. Here, the sensing of glutamate and delivery of acetylcholine mimics the signaling pathway at the neuromuscular junctions, while acetylcholine sensing and delivery can be used as a self-regulating loop to maintain normal acetylcholine levels. By defining thresholds in the sensing signal for activation of the neurotransmitter delivery, neuron-like behavior is obtained, that is, a signal is only transmitted if the stimuli reach a threshold concentration. Thus, the combined biosensor-OEIP system has been dubbed as an organic electronic biomimetic neuron.

OEIPs have also been adapted for implantation and for *in vivo* use. For this purpose, the usual planar design was converted into a tubular, narrow, and fully encapsulated device in order to be as nonintrusive and biocompatible as possible. The first device consisted of two parallel electrodes, electrolyte compartments, and channels, both with outlets at the tip of the device [40]. One side of the device served as the source and the other as the counter electrode/electrolyte, while the delivery target was the electrolyte the tip was immersed in. The syringe-shaped OEIP was implanted in close proximity to the round window membrane of the cochlear in a guinea pig, with the aim of specific chemical stimulation and also regulation of the auditory system. Through local delivery of glutamate the hearing sensitivity was reduced, as the inner hair cells were affected by the excessive glutamate concentration. Meanwhile, the outer hair cells, not

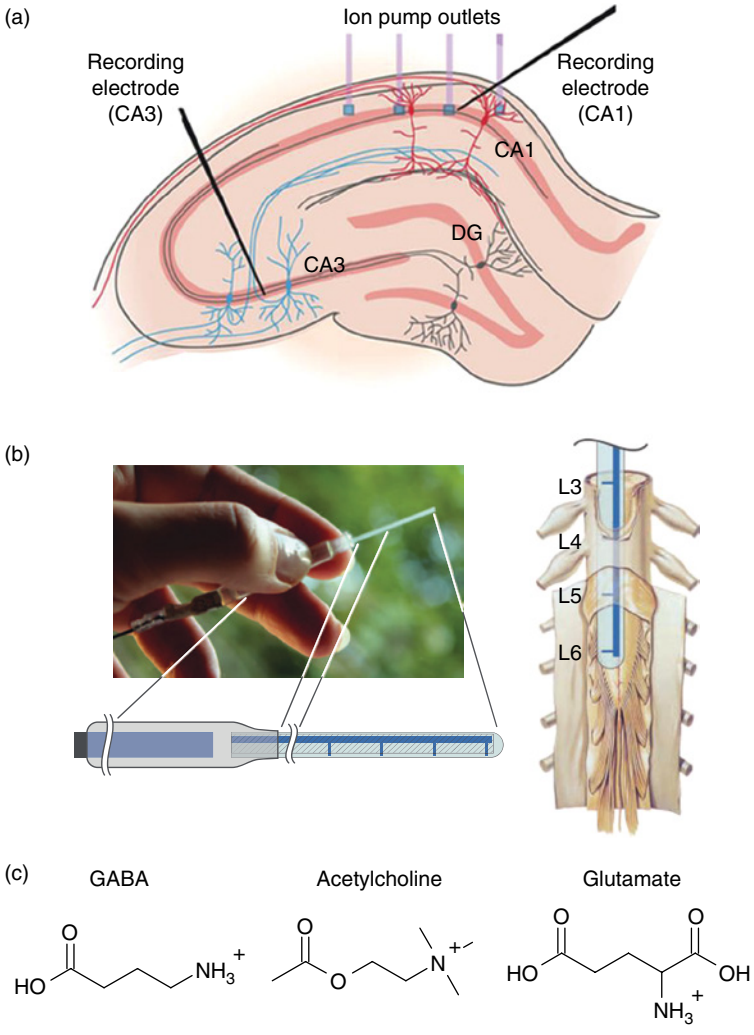

Figure 3.6 *In vitro* and *in vivo* applications of the OEIP. (a) GABA delivered through OEIP outlets placed in close proximity to the CA1 region of a mouse hippocampal slice suppressed epileptiform activity in that area, while the activity in the more distant CA3 region was unaffected. (Williamson *et al*. 2015 [34]. Reproduced with permission of John Wiley and Sons.) (b) An OEIP with four parallel outlets, spaced to match the positions of four dorsal roots (in rats) where the pain signal enters the dorsal spinal cord. Once implanted onto the spinal cord, local delivery of GABA through the device reduced the pain response in the rats. (Jonsson *et al*. 2015 [37]. Reproduced with permission of AAAS.) This work is licensed under CC BY-NC. (c) Examples of biomolecules (neurotransmitters) that have successfully been transported with the OEIP.

sensitive to glutamate, were not affected, and no effect was observed when delivering protons. This implanted OEIP thus successfully stimulated the glutamate-responsive inner hair cells (and destroyed them) through the active delivery of glutamate, without damaging or affecting other, non-targeted parts of the sensitive cochlea system.

The adaption of the OEIP to the specific biological target can also be more sophisticated. For example, to restore inhibitory pain control in a hypersensitized rat model, the channel of an OEIP was specifically designed to have one outlet aligned at each of the four dorsal roots where the pain signals enter the spinal cord (Figure 3.6b) [37]. By delivery of GABA, which inhibits the pain signal, to these specific sites the pain response threshold was significantly increased in a hypersensitive rat model. Compared to other methods for chronic pain pharmacotherapy, such as systematic administration of drugs, this implantable OEIP only affects its immediate surroundings of the nervous system and can thus potentially suppress side effects.

3.3.2 Limitations

The ability and speed of migration for a specific ion through the ion pump channel is to a large extent dependent on the size of the ion. Some examples of biomolecule ions that have been delivered with OEIPs are shown in Figure 3.6c. Large ions, such as biomacromolecules, typically have lower diffusion coefficient, resulting in a higher ionic resistance and thus require a relatively higher driving voltage. This lower diffusion coefficient also means that small coions, with higher diffusion coefficient, will be relatively easier to transport in the reverse direction, which will reduce the delivery efficiency. Additionally, the polymer in the membrane material of the channel can act as a size-exclusion mesh that prevents large molecules, such as peptides, to pass. Thus, to date, the ion pump works best for the delivery of smaller ions, such as metal ions and biomolecules with molecular weight less than ~200 $g\,mol^{-1}$, while larger molecules show low delivery speed and efficiency.

3.4 Ion Diodes, Transistors, and Circuits

Apart from just transporting ions through electrophoresis, as in OEIP devices, more complex operations involving ions are also of interest, such as ionic signal rectification or amplification. Such capabilities could enable ion-based computing and delivery systems to generate complex biomolecule signal patterns. For such operations, devices with nonlinear characteristics are needed, that is, diodes and transistors that operate on ionic signals and flows. For logic functions, schemes devised around motion of ions are inherently slow compared to their electronic counterparts, primarily owing to the several orders of magnitude lower mobility for ions. The advantage of iontronic-based logic circuits in bioelectronic applications is instead related to the opportunity to achieve advanced and complex patterns of chemical information; as opposed to the charge-only nature of an electron (or hole), an ion can have a wide range of different molecular structures, configurations, reactivity, and so on, and can thus carry information specific to biological systems and their functions. For example, an ionic transistor modulating a flow of glutamate ions will have a distinctly different effect than if the flow is represented by GABA ions, as the first molecule is an excitatory neurotransmitter while the latter is inhibitory.

3.4.1 Ion-Conducting Diodes

Diodes are nonlinear two-terminal electrical components that have significantly lower resistance in one direction. In other words, the current through the diode is dependent on the voltage polarity. Various types of ion-conducting diodes have been presented, primarily based on either nanofluidic channels or ion-exchange membranes (bipolar membranes) (Figure 3.7). Nanofluidic ion diodes typically utilize charged sidewalls along a nanometer-sized channel. The channel is divided into two sides, with either negatively or positively charged sidewalls. EDLs form along the charged sidewalls, which accumulate the counterion while repelling the coions. Owing to the small dimensions, the EDL can affect the entire channel. The ion distribution along nanofluidic diodes thus resembles a bipolar membrane. However, the EDL thickness is highly dependent on the electrolyte concentration, and decreases from 3.1 nm at 10 mM to 1.0 and 0.3 nm at 100 mM and 1 M, respectively [41]. Owing to the difficulty in fabricating single-nanometer channels, nanofluidic ion diodes perform best at low electrolyte concentrations (typically <10 mM) but poorly at higher concentrations, and thus are not promising for biological applications at physiological conditions.

Ion-exchange membranes, with fixed charges distributed throughout their bulk, can typically maintain good selectivity even at relative high surrounding ion concentration. Thus, for biological applications, diodes based on bipolar membranes are preferable. These can be manufactured by photolithography, similar to OEIPs, by connecting two channels comprising a cation- and an anion-selective membrane, forming the anode and cathode of a diode (Figure 3.8a) [44]. Micrometer-scaled bipolar membrane structures can also be obtained through photo-crosslinking polyelectrolyte gels in microfluidic systems [45]. Both these microfabricated ion diodes will exhibit current–voltage characteristics based on the forward and reverse regime of bipolar membranes.

In the forward bias regime, a positive voltage is applied to the anode terminal versus the cathode potential. Mobile ions can then migrate inside the bipolar membrane with high conductivity without formation of regions of low ion concentrations. It has been observed that counterions eventually cross the interface and become coions during forward bias [46]. The current through the bipolar membrane is thus composed of both counterion and coion migration. The main voltage drop occurs across the two ion-exchange membranes owing

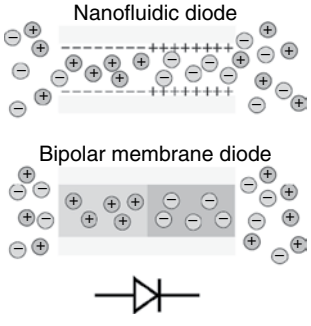

Figure 3.7 Ion diodes based on surface-charged nanofluidic channels or bipolar membranes.

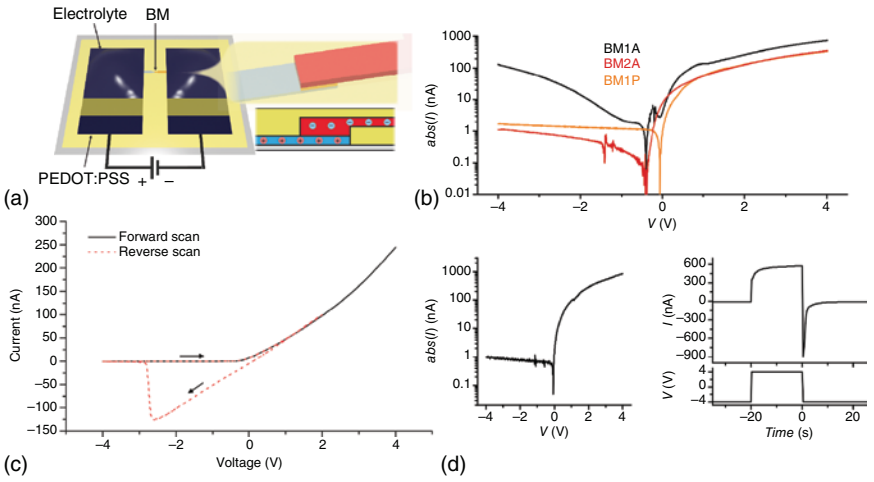

Figure 3.8 Structure and characteristics of ion bipolar membrane diodes. (a) Ion bipolar membrane diodes can be constructed by layering photolithographically patterned cation-exchange membrane (blue) and anion-exchange membrane (red), forming a bipolar membrane. The diode is ionically connected to PEDOT:PSS electrodes through two electrolytes. (Gabrielsson *et al*. 2014 [42]. Reproduced with permission of John Wiley and Sons.) (b) Ionic current rectification between forward and reverse bias for three types of bipolar membrane diodes. Water dissociation is observed in BM1A while avoided in BM2A and BM1P through the use of neutral electrolyte junction and non-amine-based anion-exchange membrane, respectively. (Gabrielsson and Berggren 2013 [43]. Reproduced with permission of AIP Publishing.) (c) Hysteresis is often observed when changing from the forward bias regime to reverse bias, due to accumulation of ions during forward bias operation. (Gabrielsson *et al*. 2012 [44]. Reproduced with permission of Royal Society of Chemistry.) (d) The performance of ion bipolar membrane diodes can be improved by minimizing the junction size, here down to 10 µm, as less charge then needs to be injected/extracted. (Gabrielsson *et al*. 2013 [43]. Reproduced with permission of AIP Publishing.)

to their bulk resistivity, and the current increases approximately linearly with applied voltage.

When a negative voltage is applied at the anode, versus the cathode potential, the reverse bias regime is obtained. As the direction of the electric field is reversed, the bipolar membrane interface becomes depleted of ions. As ionic conductivity is dependent on the concentration of ions, the interface region exhibits low conductivity. The low conductivity of the interface renders the bipolar membrane less conductive as compared to the forward bias, thus giving the current–voltage asymmetry that enables bipolar membrane diodes to rectify ion currents (Figure 3.8b). The main potential drop for the reverse bias operation occurs across the ion-depleted interface.

In addition to the ideal forward and reverse bias regimes, an additional, non-ideal diode property can be observed in some ion bipolar membrane diodes, where the reverse bias conductivity rapidly increases at higher negative voltages than ~–1 V. This is due to electric field-enhanced water dissociation, where H_2O is split into H^+ and OH^- (BM1A in Figure 3.8b). The generated H^+ and OH^- are separated by the electric field and migrate away from the interface. Corresponding

acidic and basic pH changes can be detected at the anode and cathode electrolyte, respectively. As the bipolar membrane interface is no longer depleted of ions, and as H^+ and OH^- both have high mobility, the conductivity through the ion bipolar membrane diode is significantly higher than in the true reverse bias regime. This can diminish the rectification ratio to reach below 10 at voltages beyond ±1 V [43, 44], and thus reduces the usefulness of such devices as diodes. Two strategies have been employed to avoid the water dissociation effect. First, a neutral electrolyte can be inserted into the interface of the bipolar membrane [44, 47]. This redistributes the potential drop across a longer distance, reducing the local electric field strength. Secondly, the typical amine-based anion-selective membrane can be replaced by a less catalytic phosphonium polyelectrolyte [43]. Using such approaches, rectification ratios of around 800, at ±4 V, can be obtained [43].

Hysteresis is often observed when switching an ion bipolar membrane diode from forward to reverse bias [44, 46]. This is primarily due to the accumulation of ions in the bipolar membrane interface during forward bias. In contrast to electrons and holes in semiconductor diodes, cations and anions do not recombine and annihilate (except in water formation by H^+ and OH^-), and significant amounts of ions can therefore be stored at the interface. The accumulated ions need to be removed to reach the reverse bias condition of ion depletion in the interface, and thus a delayed rectification is observed when going from forward to reverse bias operation (Figure 3.8c).

If the interface volume is small, for example, the cation- and anion-exchange membranes are in direct contact, the concentrations of accumulated ions can approach the concentration of fixed charges at either side of the bipolar membrane. This lowers the charge selectivity of the ion-exchange membranes, and thus allows ions in the interface to continue migrating along the electric field as coions in the previously prohibited side of the bipolar membrane. Conversely, if the interface volume is large, as in the case of ion bipolar membrane diodes with an intermediate neutral layer at the interface, relatively much larger amounts of ions can be accumulated before coion transport occurs. As a consequence, the hysteresis is higher for the latter type of ion bipolar membrane diodes as compared to the former case. Although generally regarded as an unwanted feature, the hysteresis in ion diodes has been suggested to be useful for iontronic memory devices [48].

The time required to switch an ion bipolar membrane diode from the nonconductive reverse bias to the conductive forward bias state, and vice versa, is highly dependent on the dimensions of the bipolar membrane interface, as this dictates the amount of ions that need to be injected or extracted from the junction. Improved switching times, from >10 s down to 4 s in both directions, have been demonstrated for ion bipolar membrane diodes when the interface lengths were reduced from 50 to 10 μm [43] (Figure 3.8d).

3.4.2 Transistors for Modulating Ion Flows

Transistors are three-terminal devices where the bias applied at one terminal modulates the current between the two other ones. In a bipolar junction transistor, the modulating terminal is called *base* and has opposite polarity compared to the emit-

ter and collector terminals between which the current is modulated. The structure resembles two connected pn-junctions forming a T-junction (Figure 3.9d). Thus, similar to ion diodes, ion bipolar junction transistors (IBJTs) can be made by connecting two bipolar membranes; for example, one anion-exchange membrane, serving as base, forms a T-junction with two cation-exchange emitter and collector membranes. The two junctions are named emitter–base (EB) and collector–base (CB), and each of them exhibits diode behavior. Depending on the selectivity of the emitter and collector (either for cations or for anions) the IBJT is either a pnp- or

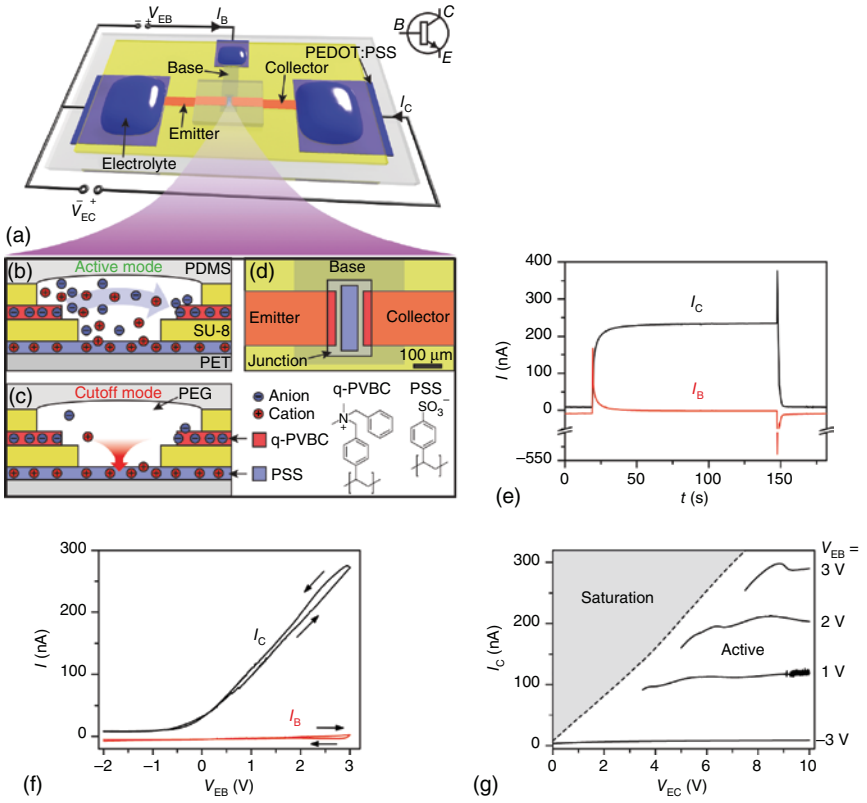

Figure 3.9 npn-IBJT device geometry, modes of operation, and characteristics. (a) The anion-selective emitter and collector are connected to a cation-selective base. The base and collector are biased versus the emitter with V_{EB} and V_{EC}, respectively, through electrolyte-covered PEDOT:PSS electrodes. (b) In the active mode $V_{EB} > 0$ V and cations are injected into the junction, enabling anions to cross between emitter and collector. (c) In the cutoff mode ions are removed from the junction through the base and collector. (d) A neutral PEG-based electrolyte separates the emitter, collector, and base. The emitter–collector distance is 100 µm. (e) Switching characteristics between cutoff ($V_{EB} = -3$ V) and active mode ($V_{EB} = +3$ V). Momentarily after the switch in V_{EB}, a spike in I_B injects/extracts cations to/from the junction. The 90% rise and 10% fall times are 9 and 3 s, respectively. (f) Transfer curve ($V_{EB} = 10$ V). I_C is low for $V_{EB} < 0$ V and increases linearly for $V_{EB} > 0$ V, while I_B is low through the scan. (g) Output characteristics. In the voltage range studied, I_C increases with V_{EB} but is almost constant with respect to V_{EC}, that is, I_C is saturated in the active mode. (Tybrandt *et al*. 2011 [49]. Reproduced with permission of American Chemical Society.)

an npn-transistor. In a pnp-IBJT, a cation current between emitter and collector (collector current, I_C) is modulated by injection and extraction of anions through the base (base current, I_B) [47], and in the complementary npn-IBJT the polarity is reversed [49].

To operate a single IBJT, the emitter, base, and collector terminals are connected to individual electrolytes and electrodes (Figure 3.9a). A voltage V_{EC} is applied between the emitter and collector electrodes in order to drive the migration of the main charge carriers from the emitter toward the collector. Another voltage (V_{EB}) is applied between the emitter and the base electrodes to enable modulation of I_C.

Depending on V_{EC} and V_{EB}, the IBJT is operated in one of four modes: active, cutoff, reverse active, or saturation. The mechanisms for ion transport in these modes are similar between the pnp- and the npn-IBJTs, differing primarily only in the polarity of the ions involved and bias potentials. Thus, the npn-configuration will be discussed in detail. Further, a configuration with symmetrical emitter–collector is assumed.

In the *active mode*, both V_{EC} and V_{EB} are positive, and $V_{EB} < V_{EC}/2$. As V_{EB} is positive, the EB junction is forward biased, and both anions and cations are injected into the junction through the emitter and base terminals, respectively, giving a positive I_B (Figure 3.9b). The increase in ion concentration leads to an increased conductivity of the junction, and anions can move across the junction. The CB junction is, on the other hand, reversely biased and tries to deplete the junction. The anions extracted through the collector give rise to a high I_C, which defines the on-current (Figure 3.9e). The potential drop across the emitter due to the on-current elevates the potential at the junction and limits the I_B as the potential across the EB junction is reduced. As I_B is low in steady state, I_C depends primarily on the collector resistance and V_{EB}, that is, I_C increases with V_{EB} (Figure 3.9f). In the active mode, the ion concentration inside the junction linearly decreases from the emitter to the collector and an ion-depleted region appears at the collector, across which anions diffuse. The ion-depleted region increases in length with increased V_{EC}, and I_C is thus almost constant versus V_{EC} (Figure 3.9g).

The *saturation mode* is established if the V_{EB} is increased above $V_{EC}/2$, so that CB also becomes forward biased. This leads to continuous accumulation of ions inside the junction and high currents (I_C and I_B). For this reason, the saturation mode is preferably avoided in IBJTs, as high ion concentration can lead to extensive swelling of the junction, which then can deteriorate the characteristics of the junction.

By reversing the V_{EB} to negative potential, both EB and CB are in reverse bias, putting the IBJT in the *cutoff mode*. Cations will then be extracted through the negative biased base (Figure 3.9c). To maintain charge neutrality in the junction the concentration of anions also decreases, primarily by extraction of anions through the higher biased collector. As the junction is depleted of ions, the conductivity becomes limited, resulting in a low I_C (off-current).

If instead a negative V_{EB} and V_{EC} are applied, the forward/reverse bias state of EB and CB is changed (as compared to the active mode), leading to the *reverse active mode*. For a symmetric IBJT this mode is equal to the active mode.

The time for switching an IBJT from cutoff to active mode, and vice versa, depends to a large extent on the dimensions of the actual junction, that is, how large a volume needs to be injected with or depleted of ions. For high-speed operation, it is therefore advantageous to design the IBJT with minimal distance between the emitter and the collector [50]. IBJTs with 2 μm emitter–collector distance have shown switching speeds of around 2 s [51]. The ratio between the I_Cs in the active and cutoff modes (the on–off ratio) is typically around 100, while the gain (ratio between I_C and I_B in active mode) is typically around 10 [47].

3.4.3 Applications

3.4.3.1 Modulating Neurotransmitter Flow

The emitter and collector of an IBJT are similar in structure to the channel of an OEIP. IBTJs can therefore be used for electrophoretic transport of ions from a source electrolyte, through the collector, junction, and emitter, to a target electrolyte. The advantage over an OEIP is that the transport can be controlled via the base terminal, thus separating the voltage used to drive the electrophoresis from the on/off signal. For example, a pnp-IBJT has been used to stimulate SH-SY5Y cells by delivery of acetylcholine, where the delivery was triggered and modulated by pulsing the EB voltage (V_{EB}) while holding the emitter–collector voltage (V_{EC}) constant (Figure 3.10) [47]. One could further connect the base input to another ionic or chemical circuit, to realize complex autoregulated delivery, for instance, feedback-regulated delivery of a neurotransmitter.

3.4.3.2 Diode Logics

The rectification property of ion bipolar membrane diodes enables them to be used in simple diode-based logic circuits for ionic computing. For example, Han *et al.* have presented integrated AND, OR, and NAND-gates manufactured in microfluidic systems filled with gelled polyelectrolytes [45]. These gates function as ordinary diode-resistor logic gates. In the AND-gate (Figure 3.11), the cathode side of two ion diodes is connected to individual input terminals, while the anode side is connected through a resistor to a positive bias supply. The logic output signal is measured as a voltage drop across the resistor. When one or both of the diodes are biased at 0 V (i.e., forward biased), the voltage drop over the resistor due to the forward bias current pulls the output voltage down toward 0 V. If, on the other hand, both diodes are biased above the positive bias supply voltage, both pathways are reverse biased and the output remains at the positive bias voltage. Additionally, the light emission from a fluorescent dye, fluorescein, acting as an anion in the bipolar membrane, enabled a visual readout of the logic state.

3.4.3.3 Transistor Logics

Diodes can only be used to realize a small range of logic gates, and they offer no signal gain. In addition, the hysteresis and the bidirectional transport observed in ion bipolar membrane diodes can be disadvantageous, especially in drug delivery applications. Current amplifying transistors are thus often more suitable for designing logics gates. IBJTs have therefore been employed to construct inverters and

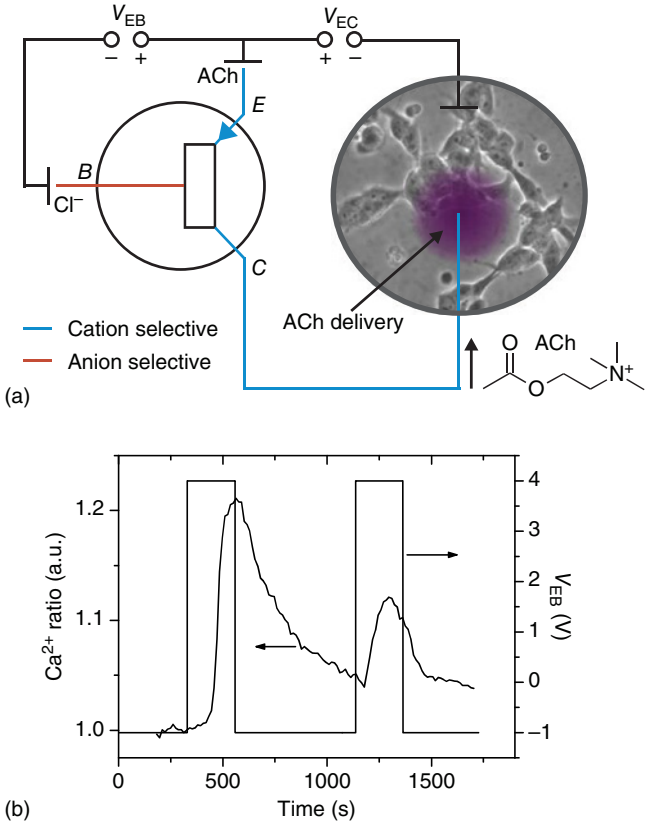

Figure 3.10 Modulation of acetylcholine neuronal signaling with a pnp-IBJT. (a) SH-SY5Y cells were cultured at the collector outlet of the IBJT, while an electrolyte containing acetylcholine was loaded at the emitter. V_{EC} is held constant at +10 V, while acetylcholine delivery is actuated through switching V_{EB} between −1 V (off) and +4 V (on). (b) Acetylcholine receptors respond to the delivered acetylcholine by opening membrane-bound ion channels resulting in an influx of Ca^{2+}, which is detected with a Ca^{2+}-sensitive fluorescent probe. (Tybrandt *et al.* 2010 [47]. Reproduced with permission of PNAS.)

NAND-gates, in both npn and complementary (using both npn and pnp) IBJT circuits [52]. These gates, including resistors, conductors, transistors, and electrodes, were integrated on single chips (Figure 3.12). Even though the characteristics for the IBJTs might not be ideal, the obtained response from the gates is feasible and shows the expected behavior. For inverters the complementary designs show higher gain and lower power consumption than the single npn-type. One severe limitation is, however, the low switching speed, typically reaching ~100 s. This could however potentially be improved by using smaller, and thus faster, transistors [51].

The reported ion transistors logic gates, especially the complementary NAND-gate including four transistors [52], show the feasibility of integrating several iontronic components into functional circuits. One of the more interesting applications for this type of ion-conducting logic gates is the delivery of chemicals and drugs in 2D or 3D grids, where the points in the array contain an ionic logic gate and could

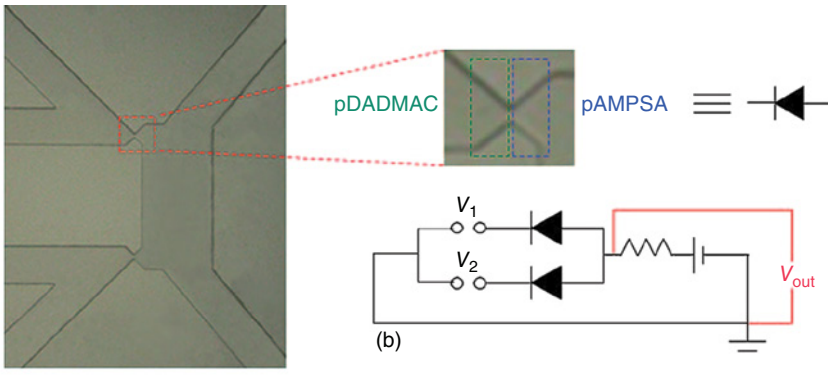

Input (V_1, V_2)		Output (V_{out})	
0	0	Low (0.35 V)	0
1	0	Low (0.4 V)	0
0	1	Low (0.4 V)	0
1	1	High (1.0 V)	1

(c)

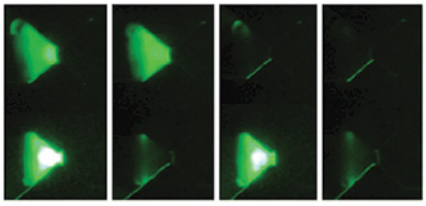

(d)

Figure 3.11 Ion diode-based AND-gate. (a) The gate contains two bipolar membranes, formed by gels of Poly(diallyldimethylammonium chloride) (pDADMAC) and poly(2-acrylamido-2-methyl-1-propanesulfonic acid) (pAMPSA). (b) Inputs (V_1 and V_2) are connected to the cathode side of the diodes, while the output is measured across the resistance of a microfluidic channel. (c) Truth table. The output is only high for the input combination $V_1 = V_2 = 1$, that is, the gate shows AND-functionality. (d) A fluorescent dye in the bipolar membranes gives a visual readout of the diode state (forward/reverse biased). (Han *et al*. 2009 [45]. Reproduced with permission of John Wiley and Sons.)

be individually addressed in an X–Y–Z manner. Such advanced delivery device would be useful to produce and control complex chemical patterns for the stimulation of target tissue functions.

3.4.3.4 Full-Wave Rectifier

Even though the use of conjugated polymers as electrode material elevates the useful safe capacity range compared to metal electrodes, such electrodes can still be electrochemically "consumed" and may produce undesired side reactions, such as pH changes, when operated for extended periods [33]. This can be a problem for iontronic devices aimed at delivering large amounts of charged molecules over extended times, especially if the dimensions of the electrode are restrained, as, for example, in systems designed for use *in vivo*.

An elegant solution to this problem is to apply a continuously alternating input voltage to the electrodes, and then rectifying the resulting ion current with the use of an ionic full-wave rectifier [42]. A commonly used circuit for full-wave rectification of alternating currents is the four-diode bridge circuit, where regardless of the

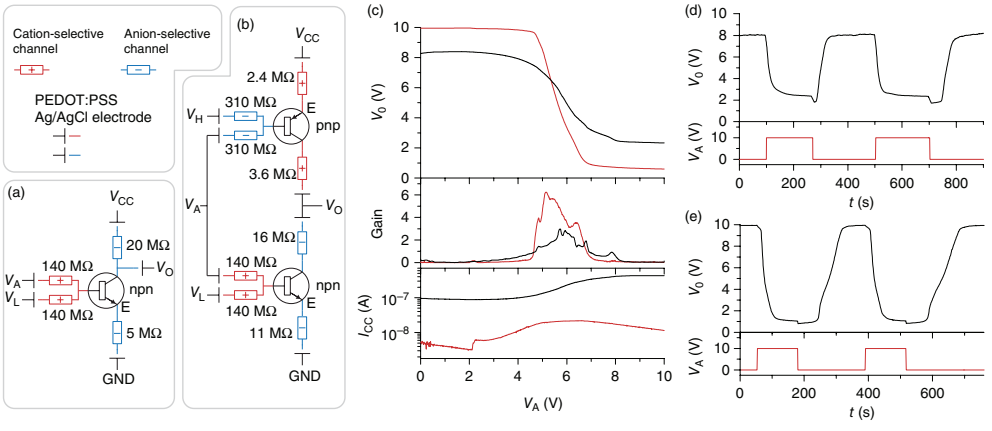

Figure 3.12 Ionic inverter gates based on IBJTs. (a) npn-Type and (b) complementary type inverter circuits. (c) The input signal V_A is inverted to the output signal V_O, that is, high V_A gives low V_O and vice versa. The complementary type inverter (red) offers better swing and gain and lower supply current (I_{CC}) than the npn-type inverter (black). (d) Pulse responses for the npn-type and (e) complementary type inverter. The response is slow owing to the slow performance of the IBJTs. (Tybrandt *et al*. 2012 [52]. Reproduced with permission of Nature Publishing Group.)

polarity of the input voltage, the polarity at the output is always the same. An equivalent ionic circuit can be produced by replacing the diodes with ion bipolar membrane diodes (Figure 3.13a). When an input voltage is applied, one input electrode is oxidized and the other is reduced, and switching the input polarity reverses the oxidation/reduction. Meanwhile, ion diode circuits located between the electrodes ensures that the voltage between the output reservoirs is always positive (Figure 3.13c,d).

By placing a channel of an ion-exchange membrane between the output reservoirs, the circuit can be used as an OEIP, where the transport of ions between the reservoirs is rectified (Figure 3.13b). This circuit was used to demonstrate electrode-independent delivery of acetylcholine (Figure 3.13e). An alternating input signal of ±8 V, with a 20 min period, was applied to the input electrodes, resulting in a steady-state input current of around ±200 nA. The ion bipolar membrane diode circuit rectified this input, at steady state, to +6.8 V over the output. Acetylcholine was loaded into the positive biased output reservoir, while the negative biased output reservoir, containing NaCl, was sampled at every switch in input polarity. The acetylcholine content of the sampled solutions was analyzed, and showed an average delivery of 1.1 nmol of acetylcholine per switch cycle, equivalent to an average delivery rate of 1.83 pmol s^{-1}, and a corresponding total delivery of 1.1 mC of charge over five periods. Owing to the alternating oxidation/reduction of the electrodes, only approximately 120 μC of electrode capacity was used. Thus, the circuit can decouple the generation of ionic currents through electrode reactions from the charge-compensating capacity of the electrode.

A potential future use for this ionic full-wave rectifier is to extend the electrode lifetime in devices intended for long-term *in vivo* applications, for example, pain relief achieved through iontronic drug delivery [37]. The device footprint of such device would preferably be as small as possible, while large output capacity is still required. With the rectifier, the electrode area can be minimized, and the limitation is instead the source compartment of the biomolecules (which at saturated concentration could likely hold sufficient therapeutic substance for long-term operation).

3.5 Conclusions

Conventional electronic devices have evolved from the first transistors introduced in the 1940s to integrated circuits and today's modern (CMOS) computer chips fabricated on silicon wafers using photolithography. For ion-conductive circuits for human–machine interfacing, we now have a basic set of individual components: conductors, resistors, diodes, and transistors. Additionally, with tools and processes borrowed from semiconductor fabrication, simple integrated ionic circuits are also realizable. Future improvements of such components and circuits will hopefully lead to a Moore's law-like development of ionic human–machine interfacing technology. Of special interest is the possibility for amplification and addressability of chemical signals offered by circuits of ion transistors, as this has the potential to enable precise and local modulation of biological processes through generation of complex, spatially and temporally fluctuating biomolecule

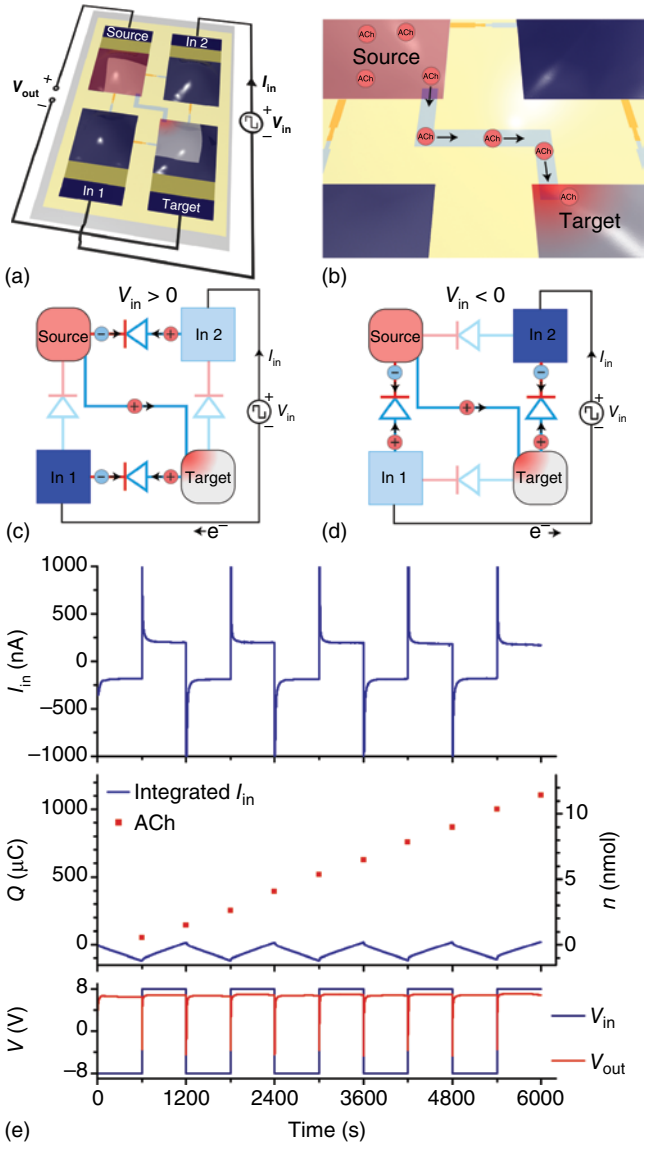

Figure 3.13 Ionic rectification of an input AC signal into a DC acetylcholine output signal. (a) The rectifying ionic bridge is biased with V_{in} at the two input PEDOT:PSS electrodes. (b) The output terminals are connected by a cation-selective channel. Acetylcholine is loaded at the source side (positively biased) and delivered to the target side (negatively biased). (c) and (d) Regardless of the input bias polarity, the four ion diodes direct the current in the same direction between the output terminals (source and target electrolytes). (e) The input current I_{in} follows V_{in}, switching between positive and negative. The voltage over the output, V_{out}, is however predominantly positive. The accumulated delivery of acetylcholine into the target suggests that the delivery rate is independent of V_{in} polarity. (Gabrielsson *et al*. 2014 [42]. Reproduced with permission of John Wiley and Sons.)

patterns in a 3D environment. Compared to, for example, the successful pacemaker using a single electrode for electronic stimulation, such ionic circuits would broaden the spectrum of biological signals the human–machine interface can leverage. Further, as the involved materials are polymer-based, and the technology lends itself to integration with organic electronics on flexible substrates, human–machine devices using ionic devices can be made biocompatible.

References

1 Polikov, V.S., Tresco, P.A., and Reichert, W.M. (2005) Response of brain tissue to chronically implanted neural electrodes. *J. Neurosci. Methods*, **148** (1), 1–18.
2 Anderson, J.M., Rodriguez, A., and Chang, D.T. (2008) Foreign body reaction to biomaterials. *Semin. Immunol.*, **20** (2), 86–100.
3 Azemi, E., Lagenaur, C.F., and Cui, X.T. (2011) The surface immobilization of the neural adhesion molecule L1 on neural probes and its effect on neuronal density and gliosis at the probe/tissue interface. *Biomaterials*, **32** (3), 681–692.
4 Cui, X., Lee, V.A., Raphael, Y., Wiler, J.A., Hetke, J.F., Anderson, D.J. *et al.* (2001) Surface modification of neural recording electrodes with conducting polymer/biomolecule blends. *J. Biomed. Mater. Res.*, **56** (2), 261–272.
5 Strumwasser, F. (1958) Long-term recording from single neurons in brain of unrestrained mammals. *Science*, **127** (3296), 469–470.
6 Fromherz, P., Offenhäusser, A., Vetter, T., and Weis, J. (1991) A neuron-silicon junction: a retzius cell of the leech on an insulated-gate field-effect transistor. *Science*, **252** (5010), 1290–1293.
7 Maynard, E.M., Nordhausen, C.T., and Normann, R.A. (1997) The utah intracortical electrode array: a recording structure for potential brain-computer interfaces. *Electroencephalogr. Clin. Neurophysiol.*, **102** (3), 228–239.
8 Connors, B.W. (2005) Synaptic transmission in the nervous system, in *Medical Physiology* (eds W.F. Boron and E.L. Boulpaep), Elsevier Saunders, Philadelphia, PA.
9 Simon, D.T., Gabrielsson, E.O., Tybrandt, K., and Berggren, M. (2016) Organic bioelectronics: bridging the signaling gap between biology and technology. *Chem. Rev.*, **116** (21), 13009–13041. doi: 10.1021/acs.chemrev.6b00146
10 Friend, R.H., Gymer, R.W., Holmes, A.B., Burroughes, J.H., Marks, R.N., Taliani, C. *et al.* (1999) Electroluminescence in conjugated polymers. *Nature*, **397** (6715), 121–128.
11 Dimitrakopoulos, C.D. and Malenfant, P.R.L. (2002) Organic thin film transistors for large area electronics. *Adv. Mater.*, **14** (2), 99–117.
12 Günes, S., Neugebauer, H., and Sariciftci, N.S. (2007) Conjugated polymer-based organic solar cells. *Chem. Rev.*, **107** (4), 1324–1338.
13 Khodagholy, D., Doublet, T., Gurfinkel, M., Quilichini, P., Ismailova, E., Leleux, P. *et al.* (2011) Highly conformable conducting polymer electrodes for *in vivo* recordings. *Adv. Mater.*, **23** (36), H268–H272.
14 Tarabella, G., Mohammadi, F.M., Coppede, N., Barbero, F., Iannotta, S., Santato, C. *et al.* (2013) New opportunities for organic electronics and bioelectronics: ions in action. *Chem. Sci.*, **4** (4), 1395–1409.

15 Guimard, N.K., Gomez, N., and Schmidt, C.E. (2007) Conducting polymers in biomedical engineering. *Prog. Polym. Sci.*, **32** (8–9), 876–921.

16 Rivnay, J., Owens, R.M., and Malliaras, G.G. (2014) The rise of organic bioelectronics. *Chem. Mater.*, **26** (1), 679–685.

17 Zinger, B. and Miller, L.L. (1984) Timed release of chemicals from polypyrrole films. *J. Am. Chem. Soc.*, **106** (22), 6861–6863.

18 Wong, J.Y., Langer, R., and Ingber, D.E. (1994) Electrically conducting polymers can noninvasively control the shape and growth of mammalian cells. *Proc. Natl. Acad. Sci. U.S.A.*, **91** (8), 3201–3204.

19 Ludwig, K.A., Uram, J.D., Yang, J., Martin, D.C., and Kipke, D.R. (2006) Chronic neural recordings using silicon microelectrode arrays electrochemically deposited with a poly(3,4-ethylenedioxythiophene) (PEDOT) film. *J. Neural Eng.*, **3** (1), 59–70.

20 Abidian, M.R., Corey, J.M., Kipke, D.R., and Martin, D.C. (2010) Conducting-polymer nanotubes improve electrical properties, mechanical adhesion, neural attachment and neurite outgrowth of neural electrodes. *Small*, **6** (3), 421–429.

21 Yang, S.Y., Kim, B.N., Zakhidov, A.A., Taylor, P.G., Lee, J.K., Ober, C.K. *et al.* (2011) Detection of transmitter release from single living cells using conducting polymer microelectrodes. *Adv. Mater.*, **23** (24), H184–H188.

22 Kontturi, K., Murtomäki, L., and Manzanares, J.A. (2008) Transport equations, in *Ionic Transport Processes in Electrochemistry and Membrane Science*, Oxford University Press, Oxford, New York.

23 Vanýsek, P. (2016) Ionic conductivity and diffusion at infinite dilution, in *Handbook of Chemistry and Physics* (ed. W.M. Haynes), CRC Press, Boca Raton, FL.

24 Hamann, C.H., Hamnett, A., and Vielstich, W. (2007) Electrode potentials and Double–Layer structures at phase boundaries, in *Electrochemistry*, 2nd edn, Wiley-VCH Verlag GmbH, Weinheim.

25 Strathmann, H. (2004) Electrochemical and thermodynamic fundamentals, in *Ion-Exchange Membrane Separation Processes*, Membrane Science and Technology, vol. **9**, Elsevier.

26 Kumar, M., Khan, M.A., Al-Othman, Z.A., and Choong, T.S.Y. (2013) Recent developments in ion-exchange membranes and their applications in electrochemical processes for *in situ* ion substitutions, separation and water splitting. *Sep. Purif. Rev.*, **42** (3), 187–261.

27 Kontturi, K., Murtomäki, L., and Manzanares, J.A. (2008) Transport in membranes, in *Ionic Transport Processes: in Electrochemistry and Membrane Science*, Oxford University Press, Oxford.

28 Frilette, V.J. (1956) Preparation and characterization of bipolar ion exchange membranes. *J. Phys. Chem.*, **60** (4), 435–439.

29 Mafe, S. and Ramirez, P. (1997) Electrochemical characterization of polymer ion-exchange bipolar membranes. *Acta Polym.*, **48** (7), 234–250.

30 Mafe, S., Ramirez, P., and Alcaraz, A. (1998) Electric field-assisted proton transfer and water dissociation at the junction of a fixed-charge bipolar membrane. *Chem. Phys. Lett.*, **294** (4–5), 406–412.

31 Pourcelly, G. (2002) Electrodialysis with bipolar membranes: principles, optimization, and applications. *Russ. J. Electrochem.*, **38** (8), 919–926.

32 Nyberg, T., Inganäs, O., and Jerregård, H. (2002) Polymer hydrogel microelectrodes for neural communication. *Biomed. Microdevices*, **4** (1), 43–52.

33 Erlandsson, P.G. and Robinson, N.D. (2011) Electrolysis-reducing electrodes for electrokinetic devices. *Electrophoresis*, **32** (6–7), 784–790.

34 Williamson, A., Rivnay, J., Kergoat, L., Jonsson, A., Inal, S., Uguz, I. *et al.* (2015) Controlling epileptiform activity with organic electronic ion pumps. *Adv. Mater.*, **27** (20), 3138–3144.

35 Isaksson, J., Kjaell, P., Nilsson, D., Robinson, N.D., Berggren, M., and Richter-Dahlfors, A. (2007) Electronic control of Ca2+ signalling in neuronal cells using an organic electronic ion pump. *Nat. Mater.*, **6** (9), 673–679.

36 Tybrandt, K., Larsson, K.C., Kurup, S., Simon, D.T., Kjall, P., Isaksson, J. *et al.* (2009) Translating electronic currents to precise acetylcholine-induced neuronal signaling using an organic electrophoretic delivery device. *Adv. Mater.*, **21** (44), 4442–4446.

37 Jonsson, A., Song, Z., Nilsson, D., Meyerson, B.A., Simon, D.T., Linderoth, B. *et al.* (2015) Therapy using implanted organic bioelectronics. *Sci. Adv.*, **1** (4), e1500039.

38 Jonsson, A., Inal, S., Uguz, L., Williamson, A.J., Kergoat, L., Rivnay, J. *et al.* (2016) Bioelectronic neural pixel: chemical stimulation and electrical sensing at the same site. *Proc. Natl. Acad. Sci. U.S.A.*, **113** (34), 9440–9445.

39 Simon, D.T., Larsson, K.C., Nilsson, D., Burström, G., Galter, D., Berggren, M. *et al.* (2015) An organic electronic biomimetic neuron enables auto-regulated neuromodulation. *Biosens. Bioelectron.*, **71** (C), 359–364.

40 Simon, D.T., Kurup, S., Larsson, K.C., Hori, R., Tybrandt, K., Goiny, M. *et al.* (2009) Organic electronics for precise delivery of neurotransmitters to modulate mammalian sensory function. *Nat. Mater.*, **8** (9), 742–746.

41 Schoch, R., Han, J., and Renaud, P. (2008) Transport phenomena in nanofluidics. *Rev. Mod. Phys.*, **80** (3), 839–883.

42 Gabrielsson, E.O., Janson, P., Tybrandt, K., Simon, D.T., and Berggren, M. (2014) A four-diode full-wave ionic current rectifier based on bipolar membranes: overcoming the limit of electrode capacity. *Adv. Mater.*, **26** (30), 5143–5147.

43 Gabrielsson, E.O. and Berggren, M. (2013) Polyphosphonium-based bipolar membranes for rectification of ionic currents. *Biomicrofluidics*, **7** (6), 064117.

44 Gabrielsson, E.O., Tybrandt, K., and Berggren, M. (2012) Ion diode logics for pH control. *Lab Chip*, **12** (14), 2507–2513.

45 Han, J.H., Kim, K.B., Kim, H.C., and Chung, T.D. (2009) Ionic circuits based on poly electrolyte diodes on a microchip. *Angew. Chem. Int. Ed.*, **48** (21), 3830–3833.

46 Han, J.-H., Kim, K.B., Bae, J.H., Kim, B.J., Kang, C.M., Kim, H.C. *et al.* (2011) Ion flow crossing over a polyelectrolyte diode on a microfluidic chip. *Small*, **7** (18), 2629–2639.

47 Tybrandt, K., Larsson, K.C., Richter-Dahlfors, A., and Berggren, M. (2010) Ion bipolar junction transistors. *Proc. Natl. Acad. Sci. U.S.A.*, **107** (22), 9929–9932.

48 Chun, H. and Chung, T.D. (2015) Iontronics. *Annu. Rev. Anal. Chem.*, **8** (1), 441–462.

49 Tybrandt, K., Gabrielsson, E.O., and Berggren, M. (2011) Toward complementary ionic circuits: the NPN ion bipolar junction transistor. *J. Am. Chem. Soc.*, **133** (26), 10141–10145.

50 Volkov, A.V., Tybrandt, K., Berggren, M., and Zozoulenko, I.V. (2014) Modeling of charge transport in ion bipolar junction transistors. *Langmuir*, **30** (3), 6999–7005.

51 Gabrielsson, E.O., Tybrandt, K., and Berggren, M. (2014) Polyphosphonium-based ion bipolar junction transistors. *Biomicrofluidics*, **8** (6), 064116.

52 Tybrandt, K., Forchheimer, R., and Berggren, M. (2012) Logic gates based on ion transistors. *Nat. Commun.*, **3**, 871.

4

Biocompatible Devices and Sustainable Processes for Green Electronics: Biocompatible Organic Electronic Devices for Sensing Applications

Kyriaki Manoli, Mohammad Yusuf Mulla, Preethi Seshadri, Amber Tiwari, Mandeep Singh, Maria Magliulo, Gerardo Palazzo, and Luisa Torsi

Dipartimento di Chimica, Università degli Studi di Bari "Aldo Moro", Via Orabona 4, 70126 Bari – Italy

4.1 Introduction

In the field of sensors and biotechnology, organic (bio)electronic devices are envisioned as promising components for flexible, biodegradable sensing tags in food packaging or on textiles [1], low-cost and disposable biosensors for *in situ* medical diagnostics, as well as for the development of artificial skin [2] and non-invasive tools for studying cell metabolism and recording neuronal activity [3]. In particular, organic thin-film transistors (OTFTs) have shown great potential for a wide variety of sensing applications. Sensors built on OTFT platforms have been proposed for label-free detection of various chemical and biological species, including detection of analytes in gaseous and aqueous or biologically relevant environments [4].

OTFTs are appealing electronic devices because of their low cost, facile fabrication, and low power consumption. As sensors, OTFTs can be operated at room temperature and offer fast, multiparametric response, signal amplification, and electronic output. The molecular structure and the morphology of organic material can be easily customized, via synthetic and surface chemistry routes, and sensing layers with specific functionalities can be obtained. To this end, several techniques have been developed for efficient immobilization of biomolecules on different types of material surfaces. Henceforth, critical sensing characteristics such as stability [5], sensitivity [6], selectivity [7], and biocompatibility [8] can be ensured. In addition, organic materials take precedence over inorganic ones because of their compatibility with flexible substrates using low-temperature and large-area fabrication processes. Currently, and thanks to the intense research in the field of organic electronics toward biodegradable and naturally occurring electroactive components [9], chemical and organic electronic (bio)sensors with low environmental and energy impact are foreseen.

The present chapter is organized as follows. First, an introduction to different types of OTFTs and their working principle is provided. Subsequently, we refer to

Green Materials for Electronics, First Edition.
Edited by Mihai Irimia-Vladu, Eric D. Glowacki, Niyazi S. Sariciftci, and Siegfried Bauer.

the architectures proposed so far for fabricating OTFT sensors and the protocols adopted for realizing sensing measurements. Then, we emphasize the most recent advances in the field of OTFT sensors in terms of device development and applications. In this section, we divide the sensors into two main categories: OTFTs chemical sensors and biosensors.

4.2 Fundamental Aspects of OTFT Sensors

Typically, an OTFT requires the following components: an organic semiconductor (OSC), an insulator, and three electrodes (contacts), namely, source, drain, and gate. The active OSC layer is located in the channel between the source and drain electrodes, whereas the gate electrode is isolated from the active channel by an insulating layer (Figure 4.1). Organic semiconducting materials can range from small molecules to oligomers and polymers. Some of the most utilized OSCs for the development of sensors are metal phthalocyanines (MPcs), pentacene, and polythiophene derivatives. Many of these materials are commercially available and biocompatible [3b, 8, 10]. Biocompatibility can be also provided by proper encapsulation [11]. Contacts are typically made of gold but conductive materials, including doped conjugated polymers, conducting metal oxides, and metal nanoparticles, are being employed as well. As gate medium, dielectric materials such as inorganic oxides, polymers, and composites can electrically isolate the semiconductor from the gate electrode. Furthermore, OTFTs gated with electrolytes are being actively used. The electrolyte can be a polymer, a water droplet, a buffer solution, or an ionic liquid [12]. Each component and the resulting interfaces are critical for the performance of the device. Sufficient

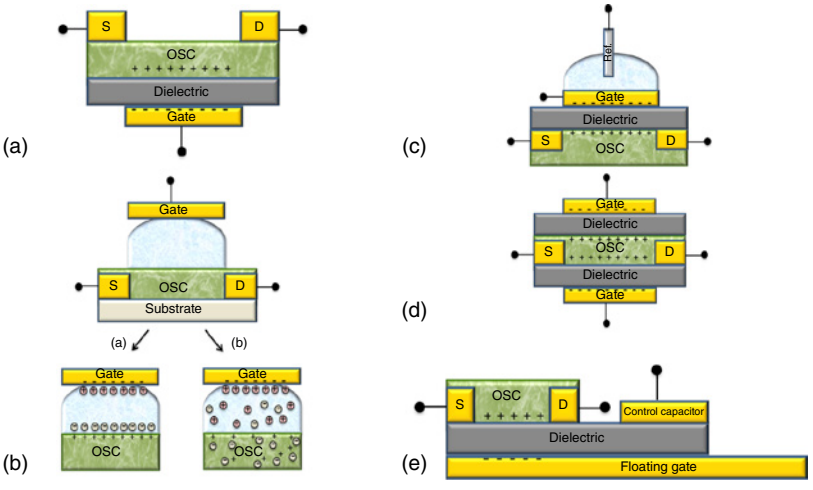

Figure 4.1 Schematic illustration of different OTFT geometries and operation principle using a p-type OSC: (A) back-gate OTFT, (B) top-gate (a) EGOFET/(b) OECT, (D) ion-sensitive OFET (ISOFET), (D) dual-gate OFET, and (E) organic charge-modulated FET (OCMFET).

control over the properties of OTFTs can be achieved through chemical design, proper choice of materials, and interface tweaking.

OTFTs operate either in a field effect transistor (FET) or an electrochemical transistor (ECT) mode. In the FET mode, the current that flows between the source and drain electrodes through the semiconductor is modulated by a perpendicular electric field. This electric field is produced by a bias applied on the gate electrode. Thereby, the semiconductor layer is capacitively coupled to the gate electrode. The magnitude of the applied gate bias determines the density of charges in the channel. Field-induced carriers in the semiconductor are confined to a few monolayers in close proximity to the semiconductor–dielectric interface, thus resulting in the formation of a two-dimensional (2D) conductive channel (Figure 4.1A). Owing to this proximity, organic field effect transistor (OFET)-based sensors rely on variations in the charge distribution across the semiconductor–dielectric interface. Electrostatic interactions and morphological and chemical changes at this interface affect greatly the charge transport. The contact–OSC interface, where carrier injection occurs, can be also subjected to such interactions upon exposure to the analyte, affecting the performance of the sensor [4c].

When instead of a dielectric the transistor is gated through an electrolyte, the electrostatic coupling of the gate to the OSC is achieved through formation of electrical double layers (EDLs) [13]. Upon gate biasing, ions in the electrolyte move and accumulate toward the gate–electrolyte and OSC–electrolyte interfaces. Polarization of the interfaces is associated to a localized large electric field that induces sizable accumulation of charged carriers in the 2D channel (Figure 4.1Ba). Under the best circumstances (high electrolyte concentration), the thickness of EDL matches the ion-surface closest approach distance (few angstroms). This situation is usually referred to as an Helmholtz's EDL and its overall capacitance is very high in the order of a few tens of microfarads per square centimeter for electrolytes, allowing operation at ultra-low voltage ranges in aqueous media [14]. In the case of customary aqueous electrolytes, the Helmholtz's EDL screens only a fraction of the surface charge, and the residual charge is compensated by a diffuse double layer – the so-called Gouy–Chapman diffuse double layer with a capacitance that is not a constant but depends on the applied potential and the ionic concentration (strictly the ionic strength). The capacitance of a Gouy–Chapman EDL equals that of a parallel plate capacitor with a thickness equal to the so-called Debye's screening length that is inversely proportional to the square root of the electrolyte concentration. The total capacitance of the electrolyte gating layer can be described as a series connection of the Helmholtz's and Gouy–Chapman capacitors and will be dominated by the smaller Gouy–Chapman capacitance. The concept of OFETs gated with electrolytes is of special technological interest because of the fast switching speeds and the high capacitance of the EDL. This type of OFETs are most commonly known as electrolyte-gated organic field effect transistors (EGOFETs). Furthermore, EGOFETs rapidly gain considerable attention as biosensing platforms, since they can be operated using water or liquid electrolytes with an ionic strength comparable to that of physiological fluids.

The electric field of the double layer not only produces electrostatic charge accumulation but can also cause ECT doping (oxidation/reduction of the

semiconductor) through percolation of ions from the electrolyte into the OSC film (Figure 4.1Bb). The occurrence of faradaic processes depends on the magnitude of the gate bias, the nature of the semiconductor, the gate material, and the electrolyte [15]. Indeed, the same device configuration can be used to operate an ECT transistor. ECT doping of the semiconductor associated with ion penetration throughout the bulk of the semiconductor layer results in three-dimensional (3D) conduction. In organic electrochemical transistor (OECTs), the 3D conductivity of the channel is modulated by reversible electrochemical doping/de-doping of the semiconductor upon application and removal of a gate bias. The OECT sensor response is, therefore, dominated by the ion diffusion process upon application of an effective gate voltage. Also, it has been shown that parameters involving device geometry, that is, gate size, morphology, and type, dimensions, and thickness of the channel, affect the performance of the sensor in terms of response time and sensitivity [16].

As sensors, OTFTs usually operate in the accumulation regime. However, most of the recent OECT sensors reported are fabricated with conducting polymers, such as poly(3,4-ethylenedioxythiophene) poly(styrenesulfonate) (PEDOT:PSS), and work in depletion. Regardless of the operation regime, the response of the sensor can be measured both statically and dynamically. In static sensing measurements, the device is electrically characterized prior to and after being exposed to the analyte, by recording I–V characteristic curves. The detection of an analyte in solution often requires the implementation of microfluidics for delivering the analyte to the sensor. Otherwise, the device is exposed to the analyte solution and measured after rinsing and drying. Static measurements allow collecting sensing information derived from changes occurring in all the device parameters. When an OTFT-based sensor is exposed to analyte vapors or solutions, a multiparametric response [17] of the transistor can be obtained by measuring changes in mobility, threshold voltage, and *on-* and *off-*current. Each of these parameters may respond differently to one or more analytes. A nice proof of this concept is the fingerprint response of an array of OSCs to a series of volatile organic compounds (VOCs), reported a few years back [18]. In dynamic mode, transient current measurements can be carried out. In this case, the transistor is operated as a resistor, under constant V_G and V_{DS}. Real-time measurements could provide useful information on the kinetics of interactions between the analyte and the sensitive layer [19]. Continuous gate biasing, however, can have detrimental effects on the electrical performance of the transistor. Decay of the drain current and threshold voltage shifts are often observed as a result of gate bias stress effect, making the sensing unreliable. Instead, strategies involving application of gate voltage pulses or incorporation of a ring oscillator circuit can diminish such issues [20].

The diverse nature of OTFT components and device layouts, alongside the significant progress made in the past decades in understanding charge transport in π-conjugated systems, material processing, and device engineering, has resulted in exciting scenarios for development of (bio)sensors. Different device geometries have been proposed for the detection of chemical and biological analytes, depending on the type of analyte, the binding characteristics of the involved (bio)recognition element, the sample matrix, and the requirements of the real-life application (*single-use sensors, on-line monitoring sensors*). Thus far, most of the OTFT sensor

geometries fall in the categories below: back-gate OTFT, top-gate EGOFET/OECT, ion-sensitive OFET (ISOFET), dual-gate OFET, and organic charge-modulated FET (OCMFET) (Figure 4.1).

4.3 OTFT: Sensing Applications

By definition a chemical sensor is an analytical device able to provide quantitative and qualitative information on its environment. It consists of a sensitive layer that interacts with chemical species, and through a transducer the chemical information is converted into a measurable signal. A subgroup of chemical sensors is biosensors. Biosensors incorporate biological molecules, such as enzymes, DNA, antibody, and bacteria, as biorecognition elements for sensing analytes. Based on the aforesaid definition, a distinction is made between OTFT chemical sensors and biosensors.

4.3.1 OTFTs: Chemical Sensors

4.3.1.1 Gas Sensors

Apart from environmental monitoring and industrial applications, gas detection is particularly important in the field of medical diagnostics and food spoilage. Many biological processes involve gases and VOCs either as reactants or as products. OSCs are generally amenable to environmentally relevant analytes, such as humidity, oxygen, or other gases and VOCs. With this in mind, OTFTs bearing a solid dielectric were initially employed as gas sensors in the early 1990s [21]. In most cases, the organic semiconductor serves as the sensing layer that is directly exposed to the analyte vapors using a back-gate configuration. OTFT gas sensors rely on weak, noncovalent interactions involving electrostatic, π-effects, and van der Waals forces. The response of the sensor depends on the chemical affinity between the involved analyte and the organic semiconductor system. Analyte–device interactions can occur at the surface of the organic semiconductor, within the grain boundaries of a poly-crystalline OSC, and at the interfaces with the dielectric or with the electrodes [22]. In several studies it has been demonstrated that the sensing mechanism is strongly correlated to parameters such as design, fabrication process, and device operating conditions. The change in the measured drain current of back-gate OFETs upon exposure to polar analytes has been found to vary depending on the morphology of the OSC film [23], the dimensions of the active channel [24], the type of dielectric interface [25], and the magnitude of the gate voltage [7a, 25, 26]. Duarte and Dodabalapur [24a] suggested that the abundance of grain boundaries in the organic film and large-scale devices give rise to grain boundary effects. On the other hand, OFETs with small channel lengths are dominated by effects occurring at the metal–OSC interface. It is also believed that high gate voltages favor charge trapping, while at lower gate voltages added charge phenomena are more possible to occur.

Furthermore, engineering of the dielectric interface has proved to be rather promising for the development of ultrasensitive OTFT sensors [27]. One commonly applied strategy for tuning the OSC–oxide interface is the use of organosilane-based

self-assembled monolayers (SAMs). In this regard, Kang *et al.* [28] studied the adsorption of moisture on pentacene-based back-gate OFETs by modifying the oxide surface, using SAMs of varying hydrophilicity. Organosilanes, holding sulfonic acid and sulfonyl chloride functional groups, have been also proposed for detection of ammonia and other amine compounds [29]. Beside SAMs, polymeric layers can be used to tailor the characteristics of the sensor. Enhancement of the sensitivity of pentacene-based sensors toward ammonia (NH_3) detection was observed, by depositing a poly(methyl methacrylate) (PMMA) film on the SiO_2 [30]. The response was further improved when the PMMA layer was treated using UV irradiation. Utilizing a polyelectrolyte as interlayer between the OSC and SiO_2, Park *et al.* [31] reported a pentacene-based humidity sensor with ultra-high sensitivity. An increase in the current and positive shifts in the threshold voltage were observed as the relative humidity was increased, whereas current decrease was found for devices fabricated using bare SiO_2. The current increase was attributed to doping of the OSC by mobile ions. The ions were released from the polyelectrolyte upon the absorption of moisture. The proposed sensor was able to detect different levels of humidity in a range from 0% to 30%. The sensor was also implemented on a flexible substrate using a thin Al_2O_3 layer as dielectric (Figure 4.2).

Polymeric dielectrics are also broadly used for the development of flexible organic electronic devices. In a recent work, Huang *et al.* [32] compared the performance of pentacene-based sensors using different polymeric dielectrics, upon exposure to NH_3. Higher responses, good signal recovery, and lower limit of detection (LOD = 1 ppm) were observed for the device gated with poly(styrene) (PS). The superior performance of the PS-gated OTFF was attributed to the formation of smaller grains of pentacene on PS. It was also suggested that PS exhibited lower surface trap density and chemical stability in the presence of ammonia. Moreover, an interesting and novel geometry for the fabrication of ultrasensitive gas sensors has been proposed by Shaymurat *et al.* [33]. In particular, a gas dielectric CuPc nanowire back-gate OFET was designed (Figure 4.3). The sensor was tested upon exposure to sulfur dioxide (SO_2). The detection limit was one

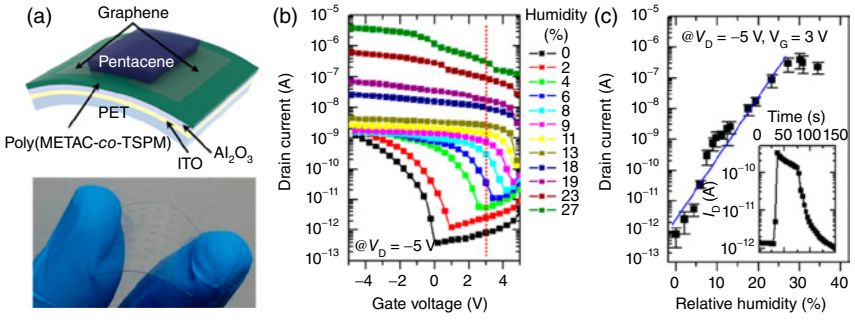

Figure 4.2 (a) Schematic diagram of a device and a photograph of the flexible humidity sensor, (b) transfer characteristics at various humidity levels ($V_D = -5$ V), and (c) plot of I_D at $V_G = 3$ V and $V_D = -5$ V as a function of the humidity level. The inset shows the dynamic response of the flexible sensor upon exposure to 6% relative humidity. (Park *et al.* 2013 [31]. Reproduced with permission of American Chemical Society.)

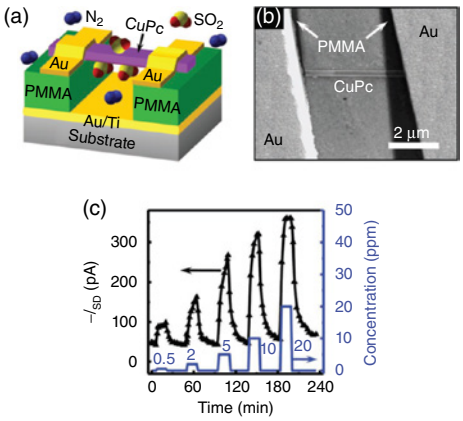

Figure 4.3 (A) The schematic illustration and (B) scanning electron microscopy (SEM) image of gas dielectric CuPc nanowire FET. (C) I_{SD} change versus time upon cycles of exposure/recovery of increasing SO_2 concentrations at $V_G = -10$ V and $V_{SD} = -15$ V at room temperature. (Shaymurat *et al.* 2013 [33]. Reproduced with permission of John Wiley and Sons.)

order of magnitude lower (0.5 ppm) compared to the LOD (10 ppm) using solid dielectric PMMA.

As far as selectivity is concerned, the degree of binding affinity between the analyte and the organic semiconductor can be tuned by introducing functional groups at the structure of the OSC, for example, at the side chains of a polymer-based OSC. Such strategies are likely to endow selectivity toward a group of analytes, such as homologous series of organic compounds (e.g., alcohols, alkanes) [34]. Specific recognition can be obtained by the presence of sophisticated receptors, either chemical or biological. Although *ad hoc* designed OSCs are beneficial in terms of enhancing the binding capacity of the active layer, undesirable effects on the electric performance are often observed. Instead, active layers formed by composite materials have been used [35]. On the other hand, the functionalized semiconductor can be deposited on top of the pristine OSC film. In the so-called bilayer structure, the first layer of OSC provides the charge transport pathway, while the second layer is responsible for interacting with the analyte [7]. The present structure has been employed successfully for selective detection of several compounds.

Among others, it is worth mentioning the pioneering contributions of Huang *et al.* [7a] and Torsi *et al.* [7b]. In the former case, the sensor displayed high selectivity and sensitivity to vapors of dimethyl phosphonate (DMPP) by incorporating terminal hydroxyl groups in the side chains of OSC. Torsi *et al.* proposed a bilayer OFET gas sensor able to differentiate the enantiomers of β-citronellol and carvone. The device consisted of an achiral alkoxyphenylene–thiophene oligomer bottom layer, while as top layer the oligomer was chemically modified with chiral side groups. Interestingly, upon exposure to the racemic mixture of β-citronellol, the response of the chiral bilayer OFET fell right between the responses of the two enantiomers. A couple of years later, Sokolov *et al.* [36] adopted the same geometry and used different calixarene-containing top layers for selective and sensitive detection of VOCs.

All the above suggest that the response of the OTFT gas sensor can be, to some extent, controlled by proper choice and process of the OTFT components, device design, and operating mode. However, the realization of OTFT gas sensors exhibiting high level of selectivity toward a target analyte is still the most challenging task. To this aim, promising are the attempts where OTFT arrays and pattern recognition algorithms are being employed [19].

4.3.1.2 Liquid Sensing

Another active area of OTFT chemical sensors is the development of sensors for detection of chemical and biological species in water, blood, or other body fluids. Utilizing P3HT as OSC and ISOFET geometry (Figure 4.4), Ji *et al.* [37] proposed a flexible sensor for measuring the concentration of potassium K^+ and hydrogen H^+ ions in the human body as indicators for acute myocardial ischemia. K^+ selectivity was achieved by using a valinomycin ionophore layer on top of the gate electrode. The size of 18-crown-6 ionophore hydrophilic interior is ideal to accommodate the K^+ ion. Tantalum pentoxide Ta_2O_5 was used as gate dielectric and H^+ ion as selective layer. The sensors were able to measure concentrations of ions in a range appropriate for the application ($[K^+]$ 33–50 mM and pH range 6.68–9.5). Different approaches to enhance the sensitivity and selectivity of ISOFET-based sensors have been attempted. Ritjareonwattu *et al.* [38] fabricated a pH sensor using P3HT as the semiconductor and PMMA as the gate insulator.

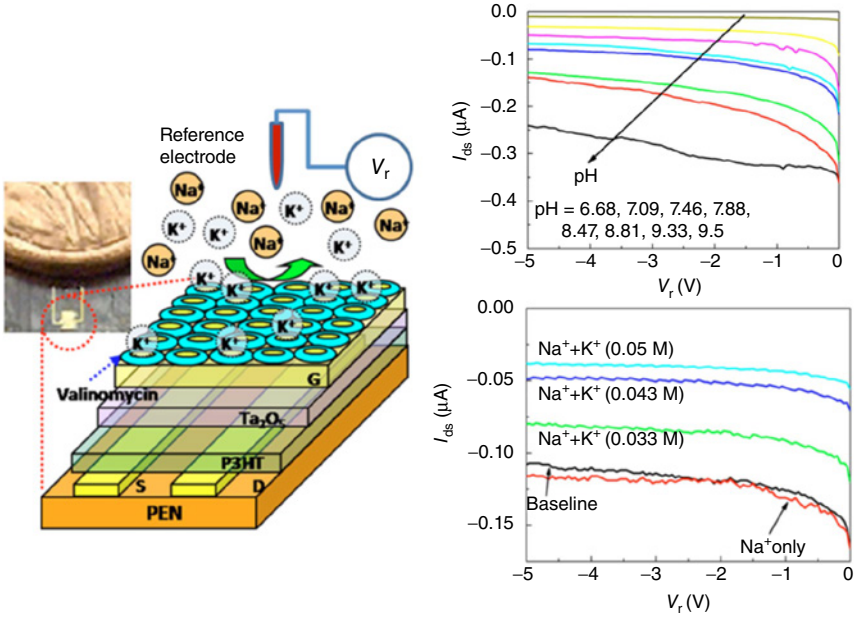

Figure 4.4 Schematic illustration of the flexible ISOFET for K^+ sensing; drain current changes versus V_r upon different pH and K^+ concentrations. (Ji *et al*. 2008 [37]. Reproduced with permission of AIP Publishing.)

Significant increase in the sensitivity of the ISOFET to H+ ions (pH range ~3.2–5.7) was observed by depositing a Langmuir–Blodgett film of arachidic acid on top of the polymeric dielectric.

Caboni *et al.* [39] overcame the limitation of using counter electrodes for pH monitoring by using OCMFET geometry. In this case, the floating gate electrode serves as the sensing layer; hence, the organic semiconductor (pentacene) does not come in contact with the analyte solution and can be properly encapsulated. The OTFT was fabricated on a flexible substrate that acted as the dielectric as well. To provide pH sensitivity, thiol-based SAMs terminated with amine functional groups were immobilized on the gold floating gate. The amino groups were able to protonize in proportion to the concentration of H_3O^+ ions in solution. Upon moving from basic to acid solutions, a shift of the threshold toward more negative values was observed. Moreover, a vertical dual-gate OTFT geometry was proposed by Spijkman *et al.* [40] as a pH sensor. The sensing mechanism was correlated to changes in the ECT potential at the second gate dielectric, quantified by threshold voltage shifts.

A seminal work was performed by Roberts *et al.* [5] where a low working voltage back-gate OFET was developed by using p-channel semiconductor 5,5′-bis-(7-dodecyl-9*H*-fluoren-2-yl)-2,2′-bithiophene (DDFTTF) and a cross-linked poly(4-vinylphenol) (PVP) as dielectric. Long-term stability in aqueous solutions of more than 10^4 electrical cycles was demonstrated. The stability was attributed to the close packing nature of the alkyl chains in the semiconductor molecular structure. Protecting the source/drain electrodes by hydrophobic fluoropolymer layer resulted in excellent stability in both stationary and flowing water. Detection up to concentrations as low as a few parts per billion for glucose, cysteine, methylphosphonic acid (MPA), and 2,4,6-trinitrobenzene (TNB) was reported (Figure 4.5). In a

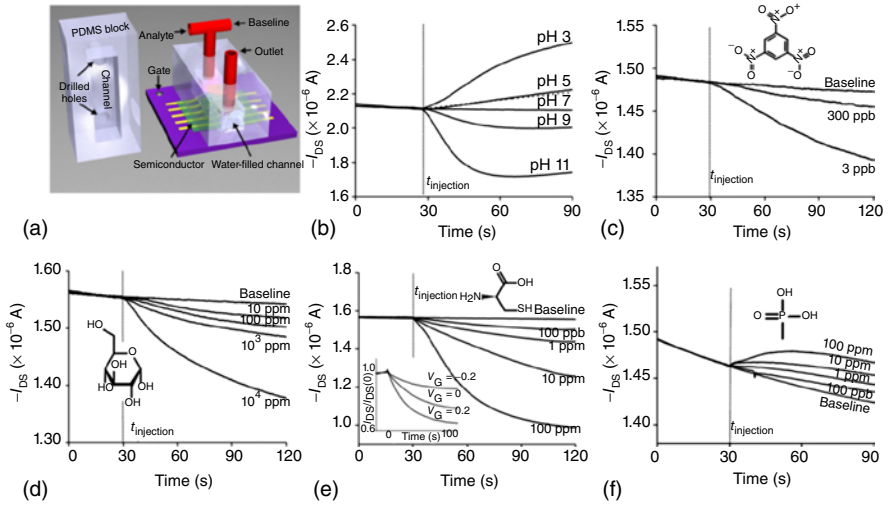

Figure 4.5 (a) Schematic showing an OTFT with DDFTTF integrated in a flow cell, (b) I_{DS} versus time response of a DDFTTF OTFT to pH. I_{DS} versus time response to (c) TNB, (d) glucose, (e) cysteine, and (f) MPA. ($V_G = -1$ V, $V_{DS} = -0.6$ V). (Roberts *et al.* 2008 [5]. Reproduced with permission of National Academy of Sciences, U.S.A.)

following work by the same group, the influence of molecular structure and film morphology on the water stability and sensor characteristics was investigated. Organic semiconductors holding different molecular structure, alkyl chain length, and film morphology were tested. After optimization, the resulting sensor was able to detect cysteine and 2,4,6-trinitrotoluene (TNT) in aqueous solutions down to 10 ppb and 40 ppm respectively [41].

Furthermore, Casalini *et al.* [42] demonstrated a label-free dopamine sensor with *in vitro* sensing capabilities and sensitivity limits ranging up to picomolar concentrations. Selectivity was assessed by immobilizing SAMs of cysteamine and 4-formylphenyl boronic acid on the gold gate electrode. The sensing mechanism was attributed to modulation of the double layer capacitance pronounced by the shift of the gate electrode work function upon dopamine adsorption. A dopamine-OECT-based sensor has been also demonstrated by Tang *et al.* [16b]. The sensing mechanism was dependent upon electro-oxidation of dopamine at the gate electrode changing the effective gate voltage of the device. The role of different gate electrodes on the sensitivity of the device was also investigated. The best LOD (0.5 nM) was achieved by Pt gate electrode among graphite, Au, and Pt/carbon-nanotube electrodes. The sensitivity of the OECT to dopamine was thus reported to be dependent on the gate electrode and the operation voltage.

Moreover, OECT devices have been extensively used for ion and pH sensing. The first studies were reported in the mid-1980s by Wrighton and coworkers. Back then, they proposed a polyaniline-based OECT for the detection of redox reagents (e.g., $Ru(NH_3)_6^{3+/2+}$ and $Fe(CN)_6^{3-/4}$) and with pH-sensing capabilities in the sensing range from 1 to 6 [43]. Effective OECT sensing with polycarbozole as active layer was demonstrated by Saxena *et al.* [44] for Cu^{2+} detection up to 2.5×10^{-6} M. The sensing mechanism, in this case, was based on measuring the conductivity variation induced by diffusion of Cu^{2+} ions from the electrolyte resulting in conformational changes in the polymer phase. Several studies have been performed in OECTs while using PEDOT:PSS as the active layer. The main approach is the introduction of an additional layer of polymeric membrane with specific ion-selective ionophores on the active channel. Mousavi *et al.* [45] developed multi-ion-selective sensors (Ca^{2+}, K^+, and Ag^+) achieving detection limits of 10^{-4} M for Ca^{2+} and K^+ and 10^{-5} M for Ag^+. In a recent study, Lin *et al.* [16a] investigated the role of the gate material on the ion-sensitive mechanism of PEDOT:PSS-based OECTs. For this purpose, different gate electrodes and in particular Au, Pt, and Ag/AgCl were tested. The gate voltage shift showed a Nernstian relationship with the ion concentration when using Ag/AgCl electrode. This was not the case for the Au and Pt gates. For all gates tested, the shift of the gate voltage was toward lower gate voltage by increasing the cation concentration in the electrolyte solution. The validations were confirmed by observing the same behaviors with different cations, such as H^+, K^+, Na^+, Ca^{2+}, and Al^{3+}. The metal ion detection limit of these devices reached down to 10^{-6} M.

4.4 OTFTs: Biosensors

OTFT devices have been widely employed for the development of biosensors, where selectivity is ensured by the integration of suitable biological recognition

elements (i.e., antibodies, enzyme, or other biomolecules) in the electronic device. As already anticipated, the OTFT platform provides several interfaces for integrating a wide range of biological recognition layers. In these biosensors, the electrical properties (mobility, threshold voltage, or capacitance of the dielectric layer) are directly affected by the biorecognition event, thus avoiding the addition of tracers or labels used in optical or ECT non-label-free transducers. In the following paragraphs, an overview of biosensing applications using OTFTs is presented by dividing them into two categories: OTFTs with solid dielectric and electrolyte-gated OTFT biosensors.

4.4.1 OTFTs with Solid Dielectric

The bilayer back-gate OFET geometry was initially adopted by several groups for the development of biosensors, and especially for the detection of DNA [46]. Herein, unlike the aforementioned bilayer-based structures in gas sensors, the biorecognition element serves as the top layer and is usually immobilized on the OSC surface (bottom layer) (Figure 4.6A). One relevant example is the bilayer OFET device proposed by Khan *et al.* [6]. In this work the OSC was modified with a thin maleic anhydride polymer layer using plasma-enhanced chemical vapor deposition (PECVD), thus enabling covalent immobilization of peptide nucleic acid strands. The device was used for *in situ* real-time detection of target

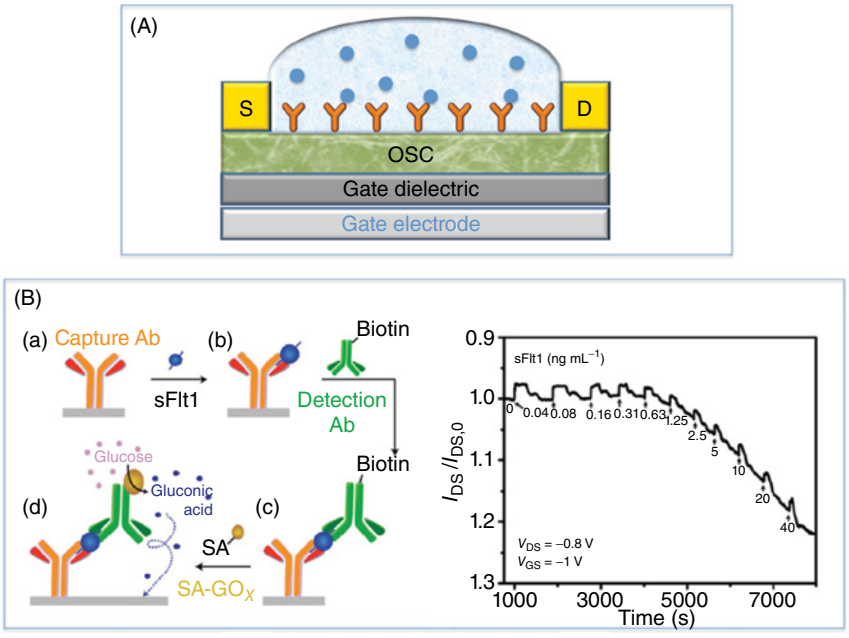

Figure 4.6 (A) Schematic structure of a back-gate bilayer OFET biosensor in which the biological recognition elements are deposited on the OSC surface. (B) Representation of the OFET ER-ELISA employed for the detection of fms-like tyrosine kinase. Transient drain current (normalized) change upon exposure to increasing concentrations of fms-like tyrosine kinase. (Hammock *et al.* 2014 [47]. Reproduced with permission of John Wiley and Sons.)

DNA molecules. The use of a thin polymeric dielectric and the integration of a microfluidic system permit the stable operation of the electronic biosensor directly in an aqueous buffer environment. The authors found that detection of charged biomarkers failed at high ionic strength. This was attributed to the extremely short Debye's length in such solutions in analogy with a similar effect observed in nanowire OFETs [48]. This is because the Debye's screening length defines the length scale at which a charged analyte can be electrically probed at the detector interface. For a Debye's length shorter than the analyte size any electrostatic effect is screened. This issue is particularly important when large recognition elements such as antibodies are integrated in the OFET device for the detection of the target analyte. To overcome this issue, Hammock *et al.* recently proposed an OFET electronic readout enzyme-linked immunosorbent assay (ER-ELISA) that is very similar to conventional ELISA methods [47]. The electronic device was based on the use of a capturing antibody layer deposited on the OSC that selectively binds the target analyte. The detection of the analyte–antibody complex was performed by using a secondary biotinylated antibody, specific for a different epitope of the analyte, and conjugated to a streptavidin-modified glucose oxidase enzyme. The reaction catalyzed by the enzyme upon addition of a glucose solution produced a change in the pH, which was measured by the OTFT device (Figure 4.6B). The detection of fms-like tyrosine kinase, a circulating anti-angiogenic factor, in both buffer and in solution, that mimics human serum down to 1.25 ng ml^{-1} concentration, was demonstrated.

Another promising back-gate configuration for the development of ultrasensitive biosensors is the functional biological interlayer (FBI)-OFET proposed by Angione *et al.* [49]. In this case, the biological recognition element is placed at the interface between the dielectric and the OSC (Figure 4.7a). Three different biosystems, namely, phospholipids (PL), purple membrane (PM), and streptavidin (SA), were investigated as prototypes. The PL FBI-OFET was employed for the detection of anesthetics such as diethyl ether and halothane [51]. The sensor was exposed to the volatile anesthetics and to acetone vapors, which is a non-anesthetic ketone with a similar vapor pressure as diethyl ether. The sensor showed good sensitivity to anesthetics, while a low response was observed in the case of acetone vapors. It was suggested that the diethyl ether molecules induce a disorder in the PL layer integrated in the OFET device affecting the 2D electronic transport at the dielectric/OSC interface. The PM FBI-OFET was utilized to study the proton translocation processes occurring at the PM (bacteriorhodopsin (bR) proteins into PL nanolamellae) upon exposure to chemical and physical external stimuli, such as low concentrations of halothane vapors or light, respectively [49]. The bR is a light-driven ion pump capable of translocating protons across the bacterial membrane as photons are absorbed. The protein is also sensitive to anesthetics as they are capable of modifying the bR local pK_a values causing an amino acid protonation/deprotonation switch. Furthermore, upon exposure to light, the bR protein structure is subjected to both a photo-induced cis/trans isomerization and a deprotonation of the bR Schiff base. The elicited changes were probed by measuring the PM FBI-OFET electrical response to the specific stimuli. The interfacial effect of the halothane interaction with the PM generated an increase in the FBI-OFET current, contrary to the negative response

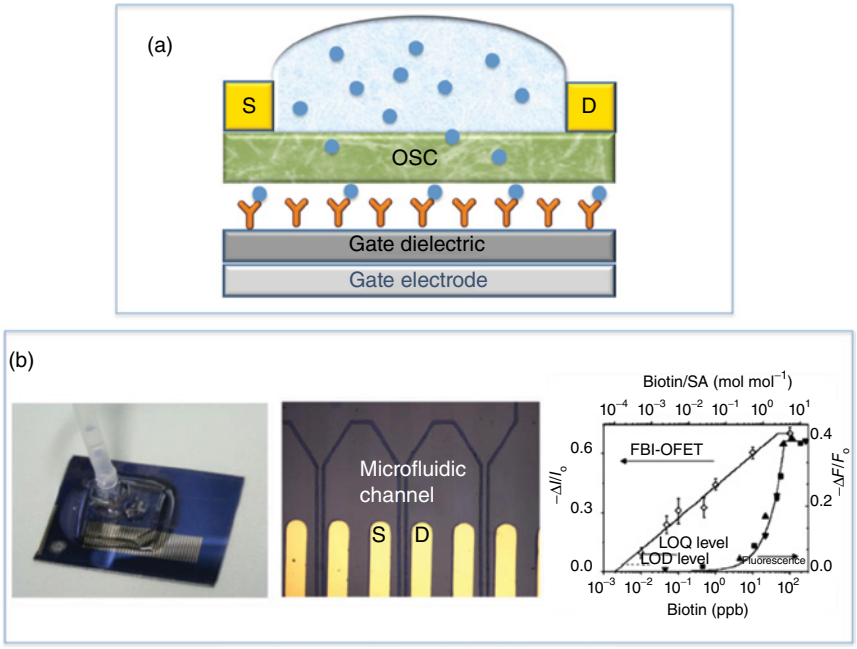

Figure 4.7 (a) Schematic structure of a back-gate FBI-OFET biosensor in which the biological recognition element is introduced on the dielectric surface underneath the organic semiconductor. (b) Pictures of the SA FBI-OFET integrated with a microfluidic system along with the relative response of the drain current of the SA FBI-OFET sensor upon exposure to different concentrations of biotin. (Magliulo *et al*. 2013 [50]. Reproduced with permission of American Chemical Society.)

obtained for a bare PL FBI-OFET. The increase in the drain current was attributed to pK_a changes in the side chain amino acids of the bR due to halothane exposure, which eventually trigger the protons release and their injection into the p-type channel by the gate field. Similar protons injection was achieved by exposing the PM FBI-OFET to green–yellow light ($\lambda > 500$ nm). Finally, the SA FBI-OFET detection capability was demonstrated by probing the SA–biotin binding (Figure 4.7b) [50]. Spin coating and layer-by-layer (LbL) assembly procedure were used to deposit the protein on the SiO_2 surface [52]. A completely different morphology of the protein layer was observed for the two deposition techniques, with the LBL deposition being more homogeneous. However in both cases, the FBI-OFET response exhibited high sensitivity, reaching detection limits of few tens of picomolar, which are comparable to those obtained with ultrasensitive nanotube- and nanowire-based FETs. Particularly, a systematic and scalable decrease in drain current was observed by exposing the SA FBI-OFET to increasing concentrations of biotin, demonstrating that OFET response is connected with the SA–biotin complex formation underneath the OSC. A set of negative control experiments, indicating selective detection of the streptavidin–biotin binding was also realized.

To avoid issues such as OSC degradation upon exposure to the analyte solution, Maddalena *et al.* [53] used a dual-gate geometry. A modified protein layer was

covalently attached on the top dielectric surface to selectively bind sulfate ions. A shift in the threshold voltage was observed upon capturing of sulfate ions by the receptor layer, owing to the added negative charges at the top dielectric. Last but not least, the OCMFET configuration has shown great potential as a biosensing platform for real-time measurements in aqueous environment [54]. Since the current geometry relies on the presence of charged molecules on the surface of the floating gate, biological interactions involving a charge variation such as the DNA hybridization or protein interactions can be studied [55]. In a first demonstration of biosensing capability, the OCMFET was used for the detection of DNA hybridization (Figure 4.8). More recently, the same device configuration has been employed for cell activity measurements [3a].

4.4.2 Electrolyte-Gated OTFT Biosensors

4.4.2.1 EGOFET Biosensors

The beginning of the electrolyte-gated transistors can be traced back to the pioneering experiments in 1950s by Bardeen and Letaw on "electrolytic analog transistor." [56] In 1955, Brattain and Garrett performed further experiments demonstrating higher field-induced charge densities at semiconductor–dielectric interfaces by employing aqueous electrolytes as gate media compared to solid dielectrics [57]. Several decades later, electrolyte gating was revisited by different groups employing solid polyelectrolytes or aqueous solutions [12a, b, 58]. To enhance the sensitivity and selectivity of EGOFET-based biosensors, the analyte-specific bioreceptor can be incorporated into the architecture of EGOFETs either on the semiconductor surface or on the surface of electrodes. This offers two interfaces that can be tailored with specific functional groups or biomolecules to enhance the selectivity and sensitivity of the EGOFET-based biosensor. The first interface is a semiconductor–electrolyte interface and the other one is a gate electrode–electrolyte interface.

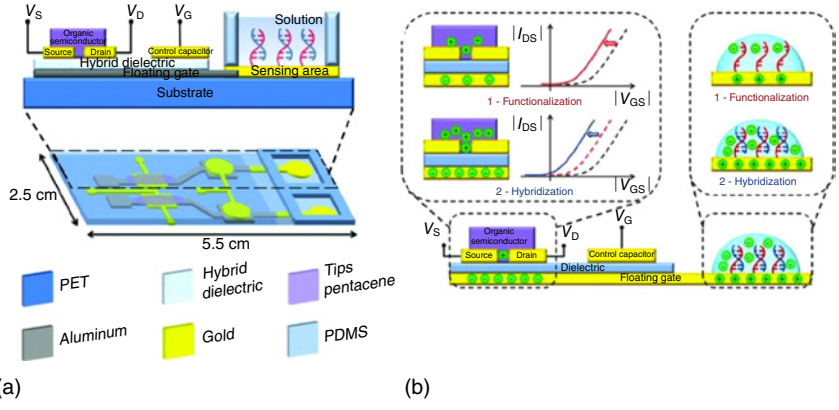

Figure 4.8 (a) Structure of the DNA charge-modulated OFET biosensor. The sensing area is completely separated from the active electronic device. (b) The device is able to operate at low voltage and a shift in the V_T is obtained upon DNA functionalization and hybridization. (Lai *et al.* 2013 [54]. Reproduced with permission of John Wiley and Sons.)

In 2012, Kergoat *et al.* [59] demonstrated the first EGOFET-based biosensor to selectively detect complimentary DNA molecules by modifying the molecular structure of OS molecule with carboxylic acid functional groups. The device consisted of poly[3(5-carboxypentyl)thiophene-2,5-diyl] bearing carboxylic acid moieties as the active layer. DNA probes were covalently attached to the carboxyl groups of the OSC via standard *N*-ethyl-*N*′-(3-diethylaminopropyl)carbodiimide/*N*-hydroxysulfosuccinimide sodium salt (EDC/NHS) coupling pure water, or phosphate-buffered saline (PBS) was employed as electrolytic gating medium and platinum wire served as gate electrode. The transfer characteristics of EGOFET upon complimentary probe hybridization showed a decrease in the OFF current for the device operated with pure water, while for non-complimentary random target no significant change was observed. On the other hand, when a high salt concentration buffer was used as gating medium, no significant changes were observed even after hybridization with a complimentary DNA probe. Also, in this case, the authors associate the sensitivity of the biosensor to the Debye's screening length. Hence, negatively charged target DNAs could be effectively detected in water-gated EGOFET because their size is below the Debye's length in pure water (hundreds of nanometers). When the ionic strength is high enough so that the Debye's length is shorter than the DNA size, the DNA detection fails. In another example of modified organic semiconductor, synthesized P3HT bearing randomly located biotin molecules at the side chains has been used to detect proteins such as negatively charged streptavidin and positively charged avidin in PBS.

The major issue of EGOFET geometry is the undesired doping of the organic semiconductor (OS) due to ionic species from electrolyte solution. This generates not only spurious signals but also degrades the OS. Cotrone *et al.* [60] demonstrated an innovative concept for addressing this problem by modifying the OS–electrolyte interface. A hydrophobic phospholipid layer was integrated with EGOFET by spin coating phospholipid lipid vesicles solution on the active area of the device. The phospholipid vesicles self-organized on the P3HT owing to their inherent amphiphilic nature to form a thin film of phospholipid bilayer (PL), which hindered the doping of the underlying OS. Recently, two interesting applications of PL integrated with EGOFET have been demonstrated. In both the cases, the biotinylated phospholipid layer (biotin–PL) was covalently attached to the surface of the organic semiconductor using carboxylic functionality rendered over the OS by PECVD process (Figure 4.9 route a) [61] or by UV cross-linking of poly(acrylic acid) (UVC-PAA) (Figure 4.9 route b) [62]. In the first case, Magliulo *et al.* [63] functionalized the P3HT surface by an ultra-thin layer of plasma-deposited ethylene acrylic acid (pdEthAA), while in the second case, a solution-processed PAA layer was cross-linked over poly[2,5-bis(3-hexadecyllthiophen-2-yl) thieno [3,2*b*]thiophene] (PBTTT) using short wavelength ($\lambda = \sim 254$ nm) UV irradiation without incorporating any chemical cross-linker. Both processes rendered carboxylic functional moieties over the surface of the organic semiconductor.

Selective label-free detection of streptavidin was demonstrated by incubating increasing concentrations of streptavidin. Upon binding of streptavidin, an increase in drain current was observed. This was ascribed to the additional negative-gating effect induced by negatively charged SA molecules attached over the p-type semiconductor–electrolyte interface. In both the cases the hydrophobic

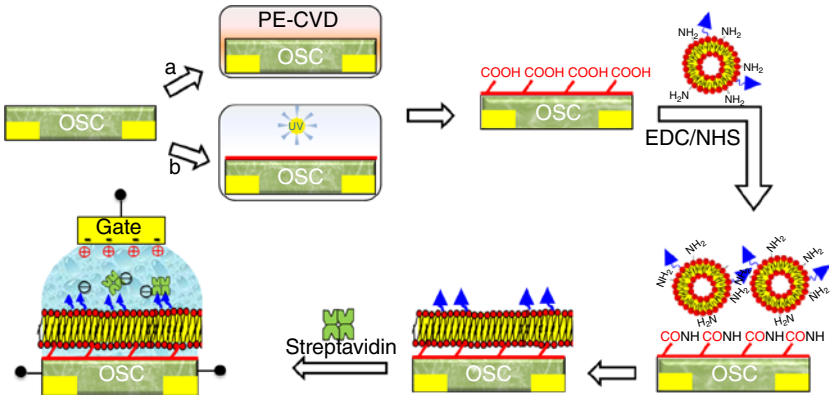

Figure 4.9 (a) PECVD and (b) UVC-PAA functionalization of the organic semiconductor surface with hydrophilic coating bearing carboxyl groups acting as anchor sites for biotin–PL covalent attachment using the EDC/NHS chemistry.

PL enhanced the performance of the EGOFET by preventing the doping of ionic species into the organic semiconductor while being gated with physiologically relevant ionic electrolytes such as PBS. The LOD of streptavidin for pdEthAA-functionalized sensor was 10 nM, while UVC-PAA functionalized EGOFET sensor was capable of detecting comparatively three orders of magnitude lower concentrations down to 10 pM.

In a following work of the same research group, the supported biotinylated lipid bilayer was further functionalized with an antibody against C-reactive protein (CRP), thus obtaining a transistor device capable of measuring the CRP concentration [64]. The EGOFET sensor, operated in highly concentrated ionic solutions (Debye's length $\lambda = 0.7$ nm), could sensitively probe the CRP binding taking place at more than 20 nm away from the transistor channel. Sensing measurements in serum were realized as well. The mechanism of sensing was related to changes in the capacitance, as an extra capacitance in series to the gating system was generated owing to the formation of Donnan's equilibria within the protein layer (Figure 4.10).

Another interesting approach of OS biofunctionalization has been recently demonstrated by Buth *et al.* [65]. The surface of α-sexithiophene (α-6T) was modified to provide hydroxyl functionality by the UV-assisted oxidation of the OSC. Penicillinase (PEN) was anchored to OSC surface using organosilane-based SAMs and EDC/NHS chemistry. The PEN acts as a catalyst and enhances the decomposition of penicillin into penicilloic acid and a proton. This generation of proton locally changes the pH of the electrolyte solution at the OS–electrolyte interface, consequently affecting the threshold voltage shift of the sensor [66]. The selective detection of penicillin was demonstrated with limit of sensitivity around 5 μM for the device operated in PBS electrolyte.

The second interface that can be easily tailored is the gate electrode–electrolyte interface. This configuration keeps the OS undisturbed by any chemical modifications, enabling optimum performance of the EGOFET device. The most widely used gate electrodes are noble metals such as gold and platinum. These

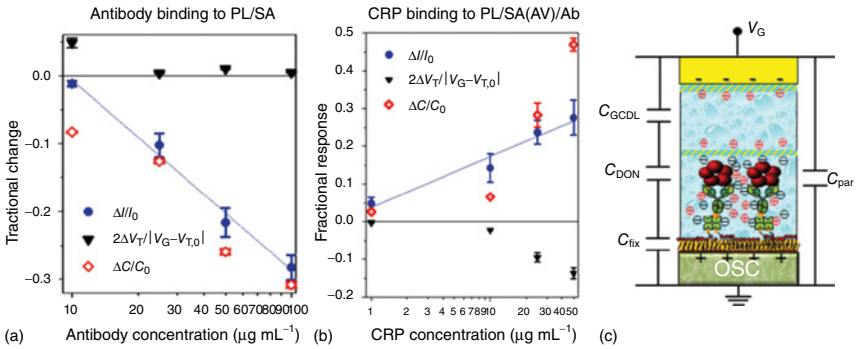

Figure 4.10 (a) Relative I_{DS} change of the PL/SA EGOFET in response to loading with antibody (blue dots). The contribution to the response of the capacitance (open red diamonds), and V_T changes (black triangles) $V_G = -0.5$ V, $V_{DS} = -0.5$ V, PBS gating solution at pH = 7.4 and $i_s = 0.163$ M. (b) I_{DS}, capacitance, and V_T fractional changes of PL/SA/Ab EGOFET in response to loading with CRP; (c) schematic of the charge arrangements in a PL/SA/Ab/CRP multilayer along with the equivalent circuit of the capacitances involved. (Palazzo *et al*. 2014 [64]. Reproduced with permission of John Wiley and Sons.)

metals can be conveniently and reproducibly functionalized using SAMs of organosulfur compounds such as thiols. The thiols bearing different functional groups at end of the tail can be employed to attach the required analyte-specific biomolecules. Moreover, the SAMs alter the capacitance and charge transfer resistance of the electrode–electrolyte interface, depending upon the chain length and the immobilized biomolecule at the end of its tail. This configuration allows us to decouple the electrical figures of merit and the contribution of capacitive changes occurring at the electrode–electrolyte interface of an EGOFET device. As previously mentioned, Casalini *et al.* [42] pioneered such an approach of sensing using the EGOFET geometry to detect dopamine neurotransmitters. More recently, such an approach of capacitance-modulated EGOFET with modified gate electrode was employed for selective differential detection of weakly charged chiral molecules down to a picomolar concentration range [67].

The gold gate electrode was modified with 3-mercaptopropionic acid (3MPA) SAMs bearing carboxylic tail groups. The porcine odorant binding proteins (pOBPs) were covalently attached to the carboxylic groups of SAM by standard EDC/NHS chemistry. The pOBP functionalized gate electrode was exposed to aqueous solutions of odorant molecules such as (*R*)-(−)-carvone and (*S*)-(+)-carvone enantiomers and 2-phenylethanol. The sensor was able to differentiate the carvone enantiomers, while the nonspecific ligand 2-phenylethanol demonstrated a relatively low response (Figure 4.11). The EGOFET sensor was able to detect subtle capacitive changes due to the interaction of surface-bound pOBPs with carvone enantiomers. The high enantioselectivity of the sensor was related to larger conformational changes upon pOBP-(*S*)-(+)-carvone interaction of the surface-confined molecular complex. Furthermore, the subtle changes in free energies of chiral interactions were determined from the electrical response of the EGOFET biosensor.

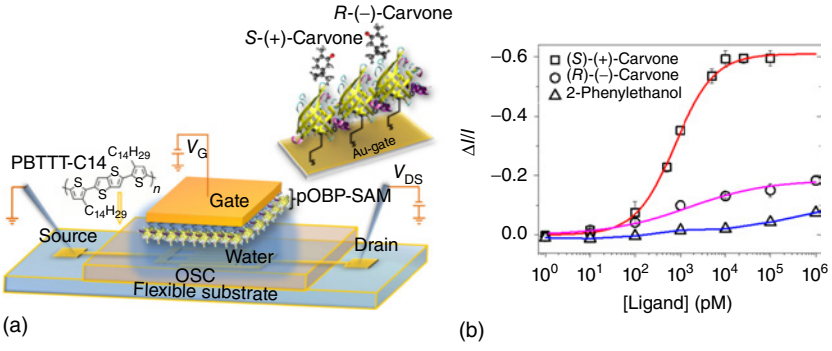

Figure 4.11 (a) Schematic illustration of the EGOFET biosensors and the biofunctionalized gold gate electrode. (b) The binding curves of variation in drain current upon exposure to the (*R*)-(–)- and (*S*)-(+)-carvone as well as the nonspecific 2-phenylethanol ligand in the concentration range from 1 to 10^6 pM. (Mulla *et al.* 2015, http://www.nature.com/articles/ncomms7010. Used under CC-BY-4.0. http://creativecommons.org/licenses/by/4.0/.)

Alternatively, biocompatible and biodegradable hydrogels can be employed to hold electrolytes and bioreceptors in EGOFET-based biosensors. In this direction, recently Dumitru *et al.* [68] demonstrated a novel jellified alginate hydrogel capsule as the gating medium for OTFTs. The transistor was fabricated on a flexible substrate and the spherical alginate capsule was formed by cross-linking a polyanionic sodium salt of alginic acid in the presence of calcium (Ca^{2+}) cations. The alginate capsule served two purposes, one as a hosting matrix for bioreceptor molecules and the second as the gating medium holding aqueous media. Hydrogels appear to provide a suitable environment for biomolecules to maintain their 3D structure since they can diffuse inside the whole matrix. Owing to their hydrophilicity, these materials are able to capture controlled amounts of aqueous solution, thus preventing the biomolecules from denaturing. In some preliminary results, it was shown that a hydrogel-gated transistor can probe enzymatic reactions occurring inside the hydrogel capsule.

4.4.2.2 OECTs Biosensors

Organic electrochemical transistors have been extensively explored as enzymatic sensors to estimate physiological parameters. Enzymes are more often integrated to the OECTs compared to the other biomolecules to date. Enzymatic OECT biosensors have been reported for detection of glucose using polyaniline PANI [69] and PEDOT:PSS [16e, 70] as active conductive layers. The enzyme can be immobilized inside the polymer matrix during synthesis, incorporated on the gate [71] or simply added in the electrolyte in solution [16e]. Several approaches have been proposed to improve the sensitivity of OECT biosensors. Most of them deal with modifications of the gate electrode. For instance, small-scale gates have shown superior performance in terms of sensitivity [72]. Gate electrodes composed of metal nanoparticles, carbon nanotubes, or graphene have been reported to enhance the sensing performance of OECT sensors by increasing the gate surface area [73]. A recent example is the work of Liao *et al.* [71] where the gate was modified with graphene or reduced graphene flakes together with glucose oxidase and

nafion/chitosan membrane. Glucose detection in the nanomolar range was achieved. Moreover, the presence of nafion/chitosan membrane prevented unwanted interferences from the uric acid and ascorbic acid that are commonly found in the biological media. The same group also developed flexible OECTs for the detection of analytes such as uric acid and glucose in saliva. A flexible polyethylene terephthalate (PET) substrate with high operational stability upon bending was employed to fabricate planar OECT sensors. The flexible design enabled conformal contact of OECTs with human body skin. Planar geometry allowed immobilization of multiple enzymes depending upon the target analytes (Figure 4.12). The sensor was successfully used for sensing analytes such as uric acid (UA), cholesterol, and glucose with low detection limits and good selectivity. Furthermore, UA and glucose levels in saliva were also detected [74]. Another interesting approach is the addition of nanoparticles to the active polymer matrix. Kergoat *et al.* detected neurotransmitters acetylcholine and glutamate [75] using electrodes made up of PEDOT:PSS and platinum nanoparticle composite. The enzymes were immobilized on the gate through BSA and glutaraldehyde coupling. The detection limit was 5 µM for the chosen analytes.

Another interesting OECT-based glucose sensor was recently shown, where polymer brushes served as a scaffold to anchor the enzyme for long-term stable sensing [76]. Unlike the widely reported OECT-glucose sensors where glucose oxidase is free in the electrolyte, the enzyme was covalently linked to the polymer brushes. Covalent binding of the enzyme with the substrate enables stable, sensitive operation over time without enzyme leakage and a preferred immobilization for chronic *in vivo* monitoring of glucose. The sensor was reported to be stable over a period of 100 days. Moreover, an all plastic, all PEDOT:PSS glucose sensor was developed where PEDOT:PSS served as all contact material and ferrocene was added as the mediator to improve the electron transfer due to the low catalytic activity of PEDOT:PSS. The sensor had a simple low-cost architecture fabricated using a one-layer fabrication process. Glucose detection in micromolar

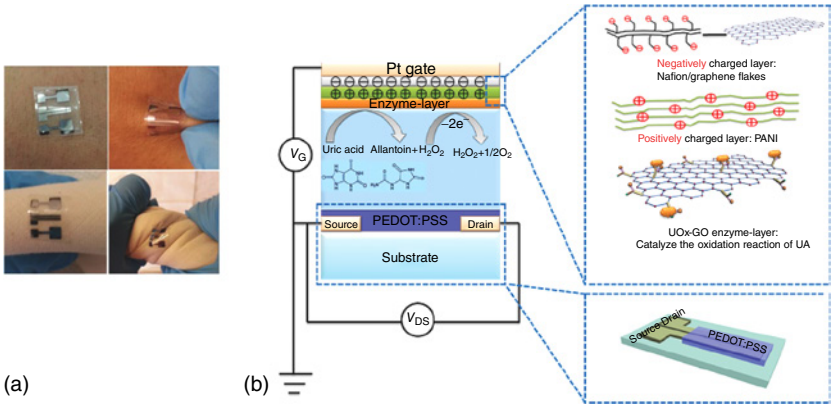

Figure 4.12 (a) Photographs for flexible OECTs attached on different surfaces and (b) schematic diagram of an OECT with a UOx-GO/PANI/Nafi on-graphene/Pt gate. (Liao *et al.* 2014 [74]. Reproduced with permission of John Wiley and Sons.)

ranges was achieved [77]. Lately, room temperature ionic liquids were used to replace traditional electrolyte solutions so as to reduce solvent evaporation and improve the stability for long-term applications. Ionic liquids are advantageous in terms of wide ECT window, high ionic strength, low evaporation rate, and so on. A long-term wearable OECT sensor incorporating an ionogel was developed by Khodagholy *et al.* for continuous monitoring of lactate in the sweat [78]. Lactate detection in a range of concentrations from 10 to 100 mM, which is relevant to the physiological levels of lactate in sweat, was reported.

Although, the majority of OECT biosensors have been focused on sensing of metabolites, nowadays, such platforms have started gaining considerable interest in the detections of biomolecules such DNA, antigens and bacteria. Some representative publications are discussed below. A PEDOT:PSS-based nucleotide sensor was developed where thiolated single-stranded DNAs were immobilized on the gold gate through thiol gold chemistry with another gate as the control gate [79]. A flexible PET was used as the substrate with integrated microfluidic system. The system was reported to be stable in culture medium and even functioned upon bending the substrates. The detection limit was 1 nM and the sensitivity was further improved to 10 pM by a pulsed enhanced hybridization process. Upon hybridization with the complementary strand, a shift in the effective gate voltage to higher values was observed. The reported mechanism was attributed to capacitance changes at the interface between the gate and the electrolyte. Lin *et al.* [80] first demonstrated a cell-based OECT biosensor incorporating PEDOT:PSS as active layer on which fibroblasts and cancer cells were cultured and monitored *in vitro.* The OECT was stable in cell culture medium and demonstrated excellent biocompatibility. Upon detachment of the cells from the active region of OECT, the transfer characteristic of the OECT shifted to a lower gate voltage by 150 mV. This shift toward lower gate voltage was attributed to the electrostatic interaction between cells and PEDOT:PSS. Additionally, the device was used for *in vitro* monitoring of the cancer cells' activities after treatment with an anticancer drug (retinoic acid). Such a cell-based sensor can be used to study cellular activities during drug screening and toxicity investigations. Similarly, an antibody immobilized on the OECTs has been used to capture whole cells. He *et al.* [81] detected bacterial enterohemorrhagic *Escherichia coli* (*E. coli*) O157:H7 using OECT where the surface of PEDOT:PSS was functionalized with anti-*E. coli* O157:H7 antibody. Such sensors can be used as disposable bacteria sensors. Recently, a highly sensitive OECT-based immunosensor to detect prostate-specific antigen (PSA) was developed with a detection limit of $1\,\mathrm{pg\,ml^{-1}}$. Such a sensor can be used for preoperative screening and diagnosis of prostate cancer [82]. Finally, a novel application of OECT has been recently presented by Leleux *et al.* [83]. Real-time recording of electrophysiological signals was performed using OECT-based biosensors. An OECT that exhibits its maximum transconductance at zero applied gate bias was designed. The proposed transistor was operated using a single power supply. The cutaneous electrical potentials served as gate potential. Clinically relevant human electrophysiological signals such as Electrocardiogram (ECG), Electrooculography (EOG), and Electroencephalography (EEG) were recorded.

4.5 Conclusions

The sensing performance of OTFT (bio)sensors working in gas or liquid environment has displayed significant advancements in terms of sensitivity and stability in the past few years. It is noteworthy that OTFT-based (bio)sensors have demonstrated their potential use in aqueous environments. This makes OTFT fit for *in vivo* or *in vitro* and *in situ* biosensing measurements. The OTFTs have covered a wide gamut of applications from detection of gases/VOCs, pH/ion, and several biological compounds to novel applications such as wearable electronics and *in vivo* and *in vitro* recording of clinically and physiologically relevant signals. The challenges yet to be accomplished are high carrier mobility and stability of current organic devices as compared to the devices of silicon or inorganic family. Another goal is to achieve low-voltage operation without sacrificing the sensing response. With the advent of the concept of green electronics, there is increasing importance of low-cost, low-power and flexible biosensors in the field of health care, quality of food, and drug development. The simplicity of biomaterials and cost effectiveness along with the ease of fabrication of OTFTs might make organic (bio)electronics as an alternative to expensive and complex complementary metal oxide semiconductor (CMOS)-based biosensors.

References

1 Liao, C., Zhang, M., Yao, M.Y., Hua, T., Li, L., and Yan, F. (2015) *Adv. Mater.*, **27**, 7679.

2 (a) Someya, T., Sekitani, T., Iba, S., Kato, Y., Kawaguchi, H., and Sakurai, T. (2004) *Proc. Natl. Acad. Sci. U.S.A.*, **101**, 9966; (b) Wu, X., Ma, Y., Zhang, G., Chu, Y., Du, J., Zhang, Y., Li, Z., Duan, Y., Fan, Z., and Huang, J. (2015) *Adv. Funct. Mater.*, **25**, 2138; (c) Schwartz, G., Tee, B.C.K., Mei, J., Appleton, A.L., Kim, D.H., Wang, H., and Bao, Z. (2013) *Nat. Commun.*, **4**, 1859; (d) O'Connor, T.F., Rajan, K.M., Printz, A.D., and Lipomi, D.J. (2015) *J. Mater. Chem. B.*, **3**, 4947

3 (a) Spanu, A., Lai, S., Cosseddu, P., Tedesco, M., Martinoia, S., and Bonfiglio, A. (2015) *Sci. Rep.*, **5**, 8807; (b) Bystrenova, E., Jelitai, M., Tonazzini, I., Lazar, A.N., Huth, M., Stoliar, P., Dionigi, C., Cacace, M.G., Nickel, B., Madarasz, E., and Biscarini, F. (2008) *Adv. Funct. Mater.*, **18**, 1751; (c) Khodagholy, D., Doublet, T., Quilichini, P., Gurfinkel, M., Leleux, P., Ghestem, A., Ismailova, E., Hervé, T., Sanaur, S., Bernard, C., and Malliaras, G.G. (2013) *Nat. Commun.*, **4**, 1575.

4 (a) Liao, C. and Yan, F. (2013) *Polym. Rev.*, **53**, 352; (b) Zhang, C., Chen, P., and Hu, W. (2015) *Chem. Soc. Rev.*, **44** (8), 2087; (c) Torsi, L., Magliulo, M., Manoli, K., and Palazzo, G. (2013) *Chem. Soc. Rev.*, **42**, 8612.

5 Roberts, M.E., Mannsfeld, S.C., Queraltó, N., Reese, C., Locklin, J., Knoll, W., and Bao, Z. (2008) *Proc. Natl. Acad. Sci. U.S.A.*, **105**, 12134.

6 Khan, H.U., Roberts, M.E., Johnson, O., Förch, R., Knoll, W., and Bao, Z. (2010) *Adv. Mater.*, **22**, 4452.

7 (a) Huang, J., Miragliotta, J., Becknell, A., and Katz, H.E. (2007) *J. Am. Chem. Soc.*, **129**, 9366; (b) Torsi, L., Farinola, G.M., Marinelli, F., Tanese, M.C., Omar, O.H., Valli, L., Babudri, F., Palmisano, F., Zambonin, P.G., and Naso, F. (2008) *Nat. Mater.*, **7**, 412.

8 Scarpa, G., Idzko, A.-L., Götz, S., and Thalhammer, S. (2010) *Macromol. Biosci.*, **10**, 378.

9 Irimia-Vladu, M. (2014) *Chem. Soc. Rev.*, **43**, 588.

10 Cramer, T., Chelli, B., Murgia, M., Barbalinardo, M., Bystrenova, E., de Leeuw, D.M., and Biscarini, F. (2013) *Phys. Chem. Chem. Phys.*, **15**, 3897.

11 Khan, H.U., Jang, J., Kim, J.-J., and Knoll, W. (2011) *J. Am. Chem. Soc.*, **133**, 2170.

12 (a) Panzer, M.J. and Frisbie, C.D. (2005) *J. Am. Chem. Soc.*, **127**, 6960; (b) Kergoat, L., Herlogsson, L., Braga, D., Piro, B., Pham, M.C., Crispin, X., Berggren, M., and Horowitz, G. (2010) *Adv. Mater.*, **22**, 2565; (c) De Tullio, D., Magliulo, M., Colafemmina, G., Manoli, K., Torsi, L., and Palazzo, G. (2013) *Sci. Adv. Mater.*, **5**, 1922.

13 Kim, S.H., Hong, K., Xie, W., Lee, K.H., Zhang, S., Lodge, T.P., and Frisbie, C.D. (2013) *Adv. Mater.*, **25**, 1822.

14 Kergoat, L., Piro, B., Berggren, M., Horowitz, G., and Pham, M.-C. (2012) *Anal. Bioanal. Chem.*, **402**, 1813.

15 (a) Laiho, A., Herlogsson, L., Forchheimer, R., Crispin, X., and Berggren, M. (2011) *Proc. Natl. Acad. Sci. U.S.A.*, **108**, 15069; (b) Larsson, O., Laiho, A., Schmickler, W., Berggren, M., and Crispin, X. (2011) *Adv. Mater.*, **23**, 4764; (c) Yuen, J.D., Dhoot, A.S., Namdas, E.B., Coates, N.E., Heeney, M., McCulloch, I., Moses, D., and Heeger, A.J. (2007) *J. Am. Chem. Soc.*, **129**, 14367; (d) Lin, F. and Lonergan, M.C. (2006) *Appl. Phys. Lett.*, **88**, 133507.

16 (a) Lin, P., Yan, F., and Chan, H.L. (2010) *ACS Appl. Mater. Interfaces*, **2**, 1637; (b) Tang, H., Lin, P., Chan, H.L., and Yan, F. (2011) *Biosens. Bioelectron.*, **26**, 4559; (c) Tarabella, G., Santato, C., Yang, S.Y., Iannotta, S., Malliaras, G.G., and Cicoira, F. (2010) *Appl. Phys. Lett.*, **97**, 123304; (d) Yaghmazadeh, O., Cicoira, F., Bernards, D.A., Yang, S.Y., Bonnassieux, Y., and Malliaras, G.G. (2011) *J. Polym. Sci., Part B: Polym. Phys.*, **49**, 34; (e) Macaya, D.J., Nikolou, M., Takamatsu, S., Mabeck, J.T., Owens, R.M., and Malliaras, G.G. (2007) *Sens. Actuators, B*, **123**, 374.

17 Torsi, L., Dodabalapur, A., Sabbatini, L., and Zambonin, P. (2000) *Sens. Actuators, B*, **67**, 312.

18 (a) Chang, J.B., Liu, V., Subramanian, V., Sivula, K., Luscombe, C., Murphy, A., Liu, J., and Fréchet, J.M. (2006) *J. Appl. Phys.*, **100**, 014506; (b) Crone, B., Dodabalapur, A., Gelperin, A., Torsi, L., Katz, H., Lovinger, A., and Bao, Z. (2001) *Appl. Phys. Lett.*, **78**, 2229.

19 Huang, W., Sinha, J., Yeh, M.-L., Hardigree, J.F.M., LeCover, R., Besar, K., Rule, A.M., Breysse, P.N., and Katz, H.E. (2013) *Adv. Funct. Mater.*, **23**, 4094.

20 (a) Manoli, K., Patrikoussakis, M.M., Magliulo, M., Dumitru, L.M., Mulla, M.Y., Sabbatini, L., and Torsi, L. (2014) *Org. Electron.*, **15**, 2372; (b) Yang, R.D., Park, J., Colesniuc, C.N., Schuller, I.K., Trogler, W.C., and Kummel, A.C. (2007) *J. Appl. Phys.*, **102**, 034515; (c) Bao, Z., Feng, Y., Dodabalapur, A., Raju, V., and Lovinger, A.J. (1997) *Chem. Mater.*, **9**, 1299.

21 (a) Laurs, H. and Heiland, G. (1987) *Thin Solid Films*, **149**, 129; (b) Assadi, A., Gustafsson, G., Willander, M., Svensson, C., and Inganäs, O. (1990) *Synth. Met.*, **37**, 123; (c) Ohmori, Y., Takahashi, H., Muro, K., Uchida, M., Kawai, T., and Yoshino, K. (1991) *Jpn. J. Appl. Phys.*, **30**, L1247.

22 Torsi, L. and Dodabalapur, A. (2005) *Anal. Chem.*, **77**, 380.

23 (a) Duarte, D., Sharma, D., Cobb, B., and Dodabalapur, A. (2011) *Appl. Phys. Lett.*, **98**, 133302; (b) Someya, T., Dodabalapur, A., Huang, J., See, K.C., and Katz, H.E. (2010) *Adv. Mater.*, **22**, 3799; (c) Torsi, L., Lovinger, A., Crone, B., Someya, T., Dodabalapur, A., Katz, H., and Gelperin, A. (2002) *J. Phys. Chem. B*, **106**, 12563; (d) Someya, T., Katz, H.E., Gelperin, A., Lovinger, A.J., and Dodabalapur, A. (2002) *Appl. Phys. Lett.*, **81**, 3079.

24 (a) Duarte, D. and Dodabalapur, A. (2012) *J. Appl. Phys.*, **111**, 044509; (b) Wang, L., Fine, D., and Dodabalapur, A. (2004) *Appl. Phys. Lett.*, **85**, 6386; (c) Wang, L., Fine, D., Khondaker, S.I., Jung, T., and Dodabalapur, A. (2006) *Sens. Actuators, B*, **113**, 539.

25 Tanese, M.C., Fine, D., Dodabalapur, A., and Torsi, L. (2005) *Biosens. Bioelectron.*, **21**, 782.

26 Li, B. and Lambeth, D.N. (2008) *Nano Lett.*, **8**, 3563.

27 Magliulo, M., Manoli, K., Macchia, E., Palazzo, G., and Torsi, L. (2014) *Adv. Mater.*, **27** (46), 7528.

28 Kang, B., Lee, W.H., Choi, H.H., Park, Y.D., and Cho, K. (2014) *RSC Adv.*, **4**, 45082.

29 Pacher, P., Lex, A., Proschek, V., Etschmaier, H., Tchernychova, E., Sezen, M., Scherf, U., Grogger, W., Trimmel, G., and Slugovc, C. (2008) *Adv. Mater.*, **20**, 3143.

30 Zan, H.-W., Tsai, W.-W., Lo, Y.-R., Wu, Y.-M., and Yang, Y.-S. (2012) *IEEE Sens. J.*, **12**, 594.

31 Park, Y.D., Kang, B., Lim, H.S., Cho, K., Kang, M.S., and Cho, J.H. (2013) *ACS Appl. Mater. Interfaces*, **5**, 8591.

32 Huang, W., Yu, J., Yu, X., and Shi, W. (2013) *Org. Electron.*, **14**, 3453.

33 Shaymurat, T., Tang, Q., Tong, Y., Dong, L., and Liu, Y. (2013) *Adv. Mater.*, **25**, 2269.

34 (a) Torsi, L., Tanese, M., Cioffi, N., Gallazzi, M., Sabbatini, L., Zambonin, P., Raos, G., Meille, S., and Giangregorio, M. (2003) *J. Phys. Chem. B*, **107**, 7589; (b) Torsi, L., Tanese, M.C., Cioffi, N., Gallazzi, M.C., Sabbatini, L., and Zambonin, P.G. (2004) *Sens. Actuators, B*, **98**, 204.

35 (a) Dudhe, R.S., Tiwari, S., Raval, H.N., Khaderbad, M.A., Singh, R., Sinha, J., Yedukondalu, M., Ravikanth, M., Kumar, A., and Ramgopal Rao, V. (2008) *Appl. Phys. Lett.*, **93**, 263306; (b) Huang, W., Besar, K., LeCover, R., Rule, A.M., Breysse, P.N., and Katz, H.E. (2012) *J. Am. Chem. Soc.*, **134**, 14650.

36 Sokolov, A.N., Roberts, M.E., Johnson, O.B., Cao, Y., and Bao, Z. (2010) *Adv. Mater.*, **22**, 2349.

37 Ji, T., Rai, P., Jung, S., and Varadan, V.K. (2008) *Appl. Phys. Lett.*, **92**, 233304.

38 Ritjareonwattu, S., Yun, Y., Pearson, C., and Petty, M.C. (2010) *Org. Electron.*, **11**, 1792.

39 Caboni, A., Orgiu, E., Scavetta, E., Barbaro, M., and Bonfiglio, A. (2009) *Appl. Phys. Lett.*, **95**, 123304.

40 Spijkman, M.J., Brondijk, J.J., Geuns, T.C., Smits, E.C., Cramer, T., Zerbetto, F., Stoliar, P., Biscarini, F., Blom, P.W., and de Leeuw, D.M. (2010) *Adv. Funct. Mater.*, **20**, 898.

41 Roberts, M.E., Mannsfeld, S.C., Tang, M.L., and Bao, Z. (2008) *Chem. Mater.*, **20**, 7332.

42 Casalini, S., Leonardi, F., Cramer, T., and Biscarini, F. (2013) *Org. Electron.*, **14**, 156.

43 Paul, E.W., Ricco, A.J., and Wrighton, M.S. (1985) *J. Phys. Chem.*, **89**, 1441.

44 Saxena, V., Shirodkar, V., and Prakash, R. (2000) *J. Solid State Electrochem.*, **4**, 234.

45 Mousavi, Z., Ekholm, A., Bobacka, J., and Ivaska, A. (2009) *Electroanalysis*, **21**, 472.

46 (a) Zhang, Q. and Subramanian, V. (2007) *Biosens. Bioelectron.*, **22**, 3182; (b) Yan, F., Mok, S.M., Yu, J., Chan, H.L., and Yang, M. (2009) *Biosens. Bioelectron.*, **24**, 1241.

47 Hammock, M.L., Knopfmacher, O., Ng, T.N., Tok, J.B.H., and Bao, Z. (2014) *Adv. Mater.*, **26**, 6138.

48 Stern, E., Wagner, R., Sigworth, F.J., Breaker, R., Fahmy, T.M., and Reed, M.A. (2007) *Nano Lett.*, **7**, 3405.

49 Angione, M.D., Cotrone, S., Magliulo, M., Mallardi, A., Altamura, D., Giannini, C., Cioffi, N., Sabbatini, L., Fratini, E., and Baglioni, P. (2012) *Proc. Natl. Acad. Sci. U.S.A.*, **109**, 6429.

50 Magliulo, M., Mallardi, A., Gristina, R., Ridi, F., Sabbatini, L., Cioffi, N., Palazzo, G., and Torsi, L. (2013) *Anal. Chem.*, **85**, 3849.

51 Angione, M.D., Magliulo, M., Cotrone, S., Mallardi, A., Altamura, D., Giannini, C., Cioffi, N., Sabbatini, L., Gobeljic, D., and Scamarcio, G. (2013) *Biosens. Bioelectron.*, **40**, 303.

52 Magliulo, M., Altamura, D., Di Franco, C., Santacroce, M.V., Manoli, K., Mallardi, A., Palazzo, G., Scamarcio, G., Giannini, C., and Torsi, L. (2014) *J. Phys. Chem. C*, **118**, 15853.

53 Maddalena, F., Kuiper, M.J., Poolman, B., Brouwer, F., Hummelen, J.C., de Leeuw, D.M., De Boer, B., and Blom, P.W. (2010) *J. Appl. Phys.*, **108**, 124501.

54 Lai, S., Demelas, M., Casula, G., Cosseddu, P., Barbaro, M., and Bonfiglio, A. (2013) *Adv. Mater.*, **25**, 103.

55 Demelas, M., Lai, S., Spanu, A., Martinoia, S., Cosseddu, P., Barbaro, M., and Bonfiglio, A. (2013) *J. Mater. Chem. B*, **1**, 3811.

56 Letaw, H. Jr. and Bardeen, J. (1954) *J. Appl. Phys.*, **25**, 600.

57 Brattain, W. and Garrett, C. (1955) *Bell Syst. Tech. J.*, **34**, 129.

58 Panzer, M.J., Newman, C.R., and Frisbie, C.D. (2005) *Appl. Phys. Lett.*, **86**, 103503.

59 Kergoat, L., Piro, B., Berggren, M., Pham, M.-C., Yassar, A., and Horowitz, G. (2012) *Org. Electron.*, **13**, 1.

60 Cotrone, S., Ambrico, M., Toss, H., Angione, M.D., Magliulo, M., Mallardi, A., Berggren, M., Palazzo, G., Horowitz, G., Ligonzo, T., and Torsi, L. (2012) *Org. Electron.*, **13**, 638.

61 Magliulo, M., Pistillo, B.R., Mulla, M.Y., Cotrone, S., Ditaranto, N., Cioffi, N., Favia, P., and Torsi, L. (2013) *Plasma Processes Polym.*, **10**, 102.

62 Mulla, M., Seshadri, P., Torsi, L., Manoli, K., Mallardi, A., Ditaranto, N., Santacroce, M., Di Franco, C., Scamarcio, G., and Magliulo, M. (2015) *J. Mater. Chem. B*, **3** (25), 5049.

63 Magliulo, M., Mallardi, A., Mulla, M.Y., Cotrone, S., Pistillo, B.R., Favia, P., Vikholm-Lundin, I., Palazzo, G., and Torsi, L. (2013) *Adv. Mater.*, **25**, 2090.

64 Palazzo, G., De Tullio, D., Magliulo, M., Mallardi, A., Intranuovo, F., Mulla, M.Y., Favia, P., Vikholm-Lundin, I., and Torsi, L. (2014) *Adv. Mater.*, **27**, 911

65 Buth, F., Donner, A., Sachsenhauser, M., Stutzmann, M., and Garrido, J.A. (2012) *Adv. Mater.*, **24**, 4511.

66 Buth, F., Kumar, D., Stutzmann, M., and Garrido, J. (2011) *Appl. Phys. Lett.*, **98**, 153302.

67 Mulla, M.Y., Tuccori, E., Magliulo, M., Lattanzi, G., Palazzo, G., Persaud, K., and Torsi, L. (2015) *Nat. Commun.*, **6**, 6010.

68 Dumitru, L., Manoli, K., Magliulo, Ligonzo, T., Palazzo, G., Torsi, L. (2015) *APL Materials*, **3**, 014904.

69 Bartlett, P. (1998) *Analyst*, **123**, 387.

70 Zhu, Z.-T., Mabeck, J.T., Zhu, C., Cady, N.C., Batt, C.A., and Malliaras, G.G. (2004) *Chem. Commun.*, **7**, 1556.

71 Liao, C., Zhang, M., Niu, L., Zheng, Z., and Yan, F. (2013) *J. Mater.Chem. B*, **1**, 3820.

72 Cicoira, F., Sessolo, M., Yaghmazadeh, O., DeFranco, J.A., Yang, S.Y., and Malliaras, G.G. (2010) *Adv. Mater.*, **22**, 1012.

73 Tang, H., Yan, F., Lin, P., Xu, J., and Chan, H.L.W. (2011) *Adv. Funct. Mater.*, **21**, 2264.

74 Liao, C., Mak, C., Zhang, M., Chan, H.L., and Yan, F. (2014) *Adv. Mater.*, **27** (4), 676.

75 Kergoat, L., Piro, B., Simon, D.T., Pham, M.C., Noël, V., and Berggren, M. (2014) *Adv. Mater.*, **26**, 5658.

76 Welch, M.E., Doublet, T., Bernard, C., Malliaras, G.G., and Ober, C.K. (2015) *J. Polym. Sci., Part A: Polym. Chem.*, **53**, 372.

77 Shim, N.Y., Bernards, D.A., Macaya, D.J., DeFranco, J.A., Nikolou, M., Owens, R.M., and Malliaras, G.G. (2009) *Sensors*, **9**, 9896.

78 Khodagholy, D., Curto, V.F., Fraser, K.J., Gurfinkel, M., Byrne, R., Diamond, D., Malliaras, G.G., Benito-Lopez, F., and Owens, R.M. (2012) *J. Mater. Chem.*, **22**, 4440.

79 Lin, P., Luo, X., Hsing, I., and Yan, F. (2011) *Adv. Mater.*, **23**, 4035.

80 Lin, P., Yan, F., Yu, J., Chan, H.L., and Yang, M. (2010) *Adv. Mater.*, **22**, 3655.

81 He, R.-X., Zhang, M., Tan, F., Leung, P.H.M., Zhao, X.-Z., Chan, H.L.W., Yang, M., and Yan, F. (2012) *J. Mater. Chem.*, **22**, 22072.

82 Kim, D.-J., Lee, N.-E., Park, J.-S., Park, I.-J., Kim, J.-G., and Cho, H.J. (2010) *Biosens. Bioelectron.*, **25**, 2477.

83 Leleux, P., Rivnay, J., Lonjaret, T., Badier, J.M., Bénar, C., Hervé, T., Chauvel, P., and Malliaras, G.G. (2015) *Adv. Healthc. Mater.*, **4**, 142.

5

Biocompatible Materials for Transient Electronics

Suk-Won Hwang[1] *and John A. Rogers*[2]

[1] *Korea University, KU-KIST Graduate School of Converging Science and Technology, 145 Anam-Ro, Seongbuk-Gu, Seoul, 02841, Republic of Korea*
[2] *University of Illinois at Urbana-Champaign, Department of Materials Science and Engineering, Frederick Seitz Materials Research Laboratory, 1304 W. Green St., Urbana, IL, 61801, USA*

5.1 Introduction

Transient electronics can be broadly defined as a *new class of technology* whose defining characteristic is the ability to physically disappear, in whole or in part, at some programmed rate or triggered time, via any of a range of different possible mechanisms including hydrolysis, dissolution, corrosion, de-polymerization, or disintegration. The mode and rate of this transience can be pre-defined or initiated by chemical or biological reactions, light, temperature, pressure, or other stimuli [1–7]. Although organic active materials can provide some utility in these types of devices, constituent materials in the highest performance transient electronic systems include ultrathin single crystalline silicon nanomembranes (Si NMs) [1–3, 8–10] or thin films of zinc oxide (ZnO) [11] for the semiconductor; magnesium (Mg), iron (Fe), zinc (Zn), molybdenum (Mo), and tungsten (W) for electrodes and interconnects [4, 12, 13]; magnesium oxide and silicon dioxide/nitride (SiO_2/SiN_x) for gate/interlayer dielectrics and passivation layers [1, 14]; biodegradable polymers (e.g., silk, poly lactic-*co*-glycolic acid (PLGA), polycaprolactone (PCL), poly lactic acid (PLA)) [1, 3], or thin metal foils for substrates/packaging materials [13]. These particular individual elements and their end products also have the advantage that they are biologically nontoxic and environmentally benign at the typically low concentrations/amounts that are associated with miniaturized electronics. Representative examples of recently reported devices include strain/temperature/pH/hydration sensors [1, 3, 10], solar cells [1], mechanical energy harvesters (MEHs) [11], wireless radio frequency (RF) power scavengers [8], multiplexed photodetectors [1], and complementary metal-oxide semiconductor (CMOS) [3, 8], all of which have reliable, high performance operational properties comparable to those of nontransient counterparts. Such diverse systems provide a promising set of building blocks toward potential applications in medically relevant uses, degradable environmental monitors/sensors, disposable consumer gadgets, and hardware-based antitamper systems. The following

Green Materials for Electronics, First Edition.
Edited by Mihai Irimia-Vladu, Eric D. Glowacki, Niyazi S. Sariciftci, and Siegfried Bauer.

sections describe the latest advances in understanding the dissolution behaviors of the key materials, as well as the characteristics of device components and other features of this emerging technology.

5.2 Mechanisms of Dissolution of Monocrystalline Silicon Nanomembranes (Si NMs)

A demonstration platform of a transient integrated circuit includes individual electronic components (an inductor, capacitor, resistor, diode, and transistor) and materials (Mg, MgO/SiO_2, Si and silk), and their dissolution behaviors in water via hydrolysis as illustrated in Figure 5.1 [1]. Si NMs represent critical elements in high-performance transient electronics that simultaneously leverage the deep base on scientific knowledge and engineering capabilities associated with the use of silicon in conventional semiconductor devices. The Si NM geometry is important because it enables planar device architectures, minimizes the amount of material that must be consumed during the transient step, and provides mechanics and processing options that are favorable for integration into substrates such as silk, degradable polymers (PLGA, PLA, PGA, PCL), and others. This format also allows access to high rates of transience while avoiding solubility limits and potentially adverse biological responses, for applications where biocompatibility is important. Si reacts with water via hydrolysis to form silicic acid ($Si(OH)_4$), according to

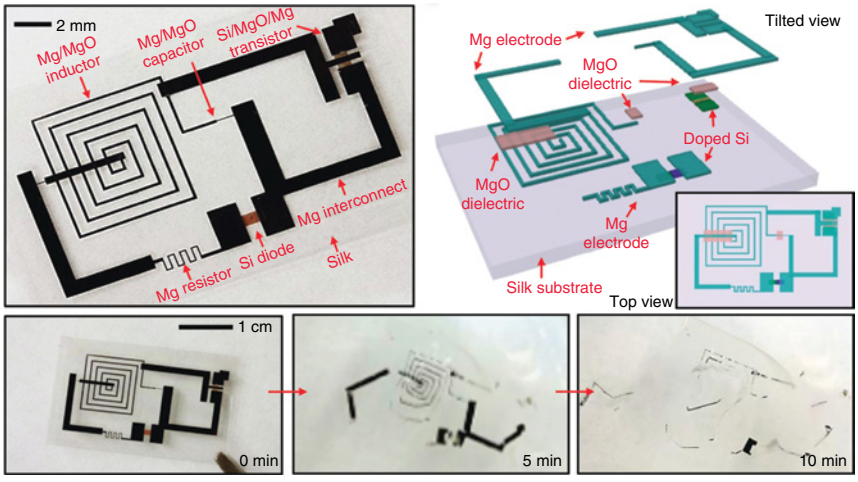

Figure 5.1 Image (top left) and schematic illustration (top right) of a representative transient integrated system, with monocrystalline silicon nanomembranes (Si NMs) for the semiconductor, magnesium (Mg) for the electrodes and interconnects, magnesium oxide (MgO) for the gate/interlayer dielectrics, and silk fibroin for the substrate. A series of images (bottom) reveals several stages of dissolution due to immersion in deionized (DI) water at room temperature. (Hwang *et al*. 2012 [1]. Reproduced with permission of AAAS.)

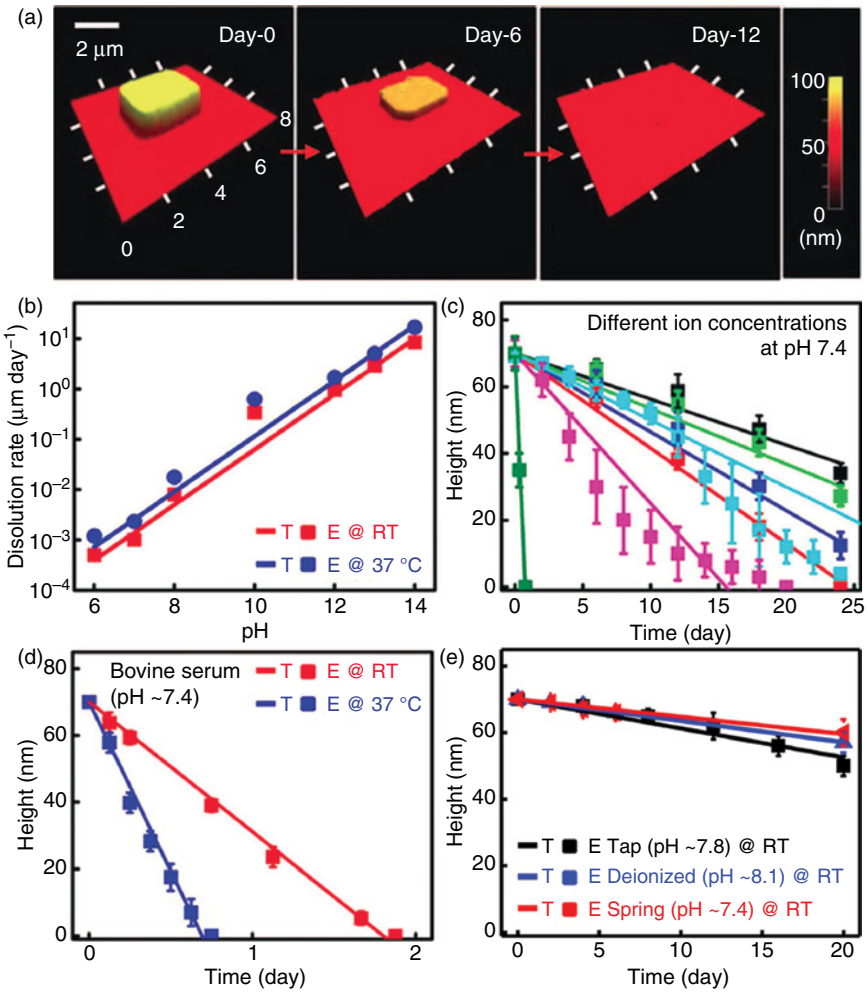

Figure 5.2 (a) A set of atomic force microscope (AFM) images of Si NMs (~70 nm) at various times of immersion in phosphate buffer saline (PBS, pH 7.4, 1 M) solution at physiological temperature (37 °C). Complete dissolution of Si NMs occurs in 2 weeks. (Hwang *et al.* 2012 [1]. Reproduced with permission of AAAS.) (b) Dissolution behaviors of Si NMs in buffer solutions with various pH values at different temperatures (room and body temperatures). (Hwang *et al.* 2014 [9]. Reproduced with permission of John Wiley and Sons.) (c) Dependence of dissolution rates on ionic concentration at a fixed pH. (Hwang *et al.* 2014 [9]. Reproduced with permission of John Wiley and Sons.) (d) Accelerated dissolution behavior in bovine serum (pH 7.4) at RT and 37 °C, respectively. (Hwang *et al.* 2014 [9]. Reproduced with permission of John Wiley and Sons.) (e) The kinetics of dissolution in various aqueous solutions at room temperature. (Hwang *et al.* 2014 [5]. Reproduced with permission of American Chemical Society.)

$$\mathrm{Si} + 4\mathrm{H_2O} \leftrightarrow \mathrm{Si(OH)_4} + 2\mathrm{H_2},$$

where the silicic acid leaves the silicon surface by diffusion, and SiO_2 can be involved as an intermediate [15–17]. The simplest model of the kinetics consid-

ers a constant surface reaction at the water–Si NM interface. The experimental results in Figure 5.2a show a set of images of Si NMs (3 μm × 3 μm × 70 nm) collected by atomic force microscopy (AFM) after different times of immersion in phosphate buffer saline (PBS, pH 7.4, 1 M) solution at a physiological temperature (37 °C). The change in thickness can be written as

$$h = h_0 - k \times t,$$

where h_0 is the initial thickness, k is the reaction constant, and t is the time [15]. The dissolution rate typically depends on the pH, whereby the rate increases as the pH increases, as in Figure 5.2b. This surface reaction can also be affected by various other factors such as temperature and ionic content/concentration in aqueous solutions and the physical/chemical properties of the Si NMs defined by the growth/deposition methods and conditions [5, 9, 13]. Studies of dissolution of silicon nanowires (Si NWs) report similar conclusions [18].

Figure 5.2c–e reveals that the kinetics of Si dissolution can vary widely, even at fixed pH, owing to the dependence on chemical composition and ion concentration of the surrounding solutions [5–9]. Another controlling factor is the Si dopant type and concentration, which are two parameters of importance in CMOS systems, solar cells, photodetectors, and others. The dissolution rates of phosphorus- or boron-doped Si NMs exhibit a significant change, in particular, at high dopant concentrations [5, 19]. Theoretical and experimental results indicate that the dissolution rate of Si NMs rapidly decreases when the concentration of either type of dopant exceeds a certain level (i.e., $10^{20}\,\mathrm{cm}^{-3}$), as reported in previous studies in other contexts [5, 19]. This feature can be observed through measured/calculated changes in electrical behaviors of the doped Si NMs. The dissolution rate of doped Si NMs remains constant (R_i) over a certain concentration, but rapidly decreases above a critical concentration (C_0). The dissolution rate can be written as

$$R = \frac{R_i}{1 + \left(C / C_0\right)^4},$$

where C is the dopant concentration.

This expression captures experimentally observed results when $C_0 = 10^{20}\,\mathrm{cm}^{-3}$ for phosphate, and $R_i = 3.08\,\mathrm{nm\,day}^{-1}$ [5, 19]. Increased/decreased doping levels offer the ability to tune the dissolution rate of silicon for use, for example, as an electrode interface material for potential applications in long- and short-term monitoring/stimulation in medical implants.

5.3 Dissolution Mechanisms of Transient Conductors and Insulators

Although the dissolution of monocrystalline silicon can be described, almost exclusively, by surface reactions, diffusion can be important for dissolution of metals for conductors, and of insulators for gate and interlayer dielectrics. In

such cases, the kinetics can be described analytically using models of reactive diffusion in which the rate-limiting step is defined by diffusion of water and hydroxide ions into the material and reaction at the same time throughout the layers. The partial differential equation for reactive diffusion is given by

$$D\frac{\partial^2 w}{\partial y^2} - kw = \frac{\partial w}{\partial t},$$

where w is the concentration of water, and D and k are the diffusivity for water and the reaction constant between porous materials and solutions, respectively [1, 17, 20].

Systematic, fundamental studies of dissolution kinetics on various metals in biological environments provide important guidelines in selecting materials for advanced transient systems. Dissolvable metals that are bioresorbable and also compatible with silicon are of primary interest: magnesium (Mg), magnesium alloy (AZ31B, 3 wt% aluminum and 1 wt% zinc), tungsten (W), zinc (Zn), and iron (Fe). Thin films of these metals deposited via either electron-beam evaporation (Mg, Fe) and/or magnetron sputtering techniques (Mg, Mg alloys, Fe, Zn, and W) allow for systematic studies of dissolution. Thin films of W deposited by chemical vapor deposition (CVD) are relevant to foundry-compatible CMOS. Dissolution experiments for metal films were performed in deionized (DI) water and simulated biofluid Hank's solution, both at room and body temperatures [1, 4]. In general, W and Fe exhibit much slower degradation rates (~few days) compared to Mg, Mg alloy, and Zn (<few hours) owing to the nonprotective nature of their hydrolysis products, namely, magnesium oxide and zinc oxide, respectively [21, 22]. The rate of change in resistance of traces of Fe becomes very slow after a certain time due to the formation of a protective iron oxide layer [23]. Compared to sputtered W films, CVD deposited W exhibits much lower resistivity and dissolution rate in DI water, suggesting its use for applications that demand slow rates of transience. A reactive diffusion model applied to the measured dissolution rate captures the experimental trends, with predictive value in determining the transience times as a function of film thickness, pH, and others [4]. The combined use of dissolvable metals with encapsulation layers allows extension of the degradation time into nearly any desired range, from minutes to months. As a foundry-compatible metal, W could be a potential candidate for contacts and interconnects of transient systems that utilize existing manufacturing processes.

The same elements, but in the form of thin foils, can serve as supporting and encapsulation layers. Related dissolution studies of metal foils conducted in buffer and Hanks' solution at 37 °C indicate some differences in dissolution rates compared to thin films. Here, the morphology and grain structure of the metal foils can influence the overall kinetics [13].

As for the gate and interlayer dielectrics, and the encapsulants, magnesium oxide (MgO), and silicon dioxide (SiO_2) or nitride (SiN_x) are attractive choices. The chemistry of dissolution of MgO and SiO_2 are related to that of magnesium and monocrystalline silicon; that is, magnesium oxide and silicon oxide react with water via

hydrolysis to form magnesium ($Mg(OH)_2$) and silicon hydroxide ($Si(OH)_4$) [1]. Evaporated films of MgO (150 nm) completely dissolve within a few hours in deionized (DI) water at room temperature, comparable to evaporated Mg films with similar thicknesses [1]. As for silicon oxide, the morphology and chemistry depend strongly on the conditions and methods for growth/deposition [1, 14]. Three different oxides show three dramatically different dissolution rates: (i) thermal oxidation (tg-oxide), (ii) plasma-enhanced chemical vapor deposition (PECVD oxide), and (iii) electron-beam evaporation (E-beam oxide). Experiments with thin film samples immersed in aqueous buffer solutions with various pH values (7–12) at room and body temperatures (37 °C), periodically inspected by spectroscopic ellipsometry and AFM, reveal the time-dependent change in thickness and surface topography. The results indicate that tg-oxides and E-beam oxides dissolve most slowly and most rapidly, respectively, under identical conditions. Differences in methods for growing tg-oxides, that is, wet and dry oxidation, do not strongly affect the corresponding dissolution rates [14]. In addition to typical factors affecting the rate, for example, temperature, pH, and ionic contents/concentration of solution, the film density and chemical composition can strongly influence the reactions. Experimental results show that thermal oxides and E-beam oxides have the highest and lowest density, respectively, thereby providing some insight into the differences. The stoichiometry of tg-oxides and PECVD oxides are close to SiO_2 (Si:O = 1 : 2), while oxygen stoichiometry of E-beam oxide is slightly higher (Si:O = 1 : 2.2). Reactive diffusion models can capture certain effects in porous materials, with the ability to account for some of the trends observed in these oxides [1, 14, 20].

The hydrolysis of silicon nitride (SiN_x) occurs in two steps: (i) oxidation into silicon oxide ($Si_3N_4 + 6H_2O \rightarrow 3SiO_2 + 4NH_3$); (ii) hydrolysis of silicon oxide ($SiO_2 + 2H_2O \rightarrow Si(OH)_4$). The overall reaction can be defined as $Si_3N_4 + 12H_2O \rightarrow 3Si(OH)_4 + 4NH_3$. Different deposition methods yield different types of nitrides, referred to as low-pressure chemical vapor deposition (LPCVD) nitride, PECVD-LF nitride (low frequency, LF) and PECVD-HF nitride (high frequency, HF). Thin films allow dissolution experiments in buffer solutions and others (bovine serum and sea water) at room and physiological temperatures (37 °C). The rate of dissolution of LPCVD nitride is lower than that of the other nitrides, possibly because of proper stoichiometry and high density. The dissolution rate of PECVD-HF nitride is much higher than that of PECVD-LF, possibly because of unfavorable stoichiometry and low density. The dependence of dissolution behaviors of these nitrides on temperature, pH, and film properties exhibits similar trends to those observed in silicon oxides. The density effect on the dissolution kinetics can also be explained, at least partly, by modified theoretical models for reactive diffusion described in the section of '2. Dissolution Studies of Different Types of Oxides' [14].

5.4 Tunable/Programmable Transience

The properties of the encapsulation layers and/or the substrates for transient electronics provide a means to tune/program the lifespan of a device, with good engineering control. Material options for the encapsulation range from inorganic materials such as MgO, SiO_2, and SiN_x to degradable polymers, such as PLGA,

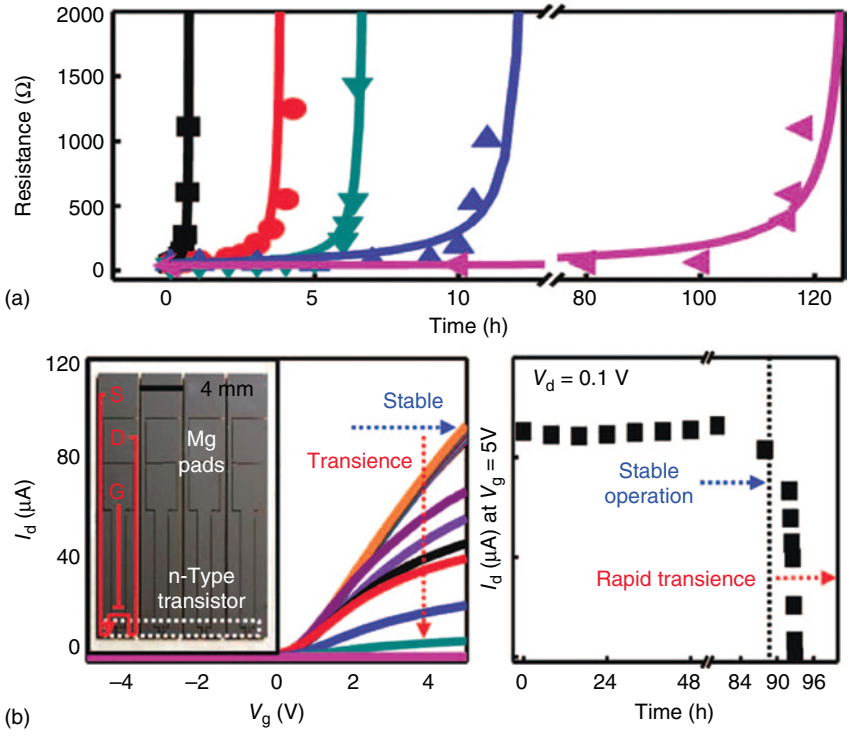

Figure 5.3 (a) Measured change in electrical resistance of serpentine Mg traces when immersed in DI water at room temperature, with combined use of encapsulation layers of MgO and crystallized silk fibroin. (Hwang *et al*. 2012 [1]. Reproduced with permission of AAAS.). (b) Practical application of the encapsulation strategy to a transient n-channel metal-oxide-semiconductor field-effect transistor (MOSFET). The drain current of the transistor shows stable operation for ~90 h, followed by rapid degradation in a relatively short timescale. This transience corresponds to two-step kinetics: (i) the thicknesses and type of encapsulation layers determine a time period for stable operation; (ii) the Mg electrodes define the second timescale.

PCL, silk films, and others, or a combined use of multiple layers of these materials. Figure 5.3a shows measured changes in electrical resistance of a meander trace of Mg, encapsulated with layers of MgO with different thicknesses, and combinations of MgO with crystallized silk films, each due to immersion in DI water at room temperature. Here, as-deposited Mg traces without any encapsulation lose their electrical continuity within an hour. A single layer of MgO with different thicknesses allows adjustment of the lifetime of the device up to 12 h, while a combination of MgO and silk extends the life to over 4 days [1]. Figure 5.3b provides an example of an encapsulation strategy at the device level using metal-oxide-semiconductor field-effect transistors (MOSFETs) with Si NMs for the semiconductor, Mg for the conductor, and MgO/SiO_2 for the gate dielectric. When partially submerged in DI water, the device exhibits stable operation for up to 90 h, that is, no degradation in measured transfer curves and drain currents. Rapid transience occurs in a short time interval that follows this period of

stable operation. Device characteristics, therefore, exhibit two-step kinetics in function: (i) The encapsulation layers determine the first timescale (stable operation); (ii) the Mg electrodes define the second (rapid transience) owing to a relatively higher rate for dissolution compared to other device materials [1]. Tuning and programming of transience behavior using this type of strategy and more complex variants of it provide important capabilities. Since the solubility of silk fibroin films in water depends on the degree of crystallinity, adjusting this parameter allows the period of device operation to be selected across a wide range, from seconds to years [24, 25].

Other encapsulating materials can be considered. A combination of multiple layers of SiO_2 and Si_3N_4 can enhance the barrier properties relative to either material individually, because of the capability of multiple layers of different materials to reduce the probability of penetrating defects. An optimized structure for long lifetime consists of triple layers of SiO_2 and Si_3N_4 in thicknesses of less than 1 μm, enabling device operation up to 10 days of continuous immersion [14].

Alternative choices rely on spin-on glass (SOG) materials with formulations similar to those widely used in the semiconductor industry for interlayer dielectric planarization application. Different SOG chemistries and processing approaches can offer a broad range of timeframes for device encapsulation [13].

5.5 Transient Electronic Systems

Materials, design layouts, manufacturing approaches, and theoretical models can be combined to yield almost any type of active or passive electrical components for transient electronic systems. Some of the most attractive options exploit bioresorbable, biocompatible inorganic electronic materials, including Si NMs and ZnO for semiconducting materials, and Mg, Fe, Zn, Mo, and W for electrodes and interconnects, and silicon dioxide (SiO_2) and magnesium oxide (MgO) as gate/interlayer dielectrics and passivation layers. Substrates and encapsulation materials include films of silk fibroin and biodegradable polymers (PLGA, PGA, PLA, and PCL). In addition to electronics, Figure 5.4a shows a schematic illustration (left) and a photograph (right) of a type of biodegradable battery, for potential use in biomedical implants for diagnosis and therapy. The battery system incorporates Mg foils as anodes, and Fe, Mo, or W foils for cathodes, with buffer solutions for the electrolyte [26]. The entire device is packaged by a degradable polyanhydride. The system dissolves in biofluids (or PBS solution), as demonstrated at an accelerated condition of 85 °C after 3 weeks. The dissolution processes include fracture and disintegration of the constituent elements into tiny pieces, each of which disappears via hydrolysis (Figure 5.4b). The details on this phase of dissolution are apparent in ZnO thin film transistors through the series of microscopic images shown in Figure 5.4c [11]. All materials of the ZnO transistor completely dissolve in DI water in 15 h; the dissolution kinetics of individual elements involve hydrolysis to produce, in case of ZnO, zinc hydroxide ($Zn(OH)_2$), according to $ZnO + H_2O \leftrightarrow Zn(OH)_2$, and other elements also dissolve in a manner similar to that described previously.

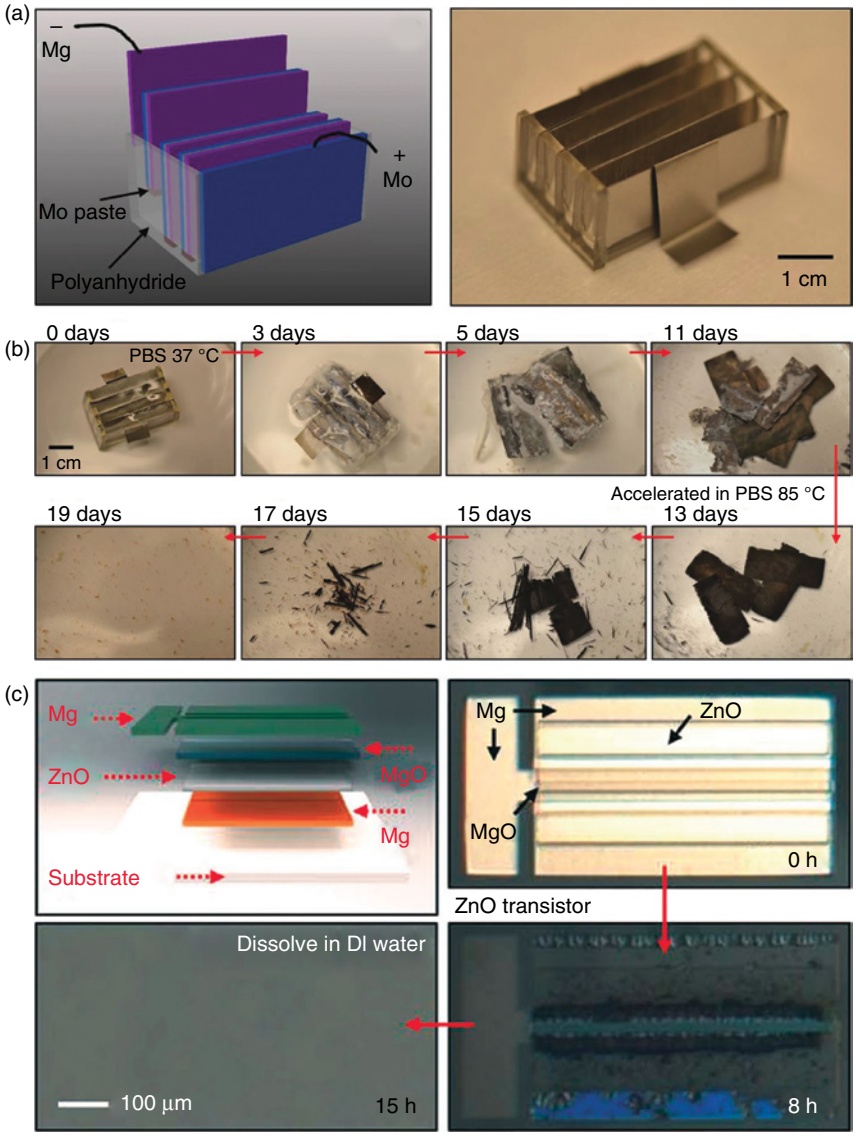

Figure 5.4 (a) Schematic illustration (left) and photograph (right) of a transient Mg–Mo battery system, and (b) images of its dissolution at various stages in accelerated condition (PBS, 85 °C). Constituent materials involve metal foils Mg and Mo for anode and cathode, polyanhydride as spacer and encasement, and PBS solution as the electrolyte. (Yin *et al*. 2014 [26]. Reproduced with permission of John Wiley and Sons.) (c) Schematic drawing and microscopic dissolution images of biodegradable ZnO-based transistors built with Mg contacts and MgO dielectrics. The device completely dissolves in DI water at RT within 15 h. (Dagdeviren *et al*. 2013 [11]. Reproduced with permission of John Wiley and Sons.)

Figure 5.5 shows various classes of transient electrical components and systems, each of which offers reliable, high-performance operation, at levels comparable to those of nontransient systems. In addition to batteries, power

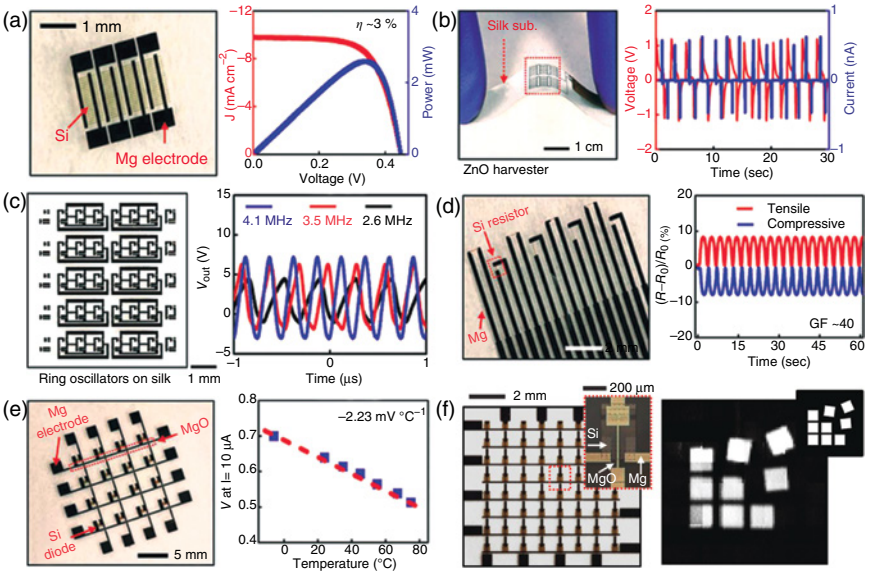

Figure 5.5 Diverse classes of transient electronic devices and systems. (a) Image and electrical characteristics of silicon solar cells, with power conversion efficiencies and fill factors of 3% and 66%, respectively. (Hwang *et al*. 2012 [1]. Reproduced with permission of AAAS.) (b) Photograph and output potential as a function of time in a ZnO mechanical energy harvesters (MEHs) during bending. (Dagdeviren *et al*. 2013 [11]. Reproduced with permission of John Wiley and Sons.) (c) Optical image and output voltage characteristics of a three-stage silicon CMOS ring oscillator that includes n- and p-channel MOSFETs. The operating frequency is up to ~4 MHz. (Hwang *et al*. 2013 [8]. Reproduced with permission of John Wiley and Sons.) (d) Image and fractional changes of resistance in a silicon strain gauge during cyclic loading. (Hwang *et al*. 2012 [1]. Reproduced with permission of AAAS.) (e) An array of silicon-based temperature sensors, and a representative device that shows a sensitivity of $-2.23\,\text{mV}\,^{\circ}\text{C}^{-1}$ at a given current value. (Hwang *et al*. 2012 [1]. Reproduced with permission of AAAS.) (f) Passive addressable array of silicon photodiodes with blocking diodes for a digital imaging system. A microscope image shows the detailed information associated with a unit cell (left inset). Captured pictures of a scanned image and logo design (inset) are shown in the right frame. (Hwang *et al*. 2012 [1]. Reproduced with permission of AAAS.)

supplies can include silicon solar cells as shown in Figure 5.5a. The device here consists of highly doped Si p–n diodes using Mg electrodes for metal contacts, to allow efficiencies for solar power conversion of ~3%, limited largely by incomplete absorption due to the thin geometry [1]. An array of MEHs based on ZnO can be constructed in a flexible format (Figure 5.5b, left), with capacitor-type geometries. During bending, the application and release of the stress generates spikes in output voltage and current in a periodic manner, matched to the mechanical stimulus (Figure 5.5b, right) [11]. In addition to wired power sources, approaches for wireless power transmission are of interest, particularly for potential applications in medical implants. One option is to use passive RF components such as inductors and capacitors for mutual inductive coupling in the near-field to a separate transmitter (external primary coil). Such systems can be constructed in a simple metal–insulator–metal (MIM) structure in which Mg forms the electrodes

(conducting traces) and SiO_2/MgO serves as the interlayer dielectrics. Inductors and capacitors exploit spiral coils and parallel plates, respectively. The operating frequencies of these RF components can be tuned by their geometries, lateral dimensions, and others parameters, with values that can extend up to 10 GHz. The experimental results in all cases are in good agreement with circuit simulations [1, 8].

A system-level, wireless RF power scavenger can deliver sufficient power for remote control of circuits that offer practical levels of functionality [8]. This type of wireless energy harvester contains a variety of components such as eight diodes, an antenna, an inductor, six capacitors, a resistor, and a silk-supporting layer. Transient PIN diodes consist of Si NMs defined as highly doped p- and n-channel regions with narrow intrinsic regions, and Mg contacts for electrodes. These PIN diodes can rectify alternating currents (AC) to direct currents (DC). Transient antennas can be manufactured by using evaporated thin films of Mg or using foils, designed to operate at 950 MHz and 2.4 GHz. Passive components, for example, inductors, capacitors, and resistors, also play key roles in impedance matching, energy storage, and current-limiters. A transient wireless RF scavenging system connected to an Mg antenna designed for operation at a frequency of 950 MHz can receive power from an RF transmitter to operate a commercial light-emitting diode (LED) at a distance of 2 m [8]. This scavenging circuit demonstrates functionality in wireless power delivery with possible utility in communication systems when integrated with silicon-based CMOS ring oscillators (Figure 5.5c) [8].

Diverse sensors, actuators, and systems can be achieved in transient formats. The left frame of Figure 5.5d presents an image of strain gauges formed using boron-doped Si NMs with Mg contacts/interconnects, where the gauge factors can reach ~40 [1]. This value compares favorably to those of state-of-the-art devices made of nontransient materials [27]. Figure 5.5d (right) shows fractional changes in resistance as a function of time during cyclic loading. Use of Si diodes and Mg resistive traces enables arrays of temperature monitors, with sensitivity of $-2.23\,mV\,°C^{-1}$ at a current of 10 μA (Si diodes) and $0.23\%\,°C^{-1}$ (Mg resistors) (Figure 5.5e) [1]. More elaborate systems that consist of silicon photodiodes with blocking diodes for readout can yield digital imagers, with the ability to capture images. A representative device consists of 64 pixels (6 × 6 array), with yields better than 90% (Figure 5.5f) [1]. Beyond these examples of silicon-based semiconductor devices and passive sensors, many other devices can be realized using these same ideas and sets of materials.

5.6 Functional Transformation via Transience

Electronic circuits that are capable of dissolving in solutions offer an opportunity for controlled, functional transformation via staged dissolution of different elements, not only to yield individual subsystems, but also to form equivalent systems with different operational behaviors. The approach utilizes variations in thicknesses and types of transient materials across the

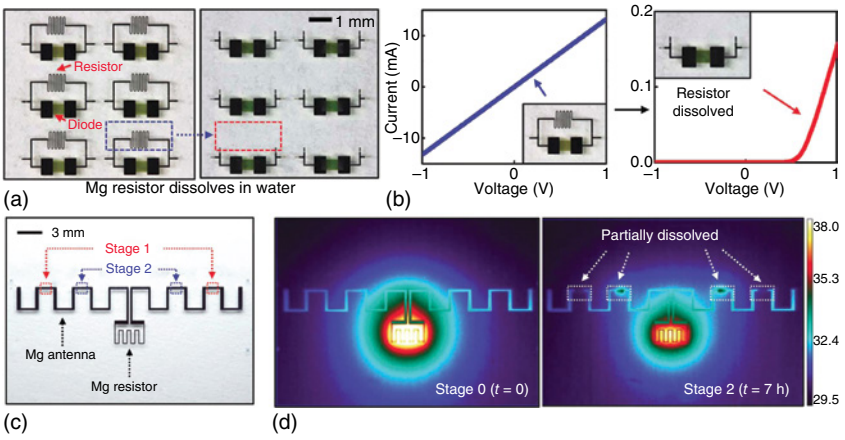

Figure 5.6 (a) A pair of optical images of transient systems consisting of Mg resistors and Si diodes, before (left) and after (right) functional transformation. (b) Most current in the circuit initially flows through a Mg resistor due to its low resistance (left), but current path changes to the silicon diode after dissolution of an Mg resistor (right). (c) Image of a passive Mg antenna component integrated with an Mg-resistive microheater for a wireless system. (d) Infrared (IR) images showing temperature changes in the microheater due to dissolution of local regions of an Mg antenna, leading to alteration of the resonance frequency. (Hwang *et al.* 2015 [12]. Reproduced with permission of John Wiley and Sons.)

system, to define a sequential dissolution process for the desired transformation. Figure 5.6a,b shows images of a combined system of simple Mg resistors with Si NM diodes and the corresponding functional behaviors of the circuit under dissolution. Here, most of the electrical current flows through resistive Mg traces at the initial state due to a resistance that is lower than that of the Si diodes. This electrical pathway is transferred into the Si p–n diodes after dissolution of the serpentine Mg resistors [12]. The duration of functional operation can be controlled by choice of thicknesses of active materials and/or their encapsulating layers. Various examples of transformation, for example, NOR to NAND gates and logic gates (NOR/NAND/inverter) to transistors, suggest applications in versatile configurations of electronic systems [12]. Similar strategies can be applied to wireless power and communication systems. Figure 5.6c presents an image of a transient Mg RF antenna integrated with an Mg heater. The system is designed such that the resonant frequency shifts by changes in geometry or direction of current flow via selective dissolution of certain regions. In this system, disconnections of a predefined area encapsulated with relatively thin layers of MgO lead to transformation in resonant frequency while other regions remain well protected with bilayers of MgO and SiO_2. Figure 5.6d illustrates multistaged transformation procedures that occur via changes in temperature, from "stage 0" (left) to "stage 2" (right), when certain regions of antenna are removed, as indicated by arrows. Similar behavior can be found in a configuration of inductive coils, whose current paths generated by an external coil are altered by removal of the local interconnects, leading to a decrease in its resonance frequency [12].

5.7 Biocompatiblity and Bioresorption

Biocompatibility and biodegradation mechanisms for transient electronic materials are critically important for envisioned applications in implantable biomedical systems. Figure 5.7a illustrates experimental arrangements for *in vitro* assessment of dissolution behaviors and toxicity of Si NMs [5]. A PDMS incubation chamber enables culturing a breast cancer cell line (MDA-MB-231) on an array of patterned Si NM dots. This type of breast cancer cell is useful in this context because of its rapid propagation and culture. Measured changes in height as a function of time in Figure 5.7b reveal the dissolution rate for the patterned Si NMs in this cell environment after removal of cells using trypsin. Complete dissolution occurs in 4 days. A set of fluorescent images of stained

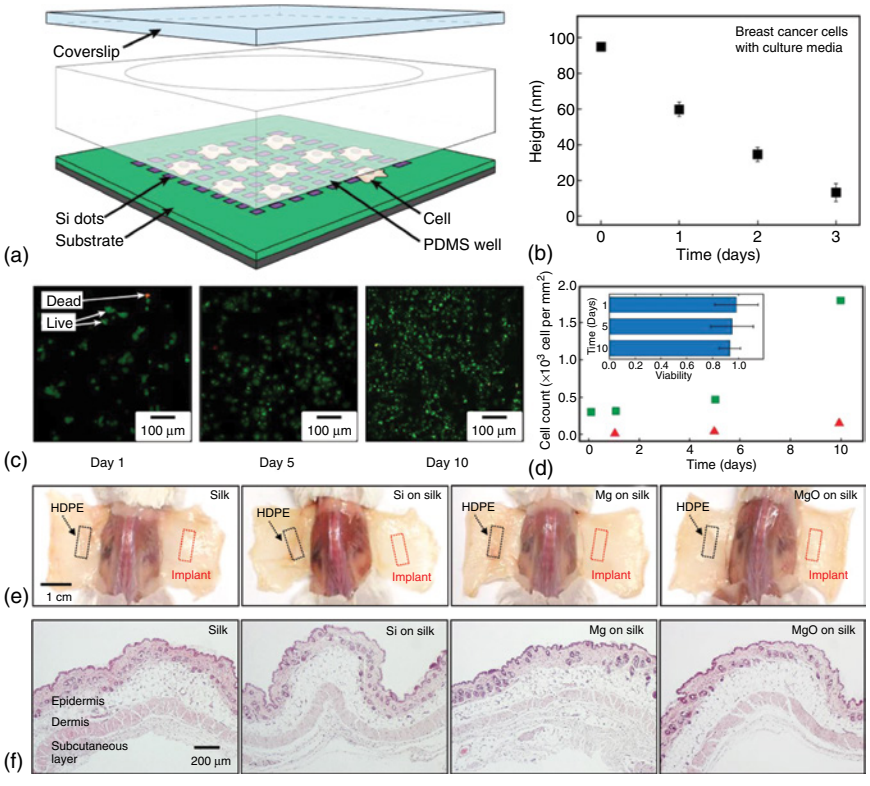

Figure 5.7 (a) Schematic illustration of an experimental structure for *in vitro* evaluation of culturing metastatic breast cancer cells on silicon NMs. (b) Measurements of changes in thickness of the Si NMs during culturing of metastatic breast cancer cells. (c) A series of fluorescent images provide information on cell viability using live/dead assay on patterned Si dots after 1, 5, and 10 days, respectively (green: live cells; red: dead cells). (d) Numbers of living and dead cells during 10 days, as counted from (c). (e) *In vivo* inspection of transient materials (left, silk; middle left, Si on silk; middle right, Mg on silk; right, MgO on silk) and control samples (HDPE) 5 weeks after implantation. (f) Histological evaluations of each material in (e) showing absence of inflammation responses. (Hwang *et al*. 2014 [5]. Reproduced with permission of American Chemical Society.)

cells in Figure 5.7c indicates viability over the course of 10 days using live/dead assays (green: living cells, red: dead cells). Corresponding statistical data in Figure 5.7d show no sign of abnormal increase in the counted live/dead cells during growth/proliferation for 10 days, although natural cell death gives rise to slight increase in the number of dead cells. The inset shows the fraction of living cells for each measurement [5].

For *in vivo* biodegradation and cytotoxicity of transient electronic components, various samples were implanted, along with controls (high-density polyethylene (HDPE), FDA approved), into mouse models. Test samples (Si NM, Mg, and MgO on silk substrates) were sterilized by ethylene oxide, and implanted at subcutaneous regions of Balb/c mice in accordance with Institutional Animal Care and Use Committee (IACUC) protocols. Figure 5.7e presents dorsal views of mice implanted with control and test samples after 5 weeks. The implanted samples were integrated into surrounding tissues with no residual signs of individual materials. The extracted tissues near the implant sites were stained with hematoxylin and eosin (H&E) to determine the inflammatory response. Histological examination of the tissues shown in Figure 5.7f reveals the absence of any inflammation, indicating that the transient materials induce no significant adverse effects [5].

5.8 Practical Applications in Medical Implants

Bioresorbable silicon electronic systems offer compelling opportunities in the development of advanced interventional and monitoring devices for assessing damage and treating injuries. Inductive Mg coils integrated with doped Si Joule heating elements (microheaters) built on silk substrates with silk packages provide transient thermal therapy systems for infection mitigation and disease treatment, where local heating can provide bacterial suppression as well as pain relief [1]. Figure 5.8a shows images of a transient wireless microheater implanted in the subdermal region of a Sprague–Dawley rat. Wireless operation at the resonant frequency with power transmission from a separate primary coil enables control of the system, in which wireless inductive coupling generates a temperature increase at the implant region (Figure 5.8b). The system consists of fully biodegradable and biocompatible materials that completely resorb into the body with duration of operation up to 15 days [1]. This timescale is dependent on the silk package, where the solubility characteristics can be tuned via the degree of crystallinity in the silk fibroin films [24, 25].

Similar technology, but with incorporation of drugs or enzymes in the silk, can yield a simple wireless drug delivery system to provide programmable control in drug release. A schematic exploded view drawing of the system and its detailed layouts appear in Figure 5.8c. Additional layers of silk loaded with drug were prepared by casting a mixture of an antibiotic and a silk solution. Sample treatment with water vapor affects an annealing of the silk matrix to provide appropriate water resistance. Figure 5.8d presents cumulative release rates for ampicillin during activation by resorbable electronic components. The rate can be adjusted by silk-related factors such as extraction time of the silk solution and

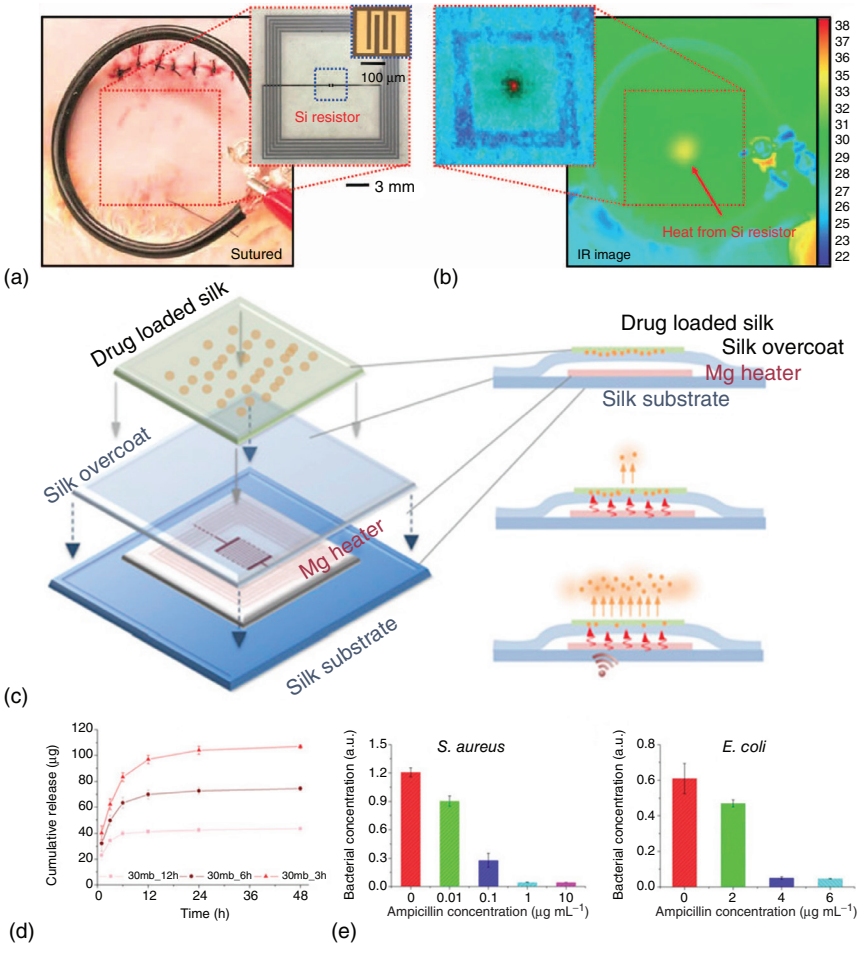

Figure 5.8 (a) Picture of a primary coil on a sutured implanted region, for transient wireless thermal therapy, with the implanted transient device shown in the inset. (Hwang *et al*. 2012 [1]. Reproduced with permission of AAAS.) (b) Thermal image from an IR camera showing localized heating (ΔT) from a transient device implanted under the subdermal region. Inset shows a magnified view of the device. (Hwang *et al*. 2012 [1]. Reproduced with permission of AAAS.) (c) Exploded view drawings of a bioresorbable wireless heater integrated with an antibiotics-doped silk film, for remotely activated drug release. (Tao *et al*. 2014 [28]. Reproduced with permission of National Academy of Sciences, U.S.A.) (d) Measurements of drug release with silk films adjusted from various conditions. (Tao *et al*. 2014 [28]. Reproduced with permission of National Academy of Sciences, U.S.A.) (e) Evaluations of a drug release system using ampicillin with different concentrations for suppressing bacterial growth (left, *Staphylococcus aureus*; right, *Escherichia coli*). (Tao *et al*. 2014 [28]. Reproduced with permission of National Academy of Sciences, U.S.A.)

water anneal time for molecular weight and crystallinity, respectively [29]. Another strategy is to regulate temperature from the microheater to alter the diffusivity of the ampicillin as well as the crystallinity of the silk [28]. Associated test results on drug delivery system show the capability of suppressing bacteria using various amounts of ampicillin (Figure 5.8e) [28].

5.9 Conclusions

As described in this chapter, silicon NMs combined with other water-soluble semiconductors, conductors, insulators, and substrates can enable diverse types of electronic systems whose key defining characteristic is an ability to dissolve via hydrolysis in natural water, biofluids, and other solutions at well-defined, controlled rates after a designated period of high-performance operation. Systematic studies of the dissolution kinetics of the constituent materials in a comprehensive range of fluids establish a baseline of understanding and, in some cases, validate models of the reactivity, which can then be used as tools to guide system design. A complete collection of transient electronic building blocks and their integration into circuits with supporting technologies provide routes to sophisticated capabilities in higher levels of transient wireless systems for envisioned applications. Because this technology can exploit silicon, it can leverage many modern, established aspects of device and circuit design using modest modifications of existing foundry fabrication processes and materials. *In vitro* and *in vivo* investigations exploit the biocompatibility of key materials for inorganic transient electronics and their efficient means for monitoring patient conditions and delivering therapy in biomedicine.

Further research efforts will focus on discovery and expansion of materials options, and development of generalized, cost-effective manufacturing approaches. A particular opportunity is in the design and optimization of advanced transient systems for implantable, multifunctional silicon interfaces to the brain, enabling high fidelity, continuous monitoring of (ECoG), intracranical pressure (ICP) and intracranical temperature (ICT), and electrical stimulation.

References

1 Hwang, S.-W., Tao, H., Kim, D.-H., Cheng, H., Song, J.-K., Rill, E., Brenckle, M.A., Panilaitis, B., Won, S.M., Kim, Y.-S., Song, Y.M., Yu, K.J., Ameen, A., Li, R., Su, Y., Yang, M., Kaplan, D.L., Zakin, M.R., Slepian, M.J., Huang, Y., Omenetto, F.G., and Rogers, J.A. (2012) *Science*, **337**, 1640.

2 Hwang, S.-W., Kim, D.-H., Tao, H., Kim, T.-I., Kim, S., Yu, K.J., Panilaitis, B., Jeong, J.-W., Song, J.-K., Omenetto, F.G., and Rogers, J.A. (2013) *Adv. Funct. Mater.*, **23**, 4087.

3 Hwang, S.-W., Song, J.-K., Huang, X., Cheng, H., Kang, S.-K., Kim, B.H., Kim, J.-H., Yu, S., Huang, Y., and Rogers, J.A. (2014) *Adv. Mater.*, **26**, 3905.

4 Yin, L., Cheng, H., Mao, S., Haasch, R., Liu, Y., Xie, X., Hwang, S.-W., Jain, H., Kang, S.-K., Su, Y., Li, R., Huang, Y., and Rogers, J.A. (2014) *Adv. Funct. Mater.*, **24**, 645.

5 Hwang, S.-W., Park, G., Edwards, C., Corbin, E.A., Kang, S.-K., Cheng, H., Song, J.-K., Kim, J.-H., Yu, S., Ng, J., Lee, J.E., Kim, J., Yee, C., Bhaduri, B., Su, Y., Omennetto, F.G., Huang, Y., Bashir, R., Goddard, L., Popescu, G., Lee, K.-M., and Rogers, J.A. (2014) *ACS Nano*, **8**, 5843.

6 Hernandez, H.L., Kang, S.-K., Lee, O.P., Hwang, S.-W., Kaitz, J.A., Inci, B., Park, C.W., Chung, S., Sottos, N.R., Moore, J.S., Rogers, J.A., and White, S.R. (2014) *Adv. Mater.*, **26**, 7637.

7 Yin, L., Farimani, A.B., Min, K., Vishal, N., Lam, J., Lee, Y.K., Aluru, N.R., and Rogers, J.A. (2015) *Adv. Mater.*, **27**, 1857.

8 Hwang, S.-W., Huang, X., Seo, J.-H., Song, J.-K., Kim, S., Hage-Ali, S., Chung, H.-J., Tao, H., Omenetto, F.G., Ma, Z., and Rogers, J.A. (2013) *Adv. Mater.*, **25**, 3526.

9 Hwang, S.-W., Park, G., Cheng, H., Song, J.-K., Kang, S.-K., Yin, L., Kim, J.-H., Omennetto, F.G., Huang, Y., Lee, K.-M., and Rogers, J.A. (2014) *Adv. Mater.*, **26**, 1992.

10 Hwang, S.-W., Lee, C.H., Cheng, H., Jeong, J.-W., Kang, S.-K., Kim, J.-H., Shin, J., Yang, J., Liu, Z., Ameer, G.A., Huang, Y., and Rogers, J.A. (2015) *Nano Lett.* **15**, 2801.

11 Dagdeviren, C., Hwang, S.-W., Su, Y., Kim, S., Cheng, H., Gur, O., Haney, R., Omenetto, F.G., Huang, Y., and Rogers, J.A. (2013) *Small*, **9**, 3398.

12 Hwang, S.-W., Kang, S.-K., Huang, X., Brenckle, M.A., Omenetto, F.G., and Rogers, J.A. (2015) *Adv. Mater.*, **27**, 47.

13 Kang, S.-K., Hwang, S.-W., Yu, S., Seo, J.-H., Corbin, E.A., Shin, J., Wie, D.S., Bashir, R., Ma, Z., and Rogers, J.A. (2015) *Adv. Funct. Mater.* **25**, 1789.

14 Kang, S.-K., Hwang, S.-W., Cheng, H., Yu, S., Kim, B.H., Kim, J.-H., Huang, Y., and Rogers, J.A. (2014) *Adv. Funct. Mater.*, **24**, 4427.

15 Rimstidt, J.D. and Barnes, H.L. (1980) *Geochim. Cosmochim. Acta*, **44**, 1683.

16 Morita, M., Ohmi, T., Hasegawa, E., Kawakami, M., and Ohwada, M. (1990) *J. Appl. Phys.*, **68**, 1272.

17 Seidel, H., Csepregi, L., Heuberger, A., and Baumgartel, H. (1990) *J. Electrochem. Soc.*, **137**, 3612.

18 Zhou, W., Dai, X., Fu, T.-M., Xie, C., Liu, J., and Lieber, C.M. (2014) *Nano Lett.*, **14**, 1614.

19 Seidel, H., Csepregi, L., Heuberger, A., and Baumgartel, H. (1990) *J. Electrochem. Soc.*, **137**, 3626.

20 Li, R., Cheng, H., Su, Y., Hwang, S.-W., Yin, L., Tao, H., Brenckle, M.A., Kim, D.-H., Omenetto, F.G., Rogers, J.A., and Huang, Y. (2013) *Adv. Funct. Mater.*, **23**, 3106.

21 Kirkland, N.T., Birbilis, N., and Staiger, M.P. (2012) *Acta Biomater.*, **8**, 925.

22 Mueller, P.P., Arnold, S., Badar, M., Bormann, D., Bach, F.-W., Drynda, A., Meyer-Lindenberg, A., Hauser, H., and Peuster, M. (2012) *J. Biomed. Mater. Res. Part A*, **100A**, 2881.

23 Zhou, J., Xu, N., and Wang, Z.L. (2006) *Adv. Mater.*, **18**, 2432.

24 Hu, X., Shmelev, K., Sun, L., Gil, E.-S., Park, S.-H., Cebe, P., and Kaplan, D.L. (2011) *Biomacromolecules*, **12**, 1686.

25 Lu, Q., Hu, X., Wang, X., Kluge, J.A., Lu, S., Cebe, P., and Kaplan, D.L. (2010) *Acta Biomater.*, **6**, 1380.

26 Yin, L., Huang, X., Xu, H., Zhang, Y., Lam, J., Cheng, J., and Rogers, J.A. (2014) *Adv. Mater.*, **26**, 3879.

27 Won, S.M., Kim, H.-S., Lu, N., Kim, D.-G., Solar, C.D., Duenas, T., Ameen, A., and Rogers, J.A. (2011) *IEEE Trans. Electron Devices*, **58**, 4074.

28 Tao, H., Hwang, S.-W., Marelli, B., An, B., Moreau, J.E., Yang, M., Brenckle, M.A., Kim, S., Kaplan, D.L., Rogers, J.A., and Omenetto, F.G. (2014) *Proc. Natl. Acad. Sci. U.S.A.*, **111**, 17385.

29 Pritchard, E.M., Valentin, T., Panilaitis, B., Omenetto, F.G., and Kaplan, D.L. (2013) *Adv. Funct. Mater.*, **23**, 854.

6

Paper Electronics

Martti Toivakka[1], Jouko Peltonen[2], and Ronald Österbacka[3]

[1] *Åbo Akademi University, Center for Functional Materials and Faculty of Science and Engineering, Laboratory of Paper Coating and Converting, Turku, Finland*
[2] *Åbo Akademi University, Center for Functional Materials and Faculty of Science and Engineering, Laboratory of Physical Chemistry, Turku, Finland*
[3] *Åbo Akademi University, Center for Functional Materials and Faculty of Science and Engineering, Laboratory of Physics, Turku, Finland*

6.1 Introduction

Paper has been a "green material" for the transfer of information for more than 2000 years. The discovery of a lightweight and flexible, plant-based substrate that could be used to store written information must be considered one of the greatest discoveries of humankind.

The possibility to store and produce information beyond the written text or graphical images has attracted considerable interest in the last 50 years. One of the first attempts to use paper as a substrate for more advanced applications was suggested by Brody and Page at Westinghouse, when they used a stenciling method to produce inorganic thin-film transistors (TFTs) on paper for flexible circuits [1, 2]. However, the concept of making electronics on paper did not catch on probably because of the difficult manufacturing process and the brittleness of the circuitry, with limited interest in paper electronics at that time being the most decisive factor. It took more than 30 years before a renewed interest in paper electronics started anew, when Berggren proposed to use printing technologies and redox-active conducting polymers as the active material to make simple electronic components and circuits on converted paper [3, 4]. The development of various printing and mass-manufacturing technologies to produce homogeneous multilayers with electronic functionalities has made flexible electronics possible, some also on paper as recently reviewed by Tobjörk and Österbacka [5].

The use of paper for electronics can be divided into different categories. First, the use of paper as a flexible substrate providing only mechanical support can help simple but high-end electronics by lamination of a plastic film with electronics between two paper sheets (e.g., for electronic paper tickets) or gluing of electronic components or silicon chips onto paper substrates. This can be considered

Green Materials for Electronics, First Edition.
Edited by Mihai Irimia-Vladu, Eric D. Glowacki, Niyazi S. Sariciftci, and Siegfried Bauer.

as electronics on paper-type applications. However, there is no particular benefit in using paper over plastic substrates for such applications and a possible loss of the recyclability might occur. When the cellulosic paper is used as an active material in, for example, sensors and actuators, it has been called electroactive paper or *smart paper*, while "electronic paper" (e-paper) refers to paper-like electronic displays, typically fabricated on plastic substrates. In this chapter, we will focus on the use of cellulosic paper as a substrate for electronics, which in our terminology is called *paper electronics*. While using paper as a substrate is difficult, since the paper surface is rough and absorptive, the use of cellulose fibers as a starting point for making a green alternative to plastics does have some advantages when combined with printing technologies.

In this chapter, we will review recent advances in achieving green electronics using cellulosic paper and fibers as a substrate for electronics. We will focus on the paper substrate, individual component development, and the use of paper for sensing purposes in both analytical and point-of-care applications.

6.2 Paper as a Substrate for Electronics

Paper is produced from plant fibers, which consist of cellulose fibrils held together by lignin and non-cellulosic polysaccharides (hemicellulose). While fibers for papermaking can, in principle, be produced from numerous plants, wood is the most common raw material source. Wood fibers are separated from each other in either chemical, mechanical, or chemimechanical pulping process, with subsequent optional bleaching to increase the brightness. These processes, together with the wood species used as raw material, yield fibers with varying surface chemistry and dimensions. Chemical pulping removes most of the lignin, hemicellulose, and extractives from the fibers, whereas they remain on and in the fibers in the mechanical processes. Pulp fibers, for which typical dimensions are 20–40 μm diameter and 1–4 mm length, can be further processed into nanofibrillar or crystalline cellulose. Cellulose micro- and nanofibrils, with diameter down to 10 nm and length between 200 and 2000 nm, can be produced through mechanical disintegration, often combined with enzymatic or chemical pretreatment. If amorphous parts of the fibrils are removed with, for example, acid hydrolysis, one obtains highly crystalline, rod-like cellulose particles with diameters as small as 5 nm and length 100–400 nm.

Pulp fibers have complex surface chemistry that is influenced by the production process. In general, fibers have ionic properties owing to the presence of hydroxyl and carboxylic acid groups. These provide the mechanical strength for the paper through hydrogen bonding and also contribute to hygroscopic properties and swelling of the fibers in the presence of water. Mechanical pulp fiber surfaces contain, in addition, phenolic groups from lignin and a complex mixture of resin and fatty acids, triglycerides, and phenolic compounds from extractives. The numerous chemicals used in papermaking bring their own complexity to the surface chemistry of paper. TEMPO (2,2,6,6-Tetramethylpiperidin-1-oxyl)-mediated oxidation, which is commonly used in production of nanocellulose, increases the fiber surface charge by incorporating carboxylic acid groups. For details on

pulping and fiber surface chemistry, see [6] for example, and for processing and characteristics of cellulosic nanomaterials [7].

Different types and differently processed wood fibers and their combinations are used to control the properties of paper as determined by end-use requirements. For example, paper intended for graphic printing, board for packaging, and tissue paper all utilize different fiber types to provide printability and mechanical and absorptivity properties, respectively. Cellulosic nanomaterials can be used to produce transparent and semitransparent films ("nanopaper"); however, large-scale production is currently not economically feasible.

Paper is traditionally made from a water-based furnish of wood fibers from which water is removed through suction and pressure, with subsequent drying. Numerous chemical additives are used to adjust paper properties; for example, alkyl ketene dimer can be used to reduce hydrophilicity and to provide wet strength, and mineral filler pigments to increase light scatter and to improve optical properties. Most paper types are further processed (converted) to better match the intended end-use application. Common surface treatment and converting processes include pigment coating to improve printability and optical properties of paper; extrusion and dispersion coating to provide barrier properties usually required in, for example, food packaging; and impregnation and lamination to create paper-based composites. For details, see [8, 9]. Converted paper products can mask much of the chemical complexity of the base paper, but introduce one, albeit more controllable, of their own. For cellulosic nanomaterials no large-scale commercial operations currently exist to process them into films or coatings. In the laboratory and on pilot scale, pressure filtration, solvent casting [10], and slot-die coating [11] have typically been used.

Obvious attractions of using paper as substrate for printed electronics and functionality include the low cost and the large existing product base that can potentially benefit from added functionality. These, combined with biodegradability, compostability, and ease of disposal through either fiber recycling or incineration, have been put forward as motivators for research into one-time use ("throw-away") paper-based electronics. A recent study on the influence of printed electronics on the recyclability of paper found the impact on industrial recycling to be insignificant [12]. Mechanical properties of paper can be considered to be an advantage since polymeric films can experience stretching during printing, which can be problematic. If stiffness is a requirement for the end use, this can easily be provided by the thicker board grades. An advantage of paper is the possibility to adjust the printability of a functional ink through modification of the paper surface, similarly as is done for graphic paper grades when targeting the traditional printing processes such as flexography or offset lithography. For example, in functional printing, controlled paper surface porosity can be used to increase print resolution, to eliminate coffee stain effect, and to improve ink adhesion. Paper, especially when coated with mineral pigments, tolerates higher temperatures than low-cost polymeric films enabling low-cost sintering of particulate metal inks with simple infrared irradiation [13]. Paper produced from wood fibers is nontransparent, but clear or high-haze transparent films can be produced from nano- and microfibrillar cellulose. In biological applications an advantage of paper can be the biocompatibility and low cytotoxicity of cellulose,

which is naturally rich in hydroxyl and carboxyl groups. In paper-based diagnostics, the pore structure of paper can provide capillary-force-driven liquid flow for microfluidic applications. The pore structure and the fiber surface chemistry can also be useful in size-based separation and chromatographic purification of analytes from biological samples [14].

Many paper properties are challenging when considering it as a substrate for printed electronics. Uncoated paper has typically high surface roughness (1–10 μm) and high porosity (10–30%) with large pores (1–5 μm), which as such require the use of very thick functional ink layers with large particle size for creation of functioning devices. Paper is also hygroscopic and has poor dimensional stability (1–5%) when moisture level in the environment changes. This can create, for example, disconnects in printed metallic conductive lines. While some paper grades tolerate higher temperatures than low-cost plastics, they usually cannot withstand temperatures above 250–300 °C, which are needed in the processing of many electric materials. The surface chemistry of paper is complex and unknown interactions between the functional materials, for example, (semi) conductive polymers and the paper surface, can be expected. Finally, if the device being fabricated requires barrier properties, unlike plastic films, the porous paper as such cannot provide them. Although micro- and nanocellulose films do have excellent gas barrier properties, they suffer from sensitivity to humidity, and the gas barrier properties are lost at relative humidity levels above 70%. A practical hurdle for producing paper electronics currently is the limited access to high-performance roll-to-roll fabrication facilities. Paper, which is by nature a dusty material, is typically not allowed in clean-room facilities used for printed electronics.

One of the main advantages of using paper as substrate for printed electronics is the opportunity to modify and adapt the paper for the targeted device and end-use application. In general, no universal or single paper for printed electronics can be developed owing to the existence of the large number of functional materials with varying properties, which are formulated as inks. Paper surface can be optimized for printability of each functional ink and printing process. For example, printing of electrodes with silver particle ink in a flexographic process benefits of paper surface porosity, which minimizes the so-called squeeze caused by excessive pressure in the printing nip, thereby increasing the print resolution (Figure 6.1). However, when printing polymeric inks, a closed surface that does not allow absorption of the functional material into the paper is required. In practice, the optimal properties of paper for printed electronics are a compromise that depends on both the functional inks and the printing methods used to fabricate the target device or product.

In general, most devices benefit from the surface smoothness of the substrate. A smooth surface enables use of narrower and thinner features without risk of disconnects. In multilayer structures, for example transistors, excessive surface roughness leads easily to penetration of one functional layer into and through another, rendering the device inoperable. Surface roughness of paper can be reduced by coating. In [15], for example, four coating layers were used to produce paper with root mean square surface roughness of 55 nm, which approaches the smoothness of low-quality plastic films. It should be noted that lateral

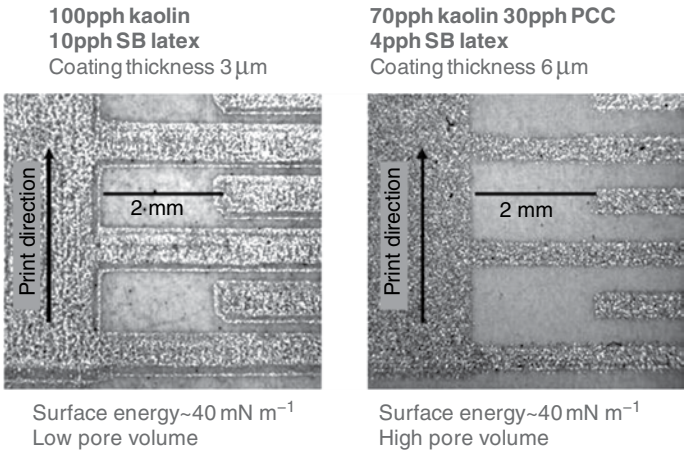

Figure 6.1 Elimination of "squeeze" for flexography printed silver electrodes by increasing the paper surface pore volume.

length scale of surface roughness (correlation length) also plays a role. Many devices can tolerate surface roughness over long distances, whereas short length scale roughness can be detrimental.

Two types of barrier properties can be required when fabricating electronic devices on paper. For most devices, a barrier, or a sealing layer, is needed to keep the functional materials on paper surface. Otherwise, both nanoparticle and polymeric inks penetrate deep into paper making it impossible to create functioning devices. Depending on the functional material, and especially the carrier fluid for the functional material, different types of barrier layers might be needed. Many functional polymers are formulated in organic solvents and a barrier against them is required. However, the barrier lifetime requirement can be quite short, that is, only needed until the functional ink has been dried in the manufacturing process. The other type of barrier, which is also common in printed electronics on plastics, is an encapsulating barrier. These are used to prevent oxygen or moisture from destroying the functionality of the device. High-performance gas barriers in conventional paper-based products are used in liquid packaging for juice. Here, an aluminum layer is either metallized or laminated onto the paper. Since paper is porous, two barrier layers would be needed to encapsulate the device, one from the top and one from below. The top barrier layer can in principle be created by atomic layer deposition of, for example Al_2O_3, which forms highly conformal coatings even on rough surfaces. In general, it appears that the paper electronics concepts proposed so far have mostly tried to avoid device architectures requiring high barrier.

Finally, the surface chemistry of paper can play a role in the performance of functional materials in contact with it. While a chemically inert surface can be created through coating to decouple the paper from the device, some surface chemical groups can potentially improve the performance of a functional material, for example, through doping [16].

Specialty papers aimed specifically at printed electronics have appeared on the market in recent years. Cross-sectional scanning electron microscope (SEM) images of a few are shown in Figure 6.2. All of the papers have multilayer coatings with very high surface smoothness, and most appear also to have some kind of a sealing layer. Products utilizing the commercial papers are, however, still missing from the market. The type of applications the commercial specialty papers are targeting is also unclear. Bollström *et al.* have proposed a multilayer specialty paper concept, shown in Figure 6.3, that can be optimized for the intended device to be fabricated together

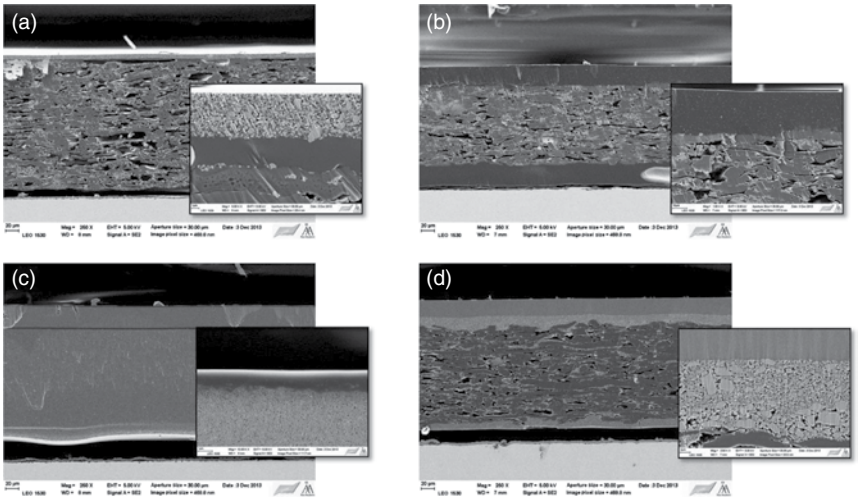

Figure 6.2 Examples of commercial papers aimed at printed electronics: (a) Arjowiggins, (b) Felix Schoeller, (c) Ilford, and (d) Printed Electronics Ltd.

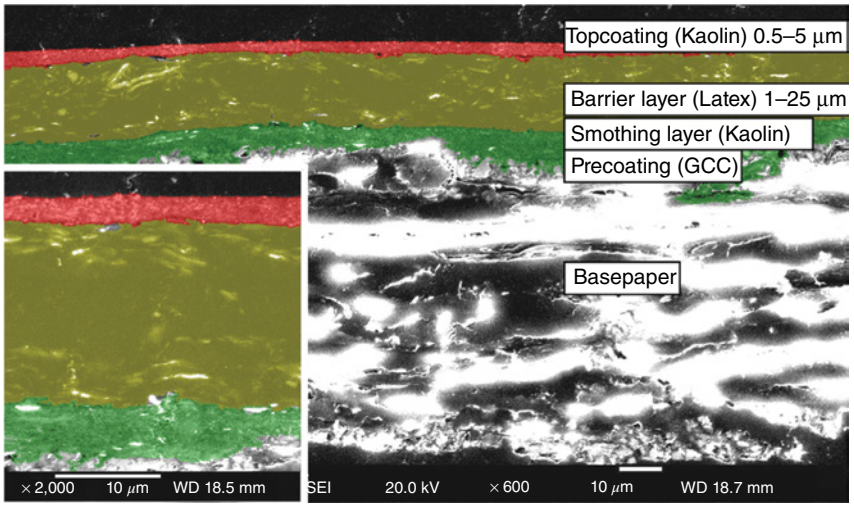

Figure 6.3 An example substrate concept for paper electronics. The different coating layers are enhanced with false coloring. (Bollström *et al*. 2009 [15]. Reproduced with permission of Elsevier.)

with the functional inks and the printing method needed [15, 17]. In this concept, surface smoothness is obtained with multiple coating layers, the barrier to maintain functional materials on paper surface with a dispersion-coated barrier layer, and the printability of the functional inks is adjusted with an ultrathin mineral coating on top. Several devices, including transistors, electrochromic pixels, gas and glucose sensors, ion-selective electrodes, simple circuits, and light-emitting electrochemical cells (LECs) have been demonstrated on the concept substrate [18–21].

In most cases, the paper substrate acts as a surface on which electronics and functional materials are deposited on. A group of its own is the type of product concepts in which the whole porous paper forms a part of the device. Here, one utilizes either functionalized fiber network, or the functional material is embedded between the fibers, which only provide mechanical support for the device. Examples include batteries, supercapacitors, and biofuel cells. A recent review of these is given by Nguyen *et al.* [22].

6.3 Application Areas for Paper Electronics

Below, a short review of potential application areas utilizing paper electronics with examples is given. The simplest products that combine printed electronics and paper material consist of printed, electrically conductive lines or meshes. Examples here include self-cooking soup packaging powered by induction [23], wallpaper that blocks electromagnetic waves [24], and an incontinence sensor [25]. Many paper electronics product concepts presented so far utilize hybrid technology, that is, they combine some aspect of printed electronics on paper with traditional silicon-based electronics. It is clear that hybrid concepts are easier to manufacture and are currently also cheaper than fully printed and integrated paper-based products. An example is radio-frequency identification (RFID) tags, in which a traditional silicon-based RFID chip is combined with an antenna that has either been printed on paper or laser-cut from on-paper-glued metallic films. Ultra high frequency (UHF) antennas have directly been inkjet-printed on to corrugated cardboards intended for packaging applications [26]. Here, an ultra-violet (UV)-curable primer layer was used to reduce surface roughness and absorptivity of the cardboard surface. North Dakota State University has developed contactless laser-assisted technology that enables transfer and assembly of ultrathin and ultrasmall RFID chips into paper. Forgery protection of products is given as a potential target application [27]. Commercially available examples of hybrid concepts include contactless smart tickets and badges with numerous uses, for example, in public transportation, for hotel and office access control, as event and tourist tickets, and in e-money applications [28]. Specialty paper with near-field communication (NFC) RFID tag embedded inside has recently been introduced to market to enable applications such as single-item product tracking and counterfeit protection [29].

Intelligent packaging systems are an area in which paper and board as packaging material can be combined with functional materials to enhance the packaging function. A common approach is to use RFID tags, sensors, indicators, and their combinations to monitor the product quality during transport

and storage, and communicate that to the supply chain logistics, or end user. For example, a smart envelope that provides remote wireless location information and opening status of a parcel has been demonstrated [30]. Opening status information can also be utilized in pharmaceutical packaging for patient adherence tracking. These types of systems record time stamps when medicine has been taken out from the package and communicate the information to, for example, a healthcare provider through a computer or a mobile communication interface [31, 32]. Most intelligent packaging concepts demonstrated so far are hybrid solutions (combination of paper electronics with traditional silicon-based electronics), which can raise environmental issues and potentially require a separate collection and recycling of the used products as mandated by regulations. This can be avoided by designing products that consist of a disposable and a non-disposable part, as is the case with the above-mentioned pharmaceutical packages: only the medical package part needs to be disposed of when all the tablets have been taken out.

An area where the combination of on-paper-printed electronics with traditional electronics is showing promise is paper-based diagnostic and sensor technologies. Through interfacing with a portable low-cost commercial electrochemical reader, for example, glucose meter used by diabetes patients, it is possible to measure numerous analytes. Whitesides' group has developed electrochemical microfluidic paper-based analytical devices (μPADs) for diagnostic and environmental testing of glucose, cholesterol, lactate, and alcohol in blood and urine [33]. Dungchai *et al.* measured glucose, lactate, and uric acid in biological samples [34]. Lu *et al.* created a paper-based electrochemical DNA sensor for point-of-care (POC) testing [35]. Pozuelo *et al.* created a paper-based chemiresistor for detection of ultralow concentrations of protein [36]. Metters *et al.* demonstrated paper-based electroanalytical sensing platforms to measure NADH and nitrite [37]. Ge *et al.* developed a photoelectrochemical paper-based device with an integrated supercapacitor amplifier and an internal light source to measure adenosine triphosphate (ATP) in human serum samples [38]. All of the above examples utilize external electric readers and often paper-based, capillary-force-driven microfluidics to transport the test sample. More control of the sample handling can be obtained with the so-called digital microfluidics, which enables single droplet manipulation through electrowetting. Paper-based digital microfluidics has recently been demonstrated by Fobel *et al.* [39]. Diagnostic and sensor technologies and applications are discussed in more detail below in Section 6.5.

Incorporation of a power source as a battery or a supercapacitor can enable stand-alone paper-based devices and make them independent of power supplies and externally powered readers. Moving toward this direction, Acreo has developed a fully, on paper or plastic, printed biosensing platform including printed amperometric sensor, battery, display, and circuitry, with only the logic component being silicon-based [40]. Zhang *et al.* created a self-powered 3D origami microfluidic electrochemiluminescence biosensing device [41]. Liu and Crooks integrated a metal-air power source and an electrochromic display to an electrochemical sensing device to create a stand-alone system and measured glucose and H_2O_2 in artificial urine samples [42].

Besides products and concepts ready for end use as exemplified above, a considerable amount of research has been devoted to development of single-device components. If a sufficiently large number of components can be fabricated on paper, a combination of these is envisioned to be used to create numerous new products analogously to silicon electronics. The basic components that can be considered for the creation of smart, stand-alone paper electronics-based products are a digital logic device (transistor), memory device, input/output device, and a power source. Recent development in these components is reviewed below.

6.4 Green Electronics on Paper

The development of single components (devices) using mass-manufacturing techniques suitable also for paper electronics has advanced enormously during the last years, mostly in the laboratory but also as commercial products. The development of air-stable materials with sufficient performance is a prerequisite for making electronics available also on paper. However, many devices require precise manufacturing, ultrasmooth, and non-absorbing surfaces, which means that different strategies for paper have to be developed. In the following section, we will take a closer look at some recent strategies and results for making the best use of paper substrates for green electronics.

6.4.1 Diode Structures

The simplest nonlinear electronic device considered here is the rectifying diode. In its simplest form it requires only a semiconductor sandwiched between two contacts. The work functions of the electrodes need to be chosen such that in forward bias efficient injection of charge carriers into the semiconductor can occur, leading to a strong voltage-dependent current through the device, while in the reverse bias, the injection is hindered because of unfavorable energy barriers with a low reverse bias current density as a result. The semiconductor is typically chosen as a wide band-gap semiconductor (insulator) able to transport the current and with energy levels matching the work function of the electrodes.

An interesting environment friendly attempt to make diodes on paper was demonstrated by Manekkathodi *et al.*, where PEDOT:PSS (poly(3,4-ethylenedioxythiophene) : polystyrene sulfonate) and vertically aligned ZnO-nanorods were grown onto Au and Ag covered photo paper using only low temperatures and a nonhazardous chemical solution [43]. The demonstrated p–n type diodes and UV photodiodes were probably suffering from the unevenness of the paper substrate, but were still functional. Another approach using nanowires was recently shown by Kopeinik *et al.*, when they used the intrinsic property of cellulose, namely, the selective binding of Ag-nanowires to the hydroxyl groups on the fibers, to form a conducting network of cellulose-silver nanowires [44]. The composite fiber structure was then covered with P3HT:PCBM (Poly(3-hexylthiophene) : Phenyl-C61-butyric acid methyl ester and aluminum to form a (weakly) rectifying diode, which also acted as a photodiode.

A different approach, also utilizing the intrinsic properties of the cellulose nanostructure, was developed by Zhang *et al.*, where chemical modifications of the cellulose fibers were made in order to produce a so called diode paper [45]. The current rectification ratio reported was 15 ± 5 V with good repeatability at room temperature typically observed when using mixed electron-to-ion conductors. The asymmetric charge distribution inside the diode paper can selectively transport cations and anions under positive and negative bias, to allow an electric current to pass in one direction while being blocked in the opposite direction. Although the mechanism is quite different from semiconductor-based p–n junctions, the phenomenon turns out to be very similar. However, the moisture content, thickness of paper, and scanning frequency will influence the performance of the diode paper.

6.4.2 Light-Emitting Paper

Light-emitting diodes are probably one of the most difficult diode structures to be made on the rough and absorptive paper substrate. The requirement of smooth surfaces and thin layers for efficient light emission in combination with transparency for light out-coupling challenges the traditional paper substrate. However, there are some recent advances that open up new ways of using cellulosic papers also as light-emitting substrates.

Purandare *et al.* reported vacuum-processed organic light-emitting diodes (OLEDs) with phosphorescent emitters fabricated on transparent cellulose paper coated with parylene [46]. The devices showed high luminance ($10\,000\,\mathrm{cd\,m^{-2}}$) and emission efficiency ($50\,\mathrm{cd\,A^{-1}}$ and $20\,\mathrm{lm\,W^{-1}}$). An alternative manufacturing approach for semitransparent OLEDs is by using a lift-off technique for semitransparent gold electrodes in the OLED structure [47]. The gold shows excellent adhesion to the epoxy, resulting in uniform OLED emission as shown in Figure 6.4. Adenine was used as the hole injecting layer on gold, increasing OLED maximum luminance and emission efficiency on cellulose. Even higher efficiencies were reported by Najafabadi *et al.* on recyclable cellulose nanocrystal substrates by using a bottom cathode of Al/LiF deposited on a 400 nm thick *N*,*N*′-di-[(1-naphthyl)-*N*,*N*′-diphenyl]-(1,1′-biphenyl)-4,4′-diamine (α-NPD) layer and a top anode of Au/MoO_3 [48]. The manufactured OLEDs achieve a maximum luminance of almost $75\,000\,\mathrm{cd\,m^{-2}}$ with a current efficacy of $53.7\,\mathrm{cd\,A^{-1}}$ at a luminance of $100\,\mathrm{cd\,m^{-2}}$ and $41.7\,\mathrm{cd\,A^{-1}}$ at $1000\,\mathrm{cd\,m^{-2}}$. The authors conclude that α-NPD layer on the cellulose nanocrystal (CNC) substrate is necessary for achieving high-performance OLEDs.

Another approach suitable for paper is using LECs, as demonstrated by Asadpoordarvish *et al.* [21]. The LEC technology seems to be of particular importance, since the light-emitting p–n junction will form also for millimeter-thick active materials and therefore is independent of the surface roughness [49]. A good fit between the LEC operation and the rough paper substrate was demonstrated through the realization of flexible and lightweight top-emitting LEC-on-paper devices, which featured a uniform light emission at a luminance of $200\,\mathrm{cd\,m^{-2}}$ and a current conversion efficacy of $1.4\,\mathrm{cd\,A^{-1}}$; see Figure 6.5. It is further notable that the entire device can be manufactured from solution under ambient air conditions using spray-coating.

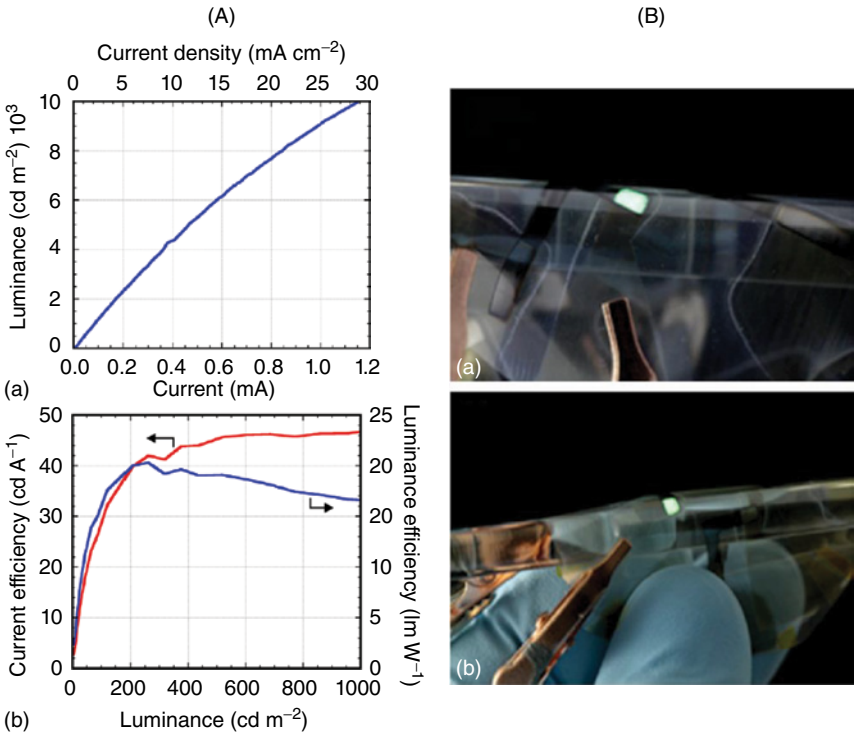

Figure 6.4 An OLED manufactured on transparent cellulose substrates showing the luminance versus current, and current efficiencies (A), and a photograph of the ready device (B). (Sumit *et al*. 2014. Reproduced with the permission of IOP Publishing.)

6.4.3 Solar Cells

Organic [50–54] and inorganic [55] solar cells, manufactured on paper as a substrate, have been demonstrated by several groups. Many of the demonstrated devices show similar features as the OLEDs, namely, a strong correlation between the surface roughness and efficiency [54]. Very smooth nanocrystalline cellulose substrates have been shown to work [54], but the use of a planarizing layer, such as metal oxides (typically ZnO) either as transferred printed [50] or laminated [51] on top of the paper substrate, has also been shown to be promising. The advantage with the metal-oxide planarizing layer is that it also acts as the charge-selective contact.

The best performing solar cell on a paper substrate today shows 4% efficiency using state-of-the-art organic photoactive blends as shown in Figure 6.6 [51]. The transparency of the top contact, MoO_3/Ag/MoO_3 in this case, has been identified as the primary limiting factor in the cell performance. However, given that the stability issue can be solved, these results indicate that high efficiencies are within reach for printable photovoltaic devices on paper.

For the inorganic solar cell, an n–i–p hydrogenated amorphous silicon (a-Si:H) cell structure was deposited by plasma-enhanced chemical vapor deposition

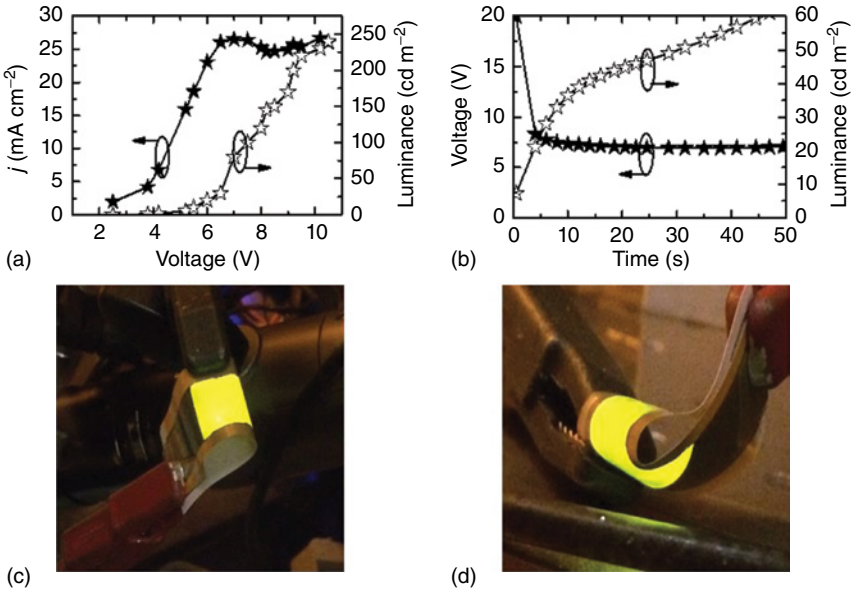

Figure 6.5 (a) The optoelectronic response of a pristine specialty paper LEC during a voltage ramp of 0.02 V s^{-1}. (b) The turn-on process of a specialty paper LEC during galvanostatic driving at $j = 14$ mA cm^{-2}. (c, d) Photographs of the uniform light emission from bent specialty paper LECs as driven by $j = 5$ mA cm^{-2}. (Asadpoordarvish *et al.* 2015 [21]. Reproduced with permission of John Wiley and Sons.)

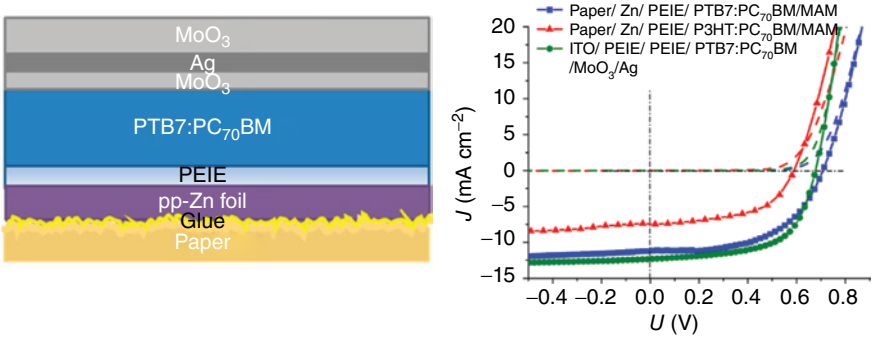

Figure 6.6 Schematic structure of the 4% inverted organic solar cell device on paper (left), and the current density–voltage (*J–V*) curves with P3HT:PC70BM (red line) and state-of-the-art PTB7:PC70BM (blue line). (Leonat *et al.* 2014 [51]. Reproduced with permission of American Chemical Society.)

(PECVD) at 150 °C. The 355 nm thick n–i–p layer was sandwiched between a bottom contact of Al/Ag and a transparent top contact of IZO on a printing paper that contained a coated layer of a hydrophilic mesoporous material. The proof of concept of using n–i–p a-Si showing an efficiency of 3.4% gives promise of further development of inorganic solar cells on paper.

6.4.4 TFTs on Paper

To make low-voltage TFTs on paper is a challenging task. After the first report of low-voltage inorganic TFTs from Fortunato *et al*. [56] where the cellulose paper also acted as the dielectric, many developments have been made. The use of metal oxides as the semiconductor with nanocrystalline cellulose as the dielectric [57–59] allows for low-voltage operation with good stability but can only be operated at low speeds owing to the ion conduction.

The increase in performance of printed or vacuum-processed organic TFTs with the use of nanocrystalline cellulose substrates [60] and planarizing dielectric layers [61–63] may enable use in memory applications [62] and as display drivers [63]. However, many of these approaches require drive voltages of >10 V, which will be problematic if used in combination with batteries, RFID, or solar cells. Recently, Zschiechang and Klauk demonstrated a low-voltage organic thin film transistor (OTFT) device with a high on–off ratio (10^6) and subthreshold swing (90 mV per decade) using no extra planarizing layers [64].

The approach of using ion modulation in combination with printable organic semiconductors for paper electronics is a very promising approach, with low-voltage operation and the possibility of truly environmentally friendly electronics. Pettersson *et al.* demonstrated the use of ionic liquids based on choline chloride (ChoCl), a vitamin cofactor, to create solution processable deep eutectic mixtures with various hydrogen bond complexators [20]. The role of the complexators is to minimize the disadvantage of the Cl^- ion penetrating the organic semiconductor and causing electrochemistry. The semiconductor layer in the transistor is also substituted with a blend of the original semiconductor and a biodegradable polymer insulator, polylactic acid. This reduces the amount of expensive semiconductor used, as also provides increased transistor performance, especially increasing the device switching speed. The environmentally friendly transistors were used to create environmentally friendly ring oscillators, logic gates, and memories on paper [20]. In Figure 6.7, the electrical characteristics of the individual transistors are shown, together with the demonstrated logic circuitry based on these devices.

6.5 Paper-Based Analytical Devices and Test Platforms

6.5.1 Paper as a Sensor Substrate

Paper has been considered as a substrate material for sensors as early as in the beginning of 1800s, when litmus paper was used for the determination of acidity of the sample [65].

The porous structure of paper enables the transport of various liquid-soluble analytes by utilizing the capillary action, which makes paper an attractive alternative for various types of sensor configurations [66–68]. Paper also fulfills many of the requirements set for POC applications by being affordable, user friendly, flexible, disposable, robust, and easily deliverable. On the other hand, more

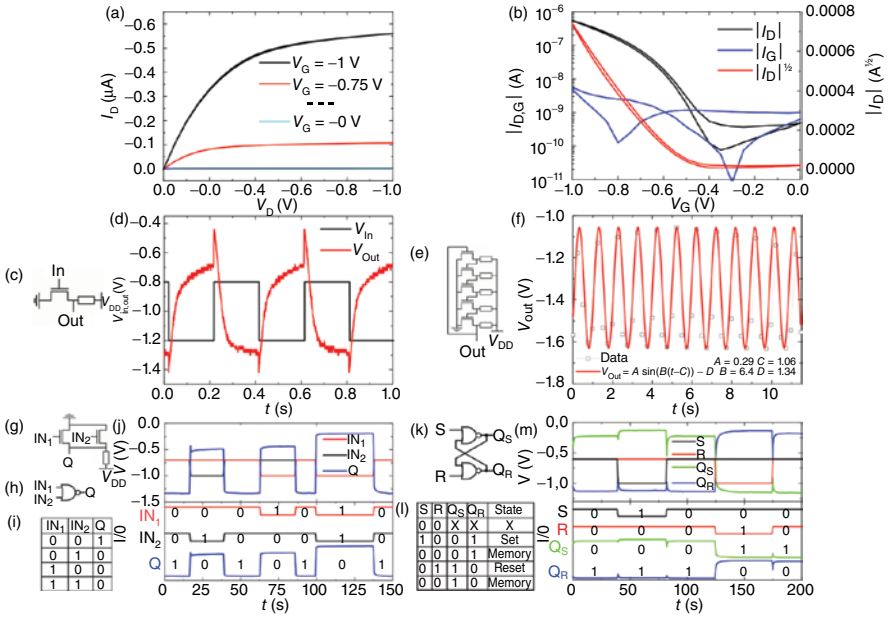

Figure 6.7 Electronic characterization of devices constructed using environmentally friendly transistors. (a) Output and (b) transfer characteristics of an individual transistor. (c) An inverter setup constructed of a transistor and resistor and the device (d) input and output characteristics. (e) Setup of a ring oscillator using five transistors and resistors and the device (f) output signal. (g) Setup of a NOR gate constructed from two transistors and one resistor. (h) The same gate drawn in component form. (i) Truth table for the NOR gate. (j) Inputs and output of the NOR gate. (k) An SR-latch in component form. (l) Truth table for the SR-latch with the inputs S and R and outputs QS and QR. (m) The inputs and outputs of the latch with the raw data in the top graph and the four channels separated in the bottom graph. All devices were measured in an inert atmosphere. (Pettersson *et al*. 2015 [20]. Reproduced with permission of John Wiley and Sons.)

advanced sensor and device design concepts incorporate the use of tailored paper substrates including controlled barrier properties and various functional materials for optical, electrical, and remote sensing as well as patterned design [5, 66, 68, 69]. The POC devices find uses especially in resource-limited locations such as in developing countries or on the field or at home [66, 70].

Another enabling factor for paper sensors is the progress in the development of ink formulations of different functional materials. The conventional high-throughput printing techniques familiar from graphical printing, as exemplified in Figure 6.8, can now be used for creating functional patterned structures and test platforms for analyzing chemical reactions or biofilm formation or cell proliferation [72]. In fact, the only limiting factor for developing novel applications is lack of imagination. Furthermore, modern printers, for example, inkjet instruments, can be equipped with several printheads for simultaneous processing of different solutions, which further boosts the possibilities for upscaling the manufacturing of smart sensor systems. This obviously offers great possibilities for dramatically reducing, for example, the healthcare costs through reduced

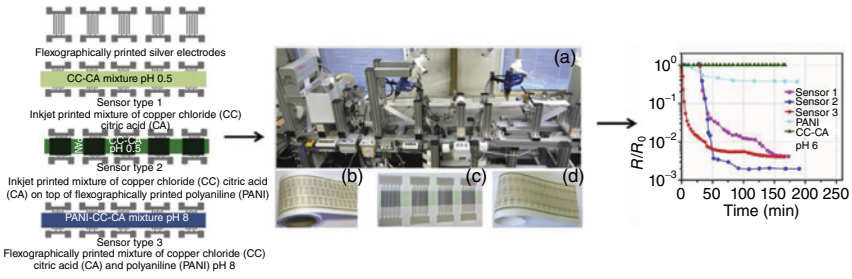

Figure 6.8 Stable ink dispersions of polyaniline (PANI) and metal salts were used for roll-to-roll printing sensors that were sensitive toward H_2S. Various combinations of the components (PANI, copper chloride, citric acid) and order of their processing in a hybrid printer (inkjet, flexography) were tested and related to the sensor performance. (Sarfraz *et al*. 2014 [71]. Reproduced with permission of Elsevier.)

production costs of different diagnostic assays [73]. These kinds of assays also enable preventive healthcare as well as rapid decision-making for patient treatment [74]. Corresponding advances can be foreseen in, for example, food quality surveillance. Recent advances in paper-based indicators, sensors, patterned test platforms, and assays as well as fluidic solutions are discussed in the following.

6.5.2 Paper-Based Microplates, Patterning

The possibility of adjusting the physicochemical properties of paper substrates by various coating and printing procedures, such as the multilayer-coated structures introduced in the previous section, allow the use of paper substrates even in applications where barrier properties against organic solvents or water are a prerequisite [5, 17].

One approach for creating fluidic structures on paper is to first make the whole paper surface hydrophobic, for example, by dipping the paper into a wax [75] and then creating hydrophilic channels by various methods – washing away regions that were covered by a mask during, for example, UV treatment [76, 77], plasma-treating the patterned areas using a metal mask [78], or inkjet-printing an "etching" solvent that dissolves the hydrophobic material [73]. Such multistep photolithographic techniques were used to produce paper-based planar alternatives for conventional three-dimensional plastic microplates [76, 77]. The liquids were absorbed into the hydrophilic paper-based zone areas where they were confined due to the hydrophobic barriers that surround the zones throughout the total paper thickness, preventing cross-contamination.

A more straightforward way is to directly apply a pattern of a hydrophobic material on the hydrophilic paper, for example, by an inkjet printer [79], a screen printer [80], an x–y plotter [81], a wax printer [77, 82, 83], or a flexographic printer [84]. The detection zones, also called *reaction arrays*, have also been constructed by one-step printing of a predetermined pattern of a hydrophobic material such as vinyl-substituted polydimethylsiloxane (PDMS) onto a coated or noncoated paper substrate [85, 86]. The geometry of the printed pattern can be

freely set through the design of the printing plate (flexographic printing) and the strong wetting/non-wetting contrast can be restricted to the very surface if the paper substrate was precoated with a barrier layer.

Besides paper, nonporous and water-resistant platforms based on nanofibrillated cellulose films have been fabricated for diagnostics [87]. The cellulose films were first oxidized to convert the primary hydroxyl groups to carboxyl groups in order to lower nonspecific adsorption. The carboxyl groups were then converted to amine-reactive ones by surface activation. Protein immobilization (antihuman IgG) was then realized by inkjet printing.

Paper-based reaction plates can bring about several advantages: the plates are fabricated from inexpensive materials; the assays can be carried out by using small sample volumes and reagent amounts; the reagents can be printed on the plates; and the disposal of biohazardous waste by incineration is easy and safe [19].

6.5.3 Paper-Based Microfluidics

Besides creating patterned structures on paper providing a wetting/non-wetting contrast, it is also possible to use paper for more complex applications in fluidics. The first paper-based microfluidic device was developed by Müller and Clegg already in 1949 for chromatographic experiments [88].

The first report on the utilization of a spontaneous capillary-driven flow in a porous support for immunoassay purposes is from 1978 by Glad and Grubb who studied the capillary migration of antigen solutions in porous strips with attached antibodies that specifically influenced the migration of the antigen solution [89].

The big boost in this field took place in the beginning of the twenty-first century through the development of μPADs [68, 76]. The improved capabilities for liquid handling have enabled the development of increasingly complex devices including those enabling sample pretreatment through filtering possibilities [70] and devices with capability for vertical and lateral transport of liquid [90].

Capillary action in a fiber network of a paper involves attractive forces between the water molecules and hydrophilic interfaces (e.g., hydroxyl groups of wood fibers), as well as the interfacial pressure difference at the meniscus within a pore [91]. The structure of the pores in the fiber network, that is, the pore size and size distribution, as well as the degree of hydrophilicity influence the speed of liquid transport, being further dependent on the properties of the liquid to be transported (e.g., surface tension and viscosity) [92]. The sample volumes needed can be reduced if liquid movement is manipulated on paper instead of inside it, which can be achieved by controlling local wettability of the paper surface either passively [93] or actively with functionalized electrodes [39].

The control of liquid movement in the channels is especially important when conducting complex (bio)chemical assays involving several liquids. The speed of the liquid flow can be, for instance, increased by sandwiching the paper substrate between polyester films [94] or decreased by printing dissolvable barriers [95]. Dissolvable barriers have been used to deliver the reagents to the test zone at different times [96]. This way, the detection limit and signal amplification can be improved [88].

6.5.4 Colorimetric (Optical) Indicators and Sensors

The main benefit of a colorimetric assay is the rapid generation of visual readouts that can be interpreted by semiskilled nonprofessionals.

Colorimetric assays are quite often based on enzymatic reactions. The simplest versions involve an oxidizing enzyme that reacts with the analyte when introduced in a reaction array [85]. Glucose oxidase is frequently used as a model system. It can be introduced to the reaction (detection) zone of a paper substrate by, for example, screen printing. Then, glucose can be dip-coated on the reaction zone. The enzyme catalyzes the oxidation of the analyte, and the by-product, hydrogen peroxide, reacts with a chromophore yielding a colorful complex. In recently reported advanced systems a set of chemoresponsive colorants is introduced in a test array enabling fingerprinting experiments, that is, discrimination of very similar analytes with high sensitivity (parts per billion level) [97]. These kinds of systems may involve vertical flow [68] or no flow at all. Devices including microfluidics have been reported where the reactants are introduced in different channels and the liquid transfer results in reactions between the channels, yielding a characteristic color response [70]. The simplest indicators yield an on/off result, that is, a color or contrast change that is easy to recognize by naked eye. Such indicators may be applicable especially in food safety monitoring [98, 99]. For more demanding use, the optical response can be calibrated, for example, for analyte concentration by using a scanner or a camera [19, 73, 76, 77]. Advanced colorimetric sensors are also capable of multianalyte sensing [73, 100, 101] and discrimination of analytes, for example, different volatile primary amines [102].

Enzymes have been used, for example, for inexpensive and easy monitoring of the concentration of carcinogenic heavy metals in water [103]. Test assays have also been developed for the diagnosis of antibodies (via enzyme-labeling) [104], food-borne pathogens [105], and viral diseases such as dengue fever [106] and malaria [107].

6.5.5 Electrical and Electro-Optical Sensors

Advances in paper substrate development [15, 108], as well as solution processing (ink formulation) and sintering of various conducting materials [13, 86], have enabled the development of a wide range of different electrical sensors. The principle of such sensors is based on the modulation of the level of conductivity of the electrode material as a result of exposure to the analyte, typically a gas. Examples of these kinds of electrode/analyte systems include graphite/moisture [109, 110], graphene oxide/nitrogen dioxide [111, 112], porous silicon/humidity [113], ITO/ethanol [114], and copper acetate–gold/hydrogen sulfide [71, 115]. In Figure 6.9 a printed NO_x sensor using reduced graphene oxide (rGO) is shown. Also, protein adsorption can be followed by a paper-based chemiresistor sensor [116, 117]. Likewise, adsorption of the analyte can generate a change of capacitance. Gold electrodes printed on a paper substrate are particularly useful for these kinds of applications because supramolecular structures can be constructed through thiol–biotin–avidin chemistry, yielding very specific impedimetric immunosensors [118].

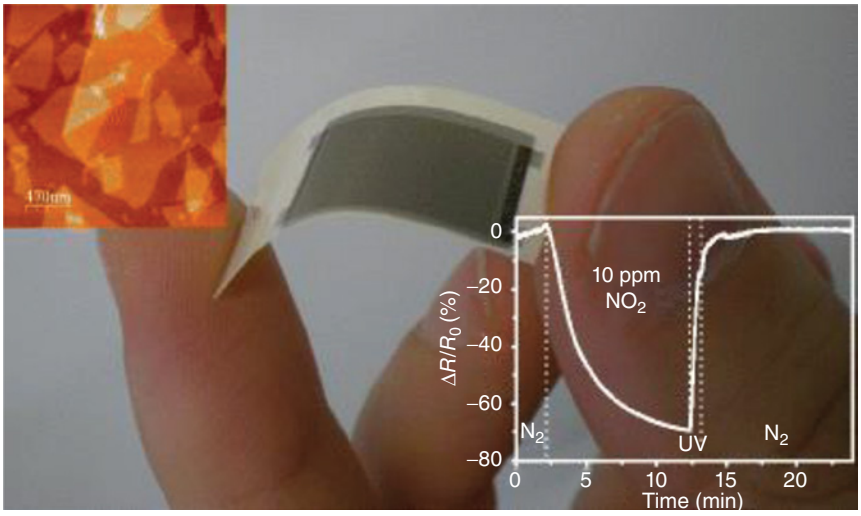

Figure 6.9 Reduced graphene oxide (rGO) based conductometric nitrogen dioxide sensitive sensor on paper. The sensor was prepared by spray-coating rGO on interdigitated silver electrodes that had been inkjet-printed on a paper substrate. The sensitivity of the sensor was high enough to detect sub-parts-per-million levels of NO_2. The adsorbed gas molecules desorbed with time, causing recovery of the sensor resistance. The desorption could be greatly accelerated by UV irradiation, enabling reversible use of the sensor. (Hassinen *et al.* 2013 [112]. Reproduced with permission of Springer.)

Conducting polymers represent yet another important group of materials that find many application possibilities in electronic chemical sensors [119–121]. Care, however, must be taken when choosing a conducting/semiconducting polymer for a certain application regarding the "green" nature of the material, that is, its recyclability and toxicity.

TFTs can also be used for biosensing applications. Liu *et al.* demonstrated a TFT-based glucose sensor that is based on the same principle as described earlier for an optical (color-change) glucose sensor, but here the reduction/oxidation reactions are used to modulate the drain voltage–current, which can be tuned through the gate voltage [122]. The sensor was encapsulated within a cellulose acetate membrane, and it yielded linear drain current–glucose concentration dependence within a concentration range of practical relevance for both a patient with diabetes and a normal patient.

Efforts have also been put on developing paper-based sensors for electro-optical sensing systems because of the readily available and quite widespread microplate readers. Microplate readers incorporate a spectrophotometer that utilizes chemiluminescence (CL) [123, 124] or electrochemiluminescence (ECL) [125, 126] as the phenomena for transducing a chemical sensing event to an optical or electrical signal. The use of this rather selective, sensitive, and dynamic (wide concentration range) technology presumes adequate transmittance of the detecting optical signal through the sample, which sets special demands for paper-based systems. Transmittance properties of paper can be improved, for example, by refraction-index-matching fluids (oils) [127].

6.5.6 Electrochemical Sensors, Assays

Electrochemistry provides a very attractive way for converting biological information into an electronic signal [128]. Numerous benefits can be related to the use of electrochemical biosensing platforms – label-free operation [129], ease of chemical modification of the electrodes [130], and the possibility of incorporating internal standards in a test stripe [131]. For example, sensors have been developed where whole blood containing a number of target analytes can be directly used without any sample clean-up prior to the measurement [132]. The novel tailored paper substrates for printed functionality together with the rapid progress in the development of stable ink formulations for various conducting materials and procedures for fabricating patterned microfluidic structures have enabled the construction of simple and cost-effective yet very versatile electrochemical cells for bioanalytical applications [88, 133–135]. These systems, since they provide an electric signal as a test result, can directly be used and connected as part of the decision-making protocols in clinical work, which makes them particularly attractive for future applications. Incorporating a printed antenna to the sensor system, thereby enabling wireless connections and remote operations, further increases the possibilities toward not only remote but also intact readout and analysis, that is, real and effective POC. For example, Li *et al.* has reported on a low-cost paper-based electrochemical enzyme-linked immunosorbent assay (ELISA) test for sensitive medical diagnosis or pathogen detection in developing countries [136]. Paper-based devices of this kind have been shown to be worthy alternatives for plastic plates when used in standard microplate readers [77] that are able to measure, for example, absorbance, fluorescence, and time-resolved fluorescence.

Several different electrochemical sensor platforms have been developed for various applications, starting from potentiometric ion sensors using paper for microfluidic sampling [137], through gold and gold/silver electrode systems and proceeding to advanced systems being made compatible with commercial electrochemical readers [33].

6.5.7 Wireless and Remote Sensing

As discussed earlier, RFID systems can be incorporated in paper and board typically as hybrid concepts combining printed electronics and conventional silicon technology. Besides tracking and identification, RFID technology is considered especially attractive also for sensor applications, enabling wireless collection of large amounts of data from a matrix of sensors. Good examples of hybrid sensor systems are those developed by the group of Tentzeris, where the antenna is printed on paper and the data is collected by an external integrated circuit (IC) [138]. These sensor systems have been applied for various applications such as for health monitoring by a skin sensor [139] or detection of different concentrations of ammonia gas [140].

When combining paper, printing, and sensing, one of the most obvious application fields is food quality control and packaging surveillance in general. Unander [141, 142] and Siden [143] have developed different types of humidity sensors, including RFID tags [143] for smart packaging applications. Sensors that are able to measure substances resulting from the spoilage process can provide

the most exact information about the state of spoilage and thereby about the edibility of the product. Sarfraz and coworkers have developed sensors for hydrogen sulfide that is produced during spoilage of, for example, poultry meat and fish, as shown in Figure 6.10 [144]. The results showed that formation of hydrogen sulfide as a result of spoilage of, for example, chicken started several days after the best-before date – information that the food production chain might be rather interested in. These sensors are applicable also in other industrial areas such as mining and environmental monitoring in general [145].

6.6 Summary and Future Outlook

In summary, many benefits brought forward for printed electronics in general are also relevant for paper electronics. These include low cost from potentially high throughput production at square meter per second levels as well as lightweight and flexibility of the thin substrate. However, paper has many challenging

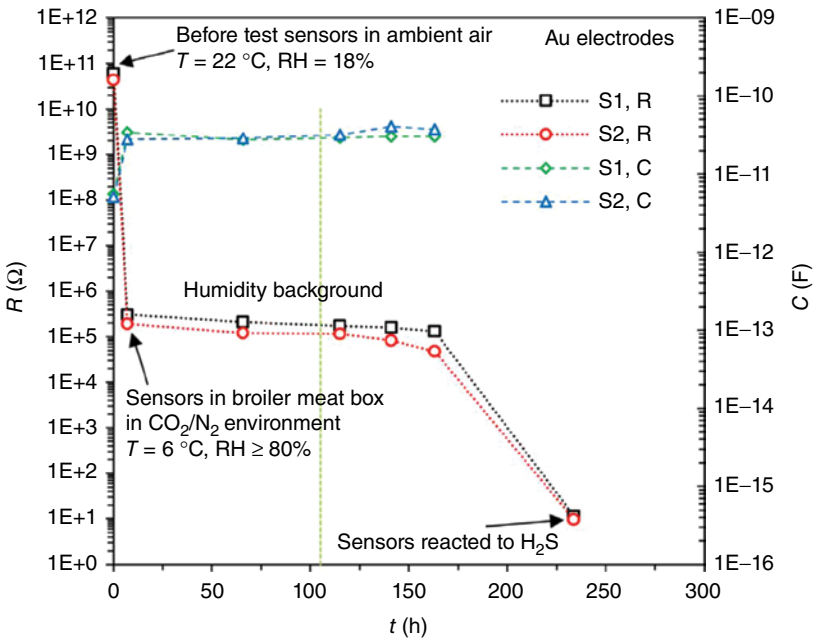

Figure 6.10 The resistance and capacitance as a function of time for paper-based sensors with interdigitated gold electrodes during the broiler meat experiment in modified atmosphere packages at +6 °C. The sensor operates by detecting hydrogen sulfide (H_2S) as an end product of the microbial metabolism. The (green) vertical dashed line indicates the end of the use-by date of the tested broiler meat batch. The earliest sensor response was detected 3.4 days after the use-by date of the tested broiler meat. The effect of humidity on resistance was more than an order of magnitude less compared to similar tests with Ag electrodes. The sensor could also be combined with a printed planar coil antenna and a printed capacitor to construct an inexpensive, wirelessly readable printed resistor-inductor-capacitor (RLC) sensor. (Koskela *et al*. 2015 [144]. Reproduced with permission of Elsevier.)

properties when considering printed electronics, including high porosity and surface roughness, complex surface chemistry, and inherent variable and irregular structure in microscopic scale. Nevertheless, this review provides examples on applications in which these challenges have been overcome. Furthermore, some of the characteristics of paper can be advantageous. Paper comes from renewable sources, is biodegradable, has a large existing product base, and can easily be modified and adapted for intended end use. Paper can be made hydrophilic or -phobic, stiff or flexible, porous or impermeable, rough or smooth, opaque or transparent. Printability of functional inks on paper can be optimized with ease for the chosen functional materials and the targeted device or product. For specific applications, for example, POC diagnostics, paper provides inexpensive and simple means for implementing microfluidics and disposal of used devices through incineration.

Although many printed electronics products that are fabricated on plastic could also be manufactured on paper, many times no real benefit can be obtained from changing the substrate; for example, replacing plastic with paper in glucose measurement strips, which have screen-printed electrodes on them, appears to have little benefit. Also, the cost advantage of paper can be lost in the high cost of the functional materials used to fabricate the devices on it. If the surface area of the device is very small, the substrate cost does not play a critical role in the total cost. Therefore, paper electronics will most probably find uses in applications where either some specific paper property is useful for fabrication or functioning of the device, or the low cost or large area is the main consideration.

References

1 Bacon, W.S. (1968) *Popular Science Vol. 193 No 5, November.* 124–125.
2 Brody, T.P. (1984) *IEEE Trans. Electron Devices*, **31**, 1614–1628.
3 Andersson, P., Nilsson, D., Svensson, P.-O., Chen, M., Malmström, A., Remonen, T., Kugler, T., and Berggren, M. (2002) *Adv. Mater.*, **14**, 1460–1464.
4 Berggren, M., Nilsson, D., and Robinson, N.D. (2007) *Nat. Mater.*, **6**, 3–5.
5 Tobjörk, D. and Österbacka, R. (2011) *Adv. Mater.*, **23**, 1935–1961.
6 Fardim, P. (ed.) (2011) *Chemical Pulping Part 1, Fibre Chemistry and Technology*, Paper Engineers' Association/Paperi ja Puu Oy, Helsinki.
7 Dufresne, A. (2012) *Nanocellulose*, de Gruyter, Berlin/Boston, MA.
8 Paltakari, J. (ed.) (2009) *Pigment Coating and Surface Sizing of Paper*, Paper Engineers' Association/Paperi ja Puu Oy, Helsinki.
9 Kuusipalo, J. (ed.) (2008) *Paper and Paperboard Converting*, Paper Engineers' Association/Paperi ja Puu Oy, Helsinki.
10 Tammelin, T., Hippi, U., and Salminen, A. (2014) Method for the preparation of NFC films on supports. European Patent Application EP2771390.
11 Kumar, V., Elfving, A., Koivula, H., Bousfield, D.W., and Toivakka, M. (2016) *Ind. Eng. Chem. Res.*, **55** (12), 3603–3613.
12 Aliaga, C., Zhang, H., Dobon, A., Hortal, M., and Beneventi, D. (2015) *Waste Manage. (Oxford)*, **38**, 41–48.

13 Tobjörk, D., Aarnio, H., Pulkkinen, P., Bollström, R., Määttänen, A., Ihalainen, P., Mäkelä, T., Peltonen, J., Toivakka, M., Tenhu, H., and Österbacka, R. (2012) *Thin Solid Films*, **520** (7), 2949–2955.

14 Khan, M.S., Thouas, G., Shen, W., Whyte, G., and Garnier, G. (2010) *Anal. Chem.*, **82** (10), 4158–4164.

15 Bollström, R., Määttänen, A., Tobjörk, D., Ihalainen, P., Kaihovirta, N., Österbacka, R., Peltonen, J., and Toivakka, M. (2009) *Org. Electron.*, **10** (5), 1020–1023.

16 Valtakari, D., Bollström, R., Toivakka, M., and Saarinen, J.J. (2015) *Thin Solid Films*, **590**, 170–176.

17 Bollström, R., Määttänen, A., Ihalainen, P., Toivakka, M., and Peltonen, J. (2014) Method for creating a substrate for printed or coated functionality, substrate, functional device and its use. European Patent 2392197.

18 Bollström, R. (2013) *Paper for printed electronics and functionality*. PhD thesis. Åbo Akademi, Turku.

19 Määttänen, A. (2014) *Printed platforms for paper-based analytical applications*. PhD thesis. Åbo Akademi, Turku.

20 Pettersson, F., Remonen, T., Adekanye, D., Zhang, Y., Wilén, C.-E., and Österbacka, R. (2015) *ChemPhysChem*, **16**, 1286–1294.

21 Asadpoordarvish, A., Sandström, A., Larsen, C., Bollström, R., Toivakka, M., Österbacka, R., and Edman, L. (2015) *Adv. Funct. Mater.*, **25**, 3238–3245.

22 Nguyen, T.H., Fraiwan, A., and Choi, S. (2014) *Biosens. Bioelectron.*, **54**, 640–649.

23 *Fulton Innovation*, http://www.cnet.com/uk/pictures/light-up-cereal-boxes-and-self-cooking-soup-powered-by-the-magic-of-induction/14/ (accessed 29 March 2017).

24 De, B.F., Eymin-Petot-Tourtollet, G., Lemaitre-Auger, P., and Vuong, T.P. (2011) Surface adaptee a filtrer une pluralite de bandes de frequencies. Patent Application PCT/FR2011/050,843.

25 *Sensible Solutions Sweden AB*, http://www.sensiblesolutions.se/ (accessed 29 March 2017).

26 Sowade, E., Göthel, F., Zichner, R., and Baumann, R.R. (2015) *Appl. Surf. Sci.*, **332**, 500–506.

27 Swedberg, C. (2013) *NDSU Researchers Develop Method for Embedding RFID in Paper, RFID Journal, February 27, 2013*.

28 Confidex, http://www.confidex.com/ (accessed 29 March 2017).

29 Powercoat, http://powercoatpaper.com/powercoat/alive/ (accessed 29 March 2017).

30 Ropas, http://www.ropas-project.eu/news/demonstrator-smart-envelope.html (accessed 29 March 2017).

31 *StoraEnso Pharma DDSi, Stora Enso Oyj*.

32 *Med-ic® Electronic Compliance Monitor, Information Mediary Corporation*.

33 Nie, Z., Deiss, F., Liu, X., Akbulut, O., and Whitesides, G.M. (2010) *Lab Chip*, **10** (22), 3163–3169.

34 Dungchai, W., Chailapakul, O., and Henry, C. (2009) *Anal. Chem.*, **81** (14), 5821–5826.

35 Lu, J., Ge, S., Ge, L., Yan, M., and Yu, J. (2012) *Electrochim. Acta*, **80**, 334–341.

36 Pozuelo, M., Blondeau, P., Novell, M., Andrade, F.J., Rius, F.X., and Riu, J. (2012) *Biosens. Bioelectron.*, **49**, 462–465.
37 Metters, J., Houssein, S., Kampouris, D., and Banks, C. (2013) *Anal. Methods*, **5**, 103–110.
38 Ge, L., Wang, P., Ge, S., Li, N., Yu, J., Yan, M., and Huang, J. (2013) *Anal. Chem.*, **85** (8), 3961–3970.
39 Fobel, R., Kirby, A., Ng, A., Farnood, R., and Wheeler, A. (2014) *Adv. Mater.*, **26** (18), 2838–2843.
40 Turner, A.P.F. (2013) *Chem. Soc. Rev.*, **42** (8), 3184.
41 Zhang, X., Li, J., Chen, C., Lou, B., Zhang, L., and Wang, E. (2013) *Chem. Commun.*, **49** (37), 3866–3868.
42 Liu, H. and Crooks, R. (2012) *Anal. Chem.*, **84** (5), 2528–2532.
43 Manekkathodi, A., Lu, M.-Y., Wang, C.W., and Chen, L.-J. (2010) *Adv. Mater.*, **22**, 4059–4063.
44 Kopeinik, H., Schennach, R., Gallik, J., Plank, H., and Friedel, B. (2015) *Cellulose*, **22**, 3425–3434.
45 Zhang, W., Zhang, X., Lu, C., Wang, Y., and Deng, Y. (2012) *J. Phys. Chem. C*, **116**, 9227–9234.
46 Purandare, S., Gomez, E.F., and Steckl, A.J. (2014) *Nanotechnology*, **25**, 094012.
47 Gomez, E.F. and Steckl, A.J. (2015) *ACS Photonics*, **2**, 439–445.
48 Najafabadi, E., Zhou, Y.H., Knauer, K.A., Fuentes-Hernandez, C., and Kippelen, B. (2014) *Appl. Phys. Lett.*, **105**, 063305.
49 Matyba, P., Maturova, K., Kemerink, M., Robinson, N.D., and Edman, L. (2009) *Nat. Mater.*, **8**, 672–676.
50 Hübler, A., Trnovec, B., Zillger, T., Ali, M., Wetzold, N., Mingebach, M., Wagenpfahl, A., Deibel, C., and Dyakonov, V. (2011) *Adv. Energy Mater.*, **1**, 1018–1022.
51 Leonat, L., Schuette White, M., Głowacki, E.D., Scharber, M.C., Zillger, T., Rühling, J., Hübler, A., and Sariciftci, N.S. (2014) *J. Phys. Chem. C*, **118**, 16813–16817.
52 Zhou, Y., Fuentes-Hernandez, C., Khan, T.M., Liu, J.-C., Hsu, J., Shim, J.W., Dindar, A., Youngblood, J.P., Moon, R.J., and Kippelen, B. (2013) *Sci. Rep.*, **3**, 1536.
53 Zhou, Y., Khan, T.M., Liu, J.-C., Fuentes-Hernandez, C., Shim, J.W., Najafabadi, E., Youngblood, J.P., Moon, R.J., and Kippelen, B. (2014) *Org. Electron.*, **15**, 661–666.
54 Vilhegas Costa, S., Pingel, P., Janietz, S., and Nogueira, A.F. (2016) *J. Appl. Polym. Sci.*, **133**, 43679–43685.
55 Águas, H., Mateus, T., Vicente, A., Gaspar, D., Mendes, M.J., Schmidt, W.A., Pereira, L., Fortunato, E., and Martins, R. (2015) *Adv. Funct. Mater.*, **25**, 3592–3598.
56 Fortunato, E., Correia, N., Barquinha, P., Pereira, L., Gonçalves, G., and Martins, R. (2008) *IEEE Electron Device Lett.*, **29**, 988–990.
57 Gaspar, D., Fernandes, S.N., de Oliveira, A.G., Fernandes, J.G., Grey, P., Pontes, R.V., Pereira, L., Martins, R., Godinho, M.H., and Fortunato, E. (2014) *Nanotechnology*, **25**, 09400.

58 Tiemann, S., Sachnov, S.J., Pettersson, F., Bollström, R., Österbacka, R., Wasserscheid, P., and Zaumseil, J. (2014) *Adv. Funct. Mater.*, **24**, 625–534.
59 Gaspar, D., Pereira, L., Delattre, A., Guerin, D., Fortunato, E., and Martins, R. (2015) *Phys. Status Solidi C*, **12**, 1421–1426.
60 Fujisaki, Y., Koga, H., Nakajima, Y., Nakata, M., Tsuji, H., Yamamoto, T., Kurita, T., Nogi, M., and Shimidzu, N. (2014) *Adv. Funct. Mater.*, **24**, 1657–1663.
61 Li, Y., Liu, C., Xu, Y., Minari, T., Darmawan, P., and Tsukagoshi, K. (2012) *Org. Electron.*, **13**, 815–819.
62 Peng, B. and Chan, P.K.L. (2014) *Org. Electron.*, **15**, 203–210.
63 Peng, B., Ren, X., Wang, Z., Wang, X., Roberts, R.C., and Chan, P.K.L. (2014) *Sci. Rep.*, **4**, 6430/1–6430/7.
64 Zschiechang, U. and Klauk, H. (2015) *Org. Electron.*, **25**, 340–344.
65 Ballerini, D.R., Li, X., and Shen, W. (2012) *Nanofluidics*, **13** (5), 769–787.
66 Liana, D.D., Raguse, B., Gooding, J.J., and Chow, E. (2012) *Sensors*, **12**, 11505–11526.
67 Yager, P., Edwards, T., Fu, E., Helton, K., Nelson, K., Tam, M.R., and Weig, B.H. (2006) *Nature*, **442**, 412–418.
68 Martinez, A.W., Phillips, S.T., and Whitesides, G.M. (2010) *Anal. Chem.*, **82**, 3–10.
69 Glavan, A.C., Martinez, R.V., Maxwell, E.J., Subramaniam, A.B., Nunes, R.M., Soh, S., and Whitesides, G.M. (2013) *Lab Chip*, **1**, 2922–2930.
70 Li, X., Ballerini, D.R., and Shen, W. (2012) *Biomicrofluidics*, **6**, 011301.
71 Sarfraz, J., Ihalainen, P., Määttänen, A., Bollström, R., Gulin-Sarfraz, T., Peltonen, J., and Lindén, M. (2014) *Colloids Surf., A*, **460**, 401–407.
72 Juvonen, H., Määttänen, A., Lauren, P., Ihalainen, P., Urtti, A., Yliperttula, M., and Peltonen, J. (2013) *Acta Biomater.*, **9**, 6704–6710.
73 Abe, K., Suzuki, K., and Citterio, D. (2008) *Anal. Chem.*, **80**, 6928–6934.
74 Giljohann, D.A. and Mirkin, C.A. (2009) *Nature*, **462**, 461–464.
75 Martinez, A.W., Phillips, S.T., Carrilho, E., Thomas, S.W., Sind, H., and Whitesides, G.M. (2008) *Anal. Chem.*, **80** (10), 3699–3707.
76 Martinez, A.W., Phillips, S.T., Butte, M.J., and Whitesides, G.M. (2007) *Angew. Chem. Int. Ed.*, **46**, 1318–1320.
77 Carrilho, E., Phillips, S.T., Vella, S.J., Martinez, A.W., and Whitesides, G.M. (2009) *Anal. Chem.*, **81**, 5990–5998.
78 Li, X., Tian, J., Nguyen, T., and Shen, W. (2008) *Anal. Chem.*, **80**, 9131–9134.
79 Dungchai, W., Chailapakul, O., and Henry, C.S. (2011) *Analyst*, **136**, 77–82.
80 Bruzewicz, D.A., Reches, M., and Whitesides, G.M. (2008) *Anal. Chem.*, **80**, 3387–3392.
81 Lu, Y., Shi, W., Jiang, L., Qin, J., and Lin, B. (2009) *Electrophoresis*, **30**, 1497–1500.
82 Olkkonen, J., Lehtinen, K., and Erho, T. (2010) *Anal. Chem.*, **82**, 10246–10250.
83 Lu, Y., Shi, W., Qin, J., and Lin, B. (2010) *Anal. Chem.*, **82**, 329–335.
84 Songjaroen, T., Dungchai, W., Chailapakul, O., and Laiwattanapaisal, W. (2011) *Talanta*, **85**, 2587–2593.
85 Määttänen, A., Fors, D., Wang, S., Valtakari, D., Ihalainen, P., and Peltonen, J. (2011) *Sens. Actuators, B*, **160**, 1404–1412.

86 Määttänen, A., Ihalainen, P., Pulkkinen, P., Wang, S., Tenhu, H., and Peltonen, J. (2012) *ACS Appl. Mater. Interfaces*, **4**, 955–964.
87 Orelma, H., Filpponen, I., Johansson, L.-S., Österberg, M., Rojas, O.J., and Laine, J. (2012) *Biointerphases*, **7**, 61.
88 Müller, R.H. and Clegg, D.L. (1949) *Anal. Chem.*, **21**, 1123–1125.
89 Glad, C. and Grubb, A.O. (1978) *Anal. Biochem.*, **85**, 180–187.
90 Martinez, A.W., Phillips, S.T., and Whitesides, G.M. (2008) *Proc. Natl. Acad. Sci. U.S.A.*, **105**, 19606–19611.
91 Gillespie, T. (1959) *J. Colloid Sci.*, **14**, 123–130.
92 Hodgson, K.T. and Berg, J.C. (1988) *J. Colloid Interface Sci.*, **121**, 22–31.
93 Songok, J. and Toivakka, M. (2016) *Microfluid. Nanofluid.*, **20** (4), 1–9.
94 Jahanshahi-Anbuhi, S., Chavan, P., Sicard, C., Leung, V., Zakir Hossain, S.M., Pelton, R., Brennan, J.D., and Filipe, C.D.M. (2012) *Lab Chip*, **12**, 5079–5085.
95 Fu, E., Lutz, B., Kauffman, P., and Yager, P. (2010) *Lab Chip*, **10**, 918–920.
96 Apilux, A., Ukita, Y., Chikae, M., Chailapakul, O., and Takamura, Y. (2012) *Lab Chip*, **13**, 126–135.
97 Askim, J.R., Mahmoudi, M., and Suslick, K.S. (2013) *Chem. Soc. Rev.*, **42**, 8649–8682.
98 Pacquit, A., Frisby, J., Diamond, D., Lau, K.T., Farrell, A., Quilty, B., and Diamond, D. (2007) *Food Chem.*, **102**, 466–470.
99 Hakola, L., Hartman, J., Honkapää, K., Laakso, P., Penttilä, R., Pitkänen, M., Rusko, E., Sipiläinen-Malm, T., and Vanttaja, I. (2013) *International Conference on Digital Printing Technologies*, pp. 253–549.
100 Vella, S.J., Beattie, P., Cademartiri, R., Laromaine, A., Martinez, A.W., Phillips, S.T., Mirica, K.A., and Whitesides, G.M. (2012) *Anal. Chem.*, **84**, 2883–2891.
101 Pollock, N.R., Rolland, J.P., Kumar, S., Beattie, P.D., Jain, S., Noubary, F., Wong, V.L., Pohlmann, R.A., Ryan, U.S., and Whitesides, G.M. (2012) *Sci. Transl. Med.*, **4**, 152ra129. doi: 10.1126/scitranslmed.3003981
102 Soga, T., Jimbo, Y., Suzuki, K., and Citterio, D. (2013) *Anal. Chem.*, **85**, 8973–8978.
103 Hossain, S.M.Z. and Brennan, J.D. (2011) *Anal. Chem.*, **83**, 8772–8778.
104 Avrameas, S. (1969) *Immunochemistry*, **6**, 43–52.
105 Jokerst, J.C., Adkins, J.A., Bisha, B., Mentele, M.M., Goodridge, L.D., and Henry, C.S. (2012) *Anal. Chem.*, **84**, 2900–2907.
106 Yager, P., Fu, E., Liang, T., Lutz, B., and Osborn, J.L. (2011) *15th International Conference on Miniaturized Systems for Chemistry and Life Sciences*, pp. 2092–2095.
107 Fu, E., Liang, T., Spicar-Mihalic, P., Houghtaling, J., Ramachandran, S., and Yager, P. (2012) *Anal. Chem.*, **84**, 4574–4579.
108 Ihalainen, P., Määttänen, A., Järnström, J., Tobjörk, D., Österbacka, R., and Peltonen, J. (2012) *J. Ind. Eng. Chem. Res.*, **51**, 6025–6036.
109 Venancio, E.C., Capparelli Mattoso, L.H., Sergio de Paula Herrmann Junior, P., and MacDiarmid, A.G. (2008) *Sens. Actuators, B*, **130**, 723–729.
110 Steffens, C., Manzoli, A., Francheschi, E., Corazza, M.L., Corazza, F.C., Vladimir Oliveira, J., and Herrmann, P.S.P. (2009) *Synth. Met.*, **159**, 2329–2332.
111 Dua, V., Surwade, S.P., Ammu, S., Agnihotra, S.R., Jain, S., Roberts, K.E., Park, S., Ruoff, R.S., and Manohar, S.K. (2010) *Angew. Chem. Int. Ed.*, **49**, 2154–2157.

112 Hassinen, J., Kauppila, J., Leiro, J., Määttänen, A., Ihalainen, P., Peltonen, J., and Lukkari, J. (2013) *Anal. Bioanal. Chem.*, **405**, 3611–3617.

113 Jalkanen, T., Mäkilä, E., Määttänen, A., Tuura, J., Kaasalainen, M., Lehto, V.-P., Ihalainen, P., Peltonen, J., and Salonen, J. (2012) *Appl. Phys. Lett.*, **101**, 263110.

114 Arena, A., Donato, N., Saitta, G., Bonavita, A., Rizzo, G., and Neri, G. (2010) *Sens. Actuators, B*, **145**, 488–494.

115 Sarfraz, J., Määttänen, A., Törngren, B., Pesonen, M., Peltonen, J., and Ihalainen, P. (2015) *RSC Adv.*, **5**, 13525–13529.

116 Pozuelo, M., Blondeau, P., Novell, M., Andrade, F.J., Rius, F.X., and Riu, J. (2013) *Biosens. Bioelectron.*, **49**, 462–465.

117 Wang, L., Chen, W., Xu, D., Shim, B.S., Zhu, Y., Sun, F., Liu, L., Peng, C., Jin, Z., Xu, C., and Kotov, N.A. (2009) *Nano Lett.*, **9**, 4147–4152.

118 Ihalainen, P., Majumdar, H., Viitala, T., Törngren, B., Näreoja, T., Määttänen, A., Sarfraz, J., Härmä, H., Yliperttula, M., Österbacka, R., and Peltonen, J. (2013) *Biosensors*, **3**, 1–17.

119 Janata, J. and Josowicz, M. (2008) *Nat. Mater.*, **2**, 19–22.

120 Gerard, M., Chaubey, A., and Malhotra, B.D. (2002) *Biosens. Bioelectron.*, **17**, 345–359.

121 Ahuja, T., Mir, I.A., Kumar, D., and Rajesh, C. (2007) *Biomaterials*, **28**, 791–805.

122 Liu, J., Agarwal, M., and Varahramyan, K. (2008) *Sens. Actuators, B*, **135**, 195–199.

123 Hemmilä, I., Dakubu, S., Mukkala, V.-M., Siitari, H., and Lövgren, T. (1984) *Anal. Biochem.*, **137**, 335–343.

124 Yu, J., Wang, S., Ge, L., and Ge, S. (2011) *Biosens. Bioelectron.*, **26**, 3284–3289.

125 Wang, S., Ge, L., Song, X., Yu, J., Ge, S., Huang, J., and Zeng, F. (2012) *Biosens. Bioelectron.*, **31**, 212–218.

126 Delaney, J.L., Hogan, C.F., Tian, J., and Shen, W. (2011) *Anal. Chem.*, **83**, 1300–1306.

127 Ellerbee, A.K., Phillips, S.T., Siegel, A.C., Mirica, K.A., Martinez, A.W., Striehl, P., Jain, N., Prentiss, M., and Whitesides, G.M. (2009) *Anal. Chem.*, **81**, 8447–8452.

128 Grieshaber, D., MacKenzie, R., Vörös, J., and Reimhult, E. (2008) *Sensors*, **8**, 1400–1458.

129 Sadik, O.A., Aluoch, A.O., and Zhou, A. (2009) *Biosens. Bioelectron.*, **24**, 2749–2765.

130 Hu, C., Bai, X., Wang, Y., Jin, W., Zhang, X., and Hu, S. (2012) *Anal. Chem.*, **84**, 3745–3750.

131 Tan, S.N., Ge, L., and Wang, W. (2010) *Anal. Chem.*, **82**, 8844–8847.

132 D'Orazio, P. (2003) *Clin. Chim. Acta*, **334**, 41–69.

133 Maxwell, E.J., Mazzeo, A., and Whitesides, G.M. (2013) *MRS Bull.*, **38**, 309–314.

134 Lan, W.-J., Maxwell, E.J., Parolo, C., Bwambok, D.K., Subramaniam, A.B., and Whitesides, G.M. (2013) *Lab Chip*, **13**, 4103–4108.

135 Määttänen, A., Vanamo, U., Ihalainen, P., Pulkkinen, P., Tenhu, H., Bobacka, J., and Peltonen, J. (2013) *Sens. Actuators, B*, **177**, 153–162.

136 Li, X.J., Nie, Z.H., Cheng, C.-M., Goodale, A.B., and Whitesides, G.M. (2010) *14th International Conference on Miniaturized Systems for Chemistry and Life Science*, pp. 1487–1489.

137 Lisak, G., Cui, J., and Bobacka, J. (2015) *Sens. Actuators, B*, **207**, 933–939.

138 Rida, A., Vyas, R., and Tentzeris, M.M. (2009) *IEEE Antennas Propag. Mag.*, **51**, 13–23.

139 Cook, B.S., Shamim, A., and Tentzeris, M.M. (2012) *IET Microwaves Antennas Propag*, **6**, 1536–1541.

140 Vyas, R. (2011) *IEEE Sens. J.*, **11**, 3139–3152.

141 Unander, T. (2008) *Characterization of low cost printed sensors for smart packaging*. PhD thesis, Mid Sweden University.

142 Unander, T. and Nilsson, H.-E. (2009) *IEEE Sens. J.*, **9**, 922–928.

143 Siden, J., Zeng, X., Unander, T., Koptyug, A., and Nilsson, H.-E. (2007) *IEEE Sensors, Conference*, pp. 308–311.

144 Koskela, J., Sarfraz, J., Ihalainen, P., Määttänen, A., Pulkkinen, P., Tenhu, H., Nieminen, T., Kilpelä, A., and Peltonen, J. (2015) Monitoring the quality of raw poultry by detecting hydrogen sulfide with printed sensors. *Sens. Actuators, B*, **218**, 89–96.

145 Abel, T., Ungerböck, B., Klimant, I., and Mayr, T. (2012) Fast responsive, optical trace level ammonia sensor for environmental monitoring. *Chem. Cent. J.*, **6** (124), 1–10.

7

Engineering DNA and Nucleobases for Present and Future Device Applications

Eliot F. Gomez and Andrew J. Steckl

University of Cincinnati, Nanoelectronics Laboratory, Department of Electrical Engineering and Computer Science, Cincinnati, OH 45221-0030, USA

7.1 The Versatile World of Nucleic Acids

7.1.1 Introduction

Deoxyribose nucleic acid (DNA) is a marvelous molecule to behold in its biological world. Transcription, translation, and replication are self-perpetuated processes for genetic expression, which all depend upon the intricate structure, organization, and special affinities of the nucleobases in the long DNA double helix [1]. Beyond biological intent, these same self-assembling mechanisms have inspired seeds of research in unconventional uses of DNA for the past 10–20 years. For example, computer scientists are building DNA-based information storage [2–4] and biological computing [5, 6] inspired by its ability to organize incalculable amounts of biological data into well-defined libraries. Nanotechnology engineers and scientists leverage the Lego®-like molecules into building blocks for elaborate nanoscale structures [7]. The long polymeric chain and negatively charged backbone, which resemble the beginning of a molecular wire, have spurred electrical engineers and material scientists to investigate electronic charge transport properties and atomic-scale electronics. We are just beginning to learn what DNA can do outside of the cell in various practical applications, such as electronic devices, nanotechnology, biosensing, information storage, and molecular engineering. Increased collaboration between different DNA fields will yield exciting new devices that control electronic and nanostructure precision with dynamic or modular platforms.

This chapter highlights several burgeoning areas of DNA electronics, nanotechnology, and molecular engineering and focuses particularly on how these three areas have shared interest for future DNA-based applications. However, the breadth of these topics is very large for a single review chapter and readers will greatly benefit from additional material in existing reviews of DNA-related subtopics. DNA in electronic applications has been the subject of several reviews, including photonic/electronic devices [8, 9] and electron transport [10, 11]. The material science of DNA was reviewed in an article [12] and was the subject of a

Green Materials for Electronics, First Edition.
Edited by Mihai Irimia-Vladu, Eric D. Glowacki, Niyazi S. Sariciftci, and Siegfried Bauer.

collection of chapters [13] covering a wide range of topics from fundamental science to electronic devices. Other notable reviews on the accomplishments of DNA origami and self-assembled structures in DNA include nanotechnology [7, 14], molecular engineering [15], and sensors [16, 17]. Although it is difficult to list all of the important reviews and contributions, the most recent work is summarized in this chapter. Additional discussion is also included on the nucleic acid bases (nucleobases), which recently have become a focus as "green" material for electronics and are showing great promise [18].

Figure 7.1 shows the three major fronts that have propelled DNA as a material for electronic and nanostructure research (primarily from a device and application emphasis perspective). The first area of research is "DNA organic electronics." This particular field of research capitalizes on key electronic properties of DNA and/or of the nucleobases for thin-film organic devices, such as the organic field-effect transistors (OFETs) and organic light-emitting diodes (OLEDs), in order to optimize device charge transport properties and improve performance. The second research area is DNA nanotechnology, which uses DNA building blocks for nanostructures, ranging from simple 2D structures to complex nanomechanical devices. The field is often called DNA origami because of its ability to fold onto itself, forming complex structures made possible by the affinities of nucleobases for each other. The third field is "DNA molecular engineering,"

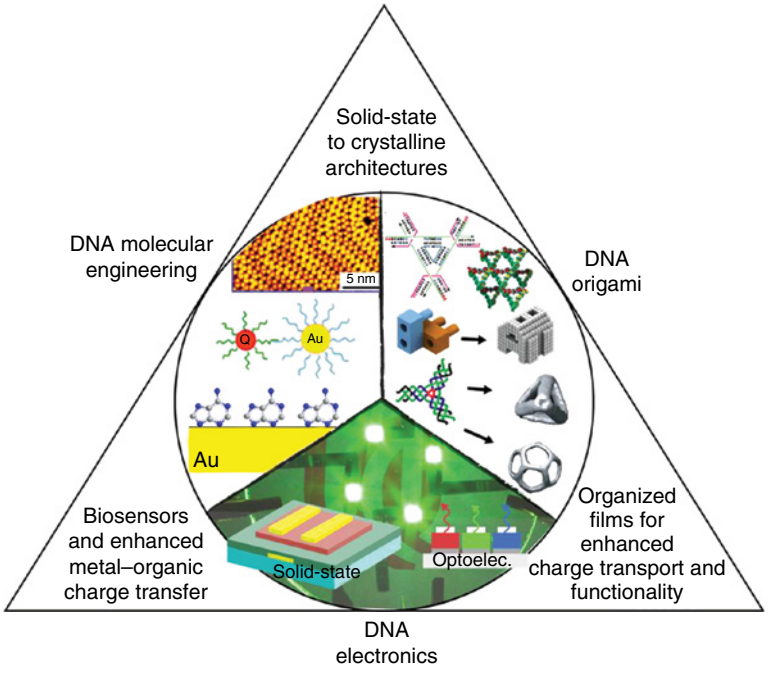

Figure 7.1 The circle encompasses the three major fields of DNA research in electronics and nanotechnology: (1) DNA origami – intermolecular bonding to form nanostructures [19–22]; (2) DNA molecular engineering – the interaction of DNA with non-DNA molecules [23–25]; and (3) DNA electronics – electronic properties in traditional solid-state devices [18]. The vertices of the triangle describe how the adjacent research fields relate to one another.

somewhat similar to DNA origami, but focusing on using DNA as a scaffold for bonds between nanoparticles. Molecular engineering also encompasses the interesting property of nucleic acid affinity for many metal electrodes, which has led to applications in biosensing and in improved metal/organic charge injection.

The vertices of the triangle in Figure 7.1 represent the fields of common interest between the three DNA-based research areas. DNA origami, for example, benefits the DNA electronics area by coupling known DNA electronic properties with self-assembled crystalline thin films to optimize device performance. DNA molecular engineering provides extensive knowledge in nucleic acid affinity to metal electrodes, which improves charge transfer between metal and organic materials and in turn creates improved biosensors. Finally, DNA molecular engineering, while very similar to DNA origami, incorporates additional functional materials, such as nanoparticles or quantum dots, into DNA scaffolds to expand material and application functionality. The triangle represents a rather simplistic view of DNA research, considering that there is an immeasurable amount of study done on the biopolymer, including research on chemical, material, genetic, and biological aspects. The discussion presented in this chapter is treated primarily from a device-oriented point of view that looks forward to applications of DNA science.

7.1.2 Natural and Artificial Synthesis Sources of Nucleic Acids

Natural DNA polymer is only 2–3 nm wide, but is composed of two conjoined nucleotide chains that can be billions of base pairs long. As illustrated in Figure 7.2, the two chains form a double-helix structure bound together by hydrogen bonds between nucleobases. Nucleotides are comprised of a phosphate group, a pentose, and a nitrogenous base (nucleobase). The DNA nucleobases are guanine (**G**), adenine (**A**), cytosine (**C**), and thymine (**T**). The ribonucleic acid (RNA) polymer, an important nucleotide chain for translating the DNA code into proteins, contains the bases **G**, **A**, **C**, and uracil (**U**). **G** has three hydrogen-bonding sites that pair with **C**, and **A** has two hydrogen-bonding sites that pair with either **T** or **U**.

Green electronics – the subject of this book – focuses on materials from environmentally responsible sources. Figure 7.3 lists a few of the natural and synthetic sources of DNA and nucleobases. DNA is found in the nucleus of every living cell, and can be extracted from plants and animals. Some sources have higher concentration of nucleic acids than others and it is easier to extract more DNA or nucleobases per volume. Salmon sperm, for example, is rich in DNA and has the added benefit of being a waste product of the fishing industry. The refining process begins by mechanically pulverizing the tissues, removing unwanted material by physical and chemical processes, combined with filtering and centrifugation to isolate pure DNA [26].

The nucleobases have historically been extracted from natural sources. Some non-mammalian sources such as wheat germ, bee pollen, and plants are known to be rich in certain bases [27–31]. The thymus, pancreas, and even bird feces are traditional sources from which bases are extracted by physical and chemical purification processes and then dried into a powder. Yeast naturally produces

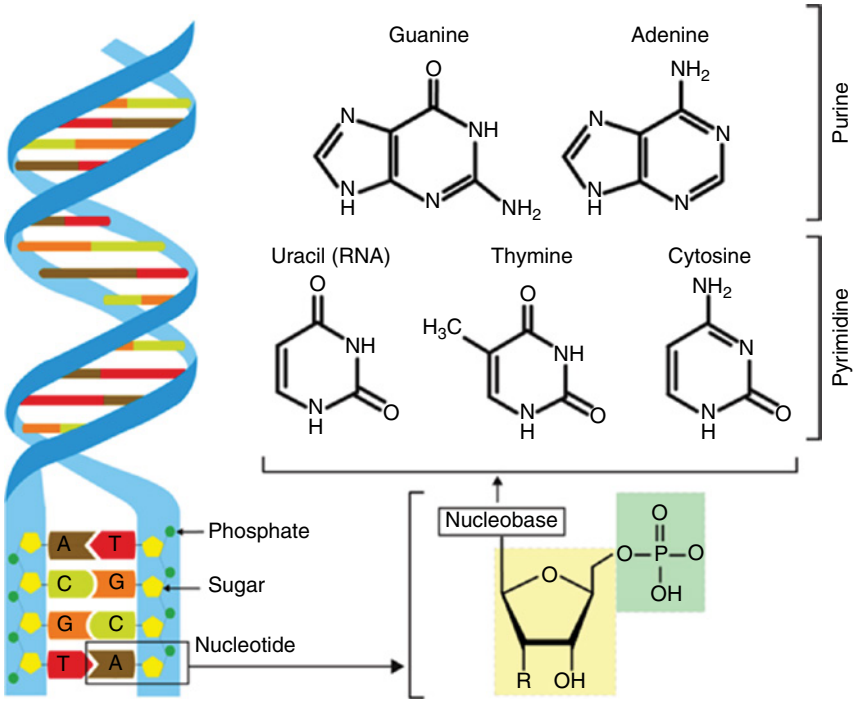

Figure 7.2 The DNA double helix consists of two interlocking and twisting chains of nucleotide units, each comprised of a sugar group, a phosphate group, and a nitrogen-containing nucleobase (either a pyrimidine or a purine). (Gomez *et al*. 2014 [18]. Reproduced with permission of John Wiley and Sons.)

	DNA	Nucleobase
Natural origin	Organ tissue Plant cells Salmon sperm	Biosynthesis (liver) Yeast Bee pollen Organ tissue Bird excrement Wheat germ
Synthetic	Solid phase synthesis Polymerase chain reaction (PCR) Molecular cloning	Abiotic reactions Fischer–Tropsch synthesis

Figure 7.3 Selected sources of natural and synthetic DNA and nucleobases.

phosphoribosyl pyrophosphate (PRPP), which is the precursor that catalyzes the synthesis of purines and pyrimidines [32, 33]. It is also known that the body metabolically produces the bases in the liver [27, 34].

Although natural sources are more desirable for green and sustainable electronics, nucleobases and DNA can also be created using synthetic processes.

Most of the bases can be derived from the Fischer–Tropsch synthesis by heating a gas mixture of CO, H_2, and CH_3 to 600 °C with a nickel–iron catalyst [35]. It also possible, although more hazardous, to create adenine from ammonia and hydrogen cyanide, as demonstrated from the work done on precursors to abiotic nucleic acids [36].

Naturally derived DNA is not always suitable for DNA nanotechnology, which requires sequence-specific strands. Oligonucleotide synthesis (a form of solid phase synthesis) has been a standard method for many years for constructing a particular DNA strand [37]. The polymerase chain reaction (PCR) is one of the most successful methods for replicating DNA strands from an existing template using an enzyme [38]. Another method, the so-called molecular cloning, can assemble DNA with cloning sites of plasmids or viral vectors in prokaryotic or eukaryotic sources [39]. While synthetic methods are available, extraction from natural sources offers the best pathway to produce large quantities of material that are relatively inexpensive and sustainable, and avoids hazardous precursors produced by artificial synthesis.

7.2 Nucleic Acids in Electronics

7.2.1 Introduction

The long DNA polymer has inspired early investigations of charge transport along its chain to adapt it as a nanowire [40]. Early studies also looked into DNA as a host for enhanced optical emission [41] of lumophores intercalated in the double-helix structure. The result was a wave of interest in using the material in organic electronics and intense investigation into DNA as an opto/electronic organic material [42]. Although attempts were made to deposit natural DNA salt (DNA^-–Na^+) into thin-film electronics, formation of uniform films from aqueous solutions was found to be difficult [43]. Therefore, the molecule was often complexed with cationic surfactants (e.g., CTAC cetyltrimethyl ammonium chloride) to its negatively charged backbone to form DNA–surfactant salts, such as DNA-–CTMA (cetyltrimethylammonium). The complexed chain could then be dissolved in alcohols and spin-coated [44].

There is a fundamental incompatibility between biomaterials and conventional organic molecules used in organic electronics, as pointed out by Solin and Inganäs [45]. Biomolecules have naturally evolved in a water-based environment and are hydrophilic, containing polar functional groups, whereas organic electronics generally use materials (polymers or small molecules) that have few polar groups and dissolve in organic solvents. A key question of both fundamental and practical importance is how the surfactant molecules alter the electronic as well as structural properties of the DNA, changing from being water soluble to organic solvent solubility, and then undergoing the critical "wet-to-dry" transition.

Interestingly, studies have indicated [46] that the DNA–surfactant complex in both wet (organic solvent solution) and dry (thin film) forms displayed chirality similar to that of DNA in aqueous form. This was explored by selecting combinations of surfactants and dye molecules that resulted in enhanced optical

characteristics. Both anionic (sulforhodamine SRh) and cationic (rhodamine perchlorate RhP) fluorescent dye molecules from the rhodamine family were found to be most likely embedded in the tails of the CTMA–surfactant molecules [47] radiating from the DNA chain rather than intercalated into the DNA double helix itself. A simplified model for this explanation is illustrated in Figure 7.4.

Early work with DNA–CTMA showed impressive versatility when incorporated as a dry film in many different types of devices, including OLEDs [42, 48], lasers [49], OFETs [50], and optical waveguides [42, 51]. However, the DNA–surfactant complex approach does present some complications in proceeding forward with next-generation devices: (i) the surfactant, a synthetic material, consists of a significant fraction of the overall complex, taking away from the goal

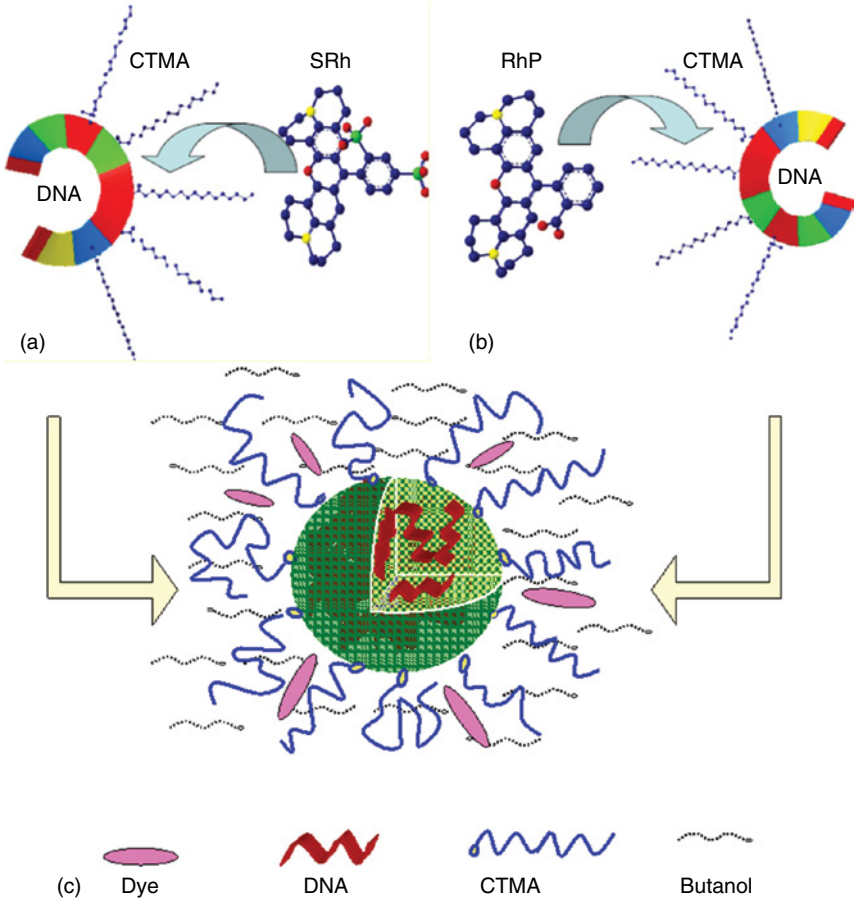

Figure 7.4 Proposed model for incorporation of (a) anionic (SRh) and (b) cationic (RhP) fluorescent dye molecules inside the DNA–surfactant (CTMA) polymer in organic solvent solution. (c) The final structure of the butanol in a micelle-like complex: DNA form together (green) and the dye (either SRh or RhP), intercalating between the CTMA strands on the outside. (You *et al*. 2009 [47]. Reproduced with permission of American Chemical Society.)

of all-natural devices; (ii) in terms of understanding and utilizing material characteristics for optimized device performance, the molecular complex makes it difficult to distinguish the electronic properties of the DNA polymer from those of the surfactant; (iii) thin-film fabrication is primarily limited to wet processing (e.g., spin-coating) in organic solvents; and (iv) the DNA complex fails to complement the working knowledge of the powerful techniques of DNA origami and molecular engineering that rely on affinity-based assembly rather than film formation of lipid films. This fourth point is especially pertinent to the future success of DNA electronics. DNA represents a unique class of organic materials that offers a potential of precise molecular control not typically offered by conventional organic electronics. Complexing the DNA with surfactants limits self-assembly properties. Retaining its ability to form well-ordered structures without the surfactant will be vital for DNA to flourish as an important material for nanotechnology and electronics.

Nucleobases, which are just beginning to emerge in organic electronics, may be able to provide more flexibility in material choice and properties. The nucleobases require no surfactant modification since they form high-quality thin films by thermal evaporation and readily integrate into typical organic electronic processes. In addition, nucleobases have a range of properties identified with its respective molecule, whereas in the case of DNA one has to resort to varying the polymer molecular weight and possibly the sequence of the polymer in order to modify charge transport and optical properties [52]. A discussion of the various known properties is presented in the next section.

7.2.2 Thin Film Properties

DNA–CTMA thin films have been well characterized, including their electrical, optical, and magnetic properties [8, 10, 12, 13]. DNA–CTMA is well known to be a good electron-blocking layer (EBL) and hole transporter in organic semiconductor devices owing to its energy levels. It has a high dielectric constant of $\kappa = 7.8$ at low frequencies (and up to $\kappa = 14$ in ceramic blends) [53] and a dielectric breakdown of 3–5 MV cm^{-1} (in sol–gel blends [54]), which has been used in capacitors and gate dielectrics. It has low optical loss in the visible range and near-IR communication wavelengths in waveguides [51].

The nucleobases have not been characterized as extensively as DNA but are rapidly proving to be a versatile set of materials for thin-film electronics. Table 7.1 summarizes many of their initial known properties. Dielectric constants range from 1.6 to 4.3 and breakdown values range from 0.9 to 3.5 MV cm^{-1}. Interestingly, **G** and **C** (with three hydrogen bonding sites) have higher dielectric constants, whereas **A** and **T** (with only two hydrogen bonding sites) have lower values [28]. The refractive index varies from 1.50 to 1.96 and temperature stability ranges from 260 to 465 °C. **G** has higher temperature stability (due to intermolecular hydrogen bonding) as well as refractive index, and **T** has both the lowest stability and refractive index [18]. Additional work needs to be done to determine conductivity of the nucleobases as thin films.

Atomic force microscopy (AFM) of thin films of the nucleobases reveals a diverse range of film quality. AFM images of 100 nm nucleobase films thermally

Table 7.1 Optoelectric properties of thin-film DNA and nucleobases for organic electronic devices.

Material	Orbitals (eV) [18, 48]		Energy gap (eV)	Dielectric constant[a]	Refractive index[b]	Thermal stability (°C)[c]	Hole mobility ($cm^2 V^{-1} s^{-1}$)	Dielectric breakdown field ($MV cm^{-1}$)
	HOMO	LUMO						
DNA–CTMA	5.6	0.9	4.7	7.8	1.54	250	0.001–0.01	3.0–3.5[d]
G	5.7	1.8	3.9	4.0	1.96	465	—	3.5
A	6.0	2.2	3.8	3.4	1.73	290	—	1.5
C	6.2	2.6	3.6	4.3	1.76	325	—	3.4
T	6.5	2.8	3.7	2.0	1.50	260	—	0.9
U	6.7	3.0	3.7	1.6	1.67	270	—	—
References	[17, 46]	[17, 46]		[18, 53]	[17, 24]	[18, 55]	[56]	[28, 54]

[a] At ~1 MHz.
[b] At 515 nm [18, 26].
[c] 95% remaining mass.
[d] Sol–gel.

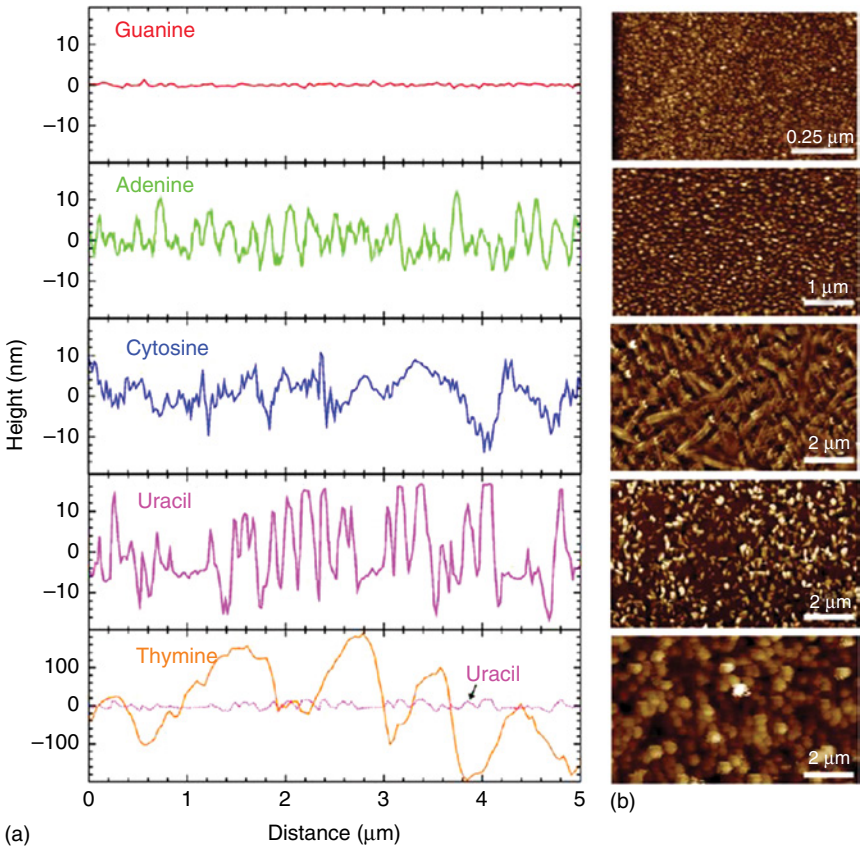

Figure 7.5 (a) Height distribution of nucleobase films sampled from corresponding AFM results and (b) AFM analysis of thin-film nucleobases (**G**, **A**, **C**, **U**, **T** from top to bottom, respectively) thermally evaporated to 100 nm on Si [57].

deposited on Si wafers are shown in Figure 7.5b. In order to compare the results, a cross-sectional view was created by sampling a 5 μm scan from each AFM image and the results plotted as vertical deflection versus horizontal distance in Figure 7.5a. The horizontal line scan was plotted on the same height scale, except for **T,** which is displayed in nearly 10 times larger in vertical range. The results show that the **G** film had the highest "quality" (i.e., lowest roughness) of the five bases with peak-to-peak range of under 1 nm, while the roughness of **T** was 100–1000 times greater than that of the other bases.

The energy levels of the nucleic acids cover a wide range of HOMO (highest occupied molecular orbital) and LUMO (lowest unoccupied molecular orbital) values, enabling selection for optimized electron and hole transport in thin films. As shown in Figure 7.6, ITO, Au, and PEDOT have higher work functions (4.7–5.1 eV) and are often used as anodes for hole injection. Al electrodes coated with LiF have a lower work function (4.1–3.1 eV) and are typically used as cathodes for electron injection. In comparison, DNA–CTMA has low HOMO/LUMO levels of 5.6/0.9 eV, resulting in its successful electron-blocking/hole transport ability in OLEDs.

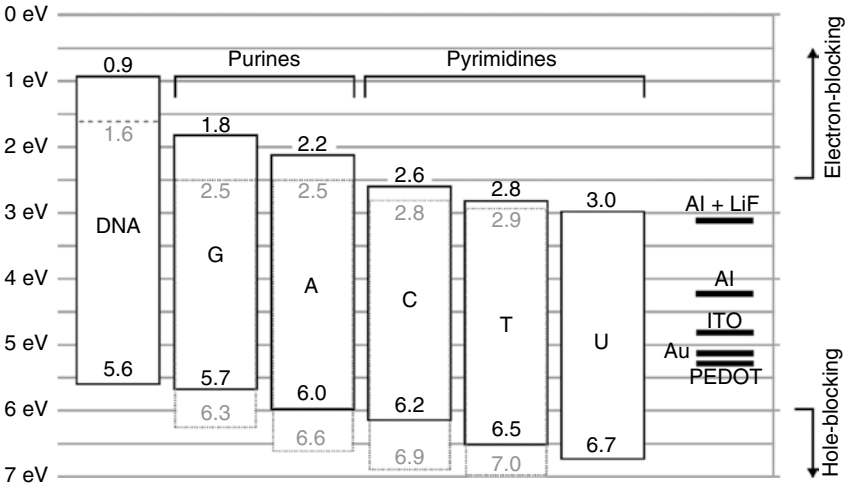

Figure 7.6 Energy levels of DNA and nucleobases showing that DNA and the purines are hole transporters while the pyrimidines have high energy levels and have electron transport abilities. Solid lines [18, 58] and dotted gray lines [59, 60] show two reported studies, as well as for DNA [48, 61].

The nucleobases have recently been explored for charge transport in thin film OLEDs demonstrating a large range of energy levels, and flexibility for charge transport control. The HOMO–LUMO energy gaps of the nucleobases are uniformly wide (3.6–3.9 eV), while the ionization potential (HOMO) increases monotonically, **G** < **A** < **C** < **T** < **U**, as seen in Figure 7.6. Consequently, **G** with the lowest ionization potential (HOMO) of 5.7 eV and an electron affinity (LUMO) of 1.8 eV is a strong hole acceptor while prohibiting electron transport. On the other hand, **U** has the highest ionization potential of 6.7 eV and the highest electron affinity of 3.0 eV, thus being a strong electron acceptor while prohibiting hole transport [18, 58]. Some variations in the reported studies exist [59, 62–66], most likely due to different measurement techniques and conditions, but the general trend among all studies is consistent. The introduction of the nucleobases has expanded the use of nucleic acids to both electron and hole transport (and blocking), offering a wide range of options for future device designs.

7.2.3 Nucleic Acids in Organic Electronic Devices

The impact of DNA-based materials in organic electronics has been surprisingly broad. This section will attempt to highlight several important devices, emphasizing some of the more recent devices and the use of nucleobases that would not have been included in past reviews.

Most of the studies and devices of DNA electronics originate from an enduring effort to verify DNA conductivity. The DNA molecule size and programmability leads it to be ideal for nanostructure electronics (see Section 7.3 for further discussion on DNA nanostructures). The first step in nanoelectronics is confirming long-range electronic conductivity along the DNA axis. It is beneficial to briefly discuss here the persevering efforts to elucidate the conduction mechanisms.

Early theoretical models [67] suggested that DNA is effectively a conducting wire and that there is sufficient delocalization to enable transport of charge over several nucleobase base pairs. It is generally believed that the conduction is via positive charge with short-range processes [68, 69]. The guanine molecule, having the highest energy HOMO, is widely accepted to be the primary carrier of the holes [69–71]. Theoretical simulation of a guanine-rich strand between two Au electrodes in Figure 7.7 shows the highest rate of hole hopping along strong localized orbitals from **G**. Despite this widely accepted model of charge transport along **G**, long-range electron transport has proved difficult to observe for a variety of reasons, resulting in a field saturated with contradictory or irreproducible results.

Many factors affect DNA–electron interactions, including electrochemical interactions with its environment and the substrates. One of the biggest difficulties lies in the intrinsic disorder and fragile nature of the native molecule with, apparently, even the slightest deformation skewing results thoroughly, as demonstrated by Heim *et al.* [72, 73]. Such changes are known to affect electronic properties from a conductor to insulator and certainly make it difficult to control any amount of current over any distance [74]. To further complicate matters, other studies [56, 75] suggested that the mechanisms of bulk material transport compared to single DNA strand are allegedly different.

In the reports, thin film layers of DNA–CTMA mobility values from ~0.001 to 0.01 $cm^2 V^{-1} s^{-1}$ were measured using time-of-flight techniques. The results suggested that the preferred routes of charge transport [75] was along the DNA backbone at low electric fields and laterally through the CTMA side-chains at high electric fields, instead of hole hopping along the nucleic acids as has typically been predicted.

A good overview of the complex nature of DNA charge transport chemistry has been summarized by Genereux and Barton [11]. A thorough review of the different reports since 2006 and comments on DNA conductivity is presented by

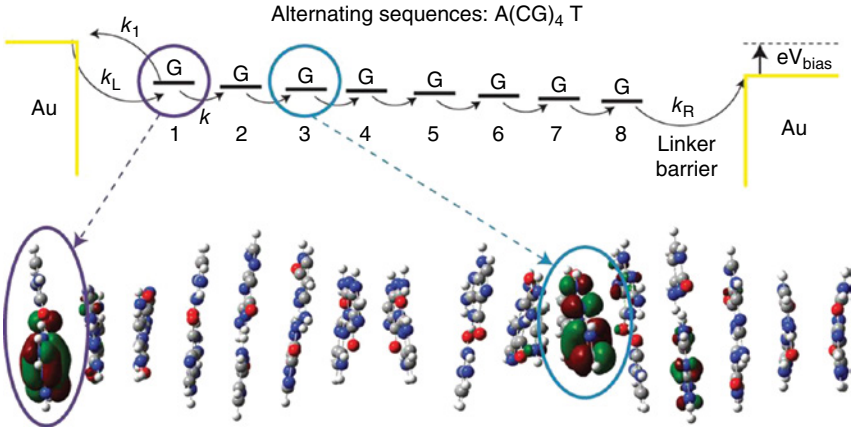

Figure 7.7 Hole hopping along HOMOs of the G bases in DNA contacted between Au electrodes in an electric field due to strong localized orbital levels in G. The hole transfer rates between G–G sites and G-electrodes are represented by constants *k*. (Xiang *et al*. 2015 [71]. Reprinted with permission of Macmillan Publishers Ltd.)

Taniguchi and Kawai [10]. The report concludes that conductivity results (ranging from insulating to semiconducting, and possibly metallic) depend on water content, base sequence, experimental environments, and doping of the DNA material being utilized. The large discrepancy and the difficulty in measuring conductivity have caused efforts to become stalemated over time.

A recent breakthrough by Livshits *et al.* [74] focuses on addressing many of the longstanding problems and may revive the field. They employ guanine-quadruplex DNA (G4-DNA), which is a guanine-only motif that forms a planar stacking. The guanine tetrad has greater rigidity than native DNA base pairs, and is thus able to withstand deformation. Gold electrodes with very sharp edge definition were evaporated using stencil lithography onto G4-DNA immobilized on an insulating (mica) surface. A conducting tip AFM simultaneously imaged and measured current along G4-DNA axis. An asymmetric current–voltage (*I–V*) characteristic was observed, with current decreasing (from ~100 to 10 pA) with increasing distance (from ~20 to 70 nm) between AFM tip and Au electrode.

The result showed an unequivocal demonstration of charge transport. Well-established *I–V* results in tandem with modeling indicate electronic transport by thermally activated hopping from one tetrad to the next, similar to mechanisms in conducting polymers. Although much work still remains in implementing more complex electrical circuits, the work offers a reliable indication of long range conductivity using nucleobases, which is a significant step forward in continuing the work on DNA-based molecular electronics.

In parallel with DNA conductivity over the years, nucleic acids have been studied in thin film devices with good success. The remaining section highlights DNA and nucleic acid thin films used in organic solid-state devices. DNA and nucleobases have been incorporated in many different components of OFETs, including the dielectric, charge injection, and semiconductor layers. Very early work used deoxyguanosine, a single-stranded DNA polymer with a **G**-only base sequence, deposited as a self-assembled p-channel for OFETs [76, 77]. This is significant because **G** is known to be a good hole transporter, and much work has been done investigating supramolecular architectures of guanosine derivatives (see review by Davis and Spada [78]). Unfortunately, no follow-up research with OFET channels using deoxyguanosine has been reported, but there may be new promise to explore this further, especially with the recent G4-DNA conduction reported by Livshits *et al.* [74].

DNA gate dielectrics has been common in OFETs since 2006. Some of the first devices contained DNA–CTMA as the gate dielectric to make memory elements, and OFETs with combined DNA–CTMA and Al_2O_3 gates that reduced hysteresis with relatively good turn-on [50]. An interesting approach [79] modified DNA with photoreactive side-chains that can result in cross-linked films upon UV irradiation, thereby changing the solubility and dielectric properties as seen in Figure 7.8. Cross-linking DNA–CTMA dielectric layers using a chemical agent is another approach [80] for improving the hysteresis of C_{60}-based OFETs. Another reported [53] modification is the formation of hybrid DNA films that incorporate high dielectric constant ceramics (such as $BaTiO_3$ and TiO_2) in order to improve the electrical properties of resultant devices. Another example of a photoactive layer incorporating the biopolymer is the DNA–CTMA:Ag nanocomposite displaying excellent memory switching effects,

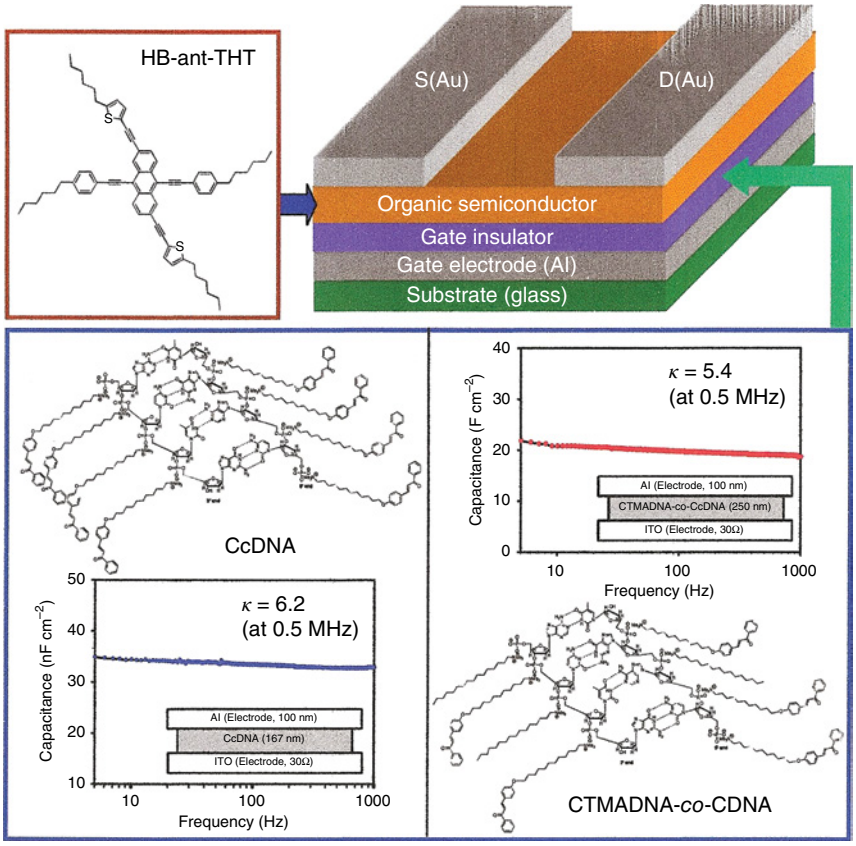

Figure 7.8 Two different DNA gate dielectrics in OTFTs using either CcDNA or CTMADNA-*co*-CcDNA (CTMA:chalcone = 3 : 7). The complexes were cross-linked under UV irradiation resulting in better gate insulations and higher field-effect mobilities. (Kim *et al*. 2010 [79]. Reproduced with permission of AIP Publishing.)

caused by the metallic affinity of DNA that induced nanoparticle synthesis upon light irradiation [81].

While DNA as a dielectric has been relatively useful, the incorporation of additional components and processes (such as surfactants, metallic or ceramic particles, cross-linking) adds complexity to the material processing and the fabrication of the eventual device. In addition, mobile ionic charges in DNA–surfactant molecules are thought [50, 80] to cause hysteresis in the electrical characteristics of OFETs. By comparison, nucleobases are small molecules that can be readily purified and produce consistent thin films by thermal evaporation. The use of nucleobases as dielectric layers in "all-natural" OFETs (see Figure 7.9a) was first demonstrated [28] by Irimia-Vladu *et al.* who reported breakdown fields of NB films ranging from ~1 to 4 MV cm^{-1}.

Lee *et al.* [59] used guanine to improve the hysteresis in inorganic semiconducting oxide (IGZO) thin-film FETs. In this case the guanine is embedded within an inorganic (Al_2O_3) dielectric layer deposited by atomic layer deposition

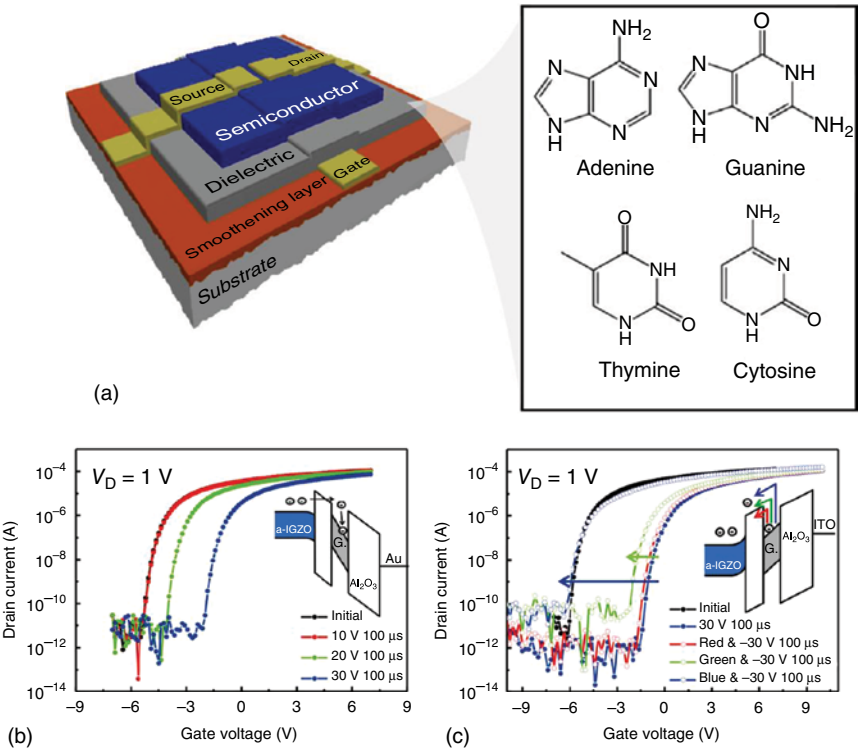

Figure 7.9 Use of nucleobases as dielectric layer in field-effect transistors: (a) dielectric layers in all-natural OFETs (Irimia-Vladu *et al*. 2010 [28]. Reproduced with permission of Elsevier.); (b) guanine in inorganic oxide semiconductor FET embedded as an interlayer within the inorganic dielectric (Al_2O_3) to improve turn-on voltage and hysteresis performance and trap charges at high electric fields (Lee *et al*. 2014 [59]. Reproduced with permission of American Chemical Society.); and (c) charges can be recovered upon exposure to high-energy (blue) photons. (Irimia-Vladu *et al*. 2010 [28]. Reproduced with permission of Elsevier.)

(ALD). The guanine is thought to getter H atoms produced during the ALD growth reaction, resulting in a more electrically stable FET operation. Interestingly, charge trapping (using voltage pulses) and de-trapping (using incident photons of sufficient energy) shown in Figure 7.9b,c, respectively, enable the use of these FETs in programmable applications. Subsequent work from the group also showed hybrid guanine/inorganic dielectric reported to improve charge injection performance [82] in nonvolatile memory inorganic (MoS_2 nanosheet) FETs offering excellent passivation and bias stress stabilization [83].

A major component of the research in DNA electronics has been related to its use in OLEDs. DNA–CTMA inserted into fluorescent OLEDs was initially reported by Hirata *et al.* [44] who investigated charge transport through several device structures and determined that the DNA layer preferentially transports holes. An OLED device with a DNA–CTMA layer was reported by Hagen *et al.* [48] to significantly improve both OLED efficiency and luminance. The performance increase was attributed [48] to the low electron affinity levels of the DNA

serving as an EBL to confine charge to the emitting layer. Nearly ideal performance was reported [42] by using DNA EBLs in phosphorescent OLEDs: maximum brightness of ~100 000 cd m^{-2} at 13 V (632 mA cm^{-2}); maximum current efficiency of ~90 cd A^{-1}; and luminous efficiency of 55 lm W^{-1} at 5 V (0.11 mA cm^{-2}). The same electron-blocking function for DNA layers was reported [84–86] in OLEDs utilizing polymer light-emitting layers as opposed to previously reported small molecule OLEDs.

All of these reports used similar methods of electron-blocking to increase emission efficiency and similar wet processing (spin-coating) to form DNA–CTMA films. DNA-CTMA deposited thin films by vacuum thermal evaporation have also been reported [55] in fluorescent OLEDs. Surprisingly, given the large molecular weight of the DNA-CTMA polymer, the method resulted in a 15 nm electron-blocking layer that also improved internal efficiency.

Maybe the most challenging and potentially most significant approach is to utilize the DNA film as the light-emitting layer, with DNA serving as the host material for lumophores. Photoluminescence from Eu complexes [55] incorporated into DNA films and electroluminescence from Ru complexes [87, 88] are among the few results that have been reported to date for this approach. Nakamura *et al.* have used [88] a DNA complex that aids in charge transfer from a phosphorescent emission to a fluorescent molecule, resulting in a voltage controlled color tunable OLED. In addition, Cho *et al.* have functionalized [89] DNA with a carbazolyl ammonium lipid as the triplet host material for a phosphorescent material system. The complexed host aids in energy transfer of triplet spin states in phosphorescent systems to emit light.

Interesting results have also been reported with organic dye molecules in DNA films and fibers. Yu *et al.* have reported [49] photoluminescence and distributed feedback lasing from sulforhodamine molecules incorporated in a DNA–CTMA layer formed on a SiO_2/Si grating. DNA–CTMA fibers formed by electrospinning and incorporating dye molecules have been reported [90] to produce stronger photoluminescence compared to equivalent thin films. Enhancement in the emission of various luminescent particles (such as quantum dots [91] and nanorods [92]) from the presence of DNA charge control layers has also been reported. Just recently, DNA was used to guide Alq3 rod crystallization in OLEDs, leveraging the DNA recognition sites to trigger photoluminescent enhancements by Alq3 [93]. These studies represent a new direction for DNA-based photonic materials, using DNA to self-assemble organic semiconductors or for new biosensor applications (see Section 7.3).

Finally, the most recent report in DNA-based luminescence comes from Reddy and Park [94], in which they complex curcumin, a natural phosphor, to CTMA in a biocrystalline form. The curcumin chromophore then readily binds to DNA. It is suggested that aligning with the DNA helix prevents aggregation-induced quenching effects. A quantum yield of 62% is achieved, making it a very promising green material for future OLEDs.

Use of DNA is emerging in other devices. Solar cells [95–97] are the most recent addition of devices benefiting from DNA. A perovskite solar cell [95] that employed DNA–CTMA reached a power conversion efficiency of 15.86%, with stable operation over 50 days in air. The mechanism relies on the electron-blocking

capability of the biopolymer, similar to its primary function in OLEDs. The results regarding biopolymers in solar cells require more attention, especially in light of the recent results with nucleobases in OLEDs (see below).

Other devices include an electrochemical supercapacitor, where the DNA is coated with a monomer of the cationic compound EDOT-N, which is a PEDOT derivative (3,4-ethylenedioxythiophene). EDOT-N binds to the negatively charged DNA backbone, intercalating into the helix structure, and self-polymerizing (using ammonium persulfate) *in situ.* The complex is formed into dry film electrodes with high porosity and large surface area. The electrode was used in an electrochemical supercapacitor by placing it in an electrolyte medium, resulting in a charge storage capacity of $32\,F\,g^{-1}$ [98].

While DNA has been investigated for OLEDs for approximately a decade, the DNA nucleobases have just recently made their appearance in OLEDs. Nucleobases have expanded the list of available materials for OLEDs with the advantage of diverse roles for each base layer. **A** and **T** have shown to have high performance as EBLs, resulting in higher efficiency and luminance performance (even exceeding previous DNA results), when used as very thin EBLs and hole transport layers (HTLs) [99]. Figure 7.10 shows results of replacing the N,N′-Di(1-naphthyl)-N,N′-diphenyl-(1,1′-biphenyl)-4,4′-diamine (NPB) and Bathocuproine (BCP) layers in the OLED structure, the EBL and hole-blocking layer (HBL) respectively, with nucleobases. The current photoemission and luminance characteristics of the resulting OLEDs follow the trend of the energy levels (see Section 7.2.2) of the nucleobases, namely **G** and **A** as EBL/HTLs and the pyrimidines **C**, **T**, and **U** as a HBL and electron transfer layer (ETL). These results greatly expand the utility of the nucleic acids and show that common organic semiconductors can be replaced with natural materials.

7.3 Nucleic Acids in Nanotechnology

7.3.1 Introduction

DNA nanotechnology leverages the self-assembling properties of DNA to build 2D and 3D nanostructures or nanomechanical devices. The discipline is often called DNA origami because of its intrinsic ability to fold onto itself with hairpin turns. Structural DNA nanotechnology has been most aptly described by Seeman, the pioneer of DNA origami for nearly 30 years, as meeting the challenge of putting "what you want where you want it in three dimensions (3D) when you want it there" [100]. Reif and LaBean groups at Duke university, responsible for many DNA assemblies, motors, and DNA computing since its early days, astutely describe DNA as a "smart glue" that can organize objects in 3D space and replicate a desired structure limitlessly for "massive parallelism" [101]. DNA nanotechnology forms complex structures by folding on itself with affinity-based nucleobases and creates structural rigidity with the phosphate-pentose backbone. The nanoscale structures have progressed beyond simple unit blocks and have emerged into applications for scaffolds and nanoscale tools [15, 101]. Figure 7.11 is based on a review [7] of the field that illustrates the two

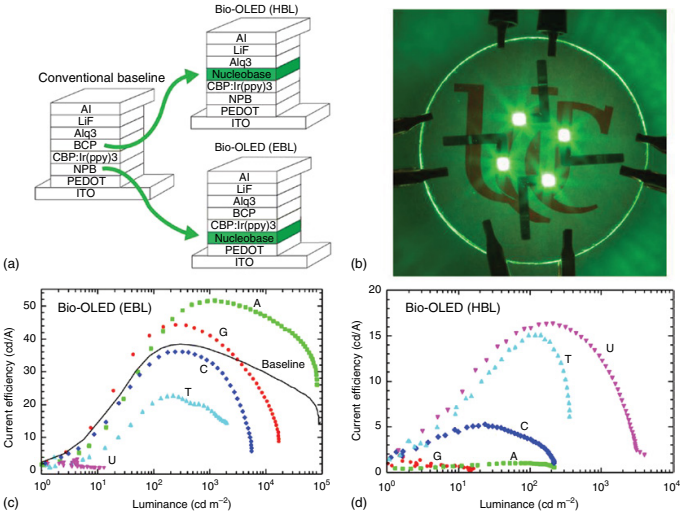

Figure 7.10 Use of nucleobases in OLED structures: (a) replacement of the HTL/EBL (NPB) and HBL (BCP) layer with nucleobases; (b) photograph of an operating OLED containing adenine EBL; (c) current emission efficiency versus luminance of the EBL-OLED showing **A** and **G** as good EBLs and of the HBL-OLED showing **T** and **U** as good HBLs (d). (Gomez *et al*. 2014 [18]. Reproduced with permission of John Wiley and Sons.)

primary approaches to DNA nanotechnology: (i) hybridization-based DNA that weaves DNA strands in pattern to create increasingly complex structures and (ii) nanoparticle-template DNA that covalently bonds nanoparticles to DNA and uses DNA as the linker to other nanoparticles.

As Figure 7.11 shows, the two major branches of DNA nanotechnology strive to increase the order and functionality of the material from simpler units. The units then repeat and join together to form 2D scaffolds and 3D lattices that eventually create functional materials. It is envisioned that the highly ordered and programmable DNA molecular arrangements will have broad applicability once fully matured. While a few applications in biosensors (Section 7.4.3) have emerged, the field has been met with great challenges. A recent review by Jones *et al*. [7] has summarized the current status of DNA nanotechnology and discussed motivation for future exploration. After many years of effort, the field has developed unfathomable precision in atomic control. However, the article acknowledges that "the hybridization-based and nanoparticle-templated subfields remain relatively isolated, with very few examples of overlap between disciplines" [7]. The authors discuss that the field has been primarily focused on controlling material at the smallest scale and synthesizing intricate nanostructures. Historically, however,

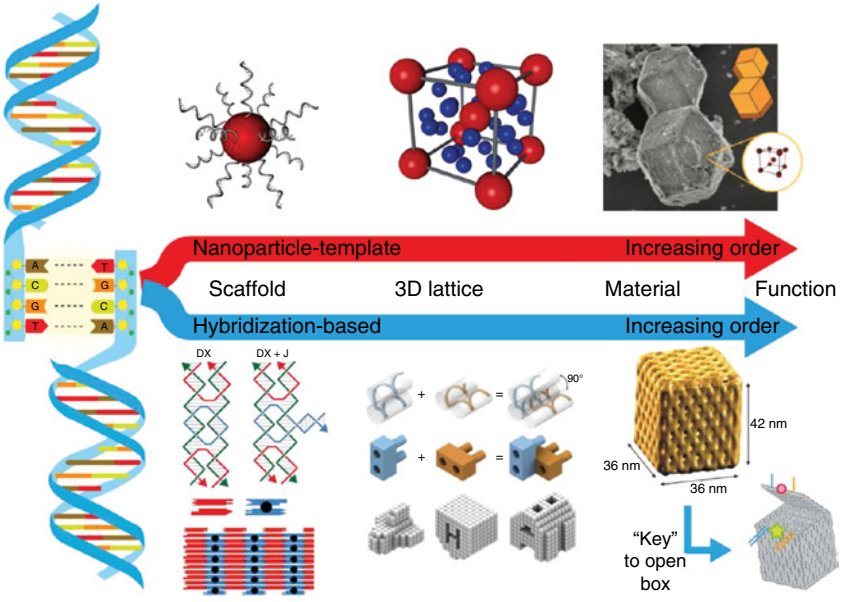

Figure 7.11 DNA nanotechnology based on sticky end DNA diverged into two fields: nanoparticle-template and hybridization-based lattice bonding. Nanoparticle-template uses DNA bound to nanoparticles to join to other nanoparticles. Hybridization-based DNA relies on sticky ends and crossovers (DNA weaving) to create rigid shapes and structures with other DNA polymers. In each respective subfield, the increasing order trend creates more functional superstructures. These two approaches have allowed a diverse set of programmable materials available for researchers in nanotechnology. (Figure adapted with permission from [7, 18, 20, 100, 102–105].)

the lasting success of nanostructures eventually depends on interaction with the macro-world.

Interfacing DNA nanotechnology with existing DNA electronics could utilize atomic manipulation to provide precise control over charge transport and device functionality. There have been a few examples of DNA origami in electronics, but the field is largely unexplored and has the potential to produce extraordinary and dynamic electronic manipulation based on highly ordered systems, a development similar to the history of inorganic semiconductors and devices.

7.3.2 DNA Nanotechnology

Both branches rely on DNA "sticky ends," which are short single-stranded protrusions from the end of the DNA polymer that bind to another sequence, either in the same strand or in a different single DNA strand, shown on the left side of Figure 7.11. This well-known technique, established from plasmid research, relies on exposing a portion of one strand of the end of a double DNA strand with the enzyme endonuclease, so that the nucleobases' affinity may result in binding to another exposed DNA strand containing the complementary sequences. Manipulating DNA is incredibly precise with well-established techniques of elongating, shortening, or otherwise modifying the strand [106]. The complementary exposed sequences stick together like Velcro® to form the glue for large superstructures.

Basic DNA origami requires the correct "sticky end" sequences and rigid structures formed by carefully placed crossovers. Crossovers are weavings of two single DNA strands that overlap and often bind together at a complimentary node. Once a basic unit is established, it is often easily repeated to create a much larger lattice. The DX (double crossover) lattice was one of the first DNA nanostructures that wove several complementary DNA strands together to provide structural integrity [104, 107]. It consists of two double helices that switch their connectivity from one helix to another to form a basic building block that can expand in both the X and Y directions. More complex variations have been made, such as the (TX) triple crossover [108]. The crossovers provide the rigidity, while the shape is created by the placement of the sticky ends. The tensegrity (word derived from "tension" and "integrity" [14]) triangle is an example of a 3D motif with extending sticky ends designed to link to itself [19, 22]. Unlike the DX motif, one of the arms is not coplanar and can create rhombohedral lattices.

To shift from a scaffold to a 3D lattice requires further rigidity. The three-point star is a complex structure created from four different crossover strands [21]. The unit binds to itself at all points and basic 3D shapes are readily formed and can be combined in several different arrangements to create polyhedral wireframes. A different approach uses "DNA bricks" that are single 32-nucleotide strands with four eight-base-pair interactions between bricks [20]. Each brick contains a 90° bend in the strand with a tail that connects with adjacent bricks in a hole and peg (Lego-like) model. Each brick can attach horizontally or vertically with its neighbors to continue construction in all dimensions. The DNA bricks form steps and cavities that have been shown to produce over 100 assortments of 3D structures, including the alphabet, symbols, and figurines with several

nanometer resolution. The DNA base sequence can be determined and synthesized resulting in a traceable and programmable system with precise control and predictable structures. The practice has become remarkably adroit at forming nanostructures, such as pillars, blocks, lattices, and even "smiley faces" with nanometer resolution [109].

Once 3D structure capability is established, more advanced materials and functions are possible. DNA origami has the advantage of motion through binding and releasing strands with enzymes to create nanomechanical motors [110] and structures that assemble and even "walk" [111–113]. Figure 7.11 shows an example of a DNA origami box that opens when a molecular "key" unlatches the structure [105], creating a possible drug delivery system. Placement, construction, and movement put the field in a position of developing interactive superstructures and dynamic systems. The long-term goals of the field are widespread, with many highlighted in the review article by Pinheiro *et al.* [15] including artificial cells, applications in cellular biophysics, and improved medical diagnostics and therapeutics.

The other main approach of DNA nanotechnology uses nanoparticle-templated DNA bonds. Instead of folding the DNA onto itself to form structures with the nucleotide chains, DNA oligonucleotides are bound to nanoparticles (such as Au nanoparticles) by strong interactions with the nucleobases and the gold surfaces or by functionalization. DNA polymers attached to these nanoparticles bind together with other template DNA and create ordered lattices of particles that otherwise would not be able to bind together. As the complexity increases, the material can be used in biosensors that bind to a variety of analytics [114–116] (see Section 7.4.3) and new materials that bind together with predictable DNA bonding instead of covalent interactions [102, 103, 117]. The hybridization and interaction of DNA with nanoparticles and metal to nucleic acid interactions, described in this chapter as DNA molecular engineering, is discussed in more detail in Section 7.4.

A very interesting application relevant to this chapter is the possible combination of DNA energy transfer and photonics. DNA origami could allow us to create complex circuitry with interconnected superstructures. Figure 7.12 shows a conceptual device [15] incorporating mechanisms of many components that have been independently considered, either theoretically or experimentally. A futuristic, but not unrealistic, "pick and place" system will require several different fields of collaboration. Functionalized DNA molecules provide tools for intended applications such as light harvesting with plasmonics; DNA origami assembles the structures in the precise locations while DNA organic electronics offers the knowledge of charge transfer.

7.3.3 Wet-to-Dry Transition

One challenging aspect of DNA origami is that it is formed in an aqueous solution under time-consuming annealing processes. In general, aqueous solutions are deleterious to most thin-film device processing and prevent direct application of conventional DNA constructs. As introduced in Section 7.2.1,

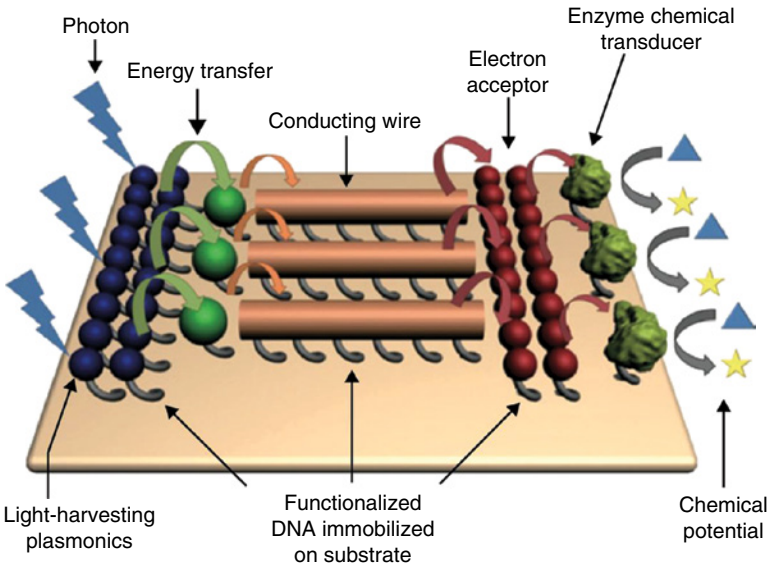

Figure 7.12 A conceptual design showing a cluster of DNA nanostructure units positioned by lattice networks and affinity bonding and functionalized by photonic molecular circuits or charge transfer/transducers. The modular design could be used as the basis for a variety of functions that could be quickly programmed and self-assembled, such as light harvesting, sensors, and chemical transducers. (Pinheiro *et al*. 2011 [15]. Reproduced with permission of Nature Publishing Group.)

DNA in aqueous solutions and thin films formed from DNA–surfactant organic solvent solutions have many similarities, thus providing a path for incorporation of crystalline DNA films. Scalability and practicality are also important aspects that need to be carefully considered, as design of even the smallest structure requires elaborate planning. There is ample opportunity to explore how such an ordered structure affects charge transport and functionality, but as yet there are few investigations to introduce DNA origami into solid-state electronics for green electronics.

Initial steps toward higher order systems in thin films could begin with DNA–CTMA. As shown in Figure 7.13a, Finch *et al.* have created [118] a wagon wheel structure of DNA bound with CTMA using DNA with sticky ends that binds to itself circularly. Upon drying, the wagon wheels retain their shape. Similarly, Figure 7.13b shows a DNA thin-film honeycomb structure created by Sun *et al.* [120] during the wet-to-dry transition. This is accomplished by DNA–surfactants and by slowly evaporating the solution to form honeycomb crystallites. Although the thin film electronic properties have not been studied, the fabrication process could be amenable to thin electronic films, while employing the relatively well-known DNA–CTMA molecules.

A polymer solar cell was reported [97] incorporating the two-dimensional DX-tile-based lattice as one of the layers. The polymer electrode, PEDOT:PSS, is dispersible in water and therefore a more involved method is required to get the

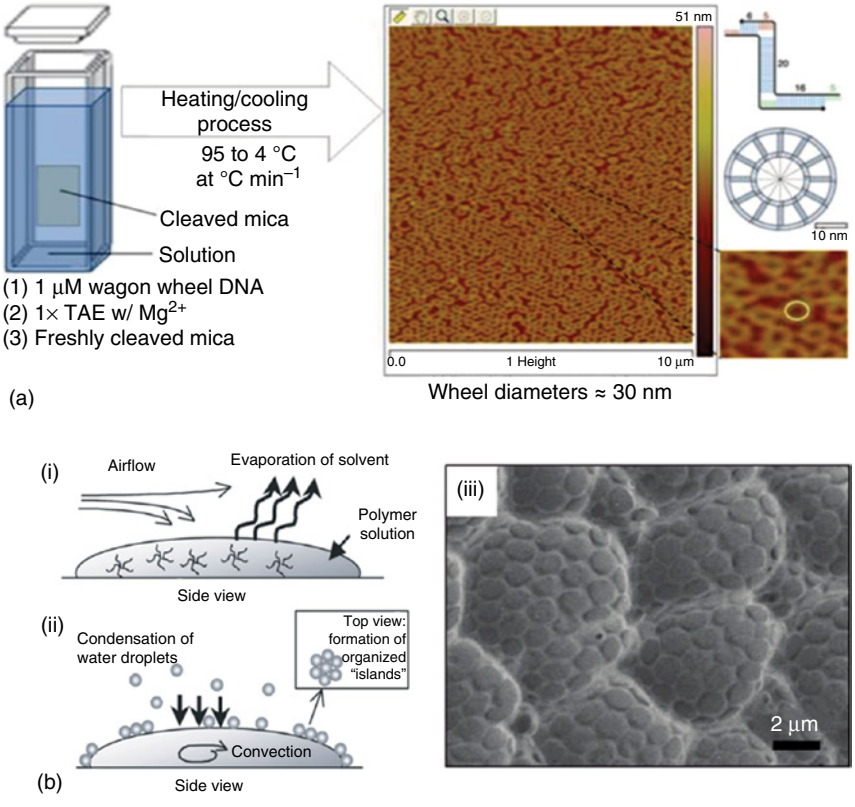

Figure 7.13 Self-arranged films that form without complex origami when transitioning from wet solutions to dry thin films [118, 119]. (a) Wagon wheel structure of DNA–CTMA circularly binding to its opposite sticky ends. (Gajria *et al*. 2011 [119]. Reproduced with permission of American Chemical Society.) (b) Gajria [119] reviews a DNA thin-film honeycomb structure created by Sun *et al*. where DNA–surfactant honeycomb crystallites are formed by controlled evaporation and condensation. (Sun *et al*. 2009 [120]. Reproduced with permission of John Wiley and Sons.)

nominally water-based DNA lattice to deposit on top. Lee *et al.* describe a dry–wet method in which the lattice was first formed in a DX configuration in a $1 \times \text{TAE/Mg}^{2+}$ buffer. The solution was centrifuged until the water evaporated and a dry DNA pellet was formed. The dry DNA DX pellet could be reformed in chlorobenzene, and the solution was dropped onto the PEDOT and annealed to leave behind a well-formed DX lattice as shown in Figure 7.14. The DNA lattice directs hole transport from the active region and blocks electrons to improve device efficiency by 10%, similar to many DNA OLED configurations. While no investigation was reported on the efficacy of the 2D lattice compared to non-latticed DNA, the work provides an effective method to exploring DNA lattices in traditional organic devices.

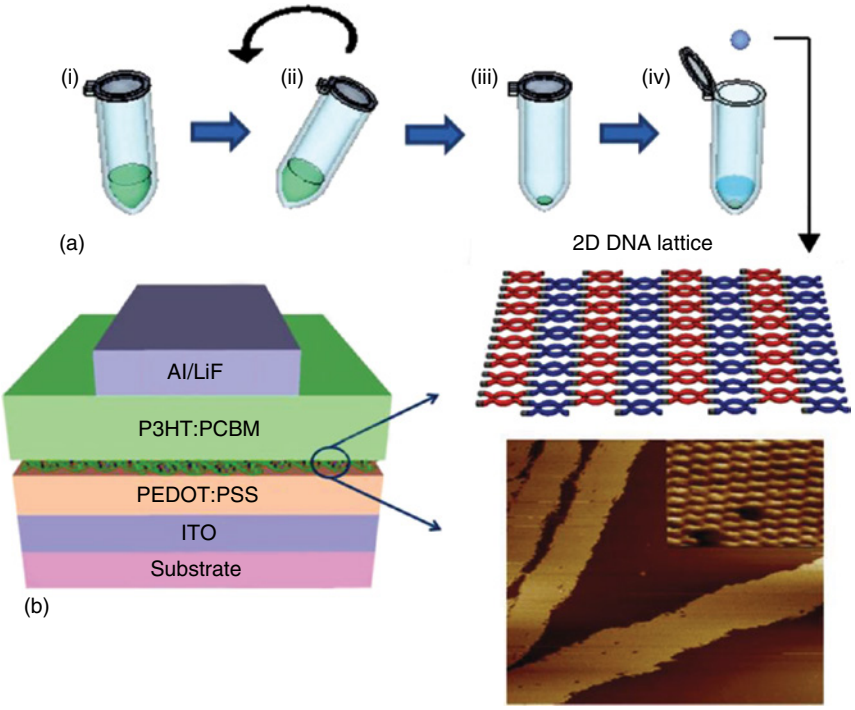

Figure 7.14 (a) Restoration of the DNA lattice into a thin film by dry–wet centrifugation processing. (b) Reconstructed DNA lattices deposited as a layer into thin-film solar cells as an electron-blocking layer. (Lee *et al*. 2011 [97]. Reproduced with permission of IOP Publishing.)

7.4 DNA Molecular Engineering

7.4.1 Introduction

The discussion on the final DNA research category for this chapter is the so-called DNA molecular engineering. DNA hybridization origami (blue section of the flow chart in Figure 7.11) is considered a separate category, primarily involving bonding of DNA strands to each other. The nanoparticle-templated DNA bonds (red section of the flow chart in Figure 7.11) are considered as part of the larger field of DNA molecular engineering, focusing on heterogeneous bonds and affinities between DNA and other materials. Within the field of DNA molecular engineering, DNA strands can be immobilized to different metallic or ionic particles and used as a template to "bond" different molecules together through a DNA linkage. Metal–nucleobase interaction (Section 7.4.2) directed by metal surfaces is also discussed.

DNA strands typically bind to nanoparticles such as quantum dots or gold nanoparticles by terminating one of the ends with either a thiol or a disulfide group causing the DNA to hybridize onto the surface with monolayer and orientation control [106]. Once the DNA strand is bound to the particle, the other end

of the DNA has a "sticky end" that is used to link to other DNA-bound particles. The DNA strands create a crystalline lattice that can control orientation, size, and frequency by substituting conventional atomic bonds with DNA links. Unlike DNA origami, intertwining strands are not necessary, since the inorganic core particles form the lattice and provide rigidity, but must follow several design rules described by Macfarlane *et al.* [103]. Since traditional molecular forces, such as electrostatic or covalent bonding, are replaced with DNA interconnection, the command over molecule placements can change the thermodynamic properties of the lattice. This could lead to new lattice arrangements that could have great potential in new material science and devices.

While much work is still necessary to bring DNA molecular engineering approach from its stable aqueous environment into traditional thin-film electronics, the vast amount of possible materials could have broad implications for electronics. Tan *et al.* [121] presents an excellent review of the field, particularly for plasmonic nanostructures templated with DNA. Gang and Tkachenko [122] also show some of the most significant achievements and challenges in the field. The field has been growing rapidly by demonstrating a growing array of structures from simple nanospheres to complex geometrical patterns such as snowflakes and hollow structures. The DNA molecular engineering field is closely tied to DNA origami, relying on a combination of different DNA motifs and plasmonic atoms, as shown in Figure 7.15, to create molecules, 2D crystals, 3D crystals, and polymers. Plasmonic nanostructures have been used for imaging in biological systems by linking quantum dots with gold nanoparticles. By using different DNA motifs and materials, there are many possibilities opening up with new organic molecules, polymers, and crystalline structures [121].

Tikhomirov *et al.* [123] provide a practical example (shown in Figure 7.16a) of how quantum dots can be linked together with short-strand DNA interconnects with precise distances, enabling effective energy transfer (in the example from green and orange to red quantum dot). A similar concept shown in Figure 7.16b by Maye *et al.* [23] shows a coupled quantum dot and an Au nanoparticle that are linked together in a heterodimer configuration to optically enhance the photoluminescence of the quantum dot by resonance with the Au nanoparticle plasmon. Samanta *et al.* [124] recently summarized several important developments of the field, and have also demonstrated a combination of DNA origami 2D lattice with DNA-templated plasmonics shown in Figure 7.16c.

7.4.2 Metal–Nucleobase Interaction and Self-assembly

Barth describes "molecular architectonics" [125] as highly ordered structures deposited onto metal substrates that self-assemble primarily by the influence of the atomic interactions and intrinsic adsorption of the substrate and surrounding molecules. DNA (and nucleobases) molecular engineering includes ongoing work in direct intrinsic adsorption affinities with metal layers that often self-assemble and bond through orbital interactions. DNA/nucleobase-to-metal affinities have been the basis of many biosensors, as well as improved electronic interaction between organic and metal interfaces. Nucleic acids have shown strong affinity for many different types of electrodes that often results in

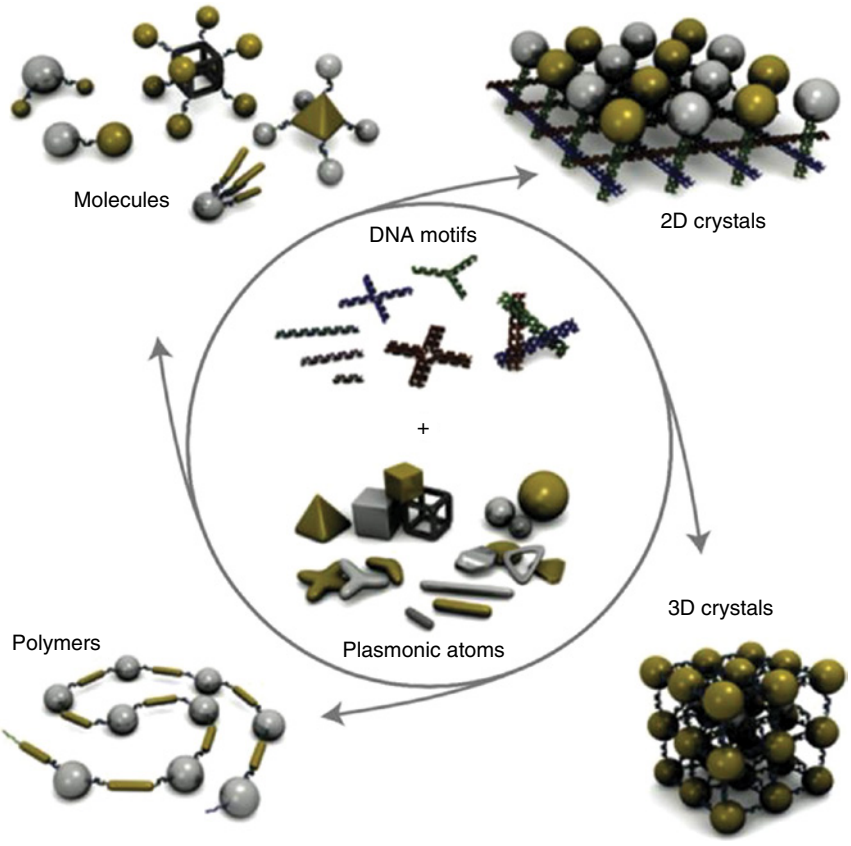

Figure 7.15 DNA nanostructure motifs functionalized with different plasmonic atoms result in molecules, 2D lattices, 3D crystals, or polymer chains that could potentially be designed with different properties. (Tan *et al*. 2011 [121]. Reproduced with permission of Nature Publishing Group.)

increased orbital overlap or order. While origami and nanotemplate bonding primarily focus on construction of nanostructures for mechanical purposes, the DNA-electrode assembly is the link between the powerful technique of DNA self-assembly and traditional solid-state electronics. This direction has initiated the introduction of ordered nucleic acids in sensors and improved metal/organic charge transfer interfaces.

The extensive knowledge of nucleobases/electrode interaction is rapidly growing, primarily for electrochemical analysis in biosensors. Sharma *et al.* [17] catalog many different electrodes and electrode modifications that have been used to detect or assemble nucleic acids. A large number of electrode materials have been investigated, including Au, Ag, Pt, Cu, ITO, TiO_2, graphene, diamond, carbon nanotubes, glassy carbon electrodes, and fullerene. While the motivation has been primarily to develop methods for DNA- or affinity-based sensing [126], the natural orbital interaction of the bases to electrodes has led to improvements in metal–organic interfaces.

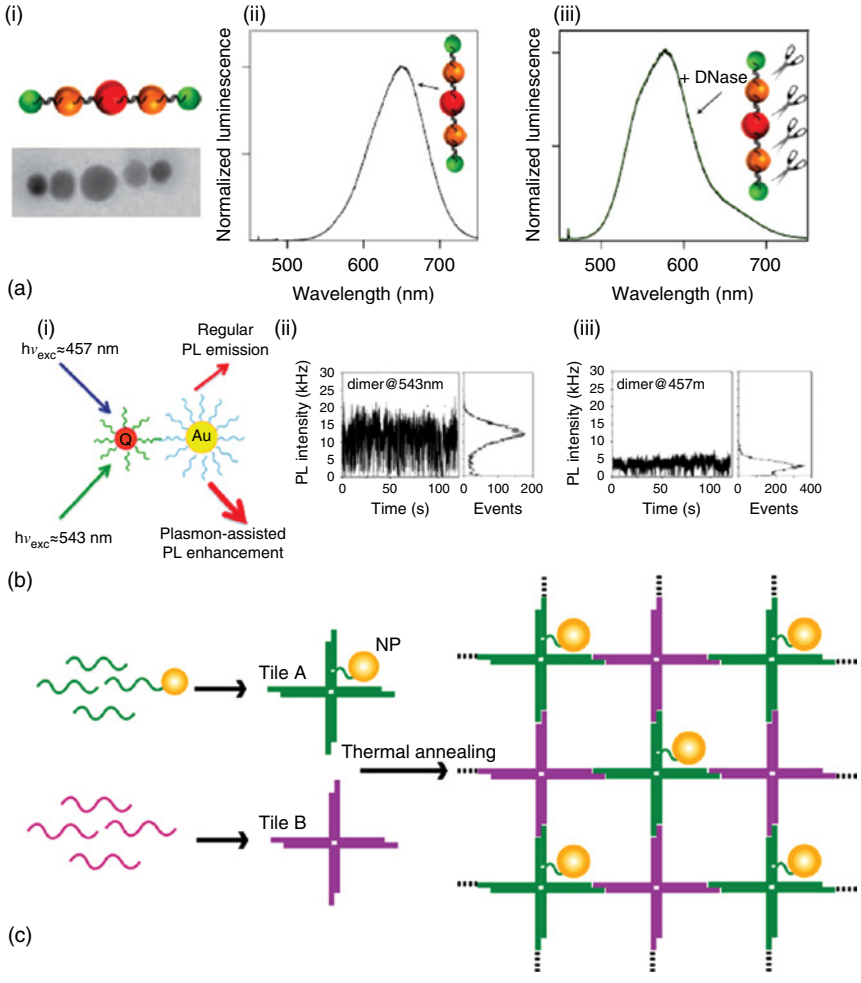

Figure 7.16 DNA molecular engineering can be used to create an array of particles. (a) (i) illustration and transmission electron microscopy (TEM) image of quantum dots linked together with DNA strands; (ii) original photoluminescence of the strand before cleaving and (iii) after cleaving. (b) (i) Quantum dot-Au nanoparticle heterodimer connected together by DNA; (ii) resonating at a precise wavelength (543 nm) inducing high fluorescence of the dye; (iii) compared to the same dimer when excited at 457 nm showing a lower fluorescent intensity. (Tikhomirov *et al.* 2011 [123]. Reproduced with permission of Nature Publishing Group.) (c) ssDNA functionalized with nanoparticles that incorporate into lattice tiles placed in designated locations [23, 123, 124]. (Samanta *et al.* 2015 [124]. Reproduced with permission of Royal Society of Chemistry.)

Nucleobases on gold electrodes have been extensively investigated [127–135] both theoretically (in density functional theory (DFT) calculations) [129, 131] and experimentally [25, 136, 137], showing an impressive capacity for self-organization, especially guanine and adenine on Au(111). Scanning tunneling microscopy (STM) images in Figure 7.17a with DFT overlays show large areas of self-assembly for adenine monolayer structures on the herringbone arrangement of Au(111) surfaces [127, 135]. X-ray diffraction revealed that adenine forms

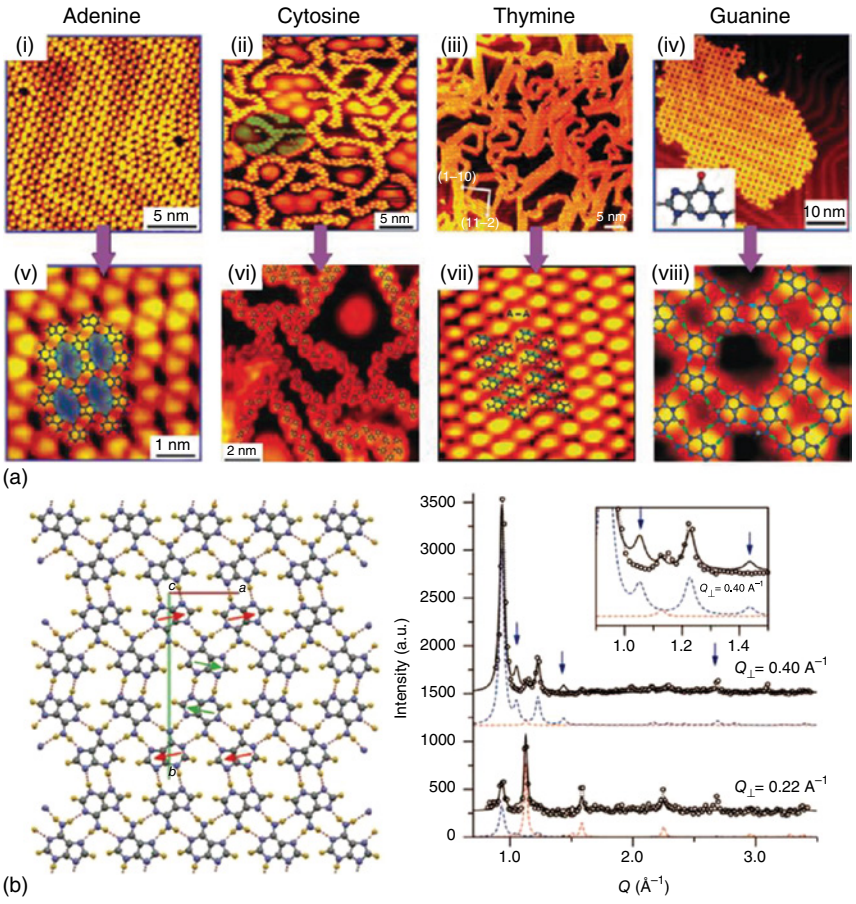

Figure 7.17 The potential of self-assembly of DNA bases on gold electrodes: (a) AFM showing the DNA bases on Au(111) [25]. (Liu *et al.* 2014, https://www.ncbi.nlm.nih.gov/pmc/articles/PMC3958828/. Used under CC-BY-3.0 http://creativecommons.org/licenses/by/3.0/.) (b) Computer simulations showing crystalline arrangement of adenine on Au(111) and confirmed with X-ray Diffraction results of adenine grown to 1000 Å [135].

"highly textured crystallite" structures that can be grown from monolayer thickness to several microns, as shown in Figure 7.17b [135]. The nucleobases show a promising advantage of self-organizing from thermal deposition onto metal surfaces without the need for designing specific DNA sequences.

The self-assembling properties coupled with orbital interactions with metal electrodes make the nucleobases a very intriguing candidate for DNA electronics. Several early papers on the topic observed the chemical and physical adsorption that supported the affinity of nucleobases to (nonoriented) gold. In 2002 Demers *et al.* [138] compared the rate of desorption between different oligonucleotide chains using thermal energy to indicate the strength of the NB-to-Au interaction. It was found that purines (guanine and adenine) have a very strong adsorption, while the pyrimidines have weaker adsorption strength purportedly "due to different types of surface binding moieties." In 2003 Kimura-Suda *et al.* [139]

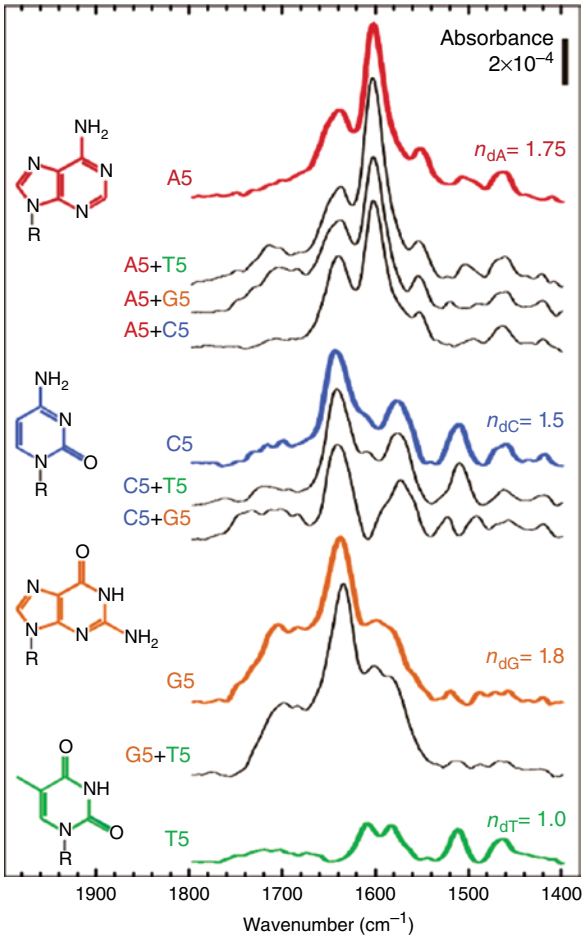

Figure 7.18 FTIR spectra of ssDNA (mixtures of different 5-mer homo-oligonucleotides) films adsorbed on Au from aqueous solutions compared to their reference spectra (bold lines). Non-bold lines show results of mixtures of two different 5-mer oligonucleotides and resultant FTIR spectra. Surface density, n ($\times 10^{14}$ nucleotides cm^{-2}), of each homo-oligonucleotide mixture was determined by XPS. (Kimura-Suda *et al*. 2003 [139]. Reproduced with permission of American Chemical Society.)

used Fourier transform infrared (FTIR) spectroscopy to determine the chemisorption of NB with equimolar mixtures of homo-oligonucleotides on Au. Figure 7.18 shows the FTIR signature of each of the oligonucleotides, as well FTIR results with mixed oligonucleotides in solution. The signature for 5-mer adenine was prominent in all oligonucleotide mixtures indicating the strong chemisorption of adenine on Au. The chemisorption was strong enough to denature the A–T bond in an oligonucleotide strand in order to preferentially bind to the bare gold electrode. The nature of chemical and physical adsorption suggests that the close proximity of the adenine to gold electrodes could influence charge injection from metal to organic layers [24].

7.4.3 DNA Biosensing

The extensive study of nucleic acid electrochemistry, well summarized by Paleček and Bartošík [140], has created a rich field of DNA biosensors. Early work showed that nucleobases could be individually discriminated on glassy carbon electrodes using cyclic voltammetry [126]. Very recently, nucleobase adsorption on graphene has pushed the efforts to develop a DNA base sensor for label-free DNA sequencing [141]. Graphene-based FETs have been fabricated with an exposed surface that allows the nucleobases to interact with the channel. Since the bases adsorb on graphene with different strengths, the change in charge carrier density due to dipole formation enables discrimination of specific bases. Although presumably no actual charge transfer occurs, the shift in work function (0.22, 0.15, 0.13, and 0.01 eV for **G**, **A**, **C**, and **T**, respectively) leads to impressively miniscule limits (1 nucleobase molecule per 10^4 nm^2 of graphene area) of detection.

In addition to traditional sequencing, properties of self-assembly on electrodes coupled with the selectivity of base pairs are ideal for biosensors for other molecules. Nucleic acids can be functionalized to receive a variety of small biomolecules [16]. The primary design uses tetrahedron nanostructures self-assembled by four oligonucleotide strands (see Figure 7.19a), as in DNA origami. The design of the tetrahedron nanostructure advantageously allows each vertex to be functionalized, for example, with fluorescent labels. In addition to ligands, the structure can fold upon itself by introducing a specific DNA sequence (Figure 7.19b,c). In another design, three of the vertices are functionalized with a thiol modification causing the structure to anchor to the gold substrate. The remaining vertex of the tetrahedron is functionalized with RNA or antibody/antigen sensors (Figure 7.19d). The tetrahedron shape has advantages over conventional hairpin sensors. Its shape and size make it exceptionally rigid and resistant to enzyme digestion. The functionalization of the three base vertices promotes proper spacing and correct orientation, and reduces overlapping to expose the sensor to the target.

Another similar application uses single-stranded DNA immobilized on Au gate electrodes of organic electrochemical transistors (OECTs) [146]. Complementary DNA strands in the analyte were detected with label-free methods by binding to the hybridized strands on the gate. The hybridization of the DNA on the gate results in gate voltage and consequently changes in the source–drain current. The device required no fluorescent label or additional antigen, relying solely on the change in work function induced by a "surface dipole formed by intrinsic charge of the DNA" [146]. The surface potential is further decreased after DNA hybridization owing to the negative charge of DNA backbone, resulting in an extremely sensitive OECT.

7.4.4 Electrode Self-assembly and Affinity in DNA Electronics

The high level organization and affinity of nucleobases and DNA on certain electrodes are also being investigated for new designs in organic electronic devices and charge injection layers. The motivation to switch to a biological hole injection layer over more established conventional charge injection layers (PEDOT, CuPC, C_{60}) has to do with the development of "green" or natural electronics and to eventually couple into the field of DNA origami. With the enormous body of

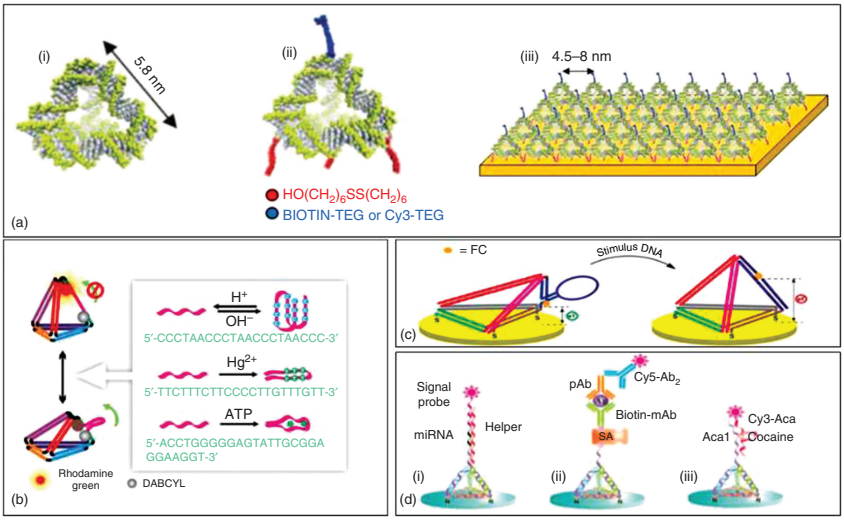

Figure 7.19 (a) Tetrahedral DNA nanostructures fixed to gold electrode and three points, with the fourth point containing a ligand. (b) The structure collapsing in chemical analyte causing either fluorescent emission or (c) electron transfer. (d) DNA tetrahedron functionalized with antibody/antigen in biosensor application [16, 142–145]. (Abi *et al*. 2014 [144]. Reprinted with permission of American Chemical Society; Li *et al*. 2014 [145]. Reprinted with permission of American Chemical Society.)

work on nucleic acid interaction with electrodes, it is somewhat surprising that more work has not been reported for charge injection layers. A few devices are highlighted here.

Several articles have recently reported on using DNA and nucleobases for charge injection layers in pentacene-based OFETs shown in Figure 7.20 [147–149]. The charge injection layer is placed between the Au source and drain electrodes and the pentacene semiconducting layer in order to facilitate charge transfer between the metal and the pentacene layers. The improvement is due to a reduced contact resistance between metal and organic layers, attributed to an interfacial dipole-induced energy shift. The effect is notable with guanine, but is even more pronounced with DNA. The DNA layer was deposited by spray-coating aqueous DNA solutions, resulting in a uniform film without the use of a surfactant [149]. Interestingly, an OFET device with "plain" DNA as an interlayer has three times greater mobility than devices using DNA–CTMA, indicating an adverse effect of the surfactant complex on charge mobility.

A similar approach by Gui *et al.* [148] fixed DNA as an injection layer by immobilizing the molecule to the electrode. This was accomplished by modifying an ssDNA with a mercapto group (SH) that binds the complex to the Au. Notable increases in both saturation current and carrier mobility were observed. The improvement is attributed to the high carrier density in the contact between the gold and the DNA complex.

The concept of a nucleic acid charge injection layer has also been extended to OLEDs by using adenine as a hole charge injection layer on Au. The results showed an improvement of OLED performance when a thin layer of adenine was deposited on Au compared to the device without the nucleobase. Luminance output for the adenine device was nearly 10 times greater than the reference device over the entire range. The current density (Figure 7.21a) of the adenine was only slightly higher, while the current efficiency exhibited an increase of three to seven times (peak values of 31.7 cd A^{-1} for adenine device vs 4.5 cd A^{-1} for conventional device) (Figure 7.21b). This provides significant evidence of enhanced hole injection from gold caused by adenine.

As was previously discussed, the adenine forms a strong chemical interaction with the Au layer [138, 139], which is attributed to the increase in the performance of the adenine OLED devices. Au surfaces are known [150] to have dipole orientations that impede hole injection, especially into organic semiconducting layers. A common hole injection layer, C_{60}, has been used to overcome this limitation. C_{60} is known to have a strong interaction with Au orbitals on the surface that causes a reversal in dipole moments due to its chemical adsorption with the metal [147, 149]. The reversed dipole favors increased charge injection from metal to organic layers. It is believed [24] that a similar mechanism of metal adsorption and dipole interaction also occurs with adenine and Au to favor increased charge injection.

This initial work has implications for the evolution of thin-film electronics toward green electronics. Furthermore, as the development of self-assembled nucleic acids on electrodes is better understood, the advantage of metal to organic interactions could play an important role in improving device performance. In addition to application in solid-state electronics, there is a wider possibility to develop the next generation of sequencing and biosensor devices.

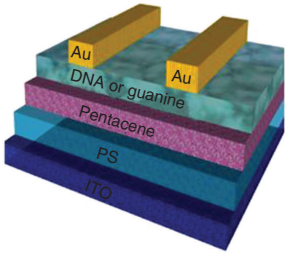

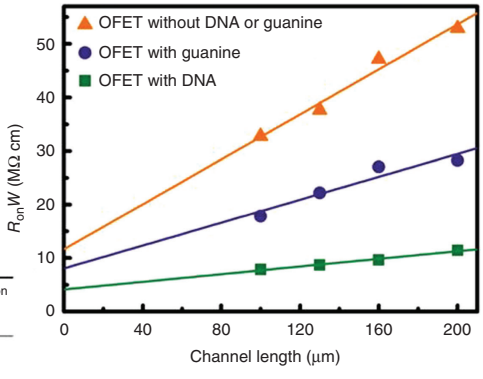

	Contact resistanc (MΩ cm)	Field-effect mobility ($cm^2 V^{-1} s^{-1}$)	Threshold voltage (V)	Saturation current (μA)
Pentacene	11.620	0.020	31	0.178
Pentacene/guanine	8.041	0.036	25	0.506
Pentacene/DNA	4.134	0.104	23	1.656

Figure 7.20 DNA or guanine used as a charge injection layer in pentacene OFETs resulting in a decrease in contact resistance ($R_{on}W$) between gold and pentacene and leading to increased field-effect mobility (μ) and lower threshold voltages. (Wei *et al*. 2014 [147]. Reproduced with permission of IOP Publishing.)

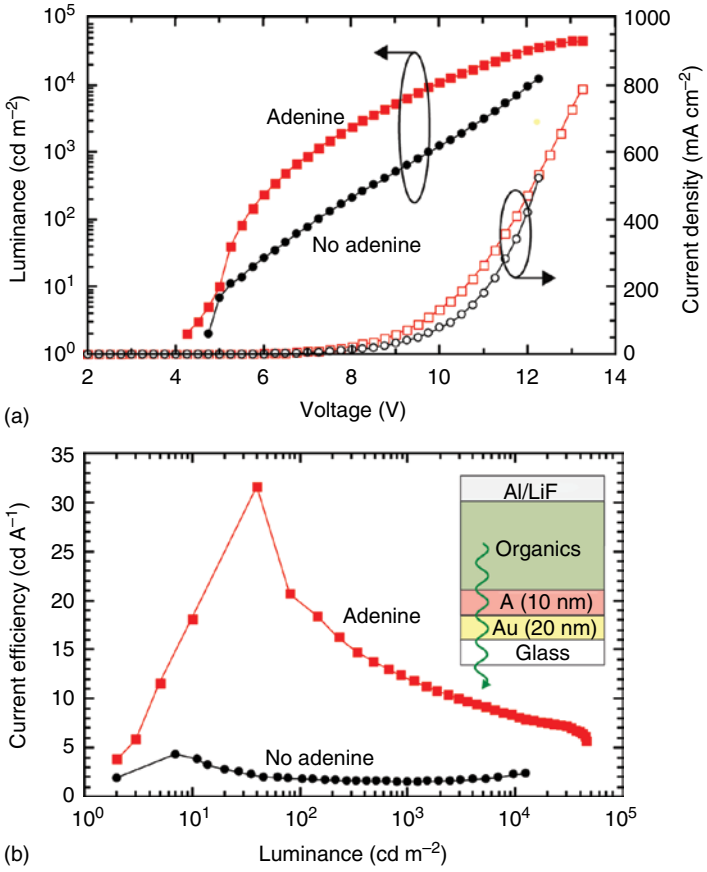

Figure 7.21 Effect of adenine on hole injection in OLEDs: (a) increased luminance versus voltage of OLED device with adenine compared to without adenine and (b) corresponding efficiency increase for adenine versus no adenine on Au (inset) OLED stack with adenine on Au [24, 57].

7.5 Summary and Future Outlook

In this chapter, we have reviewed the use of DNA and nucleobases in electronics, self-assembled origami, and molecular engineering. We have highlighted several notable reports that have been driving the trajectory of the fields for the last 20 years. The electronic properties of DNA and the nucleobases are diverse, and have been explored in a wide range of thin film solid-state devices and electronic conduction. DNA origami has been quite successful in developing tools to construct nanoscale structures with precise control. DNA molecular engineering has explored the intermolecular interactions of the bases with other materials and as a template to bind other materials together. Nucleic acids are a powerful and unparalleled set of tools for material manipulation and device design as represented in these three fields.

As we look toward the next 20 years for DNA and nucleobases, it is apparent that progress will be furthered by increased collaboration of knowledge among the fields. DNA has the opportunity to be a cornerstone in dynamic nanosystems that rely on both structural integrity and electronic manipulation made possible by self-assembled materials. DNA electronics should be intentionally designed with more ordered structures, and likewise, programming DNA origami and molecular engineering deliberately constructed with electronic application in mind. Not only will the nucleic acids be a green material, but they will also encompass a system of materials that have the unique ability for structural precision, enhanced electronic transfer, and modular systems.

Beyond the current uses of DNA, new directions of research into modified DNA materials could further expand its boundaries. For instance, peptide scaffolds, which have chemical and structural versatility, have been combined with nucleic acid base pairing interactions resulting in enhanced optical properties [151]. Other recent work has synthesized nucleobases with π-conjugated oligomers [152] resulting in tunable optoelectronic and electroactive molecules with potential use in new nucleobases, fluorescent OLEDs, or novel organic solar cell materials. Other work investigates the so-called size-expanded DNA [153], an artificial genetic system in which the nucleosides contain an additional benzene ring. The extension of the bases may offer improved opto/electronic properties [132, 154] and potential expansion for molecular engineering with gold nanoparticles [155]. New DNA derivatives such as these could provide more flexibility and functionality in material properties.

The next 20 years offer an opportunity for DNA and its nucleobases to meet progressively intricate and dynamic systems with a wide range of functionality. The nucleic acids have been shown to be highly programmable and self-assembling molecules that can conduct charge, move on command, and form the glue that link nanoparticles together. In its natural environment, the structure and affinity of DNA has been the foundation of complex biomachinery. Remarkably, this time-tested molecule continues to prove to be an indispensable architect for the modern nanoscale world.

Acknowledgments

The authors would like to acknowledge the contributions to DNA-based device research of previous graduate students in the Nanoelectronics Laboratory at the University of Cincinnati – J. Hagen, W. Li, and H. Spaeth. This research benefited greatly from a close collaboration with J. Grote and the support of the Air Force Research Laboratory over a number of years.

References

1 Alberts, B. (2008) *Molecular Biology of the Cell*, 5th edn, Garland Science.
2 Reif, J.H. *et al.* (2001) 7th International Meeting on DNA Based Computers (DNA7), Springer-Verlag, 2002, pp. 231–247.

3 Church, G.M., Gao, Y., and Kosuri, S. (2012) Next-generation digital information storage in DNA. *Science*, **337**, 1628. doi: 10.1126/science.1226355
4 Gehani, A., LaBean, T., and Reif, J. (2004) in *Aspects of Molecular Computing*, Lecture Notes in Computer Science, vol. **2950** (eds J. Nataša, P. Gheorghe, and R. Grzegorz) Chapter 12,, Springer Berlin Heidelberg, pp. 167–188.
5 Braich, R.S., Chelyapov, N., Johnson, C., Rothemund, P.W.K., and Adleman, L. (2002) Solution of a 20-variable 3-SAT problem on a DNA computer. *Science*, **296**, 499–502.
6 Reif, J.H. (2002) Successes and challenges. *Science*, **296**, 478–479. doi: 10.1126/science.1070978
7 Jones, M.R., Seeman, N.C., and Mirkin, C.A. (2015) Programmable materials and the nature of the DNA bond. *Science*, **347**, 840. doi: 10.1126/science.1260901
8 Steckl, A.J. (2007) DNA-a new material for photonics? *Nat. Photonics*, **1**, 3.
9 Kobayashi, N. and Nakamura, K. (2015) in *Electronic Processes in Organic Electronics*, Springer Series in Materials Science, vol. **209** (eds I. Hisao, K. Kazuhiro, N. Takashi, and U. Nobuo) Chapter 12,, Springer Japan, pp. 253–281.
10 Taniguchi, M. and Kawai, T. (2006) DNA electronics. *Physica E*, **33**, 1–12. doi: 10.1016/j.physe.2006.01.005
11 Genereux, J.C. and Barton, J.K. (2010) Mechanisms for DNA charge transport. *Chem. Rev.*, **110**, 1642–1662. doi: 10.1021/cr900228f
12 Kwon, Y.-W., Lee, C.H., Choi, D.-H., and Jin, J.-I. (2009) Materials science of DNA. *J. Mater. Chem.*, **19**, 1353–1380.
13 Jin, J.-I. and Grote, J. (2012) *Materials science of DNA*, CRC Press, Taylor & Francis, Boca Raton, FL.
14 Saccà, B. and Niemeyer, C.M. (2012) DNA origami: the art of folding DNA. *Angew. Chem. Int. Ed.*, **51**, 58–66.
15 Pinheiro, A.V., Han, D., Shih, W.M., and Yan, H. (2011) Challenges and opportunities for structural DNA nanotechnology. *Nat. Nanotechnol.*, **6**, 763–772.
16 Carneiro, K.M. and Greschner, A.A. (2015) Recent advances in self-assembled DNA nanosensors. *Am. J. Nano Res. Appl.*, **3**, 1–7.
17 Sharma, V., Jelen, F., and Trnkova, L. (2015) Functionalized solid electrodes for electrochemical biosensing of purine nucleobases and their analogues: a review. *Sensors*, **15**, 1564–1600.
18 Gomez, E.F., Venkatraman, V., Grote, J.G., and Steckl, A.J. (2014) Exploring the potential of nucleic acid bases in organic light emitting diodes. *Adv. Mater.* **27**, 7485–7676. doi:10.1002/adma.201403532
19 Zheng, J. *et al.* (2009) From molecular to macroscopic via the rational design of a self-assembled 3D DNA crystal. *Nature*, **461**, 74–77.
20 Ke, Y., Ong, L.L., Shih, W.M., and Yin, P. (2012) Three-dimensional structures self-assembled from DNA bricks. *Science*, **338**, 1177–1183. doi: 10.1126/science.1227268
21 He, Y. *et al.* (2008) Hierarchical self-assembly of DNA into symmetric supramolecular polyhedra. *Nature*, **452**, 198–201. doi: 10.1038/nature06597
22 Liu, D., Wang, M., Deng, Z., Walulu, R., and Mao, C. (2004) Tensegrity: construction of rigid DNA triangles with flexible four-arm DNA junctions. *J. Am. Chem. Soc.*, **126**, 2324–2325. doi: 10.1021/ja031754r

23 Maye, M.M., Gang, O., and Cotlet, M. (2010) Photoluminescence enhancement in CdSe/ZnS-DNA linked-Au nanoparticle heterodimers probed by single molecule spectroscopy. *Chem. Commun.*, **46**, 6111–6113. doi: 10.1039/C0CC00660B

24 Gomez, E.F. and Steckl, A.J. (2015) Improved performance of OLEDs on cellulose/epoxy substrate using adenine as a hole injection layer. *ACS Photonics*, **2**, 439–445. doi: 10.1021/ph500481c

25 Liu, L., Xia, D., Klausen, L.H., and Dong, M. (2014) The self-assembled behavior of DNA bases on the interface. *Int. J. Mol. Sci.*, **15**, 1901–1914.

26 Hagen, J.A. (2006) *Enhanced luminous efficiency and brightness using DNA electron blocking layers in bio-organic light emitting diodes*. PhD thesis, Doctorate of Philosophy, University of Cincinnati.

27 Lagoja, I.M. (2005) Pyrimidine as constituent of natural biologically active compounds. *Chem. Biodivers.*, **2**, 1–50.

28 Irimia-Vladu, M. *et al.* (2010) Environmentally sustainable organic field effect transistors. *Org. Electron.*, **11**, 1974–1990. doi: 10.1016/j.orgel.2010.09.007

29 Chargaff, E., Lipshitz, R., Green, C., and Hodes, M. (1951) The composition of the desoxyribonucleic acid of salmon sperm. *J. Biol. Chem.*, **192**, 223–230.

30 Davidson, J. and Waymouth, C. (1944) Tissue nucleic acids: 1. Ribonucleic acids and nucleotides in embryonic and adult tissue. *Biochem. J.*, **38**, 39–50.

31 Zamenhof, S., Brawerman, G., and Chargaff, E. (1952) On the desoxypentose nucleic acids from several microorganisms. *Biochim. Biophys. Acta*, **9**, 402–405.

32 Roman, H. (1956) A system selective for mutations affecting the synthesis of adenine in yeast. *C. R. Trav. Lab.*, **26**, 299–314.

33 Montelone, B.A. (2001) *GENE Project and Research Link 2000*, http://www.phys.ksu.edu/gene/GENEFAQ.html (accessed 13 April 2017).

34 Rosemeyer, H. (2004) The chemodiversity of purine as a constituent of natural products. *Chem. Biodivers.*, **1**, 361–401. doi: 10.1002/cbdv.200490033

35 Yang, C. and Oró, J. (1971) *Chemical Evolution and the Origin of Life; 3rd International Conference*, North-Holland Publishing Co., Amsterdam, pp. 152–167.

36 Oró, J. and Kimball, A. (1961) Synthesis of purines under possible primitive earth conditions. I. Adenine from hydrogen cyanide. *Arch. Biochem. Biophys.*, **94**, 217–227.

37 Holmberg, K. (2015) Custom Oligonucleotide Synthesis, http://www.bio.davidson.edu/Courses/Molbio/MolStudents/spring2003/Holmberg/oligonucleotide_synthesis.htm (accessed 13 April 2017).

38 Bartlett, J. and Stirling, D. (2003) in *PCR Protocols*, Methods in Molecular Biology, vol. **226** (eds B. John and S. David) Chapter 1,, Humana Press, pp. 3–6.

39 Database, J.S.E. (2015) *Molecular Cloning*, JoVE, Cambridge, MA.

40 Murphy, C. *et al.* (1993) Long-range photoinduced electron transfer through a DNA helix. *Science*, **262**, 1025–1029. doi: 10.1126/science.7802858

41 Wang, L.L., Yoshida, J., Ogata, N., Sasaki, S., and Kajiyama, T. (2001) Self-assembled supramolecular films derived from marine deoxyribonucleic acid (DNA)–cationic surfactant complexes: large-scale preparation and optical and thermal properties. *Chem. Mater.*, **13**, 1273–1281.

42 Steckl, A.J., Spaeth, H., You, H., Gomez, E., and Grote, J. (2011) DNA as an optical material. *Opt. Photonics News*, **22**, 34–39.

43 Heckman, E.M., Hagen, J.A., Yaney, P.P., Grote, J.G., and Hopkins, F.K. (2005) Processing techniques for deoxyribonucleic acid: biopolymer for photonics applications. *Appl. Phys. Lett.*, **87**, 211115. doi: 10.1063/1.2135205

44 Hirata, K. *et al.* (2004) Electroluminescence as a probe for elucidating electrical conductivity in a deoxyribonucleic acid-cetyltrimethylammonium lipid complex layer. *Appl. Phys. Lett.*, **85**, 1627. doi: 10.1063/1.1780600

45 Solin, N. and Inganäs, O. (2012) Protein nanofibrils balance colours in organic white-light-emitting diodes. *Isr. J. Chem.*, **52**, 529–539. doi: 10.1002/ijch.201100113

46 Steckl, A.J., Spaeth, H., Singh, K., Grote, J., and Naik, R. (2008) Chirality of sulforhodamine dye molecules incorporated in DNA thin films. *Appl. Phys. Lett.*, **93**, 193903. doi: 10.1063/1.3027070

47 You, H., Spaeth, H., Linhard, V., and Steckl, A.J. (2009) Role of surfactants in the interaction of dye molecules in natural DNA polymers. *Langmuir*, **25**, 11698–11702.

48 Hagen, J.A., Li, W., Steckl, A.J., and Grote, J.G. (2006) Enhanced emission efficiency in organic light-emitting diodes using deoxyribonucleic acid complex as an electron blocking layer. *Appl. Phys. Lett.*, **88**, 171109. doi: 10.1063/1.2197973

49 Yu, Z. *et al.* (2007) Photoluminescence and lasing from deoxyribonucleic acid (DNA) thin films doped with sulforhodamine. *Appl. Opt.*, **46**, 1507–1513.

50 Stadler, P. *et al.* (2007) Organic field-effect transistors and memory elements using deoxyribonucleic acid (DNA) gate dielectric. *Org. Electron.*, **8**, 648–654. doi: 10.1016/j.orgel.2007.05.003

51 Heckman, E.M., Grote, J.G., Hopkins, F.K., and Yaney, P.P. (2006) Performance of an electro-optic waveguide modulator fabricated using a deoxyribonucleic-acid-based biopolymer. *Appl. Phys. Lett.*, **89**, 181116. doi: 10.1063/1.2378400

52 Wagenknecht, H.-A. (2006) *Charge Transfer in DNA*, Wiley-VCH Verlag GmbH & Co. KGaA.

53 Ouchen, F. *et al.* (2013) Deoxyribonucleic acid-ceramic hybrid dielectrics for potential application as gate insulators in organic field effect transistors. *Appl. Phys. Lett.*, **103**, 113701. doi: 10.1063/1.4821019

54 Joyce, D.M. *et al.* (2014) Deoxyribonucleic acid-based hybrid thin films for potential application as high energy density capacitors. *J. Appl. Phys.*, **115**, 114108. doi: 10.1063/1.4868339

55 Hagen, J.A., Li, W.-X., Spaeth, H., Grote, J.G., and Steckl, A.J. (2006) Molecular beam deposition of DNA nanometer films. *Nano Lett.*, **7**, 133–137. doi: 10.1021/nl062342u

56 Yaney, P.P., Gorman, T.T., Ouchen, F., and Grote, J.G. (2012) Time-of-flight studies of hole mobilities in DNA–CTMA films fabricated and passivated in a dry environment. *J. Nanophotonics*, **6**, 063531. doi: 10.1117/1.JNP.6.063531

57 Gomez, E.F. (2015) *Investigation of DNA nucleobases for bio-organic light emitting diodes*. PhD thesis. University of Cincinnati.

58 Faber, C., Attaccalite, C., Olevano, V., Runge, E., and Blase, X. (2011) First-principles GW calculations for DNA and RNA nucleobases. *Phys. Rev. B*, **83**, 115123.

59 Lee, J. *et al.* (2014) DNA-base guanine as hydrogen getter and charge trapping layer embedded in oxide dielectrics for inorganic and organic field-effect transistors. *ACS Appl. Mater. Interfaces*, **6**, 4965–4973. doi: 10.1021/am405998d

60 Lee, Y., Lee, H., Park, S., and Yi, Y. (2012) Energy level alignment at the interfaces between typical electrodes and nucleobases: Al/adenine/indium-tin-oxide and Al/thymine/indium-tin-oxide. *Appl. Phys. Lett.*, **101**, 233305. doi: 10.1063/1.4769438

61 Lin, T.-Y. *et al.* (2011) *Proceedings of SPIE 7935, Organic Photonic Materials and Devices XIII*, 79350E.

62 Bravaya, K.B. *et al.* (2010) Electronic structure and spectroscopy of nucleic acid bases: ionization energies, ionization-induced structural changes, and photoelectron spectra. *J. Phys. Chem. A*, **114**, 12305–12317. doi: 10.1021/jp1063726

63 Pong, W. and Inouye, C.S. (1976) Vacuum ultraviolet photoemission studies of nucleic acid bases. *J. Appl. Phys.*, **47**, 3444. doi: 10.1063/1.323182

64 Urano, S., Yang, X., and LeBreton, P.R. (1989) UV photoelectron and quantum mechanical characterization of DNA and RNA bases: valence electronic structures of adenine, 1,9-dimethyl-guanine, 1-methylcytosine, thymine and uracil. *J. Mol. Struct.*, **214**, 315–328.

65 Magulick, J., Beerbom, M.M., and Schlaf, R. (2006) Comparison of ribonucleic acid homopolymer ionization energies and charge injection barriers. *J. Phys. Chem. B*, **110**, 15973–15981. doi: 10.1021/jp062231j

66 Foster, M.E. and Wong, B.M. (2012) Nonempirically tuned range-separated dft accurately predicts both fundamental and excitation gaps in DNA and RNA nucleobases. *J. Chem. Theory Comput.*, **8**, 2682–2687. doi: 10.1021/ct300420f

67 Bixon, M. *et al.* (1999) Long-range charge hopping in DNA. *Proc. Natl. Acad. Sci. U.S.A.*, **96**, 11713–11716.

68 Henderson, P.T., Jones, D., Hampikian, G., Kan, Y., and Schuster, G.B. (1999) Long-distance charge transport in duplex DNA: The phonon-assisted polaron-like hopping mechanism. *Proc. Natl. Acad. Sci. U.S.A.*, **96**, 8353–8358. doi: 10.1073/pnas.96.15.8353

69 Kawai, K., Kodera, H., Osakada, Y., and Majima, T. (2009) Sequence-independent and rapid long-range charge transfer through DNA. *Nat. Chem.*, **1**, 156–159. doi: 10.1038/nchem.171

70 Meggers, E., Michel-Beyerle, M.E., and Giese, B. (1998) Sequence dependent long range hole transport in DNA. *J. Am. Chem. Soc.*, **120**, 12950–12955. doi: 10.1021/ja983092p

71 Xiang, L. *et al.* (2015) Intermediate tunnelling–hopping regime in DNA charge transport. *Nat. Chem.*, **7**, 221–226. doi: 10.1038/nchem.2183

72 Heim, T., Deresmes, D., and Vuillaume, D. (2004) Conductivity of DNA probed by conducting–atomic force microscopy: effects of contact electrode, DNA structure, and surface interactions. *J. Appl. Phys.*, **96**, 2927–2936. doi: 10.1063/1.1769606

73 Scheer, E. (2014) Molecular electronics: a DNA that conducts. *Nat. Nanotechnol.*, **9**, 960–961. doi: 10.1038/nnano.2014.293

74 Livshits, G.I. *et al.* (2014) Long-range charge transport in single G-quadruplex DNA molecules. *Nat. Nanotechnol.*, **9**, 1040–1046. doi: 10.1038/nnano.2014.246

75 Lin, T.-Y., Chen, I.C., and Hung, Y.-C. (2012) Hole mobility characterization of DNA biopolymer by time-of-flight technique. *Appl. Phys. Lett.*, **101**, 153701. doi: 10.1063/1.4758477

76 Rinaldi, R. *et al.* (2001) Photodetectors fabricated from a self-assembly of a deoxyguanosine derivative. *Appl. Phys. Lett.*, **78**, 3541–3543. doi: 10.1063/1.1374232

77 Maruccio, G. *et al.* (2003) Field effect transistor based on a modified DNA base. *Nano Lett.*, **3**, 479–483.

78 Davis, J.T. and Spada, G.P. (2007) Supramolecular architectures generated by self-assembly of guanosine derivatives. *Chem. Soc. Rev.*, **36**, 296–313. doi: 10.1039/B600282J

79 Kim, Y.S. *et al.* (2010) High-mobility bio-organic field effect transistors with photoreactive DNAs as gate insulators. *Appl. Phys. Lett.*, **96**, 103307. doi: 10.1063/1.3299022

80 Yumusak, C., Singh, T.B., Sariciftci, N.S., and Grote, J.G. (2009) Bio-organic field effect transistors based on crosslinked deoxyribonucleic acid (DNA) gate dielectric. *Appl. Phys. Lett.*, **95**, 263304. doi: 10.1063/1.3278592

81 Hung, Y.-C., Hsu, W.-T., Lin, T.-Y., and Fruk, L. (2011) Photoinduced write-once read-many-times memory device based on DNA biopolymer nanocomposite. *Appl. Phys. Lett.*, **99**, 253301. doi: 10.1063/1.3671153

82 Lee, J., Min, S.-W., Lee, H.S., Yi, Y., and Im, S. (2014) MoS2 nanosheet channel and guanine DNA-base charge injection layer for high performance memory transistors. *J. Mater. Chem. C*, **2**, 5411–5416. doi: 10.1039/C4TC00679H

83 Lee, J. *et al.* (2015) Simultaneous protection of organic p- and n-channels in complementary inverter from aging and bias-stress by DNA-base guanine/Al_2O_3 double layer. *ACS Appl. Mater. Interfaces*, **7**, 1765–1771. doi: 10.1021/am507354p

84 Sun, Q., Chang, D.W., Dai, L., Grote, J., and Naik, R. (2008) Multilayer white polymer light-emitting diodes with deoxyribonucleic acid–cetyltrimethylammonium complex as a hole-transporting/ electron-blocking layer. *Appl. Phys. Lett.*, **92**, 251108. doi: 10.1063/1.2948864

85 Madhwal, D. *et al.* (2010) Increased luminance of MEH-PPV and PFO based PLEDs by using salmon DNA as an electron blocking layer. *J. Lumin.*, **130**, 331–333.

86 Zalar, P. *et al.* (2011) DNA electron injection interlayers for polymer light-emitting diodes. *J. Am. Chem. Soc.*, **133**, 11010–11013. doi: 10.1021/ja201868d

87 Kobayashi, N., Uemura, S., Kusabuka, K., Nakahira, T., and Takahashi, H. (2001) An organic red-emitting diode with a water-soluble DNA-polyaniline complex containing Ru(bpy). *J. Mater. Chem.*, **11**, 1766–1768. doi: 10.1039/b102882k

88 Nakamura, K., Ishikawa, T., Nishioka, D., Ushikubo, T., and Kobayashi, N. (2010) Color-tunable multilayer organic light emitting diode composed of DNA complex and tris(8-hydroxyquinolinato)aluminum. *Appl. Phys. Lett.*, **97**, 193301. doi: 10.1063/1.3512861

89 Cho, M.J. *et al.* (2010) Organic soluble deoxyribonucleic acid (DNA) bearing carbazole moieties and its blend with phosphorescent Ir(III) complexes. *J. Polym. Sci., Part A: Polym. Chem.*, **48**, 1913–1918. doi: 10.1002/pola.23958

90 Ner, Y., Grote, J.G., Stuart, J.A., and Sotzing, G.A. (2008) Enhanced fluorescence in electrospun dye-doped DNA nanofibers. *Soft Matter*, **4**, 1448–1453. doi: 10.1039/B717581G

91 Sun, Q. *et al.* (2009) Highly efficient quantum-dot light-emitting diodes with DNA–CTMA as a combined hole-transporting and electron-blocking layer. *ACS Nano*, **3**, 737–743. doi: 10.1021/nn8009079

92 Gupta, R.B., Nagpal, S., Arora, S., Bhatnagar, P.K., and Mathur, P.C. (2011) Ultraviolet electroluminescence from zinc oxide nanorods/deoxyribonucleic acid hybrid bio light-emitting diode. *J. Nanophotonics*, **5**, 059505. doi: 10.1117/1.3618630

93 Back, S.H., Park, J.H., Cui, C., and Ahn, D.J. (2016) Bio-recognitive photonics of a DNA-guided organic semiconductor. *Nat. Commun.*, **7**. doi: 10.1038/ncomms10234

94 Reddy, M.S.P. and Park, C. (2016) Bright luminescence from pure DNA-curcumin–based phosphors for bio hybrid light-emitting diodes. *Sci. Rep.*, **6**, 32306. doi: 10.1038/srep32306

95 Yusoff, A.R.b.M., Kim, J., Jang, J., and Nazeeruddin, M.K. (2016) New horizons for perovskite solar cells employing DNA–CTMA as the hole-transporting material. *ChemSusChem*, **9**, 1736–1742. doi: 10.1002/cssc.201600288

96 Dagar, J., Scarselli, M., De Crescenzi, M., and Brown, T.M. (2016) Solar cells incorporating water/alcohol-soluble electron-extracting DNA nanolayers. *ACS Energy Lett.*, **1**, 510–515. doi: 10.1021/acsenergylett.6b00192

97 Lee, K.W. *et al.* (2011) A two-dimensional DNA lattice implanted polymer solar cell. *Nanotechnology*, **22**, 375202.

98 Tang, H., Chen, L., Xing, C., Guo, Y.-G., and Wang, S. (2010) DNA-templated synthesis of cationic poly(3,4-ethylenedioxythiophene) derivative for supercapacitor electrodes. *Macromol. Rapid Commun.*, **31**, 1892–1896. doi: 10.1002/marc.201000318

99 Gomez, E.F., Venkatraman, V., Grote, J.G., and Steckl, A.J. (2014) DNA bases thymine and adenine in bio-organic light emitting diodes. *Sci. Rep.*, **4**, 7105. doi: 10.1038/srep07105

100 Seeman, N.C. (2010) Nanomaterials based on DNA. *Annu. Rev. Biochem.*, **79**, 65–87.

101 Liu, D., Park, S.H., Reif, J.H., and LaBean, T.H. (2004) DNA nanotubes self-assembled from triple-crossover tiles as templates for conductive nanowires. *Proc. Natl. Acad. Sci. U.S.A.*, **101**, 717–722. doi: 10.1073/pnas.0305860101

102 Auyeung, E. *et al.* (2014) DNA-mediated nanoparticle crystallization into Wulff polyhedra. *Nature*, **505**, 73–77. doi: 10.1038/nature12739

103 Macfarlane, R.J. *et al.* (2011) Nanoparticle superlattice engineering with DNA. *Science*, **334**, 204–208. doi: 10.1126/science.1210493

104 Winfree, E., Liu, F., Wenzler, L.A., and Seeman, N.C. (1998) Design and self-assembly of two-dimensional DNA crystals. *Nature*, **394**, 539–544.

105 Andersen, E.S. *et al.* (2009) Self-assembly of a nanoscale DNA box with a controllable lid. *Nature*, **459**, 73–76. doi: 10.1038/nature07971

106 Luo, D. (2003) The road from biology to materials. *Mater. Today*, **6**, 38–43.

107 Fu, T.J. and Seeman, N.C. (1993) DNA double-crossover molecules. *Biochemistry*, **32**, 3211–3220. doi: 10.1021/bi00064a003

108 LaBean, T.H. *et al.* (2000) Construction, analysis, ligation, and self-assembly of DNA triple crossover complexes. *J. Am. Chem. Soc.*, **122**, 1848–1860. doi: 10.1021/ja993393e

109 Rothemund, P.W.K. (2006) Folding DNA to create nanoscale shapes and patterns. *Nature*, **440**, 297–302. doi: 10.1038/nature04586

110 Li, J.J. and Tan, W. (2002) A single DNA molecule nanomotor. *Nano Lett.*, **2**, 315–318. doi: 10.1021/nl015713+

111 Gu, H., Chao, J., Xiao, S.-J., and Seeman, N.C. (2010) A proximity-based programmable DNA nanoscale assembly line. *Nature*, **465**, 202–205. doi: 10.1038/nature09026

112 Sherman, W.B. and Seeman, N.C. (2004) A precisely controlled DNA biped walking device. *Nano Lett.*, **4**, 1203–1207. doi: 10.1021/nl049527q

113 Yurke, B., Turberfield, A.J., Mills, A.P., Simmel, F.C., and Neumann, J.L. (2000) A DNA-fuelled molecular machine made of DNA. *Nature*, **406**, 605–608. doi: 10.1038/35020524

114 Condon, A. (2006) Designed DNA molecules: principles and applications of molecular nanotechnology. *Nat. Rev. Genet.*, **7**, 565–575. doi: 10.1038/nrg1892

115 Liedl, T., Sobey, T.L., and Simmel, F.C. (2007) DNA-based nanodevices. *Nano Today*, **2**, 36–41. doi: 10.1016/S1748-0132(07)70057-9

116 Polley, N., Sarkar, P.K., Chakrabarti, S., Lemmens, P., and Pal, S.K. (2016) DNA biomaterial based fiber optic sensor: characterization and application for monitoring in situ mercury pollution. *ChemistrySelect*, **1**, 2916–2922. doi: 10.1002/slct.201600391

117 Macfarlane, R.J., O'Brien, M.N., Petrosko, S.H., and Mirkin, C.A. (2013) Nucleic acid-modified nanostructures as programmable atom equivalents: forging a new "table of elements". *Angew. Chem. Int. Ed.*, **52**, 5688–5698. doi: 10.1002/anie.201209336

118 Finch, A.S., Anton, C.M., Jacob, C.M., Proctor, T.J., and Stratis-Cullum, D.N. (2012) Assembly of DNA architectures in a non-aqueous solution. *Nanomaterials*, **2**, 275–285. doi: 10.3390/nano2030275

119 Gajria, S., Neumann, T., and Tirrell, M. (2011) Self-assembly and applications of nucleic acid solid-state films. *WIREs Nanomed. Nanobiotechnol.*, **3**, 479–500. doi: 10.1002/wnan.148

120 Sun, H., Li, W., and Wu, L. (2009) Honeycomb-patterned films fabricated by self-organization of dNA–surfactant complexes. *Langmuir*, **25**, 10466–10472. doi: 10.1021/la900322d

121 Tan, S.J., Campolongo, M.J., Luo, D., and Cheng, W. (2011) Building plasmonic nanostructures with DNA. *Nat. Nanotechnol.*, **6**, 268–276.

122 Gang, O. and Tkachenko, A.V. (2016) DNA-program le particle superlattices: assembly, phases, and dynamic control. *MRS Bull.*, **41**, 381–387. doi: 10.1557/mrs.2016.92

123 Tikhomirov, G. *et al.* (2011) DNA-based programming of quantum dot valency, self-assembly and luminescence. *Nat. Nanotechnol.*, **6**, 485–490. doi: 10.1038/nnano.2011.100

124 Samanta, A., Banerjee, S., and Liu, Y. (2015) DNA nanotechnology for nanophotonic applications. *Nanoscale*, **7**, 2210–2220. doi: 10.1039/C4NR06283C

125 Barth, J.V. (2007) Molecular architectonic on metal surfaces. *Annu. Rev. Phys. Chem.*, **58**, 375–407. doi: 10.1146/annurev.physchem.56.092503.141259

126 Oliveira-Brett, A.M., Piedade, J.A.P., Silva, L.A., and Diculescu, V.C. (2004) Voltammetric determination of all DNA nucleotides. *Anal. Biochem.*, **332**, 321–329. doi: 10.1016/j.ab.2004.06.021

127 Kelly, R.E. *et al.* (2008) An investigation into the interactions between self-assembled adenine molecules and a Au (111) surface. *Small*, **4**, 1494–1500.

128 Martins, A., Queirós, A., and Silva, F. (2005) Surface-structure-sensitive adsorption of adenine on gold electrodes. *ChemPhysChem*, **6**, 1056–1060. doi: 10.1002/cphc.200400600

129 Piana, S. and Bilic, A. (2006) The nature of the adsorption of nucleobases on the gold [111] surface. *J. Phys. Chem. B*, **110**, 23467–23471.

130 Prado, C., Prieto, F., Rueda, M., Feliu, J., and Aldaz, A. (2007) Adenine adsorption on Au(111) and Au(100) electrodes: characterisation, surface reconstruction effects and thermodynamic study. *Electrochim. Acta*, **52**, 3168–3180. doi: 10.1016/j.electacta.2006.09.062

131 Rosa, M., Corni, S., and Di Felice, R. (2013) Interaction of nucleic acid bases with the Au(111) surface. *J. Chem. Theory Comput.*, **9**, 4552–4561. doi: 10.1021/ct4002416

132 Rosa, M., Sun, W., and Di Felice, R. (2013) Interaction of DNA bases with gold substrates. *J. Self-Assembly Mol. Electron. (SAME)*, **1**, 41–68.

133 Tao, N., DeRose, J., and Lindsay, S. (1993) Self-assembly of molecular superstructures studied by in situ scanning tunneling microscopy: DNA bases on gold (111). *J. Phys. Chem.*, **97**, 910–919.

134 Kwon, Y.-W., Lee, C.H., Jin, J.-I., Hwang, J.S., and Hwang, S.W. (2014) Electrical properties of nanofibers and structural characterization of DNA-Au(III) complexes. *Nanotechnology*, **25**, 205701.

135 Capitán, M.J., Otero, R., Álvarez, J., and Miranda, R. (2011) Growth of textured adenine thin films to exhibit only chiral faces. *ChemPhysChem.*, **12**, 1267–1271. doi: 10.1002/cphc.201001064

136 Kong, H. *et al.* (2014) Atomic-scale investigation on the facilitation and inhibition of guanine tautomerization at Au (111) surface. *ACS Nano*, **8**, 1804–1808. doi: 10.1021/nn4061918

137 Boland, T. and Ratner, B.D. (1994) Two-dimensional assembly of purines and pyrimidines on Au (111). *Langmuir*, **10**, 3845–3852.

138 Demers, L.M. *et al.* (2002) Thermal desorption behavior and binding properties of DNA bases and nucleosides on gold. *J. Am. Chem. Soc.*, **124**, 11248–11249. doi: 10.1021/ja0265355

139 Kimura-Suda, H., Petrovykh, D.Y., Tarlov, M.J., and Whitman, L.J. (2003) Base-dependent competitive adsorption of single-stranded DNA on gold. *J. Am. Chem. Soc.*, **125**, 9014–9015. doi: 10.1021/ja035756n

140 Paleček, E. and Bartošík, M. (2012) Electrochemistry of nucleic acids. *Chem. Rev.*, **112**, 3427–3481. doi: 10.1021/cr200303p

141 Dontschuk, N. *et al.* (2015) A graphene field-effect transistor as a molecule-specific probe of DNA nucleobases. *Nat. Commun.*, **6**, 1–7. doi: 10.1038/ncomms7563

142 Mitchell, N. *et al.* (2009) A DNA nanostructure for the functional assembly of chemical groups with tunable stoichiometry and defined nanoscale geometry. *Angew. Chem. Int. Ed.*, **48**, 525–527. doi: 10.1002/anie.200804264

143 Pei, H. *et al.* (2012) Reconfigurable three-dimensional dna nanostructures for the construction of intracellular logic sensors. *Angew. Chem. Int. Ed.*, **51**, 9020–9024. doi: 10.1002/anie.201202356

144 Abi, A. *et al.* (2014) Electrochemical switching with 3D DNA tetrahedral nanostructures self-assembled at gold electrodes. *ACS Appl. Mater. Interfaces*, **6**, 8928–8931. doi: 10.1021/am501823q

145 Li, Z. *et al.* (2014) DNA nanostructure-based universal microarray platform for high-efficiency multiplex bioanalysis in biofluids. *ACS Appl. Mater. Interfaces*, **6**, 17944–17953. doi: 10.1021/am5047735

146 Lin, P., Luo, X., Hsing, I., and Yan, F. (2011) Organic electrochemical transistors integrated in flexible microfluidic systems and used for label-free DNA sensing. *Adv. Mater.*, **23**, 4035–4040.

147 Shi, W., Yu, J., Huang, W., and Zheng, Y. (2014) Performance improvement of a pentacene organic field-effect transistor through a DNA interlayer. *J. Phys. D: Appl. Phys.*, **47**, 205402.

148 Gui, H., Wei, B., Zhang, J., and Wang, J. (2014) Improved charge injection of pentacene transistors by immobilizing DNA on gold source–drain electrodes. *Appl. Phys. A*, **115**, 759–763.

149 Shi, W., Han, S., Huang, W., and Yu, J. (2015) High mobility organic field-effect transistor based on water-soluble deoxyribonucleic acid via spray coating. *Appl. Phys. Lett.*, **106**, 043303. doi: 10.1063/1.4907325

150 Veenstra, S.C., Heeres, A., Hadziioannou, G., Sawatzky, G.A., and Jonkman, H.T. (2002) On interface dipole layers between C60 and Ag or Au. *Appl. Phys. A*, **75**, 661–666. doi: 10.1007/s003390201311

151 Berger, O. *et al.* (2015) Light-emitting self-assembled peptide nucleic acids exhibit both stacking interactions and Watson–Crick base pairing. *Nat. Nanotechnol.*, **10**, 353–360. doi: 10.1038/nnano.2015.27

152 Zerdan, R.B. *et al.* (2015) Synthesis, optical properties, and electronic structures of nucleobase-containing π-conjugated oligomers. *J. Org. Chem.*, **80**, 1828–1840. doi: 10.1021/jo502773g

153 Liu, H., Gao, J., Maynard, L., Saito, Y.D., and Kool, E.T. (2004) Toward a new genetic system with expanded dimensions: size-expanded analogues of deoxyadenosine and thymidine. *J. Am. Chem. Soc.*, **126**, 1102–1109.

154 Fuentes-Cabrera, M., Sumpter, B.G., and Wells, J.C. (2005) Size-expanded DNA bases: an ab initio study of their structural and electronic properties. *J. Phys. Chem. B*, **109**, 21135–21139. doi: 10.1021/jp055210i

155 Zhang, L., Ren, T., Yang, X., Zhou, L., and Li, X. (2013) Intermolecular interactions of a size-expanded guanine analogue with gold nanoclusters. *Int. J. Quantum Chem.*, **113**, 2234–2242. doi: 10.1002/qua.24436

8

Grotthuss Mechanism: From Proton Transport in Ion Channels to Bioprotonic Devices

Takeo Miyake[1] *and Marco Rolandi*[2]

[1] *Waseda University, Graduate School of Information, Production and System, Kitakyushu, Fukuoka, 808-0135, Japan*
[2] *University of California, Santa Cruz, Department of Electrical Engineering, Santa Cruz, CA 95064 (USA)*

8.1 Introduction

In 1804, Theodor von Grotthuss proposed a hopping mechanism for proton (H^+) transfer in chains of hydrogen-bonded water. This transfer involves the exchange of the covalent bond between an H and an O with the hydrogen bond formed by the same H with a neighboring water molecule [1–3]. At the time, water was believed to be HO and not H_2O; however, the Grotthuss mechanism stuck, and it is still used today to describe proton transport in most systems that involve hydrogen bonds including water and water bound to hydrophilic molecules such as in biological systems [4]. In nature, H^+ transport is important in a variety of processes including adenosine triphosphate (ATP) oxidative phosphorylation in mitochondria [5, 6], the HVCN1 voltage-gated proton channel in mammals [7], the light-activated proton pumping of bacteriorhodopsin in Archaea [8], proton-activated flagella in bacteria [9], the antibiotic gramicidin [10], and proton-activated bioluminescence in dinoflagellates [11]. In all of these systems, hydrogen-bonded water and hydrophilic residues form hydrogen-bonded proton wires, along which H^+ hops. In the same manner as proton hopping, proton hole (OH^-) transport occurs along the proton wires [12]. To interface with biological systems, bioelectronics includes devices that mimic biological functionality and monitor biological phenomena [13, 14]. 1D nanomaterials, such as carbon nanotubes and silicon nanowires, integrate into electronic devices that incorporate functional biological membrane proteins, channels, and pumps [15–17]. Gramicidin and bacteriorhodopsin with carbon nanotubes [18] and organic field-effect transistors [19] create biosensors with increased functionality. Ion-conductive devices such as organic electronic [20, 21] and iontronic [15] devices enable the modulation of biological functions. There are several excellent reviews on these bioelectronic devices [13, 16, 17, 20–22]. Here, we highlight recent developments from our group on proton-conducting field-effect transistors (H^+-FETs) and other semiconductor-type devices with polysaccharides that effectively mimic proton wires in ion channels [23–25]. We describe the conductivity

Green Materials for Electronics, First Edition.
Edited by Mihai Irimia-Vladu, Eric D. Glowacki, Niyazi S. Sariciftci, and Siegfried Bauer.

in these devices with a model for proton semiconductivity proposed in 1958 by Eigen and de Maeyer [26].

8.2 Proton Wires: Chains of Hydrogen Bonds and Grotthuss Mechanisms

In bulk water, charged ions transport following a simple hydrodynamic diffusion model, also known as the vehicle mechanism and described by the Einstein–Stokes equation for charged particles:

$$\mu_i = \frac{Dq}{k_B T} \tag{8.1}$$

where μ_i is the mobility of the ion, D is the diffusion constant, q is the charge of the ion, k_B is Boltzmann's constant, and T is the temperature. This model is used to describe transport of positively and negatively charged ions. However, this model greatly underestimates the mobility of H_3O^+ (Figure 8.1a) and OH^- (Figure 8.1b) in water compared with experimental results by seven and three folds respectively [27]. For example, H^+ and K^+ have similar hydrodynamic radii, and the H^+ mobility is $3.6 \times 10^{-3}\,cm^2\,s^{-1}\,V^{-1}$ [27] while the mobility for K^+ is much smaller, $0.8 \times 10^{-3}\,cm^2\,s^{-1}\,V^{-1}$ [27]. Hydrodynamic diffusion cannot be solely used to explain H^+ transport in water [3]. In 1804, Grotthuss proposed a mechanism

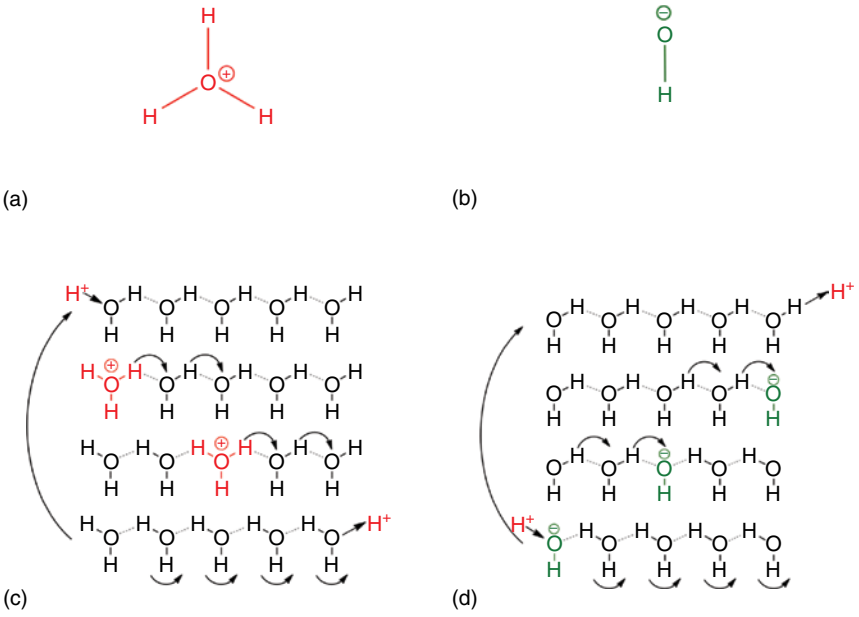

Figure 8.1 (a) Hydronium ion, (b) hydroxyl ion, (c) hop and turn Grotthuss mechanism for conductivity of H^+ as hydronium ion along a proton wire, and (d) equivalent mechanism for OH^- conductivity as proton hole along proton wire.

for proton transport along chains of hydrogen bonds in water involving hopping or tunneling of the proton from one molecule to the next (Figure 8.1c) [3]. Nagle and Morowitz postulated that this type of Grotthuss transport occurs along chains of hydrogen bonds formed by water molecules and amino acid polar residues in membrane proteins; they called these chains of hydrogen bonds proton wires [28].

In the Grotthuss mechanism, a proton hops from one molecule to the next molecule by the exchange of a hydrogen bond with a covalent bond (Figure 8.1c). However, the net movement of a proton along a single-file water chain does not result in the transfer of a unit charge, because it leaves the water chain in a polarized state. In order to accept another proton, the water chain needs to reorder itself by the transport of a Bjerrum D orientation defect that involves the rotation of the water molecules in the chain (Figure 8.1c). Therefore, the combined motion of H^+ and a D defect will translate a unit charge. In gramicidin, H^+ carries $0.68e^-$ and the Bjerrum D defect $0.32e^-$ respectively [29]. This two-step process can also support the transfer of a negatively charged OH^- "proton hole" (Figure 8.1b) along the chain. In the latter case, the reorientation occurs through the diffusion of a Bjerrum L defect instead (Figure 8.1d). Thus, protonic conductivity may involve two different charge carriers similarly to electrons and holes in semiconductors. Since it requires energy to form and translate both the ionic and Bjerrum defects, protonic conductivity is a thermally activated process and the mobility (μ_H) is described by [30]

$$\mu_H \propto \frac{1}{T}\exp\left(\frac{-E_A}{K_B T}\right) \tag{8.2}$$

where E_A is the activation energy for proton hopping or the free energy barrier that a proton overcomes in a successful hop between the sites. E_A is typically comparable to the energy required to break a hydrogen bond (~0.1 eV) in the second solvation shell, for example, Eigen cation ($H_9O_4^+$), Zundel cation ($H_5O_2^+$), H_3O^+, and H_2O [31]. Recently, the proton mobility and its motion through the water network have been investigated with theoretical and experimental molecular dynamics simulations in 2014 [32] or first-principles simulations in 2013 [33].

8.3 Proton Transport in Proton Channels

Proton channels are highly selective to proton transport across membranes. This transport is either voltage gated [34] or driven by chemical gradient [35]. All proton channels include proton wires, which are formed inside a protein cavity lined by polar amino acid residues including hydroxyl, amino, and carboxyl side groups [31, 36]. A prototypical example of these "proton wires" is the antibiotic gramicidin [29] (Figure 8.2a). Gramicidin positions itself across the cell membrane of bacteria, allows highly selective cation transfer that uncouples the membrane potential, and leads to bacterial death. The gramicidin channel has a narrow cylindrical pore that is filled with a single-file row of a dozen water molecules. Gramicidin conducts up to $2\times10^9\,H^+\,s^{-1}$, faster than any other

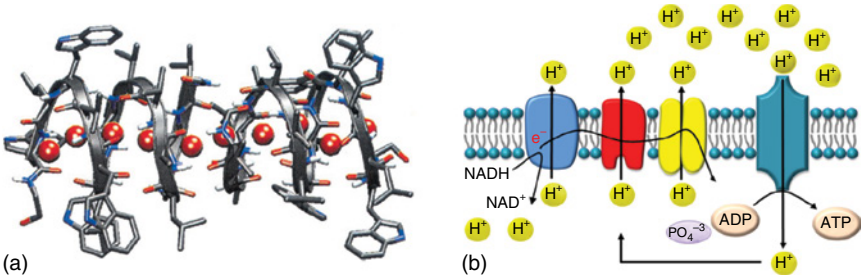

Figure 8.2 (a) Gramicidin proton channel structure. (Pomes and Roux 2002 [29]. Reproduced with permission of Elsevier.) (b) Schematic of the mitochondrial membrane. Through several channels, the products from the citric acid cycle are oxidized and pump protons in the intermembrane space. The protons such as NADH and $FADH_2$ create a protochemical potential. Rotary ATPases utilize this protochemical potential to phosphorylate ADP into ATP.

narrow-pore channel conducts any other ion. While in nature gramicidin allows the transport of other cations, when modified with CH_2OH gramicidin is a perfectly selective proton channel [3, 31]. Another proton channel is the voltage-gated proton channel HVCN1. This channel modulates signaling from the B-cell receptor following B-cell activation and histamine release from basophils, but also mediates pH-dependent activation of spermatozoa, as well as acid secretion by tracheal epithelium [7, 37, 38].

8.4 Proton Transport across Membranes and Oxidative Phosphorylation

The name "proton wire" introduced by Nagle and Morowitz describes proton transport across the mitochondrial membrane and supports the chemiosmotic theory by Peter Mitchell for oxidative phosphorylation of ATP [2, 6, 39]. ATP is used to power the metabolism of most living organisms. In oxidative phosphorylation, the energy released during the citric acid cycle in the form of product oxidation of NADH and $FADH_2$ is used to produce ATP (Figure 8.2b). During these reactions electron transfers occur across the membrane between different intramembrane proteins. The net result of these reactions is an accumulation of extra H^+ on the outside of the membrane. This proton transport process is called chemiosmosis [5, 39]. As a result of chemiosmosis, a pH gradient and an electrical potential across the membrane are established. In eukaryotes, oxidative phosphorylation occurs within the cell's intermembrane wall mitochondria. In prokaryotes, oxidative phosphorylation occurs in the cell's intermembrane space. This H^+ accumulation gives rise to a protomotive force (PMF). This PMF is expressed as

$$\mathrm{PMF} = \Delta V - 2.3\frac{RT}{F}\Delta\mathrm{pH} \tag{8.3}$$

where R is the gas constant; F, the Faraday's constant; and T, the temperature, and both the electrostatic contribution (ΔV) and the chemical contribution

(ΔpH) are taken into account. This PMF forces H^+ back across the membrane via the ATP synthase. ATP synthase in the process phosphorylates adenosine diphosphate (ADP) into ATP. Certain single cell microorganisms called phototrophic archaea use light instead of glucose to produce chemical energy in the form of ATP. The conversion of light into ATP is still mediated by protons. In halobacteria, light-activated bacteriorhodopsin (H^+ pumps) and halorhodopsin (Cl^- pump) generate proton and voltage gradients by pumping ions across the plasma membrane. In the case of the bacteriorhodopsin photocycle, transient modifications of water chains and networks are also essential to the H^+ pumping mechanism [40, 41].

8.5 Biopolymer Proton Conductors

Several biopolymers that exhibit protonic conductivity unrelated to their biological function exist in nature [23, 42–44]. Examples are fiber-like materials comprising hydrogen-bonded hydrated polypeptides or polysaccharides. In these materials, proton wires do not serve a biologically relevant proton transport role, but effectively bind together the biomolecules, increasing their strength. In these biopolymers, proton mobility typically increases with hydration level [45]:

$$\mu \propto H^d \tag{8.4}$$

where H is the water content of the material and d is the critical exponent [46].

For example, protonic conductivity in collagen increases with hydration level of the material [42, 43]. Collagen is a triple-helix polypeptide with the amino acids of glycine–proline–X and glysine–X–hydroxyproline, where X is any amino acid other than glycine, proline, or hydroxyproline [47] (Figure 8.3). Triple-helix "tropocollagen" spontaneously self-assembles into larger collagen fibrils [48]. Such fibrils have micro/nanochannels available for water that support Grotthuss-type transport. Another fibrous protein, keratin, from wool has demonstrated ionic conductivity when hydrated [49]. Keratin is also a skin protein from the outer layer of human skin. In almost the same manner as collagen formation, keratin monomers consisting of an alpha helical rod domain assemble into bundles to form intermediate filaments. Such filaments can form an H-bonded water network with amino acid groups on its side chains, and these groups contribute to H^+ transfer.

Polysaccharide biopolymers such as cellulose [44] and chitosan [23] are also proton conductors. Carboxyl-group-modified cellulose has good proton conductivity ($\sim 7.7^{-4}\,S\,cm^{-1}$) in proton exchange membranes for fuel cells [44]. Maleic anhydride [23], proline [24], and pyridine [50] groups are attached to chitosan backbone to improve its water solubility and protonic conductivity. The conductivity of the pigment eumelanin also has a strong protonic component when hydrated [51, 52]. Recently, Gorodetsky and coworkers reported the highest proton-conducting protein ($2.6 \times 10^{-3}\,S\,cm^{-1}$) by integrating squid reflectin in proton-conducting devices [25]. Reflectin is present in organelles known as iridophores in squid skin cells, which enable the squid to change the color of its skin.

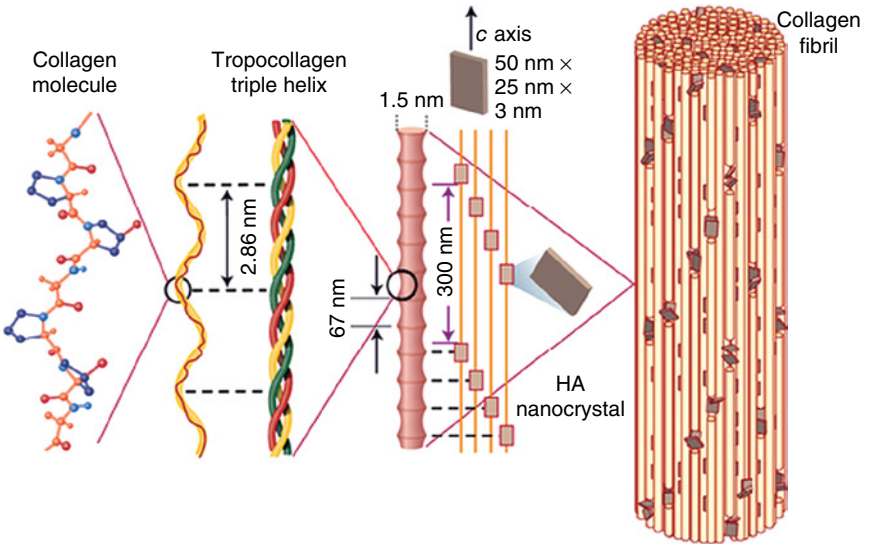

Figure 8.3 The fibers comprise several mineralized collagen fibrils, composed of collagen protein molecules (tropocollagen) formed from three chains of amino acids and nanocrystals of hydroxyapatite (HA), and linked by an organic phase to form fibril arrays. (Wegst *et al*. 2014 [48]. Reproduced with permission of Nature Publishing Group.)

8.6 Devices Based on Proton Conductors

In contrast with the widespread presence of proton conductors in biology, few examples of protonic devices exist. The first example was an ice FET reported by Petrenko and Maeno in 1987 [53]. Vanheusden *et al.* demonstrated a nonvolatile memory device based on mobile protons in SiO_2 thin films [54]. In 2008, the Yang group demonstrated electrostatically gated proton transport in mesoporous silica films [55] (Figure 8.4). Recently, such a silica-based inorganic proton conductor was applied to lateral electric double-layer capacitor for indium-zinc-oxide (IZO)-based artificial synapse [56]. With strong lateral modulation corresponding to the proton migration effect, electric current mimicked synaptic behaviors such as excitatory postsynaptic current (EPSC). In addition to their inorganic channel modulation systems, the external electric field allows an ionic modulation in organic Nafion channel [57]. O'Hayre and colleagues demonstrated electric field modulation of the proton resistance of a Nafion membrane in response to a gate bias [57].

8.7 Bioprotonic Devices: Diodes, Transistors, Memories, and Transducers

Inspired by proton channels and the Grotthuss mechanisms, our group demonstrated devices where the flow of H^+ and OH^- in biopolymers can be controlled with electric fields in a manner that is analogous to electrons and holes in semiconductors.

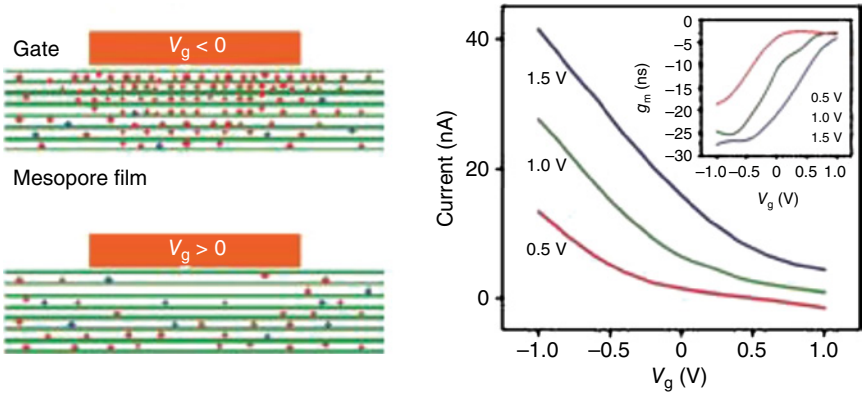

Figure 8.4 Mesoporous nanofluidic device with voltage gate electrode, which changes cation (red) and anion (blue) distribution within nanochannels and accordingly ionic current modulation. (Fan *et al*. 2008 [55]. Reproduced with permission of Nature Publishing Group.). The selected curves of transfer characteristics, current versus gate voltage for $V = 0.5$, 1, and 1.5 V respectively, all show consistent p-type gating behavior. Interestingly, a gate voltage of +1 V was able to completely switch off the apparent ionic current at low biases.

8.7.1 Protodes: PdH_x for Efficient Proton Transport at the Contact Biopolymer Interface

Most metal contacts in devices (Au, Pt) are excellent electronic conductors but poor proton conductors and are referred to as proton-blocking contacts. Palladium hydride (PdH_x) is both an electronic and a protonic conductor and can transfer proton to a channel, serving effectively as a protode (Figure 8.5a) [58]. To prove the H^+ injecting ability of PdH_x contacts, we measure the H^+ conductivity of a polysaccharide derivative where PdH_x contacts (source and drain) inject and drain protons into and from the proton-conducting channel [23, 58, 59].

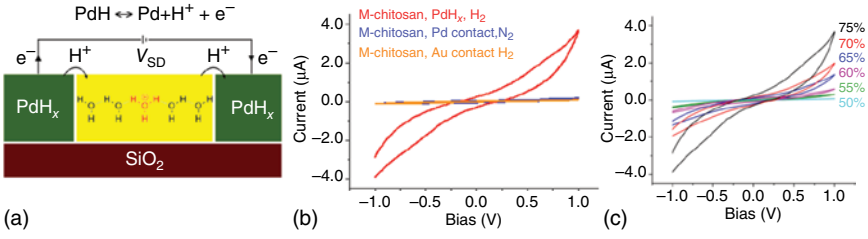

Figure 8.5 (a) Two-terminal device with PdH_x source and drain. The PdH_x source and drain inject and sink protons into and from the proton wire according to the reversible reaction $PdH \rightarrow Pd + H^+ + e^-$ going from left to right at the source and from right to left at the drain. The PdH_x source and drain are connected to outside measurement electronics that measure the electronic current to complete the circuit. (b) Current voltage characteristics of nanofiber polysaccharide thin films (1×1 cm^2, 300 μm thick) at 75% RH. Maleic chitosan measured with Au contacts (orange), Pd contacts in N_2 atmosphere (blue), PdH_x contacts in 5% H_2 atmosphere (red). (c) Conductivity as a function of humidity for a maleic chitosan thin film with PdH_x contacts in 5% H_2 atmosphere. (Zhong *et al*. 2011 [23]. Reproduced with permission of Nature Publishing Group.)

The H^+-conducting biopolymer is maleic chitosan poly(β-(1,4)-*N*-Maleoyl-D-glucosamine) and was synthesized in our laboratories [30]. Proton current using hydrogen-depleted Pd or Au contacts – both proton blocking – is small and it is attributed to electrons (Figure 8.5b). In contrast, the current using PdH_x contacts (both H^+ and electrons) increases with relative humidity (and maleic chitosan hydration level) as expected from Eq. (8.4) (Figure 8.5c) and observed in other biological macromolecules such as collagen [60], cellulose [61], and keratin [49]. Recently, with these PdH_x contacts we have observed that the protonic conductivity of the pigment eumelanin also increases with relative humidity [62].

To further understand proton transport at the interface between PdH_x and a proton conductor, we investigate the dependence of the formation and depletion of PdH_x on the potential applied to the PdH_x (V) in a water solution containing H^+ and OH^- (Figure 8.6a). First, we form PdH_x with a negative *V* applied to the

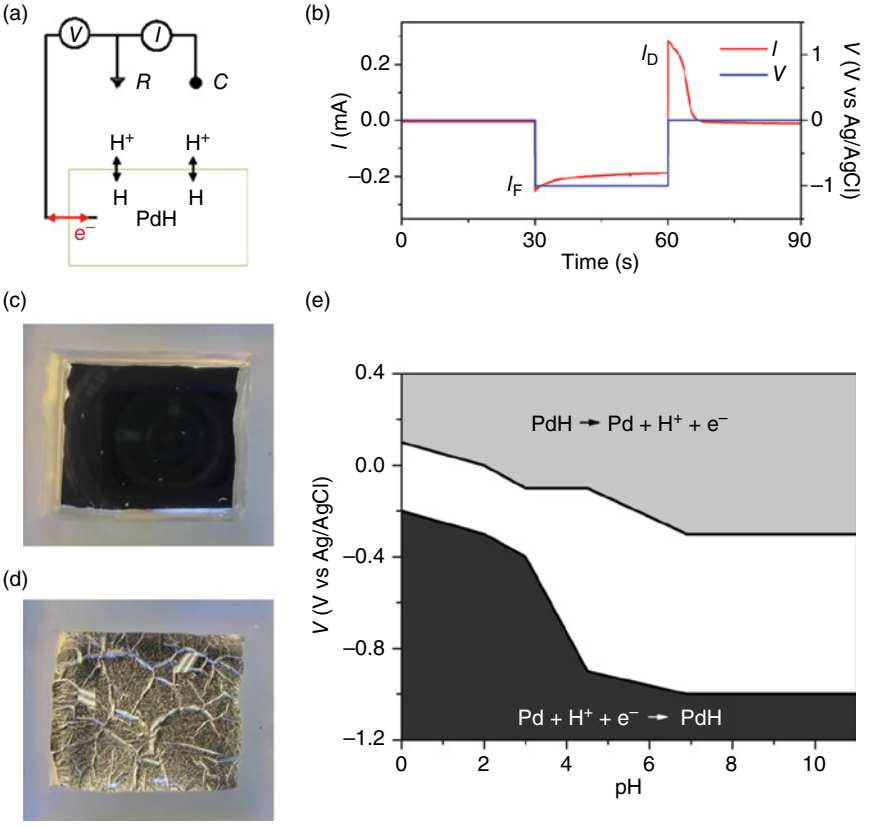

Figure 8.6 (a) Voltage-controlled Pd/PdH_x transition. Electrons and protons transfer into the Pd/PdH_x during formation and out during depletion. (b) Temporal characteristics of the PdH_x formation (at $-1.0V_F$) and depletion (at $0V_D$) in Na_2SO_4 solution (pH = 6.7). (c) Picture of Pd when the measurement starts at 0V. (d) Picture of PdH_x when a negative voltage of $-1.0V_F$ is applied; Pd absorbs protons from the solution, forming PdH. (e) pH and voltage dependence of PdH formation and depletion. (Miyake *et al*. 2015 [63]. Reproduced with permission of Nature Publishing Group.)

PdH_x contact, which we refer to as V_F. A V_F applied to the Pd induces a current of e^- to flow into the Pd, which we refer to as formation current (I_F). This e^- reduces the H^+ from solution, which is absorbed as H into the Pd to form PdH_x. Second, once the Pd is fully converted to PdH_x with $x = 0.6$, we switch V to a positive depletion voltage (V_D) at which PdH_x is expected to go back to Pd. For this specific measurement, $V_d = 0$ V. The difference in chemical potential of H^+, or protochemical potential (μ) between the PdH (μ_{PdH}) and the solution (μ_{pH}), determines whether the H^+ will transfer back to the solution. This difference is defined as [64]

$$\mu_{PdH} - \mu_{pH} = eV + K_b T \ln\left(a_{H^+} / (pH_2)^{1/2}\right) \tag{8.5}$$

where a_{H+} = activity of H^+ in solution with pH = $-\log a_{H+}$, pH_2 = hydrogen partial pressure in the Pd.

From Eq. (8.5), the protochemical potential of H^+ in the PdH_x (μ_{PdH}) for $x = 0.6$ and $V = 0$ V is the same as the protochemical potential for a solution at pH = 0 ($\mu_{pH=0}$), and is higher than the protochemical potential for a solution at pH = 6.7 ($\mu_{pH=6.7}$) [65]. As a result, for $V_D = 0$, H^+ flow from PdH_x into the solution and induce a current of e^- to flow from the electrode. This current is a product of the oxidation of H from the PdH_x into H^+ [66] (Figure 8.6b) and we refer to it as depletion current (I_d). Since I_F is affected by dielectric charging of the solution, we use the magnitude of I_d to measure the extent of PdH_x formation for a given V_F assuming that for a specific V_D all of the H^+ loaded onto the Pd for V_F return to the solution. During the formation of PdH_x, we also observe a color change in the electrode from metallic (Pd, Figure 8.6c) to white (PdH_x, Figure 8.6d), while after depletion the electrode returns to its original metallic color (Pd) [67]. Second, we investigate the dependence of the PdH_x formation and depletion on the solution pH (Figure 8.6e). We determine the threshold values for V_F and V_D for a range of pH values (0.0, 2.0, 3.0, 4.5, 6.7, and 11.0). As solution pH increases, the threshold values for V_F and V_D decrease as expected due to the influence of pH on the solution protochemical potential (1) [65]. It is interesting to note that there is a range of pH and V (area in white) in which the solution and the PdH are in equilibrium and no exchange of H^+ across the interface occurs. Threshold potentials for formation (V_F) and depletion (V_D) vary as the solution pH varies. When the reaction is proceeding very slowly the calculated formation threshold voltage depends on the reaction rate in addition to activation energy, which probably causes the nonlinear results for threshold V_F.

8.7.2 Hydrogen Diffusion inside PdH_x and Depletion: Synaptic Devices and Memories

While in the biopolymer H^+ transport is driven by drift-diffusion following Poisson's equation, H^+ transport in the PdH_x is driven by diffusion [23]. This difference in transport arises because there is no electric field in Pd and H^+ likely moves as neutral H due to the similarity in electronegativity of Pd and H. To better characterize the transfer of H^+ at the PdH_x–polymer interface, we couple PdH_x contacts with the well-studied protonic conductor, Nafion. PdH_x contacts inject and drain H^+ into and from the proton-conducting Nafion (Figure 8.7a) [23, 24, 58, 59].

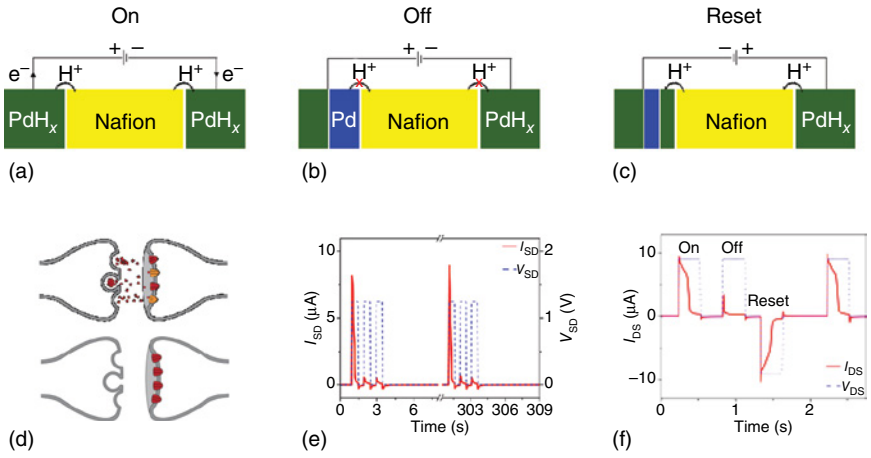

Figure 8.7 (a–c) Schematic side views of protonic synapses showing proton depletion and reuptake in the presynaptic contact. (a) ON state. (b) OFF state after a V_{SD} pulse, and the resulting I_s spike depletes the PdH_x contact of hydrogen to form Pd. (c) RESET. A negative V_{SD} injects H^+ back into the contact to form PdH_x. (d) Synaptic transmission in a chemical synapse. (e) Demonstration of ON and OFF switching in an analogous microdevice. Three positive pulses $V_{SD} = 1.25$ V, 0.25 s and a negative $V_{SD} = -1.25$ V, 0.25 s for RESET were applied. (Josberger *et al*. 2014 [67]. Reproduced with permission of John Wiley and Sons.)

For each H^+ injected into the Nafion, an excess electron is collected by the leads, which complete the circuit. H^+ current (I_{SD}) flows between the source and the drain in the protonic synapse at an external applied voltage (V_{SD}) (Figure 8.7b,d,e). The H^+ current in the Nafion channel depletes H from PdH_x and creates a concentration gradient in the PdH_x and a subsequent diffusion flux inside the contact. For low current densities, the diffusion flux in the PdH_x, the absorption of H from the H_2 atmosphere, and I_{SD} balance out and the PdH_x contacts effectively function as protodes – the protonic equivalent of electrodes. For higher current densities, as in the Nafion channel, a region of the source fully depletes H to form Pd. Pd can no longer inject H^+ in the Nafion and I_{SD} decays as a function of time. As a result, a V_{SD} pulse produces a spike in I_{SD} as the contact depletes (Figure 8.7b,e). After waiting for a determined period of time (300 s), the source replenishes H from the atmosphere and later the V_{SD} pulse results in an I_{SD} spike of the same magnitude as the first one. This type of transient behavior has previously been observed in PdH_x reversible electrodes in contact with an acidic solution [68]. This behavior is similar to short-term depression (STD) in a chemical synapse in the brain (Figure 8.7d). With these protonic devices, we demonstrated a two-terminal memory with reconfigurable "ON" and "OFF" states (Figure 8.7c,f). A protonic memory with 20 nm wide contacts would operate with only 30 fJ of energy, which is two orders of magnitude smaller than the energy used by a natural synapse (1 pJ).

8.7.3 A Phenomenological Description of Proton Transport and Acid and Base Doping

As mentioned in Section 8.2, sustained protonic conductivity requires the movement of H^+ and OH^- ions as well as Bjerrum D and L defect. The hopping

process and the associated protonic conductivity are thermally activated. This behavior of H^+ is similar to the charge carrier in electronic semiconductors. Eigen and de Maeyer first proposed a "protonic semiconductor" in 1958 "with an intrinsic (thermal) distribution of the charge carriers (protons) between a 'valence' band (H-bonded H_2O) and a conduction' band (excess protons fluctuating in H bonds)" [26]. Here, we repurpose this model to describe our complementary protonic devices. A proton wire without any H^+ or OH^- charged defects does not conduct unless an excess charge is injected from the contacts (Figure 8.8a). H^+ is equivalent to electrons in semiconductors, and acid groups are H^+ donors. OH^- ions are proton holes, and base groups are H^+ acceptors. Two kinds of energies are needed for proton transfer. The first is the activation energy. A neutral proton wire is not conductive unless energy is contributed to create a H^+ and OH^- pair (Figure 8.8c,d). The energy is defined as band gap

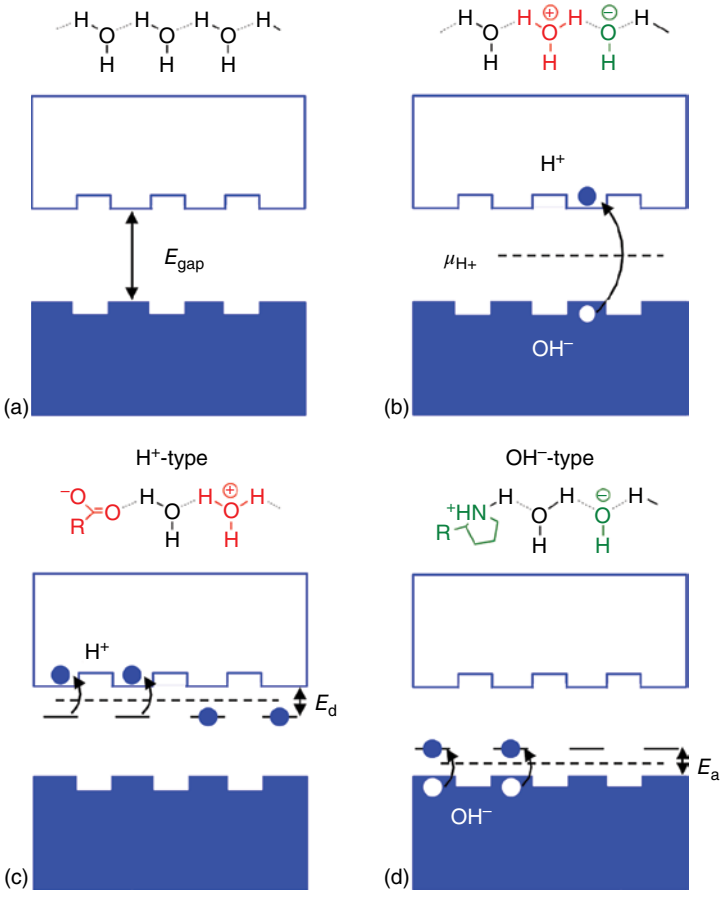

Figure 8.8 (a) Quasi-band proton wire description; (b) formation of an H^+–OH^- pair requires 0.83 eV and makes the wire conductive. (c) Acid groups in the polymer donate H^+ and create a H^+-type proton wire; (d) base groups in the polymer accept H^+ and create an OH^--type proton wire. (Deng *et al.* 2013 [24]. Reproduced with permission of Nature Publishing Group..)

energy E_{gap}. The proton wire becomes conductive by H^+ hopping from the H^+ valence band (H-bonded H_2O) to the empty H^+ conduction band (excess protons fluctuating in H bonds). The other kind of energy required for H^+ to move is hopping energy, depicted as energy wells in Figure 8.8b. The hopping energy is smaller than E_{gap}. We derive E_{gap} from the Gibbs–Helmholtz equation and the dissociation constant of water (K_w) as

$$E_{gap} = \Delta G^0 = -k_B T \ln K_w = 0.83\text{eV} \tag{8.6}$$

which is remarkably close to the thermal activation energy observed in Ref. [26]. This value for the protonic "band gap" is similar to the activation energy measured for proton-conducting biopolymers [49, 60], and is remarkably close to the band gap of traditional electronic semiconductors such as Si (1.1 eV) or Ge (0.76 eV). Not unlike Si and Ge, the conductivity of most intrinsic biological protonic conductors at room temperature is low [69]. The conductivity of proton wires can be modulated by doping with H^+ or OH^- charge carriers such as dopants (group V (P) or group III (B)) in semiconductors. The number of acid or base groups in the protonic conducting materials affects the concentration of free protons or proton holes and the conductivity. The dissociation constant of an acid/base defines its activation energy, using the same Gibbs–Helmholtz equation (Eq. (8.6)), but substituting water dissociation constant K_w to acid/base dissociation constant K_a/K_b to calculate the activation energy. The position of the protochemical potential is calculated from the activity of H^+ or the pH [2]. Qualitatively, μ^{H+} in a protonic semiconductor is affected by doping in the same way the Fermi energy in an electronic semiconductor is affected. For an intrinsic material, μ^{H+} is at mid gap. For H^+-type material, μ^{H+} is closer to the conduction band and for an OH^--type material μ^{H+} is closer to the valence band.

8.7.4 Complementary Bioprotonic Transistors

To verify the analogy of H^+-type and OH^--type protonic semiconductors with electronic semiconductors, we have demonstrated that maleic chitosan (H^+-type) and proline–chitosan (OH^--type) junction devices with proton-conducting contacts exhibit rectifying behavior equivalent to a semiconductor p–n junction [24]. We then test these materials in protonic-FET type complementary devices. In a protonic-FET, the source–drain protonic current, I_{DS}, recorded as a function of drain–source bias, V_{DS}, is controlled by changing the potential of the back gate electrode, V_{GS} (Figure 8.9).

Similarly to conventional electronic FETs, the I_{DS} modulation in the protonic FETs is described using the I_{DS} relationship in the linear regime for the gradual channel approximation [70]:

$$I_{DS} = \pm \mu_{lin} C_G \frac{W}{L}\left[\left(V_{GS} - V_{TH}\right)V_{DS}\right] \tag{8.7}$$

(+ for a negative charge carrier and – for a positive charge carrier; μ_{lin}, mobility in the linear regime; C_G, gate capacitance per unit area; W, device width; L, device length; V_{TH}, threshold gate voltage at which conduction occurs). A modification

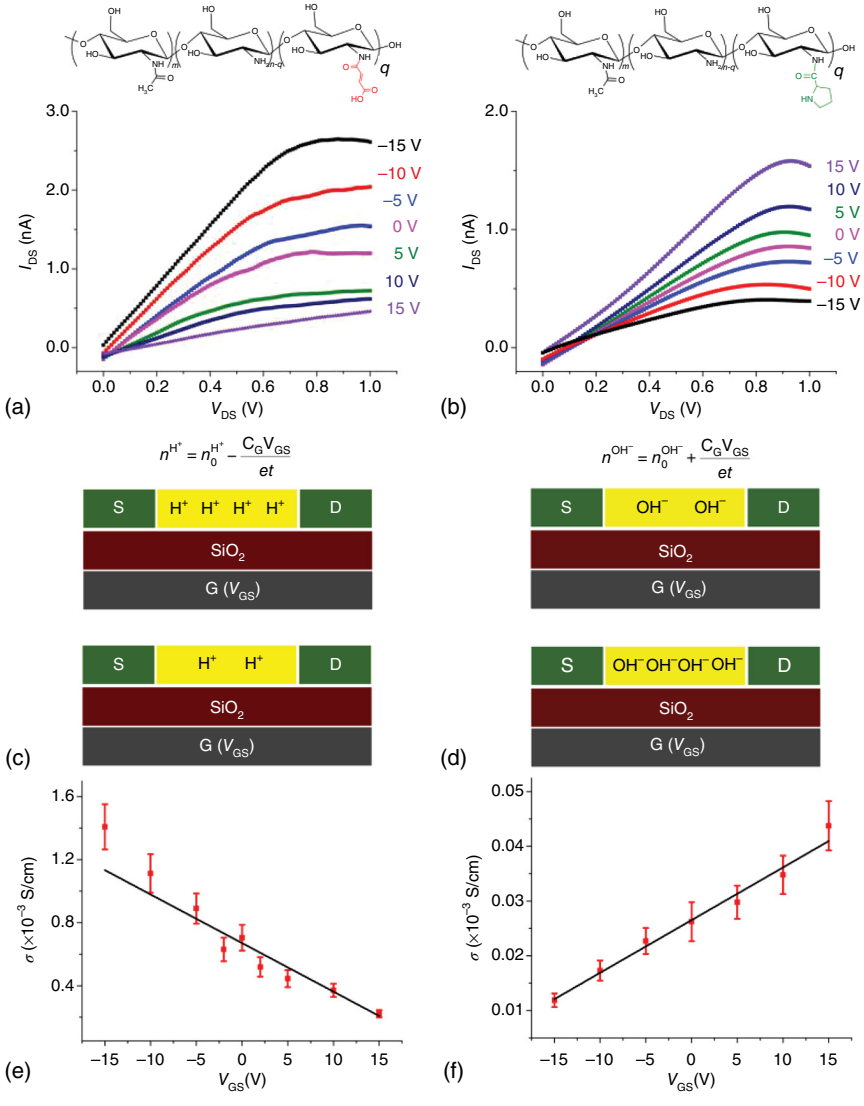

Figure 8.9 (a,b) Plots of I_{DS} as a function of V_{GS} for different V_{DS} (RH 75%) for a maleic chitosan H^+-FET and a proline–chitosan OH^- FET with PdH_x contacts. Device dimensions: length 8.6 µm, width 3.5 µm, height 82 nm for (a) and 9.6 µm, width 28 µm, height 200 nm for (b). (c,d) Schematics of H^+ and OH^- transistor capacitative charge carrier n^{H+} and n^{OH-} modulation. (e,f) Plots of σ as a function of V_{GS} and linear fit for the device in (a) and (b) respectively. For cross σ and charge density calculations the cross-sectional area of the devices was derived from Atomic Force Microscope (AFM) and the cross sections were approximated to a rectangle with $t = 66$ nm for (a) and $t = 160$ nm (b) with the same widths as the actual devices. (Deng *et al.* 2013 [24]. Reproduced with permission of Nature Publishing Group.)

is necessary because in our FETs we cannot reach V_{TH} and the devices are "ON" for $V_G = 0$ V by virtue of the acid and base doping. The resulting charge carrier density in the devices is

$$n^{H^+} = n_0^{H^+} - \frac{C_G V_{GS}}{et} \tag{8.8}$$

for H^+-FET and

$$n^{OH^-} = n_0^{OH^-} + \frac{C_G V_{GS}}{et} \tag{8.9}$$

for OH^--FET respectively (Figure 8.9c,d) and

$$J_{DS} = e\mu_{lin}^{H^+}\left(n_0^{H^+} - \frac{C_G V_{GS}}{et}\right)\varepsilon_{DS} \tag{8.10}$$

for H^+-FET and

$$J_{DS} = e\mu_{lin}^{OH^-}\left(n_0^{OH^-} + \frac{C_G V_{GS}}{et}\right)\varepsilon_{DS} \tag{8.11}$$

for OH^--FET. From this data we can derive charge carrier density and mobility for the proton-conducting chitosan. The H^+ mobility in maleic chitosan is $\sim 4.3 \times 10^{-3}\,cm^2\,V^{-1}\,s^{-1}$, which is remarkably close to the mobility of H^+ in diluted acid solutions. Recently, Gorodetsky has demonstrated the first protein based H^+-FET with the protein reflectin with similar H^+ mobility [25, 28]. Proteins are extremely attractive for these types of devices because their structure and functionality can be precisely tailored using genetic engineering. Data from the devices confirms that the acid-doped maleic chitosan behaves like a H^+-doped protonic semiconductor and that the base-doped proline–chitosan behaves like an OH^--doped protonic semiconductor.

8.7.5 Enzyme Logic Transducer

To demonstrate the flexibility of the PdH_x interface with biological systems, we integrate the Pd/PdH protode with enzyme logic (Figure 8.10) [63]. Two input signals activate glucose dehydrogenase (GDH); input A is NAD^+ and input B is glucose (Figure 8.10a). GDH requires the presence of both NAD^+ and glucose to function, effectively serving as an enzymatic AND logic [71]. The absence of glucose or NAD^+ is defined as a logic "0," while their presence is defined as logic "1." We use the formation of PdH at $V_D = -0.85\,V$ and the resulting I_D measured at $V_D = 0\,V$ as the logic output. $I_D > 0.1\,mA$ corresponds to a logic "1," while $I_D < 0.05\,mA$ corresponds to a logic 0. In the absence of either substrate (logic input "0,0," "0,1," or "1,0"), GDH is not active and the solution pH remains the same. At pH 6, a $V_F = -0.85\,V$ does not form PdH and the resulting $I_D < 0.05\,mA$. The presence of the both NAD^+ and glucose (logic "1,1") activates the biocatalytic reaction of GDH (Figure 8.10b), which produces gluconic acid and lowers the solution pH from 6.0 to 4.0. At pH 4.0, $V_F = -0.85\,V$ results in the formation of PdH. The resulting $I_D = 0.164\,mA$ at $V_D = 0\,V$ (Figure 8.10c) corresponds to a logic output 1. These results demonstrate that the Pd/PdH system can transduce proton signals from biochemical inputs into readable electronic currents.

(a)

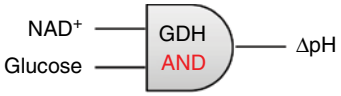

	Input A		Input B		Output		
	Logic	NAD^+	Logic	Glucose	ΔpH	I_{max}	Logic
□	0	0 mM	0	0 mM	–0.03	4 μA	0
△	0	0 mM	1	30 mM	–0.05	24 μA	0
◇	1	1 mM	0	0 mM	–0.07	7 μA	0
●	1	1 mM	1	30 mM	–1.71	167 μA	1

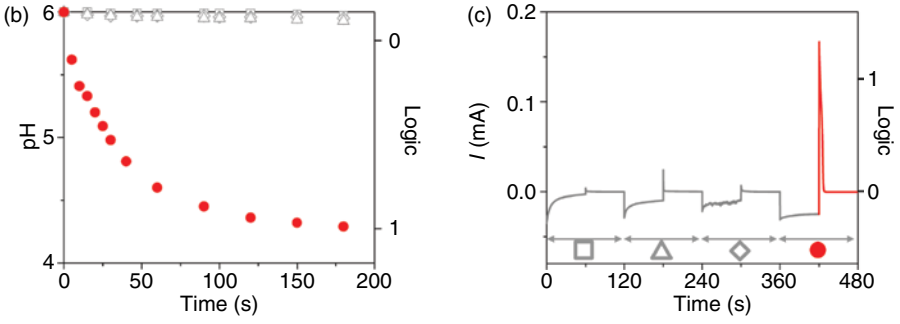

Figure 8.10 (a) Truth table for pH and current output when varying inputs as: Input A: NAD^+; Input B: glucose. An output of 1 indicates significant pH and current change; an output of 0 indicates no change and current. (b) pH change of the solution over time for varying inputs. Only when both inputs are present (1, 1) does the pH change significantly. (c) Digital readout of the protonic current with the PdH transducer controlled by enzyme logic. For each possible input (A, B), the device is first loaded at –0.85*V*, and then depleted at 0*V*. Some reduction current occurs for all negative applied voltages, but only when both inputs are present does the system display a large positive transient current at 0*V*. (Miyake *et al*. 2015 [63]. Reproduced with permission of Nature Publishing Group.)

8.8 Future Outlook

Inspired by the Grotthuss mechanisms introduced in 1804 for proton transport in proton wires, we have developed bioprotonic devices that can control and record currents of H^+ and OH^- including diodes, complementary transistors, memories, and transducers. These devices are analogous to semiconductor-based devices for electrons and holes. One of the goals for developing these devices was to provide an interface with proton-driven biological phenomena such as oxidative phosphorylation and the HCVN1 proton channel. Whether these devices will be useful in bioelectronics and translational applications remains to be seen due to very challenging fabrication as well as an on–off ratio that needs improvement for the transistors that limits practical applications. However, in developing these devices we have rediscovered PdH_x as proton-injecting contacts that can enable the DC measurement of proton currents in soft materials such as reflectin-based proteins and melanin [25, 28].

Acknowledgments

We acknowledge several students and post docs that contributed to the research reviewed here throughout the years. This work was supported by the U.S. Department of Energy (DOE), Office of Science, Basic Energy Sciences (BES), under Award #<DE-SC001044> (PdH formation and enzyme logic), the National Science Foundation CAREER Award (DMR 1150630) (bioprotonic FETs), the University of Washington, and a 3M Untenured Faculty Award. T.M. acknowledges a fellowship from the Japanese Society for the Promotion of Science. Part of this work was conducted at the Washington Nanofabrication Facility/Molecular Analysis Facility, a member of the NSF National Nanotechnology Infrastructure Network.

References

1 Nagle, J.F., Mille, M., and Morowitz, H.J. (1979) Theory of hydrogen-bonded chains in bioenergetics. *Biophys. J.*, **25**, A48–A48.
2 Nagle, J.F. and Morowitz, H.J. (1978) Molecular mechanisms for proton transport in membranes. *Proc. Natl. Acad. Sci. U.S.A.*, **75**, 298–302.
3 Cukierman, S. (2006) Et tu, Grotthuss! and other unfinished stories. *Biochim. Biophys. Acta*, **1757**, 876–885.
4 DeCoursey, T.E. (2003) Voltage-gated proton channels and other proton transfer pathways (vol 83, pg 475, 2003). *Physiol. Rev.*, **83**, 457–579.
5 Mitchell, P. (1966) Chemiosmotic coupling in oxidative and photosynthetic phosphorylation. *Biol. Rev.*, **41**, 445–502.
6 Morowitz, H.J. (1978) Proton semiconductors and energy transduction in biological-systems. *Am. J. Physiol.*, **235**, R99–R114.
7 Capasso, M., DeCoursey, T.E., and Dyer, M.J.S. (2011) pH regulation and beyond: unanticipated functions for the voltage-gated proton channel, HVCN1. *Trends Cell Biol.*, **21**, 20–28.
8 Lanyi, J.K. (2004) Bacteriorhodopsin. *Annu. Rev. Physiol.*, **66**, 665–688.
9 Walz, D. and Caplan, S.R. (2002) Bacterial flagellar motor and H+/ATP synthase: two proton-driven rotary molecular devices with different functions. *Bioelectrochemistry*, **55**, 89–92.
10 Busath, D. and Szabo, G. (1981) Gramicidin forms multi-state rectifying channels. *Nature*, **294**, 371–373.
11 Smith, S.M., Morgan, D., Musset, B., Cherny, V.V., Place, A.R., Hastings, J.W., and Decoursey, T.E. (2011) Voltage-gated proton channel in a dinoflagellate. *Proc. Natl. Acad. Sci. U. S. A.*, **108**, 18162–18167.
12 Riccardi, D., Konig, P., Prat-Resina, X., Yu, H.B., Elstner, M., Frauenheim, T., and Cui, Q. (2006) "Proton holes" in long-range proton transfer reactions in solution and enzymes: a theoretical analysis. *J. Am. Chem. Soc.*, **128**, 16302–16311.
13 Noy, A. (2011) Bionanoelectronics. *Adv. Mater.*, **23**, 807–820.
14 Richter-Dahlfors, A., Svennersten, K., Larsson, K.C., and Berggren, M. (2011) Organic bioelectronics in nanomedicine. *Biochim. Biophys. Acta*, **1810**, 276–285.

15 Leger, J., Berggren, M., and Carter, S.A. (2011) *Iontronics: Ionic Carriers in Organic Electronic Materials and Devices*, CRC Press, Boca Raton, FL.

16. Meredith, P., Bettinger, C.J., Irimia-Vladu, M., Mostert, A.B., and Schwenn, P.E. (2013) Electronic and optoelectronic materials and devices inspired by nature. *Rep. Prog. Phys.*, **76**, 034501.

17 Rivnay, J., Owens, R.M., and Malliaras, G.G. (2014) The rise of organic bioelectronics. *Chem. Mater.*, **26**, 679–685.

18 Huang, S.-C.J., Artyukhin, A.B., Misra, N., Martinez, J.A., Stroeve, P.A., Grigoropoulos, C.P., Ju, J.-W.W., and Noy, A. (2010) Carbon nanotube transistor controlled by a biological ion pump gate. *Nano Lett.*, **10**, 1812–1816.

19 Angione, M.D., Cotrone, S., Magliulo, M., Mallardi, A., Altamura, D., Giannini, C., Cioffi, N., Sabbatini, L., Fratini, E., Baglioni, P., Scamarcio, G., Palazzo, G., and Torsi, L. (2012) Interfacial electronic effects in functional biolayers integrated into organic field-effect transistors. *Proc. Natl. Acad. Sci. U.S.A.*, **109**, 6429–6434.

20 Tarabella, G., Mohammadi, F.M., Coppede, N., Barbero, F., Iannotta, S., Santato, C., and Cicoira, F. (2013) New opportunities for organic electronics and bioelectronics: ions in action. *Chem. Sci.*, **4**, 1395–1409.

21 Owens, R.M. and Malliaras, G.G. (2010) Organic electronics at the interface with biology. *MRS Bull.*, **35**, 449–456.

22 Larsson, K.C., Kjall, P., and Richter-Dahlfors, A. (2013) Organic bioelectronics for electronic-to-chemical translation in modulation of neuronal signaling and machine-to-brain interfacing. *Biochim. Biophys. Acta*, **1830**, 4334–4344.

23 Zhong, C., Deng, Y., Roudsari, A.F., Kapetanovic, A., Anantram, M.P., and Rolandi, M. (2011) A polysaccharide bioprotonic field-effect transistor. *Nat. Commun.*, **2**, 476.

24 Deng, Y., Josberger, E., Jin, J., Rousdari, A.F., Helms, B.A., Zhong, C., Anantram, M.P., and Rolandi, M. (2013) H^+-type and OH^--type biological protonic semiconductors and complementary devices. *Sci. Rep.*, **3**, 2481.

25 Ordinario, D.D., Phan, L., Walkup, W.G., Jocson, J.M., Karshalev, E., Husken, N., and Gorodetsky, A.A. (2014) Bulk protonic conductivity in a cephalopod structural protein. *Nat. Chem.*, **6**, 597–603.

26 Eigen, M. and Demaeyer, L. (1958) Self-dissociation and protonic charge transport in water and ice. *Proc. R. Soc. London, Ser. A*, **247**, 505–533.

27 Bard, A.J. and Faulkner, L.R. (2001) *Electrochemical Methods: Fundamentals and Applications*, 2nd edn, John Wiley & Sons, Inc., New York.

28 Rolandi, M. (2014) Bioelectronics: a positive future for squid proteins. *Nat. Chem.*, **6**, 563–564.

29 Pomes, R. and Roux, B. (2002) Molecular mechanism of H+ conduction in the single-file water chain of the gramicidin channel. *Biophys. J.*, **82**, 2304–2316.

30 Kumar, P.P. and Yashonath, S. (2006) Ionic conduction in the solid state. *J. Chem. Sci.*, **118**, 135–154.

31 Wraight, C.A. (2006) Chance and design – proton transfer in water, channels and bioenergetic proteins. *Biochim. Biophys. Acta*, **1757**, 886–912.

32 Park, K., Lin, W., and Paesani, F. (2014) Fast and slow proton transfer in ice: the role of the quasi-liquid layer and hydrogen-bond network. *J. Phys. Chem. B*, **118**, 8081–8089.

33 Hassanali, A., Giberti, F., Cuny, J., Kuhne, T.D., and Parrinello, M. (2013) Proton transfer through the water gossamer. *Proc. Natl. Acad. Sci. U.S.A.*, **110**, 13723–13728.

34 DeCoursey, T.E. (2008) Voltage-gated proton channels. *Cell. Mol. Life Sci.*, **65**, 2554–2573.

35 Mitchell, P. (1961) Chemiosmotic coupling in oxidative and photosynthetic phosphorylation. *Biochem. J.*, **79**, P23.

36 Nagle, J.F. and Morowitz, H.J. (1978) Molecular mechanisms for proton transport across membranes. *Biophys. J.*, **21**, A58–A58.

37 DeCoursey, T.E. (2008) Voltage-gated proton channels: what's next? *J. Physiol.*, **586**, 5305–5324.

38 DeCoursey, T.E. (2013) Voltage-gated proton channels: molecular biology, physiology, and pathophysiology of the H-V family. *Physiol. Rev.*, **93**, 599–652.

39 Mitchell, P. (2011) Chemiosmotic coupling in oxidative and photosynthetic phosphorylation. *Biochim. Biophys. Acta*, **1807**, 1507–1538.

40 Oesterhelt, D. (1976) Bacteriorhodopsin as an example of a light-driven proton pump. *Angew. Chem. Int. Ed. Engl.*, **15**, 17–24.

41 Onufriev, A., Smondyrev, A., and Bashford, D. (2003) Affinity changes driving unidirectional proton transport in the bacteriorhodopsin photocycle. *J. Mol. Biol.*, **332**, 1183–1193.

42 Hoeve, C.A. and Lue, P.C. (1974) The structure of water absorbed in collagen. I. The dielectric properties. *Biopolymers*, **13**, 1661–1680.

43 Migchels, C. and Berendse, H. (1973) Proton exchange and molecular orientation of water in hydrated collagen fibers – NMR-study of H_2o and D_2o. *J. Chem. Phys.*, **59**, 296–305.

44 Samsudin, A.S., Khairul, W.M., and Isa, M.I.N. (2012) Characterization on the potential of carboxy methylcellulose for application as proton conducting biopolymer electrolytes. *J. Non-Cryst. Solids*, **358**, 1104–1112.

45 Ashcroft, N.W. and Mermin, N.D. (1976) *Solid State Physics*, Holt, New York.

46. Bruni, F., Careri, G., and Leopold, A.C. (1989) Critical exponents of protonic percolation in maize seeds. *Phys. Rev. A*, **40**, 2803–2805.

47 Stevens, M.M. and George, J.H. (2005) Exploring and engineering the cell surface interface. *Science*, **310**, 1135–1138.

48 Wegst, U.G., Bai, H., Saiz, E., Tomsia, A.P., and Ritchie, R.O. (2014) Bioinspired structural materials. *Nat. Mater.*, **14**, 23–36.

49 Murphy, E.J. (1976) Ionic-conduction in keratin (wool). *J. Colloid Interface Sci.*, **54**, 400–408.

50 Helms, B.A., Deng, Y., and Rolandi, M. (2015) Synthesis of pyridine chitosan and its protonic conductivity. *J. Polym. Sci., Part A: Polym. Chem.*, **53**, 3.

51 Mostert, A.B., Powell, B.J., Pratt, F.L., Hanson, G.R., Sarna, T., Gentle, I.R., and Meredith, P. (2012) Role of semiconductivity and ion transport in the electrical conduction of melanin. *Proc. Natl. Acad. Sci. U.S.A.*, **109**, 8943–8947.

52 Mostert, A.B., Powell, B.J., Gentle, I.R., and Meredith, P. (2012) On the origin of electrical conductivity in the bio-electronic material melanin. *Appl. Phys. Lett.*, **100**, 093701.

53 Petrenko, V.F. and Maeno, N. (1987) Ice field transistor. *J. Phys. Paris*, **48**, 115–119.

54 Vanheusden, K., Warren, W.L., Devine, R.A.B., Fleetwood, D.M., Schwank, J.R., Shaneyfelt, M.R., Winokur, P.S., and Lemnios, Z.J. (1997) Non-volatile memory device based on mobile protons in SiO_2 thin films. *Nature*, **386**, 587–589.

55 Fan, R., Huh, S., Yan, R., Arnold, J., and Yang, P.D. (2008) Gated proton transport in aligned mesoporous silica films. *Nat. Mater.*, **7**, 303–307.

56 Zhu, L.Q., Wan, C.J., Guo, L.Q., Shi, Y., and Wan, Q. (2014) Artificial synapse network on inorganic proton conductor for neuromorphic systems. *Nat. Commun.*, **5**, 3158.

57 Deml, A.M., Bunge, A.L., Reznikov, M.A., Kolessov, A., and O'Hayre, R.P. (2012) Progress toward a solid-state ionic field effect transistor. *J. Appl. Phys.*, **111**, 074511.

58 Morgan, H., Pethig, R., and Stevens, G.T. (1986) A proton-injecting technique for the measurement of hydration-dependent protonic conductivity. *J. Phys. E: Sci. Instrum.*, **19**, 80–82.

59 Glasser, L. (1975) Proton conduction and injection in solids. *Chem. Rev.*, **75**, 21–65.

60 Bardelme, G. (1973) Electrical-conduction in hydrated collagen.1. Conductivity mechanisms. *Biopolymers*, **12**, 2289–2302.

61 Evans, B.R., O'Neill, H.M., Malyvanh, V.P., Lee, I., and Woodward, J. (2003) Palladium-bacterial cellulose membranes for fuel cells. *Biosens. Bioelectron.*, **18**, 917–923.

62 Deng, Y., Wünsche, J., Kumar, P., Di Mauro, E., Josberger, E., Sayago, J., Pezzella, A., Soavi, F., Cicoira, F., Rolandi, M., and Santato, C. (2015) Protonic and electronic transport in hydrated thin films of the pigment eumelanin. *Chem. Mater.*, **27**, 6.

63 Miyake, T., Josberger, E.E., Keene, S., Deng, Y., and Rolandi, M. (2015) An enzyme logic bioprotonic transducer. *APL Mater.*, **3**, 014906, in press.

64. Flanagan, T.B. and Lewis, F.A. (1959) Electrode potentials of the palladium + hydrogen system. *Trans Faraday Soc.*, **55**, 1409–1420.

65 Imokawa, T., Williams, K.J., and Denuault, G. (2006) Fabrication and characterization of nanostructured Pd hydride pH microelectrodes. *Anal. Chem.*, **78**, 265–271.

66 Gabrielli, C., Grand, P.P., Lasia, A., and Perrot, H. (2004) Investigation of hydrogen adsorption-absorption into thin palladium films - I. Theory. *J. Electrochem. Soc.*, **151**, A1925–A1936.

67 Josberger, E.E., Deng, Y., Sun, W., Kautz, R., and Rolandi, M. (2014) Two-terminal protonic devices with synaptic-like short-term depression and device memory. *Adv. Mater.*, **26**, 4986–4990.

68 Yang, T.H., Pyun, S., and Yoon, Y. (1997) Hydrogen transport through Pd electrode: current transient analysis. *Electrochim. Acta*, **42**, 1701–1708.

69 Christie, J.H. and Woodhead, I.M. (2002) A new model of DC conductivity of hygroscopic solids – Part 1: cellulosic materials. *Text. Res. J.*, **72**, 273–278.

70 Sze, S.M. (1982) Citation classic – physics of semiconductor-devices. *Cc/Eng. Technol. Appl. Sci.*, in Chapter 1 (7–60) and 8 (431–510).

71 Katz, E. and Privman, V. (2010) Enzyme-based logic systems for information processing. *Chem. Soc. Rev.*, **39**, 1835–1857.

9

Emulating Natural Photosynthetic Apparatus by Employing Synthetic Membrane Proteins in Polymeric Membranes

Cherng-Wen Darren Tan and Eva-Kathrin Sinner

University of Natural Resources and Life Sciences, BOKU, Department of Nanobiotechnology, Institute of Synthetic Bioarchitectures, Muthgasse 11, 2OG, 1190, Vienna, Austria

9.1 Introduction

A venerable parade of names including Thales of Miletus, Benjamin Franklin, Luigi Galvani, André-Marie Ampère, George Ohm, Ernst Werner von Siemens, and Nikola Tesla, among many others, marks the development of mankind's knowledge, and eventual harnessing, of the power of electricity [1, 2]. In this, the twenty-first century, electricity is the motive force of our technology. The second industrial revolution saw the combination of steam and electrical powers, wherein the former drove generators that provided the latter. However, the tremendous technological progress from the early nineteenth century to the present day saw an overwhelming increase in the consumption of electricity. This rapidly led to the realization that our current repertoire of methods for producing electricity may no longer be sufficient or viable. As an alternative, we turned to the sun.

Our star is already one of two primary sources of chemical energy for terrestrial life. Photoautotrophs, such as green plants, collect photons from the sun and transduce their energies into chemical potentials, driving chemical reactions and, hence, life [3]. Others in the food chain benefit by consumption of these green plants, thus inheriting the chemical potential they had generated [3].

The possibility of an analogous process, whereby the energy of photons could be transformed into electricity, was first shown in the nineteenth century. At the age of 19, Alexandre-Edmond Becquerel observed that when light was shone on acidified silver chloride, in contact with platinum electrodes, voltage and current were produced [4]. It is for this reason that the photovoltaic effect, central to the function of solar cells, is also called the *Becquerel effect*.

Today, dye-sensitized solar cells require semiconductor materials, such as ruthenium dye, which capture the energy of incident light by transferring it to their electrons [5, 6]. These excited electrons are then injected into the material of attendant electrodes and enter the circuit through which they run. However,

Green Materials for Electronics, First Edition.
Edited by Mihai Irimia-Vladu, Eric D. Glowacki, Niyazi S. Sariciftci, and Siegfried Bauer.

ruthenium is a rare and expensive metal, the mining of which has an undesirable impact on the environment. In the hope of alleviating this environmental burden, researchers turned to natural dye sensitizers as an alternative. Terrestrial photoautotrophs again serve as an inspiration.

Photosynthetic bacteria and green plants have evolved photosynthetic pigments and proteins capable of harnessing light and transducing the energy to chemical potential [7]. These include the light-harvesting complex II (LHCII) protein and its associated chlorophylls, as well as the proteins of the photosystem II (PSII) reaction center [7].

In the process of transduction, the energy of the incident light is transferred using electrons as charge carriers [8]. This process, one of the most successful evolutionary adaptations to arise, mirrors that of the photovoltaic effect [8]. In addition, such photosynthetic materials are ubiquitous and abundant, being easily found in every green plant, making them readily available at low cost. For these reasons, such naturally occurring photosensitive materials are an attractive alternative to conventional molecular dye sensitizers. In fact, photosystem I (PSI) has been used as a component of artificial photosynthetic systems as well as for the development of organic photovoltaic devices to replace silicon-based solar cells [9, 10].

However, it is the attendant LHCII proteins with their bound pigments that increase the wavelength absorption range of PSII, rendering the system more efficient [11]. Furthermore, the associated pigments have a protective effect that prevents damage to the LHCII when under intense photoexcitation [11]. Each LHCII molecule has also been found to be amenable to surface immobilization, without severe loss of its function [11]. In addition, LHCII is the most abundant membrane protein on Earth, as well as in green plants. These reasons suggested that LHCII might be more appropriate for further studies than other photosynthetic complexes.

9.2 Light-Harvesting Complex II

LHCII is the most abundant membrane protein on Earth [12]. It is found in photosynthetic bacteria, as well as in the thylakoid membrane in chloroplasts of green plants [7]. In the latter, LHCII is associated with other photosynthetic proteins forming what is called *photosystem II* (Figure 9.1) [7].

Where LHCII is the apparatus for trapping light, PSII is the instrument by which this energy is transduced into electrical and finally chemical energy. For this reason, the LHCII complex is also called the *antenna complex* [7, 13]. Each comprises three associated LHCII monomers [14]. Each monomer protein is composed of a 232 amino-acid-long polypeptide [15]. Intrinsic to the structure of each LHCII monomer in the trimer complex is the presence of eight molecules of chlorophyll *a*, six of chlorophyll *b*, two of lutein, one of neoxanthin, and one of violaxanthin, of which the latter three are known collectively as carotenoids [15, 16]. Each monomer also tightly binds one phospholipid [16].

The ability of LHCII to sensitize solar cells was demonstrated by researchers including Yu *et al.* [16, 17]. In their work, they managed to isolate LHCII with its

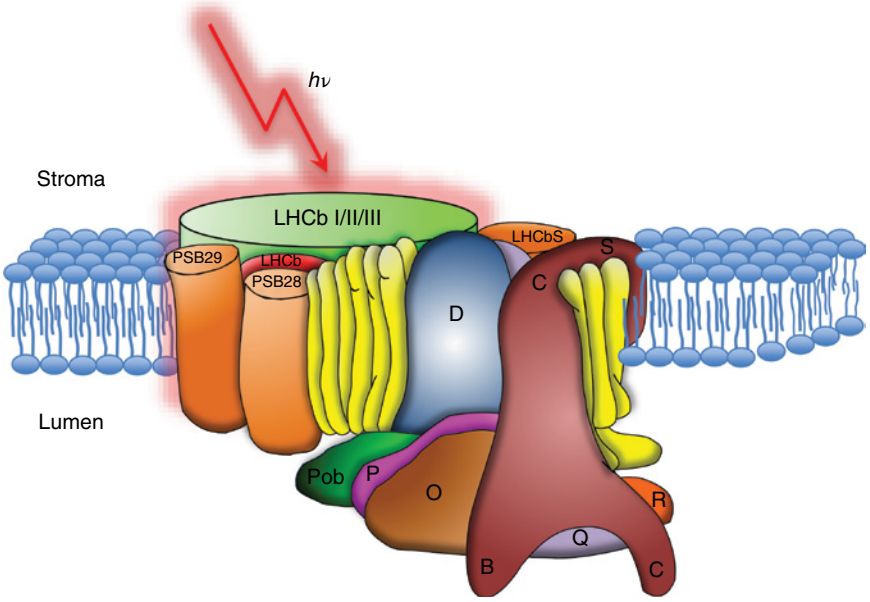

Figure 9.1 Figure showing photosystem II and its component proteins. Light (indicated by "*hν*") is received by the LHCb complex and transduced through the other components of the photosystem II complex.

associated pigments from spinach leaves by solubilizing the proteins in a detergent. They then deposited the proteins onto fluorine-doped tin oxide glass and characterized their current–voltage properties. What they found was not only that the system generated electricity upon exposure to light but also that this photocurrent increased linearly with the intensity of the incident light used. However, they did note that the LHCII might have undergone conformational change, thus affecting its performance.

The function of LHCII, as with all other membrane proteins, depends critically on its structure. The failure to adopt the appropriate protein conformation, or the loss of this structure, typically leads to loss or reduction of performance. If LHCII is to be studied in isolation from its natural environment, it is important to ensure that its structure is maintained or properly assumed. This is a concern for all membrane proteins being studied *in vitro*.

9.3 Natural Proteins in Natural Membrane Assemblies

Higher terrestrial life, such as green plants and humans, is made up of an incredible panoply of cells, numbering in the trillions for the latter [3, 18]. These are arranged into complex networks of tissue or organs, each performing minute but intricate tasks critical to the survival of the system (Figure 9.2). It is crucial that

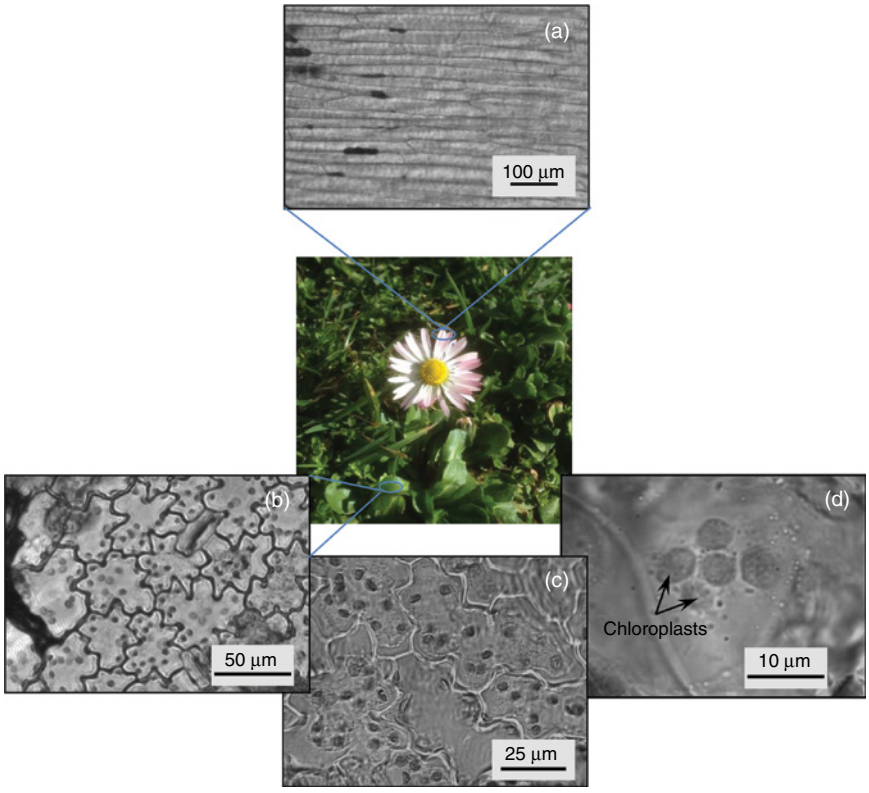

Figure 9.2 Images showing plant structures. (center) Photograph of *Bellis perennis* plant. Phase contrast micrographs of (a) flower petal cells, (b) leaf cells, (c) leaf cells at higher magnification, and (d) chloroplasts inside a leaf cell.

these cells perform their various functions in concert with other cells around them [3].

Each cell is an individual living system delineated by a bilayered lipid cell surface membrane [3]. This membrane regulates and isolates the interior of a cell from its surrounding, thus allowing it to maintain its identity and function. Organelles within cells, such as mitochondria and chloroplasts, are also bound by membranes for the same reason. However, these membranes also form a barrier to communication. Despite this isolation, a cell or organelle must still be able to sense its surroundings and respond appropriately. Like any self-sufficient machine, each membrane-bound structure needs sensors and actuators.

These functions are performed by proteins embedded in the cell surface membrane [3]. Some of these membrane proteins span the entire membrane bilayer, serving as a bridge between the environment outside and inside the cell or organelle (Figure 9.3).

These transmembrane proteins are of particular interest as they typically serve a dual purpose – that of sensing a change in the environment and subsequently effecting a change in the cell/organelle interior or behavior in response [3]. To illustrate, photosynthetic membrane proteins, such as LHCII, sense light and

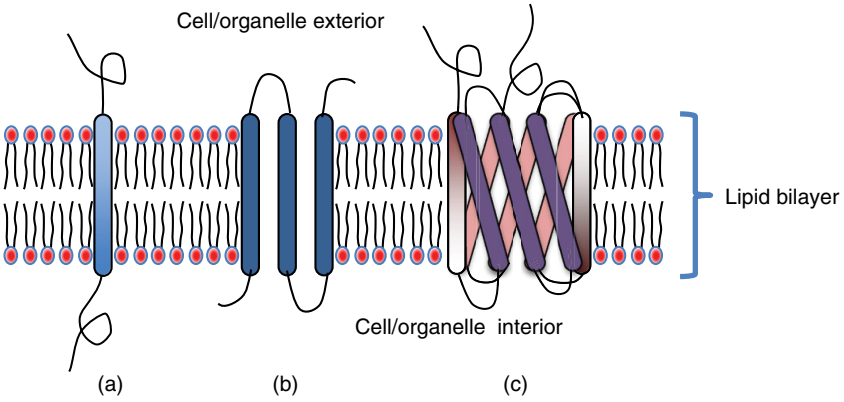

Figure 9.3 Types of membrane protein. (a) Single-pass transmembrane protein. (b) Polytopic transmembrane protein. (c) Polytopic transmembrane protein complex comprising multiple membrane proteins.

transfer or transduce this energy into work. Needless to say, any failure or inadequacy of these proteins in their function often leads to pathologies that result in malformation or illness [19]. Protein function, invariably, is dependent on protein structure.

Unlike soluble proteins, membrane proteins depend on interaction with the surrounding lipid molecules in order to maintain their structure. Depriving them of the lipids in an aqueous environment would typically result in the proteins aggregating, as the hydrophobic transmembrane domains associate in mutual shielding. For this reason, Yu *et al.* were careful to include a detergent in their LHCII preparation. Being amphiphilic, detergents would react with membrane proteins in a manner similar, though not necessarily identical, to lipids. For their native function to be probed, membrane proteins have to remain membrane bound, or be at least detergent-stabilized.

9.3.1 The Need for Reliable Test Systems

Typically, experiments on membrane proteins are performed on cultured cells expressing these proteins on their cell surface membrane [20]. These proteins are either expressed endogenously, or from appropriate expression vectors encoding the protein. However, a cell's surface membrane is decorated with other membrane proteins and this presents a challenge for researchers to distinguish the proteins of interest from the rest [21]. The presence of competing contaminants inevitably complicates the interpretation of data [22]. Furthermore, each batch of cells typically does not behave exactly as another batch in an assay, so that reproducibility between batches is poor. This is exacerbated by aging of the cells during culture, which can significantly modify their behavior during assays. Addressing this problem by using only one batch of cells for multiple tests is also impractical since the same batch of cells would likely not response identically in subsequent assays. This is due to the fact that after an assay, the cell surface cannot be restored to the same pristine state that was present at the start of the first experiment. Similarly, certain assays, such as ligand-binding assays, might cause inter-

nal changes to the cells, resulting in a form of physiological memory, which will also modify their response in subsequent tests.

Furthermore, the common use of high yield promoters such as T7 in expression vectors generally leads to overproduction of the desired protein [21, 23]. This necessarily channelizes metabolic resources to the production process, often to the detriment of the host. In some cases, the membrane proteins of interest may also be toxic, again leading to reduced host cell viability [20, 24].

In addition, specialized knowledge as well as biosafety facilities are necessary for the maintenance and testing of cells in culture [25, 26]. This presents a considerable drain in resources.

9.3.2 Membrane Proteins in Artificial Membranes

To address these difficulties, researchers have turned to the use of artificial systems that mimic the cell or organelle surface membrane, but not the entire cell or organelle [27, 28]. These are often bilayered membranes comprising phospholipids assembled into sheets, discs, or vesicles, with membrane proteins embedded in them [21, 22, 24, 27, 29–32].

When properly folded and oriented these systems would present the membrane proteins in their native conformation and orientation for testing [23, 30, 33]. This eliminates nonspecific responses common in cultured cell experiments owing to the presence of other membrane proteins, and also decouples the response of the target protein from the modulatory effects of these contaminants.

However, this approach presents two challenges: (i) a supply of pure membrane proteins is required; (ii) a means is needed to insert these proteins into the artificial membrane. Both challenges have been addressed in a variety of ways.

9.3.3 Membrane Protein Production

The production of proteins in quantity is a technology that is decades old [20, 34]. Cultured cells have been used to produce proteins of interest, often by transforming these cells with the appropriate expression vectors. The desired proteins are then purified from the broth or the host using well-established methods including immunoprecipitation and affinity chromatography [35, 36]. This method is favored by researchers, such as Harold Paulsen, for the production of LHCII in *Escherichia coli.* However, the use of cells reintroduces the need for specialized labor and infrastructure, which the use of membrane proteins in artificial membranes was supposed to obviate in the first place. Furthermore, photosynthetic complexes are difficult to purify to homogeneity, although density centrifugation methods have been widely used.

As such, alternatives such as cell lysates and recombinant protein mixes have been used to transcribe these vectors and translate the resultant mRNA into the desired protein [22, 34, 37, 38]. This can then be purified from the reaction mixtures as described above. To this end, a wide range of systems are available commercially, which provide the necessary enzymes and basic material for the expression of genes properly encoded in expression vectors. These kits are based on the wheat germ extract, reticulocyte lysate, and bacterial lysate systems [39–42].

Since protein function is critically dependent on their structure, the failure to fold the synthesized protein would produce proteins that are not functional, and so, useless for studies [19, 21, 24]. As such it is critical, when using these lysate and recombinant systems, to ensure that the nascent polypeptides are properly folded and retain this folding.

Membrane proteins are particularly difficult since they typically comprise stretches of hydrophobic domains [21]. It is the hydrophobicity of these domains that allows them to be anchored in membranes via interaction with the hydrophobic interface of the phospholipid bilayer [19]. However, it is also the interaction of these domains that causes the proteins to precipitate when in aqueous solutions. The resultant precipitates would be misfolded and hence cannot function properly. To prevent this, researchers have turned to the use of artificial membranes to mimic the protective function of the cell surface membrane [27, 29–32, 36].

9.3.4 Artificial Membranes

The use of phospholipids for the fabrication of artificial membranes readily suggests itself. Phosphatidylcholine and phosphoethanolamine are examples of phospholipids commonly used to mimic mammalian cell membranes [36, 43]. These, along with glycolipids and cholesterol, are typical components of cell membranes. Varying the ratio of these three, as well as other lipids, allows one to mimic different membranes found in cells, such as the surface, mitochondrial, and chloroplast membranes [44]. In the case of photosynthetic complexes, such as LHCII, one may choose to mimic the thylakoid membrane, which consists of phosphatidylglycerol, digalactosyl diacylglycerol, monogalactosyl diacylglycerol, and sulfoquinovosyl diacylglycerol [12].

A common technique of preparing phospholipid membranes is to dissolve the phospholipids in a volatile solvent such as dimethyl formamide and then slowly drying an aliquot in a glass container, such as a round-bottomed flask. Elevated temperatures and constant rotation ensures that the drying phospholipids form a thin, even layer against the glass surface. An aqueous saline solution is then added to rehydrate the phospholipids. Sonication or rapid stirring during this process encourages the phospholipids to dissolve thoroughly, self-assembling into bilayered vesicles in the process. These vesicles – liposomes – are then extruded through polycarbonate membranes of defined pore size to liberate nested vesicles, as well as to force the liposomes into a more uniform size distribution [45–47].

9.3.5 Integrating Protein and Membrane Production

Many methods have been devised to insert synthesized membrane protein into artificial membranes. Typically, one would first dissolve the membrane protein in a detergent solution before the addition of liposomes. At the right concentration, the detergent surrounding the proteins would also interact with the membrane lipids, allowing the protein to penetrate the bilayer. This may be facilitated by similar treatment of the liposomes with detergents, although this would also require careful selection of detergent concentration to avoid solubilizing the lipids. The detergents are then removed, leaving the proteins correctly folded and embedded in the artificial membrane. Alternatively, one could subject a mixture

of the membrane protein and liposomes to repeated freeze–thaw cycles. This presumably disrupts the membrane structure and in the process of self-assembly between cycles, the proteins have a chance to interact with the lipids and assume a folded conformation. Other methods include first immobilizing the membrane proteins against a solid surface, and then adding the lipids in aqueous medium to allow the molecules to self-assemble into a membrane around the proteins. This method offers the advantage of ensuring that the proteins are uniformly distributed and unidirectional. A recent development is *in vitro* membrane-assisted protein synthesis [22, 30, 31, 33, 48]. This is a generic phrase coined to describe those methods of producing protein-embedded artificial membranes without the use of surfactants and wherein the protein is produced in the presence of the artificial membranes. Such approaches have also produced membranes with integrated, correctly folded, and properly orientated membrane proteins [22, 23, 31, 33, 48, 49]. Users have provisionally described a process of protein insertion into the membrane that mimics part of the process that goes on in cells – namely, that the gene of interest is expressed as nominally occurs in cells, during which the nascent polypeptide, as it emerges from the ribosomes during translation, spontaneously inserts into the artificial membrane present. This process is descriptively termed *co-translational insertion* [22, 24, 31, 32, 50] (Figure 9.4). It should be noted, however, that whether the proteins are actually inserted co- or post-translationally has not yet been exhaustively probed. Nonetheless, this method seems to be universally amenable for the production of membrane-embedded proteins.

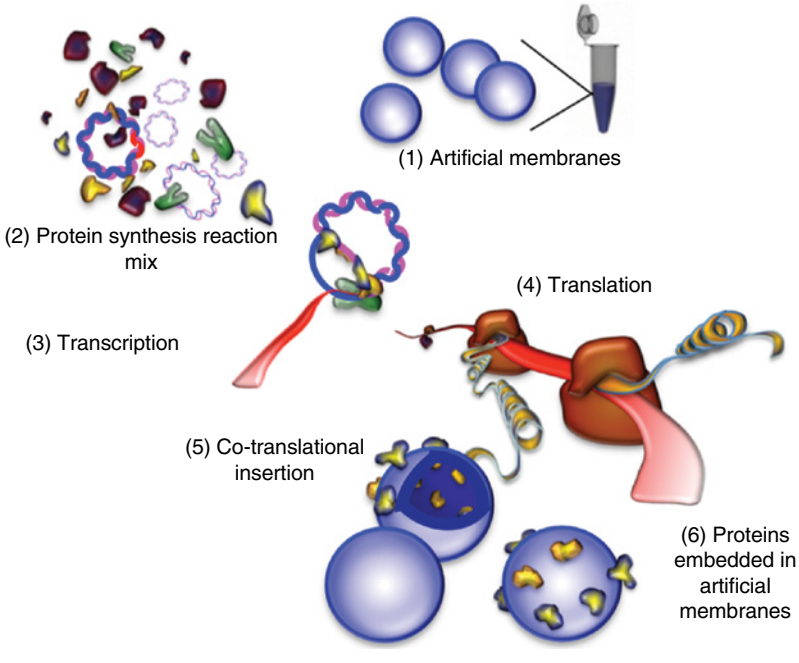

Figure 9.4 Diagram showing putative co-translational insertion during *in vitro* membrane-assisted protein synthesis (iMAPS).

9.3.6 LHCII in Artificial Lipid Membranes

Considerable work has been done by Kühlein, Paulsen, van Amerongen, and others in understanding how to produce LHCII and to preserve its structure and function. In the process, it was learnt that pigment binding in aqueous media has a crucial effect on LHCII structure, allowing it to assume, at least partially, its native conformation. The pigments also appear to have an effect on the ability of the LHCII to trimerize into functional complexes. Further stabilization of LHCII trimer complex structure appears to rely on interaction with the surrounding lipids, especially phosphatidylglycerol, for which it has a binding site.

This ability to refold partially in the presence of pigments is an advantage that few other membrane proteins offer, thus reinforcing the argument for LHCII as an appropriate choice for further development. Paulsen *et al.* managed to produce LHCII in *E. coli*, from which it was then purified. The purified protein was then reconstituted with pigments and then into thylakoid membranes isolated from pea seedlings, or mixed with lipids derived from isolated thylakoids. Thereafter, various fluorescence and surface plasmon-resonance-based characterization techniques showed that the LHCII produced retained functional characteristics similar to their native counterparts. This body of work demonstrated that LHCII removed from its native milieu and supported by artificial lipid membranes is still able to harness the energy of incident light.

9.3.7 LHCII in Artificial Polymer Membranes

Although phospholipid membranes can mimic the cell membrane, they are vulnerable to mechanical damage and instability due to oxidation of the phospholipids [27]. Furthermore, chemical modification such as glycosylation and probe labeling is not trivial for phospholipids. Once more, the search for alternatives has begun and, increasingly, researchers are looking to polymers.

The works of Hermann Staudinger and Jean-Marie Lehn helped us to understand the nature of polymers and polymer assemblies, and how they can behave in ways similar to biological systems. In time, pioneers such as Helmut Ringsdorf and Wolfgang Meier began combining proteins and polymers, showing that both can coexist and still retain their individual character. The latter especially showed that membranes composed of a triblock copolymer could mimic the hydrophilic–hydrophobic–hydrophilic layered character of lipid membranes, and even support membrane proteins embedded in them [51, 52]. As with lipid membranes, these can be produced in the form of vesicles – polymersomes – or as planar tethered membranes.

The use of polymers allows one to control the purity, chemical composition, and chemical modification of the artificial membranes to a greater degree [53]. Furthermore, polymers can be designed to be resistant to oxidation and, to a certain extent, resistant to mechanical pressure and dehydration. This last is particularly useful if the vesicles are to be analyzed using methods such as electron microscopy, wherein a vacuum is applied.

For these reasons, Sinner *et al.* chose to produce LHCII supported by a polymer membrane. Instead of phospholipids, or triblock copolymers, they chose to use an amphiphilic diblock copolymer, poly(butadiene)–poly(ethylene oxide) instead (Figure 9.5) [27, 53].

Thin film rehydration of poly(butadiene)–poly(ethylene oxide), as described for phospholipids above, results in polymersomes that mimic the bilayered membrane structure of liposomes [27]. In addition, Sinner *et al.* has used both polymersomes and tethered polymer bilayers as supporting membranes. These have proved to be able to host membrane proteins using a variety of insertion methods [27, 33, 48, 49].

Sinner has also used *in vitro* membrane-assisted protein synthesis to produce the LHCII and have it insert into the polymer membrane spontaneously. Unlike LHCII purification from a plant or bacterial source followed by detergent-assisted membrane reconstitution, this approach simplified the process of protein production as well as integration. Of particular interest is the fact the LHCII also appeared to have been incorporated into the membranes in a single, preferred orientation. In this work, LHCII was produced using a wheat-germ-based cell-free lysate. This plant-derived protein expression system was deemed most appropriate for the expression of what is, in their case, a plant photosynthetic protein. Furthermore, expression levels of the LHCII appeared to increase, to a point, with the addition of polymer material, thus allowing the group to improve the yield of membrane-bound LHCII. Fluorescence-based characterization showed that the LHCII so produced is able to effect energy transfer through its pigments upon illumination.

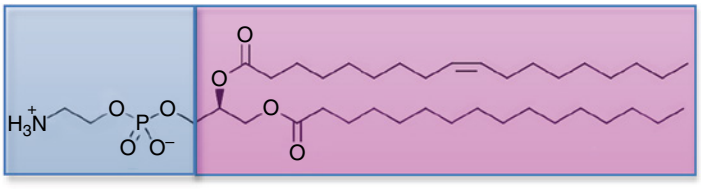

Figure 9.5 Amphiphilic nature of molecules that self-assemble into membranes. Chemical structure of (a) the phospholipid, palmitoyl-oleyl-*sn*-phosphatidylcholine and (b) the polymer, poly(butadiene)–poly(ethyeneoxide) (1,2-rich microstructure fraction, Polymer Source, USA). Regions highlighted with blue and pink boxes are hydrophilic and hydrophobic, respectively. (b) Each blue and pink strip indicates a repeat of the chemical structure highlighted in the blue and pink boxes.

9.4 Plant-Inspired Photovoltaics: The Twenty-First Century and Beyond

Recent and extensive work suggests that photosynthetic complexes, such as LHCII, might offer a viable alternative to the use of rare molecular dyes in photovoltaic systems. That these protein complexes are in abundance, being found in the leaf of every green plant around us, means that their use may not leave a harmful imprint on the biosphere. That they can also be synthesized and stabilized in artificial membranes indicates that production of functional, membrane-bound, photosynthetic complexes can be industrialized. If successful, this would mean that such complexes need not be obtained from plants, thus allowing users to avoid impinging on, and potentially depleting, the biosphere. On a final note, it should be highlighted that virtually any membrane protein, including other charge-carrying proteins such as cytochrome *c* and ubiquinone, might be synthesized and embedded in artificial membranes. As such, the production of synthetic proteins in synthetic membranes might serve as a generic means to produce functional, electroconductive membrane-bound proteins for integration into electronic systems.

List of Abbreviations

iMAPS	*in vitro* membrane-assisted protein synthesis
LHCII	light-harvesting complex II
PSII	photosystem II

References

1 Hummel, R.E. (2012) *Electronics Properties of Materials*, 4th edn, Springer.
2 Mokyr, J. (1998) *The Second Industrial Revolution, 1870-1914*, Northwestern University.
3 Alberts, B. (2013) *Essential Cell Biology*, 4th edn, New York, NY, Garland Science.
4 U.S. Department of Energy office of Energy Efficiency and Renewable Energy. (2004) *The History of Solar,* U.S. Department of Energy office of Energy Efficiency and Renewable Energy.
5 Hardin, B.E.H., Hoke, E.T., Armstrong, P.B., Yum, J.-H., Comte, P., Torres, T., Frechet, J.M.J., Nazeeruddin, M.K., Grätzel, M., and McGehee, M.D. (2009) Increased light harvesting in dye-sensitized solar cells with energy relay dyes. *Nat. Photonics*, **3** (7), 406–411.
6 Siegers, C., Wurfel, U., Zistler, M., Gores, H., Hohl-Ebinger, J., Hinsch, A. *et al.* (2008) Overcoming kinetic limitations of electron injection in the dye solar cell via coadsorption and FRET. *ChemPhysChem*, **9** (5), 793–798.
7 Barber, J. (2002) Photosystem II: a multisubunit membrane protein that oxidises water. *Curr. Opin. Struct. Biol.*, **12** (4), 523–530.

8 Lukins, P.B. (2000) Direct observation of semiconduction and photovoltaic behaviour in single molecules of the Photosystem II reaction centre. *Chem. Phys. Lett.*, **321**, 13–20.

9 Yu, D., Wang, M., Zhu, G., Ge, B., Liu, S., and Huang, F. (2015) Enhanced photocurrent production by bio-dyes of photosynthetic macromolecules on designed TiO2 film. *Sci. Rep.*, **5**, 9375.

10 Das, R.K., Killey, P.J., Segal, M., Norville, J., Yu, A.A., Wang, L., Trammell, S.A., Reddick, L.E., Kumar, R., Stellacci, F., Lebedev, N., Schnur, J., Bruce, B.D., Zhang, S., and Baldo, M. (2004) Integration of photosynthetic protein molecular complexes in solid-state electronic devices. *Nano Lett.*, **4** (6), 1079–1083.

11 Liu, J., Lauterbach, R., Paulsen, H., and Knoll, W. (2008) Immobilization of light-harvesting chlorophyll a/b complex (LHCIIb) studied by surface plasmon field-enhanced fluorescence spectroscopy. *Langmuir*, **24** (17), 9661–9667.

12 Yang, C., Boggasch, S., Haase, W., and Paulsen, H. (2006) Thermal stability of trimeric light-harvesting chlorophyll a/b complex (LHCIIb) in liposomes of thylakoid lipids. *Biochim. Biophys. Acta*, **1757** (12), 1642–1648.

13 Caffarri, S., Kouril, R., Kereiche, S., Boekema, E.J., and Croce, R. (2009) Functional architecture of higher plant photosystem II supercomplexes. *EMBO J.*, **28** (19), 3052–3063.

14 Hobe, S., Prytulla, S., Kuhlbrandt, W., and Paulsen, H. (1994) Trimerization and crystallization of reconstituted light-harvesting chlorophyll a/b complex. *EMBO J.*, **13** (15), 3423–3429.

15 Liu, Z., Yan, H., Wang, K., Kuang, T., Zhang, J., Gui, L. *et al.* (2004) Crystal structure of spinach major light-harvesting complex at 2.72 A resolution. *Nature*, **428** (6980), 287–292.

16 Yu, D., Zhu, G., Liu, S., Ge, B., and Huang, F. (2013) Photocurrent activity of light-harvesting complex II isolated from spinach and its pigments in dye-sensitized TiO2 solar cells. *Int. J. Hydrogen Energy*, **38**, 16740–16748.

17 Yang, Y., Jankowiak, R., Lin, C., Pawlak, K., Reus, M., Holzwarth, A.R. *et al.* (2014) Effect of the LHCII pigment-protein complex aggregation on photovoltaic properties of sensitized TiO2 solar cells. *Phys. Chem. Chem. Phys.*, **16** (38), 20856–20865.

18 Bianconi, E., Piovesan, A., Facchin, F., Beraudi, A., Casadei, R., Frabetti, F. *et al.* (2013) An estimation of the number of cells in the human body. *Ann. Hum. Biol.*, **40** (6), 463–471.

19 Ng, D.P., Poulsen, B.E., and Deber, C.M. (2012) Membrane protein misassembly in disease. *Biochim. Biophys. Acta*, **1818** (4), 1115–1122.

20 Katzen, F., Chang, G., and Kudlicki, W. (2005) The past, present and future of cell-free protein synthesis. *Trends Biotechnol.*, **23** (3), 150–156.

21 Seddon, A.M., Curnow, P., and Booth, P.J. (2004) Membrane proteins, lipids and detergents: not just a soap opera. *Biochim. Biophys. Acta*, **1666** (1-2), 105–117.

22 Yang, J.P., Cirico, T., Katzen, F., Peterson, T.C., and Kudlicki, W. (2011) Cell-free synthesis of a functional G protein-coupled receptor complexed with nanometer scale bilayer discs. *BMC Biotech.*, **11**, 57.

23 Ritz, S., Hulko, M., Zerfass, C., May, S., Hospach, I., Krasteva, N. *et al.* (2013) Cell-free expression of a mammalian olfactory receptor and unidirectional insertion into small unilamellar vesicles (SUVs). *Biochimie*, **95** (10), 1909–1916.

24 Lyukmanova, E.N., Shenkarev, Z.O., Khabibullina, N.F., Kopeina, G.S., Shulepko, M.A., Paramonov, A.S. *et al.* (2012) Lipid-protein nanodiscs for cell-free production of integral membrane proteins in a soluble and folded state: comparison with detergent micelles, bicelles and liposomes. *Biochim. Biophys. Acta*, **1818** (3), 349–358.

25 WHO (2004) *Laboratory Biosafety Manual*, 3rd edn, WHO Library Cataloguing-in-Publication Data.

26 NIH-CDC (2009) *Biosafety in Microbiological and Biomedical Laboratories*, 5th edn, HHS Publication.

27 Malinova, V., Nallani, M., Meier, W.P., and Sinner, E.K. (2012) Synthetic biology, inspired by synthetic chemistry. *FEBS Lett.*, **586** (15), 2146–2156.

28 Nagamori, S., Smirnova, I.N., and Kaback, H.R. (2004) Role of YidC in folding of polytopic membrane proteins. *J. Cell Biol.*, **165** (1), 53–62.

29 Giess, F., Friedrich, M.G., Heberle, J., Naumann, R.L., and Knoll, W. (2004) The protein-tethered lipid bilayer: a novel mimic of the biological membrane. *Biophys. J.*, **87** (5), 3213–3220.

30 Arimitsu, E., Ogasawara, T., Takeda, H., Sawasaki, T., Ikeda, Y., Hiasa, Y. *et al.* (2014) The ligand binding ability of dopamine D1 receptors synthesized using a wheat germ cell-free protein synthesis system with liposomes. *Eur. J. Pharmacol.*, **745**, 117–122.

31 Nozawa, A., Ogasawara, T., Matsunaga, S., Iwasaki, T., Sawasaki, T., and Endo, Y. (2011) Production and partial purification of membrane proteins using a liposome-supplemented wheat cell-free translation system. *BMC Biotech.*, **11**, 35.

32 Katzen, F., Fletcher, J.E., Yang, J.P., Kang, D., Peterson, T.C., Cappuccio, J.A. *et al.* (2008) Insertion of membrane proteins into discoidal membranes using a cell-free protein expression approach. *J. Proteome Res.*, **7** (8), 3535–3542.

33 May, S., Andreasson-Ochsner, M., Fu, Z., Low, Y.X., Tan, D., de Hoog, H.P. *et al.* (2013) In vitro expressed GPCR inserted in polymersome membranes for ligand-binding studies. *Angew. Chem. Int. Ed.*, **52** (2), 749–753.

34 Ando, E., Bernhard, F., Dötsch, V., Durst, F., Endo, Y., Ezure, T., Fox, B.G., Goren, M.A., Hori, H., Ito, M., Kanamori, T., Kanno, T., Kigawa, T., Kobayashi, I., Kobayashi, T., Kohno, T., Kuruma, Y., Löhr, F., Makino, S.-I., Markley, J.L., Matsuura, T., Mikami, S., Miyazono, K.-I., Nanamiya, H., Nishikawa, K., Nozawa, A., Ohashi, H., Ohno, S., Reckel, S., Sawasaki, T., Shikata, M., Shimizu, Y., Shrokov, V.A., Sobhanifar, S., Sunami, T., Suzuki, H., Suzuki, T., Suzuki, T., Takai, K., Takeo, S., Tanokura, M., Tsuboi, T., Torii, M., Tozawa, Y., Ueda, T., Watanabe, M., Yokogawa, T., and Yomo, T. (2010) *Cell-Free Protein Production Methods and Protocols*, Humana Press.

35 Herskovits, A.A., Shimoni, E., Minsky, A., and Bibi, E. (2002) Accumulation of endoplasmic membranes and novel membrane-bound ribosome-signal recognition particle receptor complexes in *Escherichia coli*. *J. Cell Biol.*, **159** (3), 403–410.

36 Devesa, F., Chams, V., Dinadayala, P., Stella, A., Ragas, A., Auboiroux, H. *et al.* (2002) Functional reconstitution of the HIV receptors CCR5 and CD4 in liposomes. *Eur. J. Biochem.*, **269** (21), 5163–5174.

37 Deichaite, I., Casson, L.P., Ling, H.P., and Resh, M.D. (1988) In vitro synthesis of pp60v-src: myristylation in a cell-free system. *Mol. Cell. Biol.*, **8** (10), 4295–4301.

38 Franke, C.A., Wilson, E.M., and Hruby, D.E. (1990) Use of a cell-free system to identify the vaccinia virus L1R gene product as the major late myristylated virion protein M25. *J. Virol.*, **64** (12), 5988–5996.

39 Promega. (2010) *TNT(R) Coupled Wheat Germ Extract Systems*.

40 Promega. (2009) *E. coli S30 Extract System for Circular DNA*.

41 Promega. (2014) *TNT(R) Coupled Reticulocyte Lysate Systems*.

42 New England Biolabs I. (2013) *PURExpress In Vitro Protein Synthesis Instruction Manual*.

43 Zhukovsky, M.A., Basmaciogullari, S., Pacheco, B., Wang, L., Madani, N., Haim, H. *et al.* (2010) Thermal stability of the human immunodeficiency virus type 1 (HIV-1) receptors, CD4 and CXCR4, reconstituted in proteoliposomes. *PLoS One*, **5** (10), e13249.

44 van Meer, G. and de Kroon, A.I. (2011) Lipid map of the mammalian cell. *J. Cell Sci.*, **124** (Pt 1), 5–8.

45 Hammer, D.A., Robbins, G.P., Haun, J.B., Lin, J.J., Qi, W., Smith, L.A. *et al.* (2008) Leuko-polymersomes. *Faraday Discuss.*, **139**, 129–141; discussion 213-28, 419-20.

46 Murtas, G., Kuruma, Y., Bianchini, P., Diaspro, A., and Luisi, P.L. (2007) Protein synthesis in liposomes with a minimal set of enzymes. *Biochem. Biophys. Res. Commun.*, **363** (1), 12–17.

47 van der Meel, R., Fens, M.H., Vader, P., van Solinge, W.W., Eniola-Adefeso, O., and Schiffelers, R.M. (2014) Extracellular vesicles as drug delivery systems: lessons from the liposome field. *J. Controlled Release*, **195**, 72–85.

48 Nallani, M., Andreasson-Ochsner, M., Tan, C.W., Sinner, E.K., Wisantoso, Y., Geifman-Shochat, S. *et al.* (2011) Proteopolymersomes: in vitro production of a membrane protein in polymersome membranes. *Biointerphases*, **6** (4), 153–157.

49 Tan, D.C., Wijaya, I.P., Andreasson-Ochsner, M., Vasina, E.N., Nallani, M., Hunziker, W. *et al.* (2012) A novel microfluidics-based method for probing weak protein-protein interactions. *Lab Chip*, **12** (15), 2726–2735.

50 Nozawa, A., Nanamiya, H., Miyata, T., Linka, N., Endo, Y., Weber, A.P. *et al.* (2007) A cell-free translation and proteoliposome reconstitution system for functional analysis of plant solute transporters. *Plant Cell Physiol.*, **48** (12), 1815–1820.

51 Stoenescu, R., Graff, A., and Meier, W. (2004) Asymmetric ABC-triblock copolymer membranes induce a directed insertion of membrane proteins. *Macromol. Biosci.*, **4** (10), 930–935.

52 Meier, W., Nardin, C., and Winterhalter, M. (2000) Reconstitution of channel proteins in (polymerized) ABA triblock copolymer membranes. *Angew. Chem. Int. Ed.*, **39** (24), 4599–4602.

53 Lim, S.K., de Hoong, H.-P., Parikh, A.N., Nallani, M., and Liedberg, B. (2013) Hybrid, nanoscale phospholipid/block copolymer vesicles. *Polymers*, **5**, 1102–1114.

10

Organic Optoelectronic Interfaces for Vision Restoration

Andrea Desii[1], Maria R. Antognazza[1], Fabio Benfenati[2,3], and Guglielmo Lanzani[1,4]

[1] *Center for Nano Science and Technology, Istituto Italiano di Tecnologia, 20133 Milan, Italy*
[2] *Center for Synaptic Neuroscience and Technology, Istituto Italiano di Tecnologia, 16132 Genoa, Italy*
[3] *University of Genova, Department of Experimental Medicine, 16132, Genova, Italy*
[4] *Politecnico di Milano, Dip.to di Fisica, Piazza Leonardo Da Vinci 32, 20133, Milano, Italy*

10.1 Introduction

The eye in humans and primates is a wonderful and amazing device. Far more than a simple detector, our eye can perform advanced image processing before sending data to the central nervous system (thalamus and visual cortex), forming the most complex and sophisticated sensory systems, the visual system that is the predominant sense in higher mammals and humans. The eye evolved in about 500 M years, from a patch of light-sensitive cells exposed at the surface to the complex organ we know. Partially the brain developed in order to process the increasing volume of data the eye was collecting. Charles Darwin, the father of the evolution theory, was surprised by this outcome and apparently confessed once that it was difficult, even for him, to believe that a random process achieved that much. Yet that is what happened, and apparently not just once, because other animals quite far away from us, such as the octopus, do see in color pretty much as we do. The eye is a perfect camera with adjustable lenses, a diaphragm, and a photosensitive chip made of live neural circuits. René Descartes was the first to describe in detail the functioning of the eye as a photocamera by using a calf eye he got from a slaughterhouse in which he cut the posterior wall and replaced it with tissue paper or frosted glass. He found that the visual field refracted through the eye was projected in 2D on the rear wall of the eye (Figure 10.1).

The eye is a fertile inspirer of technology. However, albeit many devices are clearly eye inspired, we still cannot fully reproduce it; perhaps we still do not even know exactly how it works at the level of the complex neuronal circuitry.

The optical system is rather simple, based on two main diopter surfaces, the cornea and the lens. The cornea is the transparent membrane separating the "aqueous humor" from the outside world. It performs the first reflection,

Green Materials for Electronics, First Edition.
Edited by Mihai Irimia-Vladu, Eric D. Glowacki, Niyazi S. Sariciftci, and Siegfried Bauer.

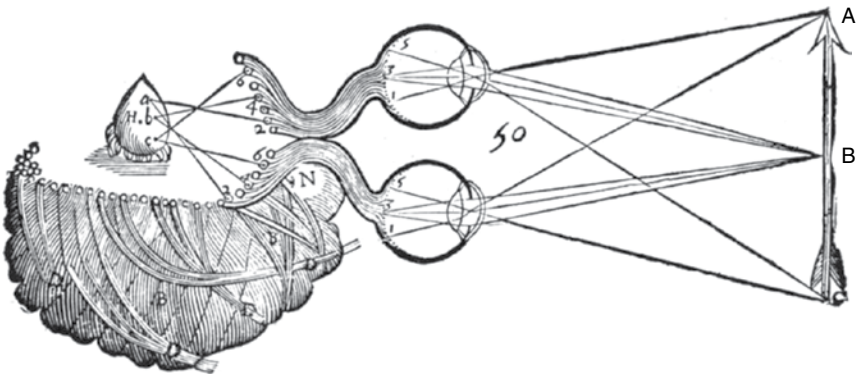

Figure 10.1 Descartes' representation of how the visual system perceives objects.

corresponding to about 4% of the incident intensity, and the first refraction. Indeed, deviations from the spherical shape in the cornea may lead to vision impairment, such as astigmatism. Light rays enter the eye and reach the main refractive body, the lens. This stays just behind an adjustable diaphragm called *iris* delimiting the light entrance (pupil). The refractive power of the lens is finely controlled by ciliary muscles that accommodate its shape to focus the image on the retina. A young kid can neatly see an object at 10 cm from his eyes. Unfortunately this ability gets lost with time, and a 50-year-old man can typically see objects not closer than 1 m or so. The reason is the loss of elasticity in the lens that can no longer be accommodated. This defect is called *presbyopia* and it is easily corrected by adopting magnifying, positive lenses, the common reading glasses. On the contrary, the spectacles for short-sighted people that correct myopia use divergent lenses (indeed a myopic eye focuses on objects just in front of the retina). In his famous novel *The lord of flies* William Golding describes a myopic young guy who sets a fire focusing sunlight with his glasses. While the literature value is out of question here, one should note that either the young guy was affected by hypermetropia (farsightedness) and thus he was using converging lenses, or this could not happen. In another famous novel Orson Wells tells about a man who could become invisible by adjusting his refractive index in order to match that of the environment. While this, as impractical as it is, could in principle work, an unaccounted consequence would be that the invisible man would be blind, for his eye could not refract light on the retina.

The eye spatially filters out incoming rays through the small pin hole called *pupil*. This is an aperture controlled by light sensors connected to muscles that adjust the diameter: wide shut in the dark and narrow in strong light. This light-induced reaction is indeed exploited in testing prosthetic retina implants on animals. An important consequence of this simple geometry is that real images are formed reversed at the bottom of the eye ball. This was known since middle age and was the subject of intense study. A camera obscura, even before the advent of photography, was based on the same geometry, appreciating the neat image that forms after spatial filtering of straight light. Canaletto, the famous Venetian painter, was using this trick to fix on canvas the patterns of his majestic scenes.

The pupil is defined by the iris, a colored pattern, very beautiful and charming, that does not have any photonic function but perhaps other kind of functions, such as attracting sexual partners. Albinos have missing pigments and do not have strong colors in their iris, which looks dim red. The pupil state is controlled by the level of light intensity in the environment through several kinds of photoreceptors, besides those in the retina and responsible for vision; other pigments such as melanopsins in the ganglion cells seem involved. Melanopsin is also responsible for the circadian rhythm of the biological clock. Under jet lag this is deranged, as we all know. Staying in the sun, powering up your melanopsins, could help re-establish the balance.

Light refracted by the lens travels through the humor vitreous to reach the retina. This is a highly transparent viscous liquid, which with aging may developed thick, opaque floating bodies, perhaps made of protein aggregates. When one of these objects intercepts an image ray, we are disturbed and we see ghost spots floating in front of us. Besides this undesired effect that occurs with age or after a trauma, the transparency of the humor is amazingly high. Essentially the only losses suffered by the incoming light rays are due to the refractive surfaces, reflecting 4% each, according to the index mismatch.

After traveling through the humor vitreous, light impinges on the inner nuclear layer that contains the ganglion cells. Then, it travels through a number of neuronal layers, horizontal cells, amacrine, and bipolar cells, to finally reach the photoreceptors. This setting is surprising. All the circuitry devoted to signal processing is just in front of the detector, as if a photonic engineer would set up his cables and preamplifier just in front of the photodiode. An engineer doing this would not be considered a very smart one. However, that is what happens in the human eye and in that of most primates. The "circuitry" is so perfectly transparent that indeed such a setting does not introduce any loss. Mueller cells, stretched across the retina section, seem to work like natural optical fibers, improving light transmission through the neuronal bodies [1]. Note that there is at least one exception to the inverted retina architecture, the octopus eye. Octopuses do see colors; indeed, they are very clever animals that can also solve simple problems. They have a retina similar to ours in composition; yet the wiring is straight, not inverse. Light strikes photoreceptors, and then the electrochemical signals propagate through the neuronal layers and reach the optic nerve. Apparently, nobody knows why it is so. A possible explanation is that a short distance between the photoreceptors and the pigmented epithelium could facilitate nourishing and regeneration of the involved pigments. Owing to the curious inverse retina the optic nerve should pierce the retina to reach the brain from the inside of the eye. This brings as a consequence a blind spot in the retina where there are no photoreceptors, which occurs right at the recollection of the ganglion cell axons to form the optic nerve. Because we have two eyes and binocular vision, we do not feel this. However, using a single eye it is possible to appreciate it.

Beside the chromophore 11-cis-retinal contained in the opsins (rhodopsin, photopsins, and melanopsins), other carotenoids in the eye have the purpose of photoprotection (such as lutein and zeaxanthin). Carotenoids are compounds predominantly made by conjugated carbon and hydrogen that are quite common in

the biosphere. The same pigments that give colors to fruit, vegetables, and leaves are indeed present in the eye to detect colors. Notably the molecular structure of the chromophore detecting light in our photoreceptors is almost identical to one half of the beta carotene molecule. During World War II, the British government spread the news that their counter air force was very successful because of the exceptional good sight of their soldiers, fed by a diet rich in carrots. This was not true of course. While we cannot exclude that carrots are beneficial for the eye, the real reason of the success was the discovery of the radar, a military secret at that time.

The eye is optimized for best performance at minimum cost. For instance, it has a broad field of view, about 150° in plane and 120° in vertical, but with variable space resolution in order to reduce the volume of data transmission. This is achieved by adopting the log-polar geometry, which is a space variant and size variant distribution of the photoreceptors. Active pixels are small (about 2.5 μm) and closely packed in the macula and get larger and sparse going radially to the periphery. The macula is devoted to high-resolution detection, with 1/60° angular resolution. Hawks and eagles have two maculas, in order to improve their vision. Other species such as squirrels, cats, dogs, and deer have a less dramatic regional specialization, and possess what is called an *area centralis* or a *visual streak*. Because the density of photoreceptors decreases moving from the macula to the peripheral region of the retina, the amount of data collected is also vastly reduced at the cost of resolution. This provides the lateral view, still of critical importance for controlling the space around us, yet not so rich in details that would make data transfer impractical. Having the same resolution on the whole range of view would require a brain about 10^4 times heavier. This smart setting of the photoreceptor has inspired the development of anthropomorphic detectors based on the log polar array. Such log-polar photodiode arrays may be used in early warning, security cameras, video surveillance systems, and robots, where the volume of the wiring connections is a serious issue [2].

The human retina contains two types of photoreceptors, rods and cones, approximately in a ratio 20 : 1 [3]. Cones are distributed radially from the fovea, a disk of a few millimeters in diameter, in a peculiar log-polar geometry. They are small (2.3 μm) and closely packed in the fovea and become sparse and larger (10 μm) in the periphery, according to the log polar geometry discussed above.

Cones are responsible, although less sensitive than rods, for daily color vision through the so-called trichromatic vision. Three subtypes of cones have been identified, namely S, M, and L, with distinct spectral responses [4], in the blue, green, and red wavelength regions respectively. However, a unique chromophore is present in all cones, namely, retinal, and the spectral tuning of the light response is achieved by modifying the local environment around the retinal molecule. During daylight activity the more sensitive rods are saturated, while under dim light they become active and cones become insensitive. Rods come in one type only, do not provide color vision, as we note in the moonlight, and have lower spatial resolution with respect to foveal vision. Because rods are not present in the fovea, a dim light can be seen better gazing at an angle. This trick was adopted by early spectroscopists, who detected weak light signals by the eye. This practice led sometimes to misconceptions such as the hypothesized form of radiation called *N-rays*. It was initially confirmed by many experiments, but subsequently found to be illusory [5].

10.2 Retinal Implants for Vision Restoration

Legal blindness is defined by the World Health Organization as a condition of visual acuity lower than 20/400 or visual field smaller than 20° in the better seeing eye. According to this definition, there were 39 millions of blind patients in 2010 worldwide [6]. Retinitis pigmentosa (RP) is the most common cause of inherited blindness, affecting an estimated 1.5 million people [7]. In this disease, photoreceptor cells gradually lose their function, leading to a progressive reduction of visual field and acuity, starting from the periphery. In the early stage of this disease, ganglion cells, amacrine, and horizontal and bipolar cells remain intact. There is no cure for RP, but several treatments are being tested. Implants able to substitute degenerate photoreceptors and to excite retinal output neurons can in principle restore visual perception [8]. This can be achieved by preprocessing an image recorded with an external camera to control an array of electrodes implanted in the retina, or by an intrinsically photosensitive implant able to transduce the optical energy into electric stimuli.

Retinal implants have been installed in three general configurations. In the epiretinal architecture, the device is placed on top of the inner retina, at the interface with the vitreous humor, in contact with ganglion cells. Subretinal devices are implanted where photoreceptors have been lost, between bipolar cells and pigmented epithelium. In the suprachoroidal configuration, the array is implanted between the choroid and the sclera, outside the retina. Two implants have been approved for commercialization (ARGUS II and Alpha-IMS) [9–12], some are undergoing clinical tests [13, 14], and several others are in the preclinical phase [15–18] (Figure 10.2).

In the epiretinal ARGUS II system (Second Sight Medical Products, Sylmar, CA) the electrode array is attached to the retina with a plastic tack that penetrates the retina and is anchored in the sclera by means of tiny barbed hooks. A foil with wires leads from the electrode array to the receiver electronics located in a capsule on the eye bulb. A pocket computer with batteries translates the video image taken by an external camera mounted on a spectacle frame into electrical impulses that are sent electromagnetically by a transmitter antenna on the spectacle frame through the periorbital tissue to a receiver coil on the eye bulb positioned next to the episcleral capsule. From there, a foil with 60 wires leads directly to the 60-electrode array, which is attached to the retinal ganglion cells whose nerve fibers form the optic nerve [21]. The other commercially available implant, Alpha-IMS (Retina Implant AG, Reutlingen, Germany), contains a chip with 1500 photodiodes, amplifiers, and electrodes in each pixel, spaced 70 μm apart. Power and control signals are generated in a small box that the patient carries. A transmitter antenna behind the ear is kept in place by a magnet in a subdermal receiver box. Power and control signals are sent wirelessly to the subdermal receiver box from which a subdermal cable leads to the eyeball, ending in a thin subretinal foil. The current injected into the retina is picked up by a return electrode. The chip is positioned on a foil that carries gold wires and is surgically implanted through a flap cut into the sclera [19].

The subretinal architecture mimics more closely the anatomy of the healthy eye. The device replaces directly the depleted photoreceptors in the outermost region

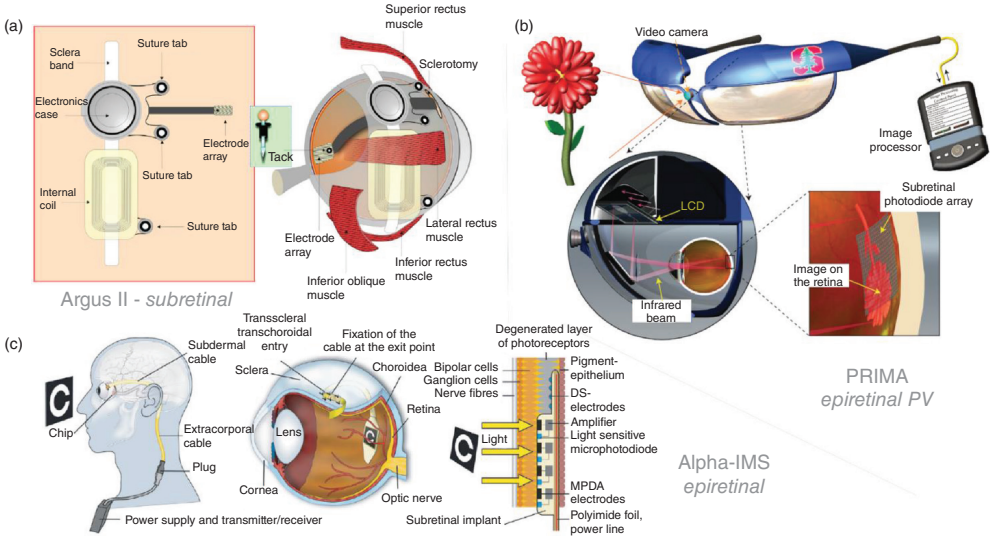

Figure 10.2 Retinal prostheses based on metal/silicon electronics. (Panel (a): Mathieson *et al*. 2012 [18]. Reproduced with permission of Nature Publishing Group; Panel (c) Zrenner *et al*. 2010 [19], http://rspb.royalsocietypublishing.org/content/early/2010/11/01/rspb.2010.1747. Used under CC-BY-4.0 http://creativecommons.org/licenses/by/4.0/; Rizzo *et al*. 2014 [20]. Reproduced with permission of Elsevier.)

of the retina. This means that the integration of the device in the visual pathway is more straightforward compared with other architectures, provided that other retinal layers are intact. In the advanced stages of retinal degenerative diseases, this is seldom the case, with retinal neurons undergoing atrophy and reconnection, modifying the signaling network. If the patient's condition allows for its implantation, a subretinal sensor can follow the natural movement of the eye and mimic more closely the physiological neural circuitry of the retina, reducing the possibility of spurious visual signaling compared to epiretinal stimulation.

The main issues with the operation of stimulating electrodes are power supply and signal control. This limits the number of electrodes that can be integrated on a single device and the potential resolution of restored vision. Each clinically tested device needs a complex surgical procedure for the installation of cables to provide power to the array. A device approaching clinical testing, the PRIMA implant (Pixium Vision, Paris, France), avoids cable implantation by projecting near-infrared (NIR) radiation on a photovoltaic device, in which silicon photodiodes in each pixel receive power and data directly through pulsed near-infrared illumination and electrically stimulate neurons [22, 23].

10.2.1 Toward an Organic Artificial Retina

All these metal–silicon artificial devices still have to face and solve major common problems: need for power supply, scarce biocompatibility, low compliance, complexity of the fabrication process, electrode number, size and geometry, high impedance levels, resistive currents, and pronounced heat production, which is very detrimental to the retinal tissue. Organic semiconductors, however, do have specific advantages in this application. They comprise single crystals, small molecules, and conjugated polymers (CPs). They are based on conjugated carbon atoms, similar to natural molecules (and to the retinal molecule in particular), thereby bearing an intrinsic affinity for biological systems. They have π-electrons delocalized along their backbone that induce strong coupling with light; indeed, many optically active compounds in nature are based on conjugated carbons (e.g., carotenoids and chlorophylls in light harvesting complexes) and the most successful applications of organic semiconductors deal with light (e.g., organic light-emitting diodes, displays, and lightning). Since their optical band gap is in the visible range and can be properly engineered by chemical tailoring, CPs are intrinsically sensitive to visible light, and a proper selection of materials allows the realization of trichromatic sensing [24]. In particular, CPs combine the outstanding mechanical properties and simple processing technologies typical of plastic with the optoelectronic properties of semiconductors. Because of their inherent softness and low degree of toxicity, they represent excellent biocompatible materials for biological applications, both *in vitro* and *in vivo*, allowing for a more intimate interface with a liquid bioenvironment. Finally, CPs are able to conduct both electrons and ions and form stable interfaces with water, opening a new communication channel between electronics and biology (Figure 10.3). The way to an organic artificial retina passes through the study of the interaction of CPs with electrically excitable biological systems. In the next section, optically activated electrical excitation of single neurons and the performance of CPs on

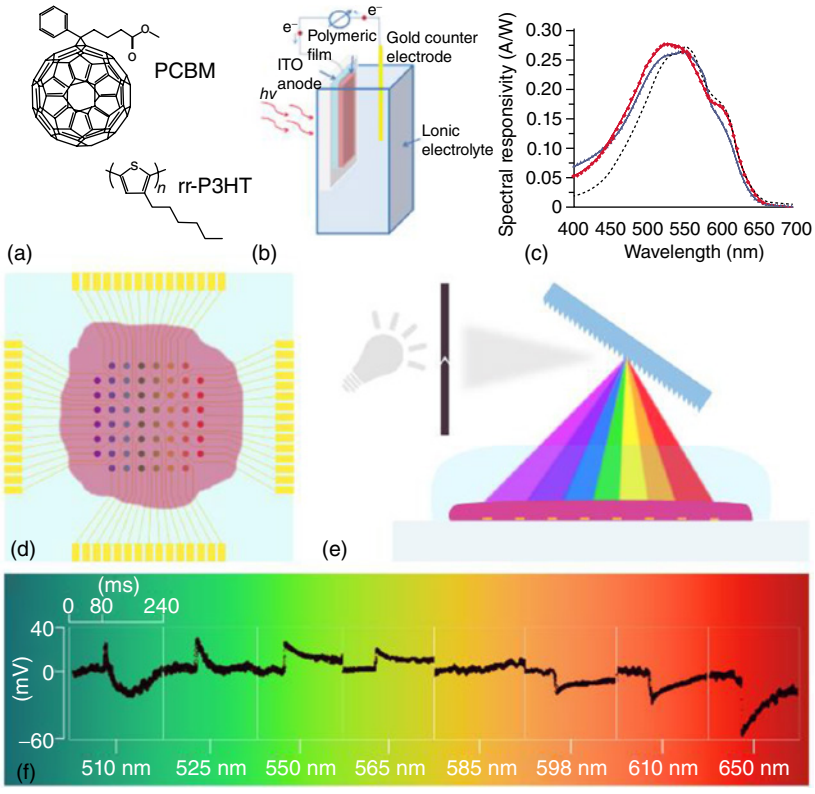

Figure 10.3 Hybrid solid–liquid cells. (a) Chemical structures of regioregular poly(3-hexylthiophene-2,5-diyl) (rr-P3HT) and phenyl-C61-butyric-acid-methyl ester (PCBM). (b) Scheme of the hybrid solid–liquid cell for modulated photocurrent spectroscopy. (c) Spectral response of the systems ITO/rr-P3HT:PCBM/NaCl/Gold (blue line and triangles) and ITO/rr-P3HT:PCBM/Ringer/Gold (red line and squares), with the saline solutions working as ionic cathodes, recorded after 12 days of immersion in minimum essential medium. Typical spectral response (in arbitrary units for direct comparison with present results) of a conventional, solid-state solar cell (ITO/rr-P3HT:PCBM (1 : 1)/Al) is reported as a reference (dashed, gray line). (Ghezzi *et al*. 2011 [25]. Reproduced with permission of Nature Publishing Group.). (d) Schematic of an 8 × 8 multielectrode array (MEA) with 60 indium tin oxide (ITO) electrodes coated with a BHJ layer. Aqueous KCl solution (100 mM) is held on top of the polymer film. (e) Various wavelengths of the visible spectrum are dispersed onto the array. (f) Photovoltage response of the ITO|BHJ|aq device as a function of various λ values of the visible spectrum. (Gautam *et al*. 2011 [26]. Reproduced with permission of American Chemical Society.)

explanted blind retinas will be discussed. These are fundamental developmental steps for the implantation of CP-based devices in animal models.

10.2.2 Cellular Photostimulation Mediated by Molecular Materials

Optical stimulation of excitable cells is emerging as an alternative to electrical and chemical stimulation methods, especially due to a higher degree of temporal and spatial resolution [27–29]. Light stimulation can be induced directly with

high-intensity pulsed laser or IR illumination, owing to processes such as membrane poration, heating, and excitation of endogenous chromophores [30–34]. In most studies, however, cell stimulation is induced by the introduction of exogenous chromophores, such as caged compounds based on γ-aminobutyric acid (GABA) and glutamate, which can be activated upon irradiation [35]. One of the most successful approaches is optogenetics, in which cells express a light-sensitive protein, used for the modulation of biological activity [36–38]. The expression of light-gated ion channels and pumps allows the control of cell excitation and inhibition [39, 40].

Another way to optically excite biological systems is to exploit the optoelectronic properties of semiconducting materials [41, 42]. It has been demonstrated that the photocurrent generated by a silicon chip kept at reverse bias is able to stimulate electrical activity in neurons grown on top of it. Pappas *et al.* obtained similar results by using a thin film of semiconducting HgTe nanoparticles [43].

10.2.3 Optoelectronic Organic Membranes for Cell Stimulation

Only recently organic semiconductors have been proposed as photoactive materials in biointerfaces. Cells live in an ion-rich watery environment. Ionic transport is a key phenomenon in cell metabolism and signaling, mediated by pumps and ion channels. Thus, the use of organic photodetectors in medical and biological applications raises an important issue in the design of bio-organic interfaces: the intimate contact between the organic semiconductor and the physiological liquid environment. In addition, the liquid electrolyte challenges organic device survival, as degradation of the metal electrode is greatly accelerated in a liquid environment. A solution to the latter problem is the realization of devices in which the metal electrode is substituted by aqueous saline solutions. It is clear that hybrid solid–liquid interfaces play a key role in bio-organic electronics, and a number of studies aiming at characterizing such an interface have been reported [44–46]. Aqueous solutions have been extensively used as gate electrodes in field-effect transistors for biological sensing, demonstrating, in some cases, optimal electronic performances and outstanding biocompatibility properties.

The biocompatibility of organic semiconductors, both molecular and polymeric materials, has been reported in various studies. Biscarini and coworkers demonstrated the adhesion and growth of primary rat neurons on pentacene thin films [47]. While cells rapidly aggregated into large assemblies on the bare semiconductor, when pentacene was coated with adhesion molecules (e.g., laminin or poly-L-lysine) the growth of neurons was comparable to that observed on glass substrates coated with the same molecules. Moreover, pentacene proved to be a suitable substrate also for the adhesion and differentiation of neural stem cells. Studies on the biocompatibility of polymeric semiconductors were first performed by Scarpa *et al.* with mouse fibroblasts grown onto poly(3-hexylthiophene-2,5-diyl) films [48]. Also in this case, the bare film proved to be a poor substrate for cellular cultures; however, after treatment with adhesion proteins or oxygen plasma, cell adhesion and growth significantly increased. Successively, Ghezzi *et al.* prepared cultures of primary rat hippocampal neurons onto both P3HT:PCBM blends and pure P3HT films coated with poly-L-lysine, observing no difference in vitality and spontaneous

electrical activity (action potential firing, synaptic currents) up to 28 days *in vitro* with respect to cultures on control substrates [25].

Several of these organic (macro)molecules have been demonstrated to work as active layers in direct contact with liquid electrolytes [26, 49–51]. In these examples, the device structure comprises an anodic contact (usually ITO) covered by the organic photosensitive layer and a saline electrolyte. Reported materials include regioregular P3HT (rr-P3HT), poly[*N*-90-heptadecanyl-2,7-carbazole-alt-5,5-(40,70-di-2-thienyl-20,10,30-benzothiadiazole)] (PCDTBT), P3OT, poly(9,9-dioctylfluorene-*co*-benzothiadiazole) (F8BT), poly[2-methoxy-5-(2-ethylhexyloxy)-1,4-phenylenevinylene] (MEH-PPV), poly[2-methoxy-5-(30,70-dimethyloctyloxy)-1,4-phenylene vinylene] (MDMO-PPV), poly [2,6-(4,4-bis-(2-ethylhexyl)-4*H*-cyclopenta[2,1-*b*:3,4-*b*0]dithiophene)-alt-4,7-(2,1,3-benzothiadiazole)] (PCPDTBT) as photoactive polymers, and poly {[*N*,*N*0-bis(2-octyldodecyl)-naphthalene-1,4,5,8-bis(dicarboximide)-2,6-diyl]-alt-5,50-(2,20-bithiophene)} (N2200) and PCBM as electron acceptors. Various electrolytes can be used for the saline solution; for direct interfacing to living cells, sodium chloride is the most interesting case, since it represents the most abundant cation of the biological extracellular fluids and of any cell culture medium. Indeed, the same device configuration shows the generation of a photocurrent in the presence of common culturing and buffering media. The main difference between hybrid and conventional organic photodetectors is related to interface phenomena between the polymer film and the electrolyte: in the hybrid device the conductance type changes from mainly electronic to ionic; in the solid-state cell, the mechanism is that of a standard Schottky barrier photodiode. The equilibrium conditions at the interface are qualitatively similar: chemical potential (Fermi level) is equalized by charge transport across the interface. Yet, the microscopic setting is dramatically different. In the solid device charge carrier migration leads to space charge separation across the interface, generating local electric fields that cause band bending. In the hybrid system, ion adsorption at the surface competes with charge transfer, also mediated by chemical reactions. A dipole layer forms at the surface, while a diffused ion layer spreads in the solution (i.e., Helmholtz layer).

In 2011, our group demonstrated that an organic photovoltaic blend (namely P3HT:PCBM) coated on a transparent ITO conducting layer is able to elicit electrical activity in primary neurons grown on top of it upon photostimulation (Figure 10.4) [25]. By recording membrane potentials by means of whole-cell patch-clamp under current-clamp configuration, it was shown that a 20 ms green light pulse (532 nm, 10–15 mW mm^{-2}) (where P3HT is strongly absorbing) evoked the generation of action potentials in neurons with great reproducibility. The response time was very rapid (around 10 ms to reach the peak of the spike) and the photostimulation process was highly spatially selective: if the light spot was moved just outside the cell body, no significant activity could be elicited in the neuron. The photophysics of the photovoltaic blend used in this study suggests a role for bulk charge photogeneration in the excitation mechanism. However, it has been found that the same transduction process of light pulses into neuronal electrical activity is obtained by using a neat P3HT film (deposited on ITO) [52]. This observation indicates that the functioning of such a hybrid interface can be quite different from that of conventional organic photovoltaic

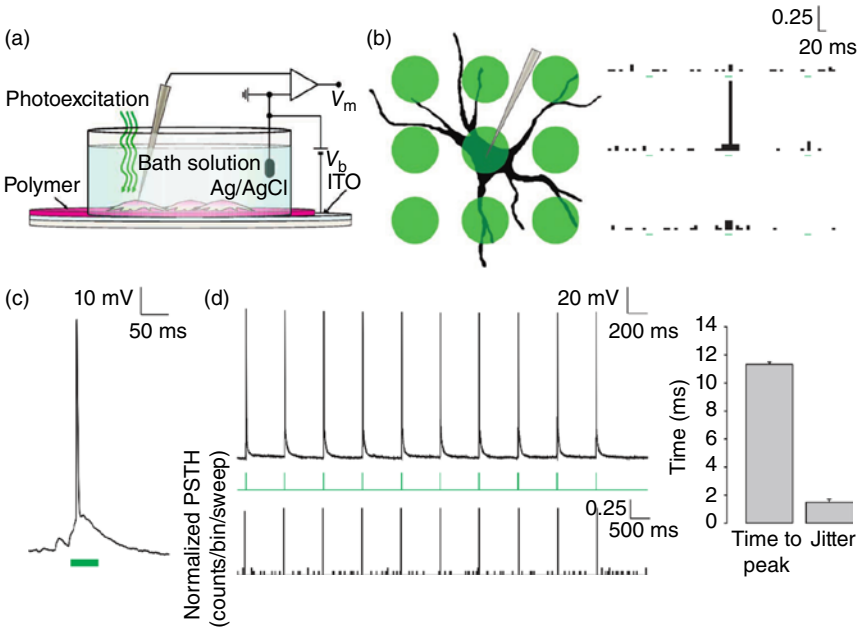

Figure 10.4 Optical stimulation of neurons cultured onto an organic optoelectronic device. (a) Scheme of the photosensing interface, with the neuronal network grown on top of the polymer active layer during patch-clamp recordings. (b) Spatial properties of the photostimulating interface. A grid of nine spots (diameter 20 µm, spacing 30 µm) was overlaid on a patched neuron and spikes were counted. Peristimulus time histograms (PSTHs) arranged in a similar grid represent the spike counts normalized for the total number of sweeps in all recorded neurons (bins 10 ms). Each histogram represents the count of the spikes recorded at the soma by the corresponding stimulation spot. (c) Action potential generation in response to a photostimulation pulse (50 ms). (d) Example of spike train generated with 20 ms pulses repeated at 1 Hz (upper panel). PSTH count was computed and normalized by considering spike trains in all recorded neurons (bottom panel; bins 20 ms). The right plot shows the latency to the spike peak with respect to the light onset computed by averaging all spikes in the train obtained from all recorded neurons and the jitter calculated as the s.d. of spike latencies measured across all recorded neurons. (Ghezzi *et al*. 2011 [25]. Reproduced with permission of Nature Publishing Group.)

devices (P3HT only solar cells have much lower efficiencies than bulk heterojunction cells with PCBM) and that faradaic currents, injected in the cleft between the device and the neuron, are not relevant. Indeed, a large body of experimental evidence suggests the presence of a capacitive coupling between the organic layer and the neuron grown on top of it. The proposed model assumes that upon photon absorption, positive charges generated in the proximity of the ITO electrode migrate into it, leaving the polymer layer negatively charged. The negative surface causes a rearrangement of the ions in the cleft, subtracting positive charges from the extracellular face of the facing cell membrane, eventually resulting in the depolarization of the cell membrane.

Photostimulation mediated by conjugated polymer membranes was demonstrated in other nonexcitable cells, namely, neocortical astrocytes and human

embryonic kidney (HEK-293) cells [53, 54]. Photoexcitation of P3HT induces a significant depolarization of the astroglial resting membrane potential: the effect is associated to an increase in whole-cell conductance at negative potentials. The magnitude of the evoked inward current density is proportional to the illumination intensity. Biophysical and pharmacological characterization suggests that the ion channel mediating the phototransduction mechanism is a chloride channel, the ClC-2 channel. In the stimulation of HEK-293 cells, on top of the capacitive charging of the polymer interface, two concomitant mechanisms were identified and characterized, leading to membrane depolarization and hyperpolarization, both mediated by a photothermal effect.

The high spatial and temporal resolution of the photoexcitation, together with the good biocompatibility properties demonstrated for the organic semiconductors, opens the way to potential applications in the field of retinal prosthetics.

10.2.4 Photoelectrical Stimulation of Explanted Blind Retinas Mediated by Optoelectronic Thin Membranes

The phenomenon of cell stimulation by polymer photoexcitation (CSP) seems naturally fitting for the artificial retina application. The goal here is to restore photosensitivity in retinas whose natural photoreceptors are damaged or lost. The retinal photoreceptors, however, are in contact with bipolar cells, and both photoreceptors and bipolar cells behave quite differently from primary brain neurons in that they do not develop action potentials, and glutamate stored in synaptic vesicles is continuously released as a function of the membrane potential from a highly specialized structure called the *ribbon* synapse. In addition, the released glutamate is recognized by distinct receptors that alternatively mediate excitatory or inhibitory effects on postsynaptic bipolar cells [55]. For the high complexity of retinal physiology, success of the polymer approach, as demonstrated for neurons, in restoring light sensitivity in retinas depleted of photoreceptors is thus not granted. Nevertheless, very recently Ghezzi *et al.* reported that such a bio-organic interface is capable of restoring light sensitivity in blind retinas *ex vivo* [52]. Acutely dissected blind retinas from albino rats subjected to light-induced photoreceptor damage were placed on P3HT-coated glass:ITO substrates with the external layers in contact with the polymer. A 10 ms light pulse (4 mW mm^{-2}) was able to stimulate the firing of retinal ganglion cells (measured by extracellular recordings in the ganglion cell layer) to levels indistinguishable from those of healthy retinas of control rats, while no significant activity correlated to the light stimulus could be recorded in blind retinas placed on substrates lacking the polymeric layer (Figure 10.5c,d). The analysis of the temporal and pharmacological characteristics of the excitation proved that ganglion cell spiking was mediated by the activation of the external cell layer in contact with the polymer. Dose–response measurements revealed a threshold intensity for photostimulation of about 0.3 mW mm^{-2}, closely matching the range of retinal irradiance during outdoor activity in the sun (0.1–10 mW mm^{-2}).

In a study by Gautam *et al.*, bulk heterojunctions (BHJs) based on conjugated polymers (P3HT:N2200) were able to provide visual cues to a blind, early-stage

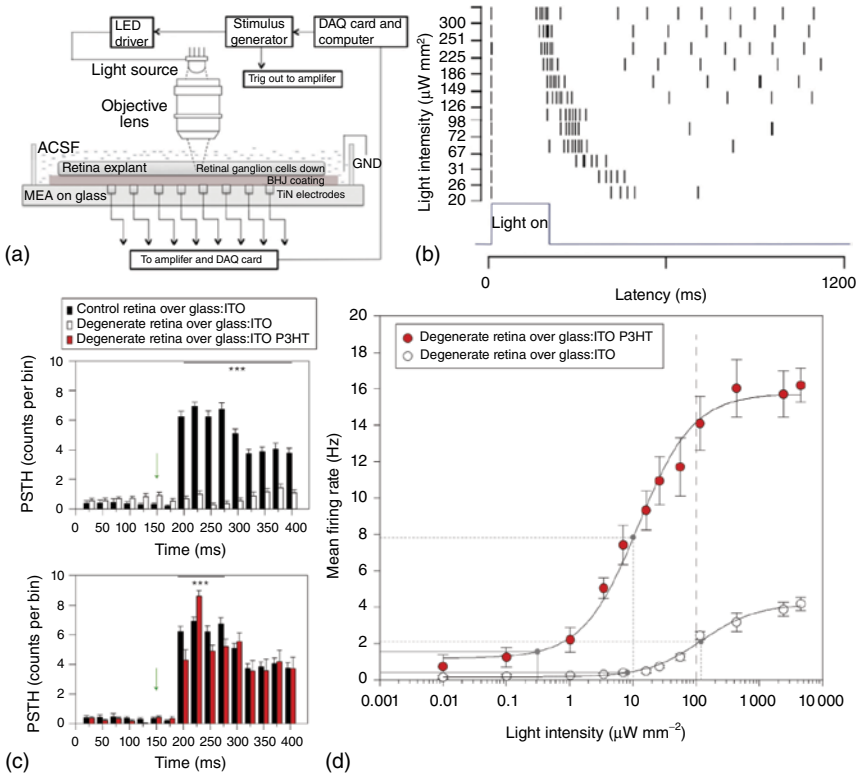

Figure 10.5 Stimulation of blind retina with organic optoelectronic membranes. (a) Schematic of the experimental setup for simultaneous photoexcitation of the BHJ layer and recording of the retinal activity using an MEA. (b) A raster plot of elicited action potentials with increasing light intensities. Each marker corresponding to a specific intensity represents an action potential. (Gautam *et al.* 2014 [56]. Reproduced with permission of John Wiley and Sons.). (c), Comparison of mean PSTHs (bin, 25 ms) obtained from control retinas on glass:ITO (black bars), degenerate retinas on glass:ITO (open bars), and degenerate retinas on P3HT-coated glass:ITO (red bars) in response to light illumination (10 ms, 4 mW mm^{-2}; green arrow). (d) Dose–response analysis of the mean firing rate versus light intensity performed in degenerate retinas over P3HT-coated glass:ITO (red dots) or glass:ITO alone (open dots). Mean firing rates were calculated in a window of 250 ms after the light pulse. Dashed line: computed maximum permissible radiant power for chronic exposure (see Methods). Dose–response curves were fitted using a sigmoidal dose–response model. Solid gray lines represent the response threshold (10% of the maximal response), and dotted gray lines represent the average half-maximum effective dose (ED50) calculated from the fitting procedure (12.11 and 120.78 mW mm^{-2}, respectively). (Ghezzi *et al.* 2013 [52]. Reproduced with permission of Nature Publishing Group.)

chick retina [56]. The explanted tissue was interfaced epiretinally with a BHJ-coated microelectrode array (MEA) and exposed to light pulses of various intensity (20–300 μW mm^{-2}), wavelength (410, 533, 570 nm), and repetition rate (1–0.01 Hz) (Figure 10.5a,b). The photoelectric signals initiated by the BHJ layer evoked neuronal activity in the ganglion cells, with features resembling the natural response of the retina to light stimulation. The average number of evoked

spikes increased with the light intensity, while the average response latency decreased. Bareket *et al*. used semiconductor membranes based on carbon nanotubes and CdSe/CdS semiconductor nanocrystals (SCNC) to photostimulate blind chick retinas [57]. Even if the films are not organic, they share with conjugated polymers most of the advantages over inorganic, silicon-based devices, one important exception being biocompatibility. To fit *in vivo* applications, the system must retain its inertness and its performance without causing toxic effects. SCNCs, especially free in solution, may induce adverse cytotoxicity effects [58, 59]. Nevertheless, the device was able to elicit ganglion cell spiking in an epiretinal configuration upon irradiation (405 nm).

The reported results demonstrate that organic semiconductors can be a valid alternative to the more traditional devices used for retinal implants, mostly based on inorganic semiconductors and/or metallic electrodes.

10.3 Perspectives

The implantation of artificial vision devices in man is a testament to the huge developments made in ophthalmology, microelectronics, biomedical engineering, and applied physics in the last decades. However, research is struggling to understand if the bionic eye can really improve the quality of life of patients. Devices based on electrode arrays fabricated using silicon microtechnology are facing issues in interfacing with the biological environment, because of heating, invasive surgical procedures, and limits in the resolution of the prostheses. All these reasons have strongly limited the success of these metal-silicon-based prostheses. Although the coupling mechanism between neural cells and the semiconducting polymer is still only partially understood, its potential impact is clear-cut. The advantages offered by organic semiconductors are manifold, and rely on material softness, reduced invasivity, very low toxicity, and enhanced biocompatibility, lack of need for external biasing, very limited and spatially confined heat production, and reduced redox reactions at the interfaces, as a consequence of the capacitive-like coupling between the artificial and the natural tissue. Another major advantage is the spatial confinement of the stimulation, which could in principle improve the limited resolution of traditional implants. There are however many open issues, regarding in particular the long-term stability of the polymeric material, the tolerability over prolonged time *in vivo*, and the optimization of the device response. Chemical engineering of substrates, anodic contacts, active materials, and encapsulation layers is expected to play a central role in the future development and implementation of organic-based retinal implants. To address these issues, research groups working on organic-based, flexible optoelectonic membranes for vision restoration are moving to preclinical testing to assess biocompatibility, stability, and function of prototype implantable devices. The work done in this area with metal- and silicon-based artificial retinas is providing invaluable cues for the implementation of surgical procedures, the choice of suitable animal models, and the evaluation of function and compliance of organic-based sensors.

References

1 Franze, K., Grosche, J., Skatchkov, S.N. *et al.* (2007) Müller cells are living optical fibers in the vertebrate retina. *Proc. Natl. Acad. Sci. U.S.A.*, **104** (20), 8287–8292.
2 Berton, F., Sandini, G., and Metta, G. (2006) Anthropomorphic visual sensors, in *Encyclopedia of Sensors* (eds C.A. Grimes, E.C. Dickey, and M.V. Pishko), ASP, American Scientific Publication, Stevenson Ranch, CA.
3 Kolb, H. Facts and Figures Concerning the Human Retina. In Webvision: The Organization of the Retina and Visual System; Kolb, H., Fernandez, E., Nelson, R., Eds.; University of Utah Health Sciences Center: Salt Lake City (UT), 1995.
4 Bowmaker, J.K. and Dartnall, H.J. (1980) Visual pigments of rods and cones in a human retina. *J. Physiol.*, **298**, 501–511.
5 Lagemann, R.T. (1977) New light on old rays: N rays. *Am. J. Phys*, **45** (3), 281–284.
6 Pascolini, D. and Mariotti, S.P. (2011) Global estimates of visual impairment: 2010. *Br. J. Ophthalmol.*, **96**, 614–618.
7 Parmeggiani, F. (2011) Clinics, epidemiology and genetics of retinitis pigmentosa. *Curr. Genomics*, **12** (4), 236–237.
8 Zrenner, E. (2002) Will retinal implants restore vision? *Science*, **295** (5557), 1022–1025.
9 Humayun, M.S., Dorn, J.D., Ahuja, A.K. *et al.* (2009) Preliminary 6 month results from the Argus™ II epiretinal prosthesis feasibility study. *Annual International Conference of the IEEE Engineering in Medicine and Biology Society 2009*, pp. 4566–4568.
10 Ahuja, A.K., Dorn, J.D., Caspi, A. *et al.* (2011) Blind subjects implanted with the Argus II retinal prosthesis are able to improve performance in a spatial-motor task. *Br. J. Ophthalmol.*, **95** (4), 539–543.
11 Rothermel, A., Liu, L., Aryan, N.P. *et al.* (2009) A CMOS chip with active pixel array and specific test features for subretinal implantation. *IEEE J. Solid-State Circuits*, **44** (1), 290–300.
12 Stingl, K., Bartz-Schmidt, K.U., Besch, D. *et al.* (2013) Artificial vision with wirelessly powered subretinal electronic implant alpha-IMS. *Proc. R. Soc. London, Ser. B*, **280** (1757), 20130077.
13 Keserü, M., Feucht, M., Bornfeld, N. *et al.* (2012) Acute electrical stimulation of the human retina with an epiretinal electrode array. *Acta Ophthalmol. (Copenh.)*, **90** (1), e1–e8.
14 Morimoto, T., Kamei, M., Nishida, K. *et al.* (2011) Chronic implantation of newly developed suprachoroidal-transretinal stimulation prosthesis in dogs. *Invest. Ophthalmol. Vis. Sci.*, **52** (9), 6785–6792.
15 Zhou, J.A., Woo, S.J., Park, S.I. *et al.* (2008) A suprachoroidal electrical retinal stimulator design for long-term animal experiments and in vivo assessment of its feasibility and biocompatibility in rabbits. *BioMed Res. Int.*, **2008**, e547428.
16 Shire, D.B., Kelly, S.K., Chen, J. *et al.* (2009) Development and implantation of a minimally invasive wireless subretinal neurostimulator. *IEEE Trans. Biomed. Eng.*, **56** (10), 2502–2511.

17 Shivdasani, M.N., Luu, C.D., Cicione, R. *et al.* (2010) Evaluation of stimulus parameters and electrode geometry for an effective suprachoroidal retinal prosthesis. *J. Neural Eng.*, **7** (3), 036008.

18 Mathieson, K., Loudin, J., Goetz, G. *et al.* (2012) Photovoltaic retinal prosthesis with high pixel density. *Nat. Photonics*, **6** (6), 391–397.

19 Zrenner, E., Bartz-Schmidt, K.U., Benav, H. *et al.* (2010) Subretinal electronic chips allow blind patients to read letters and combine them to words. *Proc. R. Soc. London, Ser. B*, **278**, 1489–1497.

20 Rizzo, S., Belting, C., Cinelli, L. *et al.* (2014) The Argus II retinal prosthesis: 12-month outcomes from a single-study center. *Am. J. Ophthalmol.*, **157** (6), 1282–1290.

21 Humayun, M.S., Dorn, J.D., da Cruz, L. *et al.* (2012) Interim results from the international trial of second sight's visual prosthesis. *Ophthalmology*, **119** (4), 779–788.

22 Mandel, Y., Goetz, G., Lavinsky, D. *et al.* (2013) Cortical responses elicited by photovoltaic subretinal prostheses exhibit similarities to visually evoked potentials. Nat. Commun., **4**, 1980.

23 Lorach, H., Goetz, G., Smith, R. *et al.* (2015) Photovoltaic restoration of sight with high visual acuity. *Nat. Med.*, **21** (5), 476–482.

24 Antognazza, M.R., Scherf, U., Monti, P., and Lanzani, G. (2007) Organic-based tristimuli colorimeter. *Appl. Phys. Lett.*, **90** (16), 163509.

25 Ghezzi, D., Antognazza, M.R., Dal Maschio, M. *et al.* (2011) A hybrid bioorganic interface for neuronal photoactivation. *Nat. Commun.*, **2**, 166.

26 Gautam, V., Bag, M., and Narayan, K.S. (2011) Single-pixel, single-layer polymer device as a tricolor sensor with signals mimicking natural photoreceptors. *J. Am. Chem. Soc.*, **133** (44), 17942–17949.

27 Callaway, E.M. and Yuste, R. (2002) Stimulating neurons with light. *Curr. Opin. Neurobiol.*, **12** (5), 587–592.

28 Sjulson, L. and Miesenböck, G. (2008) Photocontrol of neural activity: biophysical mechanisms and performance in vivo. *Chem. Rev.*, **108** (5), 1588–1602.

29 Szobota, S. and Isacoff, E.Y. (2010) Optical control of neuronal activity. *Annu. Rev. Biophys.*, **39** (1), 329–348.

30 Fork, R.L. (1971) Laser stimulation of nerve cells in aplysia. *Science*, **171** (3974), 907–908.

31 Smith, N.I., Iwanaga, S., Beppu, T. *et al.* (2006) Photostimulation of two types of Ca2+ waves in rat pheochromocytoma PC12 cells by ultrashort pulsed near-infrared laser irradiation. *Laser Phys. Lett.*, **3** (3), 154–161.

32 Hirase, H., Nikolenko, V., Goldberg, J.H., and Yuste, R. (2002) Multiphoton stimulation of neurons. *J. Neurobiol.*, **51** (3), 237–247.

33 Uzdensky, A.B. and Savransky, V.V. (1997) Single neuron response to pulse-periodic laser microirradiation. Action spectra and two-photon effect. *J. Photochem. Photobiol., B*, **39** (3), 224–228.

34 Shapiro, M.G., Homma, K., Villarreal, S. *et al.* (2012) Infrared light excites cells by changing their electrical capacitance. *Nat. Commun.*, **3**, 736.

35 Ellis-Davies, G.C.R. (2007) Caged compounds: photorelease technology for control of cellular chemistry and physiology. *Nat. Methods*, **4** (8), 619–628.

36 Fenno, L., Yizhar, O., and Deisseroth, K. (2011) The development and application of optogenetics. *Annu. Rev. Neurosci.*, **34** (1), 389–412.
37 Hegemann, P. and Möglich, A. (2011) Channelrhodopsin engineering and exploration of new optogenetic tools. *Nat. Methods*, **8** (1), 39–42.
38 Kotov, N.A., Winter, J.O., Clements, I.P. *et al.* (2009) Nanomaterials for Neural Interfaces. *Adv. Mater.*, **21** (40), 3970–4004.
39 Zhang, F., Wang, L.-P., Brauner, M. *et al.* (2007) Multimodal fast optical interrogation of neural circuitry. *Nature*, **446** (7136), 633–639.
40 Boyden, E.S., Zhang, F., Bamberg, E. *et al.* (2005) Millisecond-timescale, genetically targeted optical control of neural activity. *Nat. Neurosci.*, **8** (9), 1263–1268.
41 Fromherz, P. (2002) Electrical interfacing of nerve cells and semiconductor chips. *ChemPhysChem*, **3** (3), 276–284.
42 Fromherz, P. (2008) Joining microelectronics and microionics: nerve cells and brain tissue on semiconductor chips. *Solid-State Electron.*, **52** (9), 1364–1373.
43 Pappas, T.C., Wickramanyake, W.M.S., Jan, E. *et al.* (2007) Nanoscale engineering of a cellular interface with semiconductor nanoparticle films for photoelectric stimulation of neurons. *Nano Lett.*, **7** (2), 513–519.
44 Cramer, T., Steinbrecher, T., Koslowski, T. *et al.* (2009) Water-induced polaron formation at the pentacene surface: quantum mechanical molecular mechanics simulations. *Phys. Rev. B*, **79** (15), 155316.
45 Eisenthal, K.B. (1996) Liquid interfaces probed by second-harmonic and sum-frequency spectroscopy. *Chem. Rev.*, **96** (4), 1343–1360.
46 Svennersten, K., Larsson, K.C., Berggren, M., and Richter-Dahlfors, A. (2011) Organic bioelectronics in nanomedicine. *Biochim. Biophys. Acta – Gen. Subj.*, **1810** (3), 276–285.
47 Bystrenova, E., Jelitai, M., Tonazzini, I. *et al.* (2008) Neural networks grown on organic semiconductors. *Adv. Funct. Mater.*, **18** (12), 1751–1756.
48 Scarpa, G., Idzko, A.-L., Götz, S., and Thalhammer, S. (2010) Biocompatibility studies of functionalized regioregular poly(3-hexylthiophene) layers for sensing applications. *Macromol. Biosci.*, **10** (4), 378–383.
49 Antognazza, M.R., Ghezzi, D., Musitelli, D. *et al.* (2009) A hybrid solid–liquid polymer photodiode for the bioenvironment. *Appl. Phys. Lett.*, **94** (24), 243501.
50 Lanzarini, E., Antognazza, M.R., Biso, M. *et al.* (2012) Polymer-based photocatalytic hydrogen generation. *J. Phys. Chem. C*, **116** (20), 10944–10949.
51 Gautam, V., Bag, M., and Narayan, K.S. (2010) Dynamics of bulk polymer heterostructure/electrolyte devices. *J. Phys. Chem. Lett.*, **1** (22), 3277–3282.
52 Ghezzi, D., Antognazza, M.R., Maccarone, R. *et al.* (2013) A polymer optoelectronic interface restores light sensitivity in blind rat retinas. *Nat. Photonics*, **7** (5), 400–406.
53 Benfenati, V., Martino, N., Antognazza, M.R. *et al.* (2014) Photostimulation of whole-cell conductance in primary rat neocortical astrocytes mediated by organic semiconducting thin films. *Adv. Healthc. Mater.*, **3** (3), 392–399.
54 Martino, N., Feyen, P., Porro, M. *et al.* (2015) Photothermal cellular stimulation in functional bio-polymer interfaces. *Sci. Rep.*, **5**, 8911.
55 Wässle, H. (2004) Parallel processing in the mammalian retina. *Nat. Rev. Neurosci.*, **5** (10), 747–757.

56 Gautam, V., Rand, D., Hanein, Y., and Narayan, K.S. (2014) A polymer optoelectronic interface provides visual cues to a blind retina. *Adv. Mater.*, **26** (11), 1751–1756.

57 Bareket, L., Waiskopf, N., Rand, D. *et al.* (2014) Semiconductor nanorod–carbon nanotube biomimetic films for wire-free photostimulation of blind retinas. *Nano Lett.*, **14** (11), 6685–6692.

58 Lovrić, J., Bazzi, H.S., Cuie, Y. *et al.* (2005) Differences in subcellular distribution and toxicity of green and red emitting CdTe quantum dots. *J. Mol. Med.*, **83** (5), 377–385.

59 Chan, W.-H., Shiao, N.-H., and Lu, P.-Z. (2006) CdSe quantum dots induce apoptosis in human neuroblastoma cells via mitochondrial-dependent pathways and inhibition of survival signals. *Toxicol. Lett.*, **167** (3), 191–200.

11

Nanostructured Silica from Diatoms Microalgae: Smart Materials for Photonics and Electronics

Roberta Ragni[1], Stefania R. Cicco[2], Danilo Vona[1], and Gianluca M. Farinola[1]

[1] *Università degli Studi di Bari "Aldo Moro", Dipartimento di Chimica, via Orabona 4, 70126, Bari, Italy*
[2] *CNR-ICCOM Bari, Dipartimento di Chimica, Via Orabona, 4-70126 BARI (Italy)*

11.1 Diatoms: Living Cells in Glass Houses

The search for scalable routes to nanostructured materials with precise size, shape, and morphology represents a challenging task in current nanotechnology. Materials scientists are more and more looking at Nature as their source of inspiration for manufacturing complex architectures with ordered features from the micro- to the nanoscale. In fact, Nature provides impressive examples of living organisms capable of building three-dimensional organic and inorganic structures with highly reproducible and complex hierarchical morphologies that man-made technologies cannot yet match. This structural complexity is the result of billion years of evolution, which has optimized the ability of their components to exploit environmental factors relevant to their survival, growth, and reproduction, such as the interaction with sunlight for photosynthetic organisms. Among the organisms that have developed very complex photonic architectures, diatoms (Figure 11.1) appear particularly attractive for possible applications in materials science. Diatoms are unicellular eukaryotic microalgae ubiquitously distributed in oceans, freshwater habitats, soils, and inhospitable surfaces. Diatoms originated during or before the early Jurassic period (210–144 Mya) and for this reason, their microfossils (diatomaceous earth or diatomite) are useful tools for monitoring paleoceanographic events, environmental changes in lakes or oceans, and stratigraphic correlations [1]. Similarly to other eukaryotic algae, diatoms use photosynthesis as their energy source and convert carbon dioxide into carbohydrates. They are essential to all life on earth, producing about 20% of the oxygen we breathe by capturing atmospheric carbon [2]. The total number of diatom species worldwide is estimated to be at least 2×10^5 [3], although their classification and taxonomy is still debated [4].

These microorganisms are unique in the unicellular algae world and are attractive for applications in nanotechnology because of their nanostructured rigid cell wall,

Green Materials for Electronics, First Edition.
Edited by Mihai Irimia-Vladu, Eric D. Glowacki, Niyazi S. Sariciftci, and Siegfried Bauer.

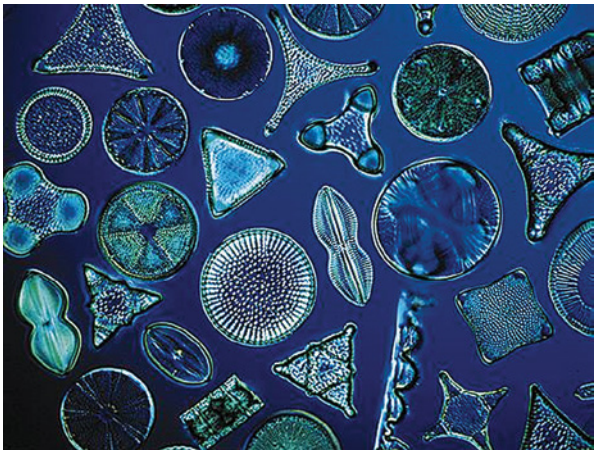

Figure 11.1 Images of silica shells of various diatoms.

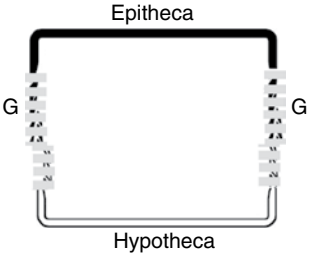

Figure 11.2 Schematic cross section through a box-like diatom frustule (G, girdle bands).

called *frustule*, made of amorphous hydrated nanoporous silica. The frustule constrains and encloses the eukaryotic protoplast, protecting it from the aqueous environment and from dangerous light wavelengths and, at the same time, controls nutrient uptake and secretion of cellular products through an intricate pattern of pores and slits on its surface. The frustule looks like a micro pillbox composed of two valves (the epitheca and the hypotheca), connected by lateral rings (girdles) that confer flexibility to the structure (Figure 11.2) [5]. Owing to their unique structure, diatoms have been defined as "living cells in glass houses" [2b].

Both valves and girdles have a specie-specific "layer-by-layer" hierarchical architecture in which every layer has a periodic nanotexturized topography with an ordered disposition of pores (areolae) whose diameter increases passing from the internal to the external layers. In spite of the fluctuation in higher taxonomic categories, a classification of diatoms can be made on the basis of frustule shape and symmetry of pore patterns: *centric* are all diatoms whose frustule has radial symmetry, while *pennate* are those in which valves are bilaterally symmetric [6]. A schematic three-dimensional (3D) cross section of a frustule of *centric* diatoms is shown in Figure 11.3: the hierarchical organization of porous plates (foramen, cribrum, and cribellum) involves pore diameters with different patterns that range from nanometers to micrometers.

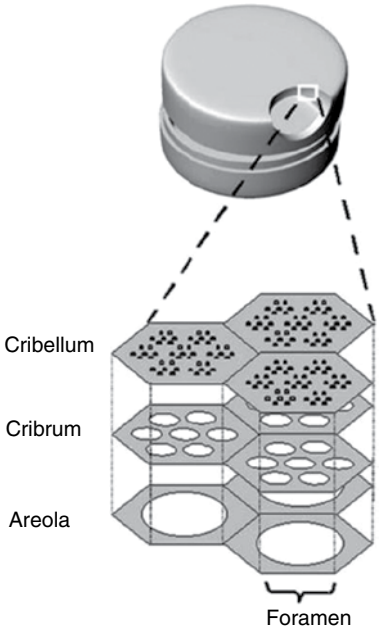

Figure 11.3 Cross -section diatom valve of a centric diatom. The honeycomb-like vertical chambers in the inner layer are called areolae. The outer siliceous thin layer membrane (cribellum) consists of very small pores. (Losic *et al*. 2007 [7b]. Reproduced with permission of Springer..)

While comprehensive diatom phylogeny is nowadays an open research topic, this is not an obstacle for utilizing the frustules of diatoms for technological applications [8]. Diatoms can be regarded as microscopic factories in which the input of nutrients and removal of metabolites are under perfect physical and chemical control by intricate patterns of channels and micro/nanopores of various shapes.

The main silicon source for biomineralization of diatoms in aquatic habitats is the orthosilicic acid $Si(OH)_4$, whose oceanic average concentration is about 70 µM, but is generally around 10 mM in surface waters where diatoms live [9]. The uptake of this element is under genetic control, which in turn implies the existence of specific gene products (proteins) guiding the precise reproduction of the biosilica pattern, generation by generation. Different gene families of silicon transporters (SITs) have been found to exhibit distinct patterns of expression through cell wall synthesis in all the diatoms investigated [10]. SITs were shown to directly interact with silicon, but they do not catalyze the silica polymerization process. Silica polymerization is in fact performed by other silicon-interacting proteins.

The mechanism by which SITs recognize and bind silicic acid is still under debate. Silica biogenesis takes place in a specialized intracellular compartment, the silica deposition vesicle (SDV, Figure 11.4) [11], which acts as a cellular "reaction vessel" where polymerization occurs according to the following equation:

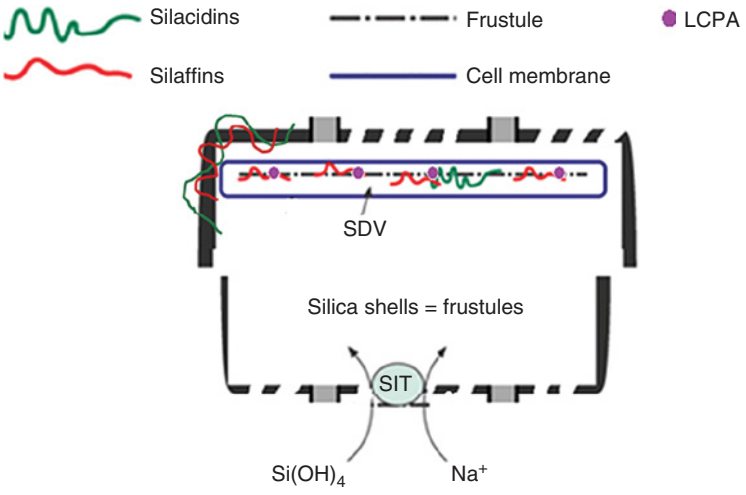

Figure 11.4 Schematic representation of silica transport and polymerization sites in diatoms.

$$n\mathrm{Si(OH)_4} \rightarrow (\mathrm{SiO_2})_n + 2n\mathrm{H_2O}$$

producing intracellular silica storage pools in which silica is believed to accumulate for the production of a new valve [12].

Silica polymerization in diatoms occurs in a very controlled way by the combined action of biomolecules whose specific role in the silica biomineralization mechanism is still under investigation. In all the diatoms species studied, in addition to polysaccharides and proteins, long-chain polyamines (LCPA) are the general components of the cells walls [13]. The polyamines extracted from the cell walls of different diatoms exhibit structural variations such as the chain length, the degree of methylation, or the position of the amino functionalities. These species-specific differences in LCPA structures support the idea of a specific role of the polyamines in creating species-specific silica nanostructures [7].

Under dissolution of the diatom biosilica using acidic conditions, phosphoproteins called *silaffins* (proteins with silica affinity) were discovered together with polyanionic peptides (derived from acidic modified peptides) called *silacidins*. The role of these proteins is to create macromolecular matrixes that can guide silica formation and precipitation [14]. Understanding the processes involved in biomineralization can eventually enable the production of nanostructured silica by biomimetic processes with minimal environmental impact. Actually, silaffins and silacidins have been extracted from the silica walls and used to induce *in vitro* precipitation of silica nanostructures (spheres, rods, or platelets) from silicic acid solution [15].

Unique properties such as biocompatibility, high surface area, tunable pore size, and versatile surface chemistry make mesoporous silica from diatoms an attractive material for many technological applications, ranging from biomedicine (drug delivery [16] and biosensing [17]) to photonics and electronics. The two latter applications are discussed in this chapter.

11.2 Diatom Frustules in Photonics and Optics

11.2.1 Diatom Frustules as Photonic Crystals

The periodic and hierarchical nanostructure of frustules is thought to be evolved to optimize the harvesting capability and photosynthetic activity of diatom cells [18]. Pores in diatoms represent "hot spots" in the formation of frustules and can be seen as "defects" that affect the natural directionality of light propagating inside the cell and enhance light absorption by chloroplasts. A diatom cell can be regarded as a "photonic box" with biosilica walls acting as photonic crystals in which very regular arrays of pores generate hierarchically ordered periodic patterns of high and low refractive index, which retain a self-similarity down to small length scales. The morphology, the average dimension, and the periodic pattern of pores in frustules are strictly dependent on the algal species. For instance, Fuhrmann *et al*. reported that frustules of the centric marine diatom *Coscinodiscus granii* have 150 µm average total diameter and show a different (hexagonal and square) periodic pattern of areolae in the valves and the girdle, respectively (Figure 11.5) [19]. Hence, both valve and girdle bands can be

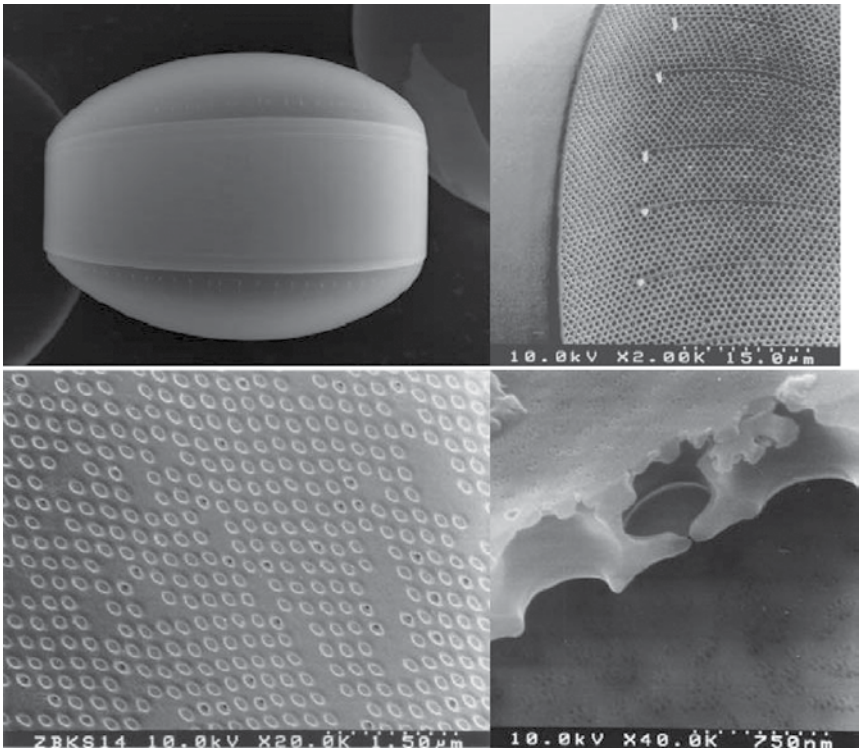

Figure 11.5 SEM images of biosilica walls. Upper row, left: frustule from *Coscinodiscus granii* species. Upper row, right: valve inside and transition with a girdle and the patterning system. Lower row, left: girdle band squared lattice, from an inside view. Lower row, right: cross section through the cell wall of the valve. (Fuhrmann *et al*. 2004 [19]. Reproduced with permission of Springer.)

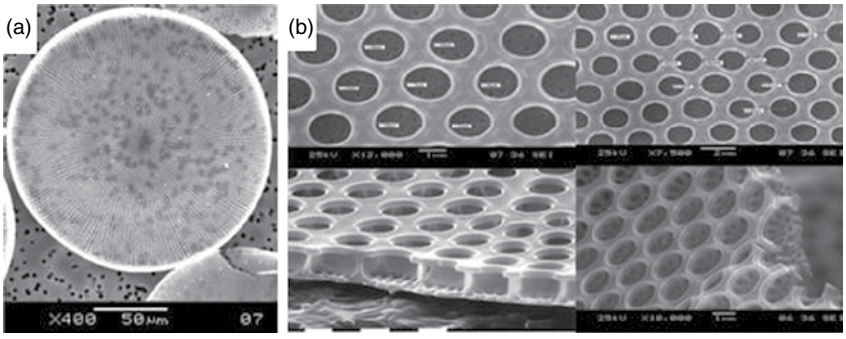

Figure 11.6 SEM images of (a) a radially symmetric valve with areolae arrays arranged in a hexagonal pattern and (b) details of the substructure of the valve with morphometric measurements of the areolae diameter, interareolae spaces, and thickness (where not reported, bar scale is 1 µm). (De Stefano *et al*. 2007 [21]. Reproduced with permission of The Optical Society.)

regarded as slab waveguide photonic crystals whose properties result from a combination of their waveguide behavior and the two-dimensional photonic band structure [20].

The highly ordered structure and the photonic crystal nature of frustules enable their application as optical microlens, filters, polarizers, waveguides, beam splitters, couplers, and laser cavities. In 2007, De Stefano *et al*. investigated the light-focusing ability of valves of the centric *Coscinodiscus wailesii* diatoms having an average diameter of 150–200 µm, an average thickness of 700 nm, and almost perfect hexagonal patterns of areolae disposed in a radial symmetric array with 2.6–2.7 µm lattice constant (i.e., the distance between the centers of two neighboring areolae) (Figure 11.6) [21].

The radial symmetry of areolae array resembles that of some man-made optical devices, such as photonic crystal fibers or phase-locked arrays of optical fibers or lasers. As a common feature of such regularly patterned systems, light propagation through their structure depends not only on the interaction with matter but also on the spatial order of the periodic lattice. In particular, on illuminating a centric *C. wailesii* valve by a red laser beam with 100 µm spot size, a coherent superposition of the light scattered by the areolae in the valve is responsible for focusing the beam to less than a 10 µm spot size at a distance of 104 µm after light transmission through the valve (Figure 11.7).

Hence, valves act as a natural microlens, which could be available on a large scale at low production cost with very precise and reproducible nanostructure. Owing to their high mechanical resistance, valves can be also easily handled by standard microneedles or microtips, thus disclosing the interesting opportunity to use them to fit the top of an optical fiber affording a lensed fiber without modifying the glass core or, similarly, they could be set up in a vertical cavity surface emitting laser.

The way in which light interacts with the highly ordered structure of *C. wailesii* biosilica shells was also explored by Noyes *et al*. who observed that diffraction and transmission of incident light by frustules is strongly wavelength dependent;

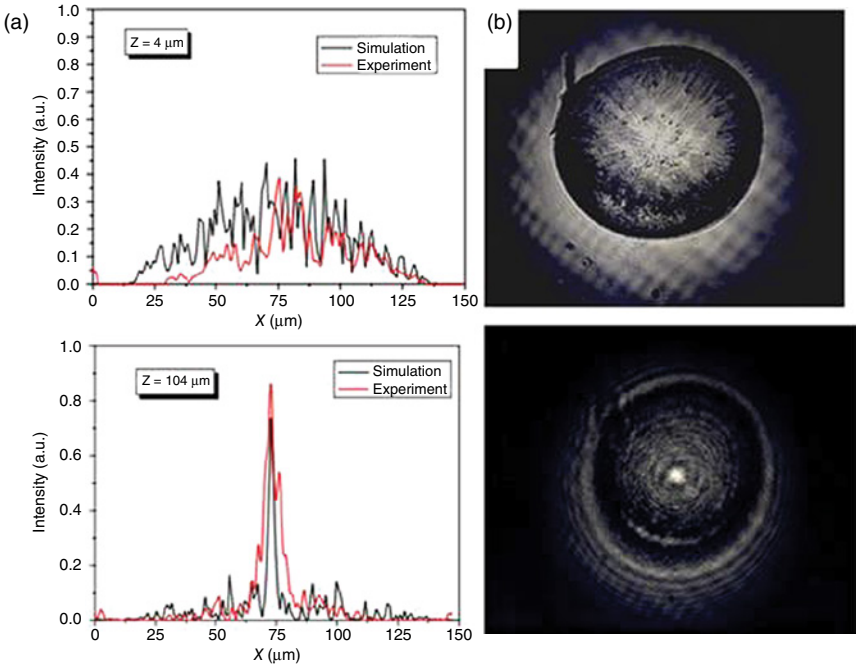

Figure 11.7 (a) The intensity distribution of transmitted light at the distance (*z*) of 4 μm (top plot) and 104 μm (bottom plot): the red line is the experimental recorded one, the black line is the numerical estimate. (b) Images of the diatom surface recorded by a CCD camera at the two distances. (De Stefano *et al.* 2007 [21]. Reproduced with permission of The Optical Society.)

in particular, transmission is more pronounced for the red light rather than for the blue and green wavelengths [22]. Yamanaka *et al.* also observed, by ultrastructural analysis, that isolated frustules of *Melosira variance* mainly absorb light in the blue wavelength region. It seems likely that diatoms have evolved their ordered biosilica shell to reduce the solar light blue component, which could lead to production of oxygen radicals responsible for an extensive oxidative damage of biomolecules inside the cells [23]. These optical features enable possible applications of frustules as optical filters.

The light-confining properties of frustules were deeply investigated by observing the transmission of partially coherent light coming from a monochromator through single valves of *C. wailesii* diatoms [24]. In particular, as a result of the superposition of wavefronts diffracted by the edges of the pores, the incoming visible light is confined, by the regular pore pattern of the diatom surface, into a spot of a few microns whose dimension and position strictly depend on wavelength. This effect was not observed for noxious ultraviolet light, explaining one of the possible evolutive advantages of the photonic properties of diatom frustules.

A similar behavior was also experimentally revealed in 2014 for single valves of *Arachnoidiscus* diatoms [25]. Also in this case, natural evolution seems to have shaped frustules to optimize the visible light exploitation and

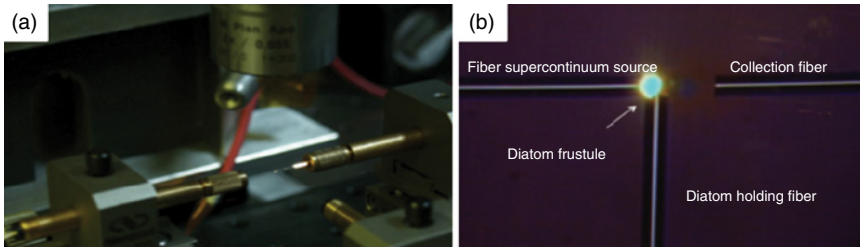

Figure 11.8 (a) Experimental setup for measurement of the tunable filter behavior of individual frustule valves. (b) Higher magnification optical image of the central region where the diatom valve is located. The transmitted light through the diatom valve is collected by the optical fiber on the right (right horizontal fiber in the image) and sent to an optical spectrum analyzer for analysis. (Kieu *et al.* 2014 [26]. Reproduced with permission of The Optical Society.)

to reduce the negative effects of UV radiations. Actually, the valves are able to interact only with the visible light, confining different monochromatic radiations in a series of hot spots whose position along the optical axis is strictly dependent on wavelength. This feature may disclose new possibilities in optics, based on the application of diatom valves as micro-monochromator elements.

The optical properties of *C. wailesii* frustules have been also investigated using the white light of a supercontinuum broadband (400–1700 nm) laser source: [26] light crosses an individual diatom valve fixed to the end of a supporting optical fiber (Figure 11.8) and the distance between the diatom valve and the light output is kept to 50–100 μm, in order to illuminate only spot regions of ~20 μm diameter on the valve surface. Such a fine imposed light spot enables probing different regions of the individual valve and evaluating the influence of the variation of pore structure on light diffraction and transmission.

As shown in Figure 11.9a, on irradiating the valve in different regions, the transmitted light intensity is reduced in correspondence to a specific wavelength that shows stronger diffraction in that location of the valve. This occurs since the variation of the intensity of transmitted light versus wavelength follows changes in the spacing of pores on the valve. Since pores located near the center are closer together than pores located near the outer rim of the valve, reduction in light transmission at shorter wavelengths (dips in Figure 11.9a) is observed near the center whereas the transmitted power at long wavelengths is reduced at the outer rim. Moreover, light interaction with the periodic pore structure of the valve is responsible for the generation of colorful patterns due to the diffraction of different applied wavelengths at different angles (Figure 11.9b): in particular, while a white light circular spot is observed when the valve is not in the light path (Figure 11.9bi), the hexagonal light scattering pattern of the beam crossing the valve results from the hexagonal periodic pore valve structure; the color of the central spot changes according to the change in the local diffraction maximum (Figure 11.9bii–iv).

The *C. wailesii* valve interaction with coherent light has been recently studied also by digital holography [27]. This technique allows clarifying the role that

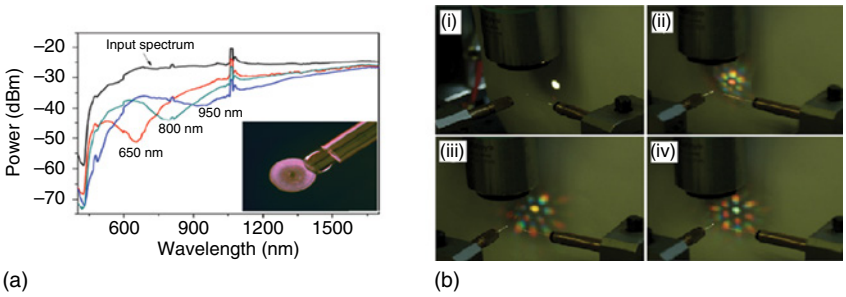

Figure 11.9 Position dependence of light transmission by a *Coscinodiscus wailesii* valve. (a) Transmission spectra corresponding to regions near the center (red), between the center and the outer valve edge (green), and near the outer valve edge (blue). Inset: optical photograph of a *Coscinodiscus wailesii* valve affixed to the supporting optical fiber. (b) Optical images of the diffraction patterns obtained from the different regions of the valve: (i) no diatom is present in the beam path, (ii–iv) the frustule valve is in the beam path. (Kieu *et al*. 2014 [26]. Reproduced with permission of The Optical Society.)

pores and valve edges play in light manipulation, discriminating the two contributions. Contrary to usual scanning microscopies, which suffer from low resolution in the direction of light propagation (i.e., the *z*-direction) and which cannot reconstruct light confinement inside the cell cytoplasm, digital holography provides a complete detection of the three-dimensional structural features of the frustule, retrieving, in far field regions, the amplitude and phase of the wavefront interacting with the frustule itself. The interferometric resolution of digital holography enables detecting the light confinement effect along the optical axis with extremely high resolution and this effect has been proved to be originated only by the diffraction of pores with no contribution from valve edges.

11.2.2 Autofluorescence of Diatom Frustules

Mesoporous silica frustules display efficient photoluminescence (PL) in the UV–blue spectral region. As reported in Figure 11.10, the PL spectra of frustules of various diatom species are almost identical (Figure 11.10a) and resemble that of

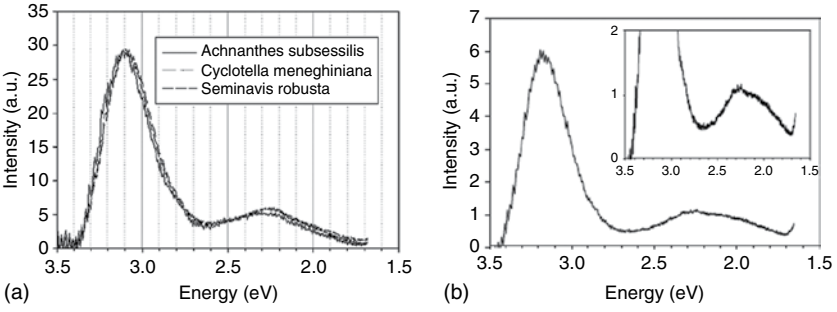

Figure 11.10 PL spectra of (a) cultured diatoms and (b) pure fused silica glass ($\lambda_{exc} = 325$ nm). (Butcher *et al*. 2005 [28]. Reproduced with permission of Elsevier.)

pure fused silica glass (Figure 11.10b), showing a strong UV–blue emission peak at 3.1 eV and a lower yellow emission contribution at 2.15 eV [28].

A more detailed photophysical characterization has been recently carried out by García-Meza *et al.* who investigated possible correlations of photoluminescence with age and surface chemistry of frustules of two pennate diatom species, namely, *Amphora* and *Gomphocymbella* [29]. It was shown that frustule photoluminescence depends on diatom aging as well as on the integrity of the biosilica shell. Only integer frustules of adult diatoms show discrete emission lines on top of the broad blue–green emission band commonly observed from porous synthetic silica and shells of young diatoms (Figure 11.11). This feature seems to be related with the morphometric and morphological changes of frustules upon aging, such as the reduction in pore diameter, the appearance of pores within pores, the deposition of more silicified girdle bands, and the appearance of pores on such bands. Moreover, the discrete emission lines seem to be associated with the ordered pore arrays of integer frustules since they disappear upon pore destruction in pulverized biosilica shells.

In a photophysical study carried out by De Stefano *et al.* [30], the autofluorescence intensity of *Thalassiosira rotula* Meunier biosilica shells has been proved to be strongly dependent on their exposure to a series of gases and volatile substances. This experimental evidence makes diatom frustules interesting biomaterials for optical sensing. In particular, upon exposure of frustules to gaseous

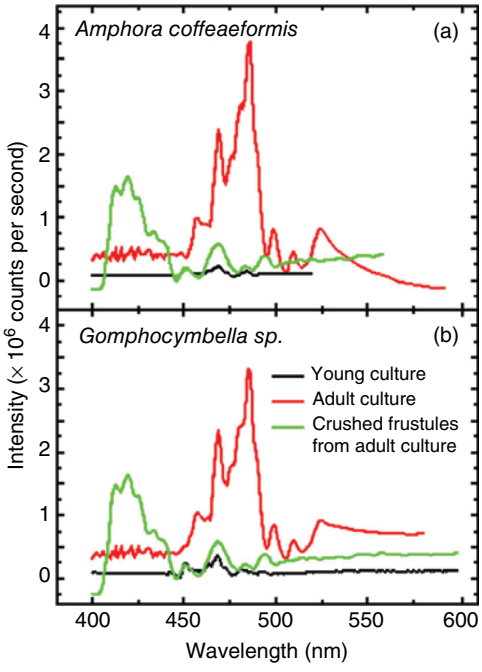

Figure 11.11 PL spectra of integer and crushed frustules from young and adult cultures of (a) *Amphora* and (b) *Gomphocymbella* diatoms. The common broad emission is subtracted to allow better visualization of the discrete set of emission lines. (Arteaga-Larios *et al.* 2014 [29]. Reproduced with permission of John Wiley and Sons.)

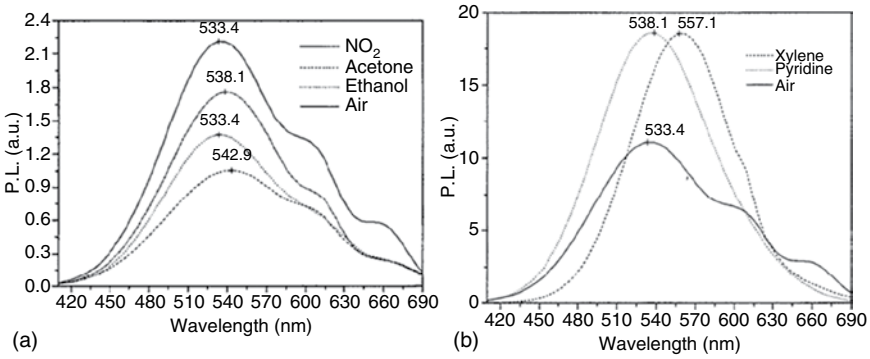

Figure 11.12 (a) Quenching and (b) enhancement of diatom frustules PL spectra in the presence of various gaseous substances. The numbers on top of each spectrum indicate the peak position as estimated by numerical fit. (De Stefano *et al.* 2005 [30]. Reproduced with permission of Nature Publishing Group.)

analytes, autofluorescence is quenched or enhanced according to the electronic nature and polarizing ability of the volatile species. As shown in Figure 11.12, electrophilic analytes, such as NO_2 or vapors of acetone and ethanol, quench frustule photoluminescence because of their electron-withdrawing effect on biosilica of the frustule surface, whereas nucleophilic gases such as vapors of xylene and pyridine have an opposite effect.

A red shift of PL is also observed for both classes of analytes as a result of the adsorption of gas molecules into the nanometer pores, which increases the average refractive index of frustules silica. Interestingly, in all cases, the observed effects on PL are reversible as soon as the analyte is removed; this suggests the possibility of employing frustules in optical sensors.

Antibody-functionalized diatom frustules have been reported as biosensor microplatforms for selective detection of immunocomplex formation. For instance, De Stefano *et al.* covalently linked, by specific spacers, a murine monoclonal antibody to the frustule surface of *Coscinodiscus concinnus Wm. Smith* diatoms and demonstrated that the interaction of the antibody with its specific peptide ligand strongly influences the photoluminescence of frustules upon excitation by a high-pressure mercury lamp [31].

Interestingly, such an effect is not observed for aspecific interactions of the antibody with other ligands. Gale *et al.* demonstrated that functionalization of *Cyclotella* sp. frustules with the nucleophilic rabbit-imunoglobulin IgG antibody enhances their intrinsic blue photoluminescence by a factor of 6 and that a further threefold enhancement of PL intensity can be detected upon immunocomplex formation with the complementary antigen (Figure 11.13) [32].

Surface-enhanced Raman scattering (SERS) immunoassay biosensors have also been recently developed by depositing goat (anti-mouse)-IgG-functionalized silver nanoparticles onto diatom biosilica shells [33]. In this case, the use of diatom frustules results in a two order magnitude increase in the detection limit of the specific mouse antigen–antiboby interaction with respect to conventional

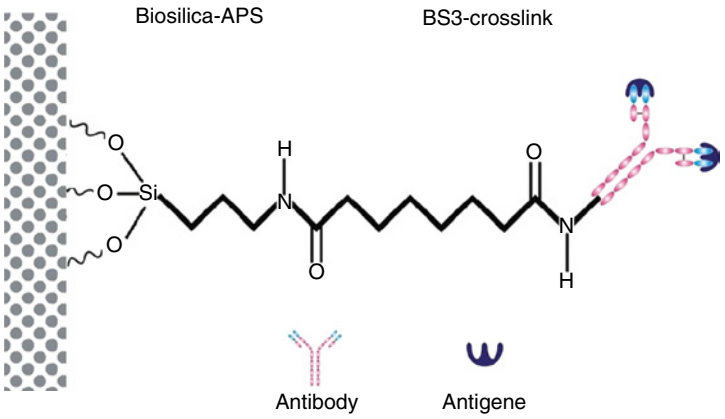

Figure 11.13 Schematic drawing of covalent linking of antibody to frustule surface by aminopropyl triethoxysilane and BS3 [bis(sulfosuccinimidyl)suberate] spacers. (Gale *et al*. 2009 [32]. Reproduced with permission of John Wiley and Sons.)

SERS sensors on flat glass. Ultrasensitive and low-cost immunoassay biosensors based on such hybrid plasmonic biosilica nanostructured materials can be expected to replace conventional optical systems in trace amount detection of cancer biomarkers for early diagnosis.

11.2.3 Functionalization of Diatom Frustules with Organic or Inorganic Emitters

Organic dyes have been frequently used as fluorescent probes to label the biosilica components in living diatoms with the aim of studying the mechanism of biomineralization. Rhodamine 123 (Figure 11.14) was first used as an *in vivo* biosilica staining agent although low accumulation efficiency limited its use [34]. Then, two organic dyes, LysoSensor blue DND-160 and LysoTracker yellow HCK-123 (Figure 11.14), were used by Desclés *et al*. for the selective imaging of biosilica in a series of living diatoms [35]. Thanks to their basic amino groups, both dyes selectively accumulate in the SDV where frustule biogenesis occurs. In particular, HCK-123 shows higher fluorescence signal-to-noise (S/N) ratio and is more stable and less detrimental for cell integrity than DND-160. Moreover, this dye allows the use of filter sets (e.g., GFP or FITC) of common confocal microscopes not equipped with UV excitation. As shown in Figure 11.14, after *in vivo* incorporation and co-deposition in the biosilica shells, both DND-160 and HCK-123 resist the harsh acid oxidative treatment with potassium permanganate and sulfuric acid used to purify the fluorescent frustules from the organic autotrophic matter. In addition, Desclés *et al.* also demonstrated that the triethoxysilyl-functionalized FITC-APS green dye (Figure 11.14) can be used as an efficient probe for *in vivo* and *in vitro* staining of frustules (Figure 11.15) [35].

Interestingly, the combined use of DND-160 and FITC-APS represents an efficient strategy for the *in vivo* monitoring of frustule exocytosis since it enables distinguishing the newly synthesized diatom-shell patterns from the pre-existing ones (Figure 11.16). Actually, in *Thalassiosira weissflogii* diatoms, biosilica

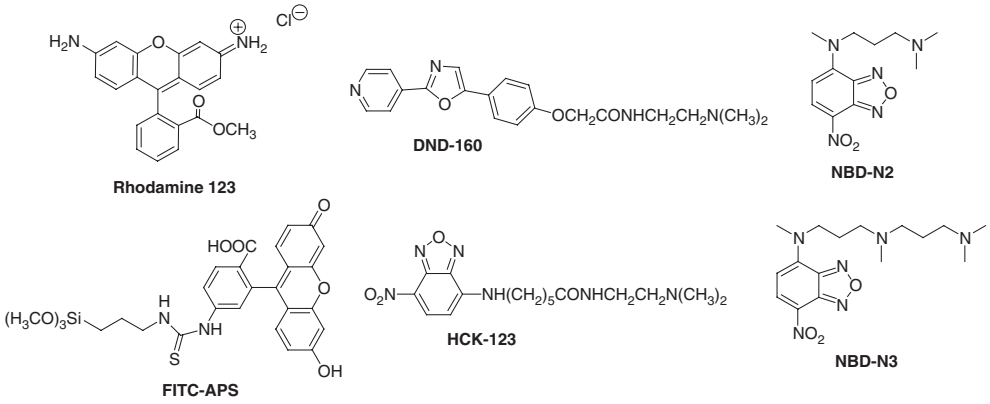

Figure 11.14 Chemical structures of organic dyes for selective frustule imaging in living diatoms

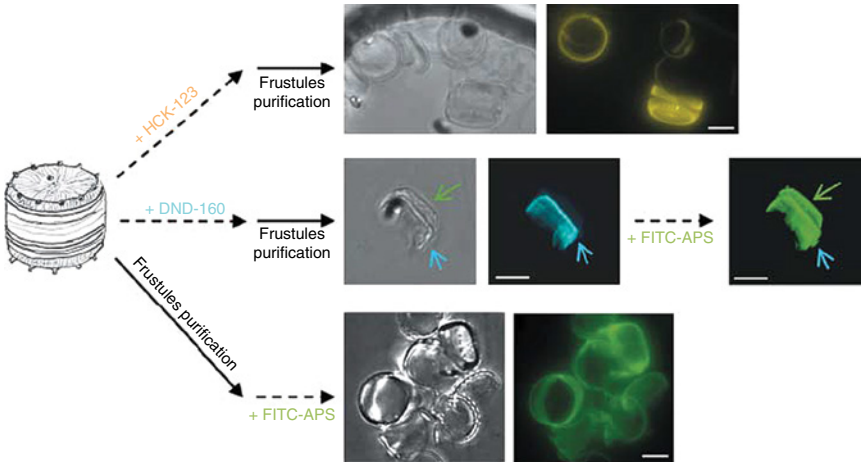

Figure 11.15 Frustules labeling with DND-160 (cyan), HCK-123 (yellow), and FITC-APS (green). DND-160 and HCK-123 are incorporated and co-deposited within newly synthesized silica structures. After incubation of DND-160 stained frustules with FITC-APS, the green arrow shows a partial frustule that is revealed only by FITC-APS labeling. Bars, 5 µm. (Desclés *et al*. 2008 [35]. Reproduced with permission of John Wiley and Sons.)

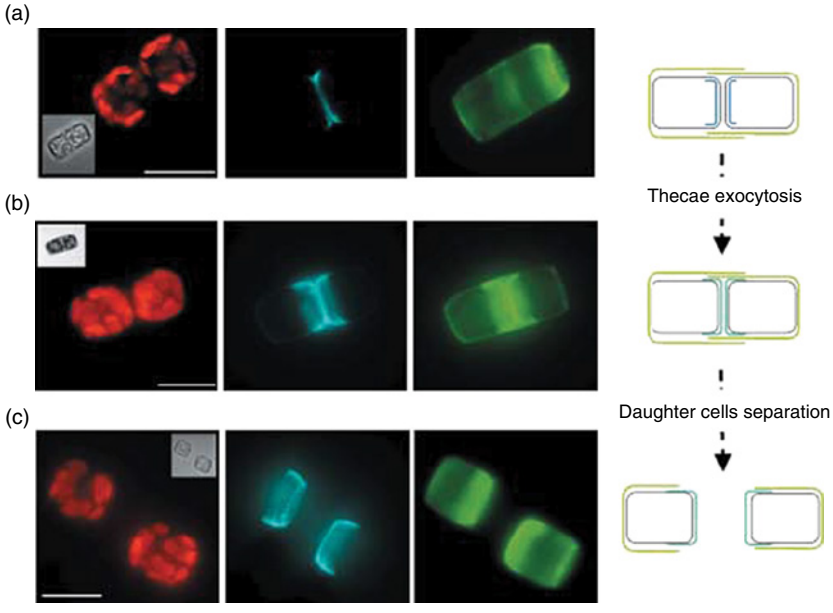

Figure 11.16 *Thalassiosira weissflogii* cells grown in the presence of DND-160 (cyan) and then labeled with FITC-APS (green) . (a) Before exocytosis, the hypothecae newly synthesized within the two daughter cells are stained only by DND-160. (b) After silica deposition vesicle (SDV) exocytosis, the new hypothecae show dual labeling with both dyes. (c) Then, the daughter cells separate and the newly formed silica material is clearly visible. Insets correspond to bright fields, and red images to chlorophyll fluorescence. (Desclés *et al*. 2008 [35]. Reproduced with permission of John Wiley and Sons.)

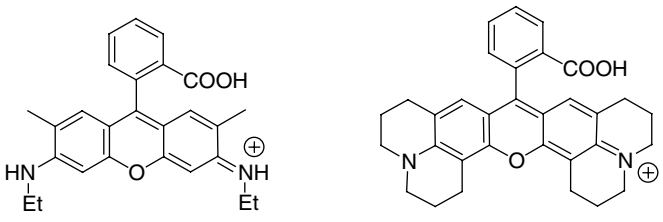

Figure 11.17 Chemical structures of Rh 19 and Rh 101 dyes.

generated inside the SDV is only accessible by DND-160 (Figure 11.16a) whereas, upon exocytosis, the new hypovalves are labeled by both DND-160 and FITC-APS dyes (Figure 11.16b), and this dual labeling is even more evident after daughter cell separation (Figure 11.16c).

More recently, highly efficient labeling of frustules was obtained with the NBD-N2 and NBD-N3 dyes (Figure 11.14) bearing oligopropylamine moieties that are very similar to those found in the diatom SDV [36].

The integration of organic fluorophores, such as laser dyes, into diatom frustules, besides being an efficient strategy to explore the natural biosilicification process, may represent a very profitable route to new biohybrid luminescent nanomaterials with potential applications such as light modulators or microresonators, since they combine the stimulated emission of the dyes with the photonic crystal behavior of the frustules. Fuhrmann *et al.* successfully incorporated *in vivo* a series of carboxyl-functionalized rhodamine laser dyes, such as Rh19 and Rh101 (Figure 11.17), in frustules of *C. granii* and *C. wailesii* diatoms and investigated light confinement effects in the resulting luminescent biosilica [37].

In particular, incubation of diatoms with the above-mentioned dyes occurs without altering frustule morphology and affords fluorescent nanostructures within 1–3 days. Moreover, significant differences can be found on comparing the PL spectrum of free Rh101 dye and Rh101 stained frustules, thus demonstrating that the local environment of nanostructured biosilica influences the emission of the incorporated dye.

Another approach used to generate highly luminescent biosilica shells consists in coating diatom frustules with green-emitting manganese and zinc oxide nanoparticles (Figure 11.18) [38]. In this case, the coating procedure is straightforward consisting in the immersion of frustules into a solution of zinc acetate dihydrate and manganese acetate. Subsequent filtration and heating at 1050 °C yields a luminescent compact, continuous, and conformal Mn-doped Zn_2SiO_4 layer on the biosilica surface.

Metal calcogenide meso- and nanostructures composed of ZnS coated frustules can be obtained by a sonochemical process leading to the deposition of ZnS nanoparticles on diatom biosilica shells [39]. The resulting structures have potential application in photonic devices since they inherit the photonic crystal behavior of the original frustules and show enhanced bandgap reflectivity due to the higher refractive index of ZnS versus silica.

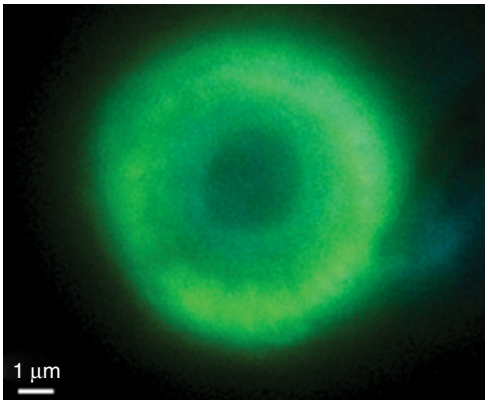

Figure 11.18 Fluorescence microscope image of a single manganese-doped Zn_2SiO_4 coated frustule of *Coscinodiscus lineatus* diatom. (Cai *et al*. 2007 [38]. Reproduced with permission of John Wiley and Sons.)

11.3 Diatom Frustules in Electronics

The application of bare frustules in electronics is limited by their insulating properties. However, frustules represent very appealing nanostructured templates useful to build up a wide variety of structures with semiconducting or conducting materials that retain the hierarchically ordered architecture of frustules. Various approaches are available to convert the biogenic silica shells into electroactive nanostructured materials. A suitable protocol consists in the *in vivo* feeding of living diatoms with metals or metal oxides and subsequent isolation of modified frustules bearing these materials in their structure. Another route consists in the deposition of a thin layer of electroactive material onto isolated biosilica shells, thus leading to hybrid nanostructures with frustule morphology composed of inner silica skeleton and a semiconducting or conducting surface. Another intriguing approach is based on the chemical conversion, by shape-preserving displacement reactions, of the diatom biosilica shells into semiconducting or conducting bioclastic materials with replicated frustule nanostructure.

11.3.1 Hybrid Metal or Metal Oxide Biosilica-Based Materials for Electronics

Electroluminescence (EL) in the visible spectral range was observed in 2008 for *Pinnularia* sp. frustules containing metabolically inserted germanium in 1.6 wt% percentage [40]. The *in vivo* Ge insertion is carried out in a bioreactor by a two-stage cell cultivation technique: [41] in the first stage, the diatom cell culture is grown up to silicon starvation, whereas in the second stage, silicon and germanium, as soluble Na_2SiO_3 and GeO_3 respectively, are co-fed to promote one cell division during Ge uptake. This technique enables dispersing Ge uniformly into the frustules and, although it does not alter their overall shape, the nanoscale pore size is modified. In fact, after the addition of soluble Ge, frustules no longer possess the thin layer of biosilica containing a subarray of 50 nm nanopores that

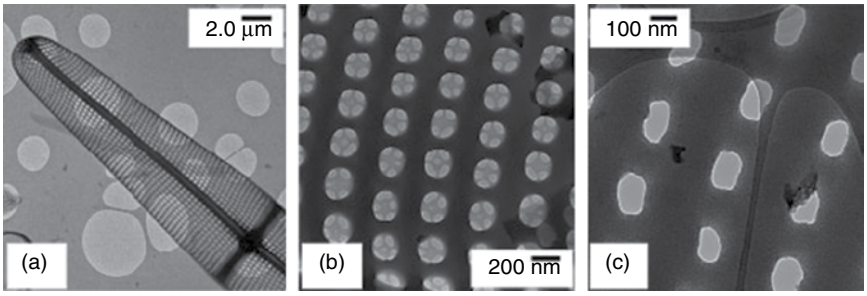

Figure 11.19 TEM images of the *Pinnularia sp.* frustule. (a) Representative valve at the end of Stage I before metabolic insertion of Ge. (b) Pore array at the end of Stage I. (c) Pore array of new representative valve at the end of Stage II of cultivation. (Jeffryes *et al*. 2008 [40]. Reproduced with permission of John Wiley and Sons.)

normally underlies the layer of 200 nm pores in frustules during the first stage (Figures 11.19b,c). Therefore, after removal of these fine features, the Ge-doped frustule valves, isolated by hydrogen peroxide treatment of cultured diatoms, strongly resemble bidimensional photonic crystal slabs.

An electroluminescent device was fabricated by spin coating these valves onto indium tin oxide coated glass substrate and subsequently depositing hafnium silicate dielectric and Al cathode layers (Figure 11.20a). The EL spectrum of such a device shows sharp line emissions in the UV–green (300–500 nm) and red–NIR (640–780 nm) ranges, whereas no EL signal is detectable for the reference diode fabricated with the same architecture using nondoped biosilica valves (Figure 11.20b).

Diatom shells have also been used in photovoltaics: hybrid titania modified frustules have been employed in efficient photoanodes for dye-sensitized solar cells (DSSCs) [42]. The metabolic insertion of titania in diatom biosilica is not efficient since the highest attainable content of titania (3.7 wt%) is low [43]. Atomic layer deposition (ALD) was also reported as a suitable method to entirely cover the frustule surface and pores with an ultrathin titania layer but, despite having great connectivity, this TiO_2 film does not reach a high surface area, which is a desirable requirement for application of the coated frustules in DSSC photoanodes [44]. This property was attained with titania nanoparticles bearing high surface/volume ratio. Titania nanoparticles deposition on diatom biosilica can be performed using a layer-by-layer approach with phytic acid as a molecular binder [45]. However, getting a sufficient number of deposition cycles to achieve good interparticle contact, keeping a high short-circuit current for DSSCs, turned out to be much time consuming. A more efficient and straightforward method has been recently reported by Toster *et al*. [42]. In his approach, a preliminary plasma treatment is carried out on frustules to activate the hydrophilic hydroxyl groups on their surface and to promote binding of these groups to titania nanoparticles. These nanoparticles are synthesized by controlled hydrolysis of titanium(IV) isopropoxide (TIP) in hexane solution and they are deposited *in situ* on the surface of the plasma-treated frustules. Subsequent calcination at 500 °C favors frustule coating with the anatase nanoparticles and the whole

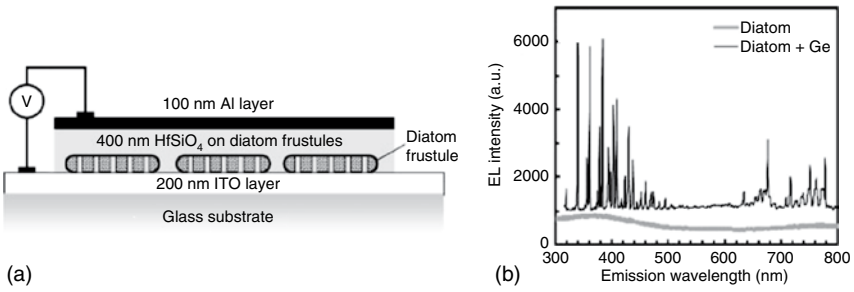

Figure 11.20 (a) Schematic drawing of Ge-doped valves based device. (b) EL spectra of diodes made with the Ge-doped and bare valves. (Jeffryes *et al*. 2008 [40]. Reproduced with permission of John Wiley and Sons.)

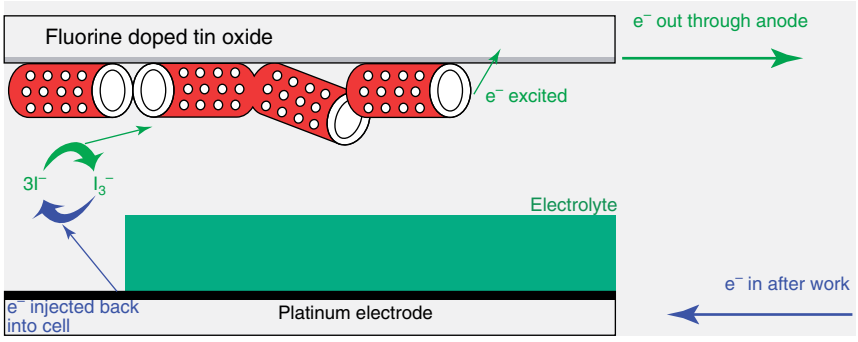

Figure 11.21 DSSC architecture incorporating titania-coated frustules. (Toster *et al*. 2013 [42]. Reproduced with permission of Royal Society of Chemistry.)

process is repeated three times to increase the thickness and connectivity of the titania film. The resulting hybrid shells are mixed in a paste of ethyl cellulose and terpineol, and then screen-printed and calcined onto fluorine-doped tin oxide (FTO) glass to afford a working electrode on which the N719 ruthenium dye sensitizer is adsorbed. The DSSC architecture is then completed, sealing this photoanode to a platinum counterelectrode and back-filling the cell with the iodide/tri-iodide electrolyte (Figure 11.21). A significant increase in energy conversion efficiency is recorded for the frustule-based DSSC with respect to a standard titania cell (4.6% vs 3.5%, respectively). This enhancement can be attributed to the light-scattering and trapping ability of frustules that increases the probability for photons to be absorbed by the dye, thus improving charge injection into the semiconductor.

11.3.2 Diatom Frustules as Templates for Three-Dimensional Replication

Two-dimensional layer-by-layer deposition techniques used in microelectronics industry are not well suited for low-cost mass production of nanostructured microdevices with complex three-dimensional shapes. Diatoms provide the possibility of large-scale production of a wide variety of intricate and patterned 3D biosilica microshells that are generated with extremely high morphological

precision by fast biological reproduction cycles. The combination of genetic precision and massive availability make diatom frustules attractive for meso- to nanodevice manufacturing. Although their silica composition is not suitable for many electronic applications, frustules can undergo bioclastic and shape-preserving inorganic conversion (BaSIC) [46] processes, leading to a wide variety of non-natural materials with retained frustule 3D morphology but completely different chemical composition.

Various BaSIC approaches to alter the composition of biosilica without losing its structural fine features have been developed, mainly relying on (i) gas/silica displacement reactions, (ii) conformal coating methods, and (iii) a combination of displacement and conformal coating processes.

For instance, high-temperature redox reaction of *Aulacoseira* cylindrical biosilica frustules with magnesium gas was used by Sandhage *et al.* to generate MgO/Si solid composites with retained frustule shape [47]. A selective dissolution of magnesia by HCl treatment allows the conversion of such composites into silicon replicas with retained frustules morphology and nanoscale features [48]. Besides being photoluminescent, these replicas exhibit rapid changes in impedance upon exposure to gaseous nitric oxide, thus allowing their application in a microscale single silicon-frustule-based gas sensor (Figure 11.22).

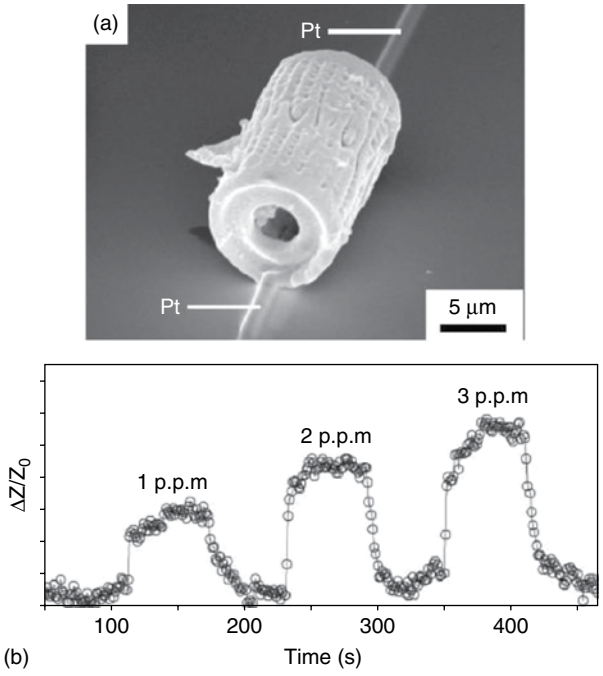

Figure 11.22 (a) Secondary electron image of a silicon replica connected to platinum electrodes in a simple gas sensor. (b) Electrical response of single silicon frustule sensor to NO gas. ΔZ is the impedance change upon exposure to NO gas and Z_0 is the sensor impedance in pure flowing argon. (Bao *et al*. 2007 [48]. Reproduced with permission of Nature Publishing Group.)

In 2014, Voelcker *et al.* have simplified the magnesiothermic reduction protocol of the *Aulacoseira* frustules biosilica and modified the surface of the resulting silicon replicas with thiol groups to enable their stable assembly on a gold-plated glass slide that can be used as the photoanode in a photoelectrochemical cell for solar energy conversion (Figure 11.23) [49]. The deposition onto silicon frustule replicas of cadmium sulfide photocatalyst has also been proved as an efficient strategy for sensitizing the photoanode and improving the photocurrent generation.

Aulacoseira biosilica frustules have been also converted, by metathetic displacement reaction with TiF_4 gas, into anatase TiO_2 replicas useful as active materials for gas sensors [50]. These nanostructures have been also exposed to hydrothermal treatment with molten $Ba(OH)_2$ or $Sr(OH)_2$, yielding $BaTiO_3$ or $SrTiO_3$ frustule replicas that, due to their ferroelectric and piezoelectric properties, may have applications in multilayer capacitors, electro-optical devices, piezoelectric actuators, passive memory storage devices, and transducers.

In 2015, Losic *et al.* reported for the first time a simple hydrothermal process converting frustules of various diatoms into their MnO_2 replicas: [51] in particular, a nanostructured layer of MnO_2 on the frustule surface is firstly deposited by heating to 160 °C the biosilica frustules dispersed into $KMnO_4$ solution. Then,

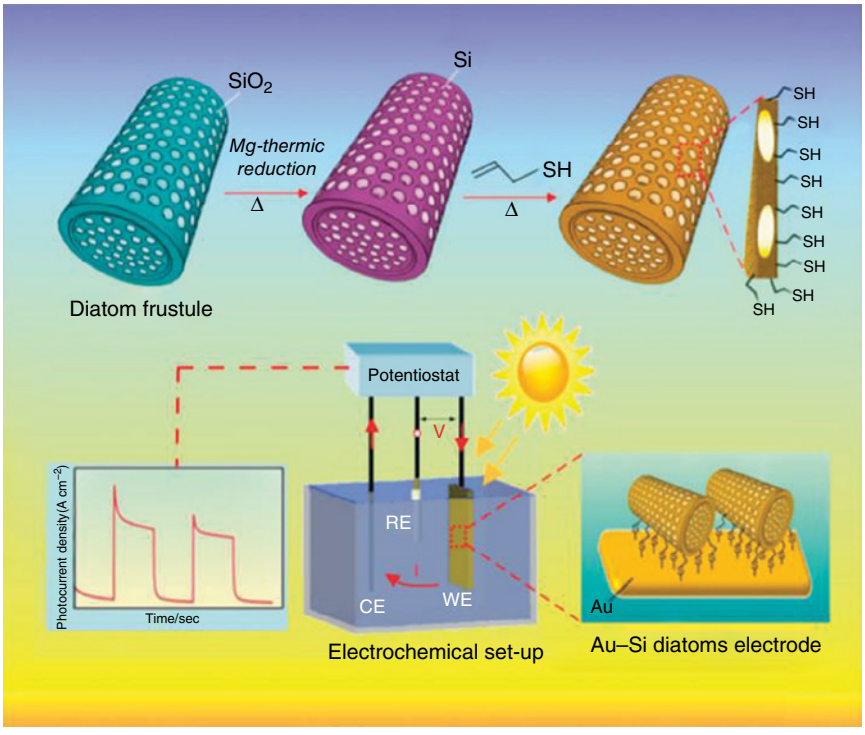

Figure 11.23 Application of thiol-modified silicon replicas in photoelectrodes for solar energy conversion. (Chandrasekaran *et al.* 2014 [49]. Reproduced with permission of Royal Society of Chemistry.)

the immersion of coated frustules into NaOH solution allows selective dissolution of the underlying biosilica and the recovery of MnO_2 replicas (Figure 11.24). These can be used as efficient electrodes in supercapacitors reaching high specific capacitance and high cycle stability (i.e., capacitance retention after 2000 cycles).

Diatoms frustules can also be converted into electronically transparent graphene replicas by a two-step procedure based on catalyst-free chemical vapor deposition (CVD) of methane and subsequent dissolution of silica with hydrofluoric acid (Figure 11.25) [52]. The high penetration and uniform deposition of gaseous methane in the complex inner channel frustule networks allow this technique to provide graphene materials that retain the 3D cylindrical morphology and all the fine structural features of native frustules. In particular, both the solid nanorods inside the areolae and the hollow channels in the frustule walls are converted into thin tube-like structures and the resulting graphene replica appears transparent and internally visible by electron microscopy. Hence, this strategy, besides disclosing the fabrication of new conducting nanostructured architectures for microelectronics, has enabled, for the first time, a clear visualization of the interior morphology of frustules, thus shedding light into the study of their morphogenesis.

Diatoms biosilica shells have been used as templates to fabricate gold nanostructures retaining the shell morphological features: various approaches are reliable for this aim, including a simple and scalable process based on the electrodeless deposition of gold onto frustules and subsequent silica removal by acid dissolution [53]. In addition, frustules are suitable templates for the fabrication of nanostructured gold films with inverse replicated structure, according to the

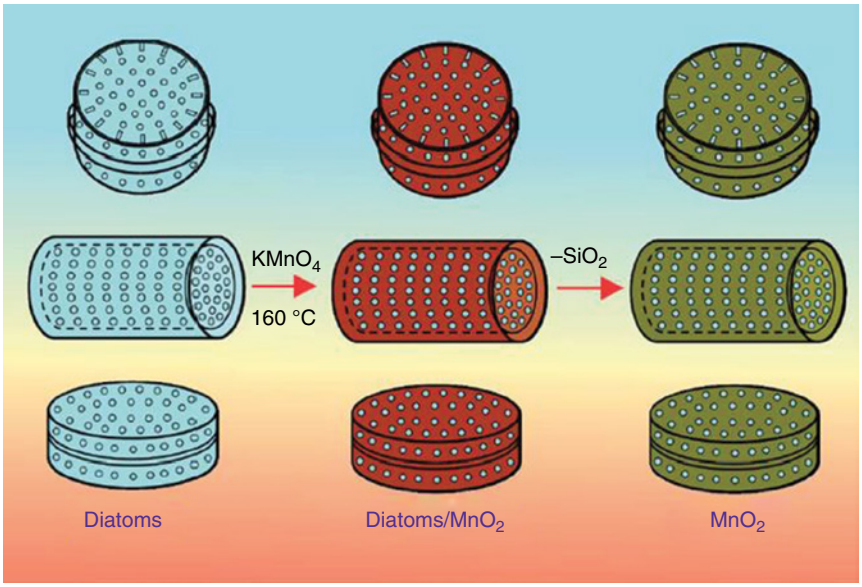

Figure 11.24 Schematic picture of the 3D MnO_2 replicas synthetic protocol. (Li *et al*. 2015 [51]. Reproduced with permission of Royal Society of Chemistry.).

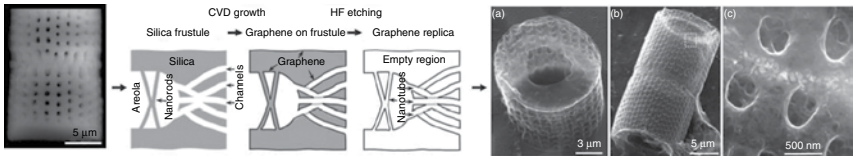

Figure 11.25 SEM image of *Aulacoseira* sp. frustule (left). Scheme of the replication process (center) and SEM images of graphene replicas (a–c, right). (Pan *et al*. 2014 [52]. Reproduced with permission of Nature Publishing Group.)

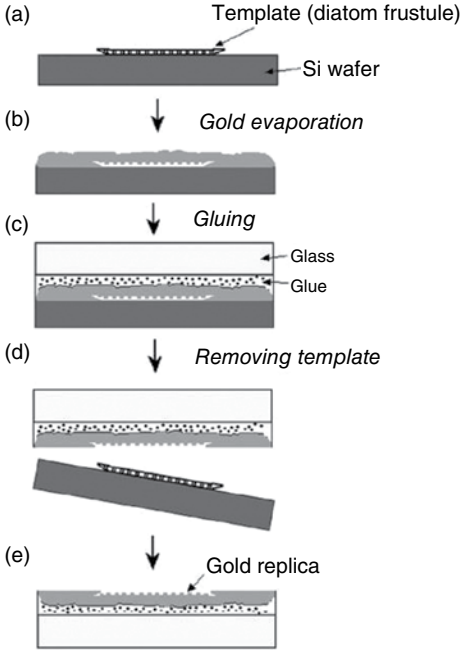

Figure 11.26 Schematic procedure for fabrication of gold nanostructures using diatom frustules as templates. (Losic *et al*. 2006 [53c]. Reproduced with permission of Royal Society of Chemistry.).

process reported in Figure 11.26. This approach represents a very useful alternative to expensive lithographic procedures and leads to complex 3D gold nanostructures with optical properties, such as the localized surface plasmon resonance (LSPR), which can enable application as components of biosensors.

11.4 Conclusions

This chapter has reported some significant results in the use of nanostructured biosilica from diatoms microalgae as a versatile source of smart nanomaterials for diverse applications in photonics and electronics. The extraordinary morphological, mechanical, and photonic properties of the beautiful structures,

evolved to optimize the interaction (survival, growth, reproduction) of the photosynthetic microorganisms with the surrounding environment, are extremely attractive. Diatoms-based nanotechnology results from creative cross-contamination of diverse fields including microbiology, chemistry, physics, materials science, and engineering.

In conclusion, we would emphasize that, in our opinion, the impact expected from these studies goes beyond the interesting applications outlined here. Diatoms nanotechnology represents a groundbreaking example of a more general approach to low-impact and high-throughput manufacturing of smart materials for photonics, electronics, and biomedicine based on production from microorganisms. Biotechnological production followed by highly selective chemical modification of the natural structures aiming to integrate or enhance their basic properties is an avenue for the development of innovative materials. Diatoms applications in photonics and electronics are among the first exciting examples of this approach.

Acknowledgments

The authors thank the Ministero dell'Istruzione dell'Università e della Ricerca (MIUR) and the University of Bari "Aldo Moro" (Project PONa3_00369 SISTEMA: "Laboratorio per lo Sviluppo Integrato delle Scienze e delle TEcnologie dei Materiali Avanzati e per dispositivi innovativi").

References

1 Smol, J.P. and Stoermer, E.F. (eds) (2010) *The Diatoms: Applications for the Environmental and Earth Sciences*, 2nd edn, Cambridge University Press.
2 (a) Werner, D. (1977) *The Biology of Diatoms*, University of California Press, Berkeley, CA; (b) Wetherbee, R. (2002) The diatom glasshouse. *Science*, **298**, 547.
3 Mann, D.G. and Droop, S.J.M. (1996) Biogeography of freshwater algae. *Hydrobiologia*, **336**, 19–32.
4 (a) Mann, D.G. (1999) The species concept in diatoms. *Phycologia*, **38** (6), 437–495; (b) Sims, P.A., Mann, D.G., and Medlin, L.K. (2006) Evolution of the diatoms: insights from fossil, biological and molecular data. *Phycologia*, **45** (4), 361–402; (c) Medlin, L. and Kaczmarska, I. (2004) Evolution of the diatoms: morphological and cytological support for the major clades and a taxonomic revision. *Phycologia*, **43**, 245–270; (d) Gordon, R. and Drum, R.W. (1994) The chemical basis for diatom morphogenesis. *Int. Rev. Cytol.*, **150**, 243–372; (e) Norten, T.A., Melkonian, M., and Andersen, R.A. (1996) Algal biodiversity. *Phycologia*, **35**, 353; (f) Mann, D.G. (2002) Diatoms: organism and image, in *Automatic Diatom Identification* (eds H. du Buf and M.M. Bayer), World Scientific, Singapore.
5 Round, F., Crawford, R., and Mann, D. (1990) *The Diatoms: Biology & Morphology of the Genera*, Cambridge University Press.

6 Williams, D.M. and Kociolek, P.J. (2007) Pursuit of a natural classification of diatoms: history, monophyly and the rejection of paraphyletic taxa. *Eur. J. Phycol.*, **42**, 313–319.

7 (a) Sumper, M. (2002) A phase separation model for the nanopatterning of diatom biosilica. *Science*, **295**, 2430–2433; (b) Losic, D., Pillar, R.J., Dilger, T., Mitchell, J.G., and Voelcker, N.H. (2007) Atomic force microscopy (AFM) characterisation of the porous silica nanostructure of two centric diatoms. *J. Porous Mater.*, **14**, 61–69.

8 (a) Drum, R.W. and Gordon, R. (2003) Star trek replicators and diatom nanotechnology. *Trends Biotechnol.*, **21**, 325–328; (b) Yang, W., Lopez, P.J., and Rosengarten, G. (2011) Diatoms: self assembled silica nanostructures, and templates for bio/chemical sensors and biomimetic membranes. *Analyst*, **136**, 42–53.

9 Hildebrand, M. (2000) in *Biomineralization: From Biology to Biotechnology and Medical Applications* (ed. E. Baeuerlein), Wiley-VCH Verlag GmbH & Co. KGaA, Weinheim, New York, pp. 171–188.

10 (a) Hildebrand, M., Dahlin, K., and Volcani, B.E. (1998) Characterization of a silicon transporter gene family in Cylindrotheca fusiformis: sequences, expression analysis, and identification of homologs in other diatoms. *Mol. Gen. Genet.*, **260**, 480–486; (b) Thamatrakoln, K., Alverson, A.J., and Hildebrand, M. (2006) Comparative sequence analysis of diatom silicon transporters: toward a mechanistic model of silicon transport. *J. Phycol.*, **42**, 822–834.

11 Drum, R.W. and Pankratz, H.S. (1964) Post mitotic fine structure of *Gomphonema parvulum*. *J. Ultrastruct. Res*, **10**, 217–223.

12 (a) Azam, F., Hemmingsen, B.B., and Volcani, B.E. (1974) Role of silicon in diatom metabolism. *Arch. Microbiol.*, **97**, 103–114; (b) Sumper, M. (2004) Biomimetic patterning of silica by long-chain polyamines. *Angew. Chem. Int. Ed.*, **43**, 2251–2254; (c) Schmid, A.M.M. and Schulz, D. (1979) Wall morphogenesis in diatoms: deposition of silica by cytoplasmic vesicles. *Protoplasma*, **100**, 267–288.

13 (a) Kroger, N., Deutzmann, R., Bergsdorf, C., and Sumper, M. (2000) Species-specific polyamines from diatoms control silica morphology. *Proc. Natl. Acad. Sci. U.S.A.*, **97**, 14133–14138; (b) Sumper, M. and Lehmann, G. (2006) Silica pattern formation in diatoms: species-specific polyamine biosynthesis. *ChemBioChem*, **9**, 1419–1427.

14 Hildebrand, M. (2008) Diatoms, biomineralization processes, and genomics. *Chem. Rev.*, **108**, 4855–4874.

15 a Pamirsky, I.E. and Golokhvast, K.S. (2013) Silaffins of diatoms: from applied biotechnology to biomedicine. *Marine Drugs*, **11** (9), 3155–3167;(b) Kröger, N., Deutzmann, R., and Sumper, M. (1999) Polycationic peptides from diatom biosilica that direct silica nanosphere formation. *Science*, **286** (5442), 1129–1132;(c) Sumper, M. and Kroger, N. (2004) Silica formation in diatoms: the function of long-chain polyamines and silaffins. *J. Mater. Chem.*, **14**, 2059–2065;(d) Belton, D.J., Patwardhan, S.V., Annenkov, V.V., Danilovtseva, E.N., and Perry, C.C. (2008) From biosilicification to tailored materials: optimizing hydrophobic domains and resistance to protonation of polyamines. *Proc. Natl. Acad. Sci. U.S.A.*, **105** (16), 5963–5968; (e) Ren-Hua, J., Dong-Dong,

Y., and Rumi, L. (2014) Biomimetic synthesis of shaped and chiral silica entities templated by organic objective materials. *Chem. Eur. J.*, **20**, 7196–7214.

16 Cicco, S.R., Vona, D., De Giglio, E., Cometa, S., Mattioli-Belmonte, M., Palumbo, F., Ragni, R., and Farinola, G.M. (2015) Chemically modified diatoms biosilica for bone cell growth with combined drug-delivery and antioxidant properties. *ChemPlusChem*, **80**, 1104–1112.

17 Nassif, N. and Livage, J. (2011) From diatoms to silica-based biohybrids. *Chem. Soc. Rev.*, **40** (2), 849–859.

18 Vrieling, E.G., Beelen, T.P.M., Van Santen, R.A., and Gieskes, W.W.C. (1999) Diatom silicon biomineralization as an inspirational source of new approaches to silica production. *J. Biotechnol.*, **70**, 39–51.

19 Fuhrmann, T., Landwehr, S., El Rharbi-Kucki, M., and Sumper, M. (2004) Diatoms as living photonic crystals. *Appl. Phys. B*, **78** (3-4), 257–260.

20 Johnson, S.G., Fan, S., Villeneuve, P.R., Joannopoulos, J.D., and Kolodziejski, L.A. (1999) Guided modes in photonic crystal slabs. *Phys. Rev. B: Condens. Matter*, **60** (8), 5751–5758.

21 De Stefano, L., Rea, I., Rendina, I., De Stefano, M., and Moretti, L. (2007) Lensless light focusing with the centric marine diatom Coscinodiscus walesii. *Opt. Express*, **15** (26), 18082–18088.

22 Noyes, J., Sumper, M., and Vukusic, P. (2008) Light manipulation in a marine diatom. *J. Mater. Res.*, **23** (12), 3229–3235.

23 Yamanaka, S., Yano, R., Usami, H., Hayashida, N., Ohguchi, M., Takeda, H., and Yoshino, K. (2008) Optical properties of diatom silica frustule with special reference to blue light. *J. Appl. Phys.*, **103** (7), 074701-1–074701-5.

24 De Tommasi, E., Rea, I., Mocella, V., Moretti, L., De Stefano, M., Rendina, I., and De Stefano, L. (2010) Multi-wavelength study of light transmitted through a single marine centric diatom. *Opt. Express*, **18** (12), 12203–12212.

25 Ferrara, M.A., Dardano, P., De Stefano, L., Rea, I., Coppola, G., Rendina, I., Congestri, R., Antonucci, A., De Stefano, M., and De Tommasi, E. (2014) Optical properties of diatom nanostructured biosilica in arachnoidiscus sp: micro-optics from mother nature. *PLoS One*, **9** (7), e103750-1–e103750-8.

26 Kieu, K., Li, C., Fang, Y., Cohoon, G., Herrera, O.D., Hildebrand, M., Sandhage, K.H., and Norwood, R.A. (2014) Structure-based optical filtering by the silica microshell of the centric marine diatom Coscinodiscus wailesii. *Opt. Express*, **22** (13), 15992–15999.

27 Di Caprio, G., Coppola, G., De Stefano, L., De Stefano, M., Antonucci, A., Congestri, R., and De Tommasi, E. (2014) Shedding light on diatom photonics by means of digital holography. *J. Biophotonics*, **7** (5), 341–350.

28 Butcher, K.S.A., Ferris, J.M., Phillips, M.R., Wintrebert-Fouquet, M., Jong Wah, J.W., Jovanovic, N., Vyverman, W., and Chepurnov, V.A. (2005) A luminescence study of porous diatoms. *Mater. Sci. Eng., C*, **25** (5-8), 658–663.

29 Arteaga-Larios, N.V., Nahmad, Y., Navarro-Contreras, H.R., Encinas, A., and García-Meza, J.V. (2014) Photoluminescence shift in frustules of two pennate diatoms and nanostructural changes to their pores. *Luminescence*, **29** (8), 969–976.

30 De Stefano, L., Rendina, I., De Stefano, M., Bismuto, A., and Maddalena, P. (2005) Marine diatoms as optical chemical sensors. *Appl. Phys. Lett.*, **87** (23), 233902-1–233902-3.

31 De Stefano, L., Rotiroti, L., De Stefano, M., Lamberti, A., Lettieri, S., Setaro, A., and Maddalena, P. (2009) Marine diatoms as optical biosensors. *Biosens. Bioelectron.*, **24** (6), 1580–1584.

32 Gale, D.K., Gutu, T., Jiao, J., Chang, C.H., and Rorrer, G.L. (2009) Photoluminescence detection of biomolecules by antibody-functionalized diatom biosilica. *Adv. Funct. Mater.*, **19** (6), 926–933.

33 Yang, J., Zhen, L., Ren, F., Campbell, J., Rorrer, G.L., and Wang, A.X. (2015) Ultra-sensitive immunoassay biosensors using hybrid plasmonic-biosilica nanostructured materials. *J. Biophotonics*, **8** (8), 659–667.

34 (a) Li, C.-W., Chu, S., and Lee, M. (1989) Characterizing the silica deposition vesicle of diatoms. *Protoplasma*, **151** (2–3), 158–163; (b) Brzezinski, M.A. and Conley, D.J. (1994) Silicon deposition during the cell cycle of Thalassiosira weissflogii (Bacillariophyceae) determined using dual rhodamine 123 and propidium iodide staining. *J. Phycol.*, **30** (1), 45–55.

35 Desclés, J., Vartanian, M., Harrak, A.E., Quinet, M., Bremond, N., Sapriel, G., Bibette, J., and Lopez, P.J. (2008) New tools for labeling silica in living diatoms. *New Phytol.*, **177** (3), 822–829.

36 Annenkov, V.V., Danilovtseva, E.N., Zelinskiy, S.N., Basharina, T.N., Safonova, T.A., Korneva, E.S., Likhoshway, Y.V., and Grachev, M.A. (2010) Novel fluorescent dyes based on oligopropylamines for the in vivo staining of eukaryotic unicellular algae. *Anal. Biochem.*, **407** (1), 44–51.

37 Kucki, M. and Fuhrmann-Lieker, T. (2012) Staining diatoms with rhodamine dyes: control of emission colour in photonic biocomposites. *J. R. Soc. Interface*, **9** (69), 727–733.

38 Cai, Y., Dickerson, M.B., Haluska, M.S., Kang, Z., Summers, C.J., and Sandhage, K.H. (2007) Manganese-doped zinc orthosilicate-bearing phosphor microparticles with controlled three-dimensional shapes derived from diatom frustules. *J. Am. Ceram. Soc.*, **90** (4), 1304–1308.

39 Zhou, H., Fan, T., Li, X., Ding, J., Zhang, D., Li, X., and Gao, Y. (2009) Bio-inspired bottom-up assembly of diatom-templated ordered porous metal chalcogenide meso/nanostructures. *Eur. J. Inorg. Chem.*, **2009** (2), 211–215.

40 Jeffryes, C., Solanki, R., Rangineni, Y., Wang, W., Chang, C.-h., and Rorrer, G.L. (2008) Electroluminescence and photoluminescence from nanostructured diatom frustules containing metabolically inserted germanium. *Adv. Mater.*, **20** (13), 2633–2637.

41 Jeffryes, C., Gutu, T., Jiao, J., and Rorrer, G.L. (2008) Two-stage photobioreactor process for the metabolic insertion of nanostructured germanium into the silica microstructure of the diatom Pinnularia sp. *Mater. Sci. Eng., C*, **28** (1), 107–118.

42 Toster, J., Iyer, K.S., Xiang, W., Rosei, F., Spiccia, L., and Raston, C.L. (2013) Diatom frustules as light traps enhance DSSC efficiency. *Nanoscale*, **5** (3), 873–876.

43 Jeffryes, C., Gutu, T., Jiao, J., and Rorrer, G.L. (2008) Metabolic insertion of nanostructured TiO_2 into the patterned biosilica of the diatom *pinnularia* sp. By a two-stage bioreactor cultivation process. *ACS Nano*, **2** (10), 2103–2112.

44 Losic, D., Triani, G., Evans, P.J., Atanacio, A., Mitchell, J.G., and Voelcker, N.H. (2006) Controlled pore structure modification of diatoms by atomic layer deposition of TiO_2. *J. Mater. Chem.*, **16** (41), 4029–4034.

45 Jia, Y.X., Han, W., Xiong, G.X., and Yang, W.S. (2008) Layer-by-layer assembly of TiO_2 colloids onto diatomite to build hierarchical porous materials. *J. Colloid Interface Sci.*, **323** (2), 326–331.
46 Sandhage, K.H., Dickerson, M.B., Huseman, P.M., Zalar, F.M., Rondon, M.R., and Sandhage, E.C. (2002) A novel hybrid route to chemically-tailored, three-dimensional oxide nanostructures: the BaSIC (bioclastic and shape-preserving inorganic conversion) process. *Ceram. Eng. Sci. Proc.*, **23** (4), 653–664.
47 Sandhage, K.H., Dickerson, M.B., Huseman, P.M., Caranna, M.A., Clifton, J.D., Bull, T.A., Heibel, T.J., Overton, W.R., and Schoenwaelder, M.E.A. (2002) Novel, bioclastic route to self-assembled, 3-D, chemically tailored meso/nanostructures: shape-preserving reactive conversion of biosilica (diatom) microshells. *Adv. Mater.*, **14** (6), 429–433.
48 Bao, Z., Weatherspoon, R.M., Shian, S., Cai, Y., Graham, P.D., Allan, S.M., Ahmad, G., Dickerson, M.B., Church, B.C., Kang, Z., Abernathy, H.W. III, Summers, C.J., Liu, M., and Sandhage, K.H. (2007) Chemical reduction of three-dimensional silica micro-assemblies into microporous silicon replicas. *Nature*, **446** (7132), 172–175.
49 Chandrasekaran, S., Sweetman, M.J., Kant, K., Skinner, W., Losic, D., Nann, T., and Voelcker, N.H. (2014) Silicon diatom frustules as nanostructured photoelectrodes. *Chem. Commun.*, **50** (72), 10441–10444.
50 (a) Dudley, S., Kalem, T., and Akinc, M. (2006) Conversion of SiO_2 diatom frustules to $BaTiO_3$ and $SrTiO_3$. *J. Am. Ceram. Soc.*, **89** (8), 2434–2439; (b) Sandhage, K.H., Allan, S.M., Dickerson, M.B., Gaddis, C.S., Shian, S., Weatherspoon, M.R., Cai, Y., Ahmad, G., Haluska, M.S., Snyder, R.L., Unocic, R.R., Zalar, F.M., Zhang, Y., Rapp, R.A., Hildebrand, M., and Palenik, B.P. (2005) Merging biological self-assembly with synthetic chemical tailoring: the potential for 3-D genetically engineered micro/nano-devices (3-D GEMS). *Int. J. Appl. Ceram. Technol.*, **2** (4), 317–326.
51 Li, F., Xing, Y., Huang, M., Li, K.L., Yu, T.T., Zhang, Y.X., and Losic, D. (2015) MnO_2 nanostructures with three-dimensional (3D) morphology replicated from diatoms for high performance supercapacitors. *J. Mater. Chem. A*, **3** (15), 7855–7861.
52 Pan, Z., Lerch, S.J.L., Xu, L., Li, X., Chuang, Y.-J., Howe, J.Y., Mahurin, S.M., Dai, S., and Hildebrand, M. (2014) Electronically transparent graphene replicas of diatoms: a new technique for the investigation of frustule morphology. *Sci. Rep.*, **4**, 6117. doi: 10.1038/srep06117
53 (a) Bao, Z., Ernst, E.M., Yoo, S., and Sandhage, K.H. (2009) Syntheses of porous self-supporting metal-nanoparticle assemblies with 3D morphologies inherited from biosilica templates (diatom frustules). *Adv. Mater.*, **21** (4), 474–478; (b) Yu, Y., Addai-Mensah, J., and Losic, D. (2010) Synthesis of self-supporting gold microstructures with three-dimensional morphologies by direct replication of diatom templates. *Langmuir*, **26** (17), 14068–14072; (c) Losic, D., Mitchell, J.G., and Voelckera, N.H. (2006) Fabrication of gold nanostructures by templating from porous diatom frustules. *New J. Chem.*, **30**, 908–914.

Index

Green Materials for Electronics, First Edition.
Edited by Mihai Irimia-Vladu, Eric D. Glowacki, Niyazi S. Sariciftci, and Siegfried Bauer.

d

q

r